THEORY OF SUBHARMONIC RESONANCE OF STORM GATES FOR VENICE LAGOON

by

PAOLO SAMMARCO

Laurea in Ingegneria Civile, Università di Roma "La Sapienza", 1989
Dottore di Ricerca in Ingegneria Idraulica, Università di Roma "La Sapienza", 1993

SUBMITTED TO THE DEPARTMENT OF CIVIL AND ENVIRONMENTAL ENGINEERING
IN PARTIAL FULFILLMENT OF THE REQUIREMENTS FOR THE DEGREE OF

DOCTOR OF PHILOSOPHY IN COASTAL ENGINEERING

at the

MASSACHUSETTS INSTITUTE OF TECHNOLOGY

September 1996

Author .....
Department of Civil and Environmental Engineering
July 30, 1996

Certified by...
Chiang C. Mei
Edmund K. Turner Professor of Civil and Environmental Engineering
Thesis Supervisor

Accepted by .....
Joseph M. Sussman
Chairman, Departmental Committee on Graduate Students

Theory of Subharmonic Resonance of Storm Gates for Venice Lagoon

by

Paolo Sammarco

Submitted to the Department of Civil and Environmental Engineering
on July 30, 1996, in partial fulfillment of the
requirements for the degree of
Doctor of Philosophy in Coastal Engineering

Abstract

This study is focused on the complex dynamics of the mobile gates designed to span the three inlets of the Venice Lagoon for flood protection (the "acqua alta" phenomenon). In calm weather the gates rest horizontally on the seabed, while in stormy weather they are raised by buoyancy so to act as a dam for keeping the high water outside the lagoon. Previous laboratory experiments with sinusoidal waves incident normally to a gate array have shown the presence of a resonant subharmonic response in which neighboring gates oscillate out of phase in a variety of ways. Linear and nonlinear theories are developed here and compared with the laboratory experiments of Tran(1996)

The linear theory predicts the eigenfrequencies and eigenmodes as functions of the geometry of the gates and channel characteristics at which this phenomenon occurs. The nonlinear theory yields an evolution equation of the Stuart-Landau type for the amplitude of the resonated eigenmode. Viscous dissipation effects are systematically included in the perturbation theory. The theoretical results, which show bifurcations involving hysteresis, are confirmed experimentally.

Chaotic envelope response to a periodically modulated incident wave is found in the solution of the time-dependent Stuart-Landau equation. Experimental proof has been given of the predicted bifurcations involving period doubling, strange attractors and frequency downshift of the response.

Thesis Supervisor: Chiang C. Mei
Title: Edmund K. Turner Professor of Civil and Environmental Engineering

Acknoledgments

Gigantic thanks to my advisor, Prof. Chiang C. Mei. My wish is to have absorbed, at least by exposure, a bit of his striking ability to find the essence of the problems and actually solve them. His exemplary capacity to strive for clarity and to conduct "fat-free" research have been inspirational to me.

Thanks to my committee members, Proff. Frank Feng, Ole Madsen and J. Nicholas Newman of MIT. Their comments and suggestions have been illuminating and decisive. Thanks to Prof. Steven Strogatz, now at Cornell, for teaching two awesome classes on nonlinear dynamics. Thanks to Prof. Alberto Noli of the University of Rome for his support in my endeavor and for constantly reminding me about engineering. Thanks to my colleague Karsten Trulsen for all our stimulating math-talks.

Thanks to Cynthia Stewart for answering all my grad-student-questions with patience and efficiency. I want to thank each end every Parsons folk with whom I have shared at least some laughs. Thanks to Sheila Frankel and Vicky Murphy for listening to all my complaints and for all the fun conversations we had. In the "early years", the great sense of humor of John Durant, the way Fernando Miralles called my name, the smiles of Anna Aurilio, Mindy Roberts, Kelly Hawk and Jenny Jay they all really cheered me. Thanks to Glenn Moglen, for finding the names Itsy and Bitsie for the two half gates in the wave basin. Thanks to Hoang Tran, the undisputed "Matlab-wiz-eletronic-master" for the help and for all the laughs we had late at night in the wave basin. Thanks to Analia Barrantes, mi ermana, for all the coffee. Thanks to my "Parsons-euro" friends Marco Marani, Carlo Procaccini and René Kim for all our nonscientific talks and for all the things we did together. All the buddies from soccer (and these include Ole Madsen!), John Durant, Jim Gawel, Orian "Thor" Gustaffsson and especially the 99% of our team, Guido Sacchi, who, in the name of our friendship, came all the way from Rome to play with me, they must all be appreciated for chasing the ball in the cold and late at night. Thanks to Edmund Carnevale for his movie reviews and thanks to Jeremy Pal for being a real "cool dude". I always wanted to be a 205-er...thanks to Kirsten Findell, Freddi-Jo Eisenberg and Lynn Reid for having given me the opportunity!

Thanks to my parents for their uncompromised inspirational example and support and for giving me the ultimate education; thanks to my brother for being "The Brother".

Finally, my friend, girlfriend, lover, sister, partner, buddy, wife, love and light of my life, Melissa, without you none of this would have been possible.

All art is at once surface and symbol.
Those who go beneath the surface do so at their peril.
Those who read the symbol do so at their peril.

OSCAR WILDE, 1889. *The picture of Dorian Gray.*

To Melissa

Contents

List of Figures

List of Tables

List of Symbols

a'	semi-thickness of the gate in m
a	nondimensional semi-thickness of the gate
a	ratio of modulation to carrier wave amplitude
a_1	ratio of modulation to carrier wave amplitude in $a = \mu a_1$
a_2	ratio of modulation to carrier wave amplitude in $a = \mu^2 a_2$
a_3	ratio of modulation to carrier wave amplitude in $a = \mu^3 a_3$
$a_{\frac{3}{2}}$	ratio of modulation to carrier wave amplitude in $a = \mu^{\frac{3}{2}} a_{\frac{3}{2}}$
a'_g	semi-thickness of a homogeneous gate
A'	incident wave amplitude in m
$\overline{A'}$	carrier wave amplitude in m
$\tilde{A}'$	modulation wave amplitude in m
A_2	nondimensional incident wave amplitude
$\overline{A}_2$	nondimensional carrier wave amplitude
$\tilde{A}_2$	nondimensional modulation wave amplitude
A^T	amplitude of the trapped wave in m
b'	modal semi-period in m
b_m	the m-th coefficient of the Fourier series of the angular displacement
b'_g	width of a homogeneous gate
B	normalized detutning in modulational resonance of a center
$\mathcal{B}_{nm}$	forcing of Bernoulli equation at the free surface, n-th order, m-th harmonic
c	common factor in the evolution equation
c_c	contraction coefficient
c_N	nonlinearity coefficient of evolution equation
c_R	radiation damping coefficient of evolution equation
c_F	coefficient of forcing in evolution equation
c_L	linear viscous damping coefficient of evolution equation
c_Q	quadratic viscous damping coefficient of evolution equation
C	linear dimensional and nondimensional buoyancy of a gate
C_n	the n-th normalization coefficient of first harmonic vertical eigenfuction expansions
C'_n	the n-th normalization coefficient of second

	harmonic vertical eigenfuction expansions
d'	distance of the center of mass of the gate from hinges
d	detuning of modulation wave from natural frequency of the center
d_2	detuning of modulation wave from natural frequency of the center in $d = \mu^2 d_2$
D	damping coefficient for response to incident wave
D	normalized detuning in modulational resonance of a center
D_n	the n-th coefficient of first harmonic eigenfunction expansion of $(z + h)$
D'_n	the n-th coefficient of second harmonic eigenfunction expansion of $(z + h)$
$\mathcal{D}_{nm}$	forcing at the gate surface, dynamic condition, n-th order, m-th harmonic
e_{11}	real part of trapped wave free survace elevation
f	loss coefficent
f_1	expansion coefficient of $f = \epsilon f_1$
f_e	loss coefficent from equivalent linearization
f_{11}	real part of trapped wave potential
f_{22}	spatial factor of forced second harmonic potential
f_c	cutoff frequency for the eigenfrequency in Hz
F_p	p-th coefficient of Fourier series of f_{22}
F_p^S	part of F_p generated by pressure on the free surface
F_p^W	part of F_p generated by pressure on the gate surface
$\mathcal{F}_{nm}$	forcing of mixed condition at the free surface, n-th order, m-th harmonic
g	gravitational acceleration on earth surface, 9.8065...
G	nondimensional eigenfrequency of the trapped wave
G	gradient function for dynamical system
G_0	nondimensional eigenfrequency of the trapped wave for zero inertia
$\mathcal{G}_{nm}$	forcing at the gate surface, kinematic condition, n-th order, m-th harmonic
h'	channel depth in m
h	nondimensional channel depth
h'_g	height of a homogeneous gate
H	Hamiltonian function
k	real root of first harmonic dispersion relation
k_n	imaginary part of n-th root of first harmonic dispersion relation
K_n	complex representation of n-root of first harmonic dispersion relation
k'	real root of second harmonic dispersion relation
k'_n	imaginary part of n-th root of second harmonic dispersion relation
K'_n	complex representation of n-root of second harmonic dispersion relation
I'	inertia of a gate in Kgm^2

I	nondimensional inertia of a gate
I_a	nondimensional added inertia of the gate
M'	mass of the gate in Kg
J	Jacobian of a two-dymensional dynamical system
p'	dimensional pressure in Pa
p	nondimensional pressure
r	1/2 for mode 1, 1/3 for mode 2
r_{11}	normalized response in modulational resonance of a center
R	reflection coefficient of incident wave
R	action variable
R_0	fixed point amplitude
R_n	n-th term of power expansion around a center
R^h	parametric equation of homoclinic orbit in hamiltonian system
s	stable nontrivial fixed point of the dynamical system
S'	first moment of inertia of the gate in Kgm
S	nondimensional first moment of inertia of the gate
t'	time in sec
t	nondimensional time
t_2	nondimensional slow time, $t_2 = \epsilon^2 t$
T	normalized time
T	transmission coefficient of incident wave
T_0	normalized time of the first Poincare' section
T_2	normalized slow time, $T_2 = \mu^2 T$
$\mathcal{T}_g'$	gravity torque on one gate in Kgm
$\mathcal{T}_p'$	fluid pressure torque on one gate Kgm
$\mathcal{T}_p'$	tangential stress torque on one gate in Kgm
$\mathcal{T}_g$	normalized gravity torque on one gate
$\mathcal{T}_p$	normalized fluid pressure torque on one gate
$\mathcal{T}_p$	normalized tangential stress torque on one gate
u	unstable nontrivial fixed point of the dynamical system
$\mathbf{u}$	velocity field
$\mathbf{U}$	rotational velocity field
$\mathbf{V}_b$	velocity of a solid boundary
W	normalized detuning of carrier wave
W_s	normalized detuning of carrier wave at a saddle node bifurcation
x'	horizontal coordinate in m
x	normalized horizontal coordinate
$\mathbf{x}_T$	tangential local coordinates in boundary layers
X	real part of normalized angular displacement of trapped mode
y'	horizontal coordinate in m

y_1', y_2'	y coordinates of one gate in m
y_1, y_2	normalized y coordinates of one gate
Y	imaginary part of normalized angular displacement of trapped mode
z'	vertical coordinate in m
z	normalized vertical coordinate
z_c'	vertical coordinate of center of mass in m
Z_1, Z_2	curves in the auxiliary plane RZ for graphical determination of fixed point
α	normalized radiation damping coefficient of evolution equation
α_{mn}	coefficient in x-dependence of wave potential series expansions
β	normalized linear viscous damping coefficient of evolution equation
β_{nm}	series expansion coeffcients of trapped wave potential
γ	normalized linear quadratic damping coefficient of evolution equation
Γ_p	p-th Fourier expansion coefficients of second order forcing on the free surface
δ	ratio between boundary layer thickness and half-modal period
ϕ_{nm}	n-th order m-th harmonic of velocity potential
Φ'	velocity potential in m^2/sec
Φ	nondimensional velocity potential
ϵ	expansion parameter, $\epsilon = A^T/b'$
λ	linearized natural frequency of oscillation around a center
Λ_p	p-th Fourier expansion coefficients of second order forcing on the gate surface
μ	ordering parameter in analysis of temporal resonance
ν	kinematic viscosity of water, $10^{-6}\ m^2/s$
Ω	angular frequency of modulation in Hz
$\Omega^{\pm}$	fluid domains separated by the gate array
ρ	density of water
ρ	action variable of temporal resonated response by modulation
ρ_g	density of homogeneous gate
π	3.14159...
Π	impedance in angular response to incident wave
Π^{α}	factor for radiation damping in Melnikov's threshold
Π^{β}	factor for viscous linear damping in Melnikov's threshold
Π^{γ}	factor for viscous quadratic damping in Melnikov's threshold
Π^{a}	factor for modulational amplitude in Melnikov's threshold
σ	normalized modulational frequency
ψ	angle variable in dynamical system
ψ^h	parametric equation of homoclinic orbit in hamiltonian system
$\boldsymbol{\tau}$	viscous stress
θ	normalized amplitude of trapped mode angular motion
θ_{nm}	n-th order m-th harmonic angular displacement
θ_{nm}^I	n-th order m-th harmonic angular displacement of gate one

θ_{nm}^{II}	n-th order m-th harmonic angular displacement of gate two
ϑ	normalized amplitude of trapped mode angular motion
Θ'	angular displacement in rad
Θ	normalized angular displacement
Θ^{I}	angular displacement of gate one
Θ^{II}	angular displacement of gate two
ξ	equation of the gate surface
η_{nm}	n-th order m-th harmonic of free surface elevation
ζ	nondimensional free surface elevation
ζ'	free surface elevation in m
ω_0	eigenfrequency in rad/sec
ω_2	coefficient of expansion about eigenfrequency, detuning

Chapter 1

Introduction

1.1 Motivation

For reducing the hazards of flooding in Venice, storm barriers have been designed to span the three inlets of Venice Lagoon. The planned barriers will consist of a series of hollow steel gates which are unconnected to each other but hinged at the bottom along a common axis on the seabed. In calm weather the gates rest horizontally on the seabed so as not to obstruct normal navigation or to impair the scenic view of the area. In stormy weather, all gates will be raised by buoyancy to an inclination of about 50° from the horizontal, and hence will act as a dam for keeping the high water outside the lagoon. The gates are otherwise free and are expected to swing to and fro in unison in normally incident waves and maintain the sea-level difference. In figure 1-1 one of the three inlet with a scheme of the proposed barrier is shown.

Laboratory experiments with sinusoidal waves incident normally on two or three gates in a narrow flume, or on a large number of gates in a wide basin, have however revealed that neighboring gates may oscillate out of phase in a variety of ways, at half of the frequency and with relatively large amplitude(Consorzio "Venezia Nuova", 1988a,b; Varisco, 1992). Some of these modal oscillations observed experimentally are schematically shown in figure 1-2. The out-of-phase motion must be understood in order to take proper measures for preserving the intended efficiency of the gates as a dam.

The scope of this work is to understand the mechanics of these modes and provide a theory that can quantify it in relation to the parameters that describe the system (gate characteristics, channel geometry and sea conditions).

To briefly describe the resonance mechanism of these modes, we note its similarity with the subharmonic resonance of edge waves on a beach. Subharmonic resonance is known to be responsible for the occurrence of long-period edge waves along a sloping shore (Guza, and Bowen, 1976; Minzoni and Whitham, 1976; Rockliff, 1978). According to the linearized theory, edge waves are the natural modes on a plane

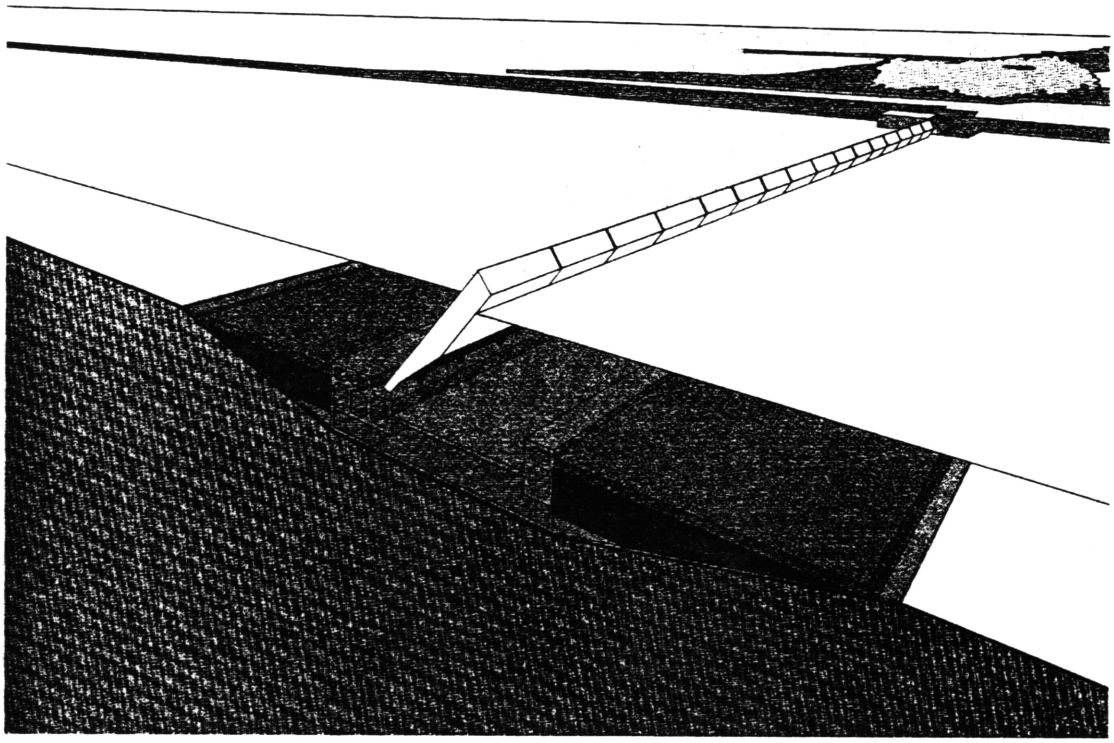

Figure 1-1: 3D view of the proposed gate barrier for the Venice Lagoon's inlets. The lagoon side is on the right side of the barrier. Reproduction from Consorzio Venezia Nuova

beach with amplitudes diminishing exponentially with distance from the shore. The lowest mode has the eigenfrequency $\omega = \sqrt{gks}$ with s the beach slope and the velocity potential:

$$\Phi_e = -\frac{igB}{\omega} e^{-kx} \cos ky \, e^{-i\omega t} + *. \tag{1.1.1}$$

For higher modes the eigenfrequencies are $\omega_n = \sqrt{2(n+1)gks}$ while the velocity potential can be expressed in terms of Laguerre polynomials. The lowest mode can be resonated by a normally incident/reflected long wave of twice the frequency,

$$\Phi_i = \frac{-igA}{2\omega} J_0\left(4\omega\,(x/gs)^{1/2}\right) e^{-2i\omega t} + *. \tag{1.1.2}$$

After a time of the order $O((\omega kA)^{-1})$, cubic nonlinearity becomes important, so is the radiation of higher harmonics which render the amplitude of resonated edge wave finite. When fully resonated the edge wave amplitude B is such that $kB = O(\sqrt{skA})$. The evolution of the edge wave amplitude is governed by the Landau-Stuart equation:

$$-i\frac{\partial B}{\partial t} = \delta B + \alpha A B^* + \beta B^2 B^* \tag{1.1.3}$$

where δ, α and β are constant coefficients depending on ω, k, s and g.

There have been suggestions that edge waves may exist near the Venice gates because of their inclination, hence can be subharmonically resonated by normally incident waves. We shall show in this chapter that gate inclination is irrelevant and that even vertical gates, as long as they are articulated, can support natural modes of trapped waves. An inviscid theory of the trapped mode will be worked out as a linear eigenvalue problem. Experiments in which real fluid effects are significant nevertheless confirm the natural frequency predicted by the inviscid theory. Laboratory evidence is then presented to show that subharmonic oscillation of vertical gates forced by normally incident waves is through the resonance of the trapped wave. Finally, scales and order of magnitude estimation prepare the groundwork for the weakly nonlinear theory developed in Chapter 2.

In Chapter 2 we shall deduce the evolution equation, similar to (1.1.3), that governs the angular motion of the gate system. Knowledge of the evolution equation allows the prediction of important quantities such as the growth rate and equilibrium amplitude of the resonated modes and therefore the maximum opening between contiguous gates. The parametric dependence of these quantities on the gate, channel, and sea characteristics is also explained.

In the inviscid theory of Chapter 2, radiation damping is the mechanism which limits the peak amplitude at resonance. In the laboratory model of the prototype, losses due to the viscosity in the fluid also limit the resonated amplitude. The gap between adjacent gates is designed to be thin (of the order of 10^{-1}m) and the corners

sharp; localized losses and vortex shedding may become important for out-of-phase motion of large amplitude. In Chapter 3, we introduce in a systematic way the frictional effects and we show that they affect the trapped wave at the third order and generate linear and quadratic terms in the evolution equation.

For uniform incident waves the evolution equation is an autonomous second order dynamical system. Chapter 4 employs the analytical methods of the dynamical system analysis to study how different dissipation mechanisms affect the resonance peaks. Theoretical predictions are then compared with laboratory experiments.

Since the three inlets of the Venice Lagoon are not likely to be subjected to strictly monocromatic waves, we consider the effects of an incident wave with slowly modulated amplitude, corresponding to a narrow-banded spectrum. With an amplitude periodic in time, the evolution equation becomes a second order nonautonomous dynamical system. In this Chapter we use local and global analysis to investigate modulational resonances and transition to chaos.

1.2 Literature review

The subharmonic oscillation phenomenon was originally observed during the first series of laboratory experiments commissioned by the *Consorzio Venezia Nuova* to a private company, Estramed Spa. These first observations were reported in a technical report of the *Consorzio Venezia Nuova* (1988a). A few months later the same phenomenon was observed at Delft Hydraulic Laboratory, and is described in another report of *Consorzio Venezia Nuova*, (1988b). In several others reports by the *Consorzio*, a variety of model tests ranging from three gates in a channel to several gates in a wave basin are described At the 23^{rd} Coastal Engineering Conference held in Venice, Italy, Varisco(1992) summarized the findings in a contribution which appears in the abstracts.

Following the Venice Conference, in Mei*et al.*(1994), it was recognized that the phenomenon was related to the existence of trapped waves. They also performed experiments to support the subharmonic resonance and conjectured the similarity to the edge wave problem known to be governed by a Stuart-Landau equation.

In the present theories, the conjecture is substantiated by working out the nonlinear boundary conditions and equation of motion up to the third order. In the nonlinear theory, several radiation and diffraction problems arise at the second order, which require of the forced second harmonic. Preliminary results of the nonlinear theory and the implications of an evolution equation of the Stuart-Landau type have been presented in Sammarco & Mei(1995).

A much simplified linear theory of the gate dynamics has been developed by Blondeaux *et al.*(1993a, b). To reduce computational labor, they considered the shallow water limit and rigid vertical gates of infinitesimal width which are allowed to slide at

the bottom, unlike the prototype gates of finite width that roll about a hinge at the bottom and are stabilized by buoyancy. They then replace the buoyancy effects by an an artificial linear spring. In Blondeaux *et al.*(1993*a*), they find that transverse modes in which energy is trapped are possible and they give the conditions that determines the frequencies, which depend on the geometry of the channel, the mass of the gate, the stiffness of the artificial linear spring and on the particular mode considered. In Blondeaux *et al.*(1993*b*), a linear instability analysis shows that the transverse modes become unstable when the gates are forced by plane incident waves. The authors find that the region of instability of each mode is typical of the Mathieu type resonance.

Recently, Vittori *et al.*(1996) have analyzed the subharmonic resonance of the trapped modes according to the simplified model of Blondeaux *et al.*(1993*a*, *b*) by a weakly nonlinear analysis. Energy is lost through radiation damping, the dissipation mechanism that limits the resonated amplitude. Their evolution equation is similar to that for the edge waves of Rockliff(1978). As in Rockliff(1978), they discuss the trivial and nontrivial equilibrium solutions and their existence in terms of the incident wave amplitude and period and they find that the null solution loses stability in transcritical and in subcritical pitchfork bifurcations. In the case of edge waves, the bifurcation diagram is tilted towards positive detuning, while in Vittori *et al.*(1996) is tilted towards negative detuning, as for the Faraday waves in a cilindrical container (Miles & Henderson, 1990; Miles, 1993).

For edge-wave problem, Miles(1990) has modeled the effect of viscosity by introducing a linear dissipation term, which in the case of edge-wave implies imperfect reflection. He has found the equilibrium solutions and has shown that the resonance curve shrinks as the dissipation increases. Moreover he has found the existence of a critical value of the incident amplitude below which the edge wave cannot be resonated.

Experiments on the implied hysteresis and jump phenomenon have been performed by Hendersen and Miles(1991) in the contest of Faraday resonance. They measured the hysteretic lines in the frequency-amplitude plane and successfully compared the hysteretic threshold with experiments, but comparison of the resonated amplitudes was not shown.

In simpler geometries, the effect of viscosity has been deduced systematically by means of a formal perturbation series by Johns(1968), Dore(1969), Greenspan (1968) and Mei and Liu(1973). These perturbation theories yields both the damping rate and the frequency shift induced by the boundary layers.

For a modulated wave amplitude, the evolution equation becomes time dependent. Gottlieb & Mei(1996) analyzed the evolution of edge waves for a modulated incident waves and the Faraday waves when the sinusoidal vertical oscillation of the container is modulated in time. Using the averaging technique, they studied the possible bifurcations leading to period doubling of the response envelope. Trulsen & Mei(1994), in the context of gravity-capillary waves, employed the multiple scales method to study

similar temporal resonances of an evolution equation without dissipation, equivalent to a time dependent Hamiltonian system with one degree of freedom.

Gottlieb & Mei(1996) have made extensive use of the Melnikov method to study global bifurcation leading to horseshoe type of nonperiodic motion. They found a threshold above which chaotic motion is possible. Such a threshold depends on radiation damping.

An unpublished paper on edge waves of Gottlieb & Mei(1995) includes the effect of linear viscous damping on the threshold given by the Melnikov method.

1.3 Linear theory of trapped modes near vertical flap gates

We are interested in eigenmodes periodic in the direction along the hinge (the axis of rotation). Hence it suffices to consider a spatial period, say $2b$, which may correspond to the width of a wave flume. We show that the variety of modes sketched in figure 1-2 and observed experimentally (Consorzio "Venezia Nuova", 1988a,b; Varisco, 1992), are theoretically possible. The present linear theory and the experiments presented in the next section are extracted from Mei *et al.*(1994).

The variety of modal shapes depends on the number of gates needed to define a period. Without loss of generality we assume that the modes are symmetric about the x axis, which may also be thought as a vertical wall. As shown in figure 1-2a, with two gates in a period the modal shape is $(+,-,+)$, i.e., every gate is in opposite phase with its immediate neighbors. Only half of the first and last gates lie in the period. With three gates the modal shape is $(+,-,-,+)$ (figure 1-2b), so that every fourth gate is in phase with the first and in opposite phase with the second and third. Similar to mode 1, only half of the first and last gates are in the period. With four gates the modal shape is $(+,0,-,0,+)$ (figure 1-2c), so that every second gate is stationary while the first and third are in opposite phase. With six gates, two modes (4 and 5) are possible: $(+,0,-,-,0,+)$ (figure 1-2d), and $(+,+,-,-,-,+,+)$ (figure 1-2e). For mode 4, the first and last gates are fully contained in the period. For longer periods the modal shapes can be even more complex.

It suffices to sketch the inviscid theory for the first two modes (two and three gates in a period). Because the motion is even in y, we can limit the analysis to the semi period $0 < y < b$ only and use a Fourier series of cosines to describe all the quantities. Let the horizontal displacement of the gates in the semiperiod $0 < y < b$ be described by

$$-(z+h)\theta(y)\mathrm{e}^{-i\omega t} + * \tag{1.3.1}$$

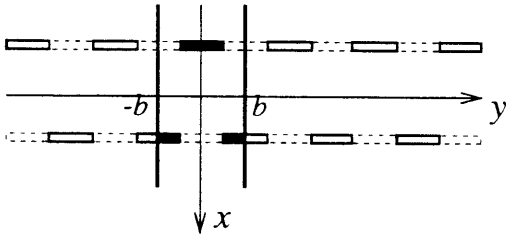

a) MODE 1

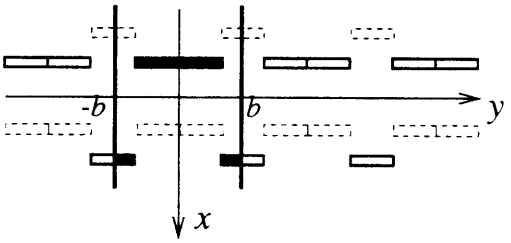

b) MODE 2

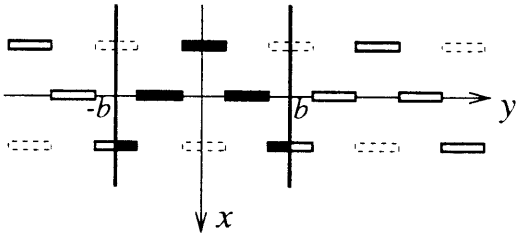

c) MODE 3

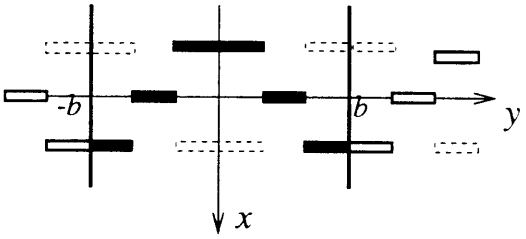

d) MODE 4

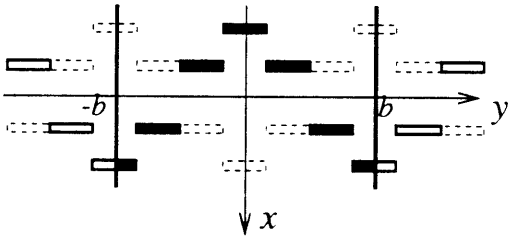

e) MODE 5

Figure 1-2: Possible modal responses.

with

$$\theta(y) = \left\{ \begin{array}{c} \theta^I \\ \theta^{II} \end{array} \right\} \quad \text{for} \quad \left\{ \begin{array}{l} 0 < y < (1-r)b \\ (1-r)b < y < b \end{array} \right. , \tag{1.3.2}$$

where $r = 1/2$ and $r = 1/3$ are respectively for mode 1 and 2 and $*$ denotes the complex conjugate. It is known (Wehausen and Laitone, 1960) that the most general solution in a long rectangular channel of width b consists of not only long-crested propagating and evanescent modes:

$$e^{-i\omega t} \left\{ \beta_{00} e^{\pm ikx} \cosh k(z+h) + \sum_{n=1}^{\infty} \beta_{0n} e^{\mp k_n x} \cos k_n (z+h) \right\} + * \tag{1.3.3}$$

but also short-crested propagating modes:

$$e^{-i\omega t} \sum_{m=1}^{M} \cos \frac{m\pi y}{b} \beta_{m0} e^{\pm i\alpha_{m0} x} \cosh k(z+h) + * \tag{1.3.4}$$

as well as evanescent modes:

$$\begin{aligned} e^{\mp i\omega t} \sum_{m=M+1}^{\infty} \beta_{m0} \cos \frac{m\pi y}{b} e^{\pm i\alpha_{m0} x} \cosh k(z+h) \\ e^{-i\omega t} \sum_{m=1}^{\infty} \cos \frac{m\pi y}{b} \sum_{n=1}^{\infty} \beta_{mn} e^{\mp \alpha_{mn} x} \cos k_n (z+h) + *, \end{aligned} \tag{1.3.5}$$

where k and k_n are real roots of the following equations

$$\omega^2 = gk \tanh kh; \quad \omega^2 = -gk_n \tan k_n h, \quad n = 1, 2, 3, ..., \tag{1.3.6}$$

while

$$\alpha_{m0} = \sqrt{k^2 - \left(\frac{m\pi}{b}\right)^2}, \quad \alpha_{mn} = \sqrt{\left(\frac{m\pi}{b}\right)^2 + k_n^2} \tag{1.3.7}$$

In the series (1.3.4) (1.3.5) M is the largest integer for which α_{M0} is real, that is

$$\frac{M\pi}{b} < k < \frac{(M+1)\pi}{b}. \tag{1.3.8}$$

This type of expansion has been used by Madsen(1973) to study wave radiation by oscillating flaps in a channel. Wave trapping near vertical gates corresponds to the state of no radiation, despite their oscillations. First the frequency must be low enough

$$k < \frac{\pi}{b} \tag{1.3.9}$$

so that no short-crested propagating modes can exist: $M = 0$. To ensure the absence

of the long-crested propagating wave, we must also require that

$$\int_0^b \theta(y)dy = 0 \tag{1.3.10}$$

which also guarantees the absence of all long-crested evanescent modes, i.e., $\beta_n = 0$ for all n. For the simple mode of(1.3.2), eq.(1.3.10) implies that

$$\theta^{II} = \theta^I \left(\frac{r-1}{r}\right). \tag{1.3.11}$$

In particular

$$\begin{aligned} \theta^{II} &= -\theta^I, \quad r = 1/2; \\ &\quad -2\theta^I, \quad r = 1/3. \end{aligned} \tag{1.3.12}$$

Hence, the angular motion of the gates $\Theta(y,t)$, for both mode 1 and 2, can be combined in one expression

$$\Theta(y,t) = \theta\, q(y)\, \mathrm{e}^{-i\omega t} + *, \quad q(y) = \left\{ \begin{array}{c} 1 \\ 1-1/r \end{array} \right\} \quad \text{for} \quad \left\{ \begin{array}{l} 0 < y < (1-r)b \\ (1-r)b < y < b \end{array} \right. . \tag{1.3.13}$$

The function $q(y)$ can also be written with the aid of the Heavyside step function H

$$q(y) = 1 - \frac{1}{r} H\left[1 - (1-r)\, b\right], \tag{1.3.14}$$

or by means of its Fourier series

$$q(y) = \sum_{m=1}^{\infty} b_m \cos\frac{m\pi y}{b}, \tag{1.3.15}$$

with coefficients

$$b_m = \frac{2}{b}\int_0^b q(y) \cos\frac{m\pi y}{b} \mathrm{d}y = \frac{2}{m\pi r} \sin m\pi(1-r). \tag{1.3.16}$$

The modal shapes 1 and 2 and their description are shown in figure 1-3.

The resulting trapped mode potential is

$$\begin{aligned} \Phi^{\pm} &= \mp \mathrm{i}\omega\theta \sum_{m=1}^{\infty} \cos\frac{m\pi y}{b} \\ &\left[\beta_{m0} \mathrm{e}^{\mp|\alpha_{m0}|(x\mp a)} \cosh k(z+h) + \sum_{n=1}^{\infty} \beta_{mn} \mathrm{e}^{\mp\alpha_{mn}(x\mp a)} \cos k_n(z+h)\right] \mathrm{e}^{-i\omega t} + *. \end{aligned} \tag{1.3.17}$$

The coefficients β_{mn} are obtained by matching the normal velocities of the gate and

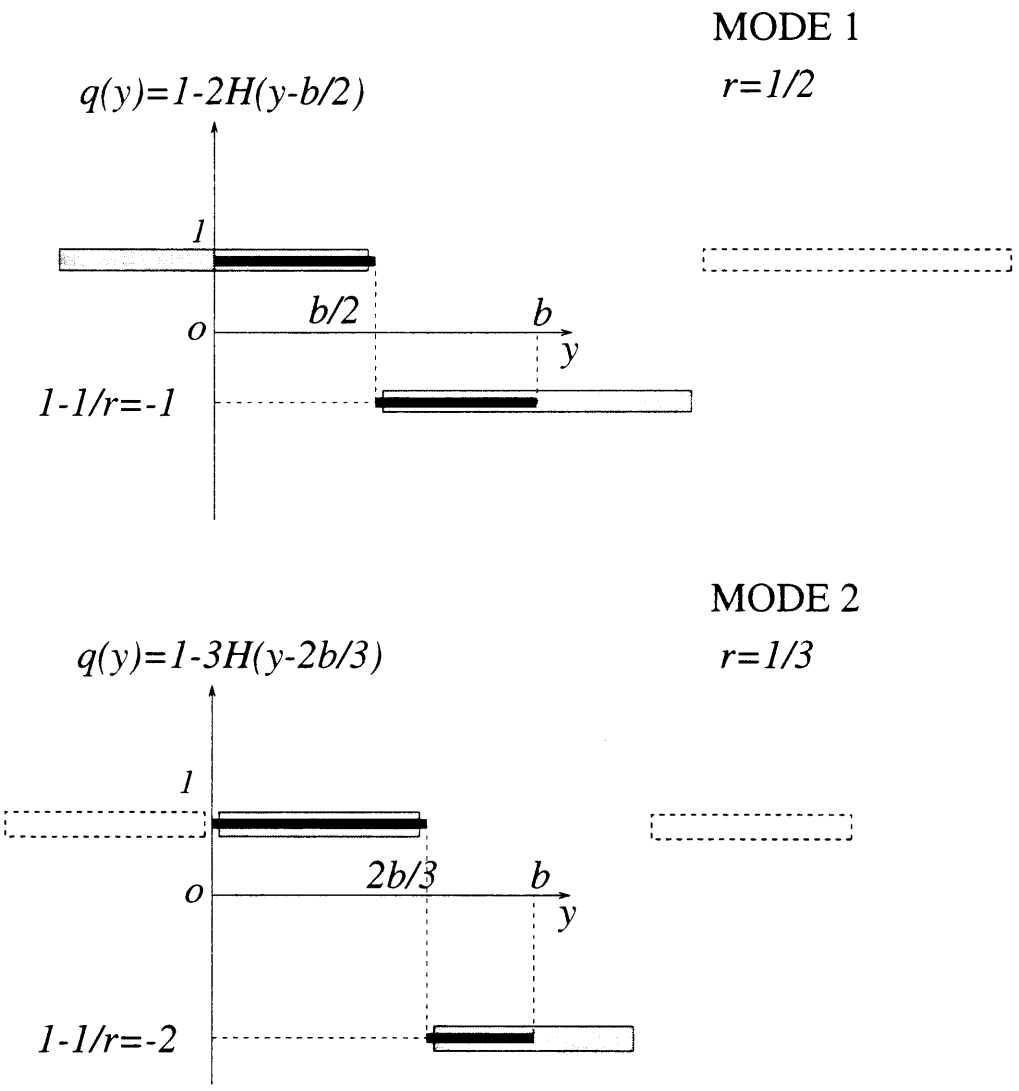

Figure 1-3: Compact representation of mode 1 and 2. The shaded rectangles represent the physical gates. The thick solid lines represent the modal shape $q(y)$

of the adjacent fluid at the gate surface $x = \pm a$:

$$\beta_{mn} = \frac{b_m D_n}{\alpha_{mn} C_n} \tag{1.3.18}$$

where

$$C_0 = \frac{1}{2}\left(h + \frac{g}{\omega^2}\sinh^2 kh\right), \quad D_0 = \frac{1}{k^2}\left[\left(\frac{h\omega^2}{g} - 1\right)\cosh kh + 1\right], \tag{1.3.19}$$

$$C_n = \frac{1}{2}\left(h - \frac{g}{\omega^2}\sin^2 k_n h\right), \quad D_n = \frac{1}{k_n^2}\left[\left(1 - \frac{h\omega^2}{g}\right)\cos k_n h - 1\right]. \tag{1.3.20}$$

The corresponding free surface height is

$$\zeta^{\pm} = \pm\frac{\omega^2}{g}\theta \sum_{m=1}^{\infty} \cos\frac{m\pi y}{b}$$
$$\left[\beta_{m0} \mathrm{e}^{\mp|\alpha_{m0}|(x\mp a)} \cosh kh + \sum_{n=1}^{\infty} \beta_{mn} \mathrm{e}^{\mp\alpha_{mn}(x\mp a)} \cos k_n h\right] \mathrm{e}^{-i\omega t} + *. \tag{1.3.21}$$

In addition to the kinematic condition on the gate surface we must consider the dynamics of a gate. Taking the gate in $0 < y < (1-r)b$ (i.e. half physical gate for mode 1 and one gate for mode 2), we apply Newton's law

$$I\Theta_{tt} + C\Theta = -2\int_0^{(1-r)b} \mathrm{d}y \int_{-h}^{0} \rho\left[\Phi_t^+\right]_{x=a} (z+h)\mathrm{d}z. \tag{1.3.22}$$

I is the moment of inertia of the gate:

$$I = I_{xx} + I_{zz} = \iiint_{V_s} \left(x^2 + (z+h)^2\right) \rho_s dV \tag{1.3.23}$$

where the subscript s denote the solid part of the gate. C is the restoring moment due to buoyancy:

$$C = \rho g(I_{xx}^a + I_z^v) - Mg(z_c + h) \tag{1.3.24}$$

with

$$I_{xx} = \iint_S x^2 dxdy, \quad I_z = \iiint_V (z+h)dV. \tag{1.3.25}$$

S denotes the cross sectional area of the gate at the water line, V the water volume displaced by the gate, and z_c is the depth of the center of mass.

The right hand side of (1.3.22) can be found from (1.3.17) to be

$$\omega^2 I_a \theta \mathrm{e}^{-\mathrm{i}\omega t} + * \tag{1.3.26}$$

where

$$I_a(\omega) = \frac{2\rho b}{\pi} \sum_{m=1}^{\infty} \sum_{n=0}^{\infty} \frac{1}{m} \beta_{mn} D_n \sin m\pi(1-r) \tag{1.3.27}$$

is the hydrodynamic moment of inertia which is function of ω and of the parameters kh and b. Combining (1.3.22) with (1.3.27) we get the eigenvalue condition for ω:

$$\omega^2(I + I_a(\omega)) = C \tag{1.3.28}$$

The amplitude θ is so far arbitrary. The free surface height of the eigenmode is given by (1.3.21).

In the next section we describe some preliminary experiments, carried out to verify the linear eigenvalue theory and better describe the essence of the phenomenon.

1.4 Experiments for two vertical gates

Simple experiments have been performed in a long wave flume to confirm the existence of the first trapped mode and the possibility of subharmonic resonance by normally incident waves.

In a glass-walled wave flume of 25 m length, 0.38 m width and 0.6 m depth, two rectangular plexi-glass boxes with triangular basis were attached to a nearly frictionless hinge on a flat plate resting on the bottom of the tank. A sketch of the experimental setup is shown in figure 1-4. To measure the free oscillations natural frequencies the two gates are displaced by equal and opposite angles from the vertical axis and then released at $t = 0$. Subsequent angular displacement $\Theta(t)$ of both gates are recorded as functions of time. Because of the thin gaps and the sharp corners, all oscillations are damped. By averaging the time between successive zero crossings, the natural period is measured for each water depth. The results are compared with the inviscid theory in figure 1-5. For each curve the structural inertia of the gate is constant. The variation of I is achieved by adding extra weight on the top of each gate. To test higher natural frequency, buoyancy is increased by adding styrofoam on the outside faces of the gates (see figure 1-4), i.e. by essentially increasing I_z in (1.3.25). The values of the resulting inertia for each of the five curves in figure 1-5 are, from the lowest to the highest, $I = 0.21, 0.196, 0.273, 0.582, 0.771$ kg m^2. The corresponding buoyancy for $h = 0.4$ m has the values $C = 33.1, 20.0, 18.62, 12.5, 8.58$ kg m^{2}s^{-2}. The first set of I (=0.21) and C (=33.1) corresponds to the configuration with styrofoam. For each inertia several water depths are tested. The agreement between theory and measurement on the natural period is good despite the presence of viscosity.

With the existence of trapped mode confirmed, we next test the possibility of subharmonic gate resonance by normally incident waves. At the far end of the tank an absorbing beach of 1/3 slope made of layers of fibrous material spans the entire width of the wave tank. In a typical experiment, monochromatic waves of a selected

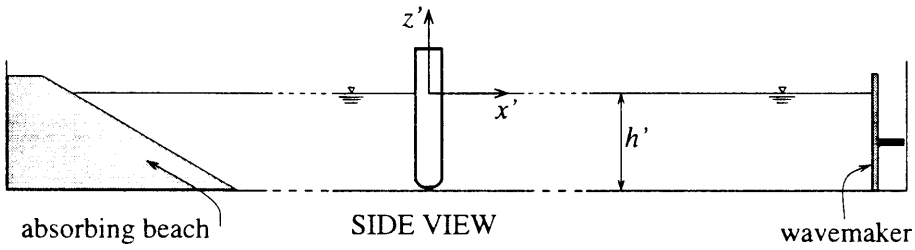

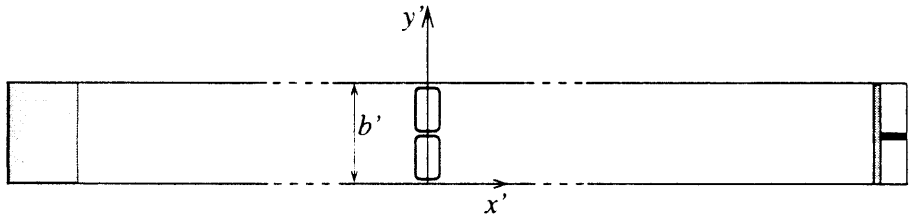

PLAN VIEW

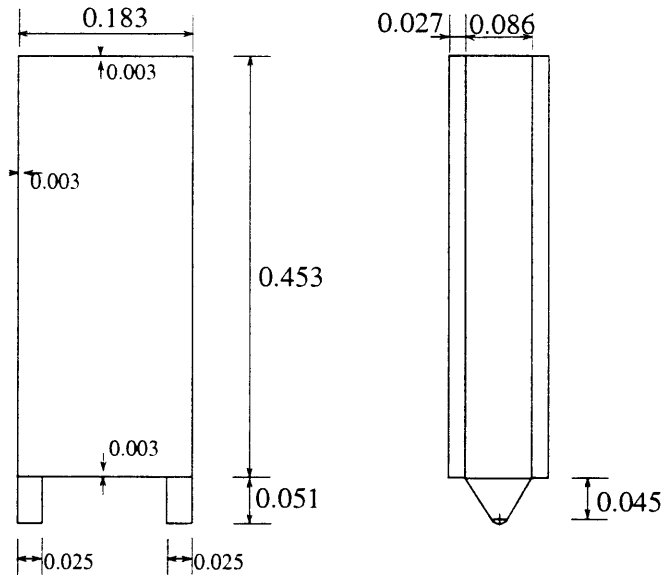

Figure 1-4: Scheme of the experimental setup in the wave flume and details of one gate

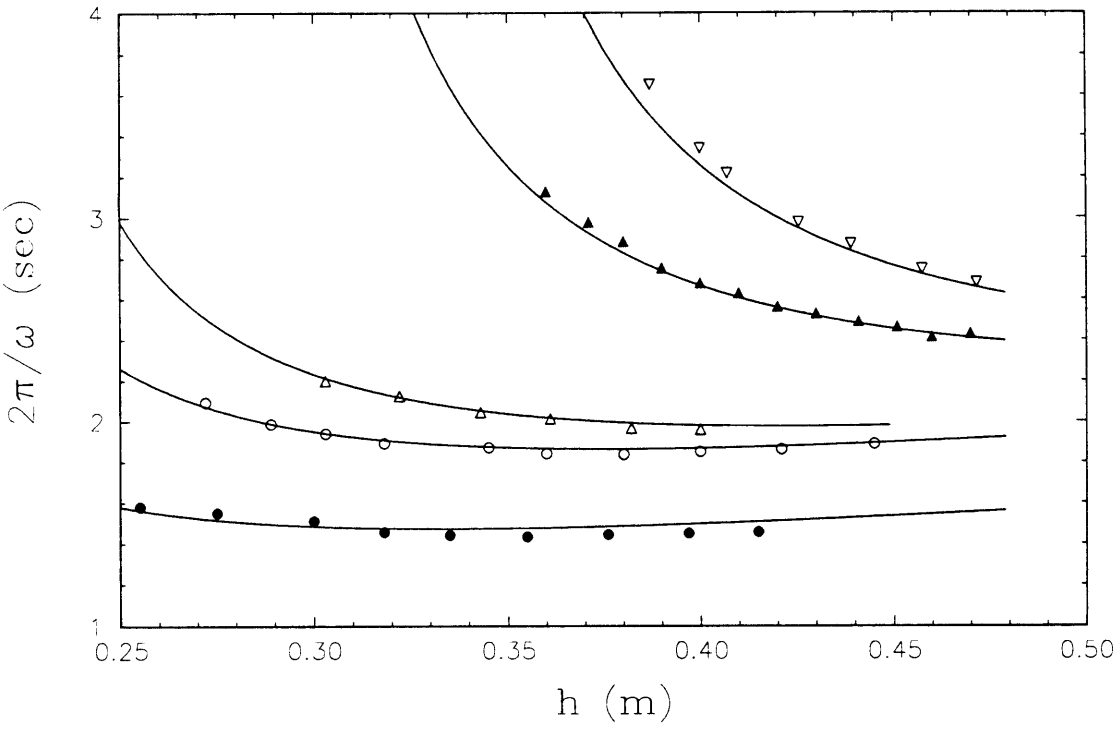

Figure 1-5: Natural frequency of gates oscillating opposite in phase in various water depth h (m). The gate inertia I corresponding to each curve is 0.21, 0.196, 0.213, 0.582, 0.771 kgm^2 from bottom to top.

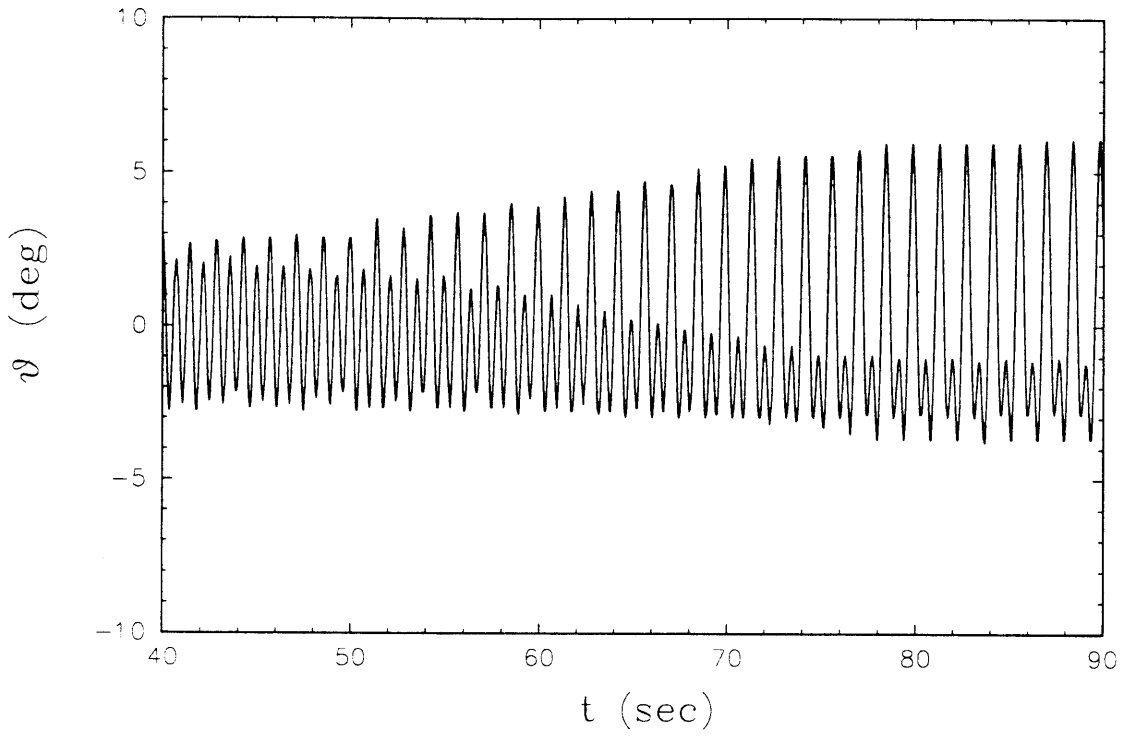

Figure 1-6: Time series of one gate showing the period doubling phenomenon.

frequency and amplitude are generated and the gates response monitored. For each of the model inertia and various water depths of figure 1-5, subharmonic resonance is sought by generating waves at nearly twice the theoretical natural frequencies. In the initial stage both gates oscillate in unison at the frequency of the incoming waves. Then, subharmonic (opposite in phase) oscillation builds up slowly until it reaches a large amplitude. This period-doubling phenomenon is the most pronounced for gates with buoyant styrofoam, as shown in figure 1-6. In this sample case $h = 0.36$ m; the linear theory predicts $f = 0.68$ Hz while the free oscillation experiments give $f = 0.698$ Hz. The forced response is the largest when the wave frequency is 1.4 Hz. The amplitude of the incident wave is $A = 0.022$ m with a steepness $kA = 0.175$.

Wave spectra of the recorded time series of the gates and of the free surface at a distance 5 m on the reflection side of the gates are taken at the sampling rate of 30 Hz and for sample times long enough to allow the system to reach a stationary condition. Figure 1-7a shows the power spectrum of the motion of one gate before the growth of the subharmonic component begins. The duration of this initial steady motion is about 50 seconds and contains more than 60 cycles, so that Fourier analysis is applicable. After the transition is complete, the signal is Fourier-analyzed again. The power spectrum in 1-7b shows the resonated subharmonic component coexisting with the synchronous component. It is noteworthy that the synchronous motion is

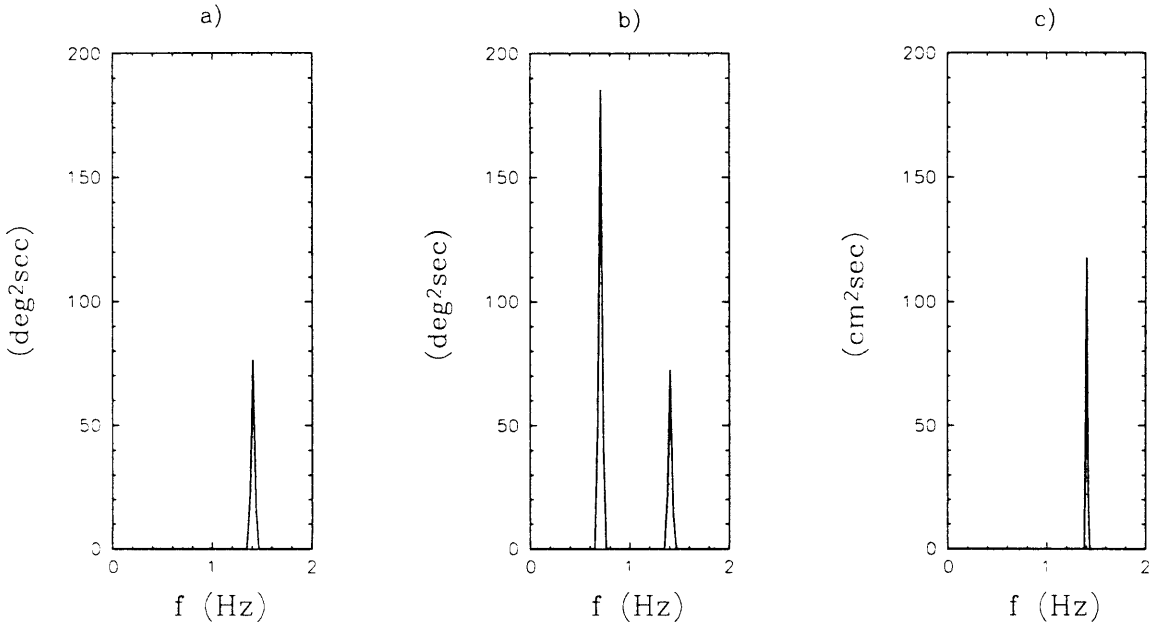

Figure 1-7: Energy spectrum of: a) one gate in the initial stage, b) the same gate in the final stage, c) water surface 5 m upstream of the gates.

unaltered during this period-doubling process. Figure 1-7c shows the free surface power spectrum for the same final stationary condition at the station five meters away from the gates.

After establishing the eigenmode, the nonlinear analysis of subharmonic resonance by normally incident waves can be carried out exactly as in the edge wave problem. The derivation and implications of such a theory is the object of the following Chapters.

1.5 Estimation of the order of magnitude

We first assess the relative order of magnitude of the trapped and incident waves in the nonlinear theory. Here we follow Mei(1989) in a similar estimation for the edge wave resonance.

Consider both the angular motion of the trapped wave Θ^T

$$\Theta^T = \theta^T e^{-i\omega t} + * \tag{1.5.29}$$

and the angular motion excited by an incident plane wave A of twice the natural

frequency

$$\Theta^A = \theta^A e^{-2i\omega t} + *, \tag{1.5.30}$$

to be present in the channel. We want to see how, through a nonlinear feedback mechanism, the first harmonic $\pm\omega$ can be forced by the incident wave at $\pm 2\omega$.

Consider for simplicity and without loss of generality, the equation of motion of the gate system. Writing on the LHS the linear part and on the RHS the possible quadratic and cubic nonlinearities that yield the first harmonic $\pm\omega$, the equation of motion is

$$\mathcal{L}\Theta^T + \mathcal{L}\Theta^A = (\Theta^T, \Theta^A) + (\Theta^T, \Theta^T, \Theta^T) + (\Theta^T, \Theta^A, \Theta^A), \tag{1.5.31}$$

where $\mathcal{L}$ is composed respectively by inertia, buoyancy and linear dynamic pressure terms

$$\mathcal{L} = I\partial_{tt} + C - \int_{-h}^{0} dz\ (z+h)\partial_t \{\text{potential}\}. \tag{1.5.32}$$

The possible harmonics forced by the RHS terms of (1.5.31) are respectively

$$(\pm\omega, \pm 3\omega) \quad (\pm\omega, \pm 3\omega) \quad (\pm\omega, \pm 3\omega, \pm 5\omega) \tag{1.5.33}$$

and their magnitudes are

$$|\theta^T||\theta^A| \qquad |\theta^T|^3 \qquad |\theta^T||\theta^A|^2 \tag{1.5.34}$$

At the beginning of resonance $|\theta^T| \ll |\theta^A|$, so the first term in (1.5.34) is the most important for resonating Θ^T. In response to this forcing, the amplitude $|\theta^T|$ is no longer constant in time. From $I\partial_{tt}\Theta^T$, a term proportional to $\partial_t|\theta^T|$, which represents the initial growth of $|\theta^T|$, is expected. Balancing the two terms, $\partial_t|\theta^T| \sim |\theta^T||\theta^A|$, we see that the time scale of resonance growth must be $\sim 1/|\theta^A|$. Consequently, two time scales are inherent in this problem: $1/\omega$ and $1/\omega|\theta^A|$. At the mature state of the resonance, equilibrium is attained, in which the cubic and quadratic nonlinearities are in balance. If we try to balance the first and third terms of (1.5.34), $|\theta^T||\theta^A| \sim |\theta^T||\theta^A|^2$, which is a contradiction. The only possible equilibrium is through the balance of the first and second terms of (1.5.34), $|\theta^T||\theta^A| \sim |\theta^T|^3$, from which $|\theta^T| \sim \sqrt{|\theta^A|}$.

Hence, if in the weakly nonlinear theory the amplitude of the trapped wave oscillating on a fast scale $1/\omega$ is scaled to be $O(1)$, then the incident wave must be $O(\epsilon)$, with $\epsilon \ll 1$ an ordering parameter, and the time scale of growth will be $1/\epsilon^2\omega$.

In the next Chapter, after normalization and Taylor expansion of the governing equations, we employ the method of multiple scales with the above relative order of magnitude in the expansions.

Chapter 2

Weakly nonlinear analysis

2.1 Introduction

In this chapter we develop the nonlinear theory of the resonance of the trapped wave introduced in section 1.3. In section 2.2 the governing equations and boundary conditions are introduced. Successively, in section 2.3 nondimensional quantities are introduced and nondimensional governing equations and boundary conditions are deduced. In section 2.4 the boundary conditions are then Taylor expanded about the mean position of the boundaries. The method of multiple scales is used in section 2.5 to deduce an evolution equation of the Stuart–Landau type that quantifies the amplitude of the trapped wave and its dependencies on the environmental parameters. A discussion of the relevant quantities of engineering interest is contained in section 2.6, while the last section addresses the possible kinematic effects of gaps present in the laboratory experiments in a wave flume.

2.2 Governing equations

Consider an array of gates in water of depth h'. The gates are hinged along a straight axis on the bottom at $z' = -h'$; the thickness of each gate is $2a'$. Let the modal period be $2b'$; the gates have width equal to b' in the case of mode 1 and $2b'/3$ in the case of mode 2 (see figure 1-3 of chapter 1). Primes are now used to denote physical quantities.

Let Θ' be the angular displacement of the two gates in the semiperiod b'

$$\Theta'(y',t') = \left\{ \begin{array}{c} \Theta'^{I} \\ \Theta'^{II} \end{array} \right\} \qquad \text{for} \qquad \left\{ \begin{array}{l} 0 < y' < (1-r)b' \\ (1-r)b' < y' < b' \end{array} \right. \tag{2.2.1}$$

where Θ'^{I} and Θ'^{II} are constants [1]. For example, the angular motion $\Theta'(y',t')$ asso-

[1] For mode 1, both gate one and two are half the physical gate. Vice versa for mode 2 gate one

ciated with the trapped wave is

$$\left\{ \begin{array}{c} \Theta'^{I} \\ \Theta'^{II} \end{array} \right\} = \left\{ \begin{array}{c} \theta'^{I} \\ \theta'^{II} \end{array} \right\} \mathrm{e}^{-\mathrm{i}\omega_0 t'} + * = \theta'(t') \left\{ \begin{array}{c} 1 \\ 1 - 1/r \end{array} \right\} \mathrm{e}^{-\mathrm{i}\omega_0 t'} + *, \quad \left\{ \begin{array}{l} 0 < y' < (1-r)b' \\ (1-r)b' < y' < b' \end{array} \right. \tag{2.2.2}$$

where $r = 1/2$ and $r = 1/3$ respectively for mode 1 and mode 2 and ω_0 is the eigenfrequency of the mode.

The fluid is inviscid and incompressible and the flow is irrotational, so that the velocity field $\mathbf{u}'$ is the gradient of a potential Φ', $\mathbf{u}'(\mathbf{x}', t') = \nabla'\Phi'(\mathbf{x}', t')$, with Φ' governed by continuity equation:

$$\nabla'^2\Phi' = 0. \tag{2.2.3}$$

∇' is the spatial gradient operator defined as $\nabla' \equiv (\partial_{x'}, \partial_{y'}, \partial_{z'})$. The fluid pressure is related to Φ' through the Bernoulli equation

$$-\frac{p'}{\rho} = gz' + \Phi'_{t'} + \frac{1}{2}|\nabla'\Phi'|^2, \tag{2.2.4}$$

where ρ is the water density and g is the gravitational acceleration. On the free surface $z' - \zeta'(x', y', t') = 0$ the pressure is atmospheric, which is chosen to be zero:

$$-g\zeta' = \Phi'_{t'} + \frac{1}{2}|\nabla'\Phi'|^2, \qquad z' = \zeta'. \tag{2.2.5}$$

The kinematic boundary condition

$$\frac{\mathrm{d}}{\mathrm{d}t}\left[z' - \zeta'(x', y', t')\right] = 0, \tag{2.2.6}$$

can be combined with the dynamic condition (2.2.5) to give the following condition on the free surface in

$$\Phi'_{t't'} + g\Phi'_{z'} + |\nabla'\Phi'|^2_{t'} + \frac{1}{2}\nabla'\Phi' \cdot \nabla'|\nabla'\Phi'|^2 = 0, \qquad z' = \zeta'. \tag{2.2.7}$$

At the horizontal bottom $z' + h' = 0$ the kinematic boundary condition

$$\frac{\mathrm{d}}{\mathrm{d}t}(z' + h') = 0, \tag{2.2.8}$$

yields:

$$\Phi'_{z'} = 0. \tag{2.2.9}$$

---

is a full gate and two is half gate.

The motion is periodic in y' with half period b'

$$\Phi'(x', y', z', t') = \Phi'(x', y' + b', z', t'). \tag{2.2.10}$$

By symmetry, (2.2.10) is equivalent to the requirement that

$$\Phi'_{y'} = 0, \qquad y' = 0, \quad y' = b'. \tag{2.2.11}$$

Therefore we can limit our analysis to a channel of width b', insisting only on condition (2.2.11), and consider only gate one and two. These two gates separate the fluid domain in two semi-infinite domains, $\Omega^{\pm}$. With reference to figure 2-1, we consider each gate to be ideal, i.e. rectilinear from the free surface down to the bottom and with only one degree of freedom: rotation about a horizontal line represented by $z' = -h'$, $x' = 0$. In order to allow analytical tractability we assume an ideal foundation such that during the gate motion the neighboring bottom remains horizontal and deforms accordingly without resistance. The position of the two faces of one gate are $x' = \pm a'$ while at rest, and $x' - \xi^{\pm}(z', t') = 0$, while in motion. For brevity, $\xi^{\pm}$ is to be interpreted for both gates, i.e. $\xi^{\pm} = \xi^{\pm\, I}$ for gate one and $\xi^{\pm} = \xi^{\pm\, II}$ for gate two.

The kinematic boundary conditions on the two sides of each gate are

$$\frac{\mathrm{d}}{\mathrm{d}t}\left[x' - \xi^{\pm}(z', t')\right] = 0, \qquad x' = \xi^{\pm} \tag{2.2.12}$$

or

$$\Phi'_{x'} = \xi^{\pm}_{t'} + \Phi'_{z'}\xi^{\pm}_{z'}, \qquad x' = \xi^{\pm}. \tag{2.2.13}$$

Note that one kinematic condition is given for each gate, that is separately on gate one, $0 < y' < (1 - r)b'$, or on gate two, $(1 - r)b' < y' < b'$. Referring to figure 2-1, Θ' represents either $\Theta'^{\,I}$ or $\Theta'^{\,II}$ and is positive when counterclockwise. For gate one or two, the horizontal displacement $\xi^{\pm}$ is then given by

$$\xi^{\pm} \equiv -(z' + h') \tan\Theta' \pm \frac{a'}{\cos\Theta'}, \tag{2.2.14}$$

Upon substitution of (2.2.14) into the kinematic condition (2.2.13) we obtain:

$$\Phi'_{x'} = \Theta'_{t'}\frac{[-(z' + h') \pm a' \sin\Theta']}{\cos^2\Theta'} - \Phi'_{z'} \tan\Theta', \qquad x' = \xi^{\pm} \tag{2.2.15}$$

The equation of motion of one gate is given by the dynamical equilibrium of torque about the horizontal axis passing through R:

$$I' \frac{\mathrm{d}^2\Theta'}{\mathrm{d}t'^2} = \mathcal{T}'_g(t') + \mathcal{T}'_p(t') + \mathcal{T}'_\nu(t'), \tag{2.2.16}$$

where I' is the second moment of the gate, $\mathcal{T}'_g$ and $\mathcal{T}'_p$ are respectively the torque

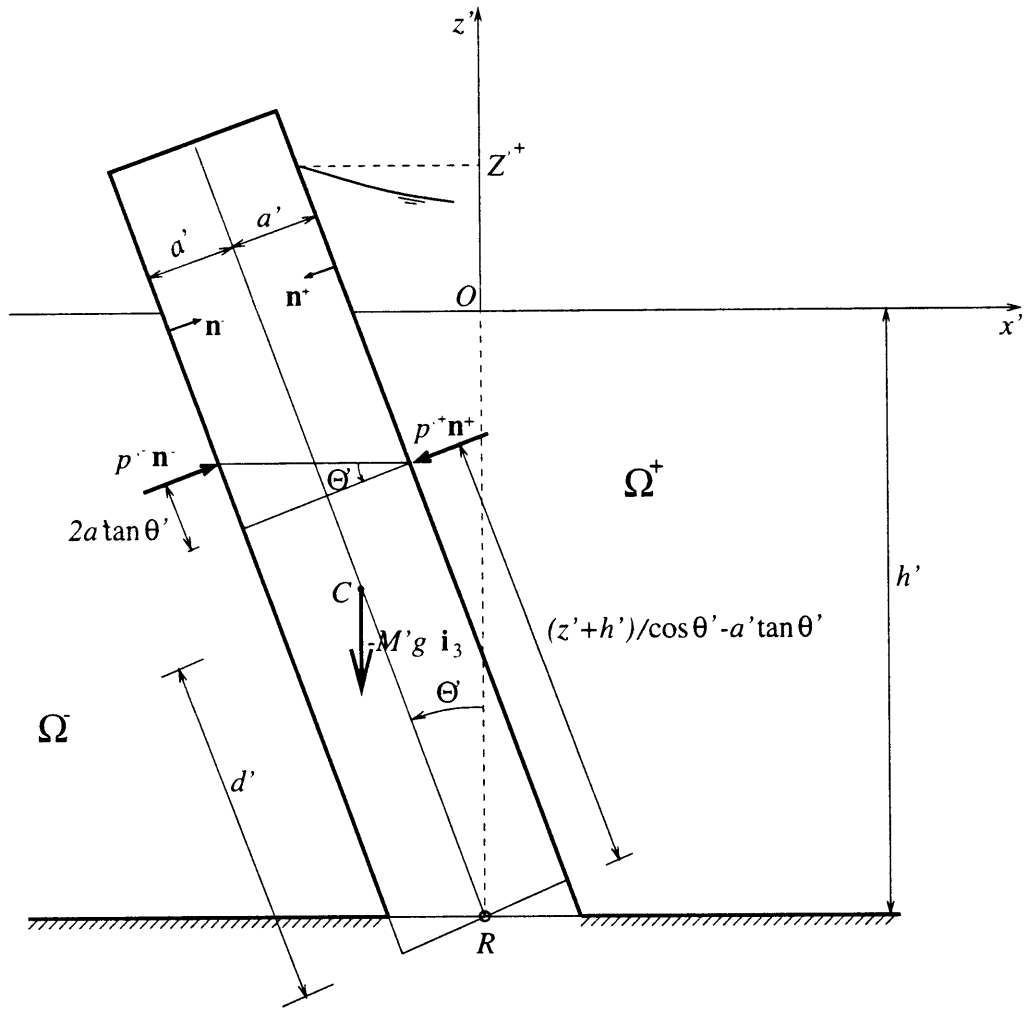

Figure 2-1: The ideal gate

induced by self weight and by the fluid pressure. $\mathcal{T}'_\nu$ is the torque induced by the viscous tangential stresses, its effect will be accounted for in chapter 3. Here we consider inviscid fluid and frictionless hinges. Torque are considered positive if counterclockwise.

If M' is the mass of the gate, $C = [x'_c(t'),\, y'_c,\, z'_c(t')]$ is the center of mass and $R = [0,\, y' \equiv y'_c,\, -h']$ is the fixed center of rotation (hinge), then the gravity torque is given by

$$\mathcal{T}'_g(t') = -\left[\overrightarrow{\mathbf{RC}} \times \left(-M' g\, \vec{\mathbf{i}}_3\right)\right] \cdot \vec{\mathbf{i}}_2 = -M' g\, x'_c \tag{2.2.17}$$

where $\vec{\mathbf{i}}_1$, $\vec{\mathbf{i}}_2$ and $\vec{\mathbf{i}}_3$ are the unit vectors of the coordinate axis and $\overrightarrow{\mathbf{RC}}$ is the vector position of the center of mass $\{x'_c,\, 0,\, z'_c + h'\}$. The minus sign is needed to account for the fact that $Ox'y'z'$ is a right handed frame of reference and so $\left[\overrightarrow{\mathbf{RC}} \times \left(-M' g \vec{\mathbf{i}}_3\right)\right] \cdot \vec{\mathbf{i}}_2$ induces clockwise rotations. Recalling that $x'_c = -d' \sin\Theta'$, with $d' = [z'_c + h']_{\Theta'=0}$ being a structural constant, and introducing the first moment of inertia of the gate $S' = M'd'$, the gravity torque becomes

$$\mathcal{T}'_g = gS' \sin\Theta'(t'). \tag{2.2.18}$$

To determine the fluid torque on the gate we decompose $\mathcal{T}'_p$ into two parts:

$$\mathcal{T}'_p = \mathcal{T}'^{+}_p + \mathcal{T}'^{-}_p, \tag{2.2.19}$$

where $\mathcal{T}'^{+}_p +$ and $\mathcal{T}'^{-}_p$ are the torque exerted by the fluid in Ω^+ and in Ω^- respectively. Such torque can be written as a surface integral on the gate surface

$$\mathcal{T}'^{\pm}_p = -\int_{G^\pm} p'^{\pm} \left(\overrightarrow{\mathbf{RP}} \times \vec{\mathbf{n}}^{\pm}\right) \cdot \vec{\mathbf{i}}_2 \, \mathrm{d}G^\pm \tag{2.2.20}$$

where $G^\pm$ is the wetted surface of the gate on the $\pm$ sides (i.e. the wetted part of $x = \xi^\pm$), P is a point on the surface $G^\pm$ and $\vec{\mathbf{n}}^{\pm}$ are the unit vectors normal to the $\pm$ sides and directed towards the gate

$$\vec{\mathbf{n}}^{\pm} = \left(\mp 1,\, 0,\, \pm\xi^\pm_{z'}\right) / \left[1 + (\xi^\pm_{z'})^2\right]^{1/2}. \tag{2.2.21}$$

Again, the minus sign is needed to account for the fact that $Ox'y'z'$ is a right handed frame of reference and so $p'^{\pm}\left(\overrightarrow{\mathbf{RP}} \times \vec{\mathbf{n}}^{\pm}\right) \cdot \vec{\mathbf{i}}_2 \, \mathrm{d}G^\pm$ induces clockwise rotations. Since $\overrightarrow{\mathbf{RP}} = (x', y', z' + h')$ and $\mathrm{d}G^\pm = \left[1 + (\xi^\pm_{z'})^2\right]^{1/2} \mathrm{d}y'\mathrm{d}z'$, we obtain by (2.2.21)

$$\mathcal{T}'^{\pm}_p = \pm \int_{y'_1}^{y'_2} \mathrm{d}y' \int_{-h'}^{Z'^{\pm}} \mathrm{d}z'\; p'^{\pm}\left(x'\xi^\pm_{z'} + z' + h'\right), \tag{2.2.22}$$

where $Z'^{\pm}$ are the projections on the $y'z'$ plane of the highest free surface on the $\pm$

sides of the gate. The limits of the integral in y' are $y'_1 = 0$, $y'_2 = (1-r)b'$ for gate one, $\Theta' = \Theta'^{I}$, or $y'_1 = (1-r)b'$, $y'_2 = b'$ for gate two, $\Theta' = \Theta'^{II}$. Using (2.2.14) for $\xi^{\pm}$ we can write the first term between parenthesis in (2.2.22) as

$$x'\xi^{\pm}_{z'} = \xi^{\pm}\xi^{\pm}_{z'} = \left[-(z'+h')\,\tan\Theta' \pm \frac{a'}{\cos\Theta'}\right](-\tan\Theta') \tag{2.2.23}$$

which can be substituted back in (2.2.22) to give the total fluid torque

$$\begin{aligned}\mathcal{T}'_p = \mathcal{T}'^{+}_p + \mathcal{T}'^{-}_p \;=\; & \int_{y'_1}^{y'_2} \mathrm{d}y' \int_{-h'}^{Z'^{+}} \mathrm{d}z'\; p'^{+}\,\frac{(z'+h'-a'\sin\Theta')}{\cos^2\Theta'} \;- \\ & \int_{y'_1}^{y'_2} \mathrm{d}y' \int_{-h'}^{Z'^{-}} \mathrm{d}z'\; p'^{-}\,\frac{(z'+h'+a'\sin\Theta')}{\cos^2\Theta'},\end{aligned} \tag{2.2.24}$$

where $Z'^{\pm}$ refers to the free surface displacements along the wetted lines

$$Z'^{\pm} = \zeta'^{\pm}(\xi^{\pm}, y', t') = \zeta'^{\pm}\left(-(\zeta'+h)\,\tan\Theta' \pm \frac{a'}{\cos\Theta'}\,, y', t'\right). \tag{2.2.25}$$

This implicit definition will be solved later through a Taylor expansion.

As a check, (2.2.24) and the equation of motion of the gate can be obtained more directly via the following geometrical considerations. Consider figure 2-1 again. The elemental pressure force on the + side is $p'^{+}\mathrm{d}G^{+}$, it is perpendicular to the gate surface and so its moment arm is equal to $(z'+h')/\cos\Theta' - a'\tan\Theta'$: the resulting elemental torque $\mathrm{d}\mathcal{T}'^{+}_p = p'^{+}\mathrm{d}G^{+}\left[(z'+h')/\cos\Theta' - a'\tan\Theta'\right]$ is positive because it induces counterclockwise rotations. By similar geometrical consideration we find that on the - side the elemental torque is instead $\mathrm{d}\mathcal{T}'^{-}_p = -p'^{-}\mathrm{d}G^{-}\left[(z'+h')/\cos\Theta' + a'\tan\Theta'\right]$; there is a minus sign in front because it induces negative rotations. Upon recognizing that $\mathrm{d}G^{\pm} = \mathrm{d}y'\mathrm{d}z'/\cos\Theta'$, we integrate on the gate surface and obtain exactly expression (2.2.24).

2.3 Nondimensional governing equations

Let A^T be the scale of the free surface oscillation generated by the motion of the gates corresponding to the trapped modes; the time scale of this motion is the natural frequency of the mode $1/\omega_0$. The gate and channel geometry is such that $h' = O(b')$.[2] For the trapped wave mode the fluid velocity scale is $\omega_0 A^T$, so that the order of magnitude of the velocity potential is $\omega_0 A^T b'$. We introduce the following

[2]For the inlet of Malamocco the proposed system has $b' = 20$ m on a mean water depth $h' = 15$ m.

nondimensional variables:

$$\mathbf{x} = \mathbf{x}'/b', \qquad t = \omega_0 t', \qquad \Phi = \Phi'/\omega_0 A^T b', \qquad \zeta = \zeta'/A^T. \tag{2.3.1}$$

The nondimensional water depth and gate half-thickness are:

$$h = h'/b', \qquad a = a'/b', \tag{2.3.2}$$

the modal period being now unity, $b = 1$. Upon substitution we obtain the following normalized equations. We distinguish solutions in $\Omega^{\pm}$ by the superscripts $\pm$. Laplace equation (2.2.3) and Bernoulli equation (2.2.4) become respectively:

$$\nabla^2 \Phi^{\pm} = 0, \tag{2.3.3}$$

$$-\frac{p'^{\pm}}{\rho \omega_0^2 b'^2} = Gz + \epsilon \Phi_t^{\pm} + \epsilon^2 \frac{1}{2} |\nabla \Phi^{\pm}|^2, \tag{2.3.4}$$

where the parameter $G = g/\omega_0^2 b'$ is $O(1)$ and $1/\sqrt{G}$ represents the nondimensional eigenfrequency. The parameter ϵ is the ratio between the amplitude of the trapped wave and the modal period, $\epsilon = A^T/b'$, and is anticipated to be much smaller than unity. The dynamic free surface boundary condition (2.2.5) becomes

$$-G\zeta^{\pm} = \Phi_t^{\pm} + \epsilon \frac{1}{2} |\nabla \Phi^{\pm}|^2, \qquad z = \epsilon \zeta^{\pm}. \tag{2.3.5}$$

On the same surface, the mixed kinematic-dynamic boundary condition (2.2.7) becomes

$$\Phi_{tt}^{\pm} + G\Phi_z^{\pm} + \epsilon |\nabla \Phi^{\pm}|_t^2 + \epsilon^2 \frac{1}{2} \nabla \Phi^{\pm} \cdot \nabla |\nabla \Phi^{\pm}|^2 = 0, \qquad z = \epsilon \zeta^{\pm}. \tag{2.3.6}$$

The kinematic conditions at the bottom of the channel becomes

$$\Phi_z^{\pm} = 0, \qquad z = -h, \tag{2.3.7}$$

while the condition of periodicity becomes

$$\Phi_y^{\pm} = 0, \qquad y = 0 \quad \text{and} \quad y = 1. \tag{2.3.8}$$

Before considering the equations on the gate, it is necessary to scale the angular motion Θ'. We recall from the linear wave–maker theory, that for a flap type wave–maker the amplitude of the generated wave is of the order of magnitude $h'\Theta'$, so that the angular displacement of the flap must be of the order $A_T/h' \sim A_T/b' = \epsilon$ radians.

Therefore we normalize the angular displacement by $\epsilon = A^T/b'$

$$\Theta = \Theta'/\epsilon. \tag{2.3.9}$$

On a gate surface

$$x = \xi^{\pm} \equiv -(z+h)\,\tan\epsilon\Theta \pm \frac{a}{\cos\epsilon\Theta}, \tag{2.3.10}$$

the kinematic boundary condition (2.2.15) now has the expression

$$\Phi_x^{\pm} = \Theta_t\,\frac{[-(z+h) \pm a\sin\epsilon\Theta]}{\cos^2\epsilon\Theta} - \Phi_z^{\pm}\tan\epsilon\Theta. \tag{2.3.11}$$

Finally, consider the dynamic boundary on one gate (2.2.16) with the expressions (2.2.18) and (2.2.24). Upon substitution of the nondimensional variables, expressing the fluid pressure through Bernoulli equation (2.3.4) we obtain after simplification:

$$\begin{aligned} I\epsilon\Theta_{tt} = {} & gS\sin\epsilon\Theta + \int_{y_1}^{y_2} \mathrm{d}y \times \\ & \left\{ -\int_{-h}^{\epsilon\zeta^+} \mathrm{d}z \left(Gz + \epsilon\Phi_t^+ + \epsilon^2\frac{1}{2}|\nabla\Phi^+|^2 \right) (z+h-a\sin\epsilon\Theta)\,/\cos^2\epsilon\Theta + \right. \\ & \left. \int_{-h}^{\epsilon\zeta^-} \mathrm{d}z \left(Gz + \epsilon\Phi_t^- + \epsilon^2\frac{1}{2}|\nabla\Phi^-|^2 \right) (z+h+a\sin\epsilon\Theta)\,/\cos^2\epsilon\Theta \right\}. \end{aligned} \tag{2.3.12}$$

In the above expression S and I are respectively the nondimensional first and second moment of the gate

$$S = S'/\rho b'^4, \qquad I = I'/\rho b'^5, \tag{2.3.13}$$

and the limits of integration in y are now $y_1 = 0$, $y_2 = 1 - r$ for gate one and $y_1 = 1 - r$, $y_2 = 1$ for gate two.

2.4 Taylor approximation of boundary conditions

The free surface boundary conditions (2.3.5) and (2.3.6), being given at $z = \epsilon\zeta$, can be Taylor–expanded about $z = 0$. For the dynamic boundary condition (2.3.5) we obtain

$$\begin{aligned} -G\zeta^{\pm} = {} & \left[\Phi_t^{\pm}\right]_{z=0} + \left[\Phi_{tz}^{\pm}\right]_{z=0}\epsilon\zeta + \frac{1}{2}\left[\Phi_{tzz}^{\pm}\right]_{z=0}\epsilon^2\zeta^2 + \left[\epsilon\frac{1}{2}|\nabla\Phi^{\pm}|^2\right]_{z=0} + \\ & \left[\epsilon\frac{1}{2}|\nabla\Phi^{\pm}|_z^2\right]_{z=0}\epsilon\zeta + O(\epsilon^3). \end{aligned} \tag{2.4.1}$$

A similar expansion for the mixed kinematic-dynamic boundary condition (2.3.6) yields

$$\left[\Phi_{tt}^{\pm}+G\Phi_{z}^{\pm}\right]_{z=0}+\left[\Phi_{ttz}^{\pm}+G\Phi_{zz}^{\pm}\right]_{z=0}\epsilon\zeta+\frac{1}{2}\left[\Phi_{ttzz}^{\pm}+G\Phi_{zzz}^{\pm}\right]_{z=0}\epsilon^{2}\zeta^{2}+$$
$$\left[\epsilon|\nabla\Phi^{\pm}|_{t}^{2}\right]_{z=0}+\left[\epsilon|\nabla\Phi^{\pm}|_{t}^{2}\right]_{z=0}\epsilon\zeta+\left[\epsilon^{2}\frac{1}{2}\nabla\Phi^{\pm}\cdot\nabla|\nabla\Phi^{\pm}|^{2}\right]_{z=0}+O(\epsilon^{3})=0. \quad (2.4.2)$$

For small ϵ all the trigonometric functions in (2.3.10),(2.3.11) and (2.3.12) can be Taylor expanded about $\Theta=0$; hence with an error of $O(\epsilon^3)$ the equation of the gate boundary (2.3.10) becomes

$$x=\xi^{\pm}\equiv\pm a-(z+h)\,\epsilon\Theta\pm\frac{a}{2}\,\epsilon^{2}\Theta^{2} \quad (2.4.3)$$

and, to the same order of approximation, the kinematic boundary condition (2.3.11) on the gates reads

$$\Phi_{x}^{\pm}=-(z+h)\,\Theta_{t}\pm a\epsilon\Theta\Theta_{t}-\Phi_{z}^{\pm}\epsilon\Theta-(z+h)\Theta_{t}\,\epsilon^{2}\Theta^{2} \quad (2.4.4)$$

The smallness of ϵ allows us to simplify further this last equation: indeed the cartesian expression of the gate surface (2.4.3) says that $x\mp a=O(\epsilon)$, i.e. that we can Taylor expand equation (2.4.4) about $x=\pm a$. Hence, the velocity potential and all its derivatives appearing in (2.4.4) , denoted generically by f, can be expanded as follows

$$f=[f]_{x=\pm a}+[f_{x}]_{x=\pm a}\left[-(z+h)\,\epsilon\Theta\pm\frac{a}{2}\,\epsilon^{2}\Theta^{2}\right]+\frac{1}{2}\,[f_{xx}]_{x=\pm a}\,[-(z+h)\,\epsilon\Theta]^{2}=$$
$$[f]_{x=\pm a}-\epsilon\,(z+h)\,\Theta\,[f_{x}]_{x=\pm a}+\epsilon^{2}\left\{\pm\frac{a}{2}\,\Theta^{2}\,[f_{x}]_{x=\pm a}+\frac{1}{2}(z+h)^{2}\Theta^{2}\,[f_{xx}]_{x=\pm a}\right\}, \quad (2.4.5)$$

with an error of $O(\epsilon^3)$. By doing so and collecting equal powers of ϵ we obtain the final form of the kinematic boundary condition, approximate to $O(\epsilon^3)$, now given on the two vertical planes $x=\pm a$:

$$\left[\Phi_{x}^{\pm}\right]_{x=\pm a}=-(z+h)\Theta_{t}+\epsilon\left\{(z+h)\Theta\left[\Phi_{xx}^{\pm}\right]_{x=\pm a}\pm a\Theta\Theta_{t}-\Theta\left[\Phi_{z}^{\pm}\right]_{x=\pm a}\right\}+$$
$$\epsilon^{2}\left\{\mp a\,\frac{\Theta^{2}}{2}\left[\Phi_{xx}^{\pm}\right]_{x=\pm a}-\frac{1}{2}(z+h)^{2}\Theta^{2}\left[\Phi_{xxx}^{\pm}\right]_{x=\pm a}-(z+h)\Theta^{2}\Theta_{t}+\right.$$
$$\left.(z+h)\Theta^{2}\left[\Phi_{zx}^{\pm}\right]_{x=\pm a}\right\}+O(\epsilon^{3}) \quad (2.4.6)$$

Next we turn to the approximation of the equation of the gate (2.3.12). The gate is a floating body, for which only second order theories are available in the literature (a complete summary of the second order theories of floating bodies can be found in Ogilvie(1982)). Here, for roll motion, we Taylor expand the equation of motion up to

third order.

As before, the Taylor expansion of the trigonometric functions simplifies to algebraic powers of $\epsilon\Theta$ both the gravity torque and the expression of the moment arms of the pressure forces on the two sides of the gate:

$$I\epsilon\Theta_{tt} = GS\left(\epsilon\Theta - \frac{\epsilon^3}{6}\Theta^3\right) + \int_{y_1}^{y_2} \mathrm{d}y \times$$
$$\left\{ -\int_{-h}^{\epsilon\zeta^+} \mathrm{d}z \left(Gz + \epsilon\Phi_t^+ + \epsilon^2\frac{1}{2}|\nabla\Phi^+|^2\right)\left[z + h - a\epsilon\Theta + (z+h)\epsilon^2\Theta^2 - \frac{5}{6}\epsilon^3\Theta^3\right] + \right.$$
$$\left. \int_{-h}^{\epsilon\zeta^-} \mathrm{d}z \left(Gz + \epsilon\Phi_t^- + \epsilon^2\frac{1}{2}|\nabla\Phi^-|^2\right)\left[z + h + a\epsilon\Theta + (z+h)\epsilon^2\Theta^2 + \frac{5}{6}\epsilon^3\Theta^3\right]\right\}. \quad (2.4.7)$$

In the last expression the inertia torque on the left hand side and the first integral on the right hand side, the gravity torque, do not need further manipulation. We note that both these terms are $O(\epsilon)$, therefore, in order to get an expression with the same approximation as before, it will be necessary to expand the fluid pressure torque integrals up to $O(\epsilon^3)$. In appendix A, we analyze separately the effect of the static pressure Gz, the linear dynamic pressure $\epsilon\Phi_t$ and of the quadratic part $\epsilon^2\frac{1}{2}|\nabla\Phi|^2$. The final result for the pressure torque $\mathcal{T}_p$ is

$$\mathcal{T}_p =$$
$$\epsilon\int_{y_1}^{y_2}\mathrm{d}y\int_{-h}^{0}\mathrm{d}z\,\{-\Delta\Phi_t(z+h)\} +$$
$$\epsilon^2\int_{y_1}^{y_2}\mathrm{d}y\int_{-h}^{0}\mathrm{d}z\left\{\Theta\Delta\Phi_{tx}(z+h)^2 + 2\,\Theta\,a\overline{\Phi_t} - \frac{1}{2}\Delta|\nabla\Phi|^2(z+h)\right\} -$$
$$\epsilon^3\int_{y_1}^{y_2}\mathrm{d}y\int_{-h}^{0}\mathrm{d}z\left\{3\,\Theta^2\,a\overline{\Phi_{tx}}(z+h) + \Theta^2\Delta\Phi_t(z+h) + \frac{1}{2}\,\Theta^2\Delta\Phi_{txx}(z+h)^3 - \right.$$
$$\left.\frac{1}{2}\,\Theta\,\Delta|\nabla\Phi|_x^2(z+h)^2 - a\Theta\,\overline{|\nabla\Phi|^2}\right\} -$$
$$\epsilon^2\int_{y_1}^{y_2}\mathrm{d}y\left\{G\,\frac{h}{2}\,\Delta\zeta^2 + h\Delta_0\left(\Phi_t\zeta\right)\right\} -$$
$$\epsilon^3\int_{y_1}^{y_2}\mathrm{d}y\left\{G\left(\frac{1}{3}\,\Delta\zeta^3 - a\Theta\,\overline{\zeta^2} - h^2\Theta\Delta\zeta\zeta_x\right) + \frac{1}{2}\,h\Delta_0\left(\Phi_{tz}\zeta^2\right) + \frac{1}{2}\Delta_0\left(\Phi_t\zeta^2\right) - \right.$$
$$\left.\Theta h^2\Delta_0\left(\Phi_t\zeta\right)_x - 2\,\Theta\,a\overline{\left(\Phi_t\zeta\right)^0} + \frac{h}{2}\,\Delta_0\left(|\nabla\Phi|^2\zeta\right)\right\} -$$
$$\epsilon\,G\,ah^2(y_2 - y_1)\,\Theta - \epsilon^3\,G\,\frac{5}{6}\,ah^2(y_2 - y_1)\,\Theta^3 + O(\epsilon^4), \quad (2.4.8)$$

where Δ and $\overline{(\cdot)}$ are shorthand notations respectively for the jumps and the averages across the gate

$$\Delta(\cdot) = \left[(\cdot)^+\right]_{x=a} - \left[(\cdot)^-\right]_{x=-a}, \qquad \overline{(\cdot)} = \frac{1}{2}\left\{\left[(\cdot)^+\right]_{x=a} + \left[(\cdot)^-\right]_{x=-a}\right\}, \quad (2.4.9)$$

$$\Delta_0(\cdot) = \left[(\cdot)^+\right]_{x=a,z=0} - \left[(\cdot)^-\right]_{x=-a,z=0}, \quad \overline{(\cdot)^0} = \frac{1}{2}\left\{\left[(\cdot)^+\right]_{x=a,z=0} + \left[(\cdot)^-\right]_{x=-a,z=0}\right\}. \tag{2.4.10}$$

Upon substitution of the above expression in the equation for the gate (2.4.7) and division by a common factor ϵ, we obtain

$$\begin{aligned}
&I\Theta_{tt} + G\left[ah^2(y_2-y_1) - S\right]\Theta + \epsilon^2\frac{G}{6}\left[5ah^2(y_2-y_1) + S\right]\Theta^3 = \\
&\quad \int_{y_1}^{y_2}\mathrm{d}y\int_{-h}^{0}\mathrm{d}z\left\{-\Delta\Phi_t(z+h)\right\} + \\
&\quad \epsilon\int_{y_1}^{y_2}\mathrm{d}y\int_{-h}^{0}\mathrm{d}z\left\{\Theta\Delta\Phi_{tx}(z+h)^2 + 2\,\Theta\,a\overline{\Phi_t} - \frac{1}{2}\Delta|\nabla\Phi|^2(z+h)\right\} - \\
&\quad \epsilon^2\int_{y_1}^{y_2}\mathrm{d}y\int_{-h}^{0}\mathrm{d}z\left\{3\,\Theta^2\,a\overline{\Phi_{tx}}(z+h) + \Theta^2\Delta\Phi_t(z+h) + \frac{1}{2}\Theta^2\Delta\Phi_{txx}(z+h)^3 - \right. \\
&\qquad\qquad \left. \frac{1}{2}\Theta\,\Delta|\nabla\Phi|_x^2(z+h)^2 - a\Theta\,\overline{|\nabla\Phi|^2}\right\} - \\
&\quad \epsilon\int_{y_1}^{y_2}\mathrm{d}y\left\{G\frac{h}{2}\Delta\zeta^2 + h\Delta_0\left(\Phi_t\zeta\right)\right\} - \\
&\quad \epsilon^2\int_{y_1}^{y_2}\mathrm{d}y\left\{G\left(\frac{1}{3}\Delta\zeta^3 - a\Theta\,\overline{\zeta^2} - h^2\Theta\Delta\zeta\zeta_x\right) + \frac{1}{2}h\Delta_0\left(\Phi_{tz}\zeta^2\right) + \frac{1}{2}\Delta_0\left(\Phi_t\zeta^2\right) - \right. \\
&\qquad \left. \Theta h^2\Delta_0\left(\Phi_t\zeta\right)_x - 2\,\Theta\,a\overline{(\Phi_t\zeta)^0} + \frac{h}{2}\Delta_0\left(|\nabla\Phi|^2\zeta\right)\right\} + O(\epsilon^3).
\end{aligned} \tag{2.4.11}$$

On the left hand side of the above expression the first, second and third terms are respectively the inertia term and the linear $O(1)$ and the nonlinear $O(\epsilon^2)$ buoyancy terms. On the right hand side the first double integral is the linear $O(1)$ pressure torque. Indeed for $\epsilon = 0$ we recover the linear theory for a floating body. The nonlinear pressure torque at both $O(\epsilon)$ and $O(\epsilon^2)$ is composed of a surface integral in y and z and a line integral at $z = 0$. This is due to the double Taylor expansion of the integrands performed both in x and z for the z integration that goes from 0 to $\epsilon\zeta^{\pm}$. We stress that all the integrals in (2.4.11) are evaluated on the fixed planes $x = \pm a$. This simplification, together with the fact that the kinematic boundary condition (2.4.6) on the gate surface is also given at $x = \pm a$ and that, similarly, the mixed condition (2.4.2) on the free surface is given on the horizontal fixed plane $z = 0$, implies that now the solution for the fluid velocity potential $\Phi^{\pm}$ has to be sought in two fixed seminfinite rectangular domains $\Omega^{\pm}$ defined by

$$\Omega^{\pm} = \left\{(x,y,z) \mid x \in [\pm a, \pm\infty],\, y \in [0,1],\, z \in [-h,0]\right\}. \tag{2.4.12}$$

For simplicity of notation we will remove in the following the square bracket symbol $[\cdot]$ that signifies evaluation at the boundaries.

2.5 Multiple scales expansion and solution of perturbation equations

In order to describe the time evolution, i.e. initial instability, growth and final equilibrium, of the amplitude of the trapped wave, we introduce $t_2 = \epsilon^2 t$ on which the amplitude of the trapped wave depends. The perturbation expansions of nondimensional fluid velocity potential, free surface elevation and gate rotation assume the form:

$$\begin{cases} \Phi^{\pm} = \Phi_1^{\pm}(x,y,z,t,t_2) + \epsilon\,\Phi_2^{\pm}(x,y,z,t,t_2) + \epsilon^2\,\Phi_3^{\pm}(x,y,z,t,t_2) + \dots \\ \zeta^{\pm} = \zeta_1^{\pm}(x,y,\quad t,t_2) + \epsilon\,\zeta_2^{\pm}(x,y,\quad t,t_2) + \epsilon^2\,\zeta_3^{\pm}(x,y,\quad t,t_2) + \dots \\ \Theta = \Theta_1(\quad y,\quad t,t_2) + \epsilon\,\Theta_2(\quad y,\quad t,t_2) + \epsilon^2\,\Theta_3(\quad y,\quad t,t_2) + \dots \end{cases} \tag{2.5.1}$$

Recall that all the expansions terms in (2.5.1) are periodic in y with unit half period; therefore the y dependence of all the quantities in (2.5.1) can be represented in a Fourier series. Having introduced the slow time scale, the t derivatives become

$$\partial_t \to \partial_t + \epsilon^2 \partial_{t_2}, \qquad \partial_{tt} \to \partial_{tt} + 2\epsilon^2 \partial_{tt_2} + O(\epsilon^4) \tag{2.5.2}$$

in accordance with the chain rule. Upon substitution of expansions (2.5.1) in the governing equation (2.3.3) and boundary condition at the bottom (2.3.7), sidewalls (2.3.8), on the free surface (2.4.2) and on the gate surface (2.4.6) (2.4.11), we obtain a set of linear governing equation and boundary conditions at each order in ϵ. They are collected below.

Laplace equation in $\Omega^{\pm}$:

$$\nabla^2 \Phi_n^{\pm} = 0, \qquad n = 1,2,3. \tag{2.5.3}$$

Free surface boundary condition:

$$\Phi_{n_{tt}}^{\pm} + G\Phi_{n_z}^{\pm} = \mathcal{F}_n^{\pm} \qquad z = 0, \tag{2.5.4}$$

where

$$\mathcal{F}_1^{\pm} = 0, \tag{2.5.5}$$

$$\mathcal{F}_2^{\pm} = -\left[\left(\Phi_{1_{ttz}}^{\pm} + G\Phi_{1_{zz}}^{\pm}\right)\zeta_1^{\pm} + \left(\nabla\Phi_1^{\pm}\cdot\nabla\Phi_1^{\pm}\right)_t\right], \tag{2.5.6}$$

$$\begin{aligned} \mathcal{F}_3^{\pm} = -\Bigg[&\left(\Phi_{2_{ttz}}^{\pm} + G\Phi_{2_{zz}}^{\pm}\right)\zeta_1^{\pm} + \left(\Phi_{1_{ttz}}^{\pm} + G\Phi_{1_{zz}}^{\pm}\right)\zeta_2^{\pm} + \frac{1}{2}\left(\Phi_{1_{ttzz}}^{\pm} + G\Phi_{1_{zzz}}^{\pm}\right)\zeta_1^{\pm^2} + \\ &2\left(\nabla\Phi_1^{\pm}\cdot\nabla\Phi_2^{\pm}\right)_t + \left(\nabla\Phi_1^{\pm}\cdot\nabla\Phi_1^{\pm}\right)_{tz}\zeta_1^{\pm} + \frac{1}{2}\nabla\Phi_1^{\pm}\cdot\nabla|\nabla\Phi_1^{\pm}|^2 + 2\Phi_{1_{tt_2}}^{\pm}\Bigg]. \end{aligned} \tag{2.5.7}$$

Bernoulli equation (2.4.1) allows us to evaluate $\zeta_n^{\pm}$ once $\Phi_n^{\pm}$ is solved

$$-G\zeta_n^{\pm} = \mathcal{B}_n^{\pm}, \qquad z = 0, \tag{2.5.8}$$

where

$$\mathcal{B}_1^{\pm} = \Phi_{1_t}^{\pm}, \tag{2.5.9}$$

$$\mathcal{B}_2^{\pm} = \Phi_{2_t}^{\pm} + \zeta_1^{\pm}\Phi_{1_{tz}}^{\pm} + \frac{1}{2}|\nabla\Phi_1^{\pm}|^2, \tag{2.5.10}$$

$$\mathcal{B}_3^{\pm} = \Phi_{3_t}^{\pm} + \zeta_1^{\pm}\Phi_{2_{tz}}^{\pm} + \zeta_2^{\pm}\Phi_{1_{tz}}^{\pm} + \nabla\Phi_1^{\pm}\cdot\nabla\Phi_2^{\pm} + \frac{1}{2}\zeta_1^{\pm^2}\Phi_{1_{tzz}}^{\pm} + \frac{1}{2}\zeta_1^{\pm}|\nabla\Phi_1^{\pm}|_z^2 + \Phi_{1_{t_2}}^{\pm}. \tag{2.5.11}$$

Bottom boundary condition:

$$\Phi_{n_z}^{\pm} = 0, \qquad z = -h. \tag{2.5.12}$$

Periodicity:

$$\Phi_{n_y}^{\pm} = 0, \qquad y = 0, \quad y = 1. \tag{2.5.13}$$

The kinematic boundary condition on the surface of one gate (2.4.6) yields:

$$\Phi_{n_x}^{\pm} = -(z+h)\Theta_{n_t} + \mathcal{G}_n^{\pm} \qquad x = \pm a, \tag{2.5.14}$$

where

$$\mathcal{G}_1^{\pm} = 0, \tag{2.5.15}$$

$$\mathcal{G}_2^{\pm} = (z+h)\Theta_1\Phi_{1_{xx}}^{\pm} \pm a\Theta_1\Theta_{1_t} - \Theta_1\Phi_{1_z}^{\pm}, \tag{2.5.16}$$

$$\mathcal{G}_3^{\pm} = (z+h)\left(\Theta_1\Phi_{2_{xx}}^{\pm} + \Theta_2\Phi_{1_{xx}}^{\pm} - \Theta_1^2\Theta_{1_t} + \Theta_1^2\Phi_{1_{zx}}^{\pm} - \Theta_{1_{t_2}}\right) - (z+h)^2\frac{1}{2}\Theta_1^2\Phi_{1_{xxx}}^{\pm} \pm a\left(\Theta_1\Theta_2\right)_t - \Theta_1\Phi_{2_z}^{\pm} - \Theta_2\Phi_{1_z}^{\pm} \mp a\frac{\Theta_1^2}{2}\Phi_{1_{xx}}^{\pm}. \tag{2.5.17}$$

Finally, the equation of motion of a gate (2.4.11) yields:

$$I\Theta_{n_{tt}} + GC\Theta_n = \int_{y_1}^{y_2}\mathrm{d}y\int_{-h}^{0}\mathrm{d}z\left\{-\Delta\Phi_{n_t}(z+h)\right\} + \mathcal{D}_n, \tag{2.5.18}$$

where

$$\mathcal{D}_1 = 0, \tag{2.5.19}$$

$$\mathcal{D}_2 = \int_{y_1}^{y_2}\mathrm{d}y\int_{-h}^{0}\mathrm{d}z\left\{-\frac{1}{2}\Delta|\nabla\Phi_1|^2(z+h) + \Theta_1\Delta\Phi_{1_{tx}}(z+h)^2 + 2\,\Theta_1\,a\overline{\Phi_{1_t}}\right\} - \int_{y_1}^{y_2}\mathrm{d}y\left\{G\frac{h}{2}\Delta\zeta_1^2 - h\Delta_0\left(\Phi_{1_t}\zeta_1\right)\right\}, \tag{2.5.20}$$

$$
\begin{aligned}
\mathcal{D}_3 = \int_{y_1}^{y_2} dy \int_{-h}^{0} dz \Big\{ & - \left[\Delta \left(\nabla\Phi_1 \cdot \nabla\Phi_2 \right) + 3\,\Theta_1^2\, a\overline{\Phi_{1_{tx}}} + \Theta_1^2 \Delta\Phi_{1_t} + \Delta\Phi_{1_{t_2}} \right] (z+h) \; + \\
& \left(\Theta_1 \Delta\Phi_{2_{tx}} + \Theta_2 \Delta\Phi_{1_{tx}} + \frac{1}{2}\,\Theta_1\, \Delta |\nabla\Phi_1|_x^2 \right) (z+h)^2 + \\
& -\frac{1}{2}\,\Theta_1^2 \Delta\Phi_{1_{txx}} (z+h)^3 + 2\,\Theta_1\, a\overline{\Phi_{2_t}} + 2\,\Theta_2\, a\overline{\Phi_{1_t}} + a\Theta_1\, \overline{|\nabla\Phi_1|^2} \Big\} - \\
& \int_{y_1}^{y_2} dy \left\{ h\Delta_0 \left(\Phi_{1_t} \zeta_2 \right) - h\Delta_0 \left(\Phi_{2_t} \zeta_1 \right) - \frac{1}{2}\, h\Delta_0 \left(\Phi_{1_{tz}} \zeta_1^2 \right) - \frac{1}{2} \Delta_0 \left(\Phi_{1_t} \zeta_1^2 \right) - \right. \\
& G \left[h\,\Delta \left(\zeta_1 \zeta_2 \right) + \frac{1}{3}\,\Delta\zeta_1^3 - a\Theta_1\, \overline{\zeta_1^2} - h^2 \Theta_1 \Delta\zeta_1 \zeta_{1_x} \right] + \\
& \left. \Theta_1 h^2 \Delta_0 \left(\Phi_{1_t} \zeta_1 \right)_x + 2\,\Theta_1\, a\overline{\left(\Phi_{1_t} \zeta_1 \right)^0} - \frac{h}{2}\, \Delta_0 \left(|\nabla\Phi_1|^2 \zeta_1 \right) \right\} - \\
& \frac{G}{6} \left[5ah^2 \left(y_2 - y_1 \right) + S \right] \Theta_1^3 - 2I\Theta_{1_{tt_2}},
\end{aligned}
\tag{2.5.21}
$$

and $C = ah^2 (y_2 - y_1) - S$ is the nondimensional buoyancy of the gate.

As seen in the introduction, the incident wave amplitude must be one order of magnitude smaller than the trapped wave; hence we assume an incident wave of amplitude $A^I = O(\epsilon)$. Let the incident wave frequency be $2\,(1 + \Delta\omega/\omega_0)$, i.e. detuned by the quantity $2\Delta\omega = 2\,(\omega - \omega_0)$ from twice the natural frequency of the trapped mode ω_0, which in nondimensional variables is equal to unity. In order for its contribution to balance the cubic terms and slow time variation at the third order, we let $\Delta\omega/\omega_0 = \epsilon^2\omega_2$.

Following the standard procedure in weakly nonlinear analysis we sort out the fast time dependence by assuming the following harmonic expansions at each order n

$$
\left\{ \Phi_n^{\pm}, \zeta_n^{\pm}, \Theta_n \right\} = \sum_{m=-n}^{n} \left\{ \phi_{nm}^{\pm}, \eta_{nm}^{\pm}, \theta_{nm} \right\} \mathrm{e}^{-\mathrm{i}m(1+\epsilon^2\omega_2)t}. \tag{2.5.22}
$$

For the functions $\{ \phi_{nm}^{\pm}, \eta_{nm}^{\pm}, \theta_{nm} \}$ to be real we also require

$$
\left\{ \phi_{nm}^{\pm}, \eta_{nm}^{\pm}, \theta_{nm} \right\} = \left\{ \phi_{n,-m}^{\pm}, \eta_{n,-m}^{\pm}, \theta_{n,-m} \right\}^* \tag{2.5.23}
$$

and $\left\{ \phi_{n0}^{\pm}, \eta_{n0}^{\pm}, \theta_{n0} \right\}$ to be real, where the superscripts * signifies the complex conjugate of the given quantity. Also the forcing terms in (2.5.4), (2.5.8), (2.5.14) and (2.5.18) can be expanded similarly

$$
\left\{ \mathcal{F}_n^{\pm}, \mathcal{B}_n^{\pm}, \mathcal{G}_n^{\pm}, \mathcal{D}_n \right\} = \sum_{m=-n}^{n} \left\{ \mathcal{F}_{nm}^{\pm}, \mathcal{B}_{nm}^{\pm}, \mathcal{G}_{nm}^{\pm}, \mathcal{D}_{nm} \right\} \mathrm{e}^{-\mathrm{i}m(1+\epsilon^2\omega_2)t}. \tag{2.5.24}
$$

with

$$
\left\{ \mathcal{F}_{nm}^{\pm}, \mathcal{B}_{nm}^{\pm}, \mathcal{G}_{nm}^{\pm}, \mathcal{D}_{nm} \right\} = \left\{ \mathcal{F}_{n,-m}^{\pm}, \mathcal{B}_{n,-m}^{\pm}, \mathcal{G}_{n,-m}^{\pm}, \mathcal{D}_{n,-m} \right\}^* \tag{2.5.25}
$$

and $\left\{\mathcal{F}^{\pm}_{n0}, \mathcal{B}^{\pm}_{n0}, \mathcal{G}^{\pm}_{n0}, \mathcal{D}_{n0}\right\}$ being real. To simplify the notation we introduce the following change of variable: $x^{\pm} = x \mp a$, in terms of which the kinematic boundary condition on the gate surface (2.5.14) is then given at $x^{\pm} = 0$.

Upon substitution of the harmonic expansions (2.5.22) into the governing equations, we get a sequence of boundary value problems in (x, y, z) at each order n and harmonic component m:

$$\nabla^2 \phi^{\pm}_{nm} = 0 \qquad \text{in} \quad \Omega^{\pm}, \tag{2.5.26}$$

$$G\phi^{\pm}_{nm_z} - m^2 \phi_{nm} = \mathcal{F}^{\pm}_{nm} \qquad z = 0, \tag{2.5.27}$$

$$\phi^{\pm}_{nm_z} = 0 \qquad z = -h, \tag{2.5.28}$$

$$\phi^{\pm}_{nm_y} = 0 \qquad y = 0,\ y = 1 \tag{2.5.29}$$

$$\phi^{\pm}_{nm_x} - \mathrm{i}\, m(z+h)\theta_{nm} = \mathcal{G}^{\pm}_{nm} \qquad x = 0, \tag{2.5.30}$$

which must be solved jointly with the equation of the gate motion for θ_{nm}

$$-m^2\, I\theta_{nm} + G\, C\, \theta_{nm} = \mathrm{i}\, m \int_{y_1}^{y_2} \mathrm{d}y \int_{-h}^{0} \mathrm{d}z \left\{\Delta\phi_{nm}(z+h)\right\} + \mathcal{D}_{nm} \qquad x = 0, \tag{2.5.31}$$

and the condition of periodicity in y

$$\phi^{\pm}_{nm_y} = 0, \qquad y = 0 \quad \text{and} \quad y = 1. \tag{2.5.32}$$

2.5.1 First order, zeroth harmonic

At $O(1)$, for the zeroth harmonic $\phi^{\pm}_{10}$, the forcing terms are also zero:

$$\mathcal{F}^{\pm}_{10} = 0, \quad \mathcal{B}^{\pm}_{10} = 0, \quad \mathcal{G}^{\pm}_{10} = 0, \quad \mathcal{D}_{10} = 0. \tag{2.5.33}$$

The problem is therefore governed by a homogeneous Laplace equation:

$$\nabla^2 \phi^{\pm}_{10} = 0 \qquad \text{in} \quad \Omega^{\pm}, \tag{2.5.34}$$

with homogeneous Neumann boundary conditions:

$$\phi^{\pm}_{10_z} = 0 \qquad \text{at} \quad z = 0 \quad \text{and} \quad z = -h, \tag{2.5.35}$$

$$\phi^{\pm}_{10_x} = 0 \qquad \text{at} \quad x = 0, \tag{2.5.36}$$

and

$$\phi^{\pm}_{10_y} = 0 \qquad \text{at} \quad y = 0,\ y = 1. \tag{2.5.37}$$

The solution is therefore independent of the fast coordinates:

$$\phi_{10}^{\pm} = \phi_{10}^{\pm}(t_2)\,. \tag{2.5.38}$$

The angular drift θ_{10} is zero; indeed the equation of motion of the gate (2.5.31) gives

$$G\,C\,\theta_{10} = 0, \tag{2.5.39}$$

which implies $\theta_{10} = 0$. Physically, there is no drift at the leading order because the restoring torque due to buoyancy is not weak. Indeed the displaced volume plays an important role in the dynamics of the gate, as can be seen in the next section, where buoyancy appears at the denominator of the eigenvalue condition that determines the eigenfrequency of the trapped wave.

2.5.2 First order, first harmonic–trapped mode

The first harmonic is the trapped wave, introduced in section 1.3. Here we present it in nondimensional variables. The forcing terms are all null

$$\mathcal{F}_{11}^{\pm} = 0, \quad \mathcal{B}_{11}^{\pm} = 0, \quad \mathcal{G}_{11}^{\pm} = 0, \quad \mathcal{D}_{11} = 0. \tag{2.5.40}$$

We look for solutions of Laplace equation

$$\nabla^2\phi_{11}^{\pm} = 0 \qquad \text{in} \quad \Omega^{\pm}, \tag{2.5.41}$$

with the following boundary conditions. Free surface boundary condition (2.5.4)

$$G\phi_{11_z}^{\pm} - \phi_{11} = 0 \qquad z = 0; \tag{2.5.42}$$

bottom boundary condition (2.5.12)

$$\phi_{11_z}^{\pm} = 0 \qquad z = -h; \tag{2.5.43}$$

condition of periodicity

$$\phi_{11_y}^{\pm} = 0 \quad y = 0,\ y = 1; \tag{2.5.44}$$

and gate surface kinematic condition (2.5.14)

$$\phi_{11_x}^{\pm} = \mathrm{i}(z+h)\theta_{11} \qquad x = 0, \tag{2.5.45}$$

where $\theta_{11}(t_2)$ is the slowing varying amplitude of the mode

$$\theta_{11} = \left\{ \begin{array}{c} \theta_{11}^{I} \\ \theta_{11}^{II} \end{array} \right\} = \theta \left\{ \begin{array}{c} 1 \\ 1 - 1/r \end{array} \right\}, \quad \left\{ \begin{array}{l} 0 < y < 1 - r \\ 1 - r < y < 1 \end{array} \right. \tag{2.5.46}$$

Let us define the modal shape q_{11} as

$$q_{11} = \left\{ \begin{array}{c} 1 \\ 1 - 1/r \end{array} \right\}, \quad \left\{ \begin{array}{l} 0 < y < 1 - r \\ 1 - r < y < 1 \end{array} \right. \tag{2.5.47}$$

and use its Fourier expansion, so that

$$\theta_{11} = \theta \, q_{11} = \theta \sum_{m=1}^{\infty} b_m \cos m\pi y, \tag{2.5.48}$$

with

$$b_m = \frac{2}{m\pi r} \sin m\pi(1 - r), \qquad m = 1, 2, \ldots \tag{2.5.49}$$

The corresponding potential is obtained by solving the homogeneous boundary value problem (2.5.41) to (2.5.45)

$$\phi_{11}^{\pm} = \mp \mathrm{i}\,\theta \sum_{m=1}^{\infty} \sum_{n=0}^{\infty} \beta_{mn} \cos m\pi y \, \cosh K_n(z + h) \, \mathrm{e}^{\mp \alpha_{mn} x} \equiv \mp \mathrm{i}\,\theta f_{11}^{\pm}(x, y, z). \tag{2.5.50}$$

The associated free surface displacement is

$$\eta_{11}^{\pm} = \pm\,\theta \frac{1}{G} \sum_{m=1}^{\infty} \sum_{n=0}^{\infty} \beta_{mn} \cos m\pi y \, \cosh K_n h \, \mathrm{e}^{\mp \alpha_{mn} x} = \pm\theta \frac{1}{G} f_{11}^{\pm}(x, y, 0) \equiv \pm\theta \, e_{11}^{\pm}(x, y). \tag{2.5.51}$$

Expressions (2.5.50) and (2.5.51) define respectively the real functions $f_{11}^{\pm}(x, y, z)$ and $e_{11}^{\pm}(x, y)$, which have the following symmetry properties about the $x = 0$ plane:

$$\begin{aligned} f_{11}^{+}(x, y, z) &= f_{11}^{-}(-x, y, z), & e_{11}^{+}(x, y) &= e_{11}^{-}(-x, y) \\ f_{11_x}^{+}(x, y, z) &= -f_{11_x}^{-}(-x, y, z), & e_{11_x}^{+}(x, y) &= -e_{11_x}^{-}(-x, y). \end{aligned} \tag{2.5.52}$$

To simplify the notation, in expression (2.5.50) we have introduced the complex nondimensional wavenumber K_n defined as

$$K_n = \left\{ \begin{array}{ll} k & \text{for } n = 0 \\ \mathrm{i}k_n & \text{for } n = 1, 2, \ldots \end{array} \right. \tag{2.5.53}$$

where k is the real root of of

$$1 = Gk \tanh kh \tag{2.5.54}$$

and the k_n are the real roots of

$$1 = -Gk_n \tan k_n h. \tag{2.5.55}$$

Hence for all $m = 1, 2, \ldots$ and $n = 0, 1, 2, \ldots$, the coefficients α_{mn} are defined by

$$\alpha_{mn} = \sqrt{m^2\pi^2 - K_n^2}. \tag{2.5.56}$$

For trapped modes all α_{mn} must be real. In the expression of the real coefficients β_{mn},

$$\beta_{mn} = \frac{b_m D_n}{\alpha_{mn} C_n}, \tag{2.5.57}$$

C_n and D_n have the nondimensional form

$$C_n = \frac{1}{2}\left(h + G\sinh^2 K_n h\right), \qquad D_n = \frac{1}{k_n^2}\left[(h/G - 1)\cosh K_n h + 1\right] \tag{2.5.58}$$

From their definitions $b_m = b_{-m}$, $\alpha_{mn} = \alpha_{-m,n}$ and therefore $\beta_{mn} = \beta_{-m,n}$. From (2.5.57) and using (2.5.49), (2.5.56) and (2.5.58) obtain

$$\beta_{mn} = \frac{4\sin m\pi(1-r)\ \left[(h/G - 1)\cosh K_n h + 1\right]}{m\pi r\, K_n^2 \sqrt{m^2\pi^2 - K_n^2}\left(h + G\sinh^2 K_n h\right)}. \tag{2.5.59}$$

The motion of the gate is governed by

$$-I\theta_{11} + G\,C\,\theta_{11} = \mathrm{i}\int_{y_1}^{y_2} \mathrm{d}y \int_{-h}^{0} \mathrm{d}z\,\{\Delta\phi_{11}(z+h)\}. \tag{2.5.60}$$

Using the expression of the potential (2.5.50) to calculate the pressure torque, the equation of motion (2.5.60) becomes an implicit equation for $G = g/\omega_0^2 b'$. The equation of motion (2.5.60) can be applied on either one of the two gates, yielding the same eigenvalue condition. Indeed, for the gate in $0 < y < 1 - r$ (half a gate for mode 1 and one gate for mode 2):

$$-I\theta_{11}^I + GC\theta_{11}^I = 2\,\theta\int_0^{1-r}\mathrm{d}y\int_{-h}^{0}\mathrm{d}z\ \sum_{m=1}^{\infty}\sum_{n=0}^{\infty}\beta_{mn}(z+h)\cos m\pi y\ \cosh K_n(z+h), \tag{2.5.61}$$

and since $\theta_{11}^I = \theta$, integration yields

$$-I + GC = I_a(G), \tag{2.5.62}$$

where the hydrodynamic added inertia is defined as

$$I_a(G) = \frac{2}{\pi}\sum_{m=1}^{\infty}\sum_{n=0}^{\infty}\frac{\beta_{mn}D_n}{m}\sin m\pi(1-r). \tag{2.5.63}$$

For mode 1, the second gate in the modal semiperiod has the same inertia and buoyancy of the first (they are two half gates). On the other hand for mode 2 the

second gate has half the inertia and buoyancy of the first (one full gate and one half gate). Therefore, if I and C are inertia and buoyancy of the first gate ($0 < y < 1-r$), then the second gate ($1-r < y < 1$) has inertia and buoyancy given by

$$\frac{r\,I}{1-r}, \qquad \frac{r\,C}{1-r}. \tag{2.5.64}$$

Application of the equation of motion for the second gate gives

$$-\frac{r\,I}{1-r}\,\theta_{11}^{II} + G\,\frac{r\,C}{1-r}\,\theta_{11}^{II} = 2\,\theta \int_{1-r}^{1} \mathrm{d}y \int_{-h}^{0} \mathrm{d}z \sum_{m=1}^{\infty}\sum_{n=0}^{\infty} \beta_{mn}(z+h)\cos m\pi y\,\cosh K_n(z+h). \tag{2.5.65}$$

Recalling that $\theta_{11}^{II} = \theta\,(r-1)/r$ and integrating the right hand side, it is immediate to recover expression (2.5.62) with (2.5.63).

We stress that q_{11}, $f_{11}^{\pm}$ and $e_{11}^{\pm}$ are all real functions, being the natural mode composed only of evanescent terms. Indeed the only complex quantities in (2.5.48), (2.5.50) and (2.5.51) are respectively θ, $\mp \mathrm{i}\theta$ and $\pm\theta$, where $\theta(t_2)$ is the unknown complex amplitude of the trapped mode to be determined.

Discussion of numerical results

In order to understand the parametric dependence of G on the geometry and inertia of the gates and on the water depth, computations are carried out for the eigenfrequencies of the step modes 1 and 2. Recall that $G = g/\omega_0^2 b' \sim T^2$, T being the natural period of the mode in sec, $C = ah^2(y_2 - y_1) - S$, $a = a'/b'$, $h = h'/b'$, $S = S'/\rho b'^4$ and $I = I'/\rho b'^5$. The choice of nondimensionalization for the inertia characteristics implies S, $I \sim 0.01 - 0.20$. In the laboratory experiments of figure 1-5, I ranges from 0.026 to 0.097.

First, the volume of the gate is fixed and the nondimensional first and second moment of inertia per unit width S and I are varied. This dependence is illustrated in figures 2-2 and 2-3 for mode 1 and mode 2 respectively. G is plotted versus I and each curve is for a different value of a, 0.05, 0.10, 0.15, 0.20, 0.30; the water depth is kept fixed at $h = 1.0$. We consider for simplicity a homogeneous gate of constant density ρ_g, height $h'_g > h'$, width b'_g, thickness $2a'_g$. It can be shown that

$$S' = \rho_g\, a'_g\, b'_g\, {h'_g}^2, \qquad I' = \frac{2}{3}\,\rho_g\, a'_g\, b'_g\, {h'_g}^3 \tag{2.5.66}$$

Thus $S' = \alpha I'$ with

$$\alpha = \frac{3}{2}\,\frac{b'}{h'_g} \tag{2.5.67}$$

In figure 2-2 and 2-3, $\alpha = 0.65$. All the different curves approach a finite value as

$(S,\ I) \to 0$, which is obtained from (2.5.62)

$$G_0 = \frac{I_a(G_0)}{ah^2(1-r)}. \tag{2.5.68}$$

Equation (2.5.68) shows that G_0 is lower for higher a, as can be seen in both figures 2-2 and 2-3. In this limit, the inertia is contributed only by the displaced fluid. An experiment that could simulate this limiting case is with gates made completely of light styrofoam. Each curve for constant a blows up to infinity as $S = \alpha I$ approaches the value that renders $C = 0$, i.e. $S = ah^2(1-r)$. Between these two limiting values G increases monotonically with I, i.e. gates with increasing inertia have increasing natural periods $T \sim \sqrt{G}$. For a fixed inertia I (fixed abscissa in figure 2-2 or 2-3), an increase of a, i.e. an increase in the displaced volume, induces a shortening of the natural period (a shift to a lower curve).

Next we fix the thickness a and test the dependence on I and S for different water depths h. In figures 2-4 and 2-5 the width a is kept constant at 0.2. Each curve is for a fixed h and increasing I. The limiting value G_0 as $I,\ S \to 0$, is still given by (2.5.68). But an increase in h, i.e. an increase in the displaced volume ah, now implies an increase in G. Indeed in a small interval of zero to low inertia I, an increase in the water depth h implies an increase in the eigenperiod G (in figures 2-4 and 2-5 for $I < 0.04$ shift to a higher curve). For "high" values of I an increase in h shortens the natural period (jump to a lower curve for $I > 0.09$). This different behavior is related to the nonlinear dependence of the added inertia I_a on h through expression (2.5.63)) and the dispersion relation (2.5.54). In figure 1-5, for low inertia (solid and empty circles) there is no decrease in the natural period for large increase in water depth! All the curves for constant h intersect and eventually tend to infinity as $S \to ah^2(1-r)$. The trend is the same: for a given h, increasing I increases monotonically the natural eigenperiod. Heavier gates oscillate slower!

Finally, us fix I and S (respectively 0.03 and 0.02) and change both a and h. We vary the nondimensional halfthickness a between 0.1 and 1.0 and the nondimensional water depth h between 0.5 and 2. The 3D plot of figure 2-6 shows the dependency of the added inertia $I_a(G)$ on a and h. While the dependence on a is very weak, the dependence on h is very strong. Indeed, as $h \to \infty$ the added inertia also grows indefinitely. For sufficiently large a, the trapped wave and so $I_a(G)$ are not defined, as will be explained in the following. In figure 2.5.2 respectively a contour plot and a 3D plot of G are shown. As seen in the previous figures, when $ah^2(1-r) \to S$ from above, $C = ah^2(1-r) - S \to 0$ and $G \to \infty$. This is a common feature shown by the left side of all the plots shown from figure 2.5.2 to figure 2-10. Physically this means that as the dimensional width b' increases (larger gate width) and/or the water depth h' or thickness a' decreases, the restoring force decreases; therefore the gate takes a longer time to move back towards the rest position and the resulting period $T \sim \sqrt{G}$

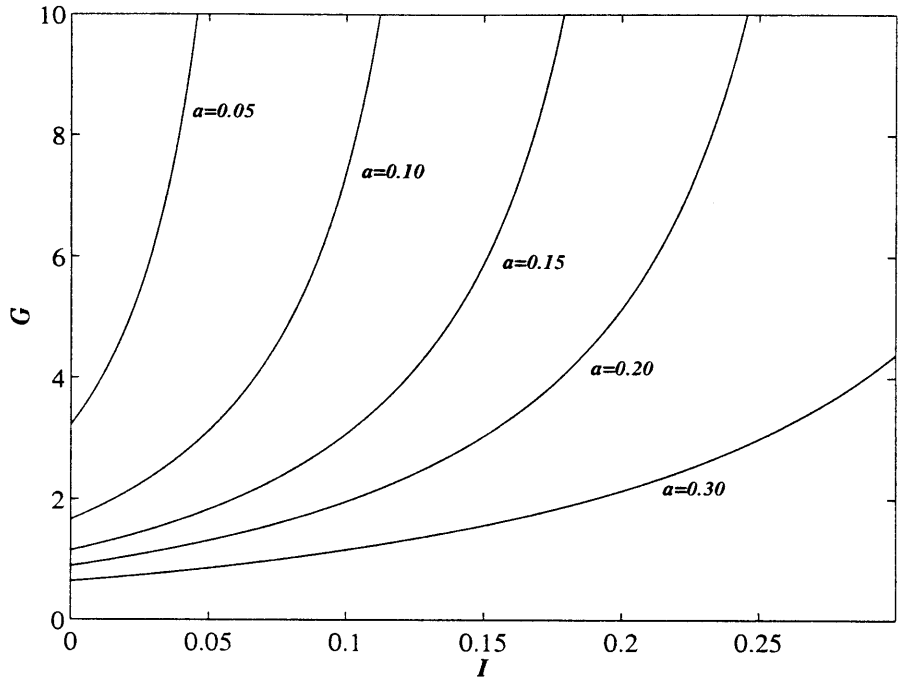

Figure 2-2: Normalized eigenperiod G of mode 1 for $h = 1$, constant values of a and varying S, I.

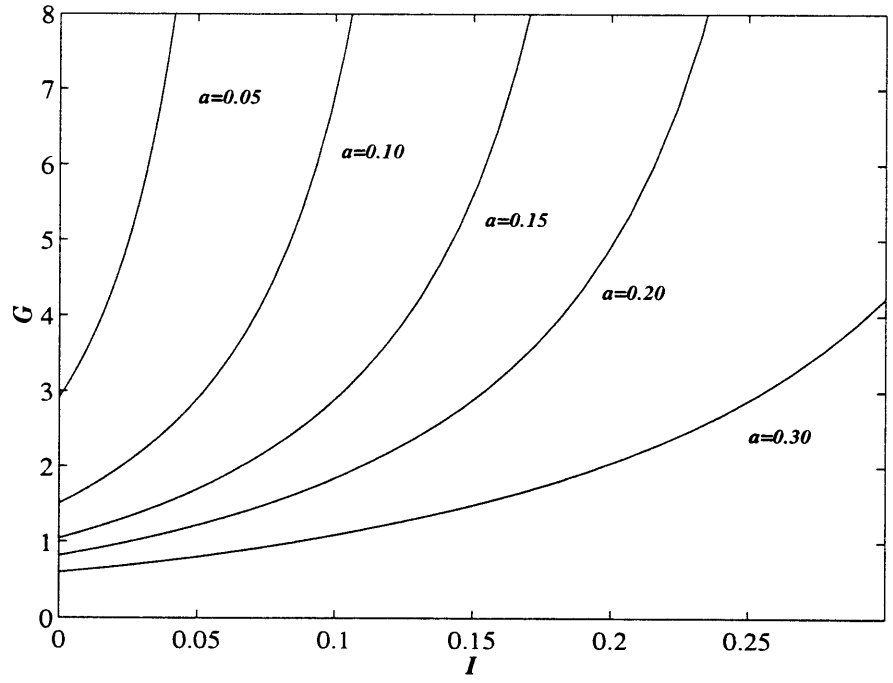

Figure 2-3: Normalized eigenperiod G of mode 2 for $h = 1$, constant values of a and varying S, I.

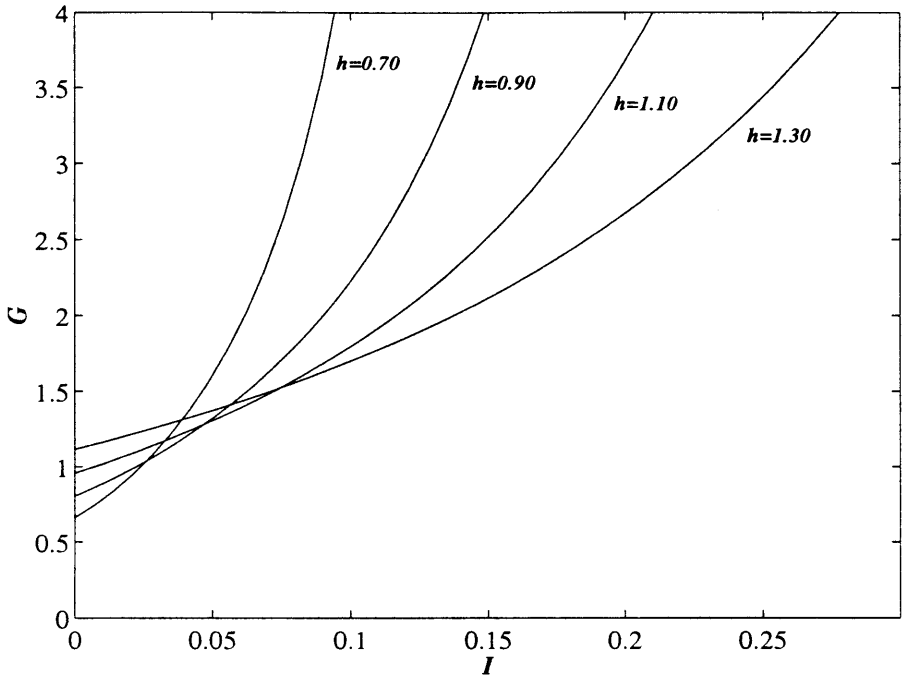

Figure 2-4: Normalized eigenperiod G of mode 1 for $a = 0.2$, constant values of h and varying S, I.

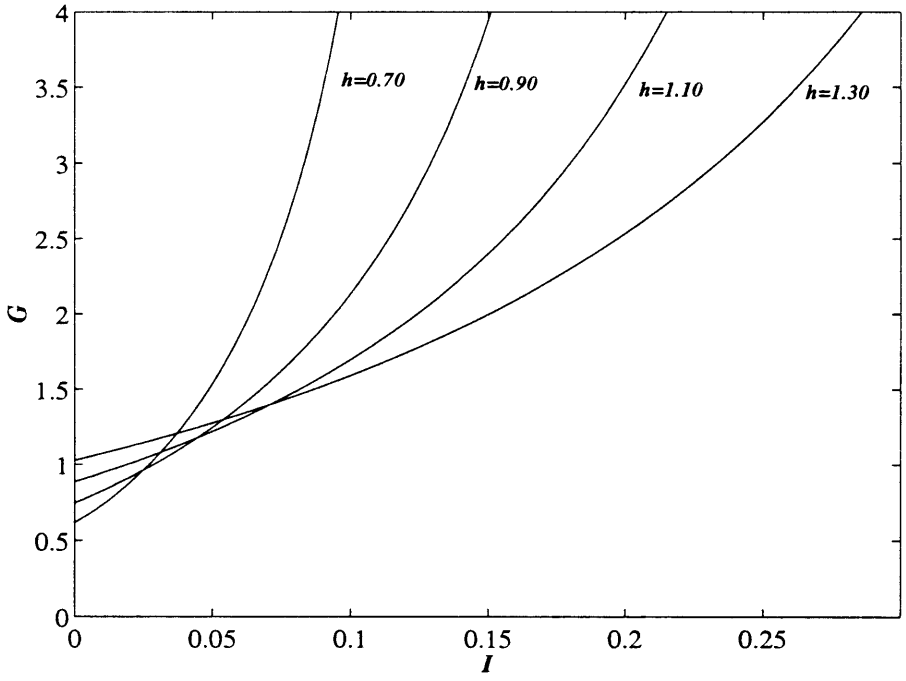

Figure 2-5: Normalized eigenperiod G of mode 2 for $a = 0.2$, constant values of h and varying S, I.

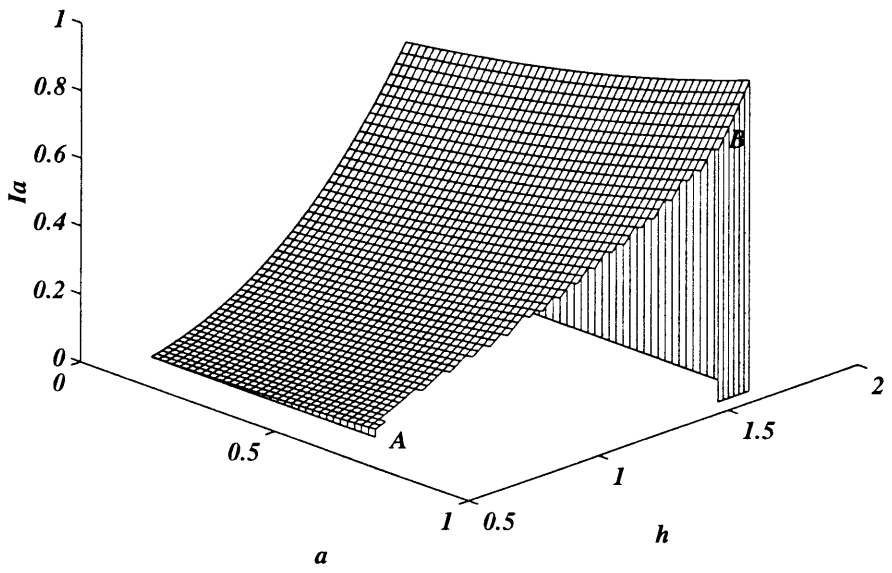

Figure 2-6: Added inertia $I_a(G)$ as a function of a and h for $I = 0.03$, $S = 0.02$. The vertical surface containing AB represents the boundary of the trapped mode.

increases. The natural period also grows indefinitely as $h \to \infty$ because $I_a(G)$ in the numerator of (2.5.62) tends to infinity, as seen in figure 2-6. Of course the limit $h \to \infty$ has no physical meaning for a gate system hinged at the bottom.

For each water depth h, the necessary condition for the existence of the trapped wave, i.e the absence of short crested propagating wave is

$$K < \pi, \tag{2.5.69}$$

where K is the root of the dispersion relationship (2.5.54). This inequality can be translated into a condition on G

$$G > \frac{1}{\pi \tanh \pi h}. \tag{2.5.70}$$

From (2.5.70), the cutoff frequency f_c in physical coordinates is

$$f_c = \frac{1}{2\pi}\sqrt{\frac{g}{b'}\pi \tanh \pi \frac{h'}{b'}}, \tag{2.5.71}$$

and increases with increasing h' or decreasing b'. For a certain combination of the parameters I, S, a, h (2.5.70) is not satisfied; the trapped mode is not possible. There-

fore, since G decreases as a increases, there is always a region bounded by AB in figure 2-6 beyond which (2.5.70) is not satisfied and the eigenmode is not possible. Physically this means that if buoyancy and restoring force are too large (large a or h), waves are radiated at the first order and no trapped wave is possible. In between the above two limiting behaviors, G is a monotonic continuous function of a and h.

In figure 2-8 we display the contour and 3D representations of G for the same set of parameters for mode 2. It can be seen that for any given a, h, mode 2 has a slightly shorter period of oscillation. This apparent decrease in period is a consequence of the choice of the nondimensionalization. In fact, for a given prototype array of gates of width b'_g, the physical modal period b' is respectively equal to b'_g for mode 1 and to $1.5\,b'_g$ for mode 2, so that the resulting natural period $T = 2\pi\sqrt{Gb'/g}$, is larger for mode 2. This statement is confirmed by numerical computation.

We repeat the computation for higher values of I and S (0.1 and 0.1 respectively). Since an increase in I and S induces an increase in G, the resulting area where the trapped wave is not possible (for the same range of a and h) is smaller. Compare the cropped areas of figure (2-9) with (2.5.2) for mode 1 and (2-10) with (2-8) for mode 2.

Finally we test the convergence of the eigensolution G as a function of the number of terms in the series representation (2.5.63) of the added inertia I_a. Figure 2-11 shows the root G of the eigenvalue condition (2.5.62) as the number of terms $m = n$ increases. After $m = n = 5$ numerical convergence is practically reached.

2.5.3 Second order, zeroth harmonic.

At the second order, the zeroth harmonic is forced by the trapped wave through quadratic nonlinearities. In view of equations (2.5.48), (2.5.50) and (2.5.51) $|\theta|^2$ can be factored out of the forcing terms of the zeroth harmonic in equation (2.5.28) to (2.5.31), leaving only the real coefficients $f_{11}^{\pm}$, $e_{11}^{\pm}$ and q_{11}. This is enough to imply that the forcing terms on the gate and the free surface are zero. In fact, the zeroth harmonic is forced only by terms of the kind $\phi_{11}\eta_{11}^* + \phi_{11}^*\eta_{11}$ (mixed condition on the free surface) or $\phi_{11}\theta_{11}^* + \phi_{11}^*\theta_{11}$ (kinematic condition on the gate surface); since ϕ_{11} is proportional to $\mathrm{i}\theta$ (no propagating modes !) and η_{11} or θ_{11} to θ, it follows

$$\phi_{11}\eta_{11}^* + \phi_{11}^*\eta_{11} = -\mathrm{i}\theta\theta^* f_{11}e_{11} + \mathrm{i}\theta^*\theta f_{11}e_{11} \equiv 0, \tag{2.5.72}$$

and

$$\phi_{11}\theta_{11}^* + \phi_{11}^*\theta_{11} = -\mathrm{i}\theta\theta^* f_{11}q_{11} + \mathrm{i}\theta^*\theta f_{11}q_{11} \equiv 0. \tag{2.5.73}$$

The forcing terms are therefore

$$\mathcal{F}_{20}^{\pm} = -G\left(\phi_{11_{zz}}^{\pm}\eta_{11}^{\pm^*} + \phi_{11_{zz}}^{\pm^*}\eta_{11}^{\pm}\right) + \phi_{11_z}^{\pm}\eta_{11}^{\pm^*} + \phi_{11_z}^{\pm^*}\eta_{11}^{\pm} =$$

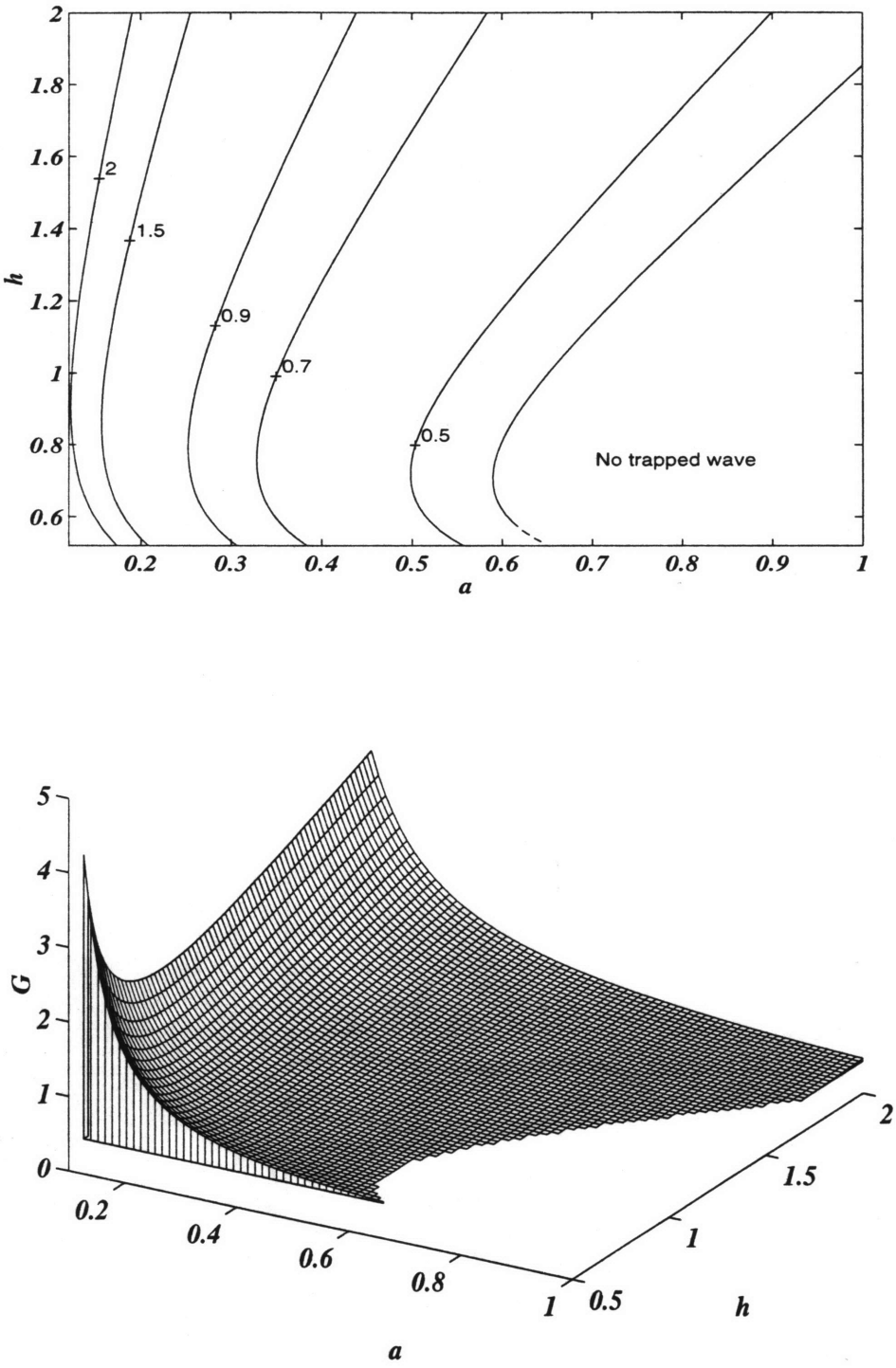

Figure 2-7: Eigenfrequency of mode 1 as a function of a and h for $I = 0.03$, $S = 0.02$. Contour and 3D plots. The labels of the contours are the values of G.

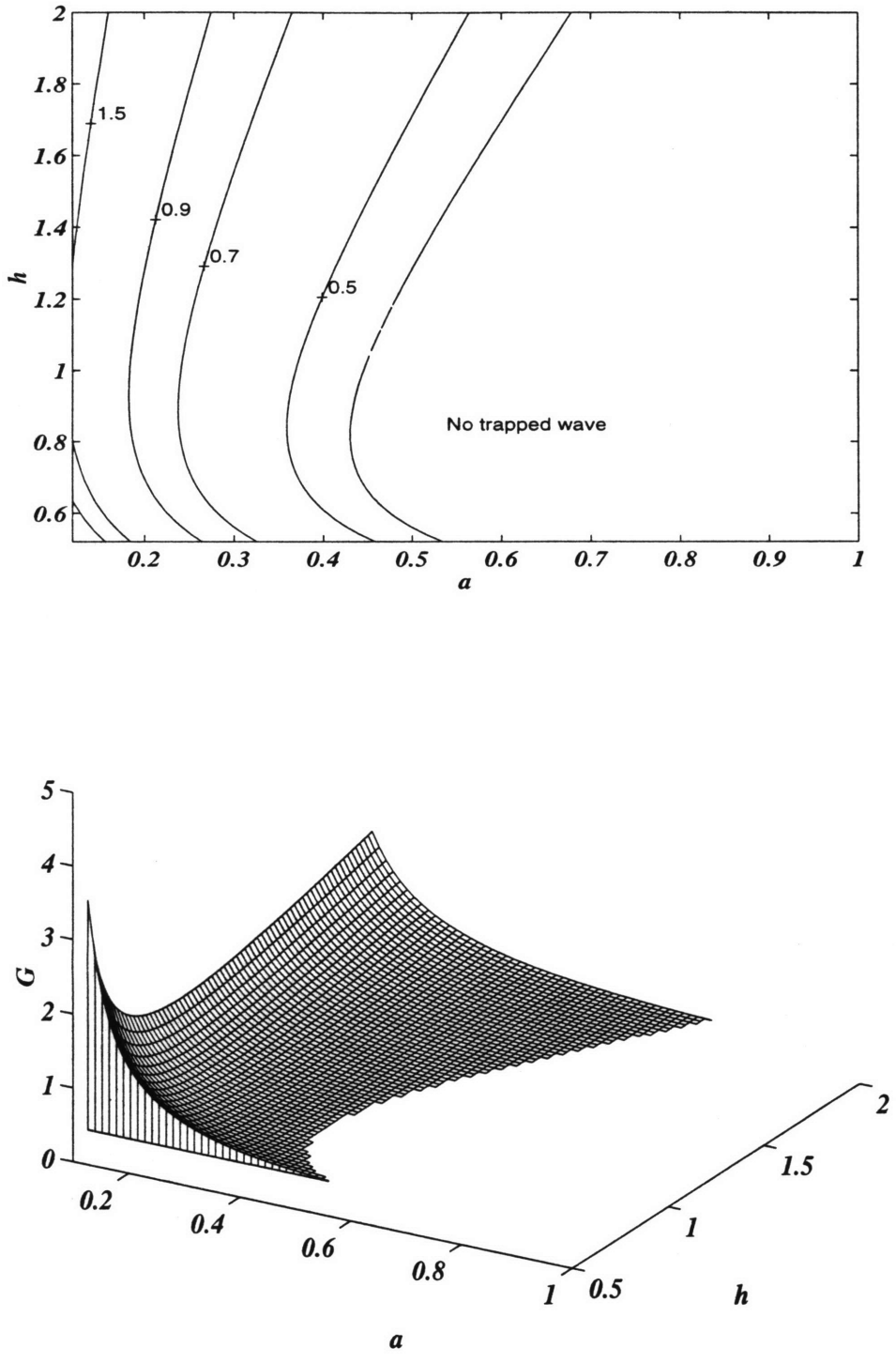

Figure 2-8: Eigenfrequency of mode 2 as a function of a and h for $I = 0.03$, $S = 0.02$. Contour and 3D plot. The labels of the contours are the values of G.

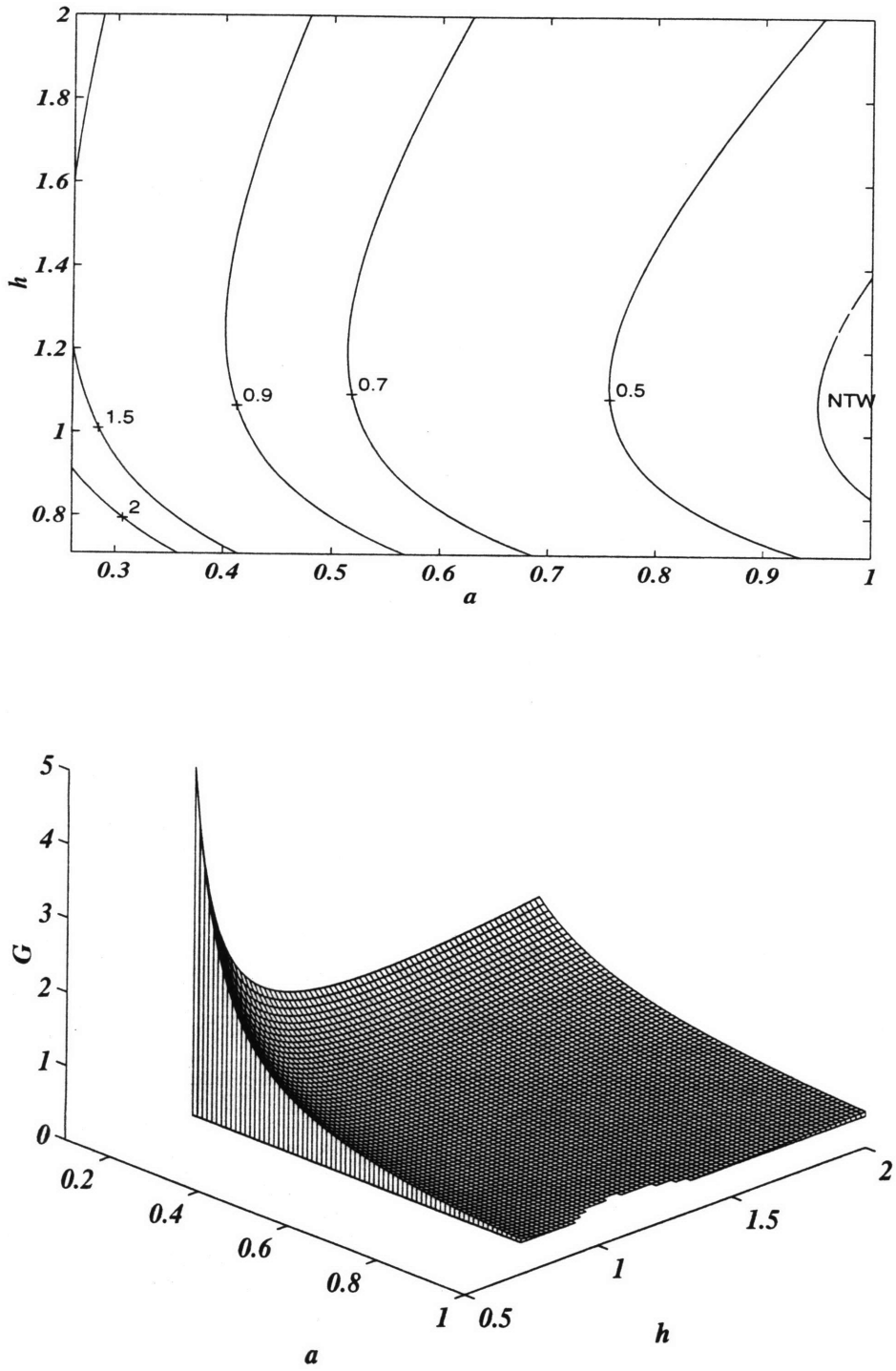

Figure 2-9: Eigenfrequency of mode 1 as a function of a and h for $I = 0.1$, $S = 0.1$. Contour and 3D plot. The labels of the contours are the values of G.

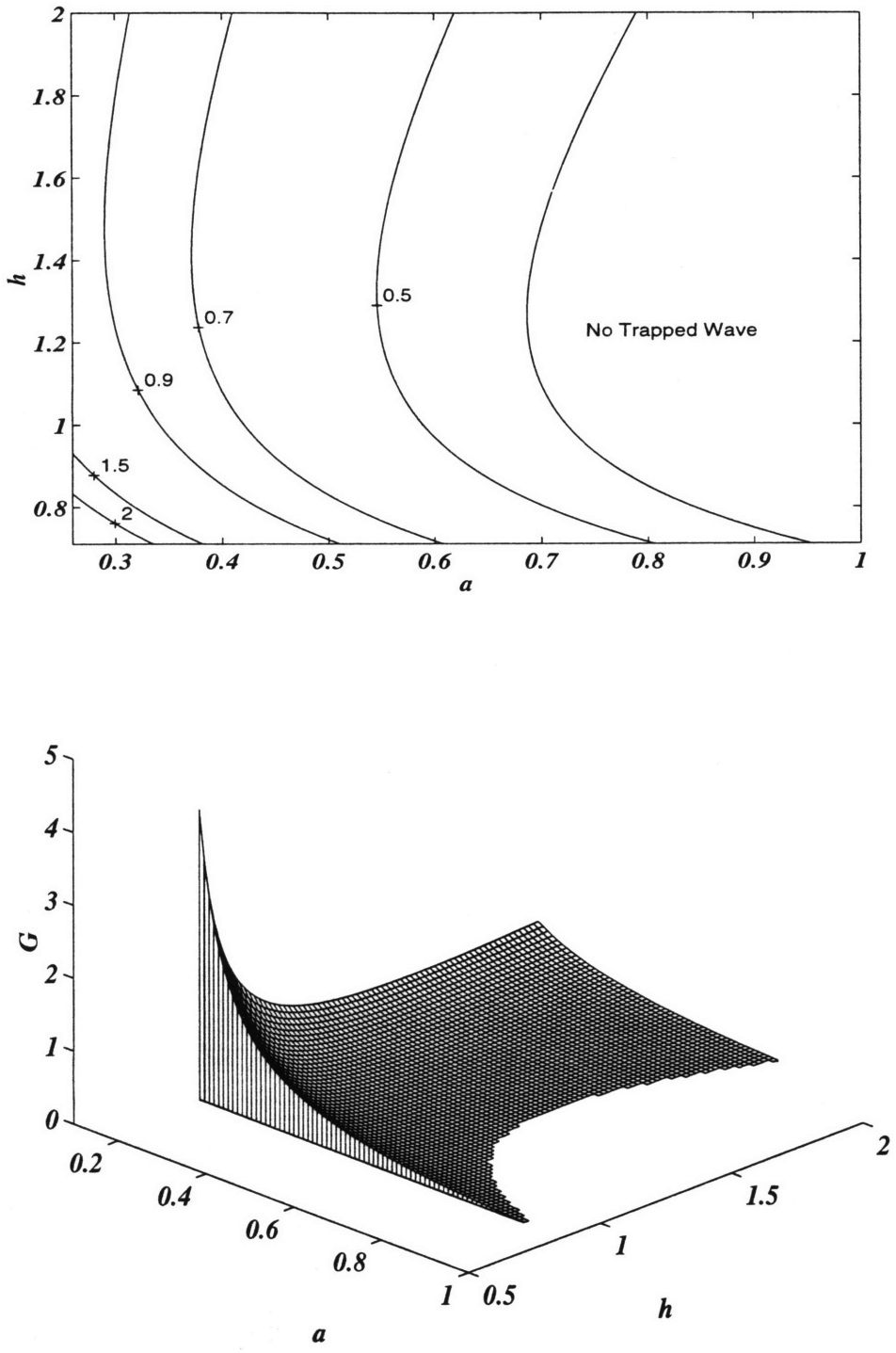

Figure 2-10: Eigenfrequency of mode 2 as a function of a and h for $I = 0.1$, $S = 0.1$. 3D plot. The labels of the contours are the values of G.

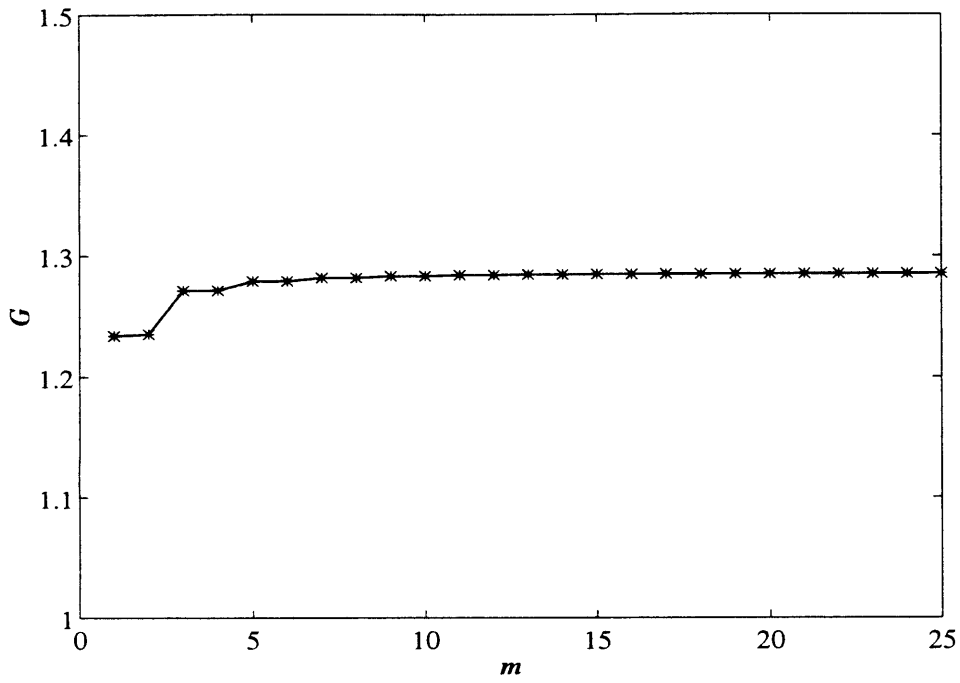

Figure 2-11: Sample of numerical test of the convergence of the eigenvalue G

$$\mathrm{i}|\theta|^2\left[G\left(f^{\pm}_{11_{zz}}e^{\pm}_{11}-f^{\pm}_{11_{zz}}e^{\pm}_{11}\right)-f^{\pm}_{11_z}e^{\pm}_{11}+f^{\pm}_{11_z}e^{\pm}_{11}\right]\equiv 0, \tag{2.5.74}$$

$$\mathcal{B}^{\pm}_{20}=-\mathrm{i}\phi^{\pm}_{11_z}\eta^{\pm^*}_{11}+\mathrm{i}\phi^{\pm^*}_{11_z}\eta^{\pm}_{11}+\nabla\phi^{\pm}_{11}\cdot\nabla\phi^{\pm^*}_{11}=|\theta|^2\left(2f^{\pm}_{11_z}e^{\pm}_{11}+|\nabla f^{\pm}_{11}|^2\right),$$

$$\mathcal{G}^{\pm}_{20}=(z+h)\left(\phi^{\pm}_{11_{xx}}\theta^{\pm^*}_{11}+\phi^{\pm^*}_{11_{xx}}\theta^{\pm}_{11}\right)-\phi^{\pm}_{11_z}\theta^{\pm^*}_{11}-\phi^{\pm^*}_{11_z}\theta^{\pm}_{11}=$$

$$\mathrm{i}|\theta|^2\left[(z+h)\left(-f^{\pm}_{11_{xx}}q_{11}+f^{\pm}_{11_{xx}}q_{11}\right)+f^{\pm}_{11_z}q_{11}-f^{\pm}_{11_z}q_{11}\right]\equiv 0, \tag{2.5.75}$$

$$\mathcal{D}_{20}=\int_{y_1}^{y_2}\mathrm{d}y\int_{-h}^{0}\mathrm{d}z\left\{-\Delta\left(\nabla\phi_{11}\cdot\nabla\phi^*_{11}\right)(z+h)+\left(\mathrm{i}\theta_{11}\Delta\phi^*_{11_x}-\mathrm{i}\theta^*_{11}\Delta\phi_{11_x}\right)(z+h)^2\right.$$

$$\left.+2\mathrm{i}\,\theta_{11}\,a\overline{\phi^*_{11}}-2\mathrm{i}\,\theta_{11}\,a\overline{\phi^*_{11}}\right\}-\int_{y_1}^{y_2}\mathrm{d}y\left\{G\,h\,\Delta\zeta_{11}\zeta^*_{11}-\mathrm{i}\,h\Delta_0\left(\phi_{11}\zeta^*_{11}\right)+\right.$$

$$\left.\mathrm{i}\,h\Delta_0\left(\phi^*_{11}\zeta_{11}\right)\right\}=|\theta|^2\int_{y_1}^{y_2}\mathrm{d}y\int_{-h}^{0}\mathrm{d}z\left\{-\Delta|\nabla f_{11}|^2(z+h)-4q_{11}\overline{f_{11_x}}(z+h)^2-\right.$$

$$\left.2a\,q_{11}\Delta f_{11}\right\}-|\theta|^2\int_{y_1}^{y_2}\mathrm{d}y\left\{G\,h\,\Delta e^2_{11}-2\,h\Delta_0\left(f_{11}e_{11}\right)\right\}\equiv 0. \tag{2.5.76}$$

$\mathcal{D}_{20}$ is zero because of the symmetry properties (2.5.52), which ensures the vanishing of all the jumps $\Delta(\cdot)$ and averages $\overline{(\cdot)}$ across the gate.

Since the forcing terms all vanish but for $\mathcal{B}_{20}$, the boundary value problem coupling $\phi^{\pm}_{20}$ and θ_{20} is identical to that governing ϕ_{10}, so that

$$\phi_{20}=\phi_{20}(t_2)\quad\text{and}\quad\theta_{20}=0, \tag{2.5.77}$$

i.e. the trapped wave does not induce any drift in the angular displacement. Instead it induces a set-down $\eta_{20}^{\pm}(x,y)$

$$\eta_{20}^{\pm} = -\frac{1}{G}\left|\theta\right|^2\left(2f_{11_z}^{\pm}e_{11}^{\pm} + \left|\nabla f_{11}^{\pm}\right|^2\right), \tag{2.5.78}$$

symmetrical with respect to $x = 0$: $\eta_{20}^{+}(x,y) = \eta_{20}^{-}(-x,y)$. This symmetry property has to be expected since the mean angular displacement is zero.

2.5.4 Second order, first harmonic

The forcing terms of the first harmonic are given by the quadratic products of the spatial gradients of $(1,0)\times(1,1)$ and by the slow time derivatives of the first harmonic $\partial_{t_2}(1,1)$. The former are all zero because $(1,0)$ depends only on t_2 and $q_{10} = 0$; the latter appear only at the third order $O(\epsilon^2)$. Hence, the forcing terms of the first harmonic are all zero

$$\mathcal{F}_{21}^{\pm} = 0, \quad \mathcal{B}_{21}^{\pm} = 0, \quad \mathcal{G}_{21}^{\pm} = 0, \quad \mathcal{D}_{21} = 0, \tag{2.5.79}$$

and the boundary value problem governing the (2, 1) harmonic is identical to the homogeneous governing the trapped wave (1, 1). Without loss of generality we choose the trivial solution $\phi_{21}^{\pm} = 0$, $\theta_{21} = 0$ and $\eta_{21}^{\pm} = 0$.

2.5.5 Second order, second harmonic

The second harmonic is forced by an incident plane wave from $x \sim \infty$ and by the trapped wave through quadratic nonlinearities. Both forcings oscillate at twice the natural frequency. Radiated waves to $\pm\infty$ are expected. At this order, the long-crested incident wave from $+\infty$ will be partly reflected and partly transmitted by the gates. The resulting linear inhomogeneous boundary value problem can be solved by separating the radiation and diffraction problems. We first examine the wave field and gate motion forced by the trapped wave.

2.5.5.a Response to nonlinear forcing

This problem is similar to the second order wave-maker theory of Fontanet(1961*a,b*), who employed Lagrangian coordinates for the description of the wave motion. For a plane wave-maker, the first order solution is composed by long-crested propagating and a series of evanescent modes (single eigenfunction expansion). Consequently he resolved a second harmonic still composed solely by long crested waves. Vice versa, in the case of the trapped wave, there are no propagating long-crested waves, but a two fold series of short-crested evanescent waves (double eigenfunction expansion).

Therefore, the second harmonic contains long- and short-crested, propagating and evanescent, modes.

We first note that a nontrivial homogeneous solution for the second harmonic is not possible. Indeed if G is the nontrivial homogeneous solution of (2.5.26) to (2.5.31) for $m = 1$, then the same equations with the same value of G and $m = 2$ have only the trivial solution.

In view of equations (2.5.48), (2.5.50) and (2.5.51), θ^2 can be factored out of the forcing terms of the second harmonic leaving only the real coefficients $f_{11}^{\pm}$, $e_{11}^{\pm}$ and q_{11}. The forcing terms read

$$\mathcal{F}_{22}^{\pm} = \phi_{11_z}^{\pm}\eta_{11}^{\pm} - G\phi_{11_{zz}}^{\pm}\eta_{11}^{\pm} + 2\mathrm{i}|\nabla\phi_{11}^{\pm}|^2 = \frac{3\,\mathrm{i}}{G^2}\,\phi_{11}^{\pm^2} - \mathrm{i}\,\phi_{11}^{\pm}\phi_{11_{zz}}^{\pm} + 2\mathrm{i}\left(\phi_{11_x}^{\pm^2} + \phi_{11_y}^{\pm^2}\right) =$$
$$\mathrm{i}\,\theta^2\left(-\frac{3}{G^2}\,f_{11}^{\pm^2} + f_{11}^{\pm}f_{11_{zz}}^{\pm} - 2f_{11_x}^{\pm^2} - 2f_{11_y}^{\pm^2}\right), \tag{2.5.80}$$

$$\mathcal{B}_{22}^{\pm} = -2\mathrm{i}\phi_{22}^{\pm} - \mathrm{i}\phi_{11_z}^{\pm}\eta_{11}^{\pm} + \frac{1}{2}|\nabla\phi_{11}^{\pm}|^2 = -2\mathrm{i}\phi_{22}^{\pm} - \theta^2\left(f_{11_z}^{\pm}e_{11}^{\pm} + \frac{1}{2}|\nabla f_{11}^{\pm}|^2\right), \tag{2.5.81}$$

$$\mathcal{G}_{22}^{\pm} = (z+h)\phi_{11_{xx}}^{\pm}\theta_{11}^{\pm} - \phi_{11_z}^{\pm}\theta_{11}^{\pm} \mp \mathrm{i}a\theta_{11}^2 =$$
$$\pm\,\mathrm{i}\,\theta^2\left[-(z+h)\,f_{11_{xx}}^{\pm}q_{11} + f_{11_z}^{\pm}q_{11} - a\,q_{11}^2\right], \tag{2.5.82}$$

$$\mathcal{D}_{22} = \int_{y_1}^{y_2}\mathrm{d}y\int_{-h}^{0}\mathrm{d}z\left\{-\frac{1}{2}\Delta|\nabla\phi_{11}|^2(z+h) - \mathrm{i}\,\theta_{11}\Delta\phi_{11_x}(z+h)^2 - 2\mathrm{i}\,\theta_{11}\,a\overline{\phi_{11}}\right\} -$$
$$\int_{y_1}^{y_2}\mathrm{d}y\left\{\frac{1}{2}G\,h\,\Delta\zeta_{11}^2 - \mathrm{i}\,h\Delta_0\left(\phi_{11}\zeta_{11}\right)\right\} =$$
$$\theta^2\int_{y_1}^{y_2}\mathrm{d}y\int_{-h}^{0}\mathrm{d}z\left\{\frac{1}{2}\Delta|\nabla f_{11}|^2(z+h) - 2q_{11}\overline{f_{11_x}}(z+h)^2 - 2a\,q_{11}\Delta f_{11}\right\} -$$
$$\theta^2\int_{y_1}^{y_2}\mathrm{d}y\left\{\frac{1}{2}\,G\,h\,\Delta e_{11}^2 - h\Delta_0\left(f_{11}e_{11}\right)\right\} \equiv 0. \tag{2.5.83}$$

The forcing term $\mathcal{D}_{22}$ vanishes because the symmetry properties (2.5.52) annihilates all the differences $\Delta(\cdot)$, $\Delta_0(\cdot)$ and the averages $\overline{(\cdot)}$ across the two sides of the gate. The forcing term $\mathcal{F}_{22}^{\pm}$ and $\mathcal{G}_{22}^{\pm}$ are even periodic functions of y, because each of the quadratic products is an even periodic function of y. Therefore $\mathcal{F}_{22}^{\pm}$ and $\mathcal{G}_{22}^{\pm}$ can also be expanded in Fourier cosine series:

$$\mathcal{F}_{22}^{\pm} \equiv \mathrm{i}\,\theta^2\left(-\frac{3}{G^2}\,f_{11}^{\pm^2} + f_{11}^{\pm}f_{11_{zz}}^{\pm} - 2f_{11_x}^{\pm^2} - 2f_{11_y}^{\pm^2}\right)_{z=0} =$$
$$\mathrm{i}\,\theta^2\sum_{p=0}^{\infty}\Gamma_p^{\pm}(x)\cos p\pi y \tag{2.5.84}$$

$$\mathcal{G}_{22}^{\pm} \equiv \pm\,\mathrm{i}\,\theta^2\left[-(z+h)\,f_{11_{xx}}^{\pm}q_{11} + f_{11_z}^{\pm}q_{11} - a\,q_{11}^2\right]_{x=0} =$$
$$\pm\,\mathrm{i}\,\theta^2\sum_{p=0}^{\infty}\Lambda_p^{\pm}(z)\cos p\pi y. \tag{2.5.85}$$

The expansion coefficients are real and are defined for $p = 0, 1, 2, \ldots$ as

$$\Gamma_p^{\pm}(x) = \epsilon_p \int_0^1 \mathrm{d}y \left(-\frac{3}{G^2} f_{11}^{\pm^2} + f_{11}^{\pm} f_{11_{zz}}^{\pm} - 2 f_{11_x}^{\pm^2} - 2 f_{11_y}^{\pm^2} \right)_{x=0} \cos p\pi y, \quad (2.5.86)$$

$$\Lambda_p^{\pm}(z) = \epsilon_p \int_0^1 \mathrm{d}y \left[-(z+h) f_{11_{xx}}^{\pm} q_{11} + f_{11_z}^{\pm} q_{11} - a\, q_{11}^2 \right]_{z=0} \cos p\pi y. \quad (2.5.87)$$

Here ϵ_p is the Jacobi symbol: $\epsilon_0 = 1$ and $\epsilon_p = 2$ for $p = 1, 2, \ldots$. We recall that $f_{11}^{\pm}$ and its derivatives are evaluated at $z = 0$ and $x = 0$ respectively in $\Gamma_p^{\pm}(x)$ and $\Lambda_p^{\pm}(z)$. Upon substitution in the above (2.5.86) (2.5.87) of the series expansions (2.5.48) for q_{11} and (2.5.50) for $f_{11}^{\pm}$ and usage of the orthogonality property of the cosine functions in the interval $y \in [0, 1]$, we can explicitly carry on the integration in y and obtain the following expressions for the expansion coefficients $\Gamma_p^{\pm}(x)$ and $\Lambda_p^{\pm}(z)$.

Forcing on the free surface:

$$\Gamma_p^{\pm}(x) = \sum_{q=-\infty, \neq 0}^{\infty} \sum_{m=0}^{\infty} \sum_{n=0}^{\infty} a_{pqmn}\, \mathrm{e}^{\mp(\alpha_{qm} + \alpha_{p+q,n})x}, \quad (2.5.88)$$

where the coefficients a_{pqmn} are

$$a_{pqmn} = \frac{\epsilon_p}{4} \beta_{qm} \beta_{p+q,n} \cosh K_m h \cosh K_n h \times \left[-\frac{3}{G^2} + K_n^2 - 2\alpha_{qm}\alpha_{p+q,n} - 2\pi^2 q(p+q) \right]. \quad (2.5.89)$$

Forcing on the gate surface:

$$\Lambda_p^{\pm}(z) = \frac{\epsilon_p}{4} \sum_{q=-\infty, \neq 0}^{\infty} b_{p+q} \left\{ -\frac{a}{2} b_q + \sum_{n=0}^{\infty} \beta_{qn} \times \left[K_n \sinh K_n(z+h) - (z+h)\alpha_{qn}^2 \cosh K_n(z+h) \right] \right\}. \quad (2.5.90)$$

Note that $\Lambda_p^+ \equiv \Lambda_p^-$, so we omit the $\pm$ superscripts and refer to both simply as Λ_p.

Because of the form of the forcing terms (2.5.84)(2.5.85), the solution of the potential and of the angular motion can be expressed in the form

$$\phi_{22}^{(\theta)^{\pm}} = \mathrm{i}\,\theta^2 f_{22}^{\pm}(x, y, z), \qquad \theta_{22}^{(\theta)} = \mathrm{i}\theta^2 q_{22}; \quad (2.5.91)$$

where q_{22} is a constant on each gate and $f_{22}^{\pm}(x, y, z)$ is complex since it represents not only the evanescent but also the propagating modes. Using the above expressions, θ^2 is factored out of the governing equations (2.5.26) to (2.5.31), and we get a boundary value problem for $f_{22}^{\pm}$

$$\nabla^2 f_{22}^{\pm} = 0 \qquad \text{in} \quad \Omega^{\pm}, \quad (2.5.92)$$

$$G f^{\pm}_{22_z} - 4 f_{22} = \sum_{p=0}^{\infty} \Gamma^{\pm}_p(x) \cos p\pi y \qquad z = 0, \tag{2.5.93}$$

$$f^{\pm}_{22_z} = 0 \qquad z = -h, \tag{2.5.94}$$

$$f^{\pm}_{22_x} - 2(z+h) q_{22} = \pm \sum_{p=0}^{\infty} \Lambda_p(z) \cos p\pi y \qquad x = 0, \tag{2.5.95}$$

$$-4\, I\, q_{22} + G\, C\, q_{22} = \mathrm{i}\, 2 \int_{y_1}^{y_2} \mathrm{d}y \int_{-h}^{0} \mathrm{d}z \, \{\Delta f_{22}(z+h)\} \qquad x = 0, \tag{2.5.96}$$

where

$$q_{22} = \left\{ \begin{array}{c} q^I \\ q^{II} \end{array} \right\}, \qquad \text{for} \quad \left\{ \begin{array}{l} 0 < y < 1 - r \\ 1 - r < y < 1 \end{array} \right. . \tag{2.5.97}$$

Let us expand $f^{\pm}_{22}$, q_{22} in Fourier series

$$f^{\pm}_{22} = \sum_{p=0}^{\infty} F^{\pm}_p(x, z) \cos p\pi y, \qquad q_{22} = \sum_{p=0}^{\infty} c_p \cos p\pi y, \tag{2.5.98}$$

with

$$c_0 = q^I(1-r) + q^{II} r, \qquad c_p = \left(q^I - q^{II}\right) \frac{\sin p\pi y}{p\pi} \tag{2.5.99}$$

Each Fourier coefficient of the above series (2.5.98) is the solution of the following reduced boundary value problem for $p = 0, 1, 2, \ldots$ in the xz plane

$$F^{\pm}_{p_{xx}} + F^{\pm}_{p_{zz}} - p^2\pi^2 F^{\pm}_p = 0 \qquad \text{in} \quad \Omega^{\pm}, \tag{2.5.100}$$

$$G F^{\pm}_{p_z} - 4 F^{\pm}_p = \Gamma^{\pm}_p(x) \qquad z = 0, \tag{2.5.101}$$

$$F^{\pm}_{p_z} = 0 \qquad z = -h, \tag{2.5.102}$$

$$F^{\pm}_{p_x} - 2(z+h)\, c_p = \pm \Lambda_p(z) \qquad x = 0, \tag{2.5.103}$$

and of the equation of motion (2.5.96). From the form of (2.5.100) to (2.5.103), we can anticipate the existence of plane propagating waves to $\pm\infty$ respectively, because of the forcing terms on the free surface $\Gamma^{\pm}_p$ and on the gate surface Λ_p.

With a view to simplifying the algebra and revealing the physics, we make the following decomposition:

$$F^{\pm}_p = F^{\pm S}_p + F^{\pm W}_p. \tag{2.5.104}$$

$F^{\pm S}_p$ is the solution of the following boundary value problem

$$F^{\pm\ S}_{p_{xx}} + F^{\pm\ S}_{p_{zz}} - p^2\pi^2 F^{\pm S}_p = 0 \qquad \text{in} \quad \Omega^{\pm}, \tag{2.5.105}$$

$$G F^{\pm S}_{p_z} - 4 F^{\pm S}_p = \Gamma^{\pm}_p(x) \qquad z = 0, \tag{2.5.106}$$

$$F^{\pm S}_{p_z} = 0 \qquad z = -h, \tag{2.5.107}$$

$$F^{\pm S}_{p_x} = 0 \qquad x = 0, \tag{2.5.108}$$

which corresponds to waves generated by an oscillating pressure on the free surface. On the other hand $F_p^{\pm W}$ is the solution of the wave–maker problem with stroke amplitude proportional to $2(z+h)\,c_p \pm \Lambda_p(z)$:

$$F_{p_{xx}}^{\pm\ W} + F_{p_{zz}}^{\pm\ W} - p^2\pi^2 F_p^{\pm W} = 0 \qquad \text{in} \quad \Omega^{\pm}, \tag{2.5.109}$$

$$GF_{p_z}^{\pm W} - 4F_p^{\pm W} = 0 \qquad z = 0, \tag{2.5.110}$$

$$F_{p_z}^{\pm W} = 0 \qquad z = -h, \tag{2.5.111}$$

$$F_{p_x}^{\pm W} = 2(z+h)c_p \pm \Lambda_p(z) \qquad x = 0. \tag{2.5.112}$$

The solution of these two linear inhomogenous problems can be obtained in terms of an eigenfunction expansion. Details are given in appendix B; here we present the final results.

Waves generated by forcing on the free surface, $F_p^{\pm S}$

$$F_p^{\pm S} = -\frac{1}{G}\sum_{l=0}^{\infty}\sum_{q=-\infty,\neq 0}^{\infty}\sum_{m=0}^{\infty}\sum_{n=0}^{\infty}\frac{\cosh K_l' h}{C_l'}\cosh K_l'(z+h)\times$$
$$\left[\mathrm{e}^{\mp(\alpha_{qm}+\alpha_{p+q,n})x} - \frac{\mathrm{i}}{\alpha_{pl}'}(\alpha_{qm}+\alpha_{p+q,n})\,\mathrm{e}^{\pm \mathrm{i}\,\alpha_{pl}' x}\right]\frac{a_{pqmn}}{(\alpha_{qm}+\alpha_{p+q,n})^2 + \alpha_{pl}'^{\,2}}. \tag{2.5.113}$$

In (2.5.113) K_l' is the wavenumber of the second harmonic and is given by

$$K_l' = \begin{cases} k' & \text{for } l = 0 \\ \mathrm{i}k_l' & \text{for } l = 1, 2, \ldots \end{cases}, \tag{2.5.114}$$

where k' is the real root of

$$4 = Gk' \tanh k'h, \tag{2.5.115}$$

and the k_l' are the real roots of

$$4 = -Gk_l' \tan k_l' h. \tag{2.5.116}$$

The coefficient C_l' has an expression similar to the first of (2.5.58)

$$C_l' = \int_{-h}^{0} \mathrm{d}z\, \cosh^2 K_l'(z+h) = h + \frac{G}{4}\sinh^2 K_l' h. \tag{2.5.117}$$

Finally, α'_{pl} is given by

$$\alpha'^2_{pl} = K'^2_l - p^2\pi^2. \tag{2.5.118}$$

Note that α_{pl}' is real not only for $p = 0$ and $l = 0$ ($\alpha_{00}' = k'$) but also for $p = 1, 2, \ldots, P$ and $l = 0$, $\alpha_{p0}' = \sqrt{k'^2 - p^2\pi^2}$, where P is the largest integer for which $k' > P\pi$; these cases correspond to one long crested propagating wave, α_{00}', and P short crested propagating wave, α_{p0}'. In the remaining cases α_{pl}' is imaginary: $\alpha_{p0}' = \mathrm{i}\sqrt{-k'^2 + p^2\pi^2}$

for $l = 0$ and $p = P+1, P+2, \ldots$, which represent short crested evanescent waves, and $\alpha'_{pl} = \mathrm{i}\sqrt{k'^2_l + p^2\pi^2}$ for $l = 1, 2, \ldots$ and $p = 0, 1, 2, \ldots$ corresponding to both long ($p = 0$) and short ($p = 1, 2, \ldots$) crested evanescent waves.

The first exponential function in (2.5.113) is always decaying as $x \to \pm\infty$ and consists of convolution products of the first order trapped wave with itself. This part of the solution is always real. The second exponential represents the waves associated with the roots of the second harmonic dispersion relation, K'_l: this second part of the solution is complex when α'_{pl} is real (propagating mode) and real when α'_{pl} is imaginary (evanescent mode). We remark that if G is sufficiently large (i.e. the dimensional eigenfrequency is sufficiently low), not only $k < \pi$ but also $k' < \pi$, which means $P = 0$, i.e. that there is only one propagating mode: the long crested $\alpha'_{00} \equiv K'_0 \equiv k'$.

Waves generated by forcing on the gate surface, $F_p^{\pm W}$

$$F_p^{\pm W} = -\mathrm{i}\sum_{l=0}^{\infty} \frac{\tilde{\Lambda}_{pl}}{\alpha'_{pl}} \cosh K'_l(z+h) \mathrm{e}^{\pm \mathrm{i}\,\alpha'_{pl}\,x}, \tag{2.5.119}$$

where

$$\tilde{\Lambda}_{pl} = \frac{\epsilon_p}{4C'_l} \sum_{q=-\infty,\neq 0}^{\infty} \left[-\frac{a\,b_q}{2K'_l} \sinh K'_l h + b_{p+q} \sum_{n=0}^{\infty} \beta_{qn} \left(C'_{nl} - \alpha^2_{qn} D'_{nl} \right) \right], \tag{2.5.120}$$

$$C'_{nl} = \int_{-h}^{0} \mathrm{d}z\, K_n \sinh K_n(z+h) \cosh K'_l(z+h) = \frac{1}{\left(K'^2_l - K^2_n\right)} \left[K^2_n + \left(\frac{4}{G^2} - K^2_n \right) \cosh K_n h \cosh K'_l h \right], \tag{2.5.121}$$

$$D'_{nl} = \int_{-h}^{0} \mathrm{d}z\, (z+h) \cosh K_n(z+h) \cosh K'_l(z+h) = \frac{1}{\left(K'^2_l - K^2_n\right)^2} \times \left\{ K^2_n + K'^2_l + \left[\frac{8}{G^2} - K^2_n - K'^2_l + \frac{3h}{G} \left(K'^2_l - K^2_n \right) \right] \cosh K_n h \cosh K'_l h \right\} \tag{2.5.122}$$

Note that for any n, l, p, not only C'_{nl} and D'_{nl}, but also (2.5.120) for $\tilde{\Lambda}_{pl}$ are real.

The angular displacement q_{22} is identically zero (with a nontrivial pressure and velocity fields, and a radiated wave!). This result can be obtained by inspection of the expressions of the forcing terms $\Gamma_p^{\pm}(x)$ and $\Lambda_p(z)$. Indeed the trapped wave solution (2.5.50)(2.5.51) is odd in x, the quadratic terms produce a forcing that is even in x on the free surface (see expression (2.5.88)), and odd in x on the gate surface (see expression (2.5.90); such a forcing therefore cannot produce any angular motion. A more detailed justification of this result, which employs the equation of motion of the

gate (2.5.96), is given in appendix B.

A straightforward application of Green's formula allows us to verify the correctness of expressions (2.5.113) and (2.5.119). Let $\partial\Omega^{\pm}$ be the boundary of $\Omega^{\pm}$ with outward normal $\vec{\mathbf{n}}$. Green's formula applied to $F_p^{\pm S}$ and $F_p^{\pm W}$ then yields:

$$\iint_{\Omega^{\pm}} \left[F_p^{\pm W}\left(\partial_{xx}+\partial_{zz}\right)F_p^{\pm S} - F_p^{\pm S}\left(\partial_{xx}+\partial_{zz}\right)F_p^{\pm W}\right]\mathrm{d}\Omega = \int_{\partial\Omega^{\pm}}\left[F_p^{\pm W}\frac{\partial F_p^{\pm S}}{\partial n} - F_p^{\pm S}\frac{\partial F_p^{\pm W}}{\partial n}\right]\mathrm{d}l. \tag{2.5.123}$$

Using the governing equations (2.5.105) to (2.5.108) for $F_p^{\pm S}$ and (2.5.109) to (2.5.112) for $F_p^{\pm W}$ (with $c_p = 0$) we obtain the identity:

$$\mp\frac{1}{G}\int_0^{\pm\infty}\mathrm{d}x\, F_p^{\pm W}(x,0)\,\Gamma_p^{\pm}(x) = \int_{-h}^{0}\mathrm{d}z\, F_p^{\pm S}(0,z)\,\Lambda_p(z). \tag{2.5.124}$$

It is easy to verify that the series (2.5.119), with coefficients given by (2.5.120), and the series (2.5.113) satisfy the above identity.

Finally, the complete expression of the second harmonic wave field forced by the trapped wave is:

$$\phi_{22}^{(\theta)\pm} = \mathrm{i}\,\theta^2 f_{22}^{\pm}(x,y,z), \qquad \theta_{22}^{(\theta)} = 0 \tag{2.5.125}$$

with

$$f_{22}^{\pm}(x,y,z) = -\sum_{p=0}^{\infty}\sum_{l=0}^{\infty}\sum_{q=-\infty,\neq 0}^{\infty}\sum_{m=0}^{\infty}\sum_{n=0}^{\infty}\frac{\cosh K_l' h}{G\,C_l'}\cosh K_l'(z+h)\,\cos p\pi y \times \frac{a_{pqmn}}{\left(\alpha_{qm}+\alpha_{p+q,n}\right)^2+{\alpha_{pl}'}^2}\left[\mathrm{e}^{\mp(\alpha_{qm}+\alpha_{p+q,n})x} - \frac{\mathrm{i}}{\alpha_{pl}'}\left(\alpha_{qm}+\alpha_{p+q,n}\right)\mathrm{e}^{\pm\mathrm{i}\,\alpha_{pl}' x}\right] - \mathrm{i}\sum_{p=0}^{\infty}\sum_{l=0}^{\infty}\frac{\tilde{\Lambda}_{pl}}{\alpha_{pl}'}\cosh K_l'(z+h)\,\cos p\pi y\,\mathrm{e}^{\pm\mathrm{i}\alpha_{pl}' x} \tag{2.5.126}$$

Note that the coefficient $\tilde{\Lambda}_{pl}$ in the above (2.5.126) is given by the double series (2.5.120), so the second summation on the right hand side (the wave maker solution) is a quadruple series; the convergence of the above series will be addressed later.

The solution for the forced wave (2.5.125) can also be sought with the aid of a Green's function rather than a direct eigenfunction expansion. We report the details of the procedure in appendix C.

Next we turn to the inhomogeneous solution for an incident wave from $x = +\infty$.

2.5.5.b Response to incident wave

This is a simple diffraction problem. The potential ϕ_{22}^I associated with an incident wave with free surface displacement in the x-z plane

$$\eta_{22}^I = \frac{A_2}{2} \mathrm{e}^{-\mathrm{i}K_0' x} \tag{2.5.127}$$

is

$$\phi_{22}^I = -\frac{\mathrm{i}GA_2}{4} \frac{\cosh K_0'(z+h)}{\cosh K_0' h} \mathrm{e}^{-\mathrm{i}K_0' x}, \tag{2.5.128}$$

where $K_0' = k'$ is the real root of the dispersion relation (2.5.115). The resulting wave field $\phi_{22}^{(A)}$ is governed by the following boundary value problem:

$$\phi_{22_{xx}}^{\pm\,(A)} + \phi_{22_{zz}}^{\pm\,(A)} = 0 \qquad \text{in} \quad \Omega^{\pm} \tag{2.5.129}$$

$$G\phi_{22_z}^{\pm\,(A)} - 4\phi_{22}^{\pm(A)} = 0 \qquad z = 0, \tag{2.5.130}$$

$$\phi_{22_z}^{\pm\,(A)} = 0 \qquad z = -h, \tag{2.5.131}$$

$$\phi_{22_x}^{+\,(A)} = 2\mathrm{i}(z+h)\theta_{22}^{(A)} - \phi_{22_x}^I \qquad x = 0^+ \tag{2.5.132}$$

$$\phi_{22_x}^{-\,(A)} = 2\mathrm{i}(z+h)\theta_{22}^{(A)} \qquad x = 0^-, \tag{2.5.133}$$

which must be solved together with the equation of motion of the gate

$$-4I\theta_{22}^{(A)} + GC\,\theta_{22}^{(A)} = \mathrm{i}2\int_{y_1}^{y_2} \mathrm{d}y \int_{-h}^{0} \mathrm{d}z \left\{ \left(\Delta\phi_{22}^{(A)} + \phi^I \right)(z+h) \right\} \qquad x = 0. \tag{2.5.134}$$

and a radiation condition at $\pm\infty$. The solution of (2.5.129) to (2.5.133), in terms of the set $\{Z_l'(z)\}$, is:

$$\phi_{22}^{+\,(A)} = \theta_{22}^{(A)} \sum_{l=0}^{\infty} \frac{D_l'}{K_l' C_l'} e^{\mathrm{i}K_l' x} \cosh K_l'(z+h) - \frac{\mathrm{i}GA_2}{4} \frac{\cosh K_0'(z+h)}{\cosh K_0' h} \mathrm{e}^{\mathrm{i}K_0' x} \tag{2.5.135}$$

and

$$\phi_{22}^{-\,(A)} = -\theta_{22}^{(A)} \sum_{l=0}^{\infty} \frac{D_l'}{K_l' C_l'} e^{-\mathrm{i}K_l' x} \cosh K_l'(z+h). \tag{2.5.136}$$

Note that only the first terms with $l = 0$ correspond to propagating waves. Substitution of the above expressions for $\phi_{22}^{\pm\,(A)}$ into the equation of motion (2.5.134) yields the forced angular motion $\theta_{22}^{(A)}$:

$$\theta_{22}^{(A)} = \frac{GD_0' A_2 / \cosh K_0' h}{-4I + GC + \sum_{l=0}^{\infty} \frac{8D_l'^2}{K_l' C_l'}} \tag{2.5.137}$$

Dropping the complex notation for K_l' and introducing the damping coefficient D and added inertia I_a as

$$D = \frac{4D_0'^2}{k'C_0'}, \qquad I_a = \sum_{l=1}^{\infty} \frac{2D_l'^2}{k_l'C_l'}, \tag{2.5.138}$$

the angular response can be rewritten as:

$$\theta_{22}^{(A)} = \frac{GD_0'A_2/\cosh K_0'h}{-4(I+I_a)+GC+2\,\mathrm{i}D}, \tag{2.5.139}$$

which is of the form of a linear oscillator with mass $I + I_a$, spring constant GC and damping (radiation) D. If we denote by Π the denominator (impedance) of (2.5.139)

$$\Pi = -4(I+I_a)+GC+2\mathrm{i}D, \tag{2.5.140}$$

the reflection and transmission coefficients R and T can be defined as

$$R = 1 + \frac{2\mathrm{i}D}{\Pi}, \qquad T = -\frac{2\mathrm{i}D}{\Pi}. \tag{2.5.141}$$

Let

$$E_l = \frac{8D_0'D_l'}{\Pi k_l'C_l'}, \qquad l = 1, 2, \ldots \tag{2.5.142}$$

then the potential assumes the expression

$$\phi_{22}^{+(A)} = -\frac{\mathrm{i}GA_2}{4\cosh K_0'h} \times \tag{2.5.143}$$

$$\left\{\cosh K_0'(z+h)\left(e^{-\mathrm{i}K_0'x} + Re^{\mathrm{i}K_0'x}\right) + \sum_{l=1}^{\infty} E_l \cosh K_l'(z+h)\, e^{\mathrm{i}K_l'x}\right\} \tag{2.5.144}$$

and

$$\phi_{22}^{-(A)} = -\frac{\mathrm{i}GA_2}{4\cosh K_0'h}\left\{\cosh K_0'(z+h)\,Te^{-\mathrm{i}K_0'x} - \sum_{l=1}^{\infty} E_l \cosh K_l'(z+h)\, e^{-\mathrm{i}K_l'x}\right\}. \tag{2.5.145}$$

The first two terms between parenthesis in (2.5.144) represent respectively the waves incoming from and reflected to ∞ (far field); the series is a local disturbance composed of evanescent modes. In expression (2.5.145) the first term is the transmitted wave propagating to $-\infty$ while the series is the local disturbance; note that the two series have the same value but opposite sign in points located symmetrically with respect to $x = 0$, i.e. the local oscillation is odd in x. It is remarkable that R and T satisfy the relations

$$|R|^2 + |T|^2 = 1 \qquad \text{and} \qquad R + T = 1. \tag{2.5.146}$$

In the following we express the solution (2.5.144)(2.5.145) as $\phi_{22}^{(A)} = \mathrm{i}A_2 g_{22}^{\pm}$ which defines $g_{22}^{\pm}$ as

$$g_{22}^{+} = -\frac{G}{4\cosh K_0' h}\left\{\cosh K_0'(z+h)\left(e^{-\mathrm{i}K_0' x} + Re^{\mathrm{i}K_0' x}\right) + \sum_{l=1}^{\infty} E_l \cosh K_l'(z+h)\, e^{\mathrm{i}K_l' x}\right\} \tag{2.5.147}$$

and

$$g_{22}^{-} = -\frac{G}{4\cosh K_0' h}\left\{\cosh K_0'(z+h)\, Te^{-\mathrm{i}K_0' x} - \sum_{l=1}^{\infty} E_l \cosh K_l'(z+h)\, e^{-\mathrm{i}K_l' x}\right\}. \tag{2.5.148}$$

Summing up, we write the total second order second harmonic solution for the potential as:

$$\phi_{22}^{\pm} = \phi_{22}^{(\theta)} + \phi_{22}^{(A)} \equiv \mathrm{i}\theta^2 f_{22}^{\pm}(x,y,z) + \mathrm{i}A_2 g_{22}^{\pm}(x,z). \tag{2.5.149}$$

The first part is forced by the trapped wave (to which radiation damping is associated) through quadratic nonlinearities, the second part is forced by the incident wave A_2. The angular motion θ_{22} is associated with the incident wave and is given by (2.5.139) which can be rewritten as

$$\theta_{22}^{(A)} = \mathrm{i}A_2 \frac{GD_0'/\cosh K_0' h}{\mathrm{i}\Pi}. \tag{2.5.150}$$

Recall that while q_{11} and $f_{11}^{\pm}$ are real functions, $f_{22}^{\pm}$, $g_{22}^{\pm}$ and q_{22} are complex.

The corresponding free surface displacement can be obtained from Bernouilli equation:

$$\eta_{22}^{\pm} = -\frac{\mathcal{B}_{22}^{\pm}}{G} = \frac{2\mathrm{i}}{G}\phi_{22}^{\pm} + \frac{\theta^2}{G}\left(2f_{11_z}^{\pm} e_{11}^{\pm} + |\nabla f_{11}^{\pm}|^2\right). \tag{2.5.151}$$

In particular the far field asymptotic expression of $\eta_{22}^{\pm}$, which involves only the propagating part of $\phi_{22}^{\pm}$ can be obtained by using (2.5.126), (2.5.144) and (2.5.145) evaluated at $z = 0$

$$\eta_{22}^{+} \sim -\frac{\mathrm{i}GA_2}{4}\left(e^{-\mathrm{i}K_0' x} + Re^{\mathrm{i}K_0' x}\right) - \theta^2 \sum_{p=0}^{P} \frac{1}{\alpha_{p0}'} \mathrm{e}^{\mathrm{i}\,\alpha_{p0}' x} \cosh K_0' h\, \cos p\pi y \times$$
$$\left[\sum_{q=-\infty,\neq 0}^{\infty} \sum_{m=0}^{\infty} \sum_{n=0}^{\infty} \frac{\cosh K_0' h}{G C_0'} \frac{a_{pqmn}\,(\alpha_{qm} + \alpha_{p+q,n})}{(\alpha_{qm} + \alpha_{p+q,n})^2 + {\alpha_{p0}'}^2} - \tilde{\Lambda}_{p0}\right] \tag{2.5.152}$$

and

$$\eta_{22}^{-} \sim -\frac{\mathrm{i}GA_2}{4} Te^{-\mathrm{i}K_0' x} - \theta^2 \sum_{p=0}^{P} \frac{1}{\alpha_{p0}'} \mathrm{e}^{-\mathrm{i}\,\alpha_{p0}' x} \cosh K_0' h\, \cos p\pi y \times$$

$$\left[\sum_{q=-\infty,\neq 0}^{\infty}\sum_{m=0}^{\infty}\sum_{n=0}^{\infty}\frac{\cosh K_0' h}{G C_0'}\frac{a_{pqmn}\left(\alpha_{qi}+\alpha_{p+q,n}\right)}{\left(\alpha_{qi}+\alpha_{p+q,n}\right)^2+{\alpha_{p0}'}^2}-\tilde{\Lambda}_{p0}\right]. \tag{2.5.153}$$

Thus away from the gates, the outgoing waves to $\pm\infty$ are the superposition of the incident, reflected and transmitted waves and the radiated waves generated nonlinearly by the trapped wave.

2.5.6 Third order, zeroth harmonic

The zeroth harmonic is not forced by the quadratic products $(2,1)\times(1,0)$ or $(2,1)\times(1,1)^*$. Because $(2,1)$ is zero (see section 2.5.3), the only forcing comes from $\partial_{t_2}(1,0)$. The zeroth harmonic forcing terms therefore are all null but for the free surface and the dynamics of the gates:

$$\mathcal{F}_{30}^{\pm}=0,\qquad \mathcal{B}_{30}^{\pm}=\phi_{10_{t_2}}^{\pm},\qquad \mathcal{G}_{30}^{\pm}=0, \tag{2.5.154}$$

$$\mathcal{D}_{30}=\int_{-h}^{0}\mathrm{d}z\left\{-\Delta\phi_{10_{t_2}}(z+h)\right\}=-\frac{h^2}{2}\Delta\phi_{10_{t_2}} \tag{2.5.155}$$

Using also the condition of periodicity, we deduce that $\phi_{30}^{\pm}$ depends only on the slow time t_2. On the free surface, a set-down $\eta_{30}^{\pm}$ is forced by the dynamic pressure

$$\eta_{30}^{\pm}=-\frac{1}{G}\phi_{10_{t_2}}^{\pm}; \tag{2.5.156}$$

the latter induces also a third order static angular displacement, as can be obtained from the equation of motion of the gate:

$$GC\theta_{30}=\int_{-h}^{0}\mathrm{d}z\,\mathcal{D}_{30}\quad\Longrightarrow\quad\theta_{30}=-\frac{h^2}{2GC}\Delta\phi_{10_{t_2}}. \tag{2.5.157}$$

2.5.7 Third order, first harmonic. Evolution equation

The first harmonic forcing terms are

$$\begin{aligned}\mathcal{F}_{31}^{\pm}=&-\Big[\left(-4\phi_{22_z}^{\pm}+G\phi_{22_{zz}}^{\pm}\right)\zeta_{11}^{*\pm}+\left(-\phi_{11_z}^{*\pm}+G\phi_{11_{zz}}^{*\pm}\right)\zeta_{22}^{\pm}+\\&\frac{1}{2}\left(-\phi_{11_{zz}}^{*\pm}+G\phi_{11_{zzz}}^{*\pm}\right)\zeta_{11}^{\pm^2}+\left(-\phi_{11_{zz}}^{\pm}+G\phi_{11_{zzz}}^{\pm}\right)|\zeta_{11}|^{\pm^2}-2\mathrm{i}\nabla\phi_{11}^{*\pm}\cdot\nabla\phi_{22}^{\pm}-\\&2\mathrm{i}\left(\nabla\phi_{11}^{\pm}\cdot\nabla\phi_{11}^{\pm}\right)_z\zeta_{11}^{*\pm}+\frac{1}{2}\nabla\phi_{11}^{*\pm}\cdot\nabla|\nabla\phi_{11}^{\pm}|^2+\nabla\phi_{11}^{\pm}\cdot\nabla\left(\nabla\phi_{11}^{\pm}\cdot\nabla\phi_{11}^{*\pm}\right)-\\&2\mathrm{i}\phi_{11_{t_2}}^{\pm}-2\omega_2\phi_{11}^{\pm}\Big]\end{aligned} \tag{2.5.158}$$

$$\mathcal{G}_{31}^{\pm}=(z+h)\left(\mathrm{i}\omega_2\theta_{11}-\theta_{11_{t_2}}+\theta_{11}^{*}\phi_{22_{xx}}^{\pm}+\theta_{22}\phi_{11_{xx}}^{*\pm}-\mathrm{i}|\theta_{11}|^2\theta_{11}+\theta_{11}^2\phi_{11_{xx}}^{*\pm}+\right.$$

$$2|\theta_{11}|^2\phi^{\pm}_{11_{zz}}\Big) + (z+h)^2\left(-\frac{1}{2}\theta_{11}^2\phi^{*\pm}_{11_{xxx}} - |\theta_{11}|^2\phi^{\pm}_{11_{xxx}}\right) \mp$$

$$\mathrm{i}a\theta^*_{11}\theta_{22} \mp a\,\frac{\theta_{11}^2}{2}\phi^{*\pm}_{11_{xx}} \mp a\,|\theta_{11}|^2\phi^{\pm}_{11_{xx}} - \theta^*_{11}\phi^{\pm}_{22_z} - \theta_{22}\phi^{*\pm}_{11_z} \tag{2.5.159}$$

$$\mathcal{D}_{31} = \int_{y_1}^{y_2}\mathrm{d}y\int_{-h}^{0}\mathrm{d}z\,\Big\{-\Big[\Delta\left(\nabla\phi^*_{11}\cdot\nabla\phi_{22}\right) + 3\mathrm{i}\theta_{11}^2 a\overline{\phi^*_{11_x}} - 6\mathrm{i}|\theta_{11}|^2 a\overline{\phi_{11_x}} + \mathrm{i}\theta_{11}^2\Delta\phi^*_{11} -$$

$$\mathrm{i}|\theta_{11}|^2\Delta\phi^*_{11} + \Delta\phi_{11_{t_2}} - \mathrm{i}\omega_2\Delta\phi_{11}\Big](z+h) - \Big[2\mathrm{i}\theta^*_{11}\Delta\phi_{22_x} + \mathrm{i}\theta_{22}\Delta\phi^*_{11_x} -$$

$$\frac{1}{2}\,\theta^*_{11}\Delta|\nabla\phi_{11}|^2_x - \theta^*_{11}\Delta\left(\nabla\phi_{11}\cdot\nabla\phi^*_{11}\right)_x\Big](z+h)^2 - \frac{\mathrm{i}}{2}\,\theta_{11}^2\Delta\phi^*_{11_{xx}}(z+h)^3 -$$

$$4\mathrm{i}\theta^*_{11}a\overline{\phi_{22}} + 2\mathrm{i}\theta_{22}a\overline{\phi^*_{11}} + a\theta^*_{11}\,\overline{|\nabla\phi_{11}|^2} + 2a\theta_{11}\,\overline{\nabla\phi_{11}\cdot\nabla\phi^*_{11}}\Big\} -$$

$$\int_{y_1}^{y_2}\mathrm{d}y\,\Big\{\,\mathrm{i}h\Delta_0\left(\phi^*_{11}\zeta_{22}\right) + 2\mathrm{i}\,h\Delta_0\left(\phi_{22}\zeta^*_{11}\right) - 2\mathrm{i}\,\theta^*_{11}a\overline{(\phi_{11}\zeta^*_{11} - \phi^*_{11}\zeta_{11})^0} -$$

$$\frac{\mathrm{i}}{2}\,h\Delta_0\left(\phi^*_{11_z}\zeta^2_{11}\right) + \mathrm{i}h\Delta_0\left(\phi_{11_z}|\zeta_{11}|^2\right) - \frac{\mathrm{i}}{2}\Delta_0\left(\phi^*_{11}\zeta^2_{11}\right) + \mathrm{i}\Delta_0\left(\phi_{11}|\zeta_{11}|^2\right) -$$

$$G\left[h\,\Delta\left(\zeta^*_{11}\zeta_{22}\right) + \Delta|\zeta_{11}|^2\zeta_{11} - a\theta^*_{11}\,\overline{\zeta^2_{11}} - 2a\theta_{11}\,\overline{|\zeta_{11}|^2} - \frac{h^2}{2}\theta^*_{11}\Delta\left(\zeta^2_{11}\right)_x -\right.$$

$$\left.h^2\theta_{11}\Delta\left(|\zeta_{11}|^2\right)_x\right] - \mathrm{i}h^2\theta^*_{11}\Delta_0\left(\phi_{11}\zeta_{11}\right)_x - \mathrm{i}h^2\theta_{11}\Delta_0\left(\phi_{11}\zeta^*_{11} - \phi^*_{11}\zeta_{11}\right)_x -$$

$$2\mathrm{i}\,\theta^*_{11}a\overline{(\phi_{11}\zeta_{11})^0} - \frac{h}{2}\,\Delta_0\left(|\nabla\phi_{11}|^2\zeta^*_{11}\right) - h\Delta_0\left(\nabla\phi_{11}\cdot\nabla\phi^*_{11}\,\zeta_{11}\right)\Big\} +$$

$$\frac{G}{2}\left[5ah^2\left(y_2-y_1\right) + S\right]|\theta_{11}|^2\theta_{11} + 2\mathrm{i}I\theta_{11_{t_2}} + 2\omega_2 I\theta_{11}, \tag{2.5.160}$$

The nontrivial solution of the homogeneous problem for $\phi^{\pm}_{31}$ is the trapped mode $\phi^{\pm}_{11}$. It is necessary therefore to impose a solvability condition. To do so we apply Green's formula to $\phi^{\pm}_{11}$ and $\phi^{\pm}_{31}$ in both domains $\Omega^{\pm}$ defined by the half modal period:

$$\iiint_{\Omega^{\pm}}\left(\phi^{\pm}_{11}\nabla^2\phi^{\pm}_{31} - \phi^{\pm}_{31}\nabla^2\phi^{\pm}_{11}\right)\mathrm{d}\Omega = \iint_{\partial\Omega^{\pm}}\left(\phi^{\pm}_{11}\frac{\partial\phi^{\pm}_{31}}{\partial n} - \phi^{\pm}_{31}\frac{\partial\phi^{\pm}_{11}}{\partial n}\right)\mathrm{d}S. \tag{2.5.161}$$

Using the governing equations for $\phi^{\pm}_{11}$ and $\phi^{\pm}_{31}$

$$0 = \mp\int_0^1\mathrm{d}y\int_{-h}^{0}\mathrm{d}z\,\left\{\phi^{\pm}_{11}\left[\mathrm{i}(z+h)\theta_{31} + \mathcal{G}^{\pm}_{31}\right] - \phi^{\pm}_{31}\left[\mathrm{i}(z+h)\theta_{11}\right]\right\} \pm$$

$$\frac{1}{G}\int_0^{\pm\infty}\mathrm{d}x\int_0^1\mathrm{d}y\,\phi^{\pm}_{11}\,\mathcal{F}^{\pm}_{31}, \tag{2.5.162}$$

and summing up the two expressions, we get

$$0 = \frac{1}{G}\int_0^1\mathrm{d}y\,\left\{\int_{-\infty}^{0}\mathrm{d}x\,\phi^{-}_{11}\,\mathcal{F}^{-}_{31} + \int_0^{\infty}\mathrm{d}x\,\phi^{+}_{11}\,\mathcal{F}^{+}_{31}\right\} - \int_0^1\mathrm{d}y\int_{-h}^{0}\mathrm{d}z\,\Delta\left(\phi_{11}\mathcal{G}_{31}\right) -$$

$$\mathrm{i}\int_0^1\mathrm{d}y\int_{-h}^{0}\mathrm{d}z\,\left[\Delta\phi_{11}\theta_{31} - \Delta\phi_{31}\theta_{11}\right](z+h). \tag{2.5.163}$$

On the right hand side of the last integral, θ_{31} and $\phi_{31}^{\pm}$ are still unknown. We now resort to the equation of motion of the gates. Let θ_{31} be given by

$$\theta_{31} = \left\{ \begin{array}{c} \theta_{31}^{I} \\ \theta_{11}^{II} \end{array} \right\}, \qquad \text{for} \quad \left\{ \begin{array}{l} 0 < y < 1-r \\ 1-r < y < 1 \end{array} \right. . \tag{2.5.164}$$

Multiplication of the first order first harmonic parts of (2.5.60) by θ_{31} yields respectively for gates one and two

$$(-I + GC)\,\theta_{11}^{I}\theta_{31}^{I} = \mathrm{i}\int_{0}^{1-r}\mathrm{d}y\int_{-h}^{0}\mathrm{d}z\left\{\Delta\phi_{11}\theta_{31}^{I}(z+h)\right\}, \tag{2.5.165}$$

$$\frac{r}{1-r}\,(-I + GC)\,\theta_{11}^{II}\theta_{31}^{II} = \mathrm{i}\int_{1-r}^{1}\mathrm{d}y\int_{-h}^{0}\mathrm{d}z\left\{\Delta\phi_{11}\theta_{31}^{II}(z+h)\right\}, \tag{2.5.166}$$

Similarly, multiplying (2.5.31) for ($n = 3$, $m = 1$) harmonic multiplication by θ_{11} yields respectively for gates one and two

$$(-I + GC)\,\theta_{31}^{I}\theta_{11}^{I} = \mathrm{i}\int_{0}^{1-r}\mathrm{d}y\int_{-h}^{0}\mathrm{d}z\left\{\Delta\phi_{31}\theta_{11}^{I}(z+h)\right\} + \mathcal{D}_{31}^{I}\theta_{11}^{I}, \tag{2.5.167}$$

$$\frac{r}{1-r}\,(-I + GC)\,\theta_{31}^{II}\theta_{11}^{II} = \mathrm{i}\int_{1-r}^{1}\mathrm{d}y\int_{-h}^{0}\mathrm{d}z\left\{\Delta\phi_{31}\theta_{11}^{II}(z+h)\right\} + \mathcal{D}_{31}^{II}\theta_{11}^{II}, \tag{2.5.168}$$

where $\mathcal{D}_{31}^{I}$ and $\mathcal{D}_{31}^{II}$ represent expression (2.5.160) for gate one and gate two respectively, i.e. for $y_1 = 0$, $y_2 = 1-r$ and for $y_1 = 1-r$, $y_2 = 1$.

Subtracting the sum of (2.5.167) and (2.5.168) from the sum of (2.5.165) and (2.5.166) gives

$$0 = \mathrm{i}\int_{0}^{1}\mathrm{d}y\int_{-h}^{0}\mathrm{d}z\,\left[\Delta\phi_{11}\theta_{31} - \Delta\phi_{31}\theta_{11}\right](z+h) - \mathcal{D}_{31}^{I}\theta_{11}^{I} - \mathcal{D}_{31}^{II}\theta_{11}^{II}. \tag{2.5.169}$$

The first integral on the right hand side is exactly the last integral of the Green's formula (2.5.163). Hence the latter can be expressed in terms of only the forcing terms of the (3,1) harmonic:

$$0 = \frac{1}{G}\int_{0}^{1}\mathrm{d}y\left\{\int_{-\infty}^{0}\mathrm{d}x\,\phi_{11}^{-}\mathcal{F}_{31}^{-} + \int_{0}^{\infty}\mathrm{d}x\,\phi_{11}^{+}\mathcal{F}_{31}^{+}\right\} - \int_{0}^{1}\mathrm{d}y\int_{-h}^{0}\mathrm{d}z\,\Delta\,(\phi_{11}\mathcal{G}_{31}) - \mathcal{D}_{31}\theta_{11}, \tag{2.5.170}$$

where $\mathcal{D}_{31}\theta_{11}$ means the summation $\mathcal{D}_{31}^{I}\theta_{11}^{I} + \mathcal{D}_{31}^{II}\theta_{11}^{II}$.

Using expressions (2.5.48) and (2.5.50) respectively for θ_{11} and $\phi_{11}^{\pm}$, we can simplify the amplitude of the trapped wave θ and obtain

$$0 = \frac{1}{G}\int_{0}^{1}\mathrm{d}y\left\{\int_{-\infty}^{0}\mathrm{d}x\,f_{11}^{-}\mathcal{F}_{31}^{-} - \int_{0}^{\infty}\mathrm{d}x\,f_{11}^{+}\mathcal{F}_{31}^{+}\right\} - 2\int_{0}^{1}\mathrm{d}y\int_{-h}^{0}\mathrm{d}z\,\overline{f_{11}\mathcal{G}_{31}} + \mathrm{i}\,\mathcal{D}_{31}\,q_{11}, \tag{2.5.171}$$

where now $\mathcal{D}_{31}q_{11}$ means the summation $\mathcal{D}_{31}^{I} + \mathcal{D}_{31}^{II}\,(1 - 1/r)$.

Using the expressions for the forcing terms we carry out the surface integrals on

the right hand side of (2.5.171). Such integrals are computationally involved because they contain terms which consist of up to a sevenfold series (quadratic products of first order trapped wave and second order forced wave). It is possible though to simplify much further the expressions of the forcing terms by systematically making use of the governing equation and boundary conditions at first and second order. In the following we outline the procedure. Consider the first two surface integrals on the right hand side involving $\mathcal{F}_{31}^{\pm}$. We first substitute $\zeta_{nm}^{\pm} = -\mathcal{B}_{nm}^{\pm}/G$ for $n = 1$, $m = 1$ and $n = 2$, $m = 2$ so that $\mathcal{F}_{31}^{\pm}$ is expressed in terms of the velocity potential only. For the same harmonics, Laplace equation is used to substitute $\phi_{nm_{zz}}^{\pm} = -\phi_{nm_{xx}}^{\pm} - \phi_{nm_{zz}}^{\pm}$, and the boundary condition on the free surface is used to substitute $\phi_{nm_z}^{\pm} = \phi_{nm}^{\pm}/G + \mathcal{F}_{nm}^{\pm}/G$. In such a way the z derivatives of all orders (i.e. the derivatives orthogonal to the plane of integration) disappear from the expression of $\mathcal{F}_{31}^{\pm}$. In the second surface integral we proceed similarly: for $n = 1$, $m = 1$ and $n = 2$, $m = 2$, we first use Laplace equation to write $\phi_{nm_{xx}}^{\pm} = -\phi_{nm_{yy}}^{\pm} - \phi_{nm_{zz}}^{\pm}$, then make repeated use of the boundary condition on the gate surface $\phi_{nm}^{\pm} = \mathrm{i}m(z+h)\theta_{nm} + \mathcal{G}_{nm}^{\pm}$. In such a way the x derivatives are eliminated from the expression of $\mathcal{G}_{31}^{\pm}$. In the expression of $\mathcal{D}_{31}$ we proceed in the same manner as for $\mathcal{G}_{31}^{\pm}$ and eliminate $\zeta_{nm}^{\pm}$ through Bernoulli equation. Note that $\mathcal{D}_{31}$ is itself composed of an integral in z from $-h$ to 0 and a part evaluated at $z = 0$, as can be seen in (2.5.160): the second and third integrals on the right hand side are therefore both on the gate surface. We then substitute the expressions

$$\phi_{11}^{\pm} = \mp \mathrm{i}\,\theta f_{11}^{\pm}(x,y,z) \quad \text{and} \quad \phi_{22}^{\pm} = \mathrm{i}\theta^2 f_{22}^{\pm}(x,y,z) + \mathrm{i}A_2 g_{22}^{\pm}(x,z). \tag{2.5.172}$$

Since $f_{11}^{\pm}$ has the symmetry property (2.5.52), so does the second harmonic forced by the trapped wave: $f_{22}^{\pm}(x,y,z) = f_{22}^{\pm}(-x,y,z)$, as can be deduced from expression (2.5.126). Such properties decrease further the computational domain: indeed whenever $g_{22}^{\pm}$ is not present, i.e. in all but the terms involving A_2, the integration can be carried in Ω^+ only and the result multiplicated by 2.

Carrying out the integrals, the right hand side of (2.5.171) becomes

$$\begin{aligned}\frac{1}{G}\int_0^1 \mathrm{d}y \left\{\int_{-\infty}^0 \mathrm{d}x\, f_{11}^- \mathcal{F}_{31}^- - \int_0^\infty \mathrm{d}x\, f_{11}^+ \mathcal{F}_{31}^+\right\} - 2\int_0^1 \mathrm{d}y \int_{-h}^0 \mathrm{d}z\, \overline{f_{11}\mathcal{G}_{31}} + \mathrm{i}\,\mathcal{D}_{31}\, q_{11} = \\ c\left\{-\theta_{t_2} + \mathrm{i}\omega_2\theta + \mathrm{i}\theta^2\theta^*\,(c_N + \mathrm{i}\,c_R) + \mathrm{i}A_2\theta^*\,c_F\right\},\end{aligned} \tag{2.5.173}$$

which, upon multiplication by i and division by c, gives finally the evolution equation

$$-\mathrm{i}\theta_{t_2} = \omega_2\theta + \theta^2\theta^*\,(c_N + \mathrm{i}\,c_R) + A_2\theta^*\,c_F. \tag{2.5.174}$$

The coefficients c_N, c_R, c_F represents respectively nonlinearity, radiation damping and forcing by the incident wave. Their complete expressions can be found in appendix C. They are respectively composed of an integral on the free surface, on the gate surface and on the water line $x = 0$, $z = 0$. Both c and c_F can be evaluated an-

alytically in a straightforward manner. The evaluation of c_N and c_R is instead much more algebraically involved since it contains the products of f_{22}^+ and f_{11}^+: numerical integration is used, which is computationally less demanding than the summation of the series that would result from an explicit integration.

In summary, we have found the evolution equation which describes the evolution of the amplitude of the trapped wave θ for a given incident wave amplitude A_2. All the coefficients c to c_F depend on the nondimensional thickness (a) and inertial (M, S, I) characteristics of the gate both explicitly (c, c_N and c_R) and implicitly through G. The dependence on the nondimensional water depth h is present in all coefficients, both explicitly and implicitly, through G. Therefore for a given incident wave amplitude, we can parametrically deduce all quantities of interest. This will be pursued in the next section. The result of a sample numerical calculation of c, c_N, c_R, c_F for fixed water depth, $h = 1$, and varying a, $S = 0.65I$ is shown in figure 2-12. The coefficient c does not vary significally with S, I and a and is always nonzero. Note that the computation for $a = 0.1$ ends at $S_{max} = ah^2(1 - r)/\alpha = 0.153$, the value of the first moment that renders zero the buoyancy C. The coefficients c_N, c_R, c_F decrease with increasing S, I and decreasing a. It is noteworthy that as the inertia of the gate increases, radiation damping decreases, (c_R in figure 2-12), together with the forcing efficiency (c_F in figure 2-12). This will be analyzed in the next section.

It is straightforward to recover the evolution equation in terms of the physical variables. Multiplication of (2.5.174) by ϵ^3 yields an evolution equation for the complex amplitude of the angular motion in radians, θ'

$$-\frac{\mathrm{i}}{\omega_0}\theta'_{t'} = \frac{\Delta\omega}{\omega_0}\theta' + \theta'^2\theta'^* (c_N + \mathrm{i}\, c_R) + \frac{A'}{b'}\theta'^* c_F. \qquad (2.5.175)$$

where we recall t' is time measured in seconds, b', A' are modal period and incident wave amplitude measured in meters.

Finally, we assess for mode 1 the numerical convergence of the values of the coefficients of the evolution equation, c_N, c_R, c_F. In figure 2-13, the four coefficients are plotted versus the number of terms kept in all the series expansions (2.5.50) (2.5.149) with (2.5.126) and (2.5.144) and (2.5.145) of the potential ϕ_{11}, ϕ_{22}. The parameters are $a = 0.2$, $h = 1.0$, $S = 0.015$, $I = 0.015$. All the coefficients reach a final value for large enough m. The slowest convergence is presented by c_N which becomes stable when at least 20 terms are kept. This is no surprise, since c_N is obtained by integration on the boundary of all the evanescent terms from $p = P + 1$ to $p = \infty$ of the second harmonic f_{22} (see expression (2.5.126)). The computation of this coefficient is a demanding numerical task since it requires the pointwise evaluation on the boundary of a 5 fold series, i.e. the sum of 20^5 products for each grid point.

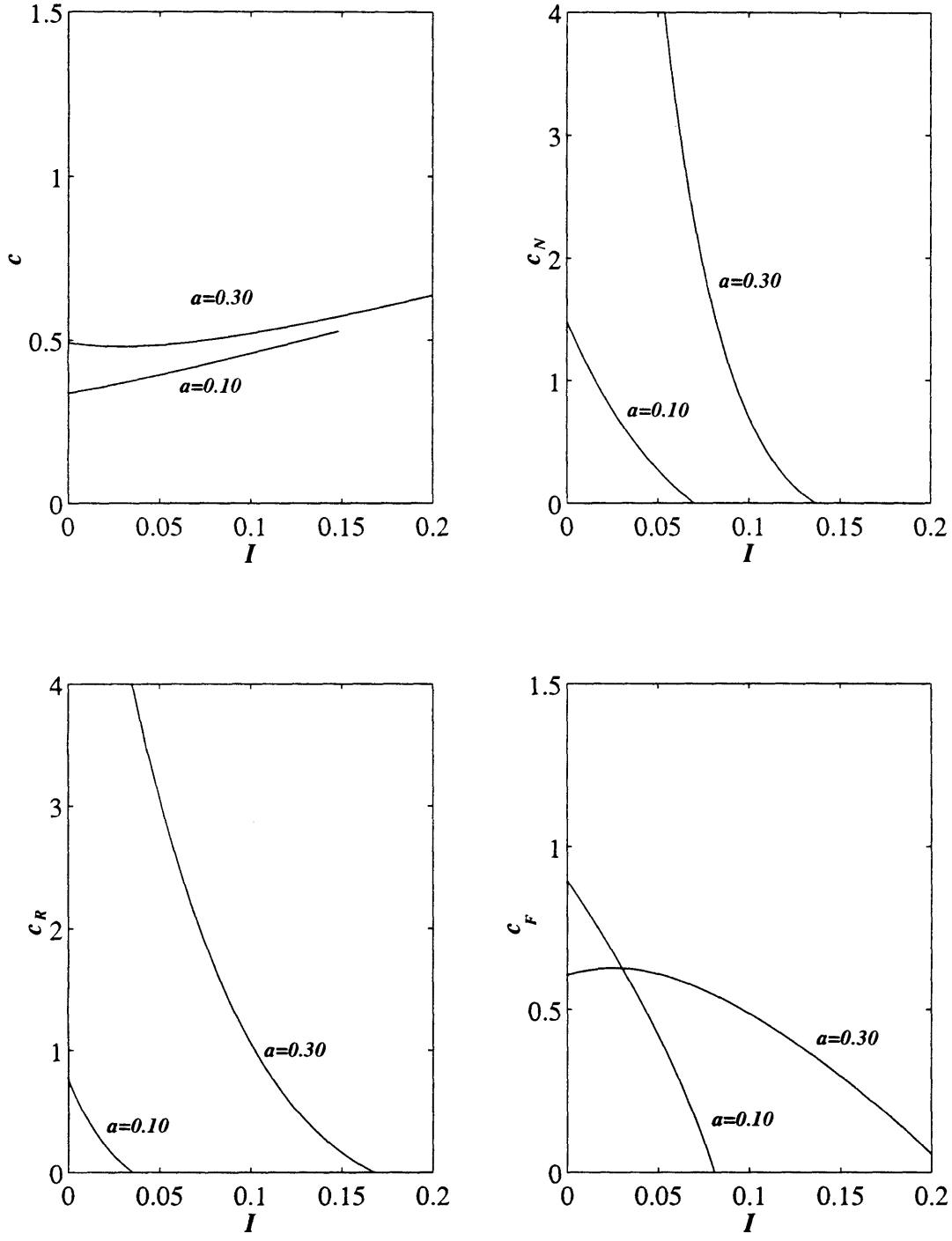

Figure 2-12: Coefficients of the evolution equations for fixed $h = 1$ and varying $S = 0.65I$; $a = 0.1$ and 0.3

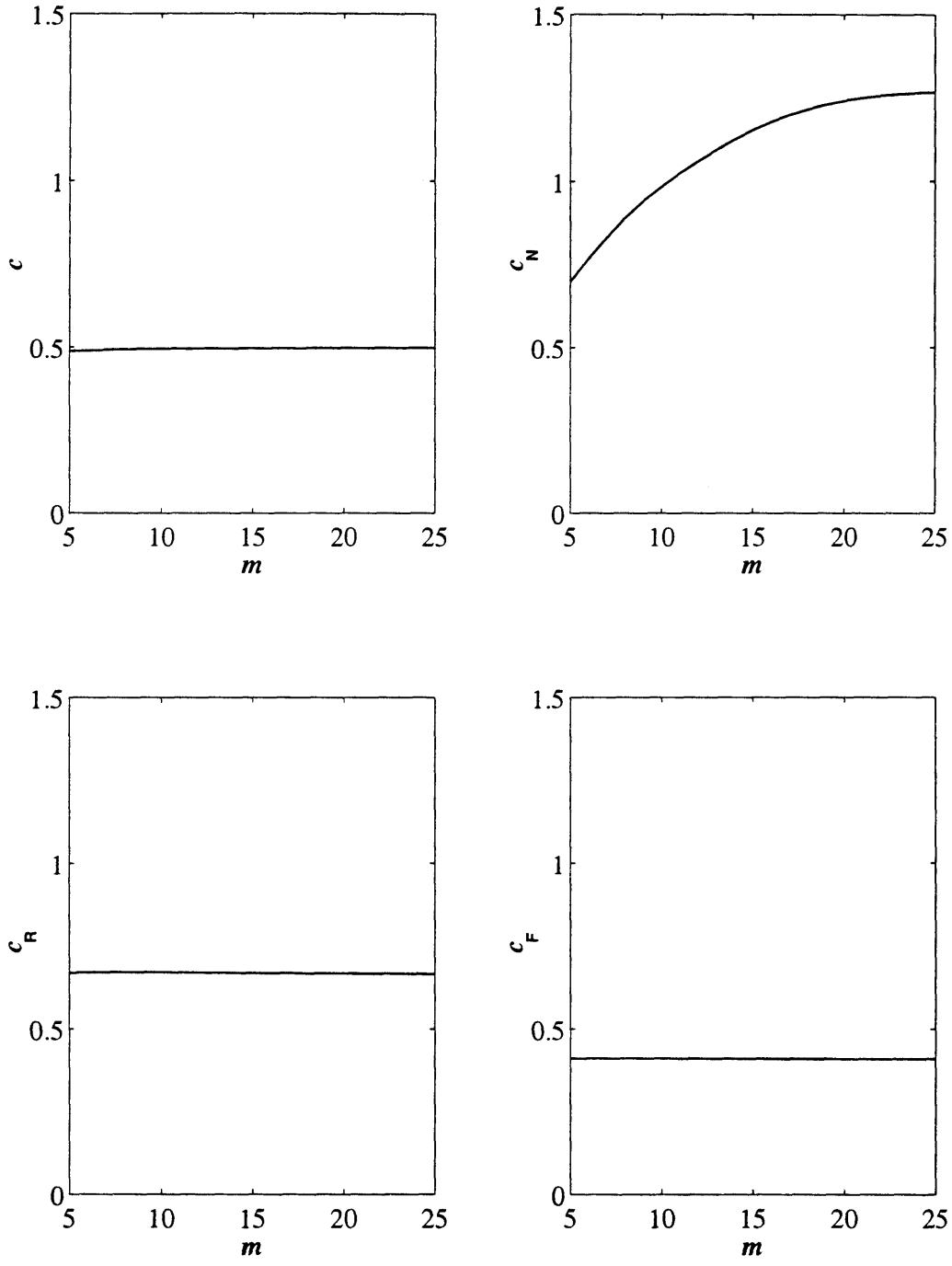

Figure 2-13: Sample of numerical tests of the convergence of all the coefficients of the evolution equation

2.6 Effects of gate and channel characteristics on steady resonance - preliminary deductions

As a preliminary analysis of the evolution equation we first examine the equilibrium amplitude of resonated mode $|\theta|_0$. By setting $\partial_{t_2} = 0$ in (2.5.174) we get

$$\omega_2\theta + \theta^2\theta^* \ (c_N + \mathrm{i}c_R) + A_2\theta^* \, c_F = 0, \tag{2.6.1}$$

which can be solved for $|\theta|^2$

$$|\theta|_0^2 = \frac{1}{{c_N}^2 + {c_R}^2}\left[\sqrt{({c_N}^2 + {c_R}^2)\left(c_F A_2\right)^2 - \left(c_R\omega_2\right)^2} - c_N\omega_2\right]. \tag{2.6.2}$$

By letting

$$\frac{\partial|\theta|_0^2}{\partial\omega_2} = 0, \tag{2.6.3}$$

we find the maximum angular displacement of the resonated trapped wave

$$|\theta|_{0_{max}} = \sqrt{\frac{c_F}{c_R}}\, A_2, \tag{2.6.4}$$

which does not occur at perfect resonance ($\omega_2 = 0$), but for a lower incident wave frequency with detuning

$$\omega_2 = -\frac{c_N c_F}{c_R}\, A_2. \tag{2.6.5}$$

Thus for a given incident wave A_2, the smaller the square root of c_F/c_R reduces the resonated amplitude. We refer to the square root of the ratio c_F/c_R as the amplification factor; it represents the result of the balance between the forcing by the incident wave, c_F, and the radiation damping, c_R. Expressions (2.6.4), (2.6.5) show that c_N affects the frequency at which the maximum response is attained but not the resonant amplitude itself.

The second information of engineering interest is the width of the frequency band in which linear instability occurs. A small interval would render the resonance less likely to be observable. In the early experiments Mei*etal*(1994) found that some configurations with small thickness a and large inertia I could not be resonated. On the other hand thicker gates (larger a with styrofoam additions) are easily resonated for a relatively large bandwidth of frequencies. Suggested by these experimental observations, we examine the theoretical interval of instability of the trapped wave.

Consider a complex perturbation $\Delta\theta = \Delta X + \mathrm{i}\Delta Y$ of the null solution $\theta = 0$, with $|\Delta\theta| \ll 1$. The linearized system governing ΔX, ΔY can be obtained from (2.5.174)

after separating real and imaginary parts

$$\frac{\mathrm{d}}{\mathrm{d}t_2}\Delta X = (c_F A_2 - \omega_2)\,\Delta Y, \tag{2.6.6}$$

$$\frac{\mathrm{d}}{\mathrm{d}t_2}\Delta Y = (c_F A_2 + \omega_2)\,\Delta X. \tag{2.6.7}$$

Therefore, unbounded exponential growth occurs whenever

$$(c_F A_2)^2 - \omega_2^2 > 0, \tag{2.6.8}$$

i.e. for a given wave amplitude A_2, whenever the frequency detuning $|\omega_2|$ is smaller than $c_F A_2$. Thus for a given incident wave, the smaller c_F reduces the bandwidth of linear instability. We refer at c_F also as the bandwidth of instability.

Guided by this preliminary analysis, we discuss the dependencies of the ratio $\sqrt{c_F/c_R}$ (amplification factor) and of c_F (bandwidth of instability) on the gate and channel properties, following the same path of section 2.5.2 for G.

In figures 2-14 and 2-15 the water depth is fixed, $h = 1$, and first and second moment of inertia S, I are increased from zero. Different values of a are tested, 0.05, 0.10, 0.15, 0.20, 0.30. The amplification factor versus the inertia I, with $S = 0.65I$, is plotted in figure 2-14. The dependence is similar to the dependence of G of figure 2-2. For $I \to 0$ the amplification factor approaches a finite value. For increasing value of the inertia, the factor also increases and becomes unbounded as $S \to ah^2(1-r)$. Therefore, the heavier the gate, not only the longer the natural period, but also the larger the angular response. Heavier gates oscillates slower and with larger amplitude! For any fixed value of the inertia (fixed abscissa in figure 2-14), an increase in a induces a decrease in the response. Referring to figure 2-15, let us choose a value of a. As the inertia increases, (the response increases) the bandwidth of instability decreases. It eventually becomes zero when the natural period and the angular response become infinite! So, for fixed displaced volume ah, heavier gates have a larger resonant response which is however more difficult to excite. For any fixed value of the inertia (fixed abscissa in figure 2-15), an increase in a induces an increase in the bandwidth of instability. This explains the difficulty of resonating the heavier gates for the experiments described in figure 1-5. For example, the third curve (empty triangles) had $I \simeq 0.06$ and $a \simeq 0.11$; around $h' = 0.38$ m, i.e. $h = 1$, the gate could hardly be resonated. The representative point in figure 2-2 falls in the region of very small bandwidth of instability. It also explains why the addition of styrofoam rendered the resonance more easily observable: the extra pieces increased the value of a leaving the inertia moments S and I almost unchanged, i.e. increased the bandwidth of instability.

The same features seen for mode 1 are observed for mode 2 in figures 2-16 and 2-16. Each curve of figure 2-16 is lower than the corresponding one in figure 2-14;

hence, for the same parameters, the amplification factor is always smaller than the one of mode 1. The maximum opening between neighboring gates is attained if mode 1 rather than mode 2 is excited. No sensible difference is observed in the size of the bandwidth of instability.

In the second set of computations the thickness a is kept constant and the dependence on I and S for different water depths h is tested. In figures 2-18 and 2-19 the width a is fixed at 0.2. Each curve is for a fixed value of h and increasing values of I (and S). The trend is the same as in figures 2-14, 2-15 for fixed h, increasing I and various a. The amplification factor increases with increasing I and is smaller for larger water depth h (the larger the displaced volume ah, the smaller the response). On the other hand, the bandwidth of instability decreases with increasing I and is larger for larger h. Therefore, if the goal is to maximize the features of the phenomenon, as in a laboratory experiment, the optimal gate should have small inertia and large buoyancy ah, which confirms early experimental findings. More delicate is the choice that minimize the phenomenon, since smaller response is associated with larger instability bandwidth and viceversa.

The same features seen for mode 1 are observed for mode 2 in figures 2-20 and 2-21. The angular response for the same set of parameters is smaller than the one attained in mode 1, while the bandwidth of instability is hardly changed.

Suggestions have been made to increase the width of the prototype gates b' with the intent of increasing the natural period $\sqrt{G}$ and shifting it outside the range of the periods of the local incident gravity waves. Such decrease in $a = a'/b'$, $h = h'/b'$, $S' = S/\rho b'^3$ and $I' = I/\rho b'^4$ should lead to the desired goal, as can be seen in all figures 2-2 2-3 2-4 2-4. The present nonlinear instability analysis shows that, because of the strong decrease in I and S, such a gain might come with an undesired increase of both the angular response and the bandwidth of instability.

To gain more insight, we now fix the inertia moments S and I and evaluate the combined change in a and h. We recall that, in dimensional variables, this can be obtained only by leaving the modal semi–period b' fixed and changing the thickness a' and water depth h'. In figure 2-22 a contour and 3D plots of the amplification factor are presented. It is confirmed that as the displaced volume ah decreases the same inertia give a higher response. On the other hand, more voluminous gates, larger a' in deeper water h', have a smaller response. Conversely, it is reconfirmed in figure 2-23 that for more voluminous gates the bandwidth of instability is larger, while it approaches zero for skinnier gates, so that a very large response is less likely to be excited. The contour plot shows that there is an optimum buoyancy ah^2 that renders maximum the bandwidth of instability.

Mode 2 has features similar to mode 1, but has smaller amplification factor, as can be seen by comparing figure 2-24 for mode 2 with figure 2-22 for mode 1. An optimal shape that maximize the bandwidth of instability is present also for mode 2.

When the inertia is larger, in order for the mode to be possible, larger a' and h'

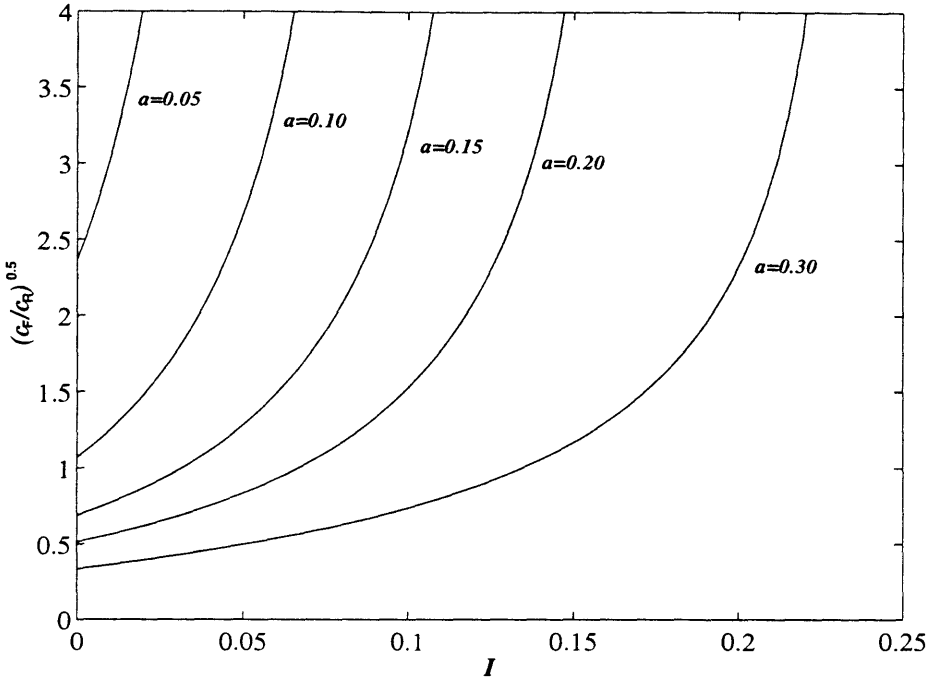

Figure 2-14: Amplification factor of mode 1 for $h = 1$ and varying a, I and $S = 0.65I$.

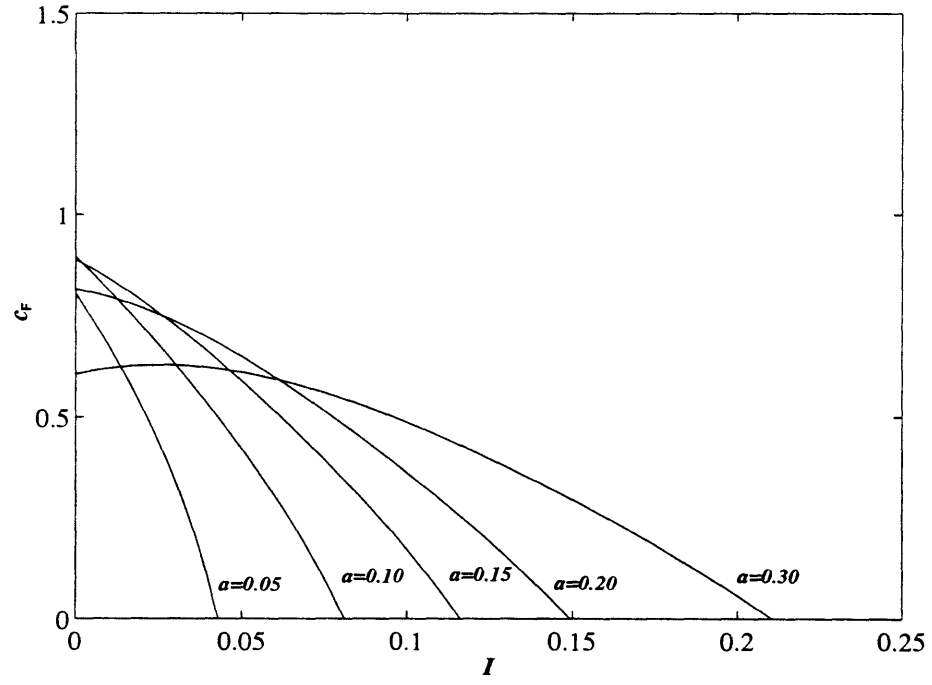

Figure 2-15: Bandwidth of instability of mode 1 for $h = 1$ and varying a, I and $S = 0.65I$.

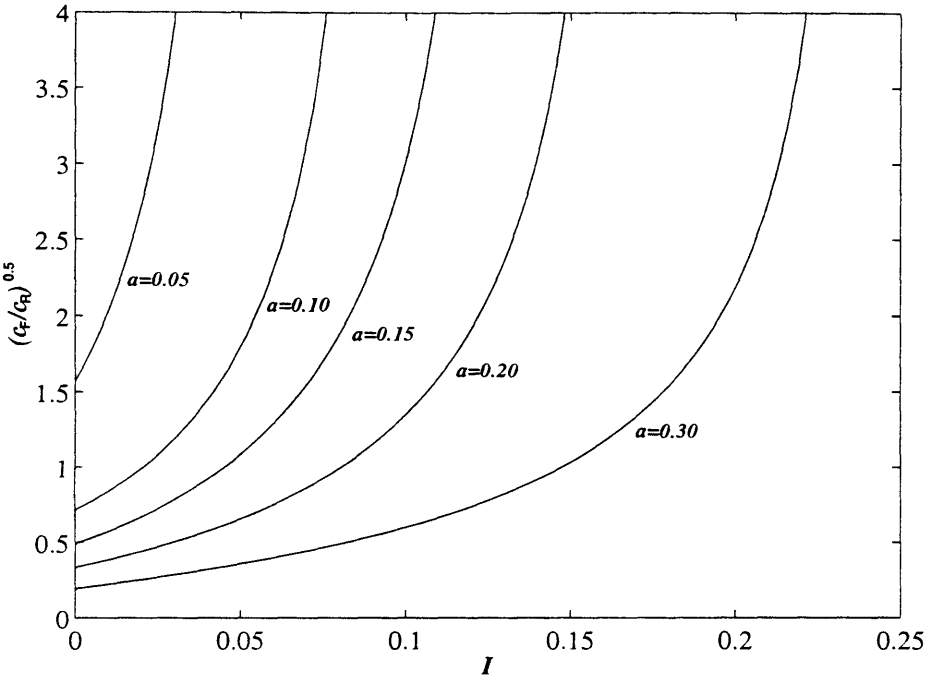

Figure 2-16: Amplification factor of mode 2 for $h = 1$ and varying a, I and $S = 0.65I$.

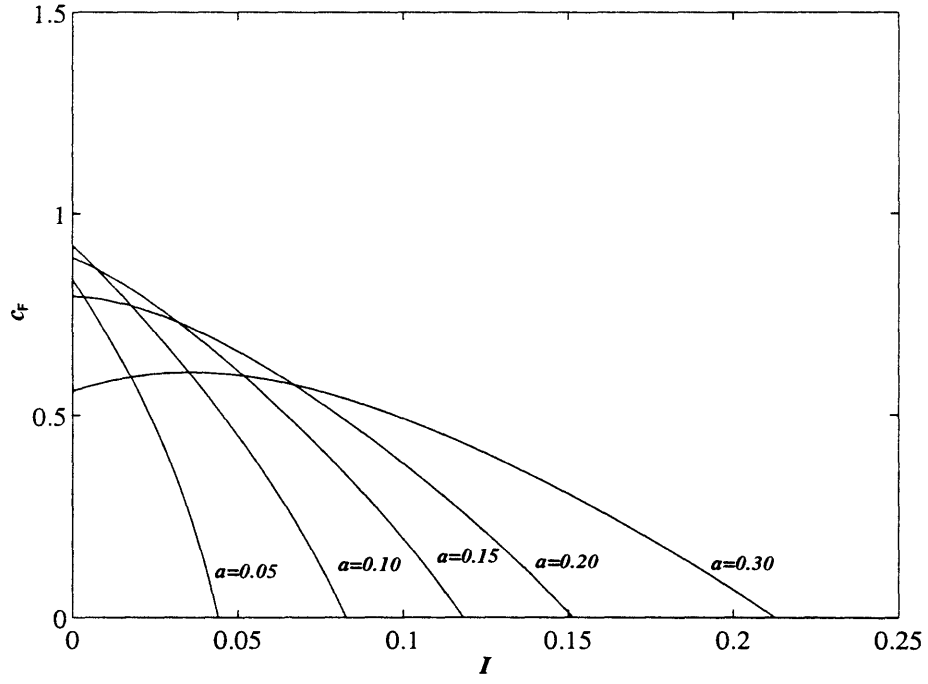

Figure 2-17: Bandwidth of instability of mode 2 for $h = 1$ and varying a, I and $S = 0.65I$.

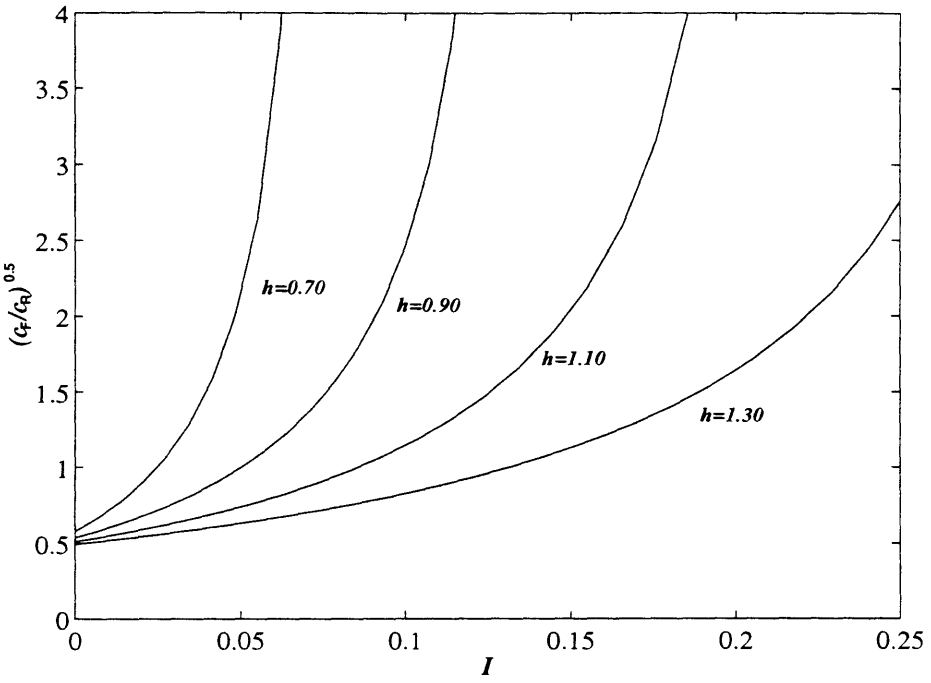

Figure 2-18: Amplification factor of mode 1 for $a = 0.2$ and varying h, I and $S = 0.65I$.

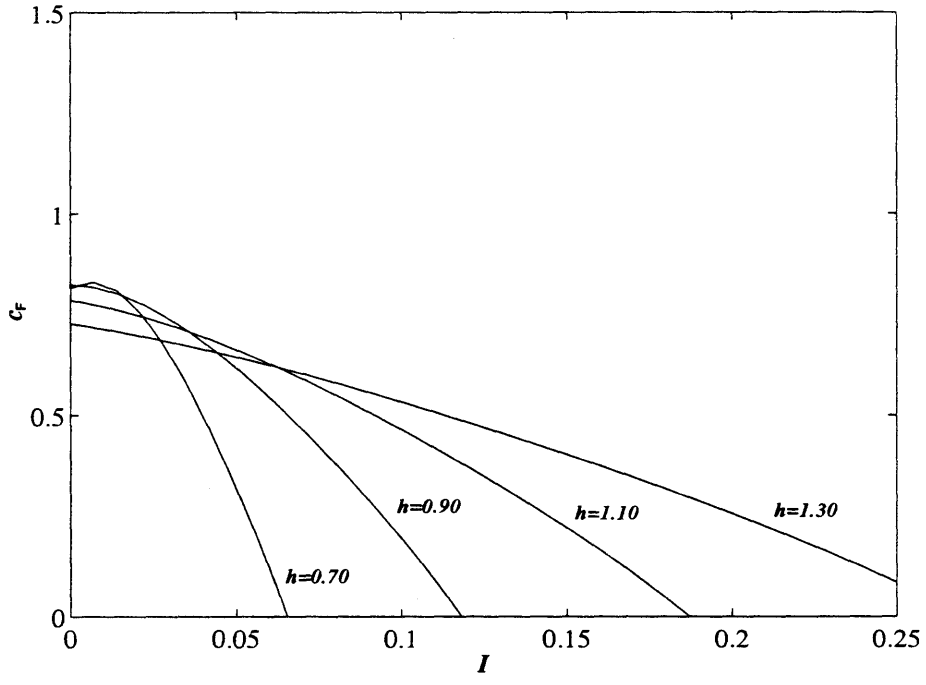

Figure 2-19: Bandwidth of instability of mode 1 for $a = 0.2$ and varying h, I and $S = 0.65I$.

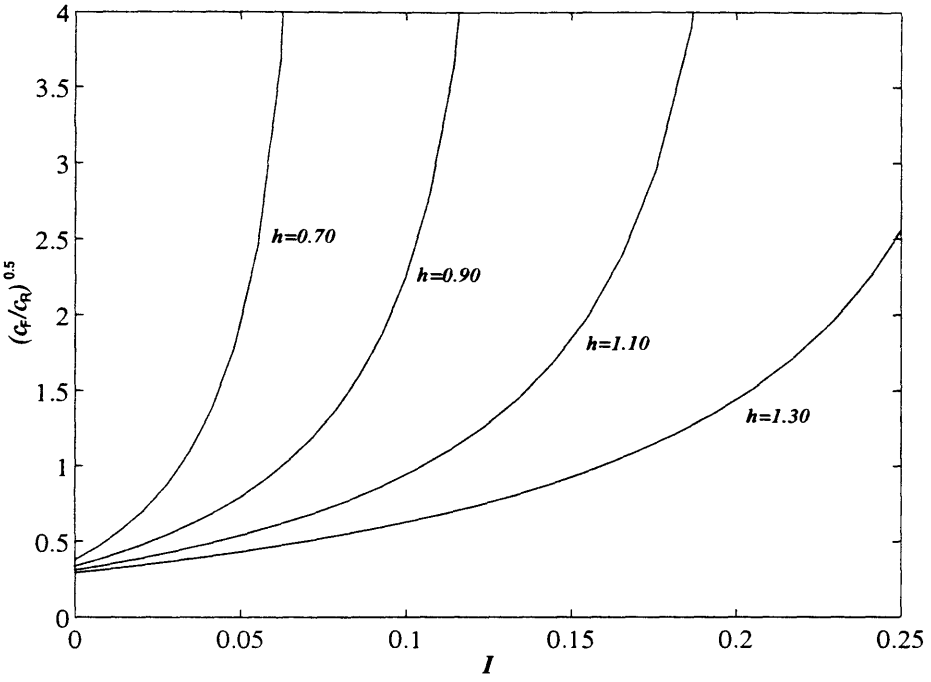

Figure 2-20: Amplification factor of mode 2 for $h = 1$ and varying h, I and $S = 0.65I$.

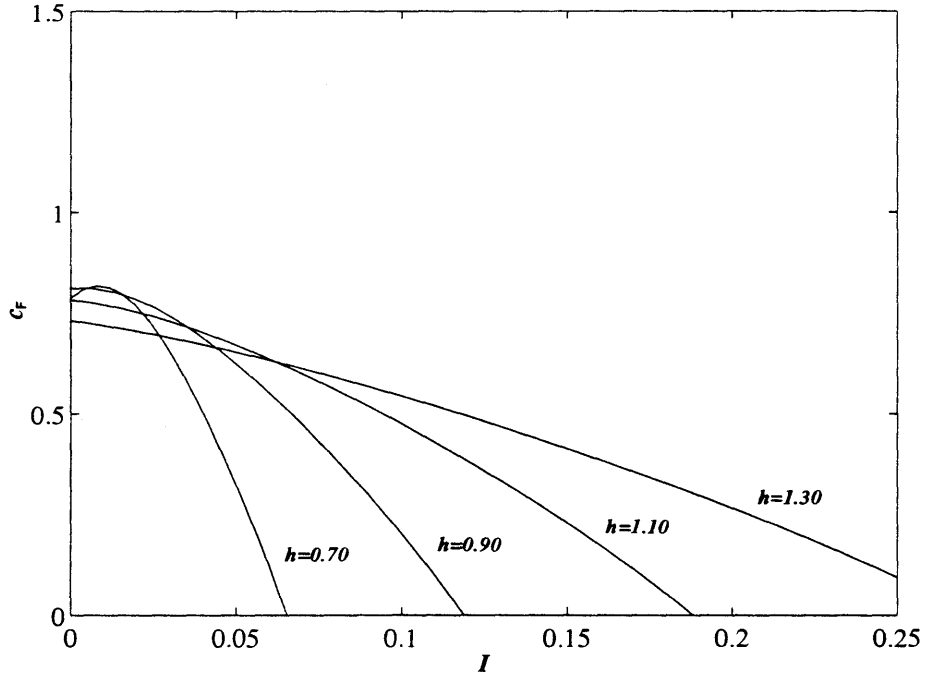

Figure 2-21: Bandwidth of instability of mode 2 for $h = 1$ and varying h, I and $S = 0.65I$.

ranges must be considered (as a rule of thumb, heavier gates need more volume for their dynamical equilibrium). This is seen in figures 2-26 to 2-29 where the inertia moments are chose to be $S = 0.1$ and $I = 0.1$. Figures 2-26 and 2-27 show the amplification factor and the bandwidth of instability for mode 1, while 2-28 and 2-29 are for mode 2. Even for this larger values of the inertia, amplification factor is slightly smaller for mode 2 and the bandwidth of instability presents a maximum.

2.7 On the gaps next to the flume walls

We assess the wall gap effect, peculiar to the laboratory experiments in the wave channel. Consider the experimental setup of figure 1-4, which models the half period b' of the modal shape of mode 1. For construction reasons two gaps of width s' exist between the walls and the gates, at $y' = 0$ and $y' = b'$. These two gaps must not be confused with the structural gaps between one gate and the other, of which only one is present at $y' = b'/2$.

Associated with the trapped mode oscillation, on the $\pm$ sides of the gates, the free surface oscillates out of phase by π (as can be deduced from (2.5.51)) with an associated oscillating pressure difference. Thus, the pressure difference forces a flux between the wall gaps, as is schematically indicated in figure 2-30. Note that the pressure difference is maximum exactly in correspondence of the wall gaps and is zero at the structural gap at $y' = b'/2$. The alternating jets along the two walls do not radiate any waves and therefore do not cause any radiation damping of the motion. This result is a simple consequence of the wave maker theory. Indeed, the long-crested radiated wave has amplitude β_{00} proportional to the mean velocity distribution across the channel

$$\beta_{00} = \int_0^{b'} \mathrm{d}y'\, U(y') = Us' - Us' = 0. \tag{2.7.1}$$

Besides, the short-crested wave are all evenescent because the jets oscillate at the frequency of the trapped wave, which by definition is composed by only evanescent modes.

Hence, the wave field generated by this velocity distribution is made entirely by short-crested evanescent modes. The only effect of these jets is to decrease the added inertia. This can be seen from at the expression of the potential $\Phi_g^{\pm} = \phi_g^{\pm} \exp(-it) + *$ generated by the alternating fluxes supposed constant through the water depth

$$\phi_g^{\pm} = \mp sU \sum_{m=0}^{\infty} \sum_{n=0}^{\infty} \frac{4 \sinh K_n h}{\alpha_{2m+1,n} C_n K_n} \cos(2m+1)\pi y \, \cosh K_n(z+h)\, \mathrm{e}^{\mp \alpha_{2m+1,n} x}, \tag{2.7.2}$$

where $s = s'/b' \ll 1$ is the nondimensional gap width. The integral of the pressure force of the gate system, would give an added inertia of the form sI_{a_g}, with $I_{a_g} = O(1)$. Now, in the experiments, $s = 0.007 \sim O(\epsilon^3)$; the inertia effect is therefore small and

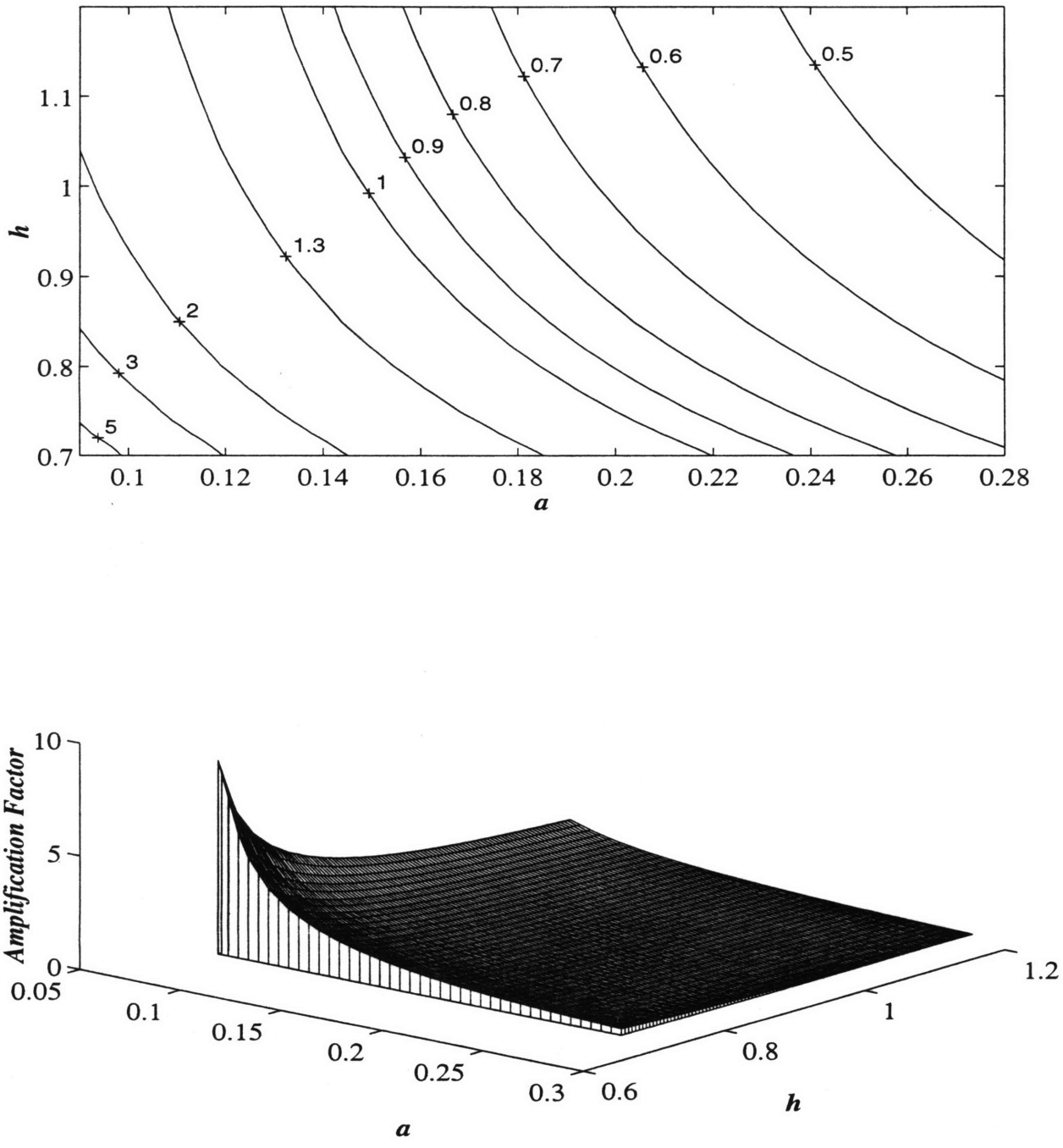

Figure 2-22: Contour and 3D plots of the amplification factor for fixed inertia moments $I = 0.03$, $S = 0.02$ and varying a and h; mode 1

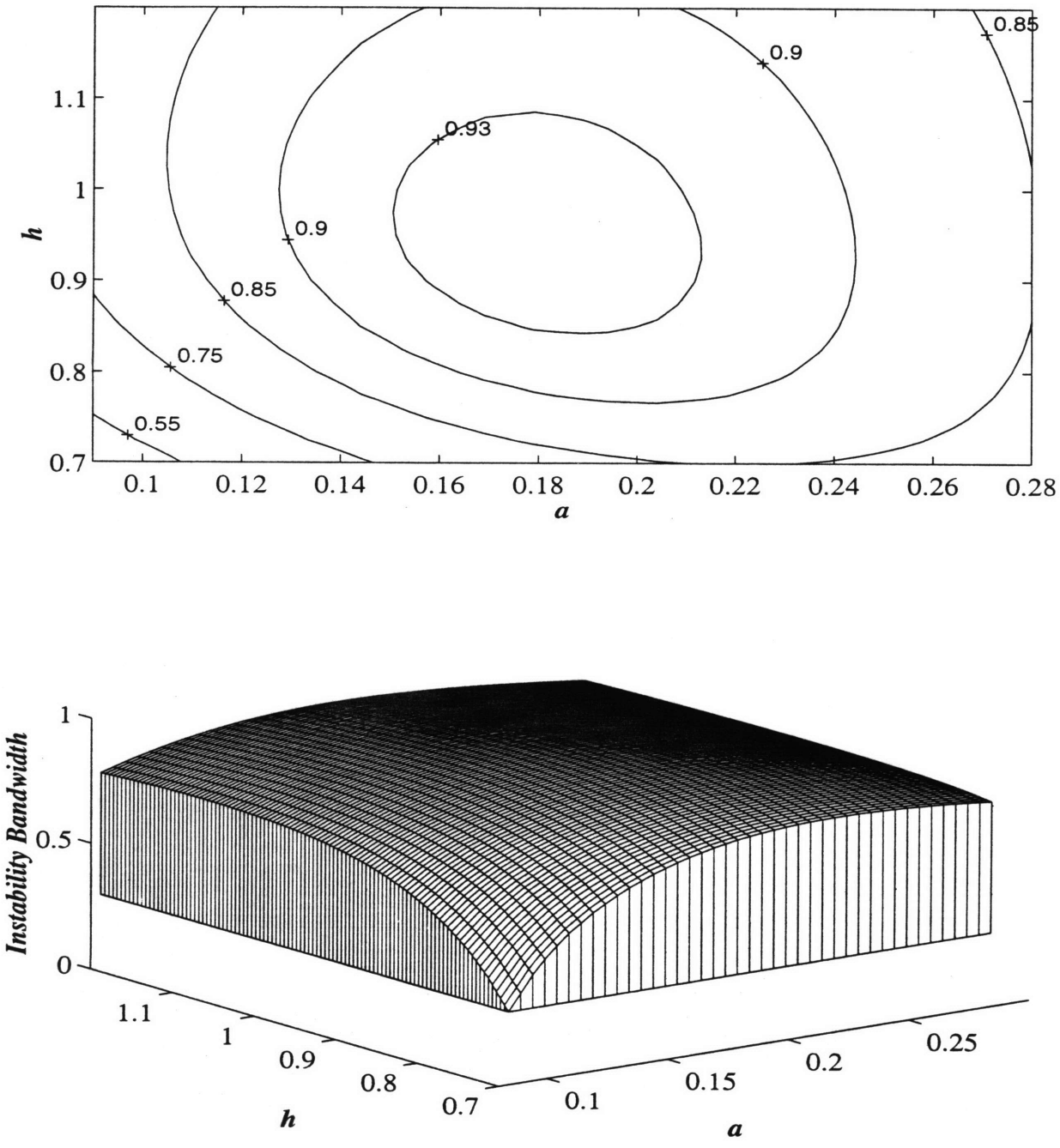

Figure 2-23: Contour and 3D plots of the bandwidth of instability for fixed inertia moments $I = 0.03$, $S = 0.02$ and varying a and h; mode 1

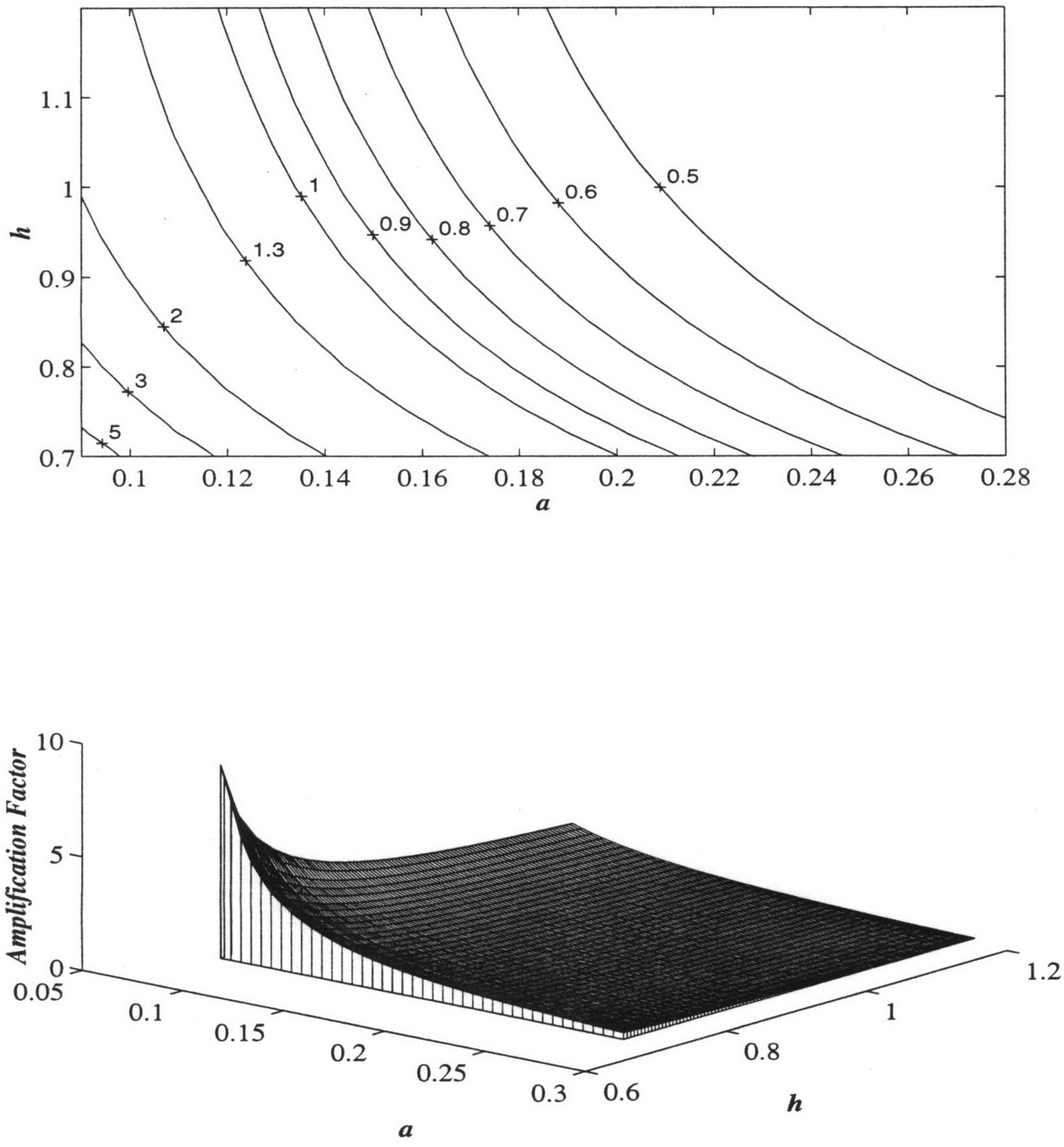

Figure 2-24: Same as figure 2-22 but for mode 2

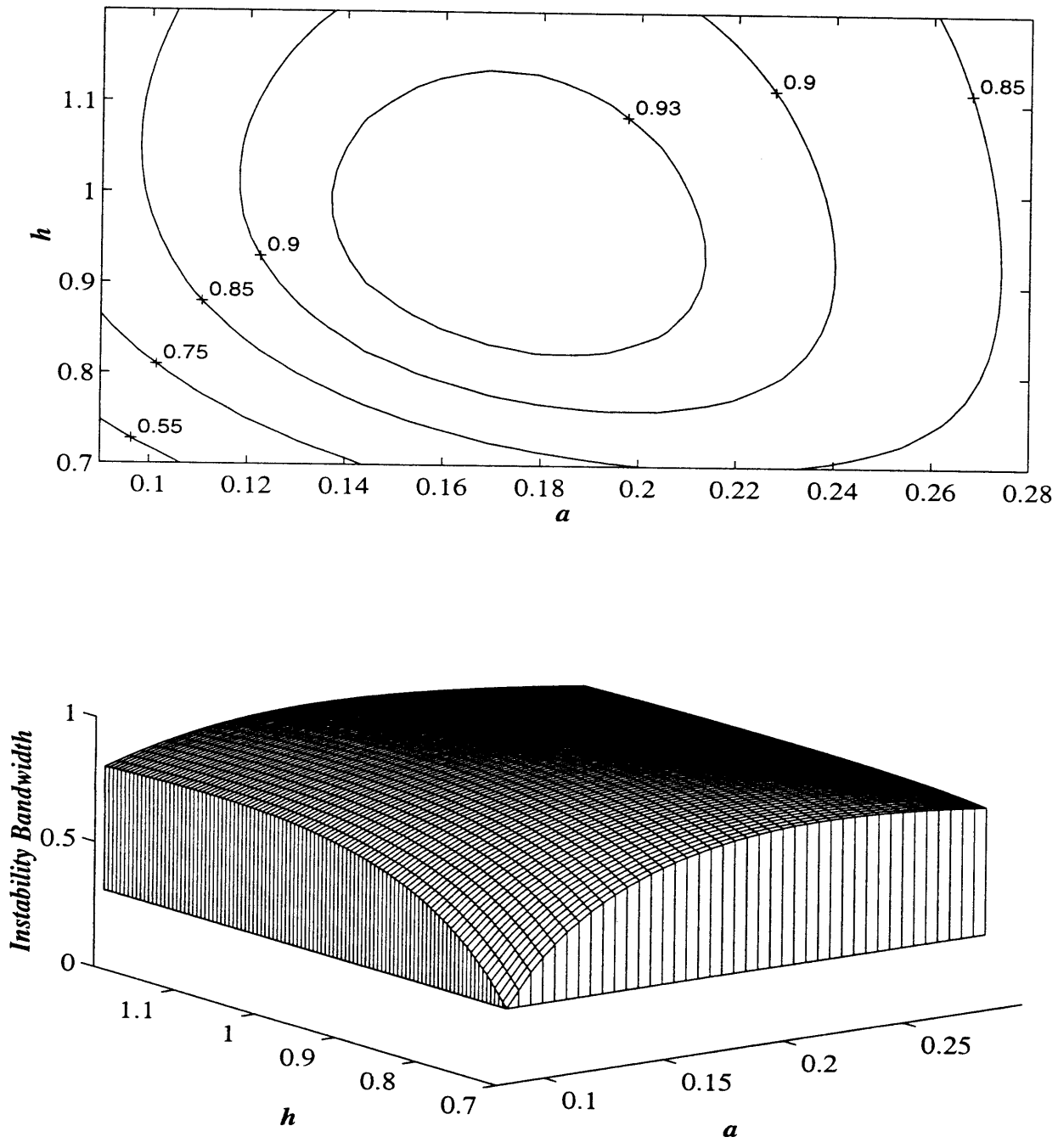

Figure 2-25: Same as figure 2-23 but for mode 2

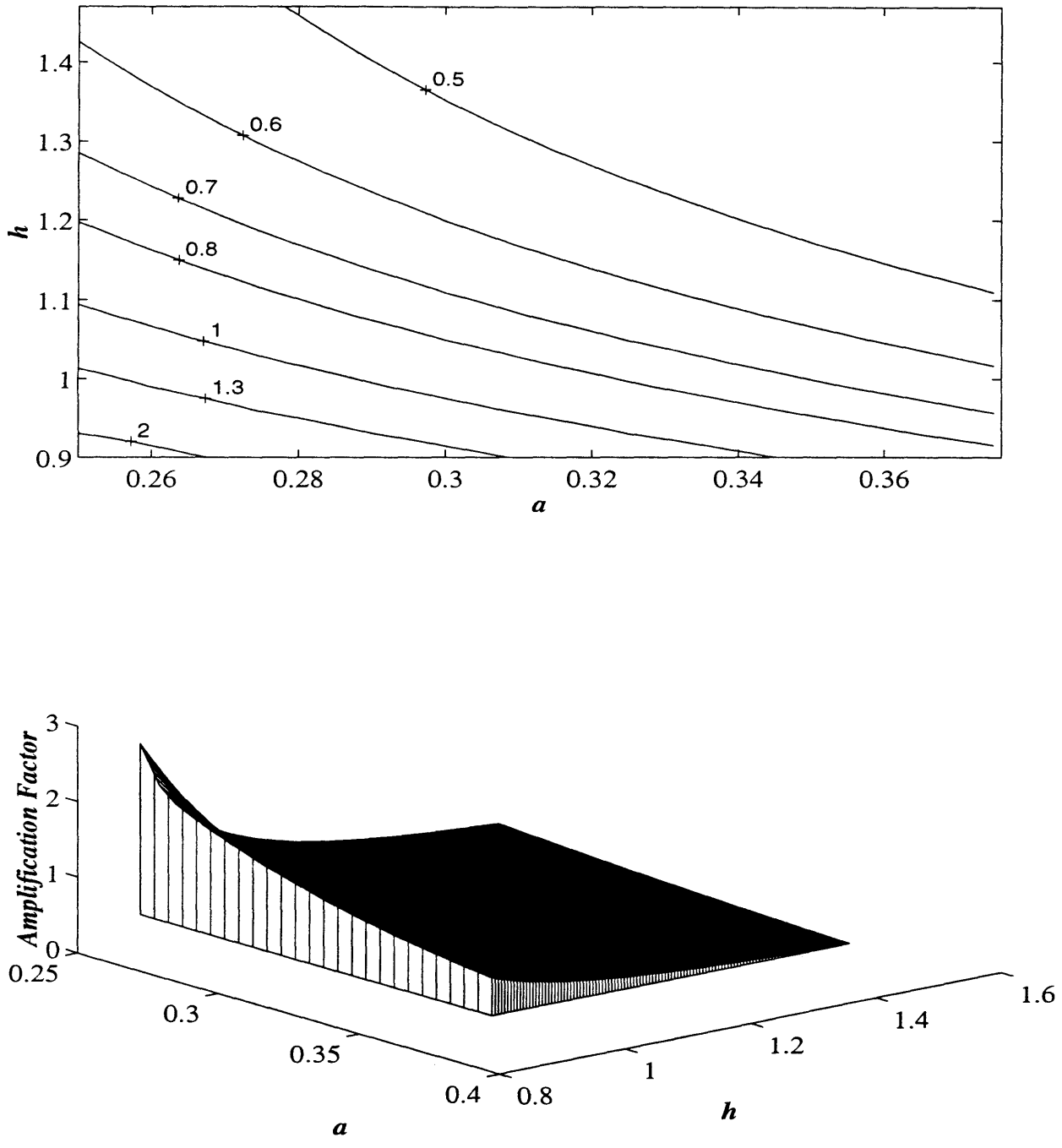

Figure 2-26: Contour and 3D plots of the amplification factor for fixed inertia moments $I = 0.1$, $S = 0.1$ and varying a and h; mode 1

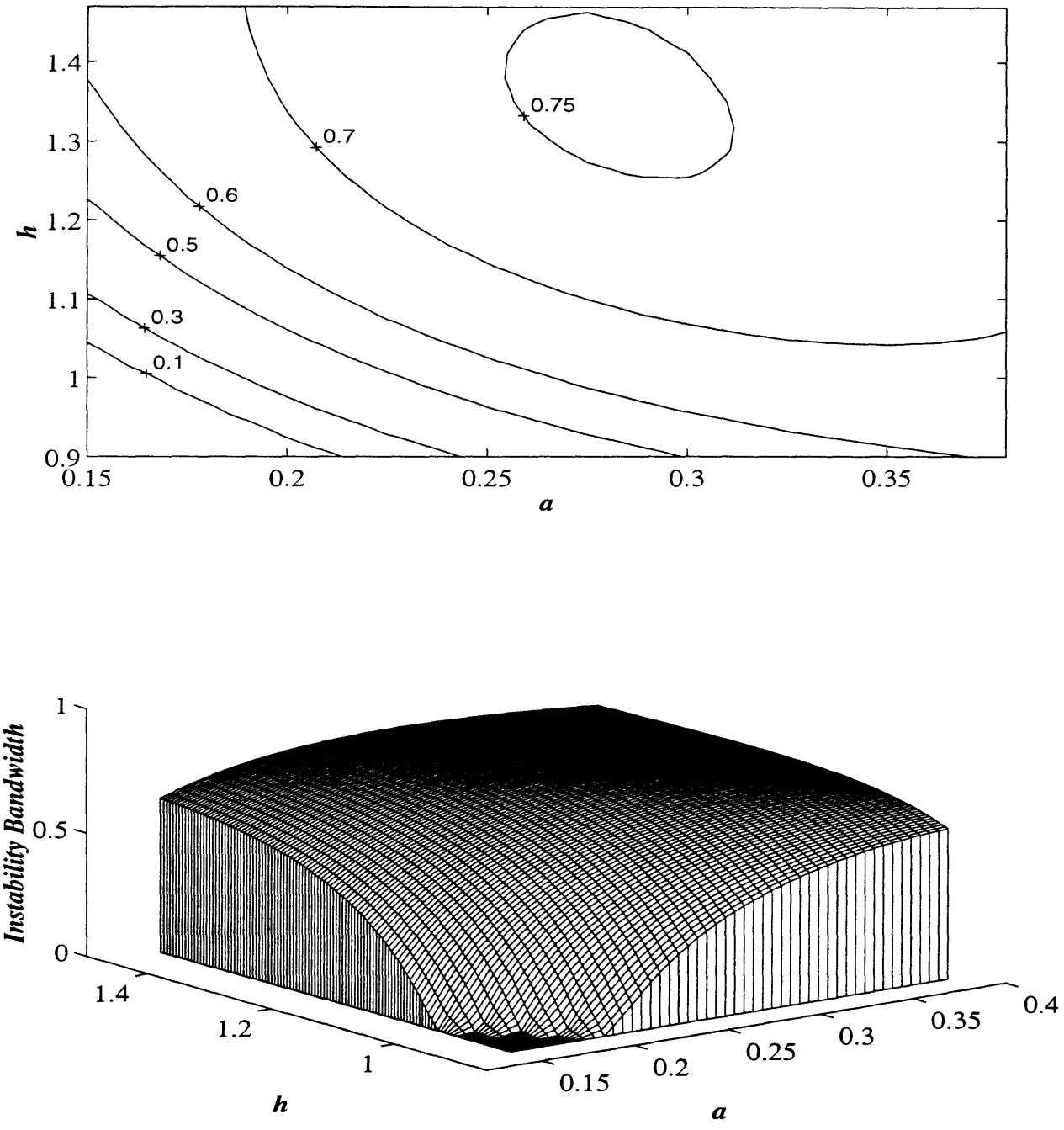

Figure 2-27: Contour and 3D plots of the bandwidth of instability for fixed inertia moments $I = 0.1$, $S = 0.1$ and varying a and h; mode 1

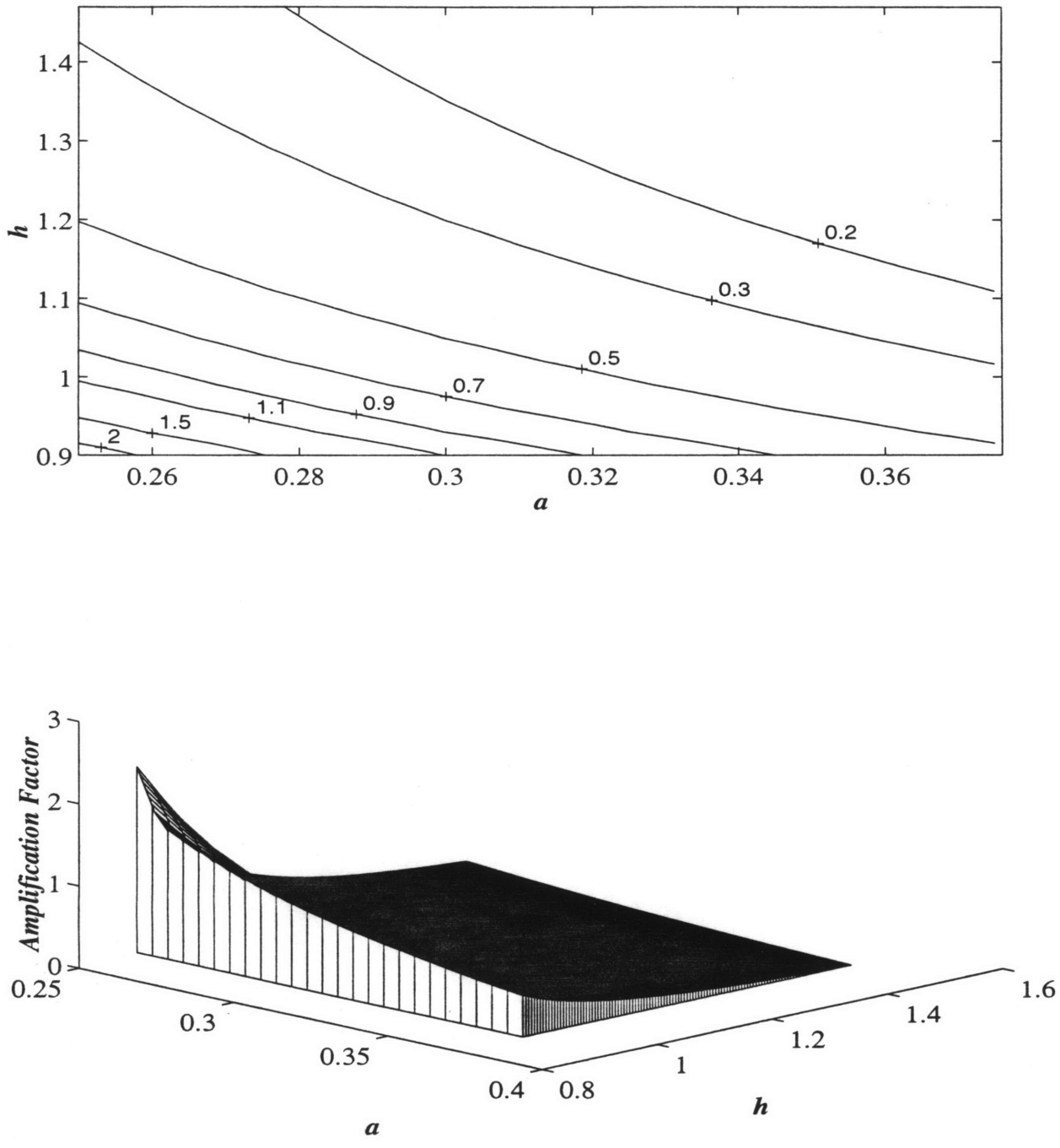

Figure 2-28: Same as figure 2-26 but for mode 2

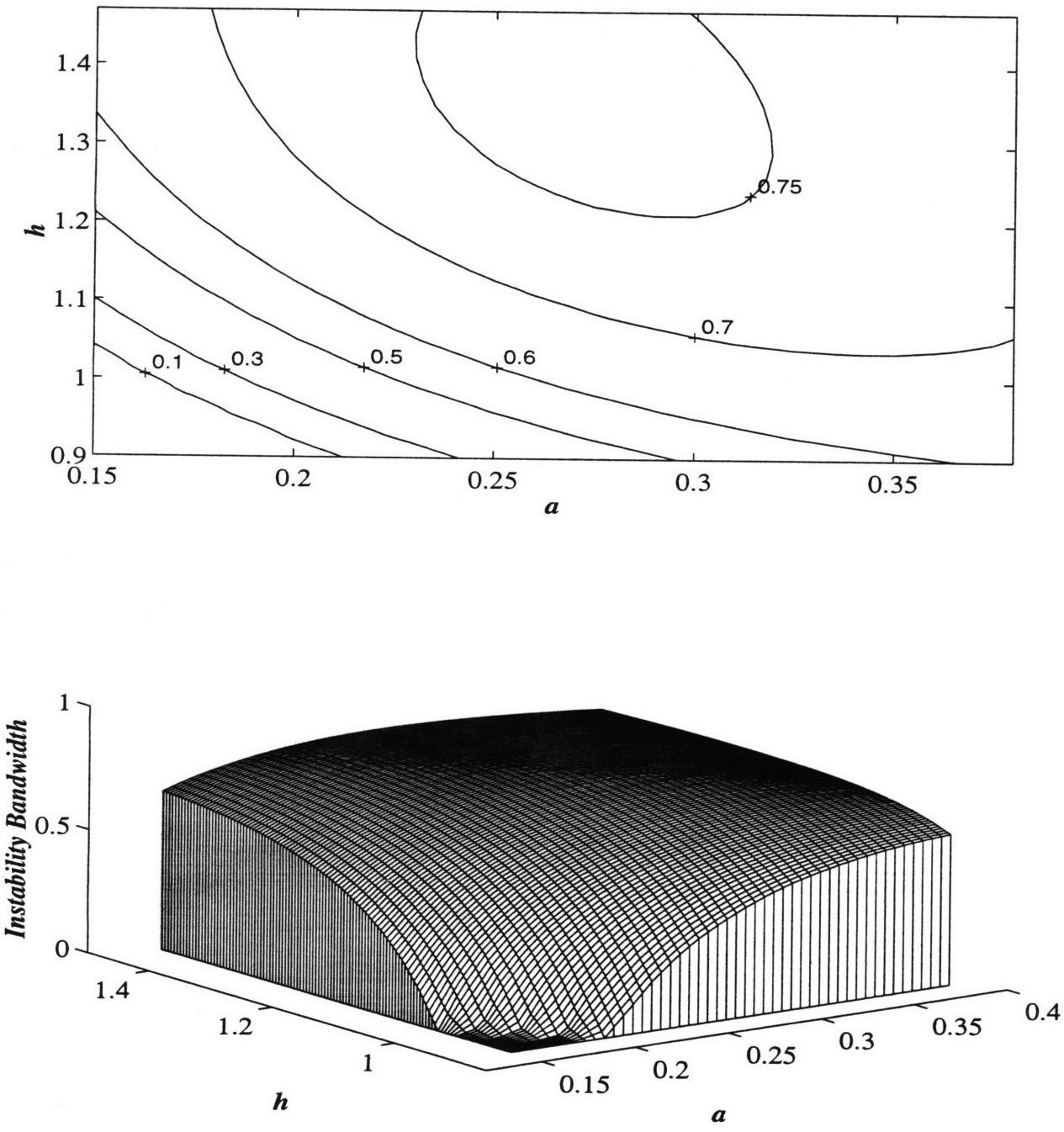

Figure 2-29: Same as figure 2-27 but for mode 2

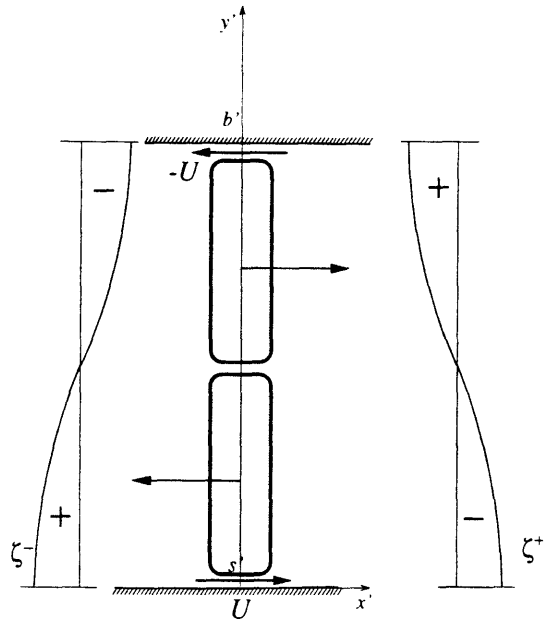

Figure 2-30: Oscillating jets due to the presence of the gaps along the channel walls.

negligible.

Chapter 3

The frictional effects

In this section we assess the real–fluid effects on the gate motion in the experiments, i.e. viscosity on the solid boundaries and in the structural gaps between the gates.

Dissipation takes place in the boundary layers at the gates surface, at the bottom surface or at the vertical walls of a laboratory flume; the fluid shear stress exert a torque on the gate. All these effect contribute to dampen the motion. In section 3.1 we show how the modeling of these viscous dissipation mechanisms is obtained by a formal perturbation analysis. Section 3.2 details the deduction of the resulting linear damping term in the evolution equation of the trapped wave amplitude.

In the prototype the gates consist of rigid structures separated by gaps of the order $O(0.2)$ m. During the out–of–phase motion associated with the trapped wave, the normal component of the fluid velocity on the gates surface reverses direction in a very short but non zero distance (the gap width); for large amplitude of motion, flow can separate at the edges of the gates. A heuristic order of magnitude estimation of this effect is presented in section 3.3

3.1 Preliminary analysis of viscous damping

For a real fluid, along all the solid boundaries a no–slip boundary condition applies and an oscillating boundary layer develops. For laboratory experiments the hypothesis of a laminar boundary layer is approximately valid [1]. The effect of this boundary layer can be represented by means of a perturbation series. Here we follow the approach of Johns(1968), Dore(1969), Greenspan (1968) and Mei and Liu(1973), as summarized in Mei(1989). We first outline the procedure and highlight the salient points, then in the next section we apply it to the trapped wave.

[1] For our experiments in the wave flume, the amplitude of the trapped wave is $A^T = 0.01$ m, the eigenfrequency is $\omega_0 = 4.4$ rad/sec, the Reynolds number is $\mathrm{Re} = \omega_0 {A^T}^2/\nu \sim 400$, within the region of laminar motion. In the prototype case, typical values are $A^T = 0.1$, $\omega_0 = 1$, $\mathrm{Re} \sim 10000$ so that an equivalent viscosity would then be necessary

We start from the linearized form of the governing equations and boundary conditions for viscous flow; as will be shown later, this is consistent with the nonlinear inviscid theory of the previous chapter 2.

Using dimensional coordinates, the linearized equation of motion for infinitesimal amplitude is

$$\frac{\partial \mathbf{u}'}{\partial t'} = -g\mathbf{i_z} - \frac{1}{\rho}\nabla' p' + \nu \nabla'^2 \mathbf{u}'. \tag{3.1.1}$$

where ν is the kinematic viscosity. The velocity vector $\mathbf{u}' = (u', v', w')$ can be taken as the sum of an irrotational and a solenoidal vector

$$\mathbf{u}' = \nabla' \Phi' + \mathbf{U}', \tag{3.1.2}$$

with $\mathbf{U}'$ being the solenoidal part, that is $\nabla' \cdot \mathbf{U}' = 0$.

Let

$$p' = -\rho g z' - \rho \Phi'_{t'}, \tag{3.1.3}$$

substitution of equations (3.1.2) and (3.1.3) into (3.1.1), yields

$$\frac{\partial \mathbf{U}'}{\partial t'} = \nu \nabla'^2 \mathbf{U}', \tag{3.1.4}$$

where use has been made of Laplace equation for Φ'.

A no-slip boundary condition must be assigned on the solid walls

$$\nabla' \Phi' + \mathbf{U}' = \mathbf{V}'_b, \tag{3.1.5}$$

where $\mathbf{V}'_b$ is the velocity of the solid boundary (zero for fixed boundaries such as the bottom or the side–walls of a laboratory flume). It can be decomposed in a normal and a parallel component to the boundary itself

$$\mathbf{V}'_b = \mathbf{V}'^{\perp}_b + \mathbf{V}'^{\parallel}_b. \tag{3.1.6}$$

On the free surface, the linearized kinematic condition reads

$$\zeta'_{t'} = \Phi'_z + W', \tag{3.1.7}$$

and the dynamic condition requires the vanishing of the normal stress

$$\Phi'_{t'} + g\zeta' + 2\nu w'_{z'} = 0. \tag{3.1.8}$$

In terms of the nondimensional variables defined in (2.3.1) and (2.3.2) of section

2.3 and of the nondimensional velocity and pressure

$$\mathbf{u} = \frac{\mathbf{u}'}{\omega_0 A^T}, \qquad p = \frac{p'}{\rho \omega_0^2 b' A^T}, \tag{3.1.9}$$

the governing equations become as follows:

$$\mathbf{u} = \nabla\Phi + \mathbf{U}, \tag{3.1.10}$$

$$\nabla^2\Phi = 0, \tag{3.1.11}$$

$$\nabla \cdot \mathbf{U} = 0, \tag{3.1.12}$$

$$p = -\Phi_t, \tag{3.1.13}$$

$$\mathbf{U}_t = \delta^2 \nabla^2 \mathbf{U}, \tag{3.1.14}$$

where the dimensionless parameter $\delta \ll 1$ is defined by

$$\delta = \frac{\sqrt{\nu/\omega_0}}{b'}; \tag{3.1.15}$$

it is the ratio of the amplitude of the oscillating laminar boundary layer $\sqrt{\nu/\omega_0}$ to the modal period b'.

The dimensionless boundary conditions are

$$\nabla\Phi + \mathbf{U} = \mathbf{V}_b, \qquad \text{on } S \text{ (solid surface)} \tag{3.1.16}$$

$$\zeta_t = \Phi_z + W, \quad \text{on} \quad z = 0 \tag{3.1.17}$$

$$\Phi_t + G\zeta + 2\delta^2 w_z = 0 \qquad \text{on} \quad z = 0. \tag{3.1.18}$$

The last two equation at $z = 0$ can be combined to give

$$G\Phi_z + \Phi_{tt} + W + 2\delta^2 w_{zt} = 0. \tag{3.1.19}$$

The vertical component W of the rotational velocity is of the same order as the other terms only in a thin strip of the meniscus boundary layer at the contact of the free surface with the solid boundaries and is much less anywhere. Therefore its global effect can only be felt at the order $O(\delta)$.

In our experiments in the wave channel the typical values are $\epsilon = A^T/b' = 0.015/0.38$, $\epsilon^2 = 0.0015$ and $\delta = \sqrt{10^{-6}/2\pi 0.7}\ /0.38 = 0.0013$. Hence $\delta = O(\epsilon^2)$, implying that viscous damping is of comparable importance as nonlinearity. From here on we shall let $\delta = \epsilon^2\delta_2$ with $\delta_2 = O(1)$.

Expecting that the rotational part $\mathbf{U}$ varies rapidly within the nondimensional

distance $O(\delta)$, we introduce a boundary–layer coordinate

$$\xi = \frac{x_N}{\epsilon^2} \qquad \text{so that} \quad \mathbf{U} = \mathbf{U}(\xi, \mathbf{x}_T) \tag{3.1.20}$$

where $\xi, \mathbf{x}_T$ form a locally rectangular coordinate system with the normal coordinate x_N pointing inwards the fluid and therefore opposite to the outward normal $\mathbf{n}$.

The continuity equation (3.1.12) then becomes

$$-\frac{\partial \mathbf{n}\cdot\mathbf{U}}{\partial \xi} + \epsilon^2 \left(\frac{\partial U_{T_1}}{\partial x_{T_1}} + \frac{\partial U_{T_2}}{\partial x_{T_2}} \right) = 0. \tag{3.1.21}$$

We now introduce a perturbation expansion in powers of ϵ^2. Because damping will affect the flow on a slow time scale $1/\epsilon^2\omega_0$ we let the terms of the series depend also on $t_2 = \epsilon^2 t$. Therefore

$$\Phi = \left[\phi_{11}(\mathbf{x}, t_2) + \epsilon^2 \phi_{31}(\mathbf{x}, t_2) + O(\epsilon^4) \right] \mathrm{e}^{-\mathrm{i}t} + *, \tag{3.1.22}$$

$$\mathbf{U} = \left[\mathbf{U}_{11}(\xi, \mathbf{x}_T, t_2) + \epsilon^2 \mathbf{U}_{31}(\xi, \mathbf{x}_T, t_2) + O(\epsilon^4) \right] \mathrm{e}^{-\mathrm{i}t} + *. \tag{3.1.23}$$

Substituting in the governing equations (3.1.11), (3.1.21) and boundary conditions (3.1.16), (3.1.19), a sequence of linear problems is obtained.

(i) *Inviscid solution at* $O(1)$*:*

$$\nabla^2 \phi_{11} = 0, \tag{3.1.24}$$

$$\mathbf{n}\cdot\nabla\phi_{11} - \left| \mathbf{V}^{\perp}_{b_{11}} \right| = 0, \qquad \text{on } S \tag{3.1.25}$$

$$G\phi_{11_z} - \phi_{11} = 0 \qquad \text{on } S_F \quad z = 0. \tag{3.1.26}$$

In the present case, the inviscid solution is the trapped wave of eigenfrequency ω_0. Note that W is not present at this order because of its small area of effectiveness. This solution gives rise to a nonzero tangential velocity on S, which is to be corrected by the rotational part $\mathbf{U}_{11}$.

(ii) *Boundary layer correction at* $O(1)$*:*

$$\frac{\partial^2 \mathbf{U}^{\parallel}_{11}}{\partial \xi^2} = -\mathrm{i}\mathbf{U}^{\parallel}_{11}, \tag{3.1.27}$$

$$\mathbf{U}^{\parallel}_{11} = -\nabla\phi^{\parallel}_{11} + \mathbf{V}^{\parallel}_{b_{11}}, \qquad \text{on } S \tag{3.1.28}$$

$$\mathbf{U}^{\parallel}_{11} \to 0 \qquad \xi \to \infty. \tag{3.1.29}$$

Note that $\mathbf{U}_{11}$ is tangential to the solid boundary S, that is, $\mathbf{n}\cdot\mathbf{U}_{11} = 0$. The

continuity equation gives

$$-\frac{\partial \mathbf{n}\cdot\mathbf{U}_{31}}{\partial\xi}+\left(\frac{\partial U_{T_1}}{\partial x_{T_1}}+\frac{\partial U_{T_2}}{\partial x_{T_2}}\right)_{11}=0, \tag{3.1.30}$$

from which $\mathbf{n}\cdot\mathbf{U}_{31}$ can be integrated across the boundary layer (from ξ to $\xi\to\infty$) subject to the condition that $\mathbf{n}\cdot\mathbf{U}_{31}=0$ at $\xi\sim\infty$. In general $(\mathbf{n}\cdot\mathbf{U}_{31})$ is nonzero at the wall S ($\xi=0$) and must be canceled by $\phi_{31\,x_N}$ at the order $O(\epsilon^2)$.

(iii) *Inviscid solution at* $O(\epsilon^2)$*:*

$$\nabla^2\phi_{31}=0, \tag{3.1.31}$$

$$\mathbf{n}\cdot\nabla\phi_{31}-\left|\mathbf{V}^{\perp}_{b_{31}}\right|=-\left[\mathbf{n}\cdot\mathbf{U}_{31}\right]_S, \qquad \text{on } S \tag{3.1.32}$$

$$G\phi_{31_z}-\phi_{31}=2\mathrm{i}\phi_{11t_2}-G\,\frac{W_{11}}{\epsilon^2} \qquad \text{on } S_F \quad z=0. \tag{3.1.33}$$

In the last condition the effect of W_{11} is $O(1)$ since the thickness of the boundary layer is only $O(\epsilon^2)$.

Now problem (i) is homogeneous and is an eigenvalue problem with nontrivial solution (the trapped wave in the present context). Problem (ii) is the classical Stokes' problem of a plate oscillating in its own plane and its solution is

$$\mathbf{U}^{\parallel}_{11}=\left[-\nabla\phi_{11}+\mathbf{V}^{\parallel}_{b_{11}}\right]_S\Gamma(\xi), \qquad \Gamma(\xi)=\mathrm{e}^{-(1-\mathrm{i})\xi/\sqrt{2}}, \tag{3.1.34}$$

which can be used to obtain $\mathbf{n}\cdot\mathbf{U}_{31}$ by integrating (3.1.30). Problem (iii) for ϕ_{31} has the homogeneous part identical to problem (i) for ϕ_{11}, which has nontrivial solutions. We therefore invoke the Fredholm alternative, that is, we apply Green's formula to ϕ_{11} and ϕ_{31} in the fluid domain Ω with boundary $\partial\Omega=S+S_F$

$$\iiint_{\Omega}\left(\phi_{11}\nabla^2\phi_{31}-\phi_{31}\nabla^2\phi_{11}\right)\mathrm{d}\Omega=\iint_{\partial\Omega}\left(\phi_{11}\frac{\partial\phi_{31}}{\partial n}-\phi_{31}\frac{\partial\phi_{11}}{\partial n}\right)\mathrm{d}S, \tag{3.1.35}$$

and use all the governing equations and boundary conditions of problems (i) and (iii) to obtain

$$0=2\mathrm{i}\iint_{S_F}\phi_{11}\phi_{11t_2}\,\mathrm{d}S-\iint_{S_F}\phi_{11}\,\frac{W_{11}}{\epsilon^2}\,\mathrm{d}S-\iint_{S}\phi_{11}\,\left[\mathbf{n}\cdot\mathbf{U}_{31}\right]_S\,\mathrm{d}S. \tag{3.1.36}$$

The above expression (3.1.36) is an evolution equation for ϕ_{11}, whose slow time derivative ∂_{t_2} (first integral on the RHS) is balanced by the viscous effects (second and third integral) [2]. The result implies a slow time exponential attenuation of the amplitude

[2]Mei(1989) details the procedure of allowing a perturbation expansion in ω, that is $\omega=\omega_0+\epsilon^2\,\omega_1+O(\epsilon^4)$, and determines the complex correction ω_1 from application of Green's formula. The two approaches give the same result.

of ϕ_{11}.

3.2 Modification of the evolution equation by viscosity

We now extend the perturbation analysis to modify the evolution equation.

3.2.1 Perturbation expansions and Green's formula

For the trapped wave, the perturbation series for the rotational part $\mathbf{U}$ is

$$\mathbf{U} = \left[\mathbf{U}_{11}\left(\xi, \mathbf{x}_T, t_2\right) + \epsilon^2\, \delta_2 \mathbf{U}_{31}\left(\xi, \mathbf{x}_T, t_2\right) + O(\epsilon^4)\right] \mathrm{e}^{-\mathrm{i}t} + *. \tag{3.2.1}$$

Since the analysis for both fluid regions, Ω^+ and Ω^-, are similar, we shall not make the distinctions and use the symbol ϕ & $\mathbf{U}$ for $x \in \Omega$ to mean $\phi^\pm$ & $\mathbf{U}^\pm$ for $x \in \Omega^\pm$. The perturbed problems are as follows.

(i) *Inviscid solution at* $O(1)$*:*

$$\nabla^2 \phi_{11} = 0 \qquad \text{in} \quad \Omega, \tag{3.2.2}$$

$$G\phi_{11_z} - \phi_{11} = 0 \qquad \text{on } S_F,\ z = 0, \tag{3.2.3}$$

$$\phi_{11_z} = 0 \qquad \text{on } S_B,\ z = -h, \tag{3.2.4}$$

$$\phi_{11_y} = 0 \qquad \text{on } S_W,\ y = 0,\ y = 1 \tag{3.2.5}$$

$$\phi_{11_x} - \mathrm{i}\,(z+h)\theta_{11} = 0 \qquad \text{on } S_G,\ x = 0, \tag{3.2.6}$$

where S_F, S_B, S_W, S_G denote respectively the free surface, the bottom surface, the wall surface (of a laboratory flume) and the gates surface. The solution is the trapped wave seen in section 2.5.2.

(ii) *Boundary layer correction at* $O(1)$*:*

$$\frac{\partial^2 \mathbf{U}_{11}^{\parallel}}{\partial \xi^2} = -\mathrm{i}\mathbf{U}_{11}, \tag{3.2.7}$$

$$\mathbf{U}_{11}^{\parallel} = -\nabla \phi_{11}, \qquad \text{on } S_B,\ S_W,\ S_G \tag{3.2.8}$$

$$\mathbf{U}_{11}^{\parallel} \to 0 \qquad \xi \to \infty. \tag{3.2.9}$$

Once $\mathbf{U}_{11}$ is found, integrate the continuity equation

$$-\frac{\partial \mathbf{n}\cdot\mathbf{U}_{31}}{\partial \xi} + \left(\frac{\partial U_{T_1}}{\partial x_{T_1}} + \frac{\partial U_{T_2}}{\partial x_{T_2}}\right)_{11} = 0, \tag{3.2.10}$$

from $\xi = 0$ to $\xi = \infty$ to obtain $\mathbf{n}\cdot\mathbf{U}_{31}$ at the boundaries S, $\xi = 0$.

(iii) *Inviscid solution at $O(\epsilon^2)$:* The second order $O(\epsilon)$ solution is unaffected by the rotational part. The correction for $\mathbf{n}\cdot\mathbf{U}_{31}$ being nonzero on S must be given by $\partial\phi_{31}/\partial n$. The governing equation are then

$$\begin{aligned}
\nabla^2\phi_{31} &= 0 && \text{in } \Omega, && (3.2.11)\\
G\phi_{31_z} - \phi_{31} &= \mathcal{F}_{31} - G\,W_{11}/\epsilon^2 && \text{on } S_F,\ z=0, && (3.2.12)\\
\phi_{31_z} &= \delta_2\left[\mathbf{n}\cdot\mathbf{U}_{31}\right]_{S_B} && \text{on } S_B,\ z=-h, && (3.2.13)\\
\phi_{31_y} &= \delta_2\left[\mathbf{n}\cdot\mathbf{U}_{31}\right]_{S_W} && \text{on } S_W,\ y=0, && (3.2.14)\\
\phi_{31_y} &= -\delta_2\left[\mathbf{n}\cdot\mathbf{U}_{31}\right]_{S_W} && \text{on } S_W,\ y=1, && (3.2.15)\\
\phi_{31_x} - \mathrm{i}\,(z+h)\theta_{31} &= \mathcal{G}_{31} \mp \delta_2\left[\mathbf{n}\cdot\mathbf{U}_{31}\right]_{S_G} && \text{on } S_G,\ x=0. && (3.2.16)
\end{aligned}$$

where the forcing terms $\mathcal{F}_{31}$ and $\mathcal{G}_{31}$ are given by (2.5.158) (2.5.159) of section 2.5.7. A inhomogeneous term arises also in the equation of motion of the gate, as a result of the fluid shear stresses action. For clarity this term is analyzed in section 3.2.3

Compared with the third order first harmonic problem analyzed in section 2.5.7, this solution has not only extra forcing terms on the free surface S_F and the gate surface S_G, namely $-G\,W_{11}/\epsilon^2$ and $-\delta_2\left[\mathbf{n}\cdot\mathbf{U}_{31}\right]_{S_G}$, but is also forced at the bottom S_B (right hand side of (3.2.13)) and the side walls S_W (right hand side of (3.2.14) and (3.2.15)). Enforcing the Fredholm alternative, that is applying Green's formula to ϕ_{11} and ϕ_{31} and carrying out the same steps of section 2.5.7 that brought from (2.5.162) to (2.5.171), yields a revised version of (2.5.171)

$$\begin{aligned}
0 = {} & \frac{1}{G}\int_0^1 \mathrm{d}y\left\{\int_{-\infty}^0 \mathrm{d}x\, f_{11}^-\,\mathcal{F}_{31}^- - \int_0^\infty \mathrm{d}x\, f_{11}^+\,\mathcal{F}_{31}^+\right\} - 2\int_0^1 \mathrm{d}y\int_{-h}^0 \mathrm{d}z\,\overline{f_{11}\mathcal{G}_{31}} + \mathrm{i}\,\mathcal{D}_{31}\,q_{11} - \\
& \int_0^1 \mathrm{d}y\left\{\int_{-\infty}^0 \mathrm{d}x\, f_{11}^-\,W_{11}^-/\epsilon^2 + \int_0^\infty \mathrm{d}x\, f_{11}^+\,W_{11}^+/\epsilon^2\right\} + \delta_2\int_0^1 \mathrm{d}y\int_{-h}^0 \mathrm{d}z\,\Delta\left(f_{11}\left[\mathbf{n}\cdot\mathbf{U}_{31}\right]_{S_G}\right) - \\
& \delta_2\int_{-h}^0 \mathrm{d}z\left\{\int_{-\infty}^0 \mathrm{d}x\, f_{11}^-\left[\mathbf{n}\cdot\mathbf{U}_{31}^-\right]_{S_W} - \int_0^\infty \mathrm{d}x\, f_{11}^+\left[\mathbf{n}\cdot\mathbf{U}_{31}^+\right]_{S_W}\right\}_{y=0} + \\
& \delta_2\int_{-h}^0 \mathrm{d}z\left\{\int_{-\infty}^0 \mathrm{d}x\, f_{11}^-\left[\mathbf{n}\cdot\mathbf{U}_{31}^-\right]_{S_W} - \int_0^\infty \mathrm{d}x\, f_{11}^+\left[\mathbf{n}\cdot\mathbf{U}_{31}^+\right]_{S_W}\right\}_{y=1} - \\
& \delta_2\int_0^1 \mathrm{d}y\left\{\int_{-\infty}^0 \mathrm{d}x\, f_{11}^-\left[\mathbf{n}\cdot\mathbf{U}_{31}^-\right]_{S_B} - \int_0^\infty \mathrm{d}x\, f_{11}^+\left[\mathbf{n}\cdot\mathbf{U}_{31}^+\right]_{S_B}\right\}. \qquad (3.2.17)
\end{aligned}$$

From (3.2.17) we then deduce the evolution equation, whose final expression is identical to (2.5.174) but for the extra term in δ_2 that arises from the last nine integrals in (3.2.17). Details are given in the next section.

In the last equation, the term $\mathcal{D}_{31}$ on the first line arose from the dynamical equation of the gate and must be corrected for frictional torque due to viscous stresses on the gate surface, which include the front, back and the sides forming the gaps. All surface integrals in the second to fourth line must be evaluated by working out the detailed rotational flow in the boundary layers on the flume walls, flume bottom, and

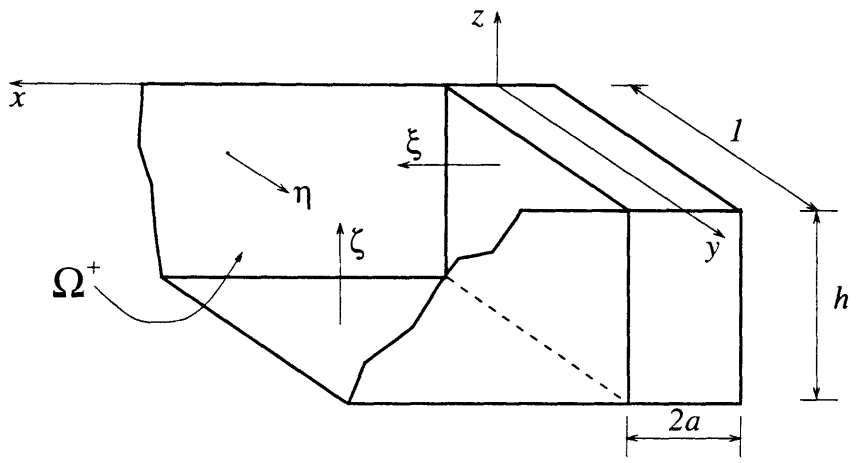

Figure 3-1: Experimental channel and boundary layer coordinates.

the front and back surfaces of the gate. We first consider the surface integrals.

3.2.2 Contributions from surface integrals

With reference to figure 3-1 we introduce the following boundary layer coordinates

$$\xi = \frac{x}{\delta}, \quad \eta = \frac{y}{\delta}, \quad \eta' = \frac{y+1}{\delta}, \quad \zeta = \frac{z+h}{\delta}, \quad \text{with} \quad \delta = \epsilon^2 \delta_2, \tag{3.2.18}$$

for the boundary layers next to, respectively, the gate, the sidewall at $y = 0$, the sidewall at $y = 1$ and the bottom.

The leading order boundary layer velocity corrections $\mathbf{U}_{11}$ are

$$\mathbf{U}_{11_G} = \left\{ \begin{array}{c} U_{11_G} \\ V_{11_G} \\ W_{11_G} \end{array} \right\} = \left\{ \begin{array}{c} 0 \\ -\phi_{11_y} \\ -\phi_{11_z} \end{array} \right\}_{x=0} \Gamma(\xi), \tag{3.2.19}$$

near the gate surface,

$$\mathbf{U}_{11_W} = \left\{ \begin{array}{c} U_{11_W} \\ V_{11_W} \\ W_{11_W} \end{array} \right\} = \left\{ \begin{array}{c} -\phi_{11_x} \\ 0 \\ -\phi_{11_z} \end{array} \right\}_{y=0} \Gamma(\eta), \tag{3.2.20}$$

near the side wall at $y = 0$,

$$\mathbf{U}_{11_W} = \left\{ \begin{array}{c} U_{11_W} \\ V_{11_W} \\ W_{11_W} \end{array} \right\} = \left\{ \begin{array}{c} -\phi_{11_x} \\ 0 \\ -\phi_{11_z} \end{array} \right\}_{y=1} \Gamma(\eta'), \tag{3.2.21}$$

near the side wall at $y = 1$, and

$$\mathbf{U}_{11_B} = \left\{ \begin{array}{c} U_{11_B} \\ V_{11_B} \\ W_{11_B} \end{array} \right\} = \left\{ \begin{array}{c} -\phi_{11_x} \\ -\phi_{11_y} \\ 0 \end{array} \right\}_{x=0} \Gamma(\zeta), \tag{3.2.22}$$

near the bottom, with Γ being Stokes solution as defined by (3.1.34). The induced velocity normal to the solid boundary is obtained by integrating continuity equation (3.2.10) from 0 to ∞. We obtain respectively

$$[\mathbf{n} \cdot \mathbf{U}_{31}]_{S_G} = \int_{\infty}^{0} \mathrm{d}\xi \left(V_{11_{Gy}} + W_{11_{Gz}} \right) = \int_{0}^{\infty} \mathrm{d}\xi \, \Gamma(\xi) \left(\phi_{11_{yy}} + \phi_{11_{zz}} \right)_{x=0} =$$
$$\pm \frac{\mathrm{i}-1}{\sqrt{2}} \theta \sum_{m=1} \sum_{n=0} \beta_{mn} \alpha_{mn}^2 \cos m\pi y \, \cosh K_n(z+h), \tag{3.2.23}$$

for the gate surface;

$$[\mathbf{n} \cdot \mathbf{U}_{31}]_{S_W} = \int_{\infty}^{0} \mathrm{d}\eta \, \left(U_{11_{W}x} + W_{11_{W}z} \right) = \int_{0}^{\infty} \mathrm{d}\eta \, \Gamma(\eta) \left(\phi_{11_{xx}} + \phi_{11_{zz}} \right)_{y=0} =$$
$$\pm \frac{\mathrm{i}-1}{\sqrt{2}} \theta \sum_{m=1} \sum_{n=0} \beta_{mn} (-m^2\pi^2) \, \cosh K_n(z+h) \, \mathrm{e}^{-\alpha_{mn}x} \tag{3.2.24}$$

for the side wall at $y = 0$;

$$[\mathbf{n} \cdot \mathbf{U}_{31}]_{S_W} = \int_{\infty}^{0} \mathrm{d}\eta \, \left(U_{11_{W}x} + W_{11_{W}z} \right) = \int_{0}^{\infty} \mathrm{d}\eta \, \Gamma(\eta) \left(\phi_{11_{xx}} + \phi_{11_{zz}} \right)_{y=1} =$$
$$\pm \frac{\mathrm{i}-1}{\sqrt{2}} \theta \sum_{m=1} \sum_{n=0} \beta_{mn} (-m^2\pi^2) \, \cos m\pi \, \cosh K_n(z+h) \, \mathrm{e}^{-\alpha_{mn}x} \tag{3.2.25}$$

for the side wall at $y = 1$;

$$[\mathbf{n} \cdot \mathbf{U}_{31}]_{S_B} = \int_{\infty}^{0} \mathrm{d}\zeta \, \left(U_{11_{B}x} + W_{11_{B}z} \right) = \int_{0}^{\infty} \mathrm{d}\zeta \, \Gamma(\zeta) \left(\phi_{11_{xx}} + \phi_{11_{zz}} \right)_{z=-h} =$$
$$\pm \frac{\mathrm{i}-1}{\sqrt{2}} \theta \sum_{m=1} \sum_{n=0} \beta_{mn} K_n^2 \, \cos m\pi y \, \mathrm{e}^{-\alpha_{mn}x} \tag{3.2.26}$$

for the bottom surface; use has been made of expression (2.5.50) for ϕ_{11} and of the fact that

$$\int_{0}^{\infty} \mathrm{d}x \, \Gamma(x) = \frac{1+\mathrm{i}}{\sqrt{2}}. \tag{3.2.27}$$

The contribution to the surface integrals of equation (3.2.17) are then evaluated as follows.

Gate surface S_G:

$$\delta_2 \int_0^1 \mathrm{d}y \int_{-h}^0 \mathrm{d}z \, \Delta \left(f_{11} \left[\mathbf{n} \cdot \mathbf{U}_{31} \right]_{S_G} \right) = \delta_2 \frac{\mathrm{i}-1}{\sqrt{2}} \theta \sum_{m=1} \sum_{n=0} \alpha_{mn}^2 \beta_{mn}^2 C_n, \tag{3.2.28}$$

where use has been made of (3.2.23) and (2.5.50).

Side walls S_W:

$$\begin{aligned} -\delta_2 \int_{-h}^0 \mathrm{d}z \left\{ \int_{-\infty}^0 \mathrm{d}x \, f_{11}^- \left[\mathbf{n} \cdot \mathbf{U}_{31}^- \right]_{S_W} - \int_0^\infty \mathrm{d}x \, f_{11}^+ \left[\mathbf{n} \cdot \mathbf{U}_{31}^+ \right]_{S_W} \right\}_{y=0} + \\ \delta_2 \int_{-h}^0 \mathrm{d}z \left\{ \int_{-\infty}^0 \mathrm{d}x \, f_{11}^- \left[\mathbf{n} \cdot \mathbf{U}_{31}^- \right]_{S_W} - \int_0^\infty \mathrm{d}x \, f_{11}^+ \left[\mathbf{n} \cdot \mathbf{U}_{31}^+ \right]_{S_W} \right\}_{y=1} = \\ -\delta_2 \frac{\mathrm{i}-1}{\sqrt{2}} \theta \, 2\pi^2 \sum_{m=1} \sum_{n=0} \sum_{n'=0} \frac{m^2 \beta_{mn} \beta_{mn'} \left(1 - \cos m\pi\right)}{\alpha_{mn} + \alpha_{mn'}} \end{aligned} \tag{3.2.29}$$

where use has been made of (3.2.24), (3.2.25) and (2.5.50).

Bottom S_B:

$$\begin{aligned} -\delta_2 \int_0^1 \mathrm{d}y \left\{ \int_{-\infty}^0 \mathrm{d}x \, f_{11}^- \left[\mathbf{n} \cdot \mathbf{U}_{31}^- \right]_{S_B} - \int_0^\infty \mathrm{d}x \, f_{11}^+ \left[\mathbf{n} \cdot \mathbf{U}_{31}^+ \right]_{S_B} \right\} = \\ \delta_2 \frac{\mathrm{i}-1}{\sqrt{2}} \theta \, \frac{1}{2} \sum_{m=1} \sum_{n=0} \sum_{n'=0} \frac{\beta_{mn} \beta_{mn'} K_{n'}^2}{\alpha_{mn} + \alpha_{mn'}} \end{aligned} \tag{3.2.30}$$

where use has been made of (3.2.26) and (2.5.50).

Free Surface S_F:

The vertical component W_{11} is zero on the free surface except for the meniscous boundary layers along the wetting line on the gate surface and the side walls. Therefore we can split the integrals into three parts:

$$\begin{aligned} -\int_0^1 \mathrm{d}y \left\{ \int_{-\infty}^0 \mathrm{d}x \, f_{11}^- \, W_{11}^-/\epsilon^2 + \int_0^\infty \mathrm{d}x \, f_{11}^+ \, W_{11}^+/\epsilon^2 \right\} = \\ -2\,\delta_2 \left\{ \int_0^1 \mathrm{d}y \int_0^\infty \mathrm{d}\xi \, f_{11}^+ \, W_{11_G}^+ + \int_0^\infty \mathrm{d}\eta \int_0^\infty \mathrm{d}x \, f_{11}^+ \, W_{11_W}^+ + \int_0^\infty \mathrm{d}\eta' \int_0^\infty \mathrm{d}x \, f_{11}^+ \, W_{11_W}^+ \right\} = \\ \delta_2 \frac{\mathrm{i}-1}{\sqrt{2}} \theta \, \frac{1}{G} \left\{ \sum_{m=1} \sum_{n=0} \sum_{n'=0} \beta_{mn} \beta_{mn'} \cosh K_n h \, \cosh K_{n'} h + \right. \\ \left. 2 \sum_{m=1} \sum_{n=0} \sum_{m'=1} \sum_{n'=0} \frac{\beta_{mn} \beta_{m'n'} \left(1 - \cos m\pi\right)}{\alpha_{mn} + \alpha_{m'n'}} \cosh K_n h \, \cosh K_{n'} h. \right\} \end{aligned} \tag{3.2.31}$$

When the integrals (3.2.28), (3.2.29), (3.2.30) and (3.2.31) are added, a new term

must be added to the right hand side of (3.2.17)

$$-\mathrm{i}\theta_{t_2} = \omega_2\theta + \theta^2\theta^* \, (c_N + \mathrm{i}\, c_R) + A_2\theta^* \, c_F + (1+\mathrm{i}) \, \delta_2 \, \theta \, c'_L, \tag{3.2.32}$$

where c'_L is

$$c'_L = \frac{1}{c\sqrt{2}} \sum_{m=1} \sum_{n=0} \left\{ \alpha_{mn}^2 \beta_{mn}^2 C_n + \sum_{n'=0} \left[\frac{\beta_{mn}\beta_{mn'} \left(K_{n'}^2 - 2\pi^2 m^2 \left(1 - \cos m\pi\right)\right)}{\alpha_{mn} + \alpha_{mn'}} + \right.\right.$$
$$\left.\left. \frac{1}{G} \beta_{mn} \cosh K_n h \, \cosh K_{n'} h \left(\beta_{mn'} + 2 \sum_{m'=1} \frac{\beta_{m'n'} \left(1 - \cos m\pi\right)}{\alpha_{mn} + \alpha_{m'n'}} \right) \right] \right\} \tag{3.2.33}$$

Note that in (3.2.33) the term $-2\pi^2 m^2 \left(1 - \cos m\pi\right)$ and last summation in m' (arising respectively from (3.2.29) and (3.2.31)) are the contribution of the sidewalls, therefore representative of a laboratory channel. For a prototype or a laboratory basin with many gates, the sidewalls are absent and the expression of c'_L to be used is

$$c'_L = \frac{1}{c\sqrt{2}} \sum_{m=1} \sum_{n=0} \left\{ \alpha_{mn}^2 \beta_{mn}^2 C_n + \right.$$
$$\left. \sum_{n'=0} \left[\frac{\beta_{mn}\beta_{mn'} K_{n'}^2}{\alpha_{mn} + \alpha_{mn'}} + \frac{1}{G} \beta_{mn}\beta_{mn'} \cosh K_n h \, \cosh K_{n'} h \right] \right\}. \tag{3.2.34}$$

The discussion of the parametric dependence of c'_L is postponed to the end of the next section.

3.2.3 Viscous torque on the gates

On the gate there are viscous torque on the front and back surfaces and on the sides forming the gap. These torque must be accounted for in the dynamical equation of the gate by modifying $\mathcal{D}_{31}$.

The nondimensional viscous stress $\boldsymbol{\tau}$ is an $O(\epsilon^2)$ quantity

$$\boldsymbol{\tau} = \left[\, \epsilon^2 \, \delta_2 \, \boldsymbol{\tau}_{31} \left(\xi, \mathbf{x}_T\right) + O(\epsilon^4) \, \right] \mathrm{e}^{-\mathrm{i}(1+\epsilon^2\omega_2)t} + *, \tag{3.2.35}$$

is used to evaluate the viscous torque on the gates. The dimensionless amplitude $\boldsymbol{\tau}_{31}$ can be calculated once the boundary layer correction $\mathbf{U}_{11\,G}$ is known according to

$$\boldsymbol{\tau}_{31} = \left\{ \begin{array}{c} \tau_{\xi x_{31}} \\ \tau_{\xi y_{31}} \\ \tau_{\xi z_{31}} \end{array} \right\} = \frac{\partial}{\partial \xi} \left\{ \begin{array}{c} U_{11_G} \\ V_{11_G} \\ W_{11_G} \end{array} \right\}_{\xi=0} = \left\{ \begin{array}{c} 0 \\ -\phi_{11_y} \\ -\phi_{11_z} \end{array} \right\} \left[\frac{\mathrm{d}\Gamma(\xi)}{\mathrm{d}\xi} \right]_{\xi=0} = \left\{ \begin{array}{c} 0 \\ -\phi^+_{11_y} \\ -\phi^+_{11_z} \end{array} \right\} \frac{(\mathrm{i}-1)}{\sqrt{2}} \tag{3.2.36}$$

On the front and back of the gate, the only component of the tangential stress that induces rotation is $\delta_2 \tau_{\xi z_{31}}$ (see figure 3-2), with a moment arm equal to a (semithick-

ness of the gate). The total viscous torque acting on the gate is then

$$\mathcal{T}_{\nu 31} = \int_{y_1}^{y_2} \mathrm{d}y \int_{-h}^{0} \mathrm{d}z \, 2a \left(-\delta_2 \tau_{\xi z 31} \right) \tag{3.2.37}$$

Using expression (3.2.36) for $\tau_{\xi z 31}$,

$$\mathcal{T}_{\nu 31} = \delta_2 \sqrt{2}\, a \, (\mathrm{i} - 1) \int_{y_1}^{y_2} \mathrm{d}y \int_{-h}^{0} \mathrm{d}z \, \phi^{+}_{11_z} = \delta_2 \sqrt{2}\, a \, (\mathrm{i} - 1) \int_{y_1}^{y_2} \mathrm{d}y \left[\phi^{+}_{11} \right]_{z=-h}^{z=0} \tag{3.2.38}$$

must be added to the expression (2.5.160) of the forcing term $\mathcal{D}_{31}$ of the equation of motion of the gate. The following term must be added to the right hand side of (2.5.171)

$$\mathrm{i}\, \mathcal{D}_{\nu 31}\, q_{11} = \mathrm{i} \left[\mathcal{T}^{I}_{\nu 31} + \mathcal{T}^{II}_{\nu 31} \, (1 - 1/r) \right] = (\mathrm{i} - 1)\, \delta_2\, \theta\, \frac{a}{\sqrt{2}} \sum_{m=1} \sum_{n=0} b_m \beta_{mn} \left(\cosh K_n h - 1 \right), \tag{3.2.39}$$

where use has been made of the series representation (2.5.50). Upon multiplication by $-\mathrm{i}$ and division by c, expression (3.2.39) can be cast in (3.2.32) in the form $(1 + \mathrm{i})\ \delta_2\, \theta\, c''_L$ with

$$c''_L = \frac{a}{c\sqrt{2}} \sum_{m=1} \sum_{n=0} b_m \beta_{mn} \left(\cosh K_n h - 1 \right). \tag{3.2.40}$$

A second contribution to the viscous torque is given by the stresses acting on the sides of the gates that limit the structural gaps. These sides, whose area is $2ah$, are parallel to the x axis and intersect the y axis at $y = 1 - r$ (see figure 3-2). The inviscid diffraction theory developed in the previous chapter does not take into account the flow field on these parts of the gate surface. Still, an estimation must be developed.

The thickness of the oscillatory boundary layer which develops on each side of the gap is $O(\sqrt{\nu/\omega_0})$, always smaller than the gap width. In the laboratory experiments, $\sqrt{\nu/\omega} = 0.5$ mm, while the gap width is $\delta' = 5$ mm. Therefore the two facing boundary layers are always well separated. When the gates oscillate at its natural frequency, the boundary layers which develop on the sides of the gap can be approximated by the one of an oscillating plate with local horizontal velocity U^p_{11} imposed by the angular motion of the gates

$$U^p_{11} = \mathrm{i}(z + h)\, \theta \left\{ \begin{array}{c} 1 \\ 1 - 1/r \end{array} \right\}, \tag{3.2.41}$$

respectively for gate one and gate two. To solve this Stokes' problem, let

$$\eta = \frac{y - 1 + r}{\delta} \tag{3.2.42}$$

be the boundary layer coordinate. The solution for the boundary layer velocity is

$$\mathbf{U}_{11gap} = \left\{ \begin{array}{c} U_{11}^p \\ 0 \\ 0 \end{array} \right\} \Gamma(\eta), \tag{3.2.43}$$

with an associated (3,1) harmonic of the tangential stress

$$\tau_{\eta x 31} = U_{11}^p \frac{(\mathrm{i} - 1)}{\sqrt{2}} \tag{3.2.44}$$

The torque $\mathcal{T}_{\nu 31}$ can be obtained by integration of the elemental torque on the surface

$$\mathcal{T}_{\nu 31} = \int_{-h}^{0} \mathrm{d}z \, 2a \left(-\delta_2 \tau_{\eta x 31}\right) (z + h) = \sqrt{2}\, a \delta_2 \, (1 - \mathrm{i}) \int_{-h}^{0} \mathrm{d}z \, U_{11}^p \, (z + h) \tag{3.2.45}$$

Carrying out the integration in (3.2.45) and recalling that for mode 2 ($r = 1/3$) gate one has two wetted side, at $y = 0$ and $y = 1 - r$, obtain

$$\mathcal{T}_{\nu 31} = (1 + \mathrm{i})\, \delta_2 \theta \frac{\sqrt{2}}{3} a h^3 \left\{ \begin{array}{c} 1/r - 1 \\ 1 - 1/r \end{array} \right\}, \tag{3.2.46}$$

respectively for gate one and gate two. This (3,1) harmonic must also be added to (2.5.160) of the forcing term $\mathcal{D}_{31}$ of the equation of motion of the gate. The contribution to the last integral on the right hand side of (2.5.171) is therefore

$$\mathrm{i}\mathcal{D}_{\nu 31}\, q_{11} = \mathrm{i}\left[\mathcal{T}_{\nu 31}^{I} + \mathcal{T}_{\nu 31}^{II}\,(1 - 1/r)\right] = (\mathrm{i} - 1)\delta_2 \theta \frac{\sqrt{2}}{3} a h^3 \frac{1}{r}\left(\frac{1}{r} - 1\right) \tag{3.2.47}$$

Expression (3.2.47) is similar in form to (3.2.39) and therefore yields in the evolution equation a linear damping term of the form $(1 + \mathrm{i})\, \delta_2\, \theta\, c_L'''$, with

$$c_L''' = \frac{1}{c}\left[\frac{a}{\sqrt{2}} \sum_{i=1} \sum_{j=0} \beta_{ij} b_i \left(\cosh K_j h - 1\right) + \frac{\sqrt{2}}{3} a h^3 \frac{1}{r}\left(\frac{1}{r} - 1\right)\right]. \tag{3.2.48}$$

In the case of the laboratory experiments in the channel for mode 1 ($r = 1/2$), two extra gaps are present near the channel wall at $y = 0$ and $y = 1$ which are not present in a wide basin with many gates or in the prototype. To account for these extra gaps, multiply expression (3.2.48) by 2.

This last expression completes the panorama of viscous effects induced by laminar

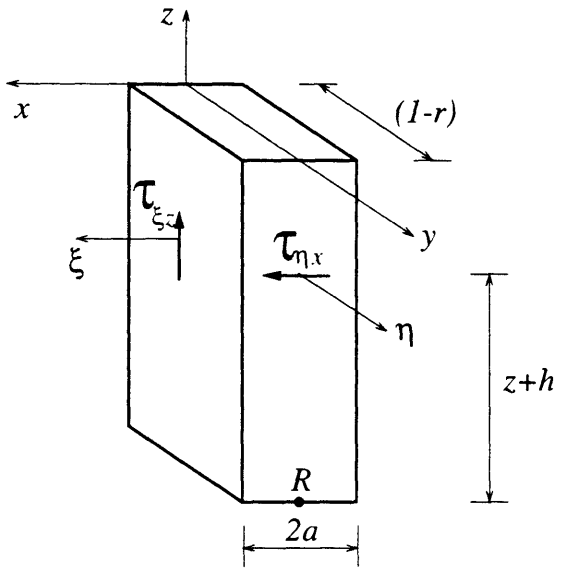

Figure 3-2: A 3d view of the model gate and acting shear stress.

boundary layers. We can define one coefficient c_L representing viscous effects

$$c_L = c_L' + c_L'' + c_L''' = \frac{1}{c\sqrt{2}} \sum_{m=1} \sum_{n=0} \left\{ \alpha_{mn}^2 \beta_{mn}^2 C_n + \sum_{n'=0} \left[\frac{\beta_{mn}\beta_{mn'}\left(K_{n'}^2 - 4\pi^2 m^2\right)}{\alpha_{mn} + \alpha_{mn'}} + \right.\right.$$
$$\left.\left. \frac{1}{G}\beta_{mn} \cosh K_n h \cosh K_{n'} h \left(\beta_{mn'} + 4 \sum_{m'=1} \frac{\beta_{m'n'}}{\alpha_{mn} + \alpha_{m'n'}} \right) \right] \right\} +$$
$$\frac{1}{c} \left[\frac{a}{\sqrt{2}} \sum_{i=1} \sum_{j=0} \beta_{ij} b_i \left(\cosh K_j h - 1\right) + \frac{\sqrt{2}}{3} a h^3 \frac{1}{r} \left(\frac{1}{r} - 1 \right) \right] \quad (3.2.49)$$

The evolution equation including the viscous effects may now be written

$$-\mathrm{i}\theta_{t_2} = \omega_2 \theta + \theta^2 \theta^* \left(c_N + \mathrm{i}\, c_R\right) + A_2 \theta^* c_F + (1 + \mathrm{i})\, \delta_2\, \theta\, c_L, \quad (3.2.50)$$

whose dimensional form reads

$$-\frac{\mathrm{i}}{\omega}\theta_{t'}' = \frac{\Delta\omega}{\omega}\theta' + \theta'^2\theta'^* \left(c_N + \mathrm{i}\, c_R\right) + \frac{A'}{b'}\theta'^* c_F + (1 + \mathrm{i})\, \delta\, \theta'\, c_L, \quad (3.2.51)$$

The coefficient c_L in (3.2.49) depends on the gate characteristics (S, I, a) implicitly through G and explicitly on a; it depends on the channel geometry h both explicitly and implicitly through G. In figure 3-3 the dependence of c_L on $a, S = 0.65I$ for

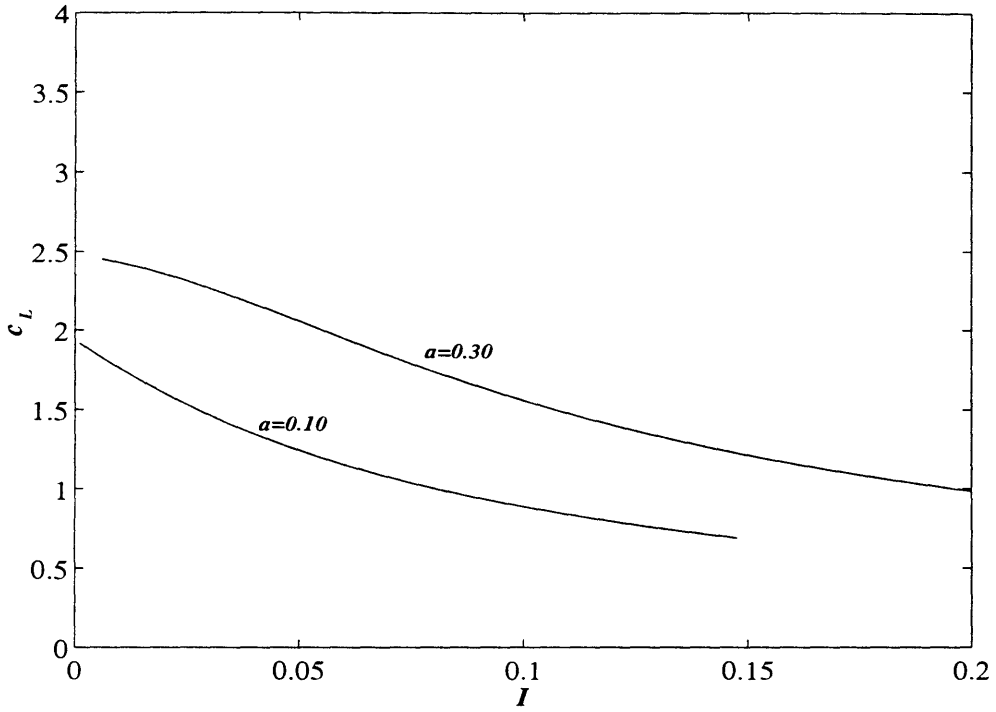

Figure 3-3: Linear viscous coefficient c_L for mode 1 and for laboratory flume with sidewalls effect, expression 3.2.49. Computations are for $h = 1.0$ and varying $S = 0.65I$; $a = 0.1$ and 0.3

fixed $h = 1$ is shown, while figure 3-4 shows the dependence of c_L on $h, S = 0.65I$ for fixed $a = 0.2$. As the inertia increases c_L decreases, that is heavier gates have lesser important viscous damping. For fixed I, an increase in a or h, i.e. an increase in the displaced volume, causes an increase in the value of c_L: more buoyant gates have more important viscous damping.

It is well known that in the laboratory experiments meniscous effects on the tank walls can be as significant as the dissipation in the boundary layers. The theoretical estimates derived here may serve as a guide for the form and order of magnitude as will be examined in a later session when experiments are discussed.

3.3 The effect of separation at the gate edges

For gate with sharp corners or rounded corners at large amplitude motion, separation and vortex shedding occurs alternatively on the two sides of the gate system. A sketch of the phenomenon is shown in figure 3-5. To assess the dynamic effects induced by this phenomenon, we consider a simple model of the gates moving in a piston-like manner rather than as a swinging flap, with a velocity approximated by the vertical

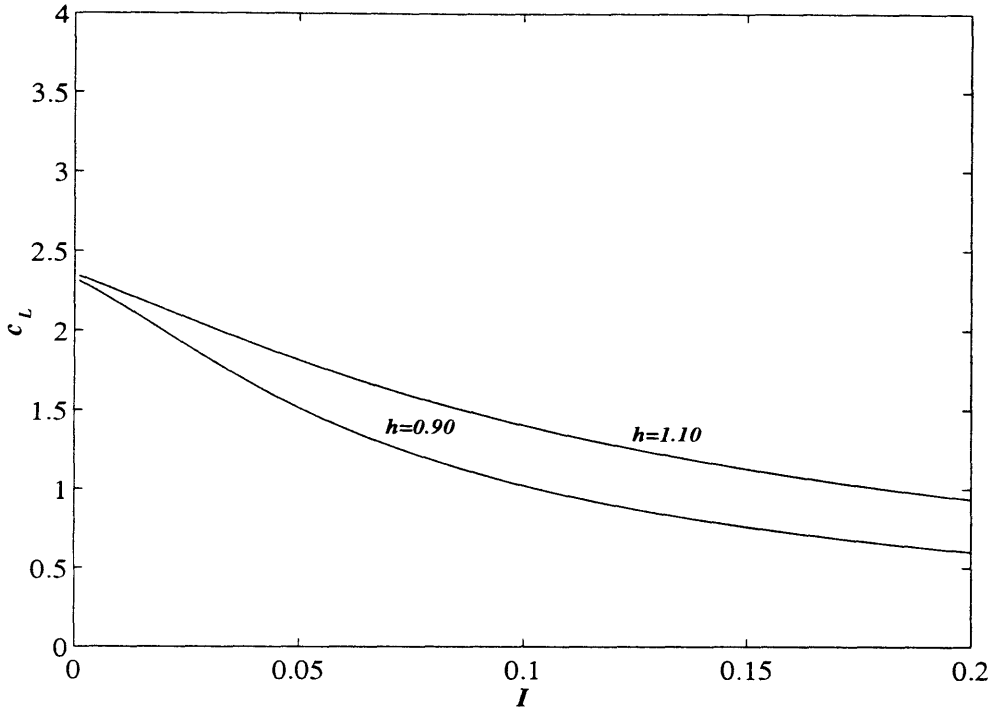

Figure 3-4: Linear viscous coefficient c_L for mode 1 and for laboratory flume with sidewalls effect, expression 3.2.49. for fixed $a = 0.2$ and varying $S = 0.65I$; Computations are for $a = 0.2$ and varying $S = 0.65I$; $h = 0.9$ and 1.1

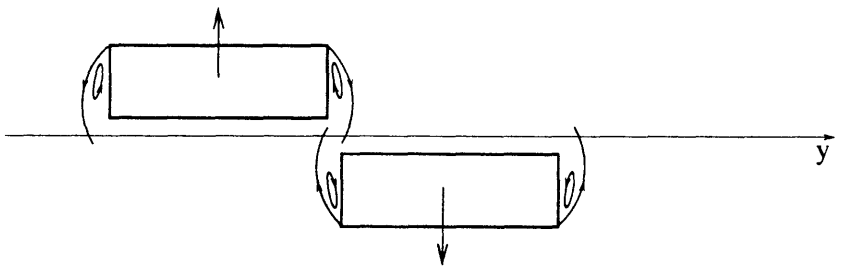

Figure 3-5: Schematic view of the separation phenomenon at the gate system corners

mean of the gate velocity

$$U' = -\frac{1}{h}\int_{-h}^{0} \mathrm{d}z'\,(z'+h')\Theta'_{1_t} = -\frac{h'}{2}\,\Theta'_{1_t}. \tag{3.3.1}$$

Consider a frame of reference fixed on one gate so that the gate is immersed in an oscillatory flow. A simplified model is the one of a constriction in a channel with a uniform oscillating flow, as is represented in figure 3-6a,b. In the picture, the gates, oscillating as in mode 1, are represented by the shaded squares denoted by 1 and 2. Figure 3-6a is for the first half cycle; when the flow reverses, the situation is depicted in figure 3-6b. Note that the picture is for gate 1 only. The same considerations apply for gate 2.

We are interested in evaluating the force acting on the constriction face GG' located at $x' = x'_0$, as a result of the presence of the corner G'. Due to this corner the fluid separates from the wall at G' creating a jet, which, after an expansion, reattaches to the wall downstream at C''. Strictly speaking, we are making the simplifying hypothesis that the distance $G'C''$ is shorter than the gate thickness $2a'$, so that the flow adheres again on the gate surface. A second strong simplification is to neglect that in the real case the gate are at their peak velocity (at which flow separation is most likely to occur) when they pass through the vertical position, i.e. when they are aligned, and not out of phase like in figure 3-6. This is not a limitation since the aim of this model is to evalute the order of magnitude of the effects of the phenomenon.

In BB' the fluid is again uniform across the section. Note that because the section of the channel changes from S to rS, the fluid accelerates with a resulting net pressure force on GG'. Such a force has been already thoroughly described by the added inertia in the trapped mode solution ϕ_{11} and therefore will have to be subtracted the from the total force that we are about to derive. For completeness we analyze the phenomenon using dimensional quantities and introduce later scaling and nondimensionalization.

In the region of accelerating flow between section AA' at $x' = x'_-$ and the section of minimum area CC' (*vena contracta*) at $x' = x'_c$, dissipation is negligible and Bernoulli equation applies

$$p'_- - p'_c + \frac{\rho}{2}\left({u'_-}^2 - {u'_c}^2\right) - \rho\frac{\partial}{\partial t}\int_{x'_-}^{x'_c} \mathrm{d}x\,u' = 0, \tag{3.3.2}$$

where $p' = \rho g\zeta'$ is the dimensional pressure within the fluid. It is assumed that at both station the transverse variation is negligible. If $u'_- = U'$, with U' given by (3.3.1), continuity requires

$$S'u'_- = c_c r S' u'_c = r S' u'_+, \tag{3.3.3}$$

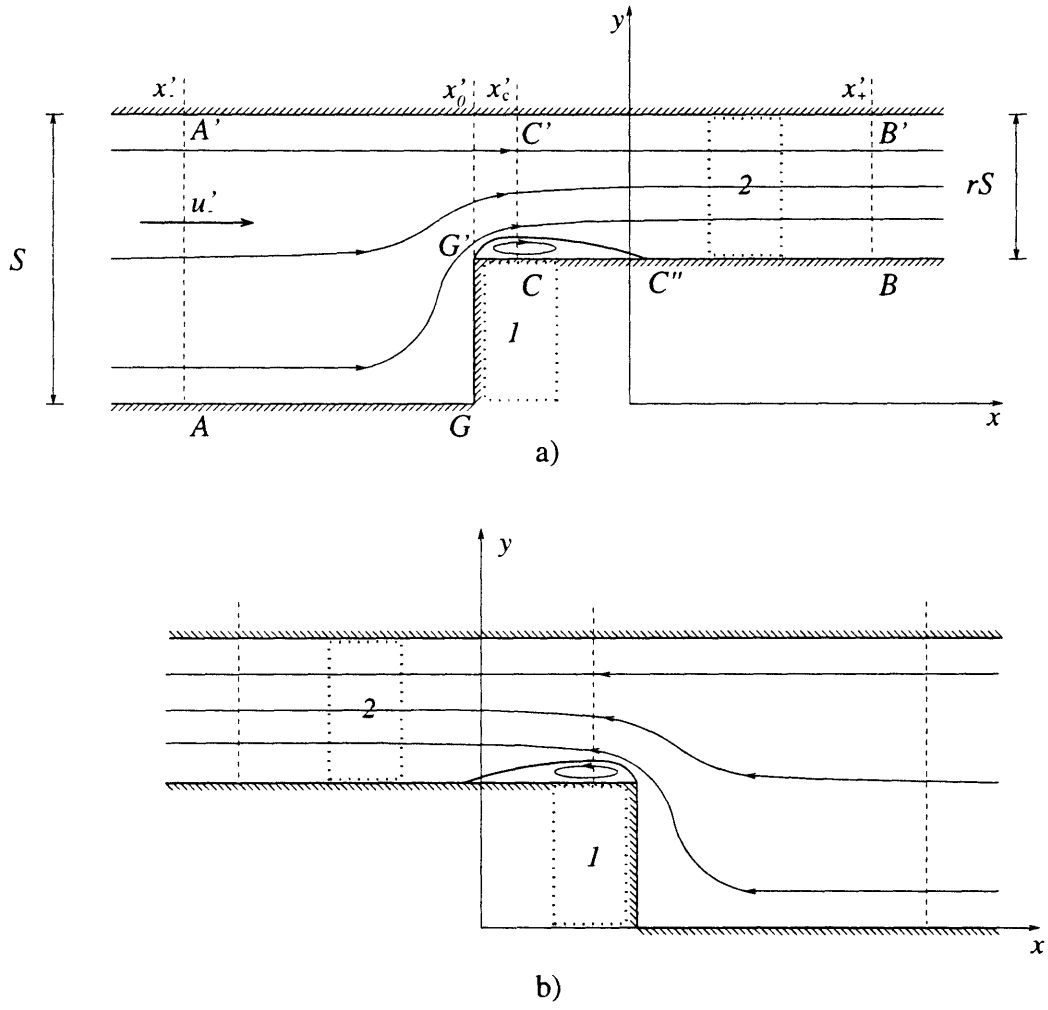

Figure 3-6: Simple model for the separation due to corners. Model is shown for gate one. a) gate one moving to the left; b) gate one moving to the right

where $S' = b'h'$ is the cross section area of the channel, c_c is the contraction coefficient and u'_c is the velocity in CC'. We now apply global momentum conservation to the control volume $AA'GG'CC'$. In the eddy zone outside the jet and behind G', velocity is very low so that the pressure is uniform across it and equal to that in the jet, p'_c. If $-F'_{tot}$ is the force that the channel exerts on the fluid through GG', the balance of total momentum requires

$$F'_{tot} - p'_- S' + p'_c r S' - \rho {u'_-}^2 S' + \rho {u'_c}^2 c r S' + \rho \frac{\partial}{\partial t} \int_{x'_-}^{x'_c} \mathrm{d}x\, u' S'(x') = 0. \tag{3.3.4}$$

where with $S'(x')$ we have indicated S', in the channel $x' < x'_0$, and the cross sectional area of the jet S'_J in the channel $x' > x'_0$. Using (3.3.2) and the first of (3.3.3) for pressure and velocity in the *vena contracta*, p'_c and u'_c, and substituting back into (3.3.4) we obtain

$$F'_{tot} = (1-r)\, p_- S + \rho {u'_-}^2 S \left(1 - \frac{r}{2} + \frac{1}{2 r c_c^2} - \frac{1}{r c_c}\right) + (r-1)\, \rho S' \frac{\partial}{\partial t} \int_{x'_-}^{x'_0} \mathrm{d}x'\, u'. \tag{3.3.5}$$

If we now consider flow without a *vena contacta* and therefore always adhering to GB, there is still a force $-F_p$ that GG' exerts on the fluid in order to accelerate it into the narrower channel of section rS'. In this case Bernoulli equation applies from x'_- all the way to x'_+

$$p'_- - p'_+ + \frac{\rho}{2}\left({u'_-}^2 - {u'_+}^2\right) - \rho \frac{\partial}{\partial t} \int_{x'_-}^{x'_+} \mathrm{d}x'\, u' = 0. \tag{3.3.6}$$

Application of momentum conservation to the fluid in $AGG'BB'$ yields

$$F'_p - p'_- S' + p'_+ r S' - \rho {u'_-}^2 S' + \rho {u'_+}^2 r S' + \rho \frac{\partial}{\partial t} \int_{x'_-}^{x'_+} \mathrm{d}x'\, u' S'(x') = 0. \tag{3.3.7}$$

Using (3.3.6) for p_+ and the second of (3.3.3) for u'_+ we obtain

$$F'_p = (1-r)\, p_- S + \rho {u'_-}^2 S \left(1 - \frac{r}{2} - \frac{1}{2r}\right) + (r-1)\, \rho S' \frac{\partial}{\partial t} \int_{x'_-}^{x'_0} \mathrm{d}x'\, u'. \tag{3.3.8}$$

and because $F'_{tot} = F'_v + F'_p$, the net force F'_v due to the sudden expansion of the jet between C and C'' can be obtained subtracting (3.3.8) from (3.3.5)

$$F'_v = F'_{tot} - F'_p = \rho {u'_-}^2 S \frac{1}{2r} \left(\frac{1}{c_c} - 1\right)^2. \tag{3.3.9}$$

When we consider the second half of a cycle, the flow to be considered is depicted in figure 3-6b. The resulting force has the same intensity but opposite direction;

therefore in order to account for both flow directions we write

$$F'_v = \rho b' h' |u'_-| u'_- \frac{1}{2r} \left(\frac{1}{c_c} - 1 \right)^2 . \tag{3.3.10}$$

The resulting torque on gate one, $\mathcal{T}'^I_v$, is obtained upon multiplication of the moment arm $h'/2$

$$\mathcal{T}'^I_v = \frac{1}{2} \rho b' h'^2 |u'_-| u'_- \frac{1}{2r} \left(\frac{1}{c_c} - 1 \right)^2 . \tag{3.3.11}$$

When we consider the force acting on gate 2 (see figure 3-6), we have to consider a channel section changing from S' to $(1-r)S'$. Repeating the same arguments, the torque is found to be

$$\mathcal{T}'^{II}_v = \frac{1}{2} \rho b' h'^2 |u'_-| u'_- \frac{1}{2(1-r)} \left(\frac{1}{c_c} - 1 \right)^2 , \tag{3.3.12}$$

We can define the loss coefficient f as

$$f = \frac{1}{4} \left(\frac{1}{c_c} - 1 \right)^2 , \tag{3.3.13}$$

so that the torque on the gates can be written

$$\mathcal{T}'_v = f \rho b' h'^2 |u'_-| u'_- \left\{ \begin{array}{c} 1/r \\ 1/(1-r) \end{array} \right\} . \tag{3.3.14}$$

Expression (3.3.14) is nonlinear in u'_- and can be further simplified by the method of equivalent linearization, i.e. if we require that the torque $\mathcal{T}'_v$ can be expressed as

$$\mathcal{T}'_v = f_e \, \rho b' h'^2 u'_- \left\{ \begin{array}{c} 1/r \\ 1/(1-r) \end{array} \right\} , \tag{3.3.15}$$

and then determine f_e by imposing that the energy dissipated in one period, calculated according to expressions (3.3.14) and (3.3.15) is the same

$$\int_0^{2\pi/\omega} \mathrm{d}t' \, f h'^2 \rho |u'_-| {u'_-}^2 = \int_0^{2\pi/\omega} \mathrm{d}t' \, f_e h'^2 \rho {u'_-}^2 , \tag{3.3.16}$$

from which

$$f_e = f \frac{\int_0^{2\pi/\omega} \mathrm{d}t' \, |u'_-| {u'_-}^2}{\int_0^{2\pi/\omega} \mathrm{d}t' \, {u'_-}^2} . \tag{3.3.17}$$

Expression (3.3.17) can also be obtained by requiring the mean square of the error to be minimum.

Because to leading order u'_- is a harmonic function of frequency ω, phase ψ' and

amplitude $\overline{u}'_-$

$$u'_- = \overline{u}'_- \cos(\omega t' + \psi'), \tag{3.3.18}$$

evaluation of the integrals in (3.3.17) is straightforward

$$f_e = \frac{8}{3\pi} f \overline{u}'_-. \tag{3.3.19}$$

f_e is therefore a function dependent on the amplitude of the harmonic oscillation. Expression (3.3.15) then becomes

$$\mathcal{T}'_v = \frac{8}{3\pi} f b' \rho h'^2 \overline{u}'_- u'_- \left\{ \begin{array}{c} 1/r \\ 1/(1-r) \end{array} \right\}. \tag{3.3.20}$$

The above expression can then be recast in nondimensional form upon introduction of the familiar nondimensional variables $h = h'/b'$, $u = u'/\epsilon\omega_0 b'$

$$\mathcal{T}'_v = \epsilon\rho\omega_0 b'^5 \left(\epsilon \frac{8}{3\pi} f \rho h^2 \overline{u}_- u_-\right) \left\{ \begin{array}{c} 1/r \\ 1/(1-r) \end{array} \right\}. \tag{3.3.21}$$

The nondimensional torque that must be added to expression (2.4.11) is then

$$\mathcal{T}_v = \epsilon \frac{8}{3\pi} f h^2 \overline{u}_- u_- \left\{ \begin{array}{c} 1/r \\ 1/(1-r) \end{array} \right\}. \tag{3.3.22}$$

Recall that to the leading order

$$u_- = -\frac{h}{2}\Theta_{1_t} = \mathrm{i}\frac{h}{2} \left\{ \begin{array}{c} 1 \\ 1-1/r \end{array} \right\} \theta \, \mathrm{e}^{-\mathrm{i}t} + *, \tag{3.3.23}$$

respectively for the gate one and gate two.

The contraction coefficient c_c for the flow considered is close to unity, therefore from expression (3.3.13) we deduce $f \ll 1$. Let $f = \epsilon f_1$, the torque (3.3.22) is then a third order $O(\epsilon^2)$ quantity and forces the first harmonic in the equation of gate motion with the term

$$\mathcal{T}_{v31} = \mathrm{i}\frac{2}{3\pi} f_1 h^4 |\theta|\theta \left\{ \begin{array}{c} 1/r \\ -1/r \end{array} \right\} \tag{3.3.24}$$

which appears as an extra term in (2.5.160). Finally, in the last integral of the solvability condition (2.5.171) appears a new term

$$\mathrm{i}\mathcal{D}_{\nu 31} q_{11} = \mathrm{i}\left[\mathcal{T}^I_{\nu 31} + \mathcal{T}^{II}_{\nu 31}(1-1/r)\right] = -\frac{2}{3\pi} f_1 h^4 |\theta|\theta \frac{1}{r^2}. \tag{3.3.25}$$

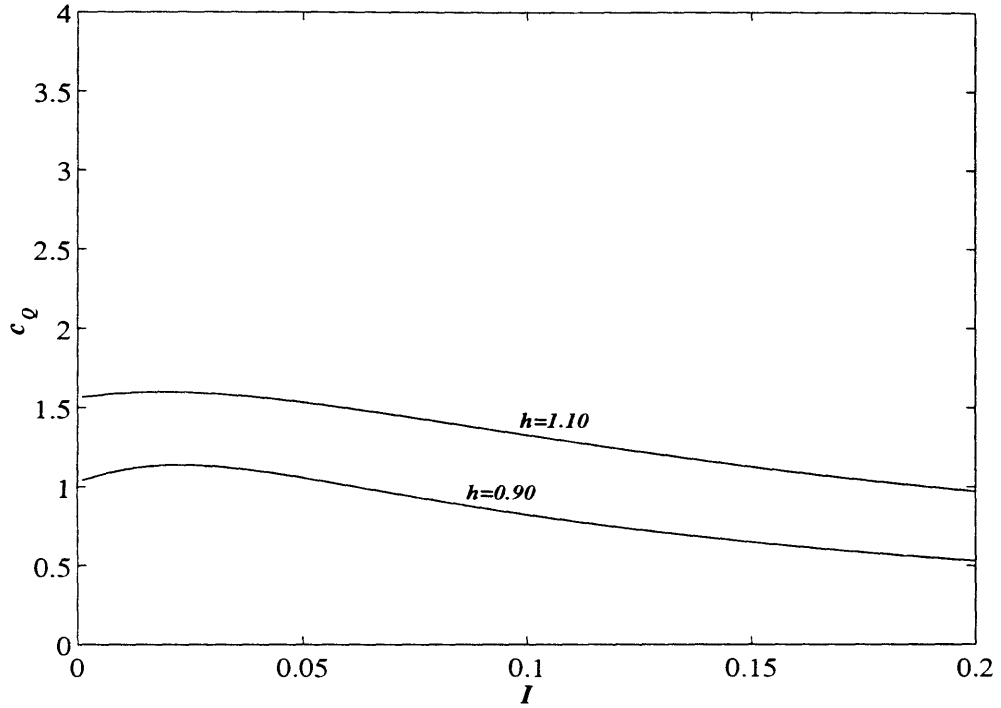

Figure 3-7: Quadratic viscous damping coefficient c_Q of the evolution equations for fixed $a = 0.2$ and varying $S = 0.65I$; $h = 0.9$ and 1.1

Defining the coefficient c_Q as

$$c_Q = \frac{1}{c}\,\frac{2h^4}{3\pi r^2}, \tag{3.3.26}$$

we find that the final evolution equation (3.2.50) has an extra term (the latter) on the right hand side

$$-\,\mathrm{i}\theta_{t_2} = \omega_2\theta + \theta^2\theta^*\,(c_N + \mathrm{i}\,c_R) + A_2\theta^*\,c_F + (1+\mathrm{i})\,\delta_2\,\theta\,c_L + \mathrm{i}f_1\,|\theta|\,\theta\,c_Q \tag{3.3.27}$$

The above evolution equation now gives a more realistic description of dissipative effects. c_R is the cubic damping associated with radiation of the second harmonic. c_L is the linear damping associated with viscous dissipation (boundary layers effect). The quadratic damping c_Q is associated with fluid separation effect. Its dependence on I for fixed $a = 0.2$ and different values of h is shown in figure 3-7. As I increases c_Q decreases mildly. There is a stronger dependence of c_Q on h as both its definition (3.3.26) and figure 3-7 show.

Finally, when the gates have sharp corners and therefore separation occurs, there are no laminar boundary layers on the two sides of the gaps and c_L must contain only the effect of the laminar boundary layer on the faces of the gates, i.e. (3.2.40) is to be

used. When the corners are rounded, as in the case of the experiments, separation is less likely to occur, so that the expression for c_L to be used is (3.2.48) and c_Q is to be set to zero. If we multiply (3.3.27) by θ^*, the complex conjugate of (3.3.27) by θ and subtract the resulting two expressions, we obtain

$$|\theta|^2_{t_2} = -|\theta|^4 c_R + A_2 \mathrm{Im}\theta^2 \, c_F - \delta_2 \, |\theta|^2 c_L - f_1 |\theta|^3 c_Q. \tag{3.3.28}$$

The above energy equation states the change of the trapped wave is due to energy input with the incoming wave (the second term on the RHS) and to the linear, quadratic and cubic damping effects.

Multiplying (3.3.27) by ϵ^3 we obtain the evolution equation in terms of the physical variables

$$-\frac{\mathrm{i}}{\omega_0}\,\theta'_{t'} = \frac{\Delta\omega}{\omega_0}\,\theta' + \theta'^2\theta'^* \,(c_N + \mathrm{i}\,c_R) + \frac{A'}{b'}\,\theta'^*\,c_F + (1+\mathrm{i})\,\delta\,\theta'\,c_L + \mathrm{i}f\,|\theta'|\,\theta'\,c_Q, \tag{3.3.29}$$

where we recall that θ' is in rad, ω_0 is the natural angular frequency in rad/sec, A' is the incident wave amplitude in meters, b' the modal half period in meters, δ is the ratio $\sqrt{\nu/\omega_0}/b'$, f is the quadratic loss coefficient and t' is time in seconds; all the c's are numerical coefficients.

3.3.1 Estimation of the loss coefficient f

In the previous section we have assessed the effect of flow separation on the evolution equation. However such analysis is only qualitative and has served the purpose of justifying the presence of a quadratic term in the evolution equation. If we want to maintain the validity of expression (3.3.26) for the coefficient c_Q, then all the uncertainties of the heuristic model can be thought of being included in the numerical value of the coefficient f, whose formal expression (3.3.13) requires the knowledge of the contraction coefficient c_c.

In the spirit of the present order of magnitude estimation, we shall estimate c_c by using the solution of Von Mises for the free streamlines following an aperture with inclined walls. Figure 3-8 is taken from Daily & Harleman(1966) and gives the coefficient c_c for various geometrical ratios b/a and angle of attack α. With reference to the symbols of figure 3-8, from the ratio b/a we get the value of c_c, which in turn is introduced in (3.3.13) to give f

$$\begin{array}{llllll} \text{Mode 1} \rightarrow & b/a = 1/2, & \alpha = 90, & c_c = 0.64, & f = 0.08 \\ \text{Mode 2} \rightarrow & b/a = 1/3, & \alpha = 90, & c_c = 0.62, & f = 0.09 \end{array} \tag{3.3.30}$$

It is only through comparison with experimental data that quantitative assessment of the quadratic dissipation term can be obtained.

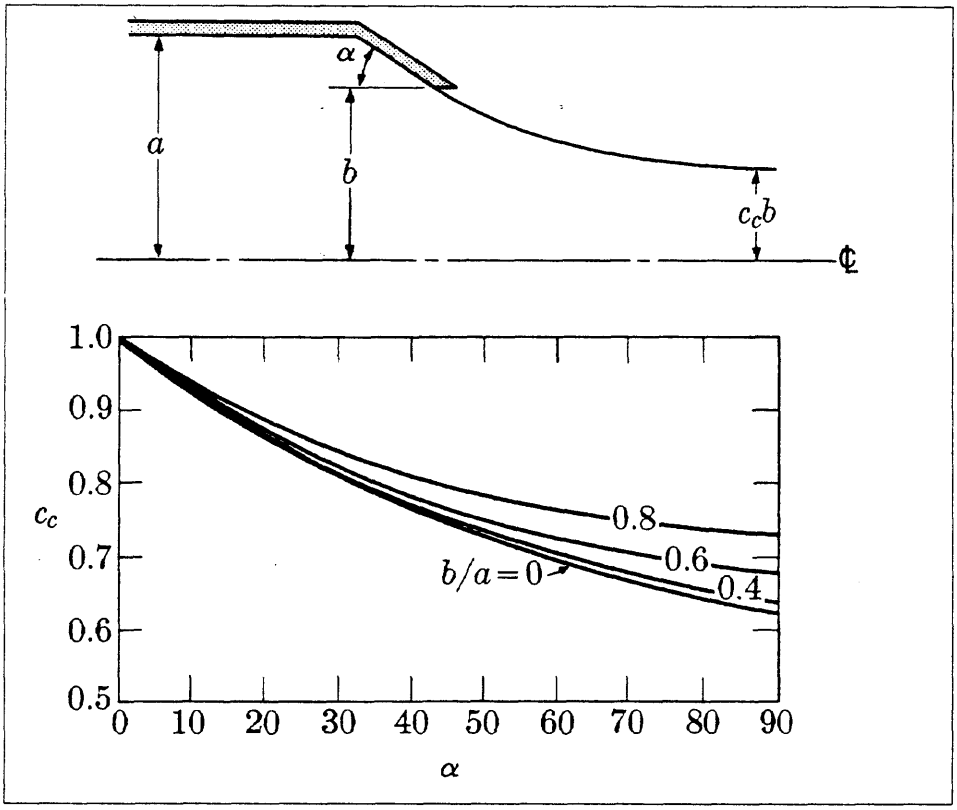

Figure 3-8: Free streamline flow from an aperture (from Daily & Harleman(1966)).

3.4 Validation of the theory with experiments

The experiments of Tran(1996) consist of free and forced oscillations. In the free oscillation experiments, the two gates are first displaced by equal and opposite angles from the vertical axis and then released. Then, the angular displacement $\Theta'_e(t') = \theta'_e(t')\cos(\omega t' - \psi_e)$ of both gates are recorded as a function of time. To allow the modal shape of the free surface to build up, the first cycle of each time series is cut, so that the initial condition to be compared with the theory is given by the first peak after the release. The forced oscillation experiments will be discussed later in section 4.4.

For free oscillations, equation (3.3.29) does not contain the forcing term $c_F A'/b'\,\theta'^*$ and the detuning term $\Delta\omega/\omega_0\,\theta'$

$$-\frac{\mathrm{i}}{\omega_0}\,\theta'_{t'} = \delta\, c_L\,\theta' + (c_N + \mathrm{i}c_R)\,\theta'^2\theta'^* + \mathrm{i}\,\delta\, c_L\,\theta' + \mathrm{i}\,f c_Q|\theta'|\,\theta'. \tag{3.4.1}$$

Therefore, using polar coordinates $\theta' = R\mathrm{e}^{\mathrm{i}\psi}$, the resulting amplitude equation in R decouples from the equation for ψ

$$R_{t'} = -\omega_0\, R\left(c_R R^2 + c_Q R + c_L\right), \tag{3.4.2}$$

The solution of (3.4.2) can only be found in implicit form, $t' = t'(R;\, R_0)$, where t'=0 for $R = R_0$.

For $4c_R c_L/{c_Q}^2 < 1$

$$t' = \frac{1}{2c_L\omega_0}\left\{\log\left[\frac{c_R + c_L R^{-2} + c_Q R^{-1}}{c_R + c_L R_0^{-2} + c_Q R_0^{-1}}\right] + \frac{1}{C}\log\left[\frac{2c_R R + c_Q\,(R/R_0+1) + 2c_L R_0^{-1} + C\,(R/R_0 - 1)}{2c_R R + c_Q\,(R/R_0+1) + 2c_L R_0^{-1} + C\,(R/R_0 - 1)}\right]\right\} \tag{3.4.3}$$

where for brevity $C = (1 - 4c_R c_L/{c_Q}^2)^{1/2}$,

For $4c_R c_L/{c_Q}^2 > 1$

$$t' = \frac{1}{2c_L\omega_0}\left\{\log\left[\frac{c_R + c_L R^{-2} + c_Q R^{-1}}{c_R + c_L R_0^{-2} + c_Q R_0^{-1}}\right] + \frac{2}{C}\,\mathrm{atan}\left[\frac{C(R - R_0)}{2c_L + 2c_R R R_0 + c_Q(R + R_0)}\right]\right\}, \tag{3.4.4}$$

with $C = (4c_R c_L/{c_Q}^2 - 1)^{1/2}$. Next we compare the theoretical solution with the free oscillation experiments in the wave channel and in the wave basin.

3.4.1 Experiments in the wave channel

Theoretical viscous dissipation coefficients

In table 3.1 the parameters characterizing the laboratory setup in the channel are summarized. The geometry of the channel and the gate was depicted in figure 1-4. The mass M' is weighted on a precision scale. The distance d' of the center of mass from the center of rotation is measured by a strain gage. Finally the inertia I' is evaluated from the period of the small amplitude oscillations in air of the gate hanging upside down.

For these set of data the nondimensional eigenfrequency of mode 1 is calculated to be $G = 1.305$, which correspond to a frequency of $\omega_0/2\pi = 0.713$ Hz. Next the c's are calculated to be

$$c_N = 2.49,\ c_R = 1.47,\ c_F = 0.90,\ c_L = 2.10,\ c_Q = 1.84, \tag{3.4.5}$$

while δ is obtained from (3.1.15) once ω_0 is known, $\delta = 0.0013$. The loss coefficient f has been determined in section 3.3.1 to be 0.08 for mode 1. In the case of the experiments in the wave channel, the flow between the wall gaps analyzed in section 2.7 is a source of additional viscous dissipation (but not of radiation damping, see section 2.7). The associated energy loss is hard to estimate in the present perturbation scheme. A crude estimation can be obtained by using a slightly higher value of f, say 0.1. Therefore

$$\delta\, c_L = 0.0028, \qquad f c_Q = 0.184. \tag{3.4.6}$$

In the experiments, several initial conditions are tested, ranging from about 4 to 10 deg. Two sample time series for one of the two gates are shown in figure 3-9, with initial conditions respectively of 5 and 9.2 deg. The maxima of the time series are indicated by asterisks.

For each experimental time series, the absolute values of the minima are taken and, together with the maxima, are compared with the theoretical envelope. The result is shown in figure 3-10 for the same time series of figure 3-9. Clearly, the theory overpredicts the gate displacement. This is likely to be due to the fact that the linear damping coefficient c_L does not contain all possible linear damping effect, such as the effects of the friction of the hinges, of the measurement devise (potentiometer). Similarly, the quadratic damping term $f c_Q$ does not account for other sources of damping such as radiation of harmonics of higher order. For example, interaction of the second order forced second harmonic with the first order trapped wave, forces at the third order propagating modes in the third harmonic, which are negligible within the order of approximation of the evolution equation, but are always present in the laboratory experiments. In other words, the estimated δc_L and $f c_Q$ are not large enough.

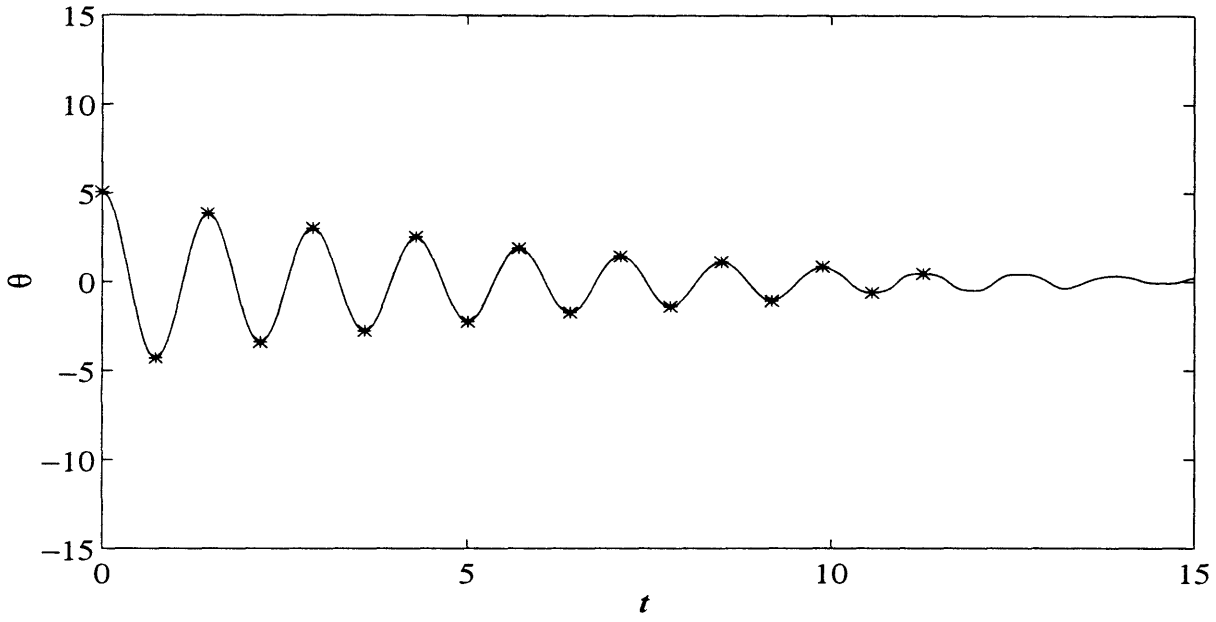

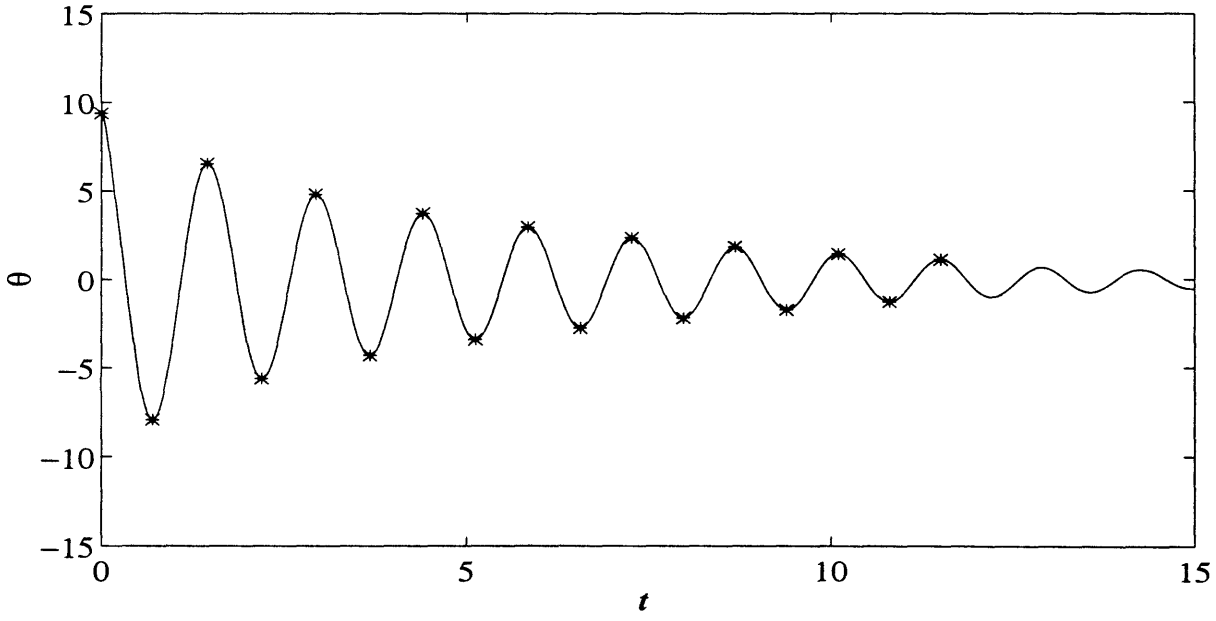

Figure 3-9: Sample free oscillation experiments. The asterisks indicate the maximum used to fit the theoretical envelope.

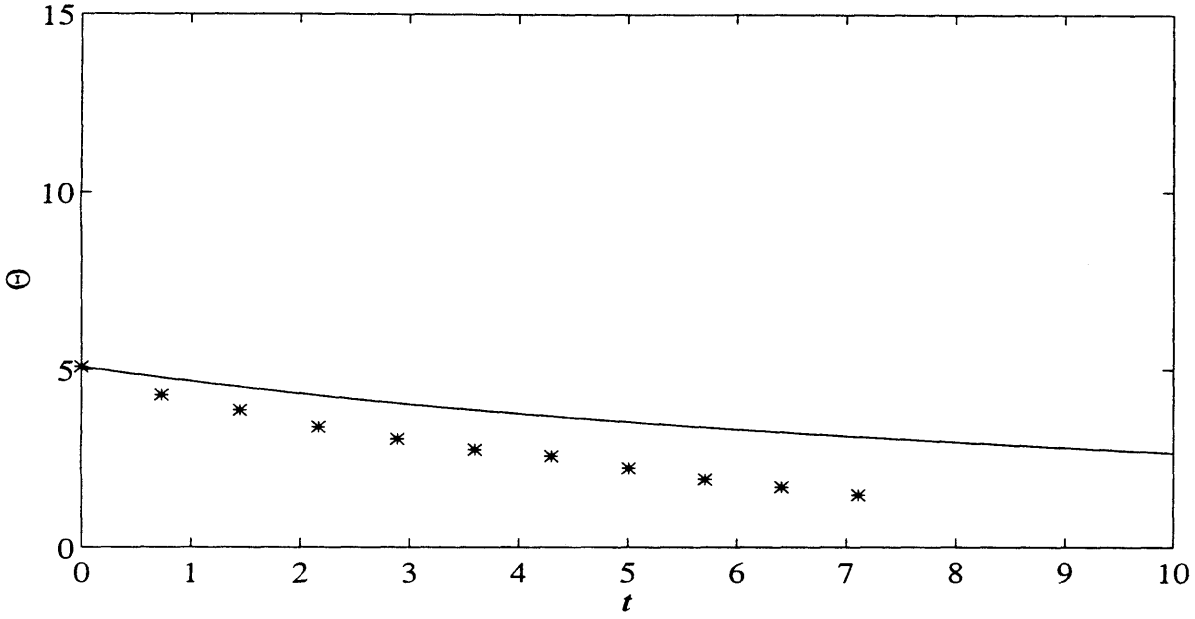

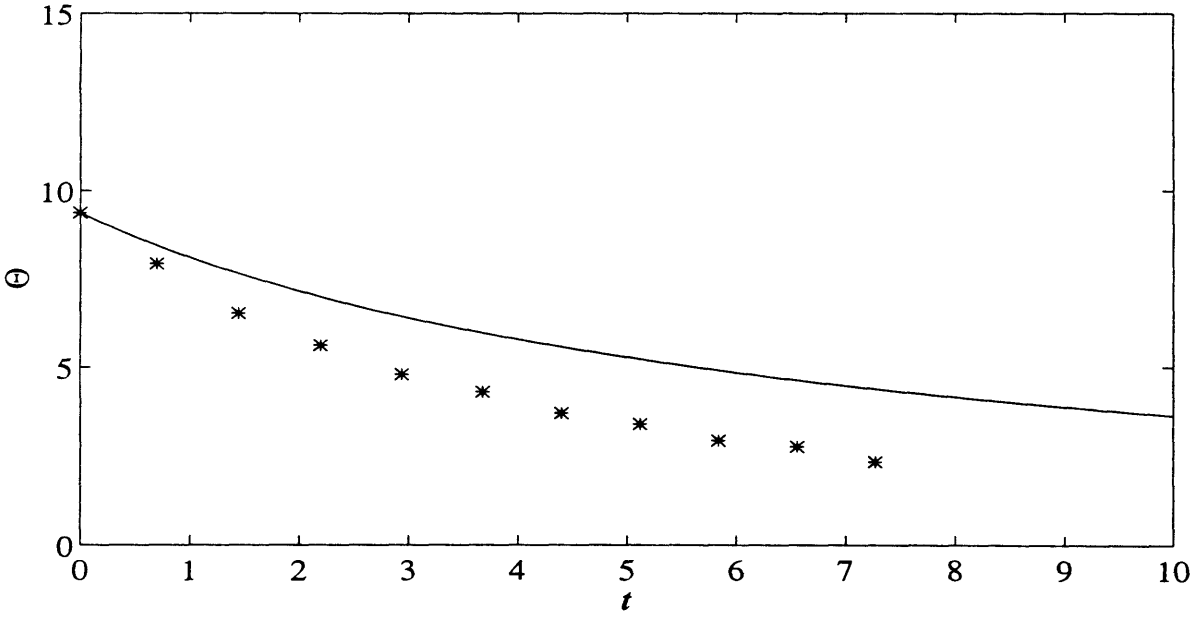

Figure 3-10: Comparison of the theoretical envelope (solid line) with the free oscillation experiments, denoted by asterisks.

DIMENSIONAL DATA		NONDIMENSIONAL DATA	
I'	0.106 kg m^2	I	0.014
M'	1.271 kg	M	0.023
d'	0.232 m	d	0.617
$S'=M'd'$	0.295 kg m	$S=Md$	0.014
a'	0.070 m	a	0.187
h'	0.370 m	h	0.992
b'	0.376 m	b	1
ρ	1.004 Mg m^3		

Table 3.1: Geometrical and inertial parameters of the channel experiments.

Fitted viscous dissipation coefficients

In the previous section we recognized the need to determine values of δc_L and $f c_Q$ that better fit the data. This can be achieved by finding a combination that minimize the distance of the theoretical envelope from the experimental time series. That is, the distance from the theoretical envelope is summed for all experimental data points to give an estimator E of the fitting

$$E = \sum_i (\theta' - \theta'_e)_i^2 , \tag{3.4.7}$$

where i extends to all the experimental data points. Then, an exhaustive search of the minimum of E in the parameter plane $\delta c_L \sim f c_Q$ is performed. The combination of viscous damping coefficients that minimize (3.4.7) is

$$\delta\, c_L = 0.009, \qquad f c_Q = 0.291. \tag{3.4.8}$$

Keeping the same theoretical values of δ and f, this corresponds to $c_L = 6.10$ and $c_Q = 2.91$, which must be compared with the theoretical values estimated in the previous section: $c_L = 2.10$ and $c_Q = 1.84$. An equivalent interpretation can be obtained by letting this larger dissipation be modeled by a larger equivalent boundary layer thickness δ and loss coefficient f, while retaining the theoretical values of c_L and c_Q. This yields $\delta = 0.0042$ and $f = 0.1580$, to be now compared with the theoretical $\delta = 0.0013$ and $f = 0.10$. In both cases the new values are respectively about three

and one and a half times the theoretical ones. Note that comparison of the theoretical and experimental value of the quadratic term is only an exercise, considered the spirit of order-of-magnitude estimation in which the quadratic term was obtained.

Naturally, with these new values, the experimental time series and theoretical envelopes are in agreement, as can be seen in figure 3-11.

3.4.2 Experiments in the wave basin

Theoretical viscous dissipation coefficients

In the Gunther wave basin Tran(1996) has conducted a detailed experimental investigation of the possible modulational resonances of the envelope of the trapped wave. The experimental setup consists of an array of eleven full gates and two half gates places in a partition of the wave basin bounded by vertical walls. The two half gates are positioned by the vertical walls, so that modal periodicity is assured. Incident waves are generated at one end and absorbed by a beach at the other. For a detailed description of the setup see Tran(1996). Here we report the theoretical calculation of the coefficients of the evolution equation for the particular gate and channel configuration and the fitting of the viscous dissipation coefficients to the free oscillation data.

The dimensions of the gate for the wave basin experiments are reported in figure 3-12. In table 3.2 the parameters characterizing the gate setup are summarized. The mass M' is weighted on a precision scale. The distance d' of the center of mass from the center of rotation and the inertia I' are simply evaluated from the geometry of the set-up.

For these data the nondimensional eigenfrequency of mode 1 is calculated to be $G = 2.040$, which corresponds to a frequency of $\omega_0/2\pi = 0.698$ Hz. Next, the c's and δ are calculated to be

$$c_N = 27.330,\ c_R = 2.271,\ c_F = 1.630,\ c_L = 1.706,\ c_Q = 4.250,\ \delta = 0.0018, \quad (3.4.9)$$

while f was evaluated in section 3.3.1 to be 0.08 for mode 1. Note that in this case, unlike the wave channel, the gap walls are only at the two ends of the gate array and have absolutely negligible effects on the dynamics. Hence we use the original value $f = 0.08$ and expression (3.2.34) for the quota c'_L of the linear viscous dissipation coefficient c_L.

For these values we obtain the theoretical estimates

$$\delta c_L = 0.0031, \qquad f c_Q = 0.34, \quad (3.4.10)$$

Also for the basin set-up, we performed free oscillation experiments and made comparisons similar to section 3.4.1, which lead to the same conclusions, that is the

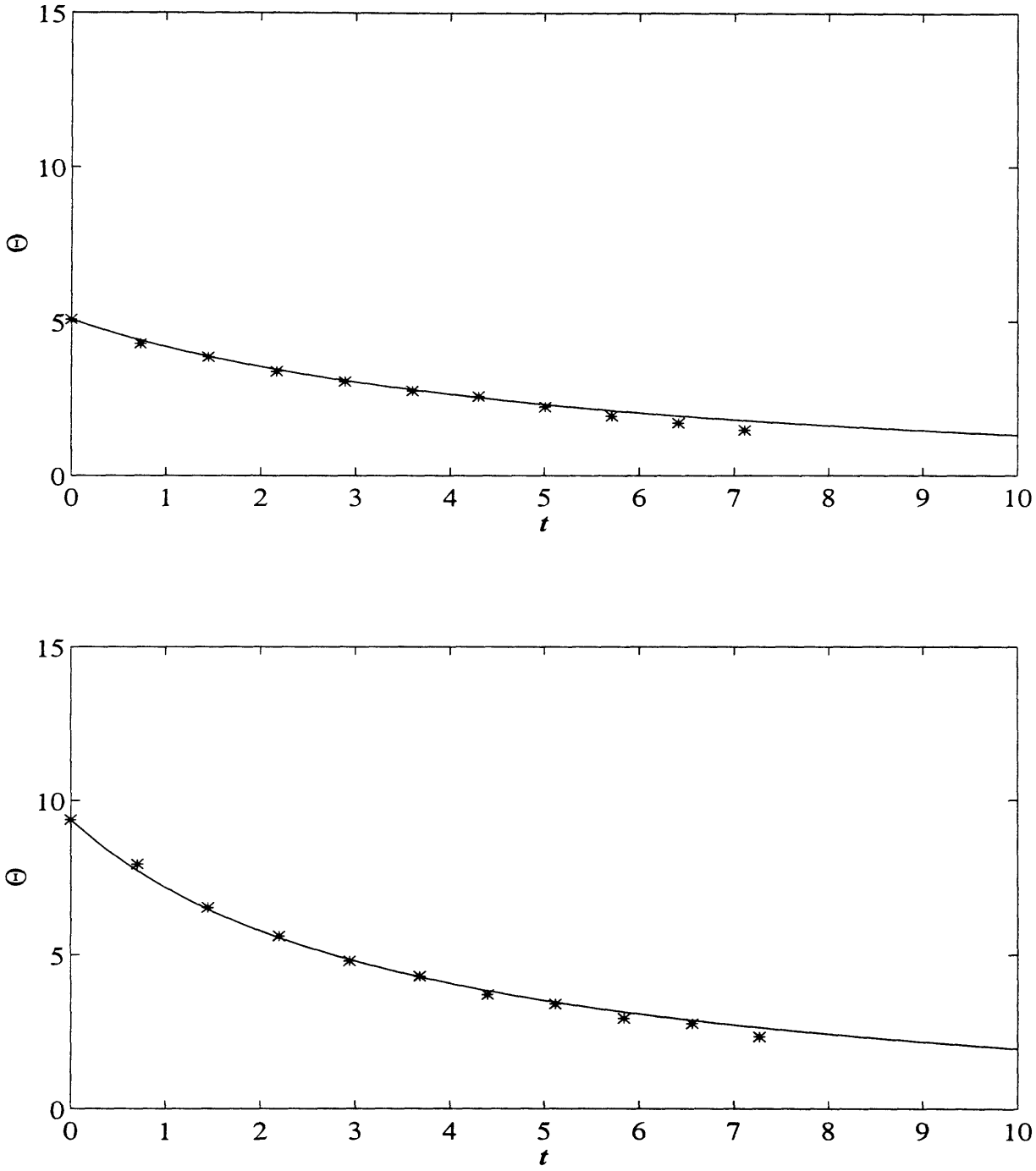

Figure 3-11: The same experimental time series of figure 3-9 compared with the theoretical envelope in the case of linear and quadratic viscous damping

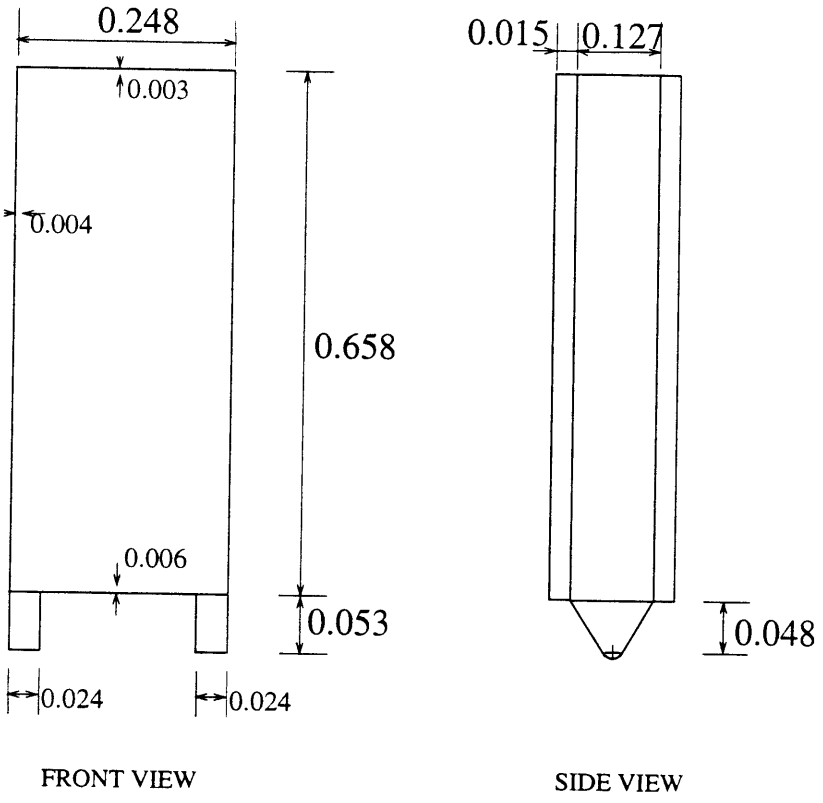

Figure 3-12: Details of one gate of the array for the wave basin experiments

DIMENSIONAL DATA		NONDIMENSIONAL DATA	
I'	0.320 kg m^2	I	0.302
M'	1.670 kg	M	0.102
d'	0.352 m	d	1.386
$S'=M'd'$	0.588 kg m	$S=Md$	0.141
a'	0.079 m	a	0.309
h'	0.590 m	h	2.323
b'	0.254 m	b	1
ρ	1.004 Mg m^3		

Table 3.2: Geometrical and inertial parameters of the wave basin experiments.

need to account for a larger amount of damping. For brevity the plots are omitted.

Fitted viscous dissipation coefficients

Using the same exhaustive search of section 3.4.1, we have determined the linear and quadratic viscous dissipation terms that best fit the data

$$\delta c_L = 0.010, \qquad f c_Q = 0.48. \tag{3.4.11}$$

As seen in section 3.4.1, the increased dissipation can be thought of being given by larger $c_L = 5.5$ and $c_Q = 6.0$ (as compared with the theoretical values (3.4.9)), or by larger $\delta = 0.0058$ and $f = 0.113$ (as compared with $\delta = 0.0018$ and $f = 0.08$).

Chapter 4

Uniform incident wave

4.1 Introduction

For simplicity we first rewrite the evolution equation in the most complete form that include the linear and quadratic dissipation terms

$$-\mathrm{i}\theta_{t_2} = \omega_2\theta + (c_N + \mathrm{i}\,c_R)\,\theta^2\theta^* + c_F A_2\,\theta^* + (1+\mathrm{i})\,\delta_2 c_L\,\theta + \mathrm{i}\,f_1 c_Q|\theta|\,\theta. \qquad (4.1.1)$$

In this chapter, an incident wave of constant amplitude $A_2 = \overline{A}_2$, is examined for the resonated equilibrium solutions and their dependence on detuning ω_2. Equation 4.1.1 has been studied by Rockliff(1978) for the edge wave. The author considered the effect of detuning for inviscid fluid, i.e. for $c_L = c_Q = 0$ and revealed the possibility of hysteresis phenomena. In the case of edge waves, the coefficient c_N is negative, causing a tilt of the bifurcation diagram towards positive detuning, as opposed to the present case. Still for edge waves, Miles(1990) considered the effect of viscosity by introducing a linear dissipation term without the real part, and studied its effect of imperfect reflection.

Our ultimate goal in chapter 5 is for a modulated wave amplitude modeling a narrow banded spectrum

$$A_2 = \overline{A}_2 + \tilde{A}_2 \cos\Omega_2 t_2, \qquad (4.1.2)$$

where Ω_2 and $\tilde{A}_2$ are the frequency and amplitude of the modulation. The evolution equation is then

$$-\mathrm{i}\theta_{t_2} = \omega_2\theta + (c_N + \mathrm{i}\,c_R)\,\theta^2\theta^* + c_F\left(\overline{A}_2 + \tilde{A}_2\cos\Omega_2 t_2\right)\theta^* + (1+\mathrm{i})\,\delta_2 c_L\,\theta + \mathrm{i}\,f_1 c_Q|\theta|\theta. \qquad (4.1.3)$$

Note that equation (4.1.1) is the particular case of (4.1.3) for $\tilde{A}_2 = 0$.

The nondimensional quantities in equation (4.1.3) have served their purpose and

can now be abandoned in favor of the representation in terms of the physical quantities

$$-\frac{\mathrm{i}}{\omega_0}\theta'_{t'} = \frac{\Delta\omega}{\omega_0}\theta' + (c_N + \mathrm{i}\,c_R)\,\theta'^2\theta'^* + c_F\left(\frac{\overline{A'}}{b'} + \frac{\tilde{A}'}{b'}\cos\Omega t'\right)\theta'^* + (1+\mathrm{i})\;\delta c_L\,\theta' + \mathrm{i}\,f c_Q|\theta'|\,\theta'. \tag{4.1.4}$$

We recall that in (4.1.4) θ' is in rad, ω_0 is the natural angular frequency in rad/sec, $\overline{A'}$ and $\tilde{A}'$ are steady and oscillating part of the incident wave amplitude in meters, b' the modal half period in meters, δ is the ratio $\sqrt{\nu/\omega_0}/b'$, f is the quadratic loss coefficient and t' is time in seconds; all the c's are numerical coefficients. The modulational frequency is defined as $\Omega = \epsilon^2\Omega_2\,\omega_0$ and measured in rad/sec.

To simplify the analysis of (4.1.4) we introduce the following nondimensional parameters and variables

$$\alpha = \frac{c_R}{c_N}, \qquad \beta = \frac{\delta\,c_L}{c_F\,\overline{A'}/b'}, \qquad \gamma = \frac{f\,c_Q}{\sqrt{c_N\,c_F\,\overline{A'}/b'}},$$
$$W = \frac{\Delta\omega/\omega_0}{c_F\,\overline{A'}/b'}, \qquad \vartheta = \sqrt{\frac{c_N}{c_F}}\,\frac{\theta'}{\sqrt{\overline{A'}/b'}}, \qquad T = c_F\,\frac{\overline{A'}}{b'}\,\omega_0 t'. \tag{4.1.5}$$

In terms of these parameters the evolution equation becomes

$$-\mathrm{i}\vartheta_T = W\,\vartheta + (1+\mathrm{i}\,\alpha)\,\vartheta^2\vartheta^* + (1 + a\cos\sigma T)\,\vartheta^* + (1+\mathrm{i})\;\beta\,\vartheta + \mathrm{i}\,\gamma|\vartheta|\,\vartheta, \tag{4.1.6}$$

where a and σ are respectively the normalized amplitude and frequency of modulation of the incident wave

$$a = \frac{\tilde{A}'}{\overline{A'}}, \qquad \sigma = \frac{\Omega}{\omega_0\,c_F\,\overline{A'}/b'}. \tag{4.1.7}$$

From their definitions (4.1.5) it is clear that α represents the normalized damping due to radiation, β the normalized linear viscous damping and γ the normalized quadratic viscous damping. α is independent of $\overline{A}/b'$, unlike β and γ. W represents the normalized detuning. The angular displacement ϑ is essentially the ratio between the angular displacement θ' and the square root of incident wave amplitude divided by the modal half period, $\overline{A'}/b'$, in agreement with the expected dependence $\theta' \sim \sqrt{\overline{A'}/b'}$.

We now turn to the object of this chapter, the case of steady incident wave amplitude $A_2 = \overline{A}_2$. Setting $a = 0$ in (4.1.6) yields

$$-\mathrm{i}\vartheta_T = W\,\vartheta + \vartheta^2\vartheta^*\;(1+\mathrm{i}\alpha) + \vartheta^* + (1+\mathrm{i})\,\beta\,\vartheta + \mathrm{i}\gamma|\vartheta|\,\vartheta. \tag{4.1.8}$$

Simple inspection shows that equation (4.1.8) has a symmetry property, i.e. if ϑ is a solution, so is $-\vartheta$. In section 4.2 we look at the case with radiation and linear viscous damping. In the following section the quadratic damping coefficient γ is also included, so that the complete picture of linear and quadratic viscous damping coefficients is

taken.

4.2 Linear viscous damping

For understanding the later section we first reexamine the case with only linear damping, which has been studied before by Miles(1990).

For $\gamma = 0$, (4.1.8) becomes

$$-\mathrm{i}\vartheta_T = W\vartheta + \vartheta^2\vartheta^*(1+\mathrm{i}\alpha) + \vartheta^* + (1+\mathrm{i})\beta\vartheta. \tag{4.2.1}$$

Separating the amplitude and the phase $\vartheta = \mathrm{i}|\vartheta|\mathrm{e}^{\mathrm{i}\psi}$ and introducing the action R, $R = |\vartheta|^2$, we obtain from (4.2.1) an equivalent dynamical system in R and ψ

$$\begin{cases} R_T = -2R(\alpha R + \sin 2\psi + \beta) \equiv -H_\psi - G_R \\ \\ \psi_T = W + R + \beta - \cos 2\psi \equiv H_R - G_\psi, \end{cases} \tag{4.2.2}$$

where the hamiltonian $H(R,\psi)$ has the expression

$$H(R,\psi) = \frac{1}{2}R^2 + R(W+\beta) - R\cos 2\psi, \tag{4.2.3}$$

and G is the gradient function associated with radiation and linear viscous damping

$$G(R,\psi) = \frac{2}{3}\alpha R^3 + 2\beta R^2. \tag{4.2.4}$$

The dynamical system (4.2.2) is periodic in ψ with period equal to π, as can be checked upon substitution of $\psi + \pi$ in (4.2.2). Periodicity in ψ is a manifestation of the symmetry property of (4.1.8).

4.2.1 Fixed points and their stability

Fixed points are defined by $R_T = \psi_T = 0$ and represent the resonated equilibrium amplitudes.

Trivial fixed point

System (4.2.2) admits the trivial solution $R_0 = 0$, $\cos 2\psi_0 = W + \beta$. Its stability can be obtained by looking at the stability of a perturbation in R. Let $R = 0 + R'$, with $R' \ll 1$, linearizing the first of (4.2.2) obtain

$$R'_T = -2\beta R' \mp \sqrt{1-(W+\beta)^2}, \tag{4.2.5}$$

from which

$$R' \propto \mathrm{e}^{2\left(\mp\sqrt{1-(W+\beta)^2}-\beta\right)T}. \tag{4.2.6}$$

Therefore the trivial fixed point is unstable for $|W+\beta| < \sqrt{1-\beta^2}$, stable otherwise. Note that in order for the region of instability to exist, the normalized linear damping coefficient β must satisfy $\beta < 1$. Using the definition (4.1.5) for β, it follows that for a given linear damping coefficient $\delta\, c_L$, instability of the trivial solution occurs only if $\overline{A'}/b'$ is larger than a threshold

$$\frac{\overline{A'}}{b'} > \frac{\delta\, c_L}{c_F}. \tag{4.2.7}$$

Nontrivial fixed points

Solving (4.2.2) for $\cos 2\psi$ and $\sin 2\psi$ and summing the squares, we get a quadratic equation in R

$$\left(1+\alpha^2\right) R^2 + 2\left(W+\beta+\alpha\beta\right) R + \left(W+\beta\right)^2 = 1-\beta^2, \tag{4.2.8}$$

whose roots R_0 are the nontrivial fixed points. The corresponding phase ψ_0 is then given by

$$\cos 2\psi_0 = W+\beta+R_0. \tag{4.2.9}$$

Solution of (4.2.8) gives

$$R_0^{\pm} = \frac{1}{1+\alpha^2}\left\{-W-\beta-\alpha\beta \pm \sqrt{1+\alpha^2-\left[\alpha\left(W+\beta\right)-\beta\right]^2}\right\}. \tag{4.2.10}$$

We will refer to s as the fixed point whose action is R_0^+, and to u as the fixed point with action R_0^-. Existence of the real square root in (4.2.10) requires

$$\frac{\beta}{\alpha} - \sqrt{1+\frac{1}{\alpha^2}} - \beta < W < \frac{\beta}{\alpha} + \sqrt{1+\frac{1}{\alpha^2}} - \beta. \tag{4.2.11}$$

The left value of the above inequality is the value of W for which the square root of (4.2.10) is zero and therefore $R_0^+ \equiv R_0^-$. As will be detailed later this is a condition for a saddle node bifurcation. We denote

$$W_s = \frac{\beta}{\alpha} - \sqrt{1+\frac{1}{\alpha^2}} - \beta. \tag{4.2.12}$$

The requirements $R_0^{\pm} > 0$ yield respectively $W < -\sqrt{1-\beta^2} - \beta$ for u and $W < \sqrt{1-\beta^2} - \beta$ for s. Therefore u exists in the interval $W_s < W < -\sqrt{1-\beta^2} - \beta$, while s exists in the interval $W_s < W < \sqrt{1-\beta^2} - \beta$. Clearly, if $\beta > 1/\sqrt{1+\alpha^2}$, then $-\sqrt{1-\beta^2} - \beta < W_s$ and the region of existence of u is zero and s is the only nontrivial root. Furthermore, s is now defined in $|W+\beta| < \sqrt{1-\beta^2}$.

Hence, depending on the values of α, β there can be three different responses. For any given α, if $\beta > 1$ there are no nontrivial solution. For $1 > \beta > 1/\sqrt{1+\alpha^2}$ there is one nontrivial solution, s. Finally, for $1/\sqrt{1+\alpha^2} > \beta > 0$ two nontrivial solutions are possible, s and u. The smaller α, the wider the interval of β in which s and u coexist.

Stability of the nontrivial fixed points can be found by evaluating the Jacobian in $R_0^{\pm}$, $\psi_0^{\pm}$

$$J(R_0^{\pm}, \psi_0) = \begin{bmatrix} -2\alpha R_0^{\pm} & -4R_0^{\pm}\left(W+\beta+R_0^{\pm}\right) \\ 1 & -2\alpha R_0^{\pm} - 2\beta \end{bmatrix}, \tag{4.2.13}$$

and calculating the corresponding eigenvalues

$$\lambda_{1,2} = -2\alpha R_0^{\pm} - \beta \pm \sqrt{-4R_0^{\pm}\left(W+\beta+R_0^{\pm}\right) + \beta^2}. \tag{4.2.14}$$

The fixed point is unstable if and only if $\lambda_1 > 0$, i.e.

$$-4R_0^{\pm}\left\{\left(1+\alpha^2\right)R_0^{\pm} + W + \beta + \alpha\beta\right\} > 0 \tag{4.2.15}$$

and, since $R_0^{\pm} > 0$, the latter condition becomes

$$R_0^{\pm} < \frac{-W-\beta-\alpha\beta}{1+\alpha^2}. \tag{4.2.16}$$

By comparing with expression (4.2.10) it is immediate to deduce that s is always stable, while u is always unstable.

The panorama of the fixed points existence and stability is summarized hereafter.

- $\beta > 1$. There is only the trivial solution, stable for any W.
- $1 > \beta > 1/\sqrt{1+\alpha^2}$. There is one stable nontrivial solution, s, for $|W+\beta| < \sqrt{1-\beta^2}$; the trivial solution is unstable for $|W+\beta| < \sqrt{1-\beta^2}$, stable otherwise.
- $1/\sqrt{1+\alpha^2} > \beta > 0$. There is one stable nontrivial solution, s, for $W_S < W < \sqrt{1-\beta^2} - \beta$ and one unstable nontrivial solution, u, for $W_S < W < -\sqrt{1-\beta^2} - \beta$ coexisting with both s and the trivial solution, the latter being unstable for $|W+\beta| < \sqrt{1-\beta^2}$, stable otherwise.

Sample $R-\psi$ phase planes representative of the four possible scenarios of the last case are depicted in figure 4-1 for $\alpha = \beta = 0.20$. For these values, (4.2.12) yields $W_s = -4.30$ and $\sqrt{1-\beta^2} = 0.98$. Figure4-1a shows the phase plane for $W = 2 > \sqrt{1-\beta^2} - \beta$, when the only fixed point is the origin, represented by the line $R = 0$. Figure 4-1b shows the phase plane for $W = -\beta = -0.20$, when the nontrivial fixed point s is present. Trajectories diverge from the origin and end in s. Figure4-1c, shows the phase plane for $W = W_s/2 = -2.15$ when both s and u exist.

The origin is stable, so that trajectories converge either to s or to the origin. Finally for $W < -W_s$, the only fixed point is the origin, as can be seen in figure 4-1d.

4.2.2 Bifurcation diagram and hysteresis

A bifurcation diagram, i.e. a plot of the fixed point action $R_0(W;\alpha,\beta)$ versus W for given α, β is shown figure 4-2. The unstable branches (the origin for $|W+\beta| < \sqrt{1-\beta^2}$ and the nontrivial fixed point u) are denoted by a dashed line. Solid lines represent stable fixed points, i.e. the nontrivial stable fixed point s and the origin in its region of stability ($|W+\beta| > \sqrt{1-\beta^2}$).

In figure 4-2 we choose $\alpha = 0.40$. Correspondingly, from the analysis of the previous section we see that both s and u are defined when $0 < \beta < 1/\sqrt{1+\alpha^2} = 0.93$, while only s exists when $0.93 < \beta < 1$. The nontrivial fixed points do not exist for $\beta > 1$.

In figure 4-2a we choose $\beta = 0.4$, so that both s and u exist. The trivial fixed point is unstable for $|W+0.4| < \sqrt{1-\beta^2} = 0.92$; from (4.2.12) obtain $W_s = -2.09$. The bifurcation at $R = 0$, $W = \sqrt{1-\beta^2} - \beta = 0.52$ is a transcritical pitchfork bifurcation (indicated by TP), while the one at $R = 0$, $W = -\sqrt{1-\beta^2} - \beta = -1.32$ is subcritical (indicated by SP). The bifurcation in which the two nontrivial fixed point s and u coalesce, at $W = W_s = -2.09$, $R = 1/\alpha\sqrt{1+\alpha^2} - \beta/\alpha = 1.32$, is a saddle node bifurcation (indicated by SN).

In figure 4-2b for $\alpha = 0.4$, β takes the marginal value for which the interval of existence of u is zero, $\beta = 1/\sqrt{1+\alpha^2} = 0.93$. The only nontrivial fixed point is s; $W_s \equiv -\sqrt{1-\beta^2} - \beta = -1.27$. The bifurcations at $W = \sqrt{1-\beta^2} - \beta = -0.56$ and at $W = W_s = -1.27$ are both transcritical pitchfork.

We stress that increasing the value of β from 0.4 to 0.93 has shrunk the interval of instability from 1.84 to 0.68; this can be clearly seen by comparing figure 4-2a to 4-2b.

The maximum value of the stable nontrivial roots, $R_{0\,max}^{+}(\alpha,\beta)$, is the maximum of the curve $R_0^+(W;\alpha,\beta)$ (solid line of figure 4-2). It is obtained for a detuning W such that

$$\frac{\mathrm{d}R_0^+}{\mathrm{d}W} = 0 \tag{4.2.17}$$

which gives

$$R_{0\,max}^{+} = \frac{1-\beta}{\alpha} \quad \text{for} \quad W = -R_{0\,max}^{+} - \beta. \tag{4.2.18}$$

The same result can be obtained with less algebra if we look for the maximum of the quadratic polynomial that defines $R_0^{\pm}$

$$\frac{\mathrm{d}}{\mathrm{d}W}(4.2.8) = 0. \tag{4.2.19}$$

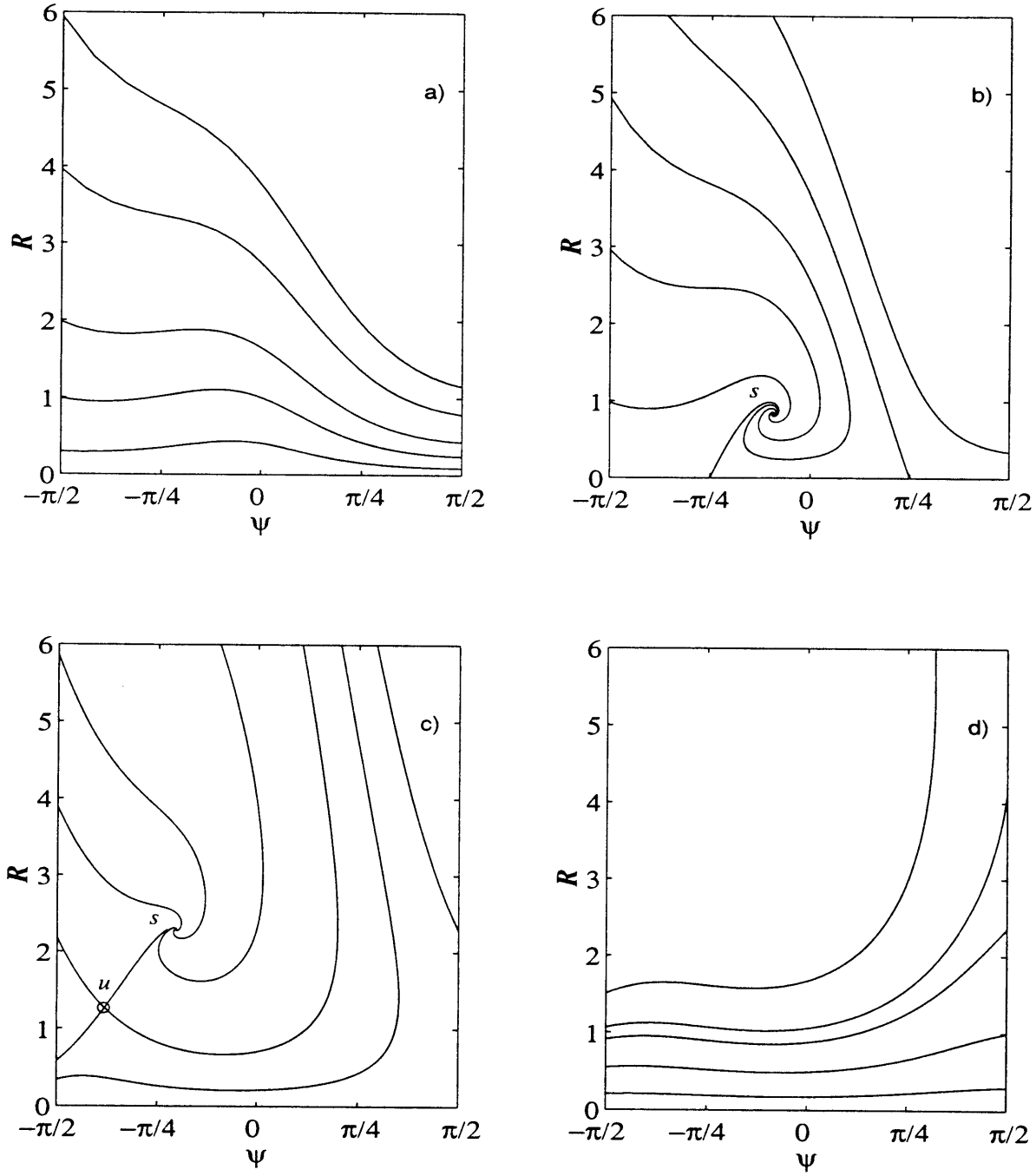

Figure 4-1: Phase plane samples in action–angle coordinates. a) $W = 2.00$, stable trivial fixed point, trajectories flow from left to right and approach the line $R = 0$. b) $W = -0.20$, one stable nontrivial f.p., s; the trivial f.p. is unstable. c) $W = -2.15$ two nontrivial f.p.'s: s and the saddle u; the trivial f.p. is stable. d) $W = -6.20$, stable trivial fixed point, trajectories flow from right to left

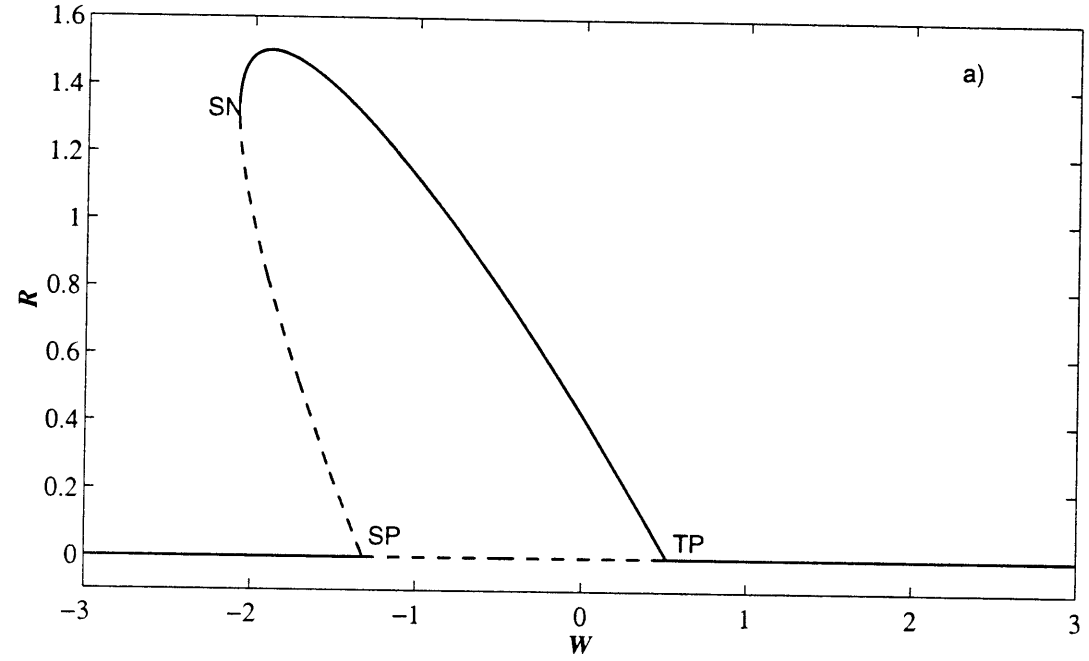

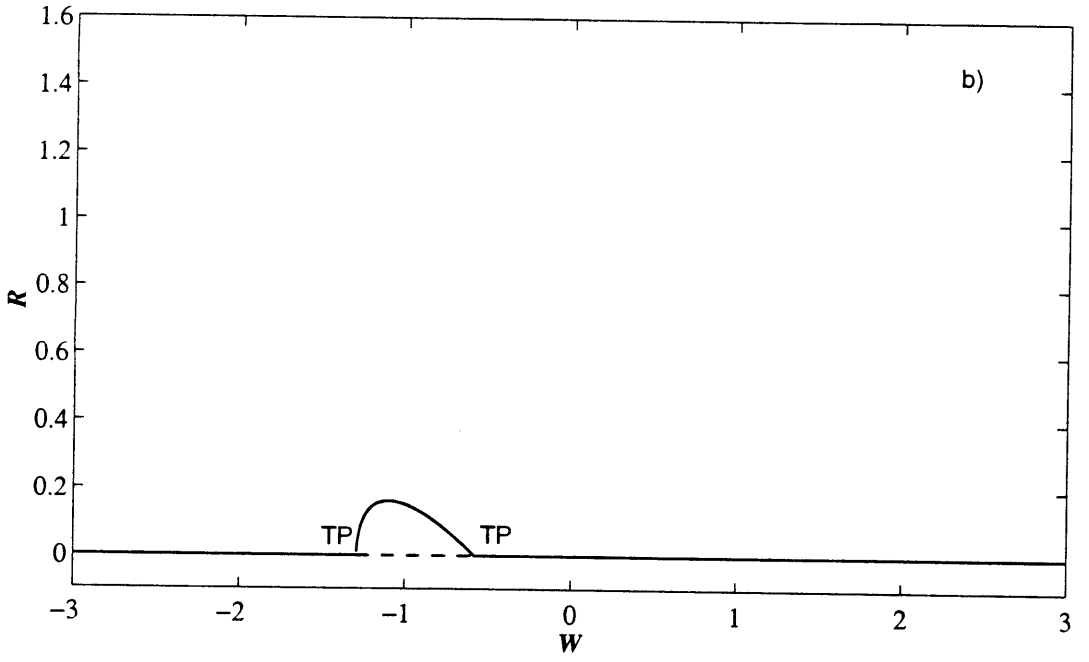

Figure 4-2: Bifurcation diagrams $R_0(W;\, \alpha, \beta)$ for $\alpha = 0.40$ a) $\beta = 0.40$, both s and u exist. b) $\beta = 0.93$, only s is possible.

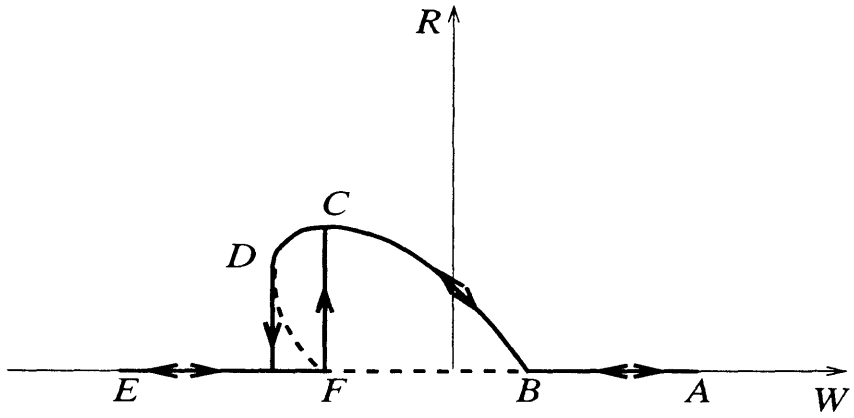

Figure 4-3: Hysteretic cycle and jump phenomenon as W varies.

As was also pointed out by Rockliff(1978) for the edge wave problem without viscous damping, the bifurcation diagram of figure 4-2a presents both a jump and an hysteresis phenomena in frequency, as is qualitatively shown in figure 4-3. Suppose that we start from point A and slowly decrease W through zero and then to negative values. We will then move first on AB then on the nontrivial branch passing through C down until D. At this point if we decrease further W the only fixed point possible is $R_0 = 0$ and so the point jumps on that line and stays there until we reach point E, say. If we now start increasing W, the representative point will stay on the $R = 0$ line until we reach point F ($W = -\sqrt{1-\beta^2} - \beta$), where the origin becomes unstable and the representative point is forced to jump on the unstable branch in C and move back towards A as we keep on increasing W. In this way an hysteretic cycle has been performed. Such phenomenon has been investigated experimentally by Tran(1996) and will be explained in section 4.4.

Region of instability in the $\Delta\omega/\omega_0\,\delta - \overline{A'}/b'\,\delta$ *plane*

In the interval $|W+\beta| < \sqrt{1-\beta^2}$ the only possible stable solution is the nontrivial solution; physically, this is the interval where the subharmonic motion will take place regardless of the initial conditions. Using the definition (4.1.5) of β and W the interval is mapped in a region of the $\Delta\omega/\omega_0\,\delta - \overline{A'}/b'\,\delta$ plane delimited by the hyperbola defined by $|W+\beta| = \sqrt{1-\beta^2}$, which reads

$$\frac{\Delta\omega}{\omega_0\,\delta} = \pm\sqrt{c_F^2\left(\frac{\overline{A'}}{b'\,\delta}\right)^2 - c_L^2} - c_L, \tag{4.2.20}$$

where $\delta; c_F, c_L$ contain the information of fluid viscosity and the gate and channel

geometry. The vertex of the hyperbola lies at

$$\frac{\Delta\omega}{\omega_0\,\delta} = -c_L, \qquad \frac{\overline{A'}}{b'\,\delta} = \frac{c_L}{c_F}. \tag{4.2.21}$$

The latter represents the marginal condition $W = -\beta$, $\beta = 1$ that denotes the onset of instability and the existence of the nontrivial root s.

In figure 4-4 the hyperbola (4.2.20) is plotted for the gate and channel characteristics of the experimental set-up in the wave channel, whose coefficients were found in section 3.4.1, expressions (3.4.5) and (3.4.6).

Along the + branch of (4.2.20), denoted by TP in figure 4-4, the origin loses stability in a transcritical pitchfork bifurcation; along the - branch, denoted instead by SP, the origin loses stability in a subcritical pitchfork bifurcation (compare with the points TP and SP of figure 4-2). Whenever the detuning $\Delta\omega$ and amplitude $\overline{A'}$ of the incident wave fall inside the hyperbola, a finite amplitude trapped wave will take place. We refer to the area above the hyperbola as the region of instability (the union of II and III in figure 4-4). Note that the larger is c_F, the larger is the region of instability. Indeed in section 2.6 this ratio has been referred to as bandwidth of instability. The dependence of c_F on the gate characteristics and water depth has been already discussed in section 2.6.

Using (4.1.5) and (4.2.12), the threshold for a saddle–node bifurcation $W = W_s$ is mapped instead onto a line

$$\frac{\Delta\omega}{\omega_0\,\delta} = -\frac{\overline{A'}}{b'\,\delta}\,c_F\sqrt{1+\left(\frac{c_N}{c_R}\right)^2} + c_L\left(\frac{c_N}{c_R}-1\right) \tag{4.2.22}$$

which is denoted by SN in figure 4-4. The line SN is tangent to the - branch of the hyperbola (4.2.20) at the point

$$\frac{\Delta\omega}{\omega_0\,\delta} = -c_L\left(1+\frac{c_R}{c_N}\right), \qquad \frac{\overline{A'}}{b'\,\delta} = \frac{c_L}{c_F}\sqrt{1+\left(\frac{c_R}{c_N}\right)^2}. \tag{4.2.23}$$

These coordinates correspond to the second marginal condition that denotes the existence of the two non trivial roots s and u, that is $\beta = 1/\sqrt{1+\alpha^2}$, $W \equiv W_s \equiv \sqrt{1-\beta^2} - \beta = -\beta\,(1+\alpha)$.

The horizontal dashed line passing for the point of tangency separate the region of instability in two region, II and III. In region II if we fix the amplitude $\overline{A'}$ and vary $\Delta\omega$, the bifurcation diagram is similar to figure 4-2b, i.e. the nontrivial solution starts and ends at $R = 0$ with two transcritical pitchfork bifurcation. Therefore more properly the curve TP is the union of the + branch of the hyperbola with the part of the - branch that goes from the vertex to the point of tangency with SN. On the other hand, in region III, the bifurcation diagram is similar to figure 4-2a, i.e. at SP the value of s is nonzero and extends continuously in the hysteresis interval.

The hysteresis interval $W \in \left[W_s, -\sqrt{1-\beta^2} - \beta\right]$ of figure 4-2, maps onto region IV delimited by SP and SN in the $\Delta\omega/\omega_0\,\delta - \overline{A'}/b'\,\delta$ plane.

From expression (4.2.22) we deduce that an increase of the value of the cubic damping coefficient c_R shrinks the hysteresis region by increasing the slope of the line SN, which therefore moves towards SP; a decrease in c_N has the same effect.

In summary, the $\Delta\omega/\omega_0\,\delta - \overline{A'}/b'\,\delta$ plane plane is divided in the following regions.

- Region I. Only one stable trivial fixed point. Subharmonic resonance does not occur.
- Region II. The trivial fixed point is unstable and coexist with one stable non-trivial one (s); subharmonic resonance always occur; no jumps in the response are possible.
- Region III. Like II but now jumps in the response are possible along SP.
- Region IV. One stable trivial fixed points coexisting with two nontrivial fixed point (s and u). Subharmonic resonance is conditional and jumps in the response are possible along SP and SN.

4.2.3 Graphical determination of nontrivial fixed points

To find the nontrivial roots and discuss their stability we can use also a graphical approach, useful when an explicit solution is not possible. For more examples on the usage of the graphical methods see Jordan & Smith(1986).

Define two curves $Z_1 = 1-\beta^2$ and $Z_2 = (1+\alpha^2)\,R^2+2\,(W+\beta+\alpha\beta)\,R+(W+\beta)^2$ and consider an auxiliary ZR plane as in figure 4-5. The nontrivial roots R_0 are given by the abscissa of the points of intersection of Z_1 and Z_2 in the region $R > 0$.

The curve Z_2 lies always in the half-plane $Z > 0$. If $\beta > 1$ the line Z_1 lies below $Z = 0$ and no intersections are possible; this corresponds to the first marginal condition for the existence of a nontrivial fixed point that was found analytically in the previous subsection.

Indeed Z_2 intersects the Z axis at $Z = (W+\beta)^2$. Therefore, for $W > \sqrt{1-\beta^2}-\beta$, Z_2 has no intersections with Z_1, as can be seen in figure 4-5a. In the interval $W \in [-\sqrt{1-\beta^2} - \beta, \sqrt{1-\beta^2} - \beta]$ there is one intersection and s is the corresponding fixed point, as shown in figure 4-5b. At $W = -\sqrt{1-\beta^2} - \beta$ a second intersection is born, which continue to exist in the interval $W \in \left[W_s, -\sqrt{1-\beta^2} - \beta\right]$, with $W_s < 0$. The new fixed point u is shown together with in s figure 4-5c. The two intersections collide when $W = W_s$, i.e. when Z_2 is tangent to Z_1. For $W < W_s$ no intersections are possible since Z_2 lies above Z_1, as can be seen in figure 4-5d. Therefore at $W = W_s$, the fixed points s and u undergo a saddle-node bifurcation. The value W_s can be

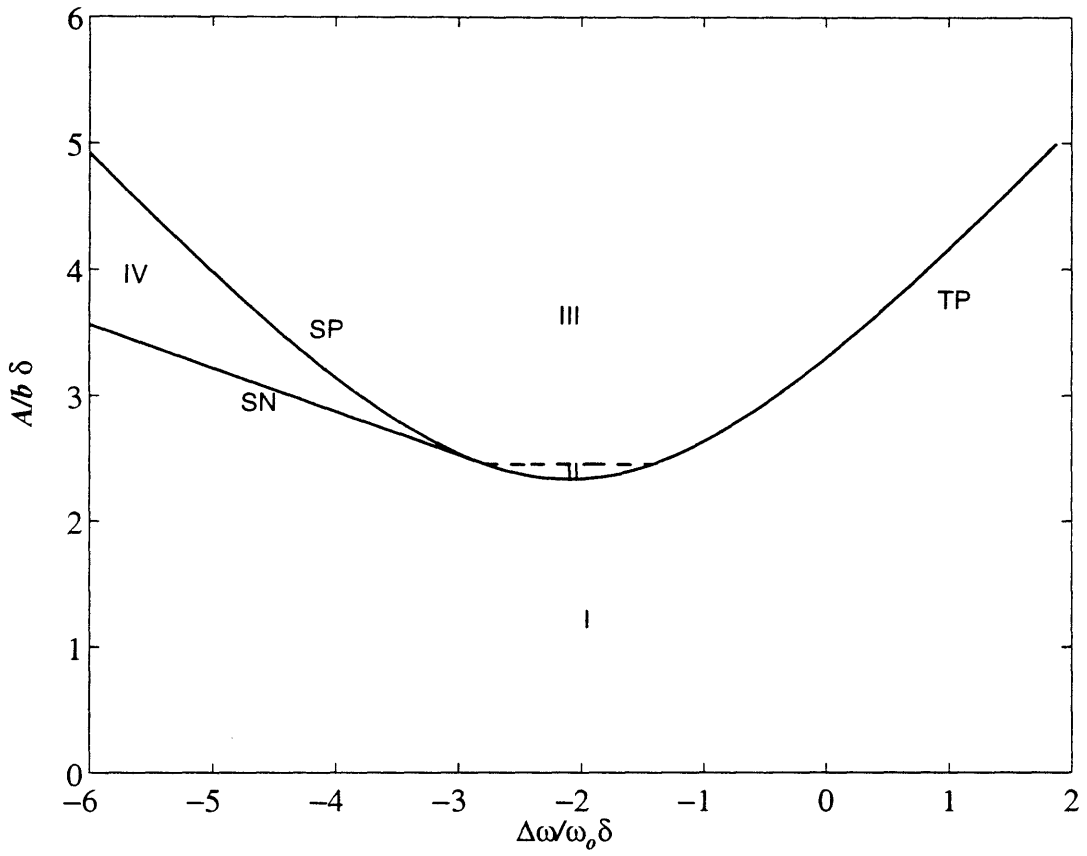

Figure 4-4: The regions of instability and hysteresis in the $\Delta\omega/\omega_0\,\delta - \overline{A'}/b'\,\delta$ plane for linear viscous damping. Region I: stable trivial fixed point. Region II and III: unstable trivial fixed point coexisting with s (region of instability). Region IV: stable trivial fixed fixed point coexisting with s and u (region of hysteresis)

found by solving for R and W under the condition for a tangent intersection

$$Z_2 = Z_1, \qquad \frac{\mathrm{d}Z_2}{\mathrm{d}R} = 0, \tag{4.2.24}$$

which gives exactly (4.2.12)

$$W_s = \frac{\beta}{\alpha} - \sqrt{1 + \frac{1}{\alpha^2}} - \beta. \tag{4.2.25}$$

The intersection corresponding to u does not exist if the Z coordinate of the vertex of Z_2, given by

$$(W + \beta)^2 - (W + \beta + \alpha\beta)^2/(1 + \alpha^2) \tag{4.2.26}$$

is above Z_1, when $W = -\sqrt{1 - \beta^2} - \beta$. Imposing such condition gives

$$\beta > \frac{1}{\sqrt{1 + \alpha^2}}, \tag{4.2.27}$$

i.e. the second marginal condition found analytically in the previous subsection.

The graphical approach tells us also the stability of the fixed points. The Jacobian at R_0, ψ_0 is

$$J(R_0, \psi_0) = \begin{bmatrix} -2\alpha R_0 & -4R_0\,(W + \beta + R_0) \\ 1 & -2\alpha R_0 - 2\beta \end{bmatrix}, \tag{4.2.28}$$

and the eigenvalues are given by

$$\lambda_{1,2} = -2\alpha R_0 - \beta \pm \sqrt{-4R_0\,(W + \beta + R_0) + \beta^2}. \tag{4.2.29}$$

The fixed point is unstable if and only if $\lambda_1 > 0$, i.e.

$$\begin{aligned} -2R_0 \left\{ 2\left(1 + \alpha^2\right) R_0 + 2W + 2\beta + 2\alpha\beta \right\} \equiv \\ -2R_0 \left\{ \left. \frac{\mathrm{d}Z_2}{\mathrm{d}R} \right|_{R=R_0} \right\} > 0. \end{aligned} \tag{4.2.30}$$

Since $R_0 > 0$ by definition, the only possibility for a fixed point to be unstable is

$$\left. \frac{\mathrm{d}Z_2}{\mathrm{d}R} \right|_{R=R_0} < 0. \tag{4.2.31}$$

From the slope of Z_2 at the points of intersection in figure 4-5b and c, we deduce that, in their respective region of existence, s is always stable (sink) while u is always unstable (saddle).

Finally, we turn to the representation of the dynamical system in cartesian coordinates. Separating the real and imaginary part $\vartheta = X + \mathrm{i}Y$ in (4.1.8), obtain a

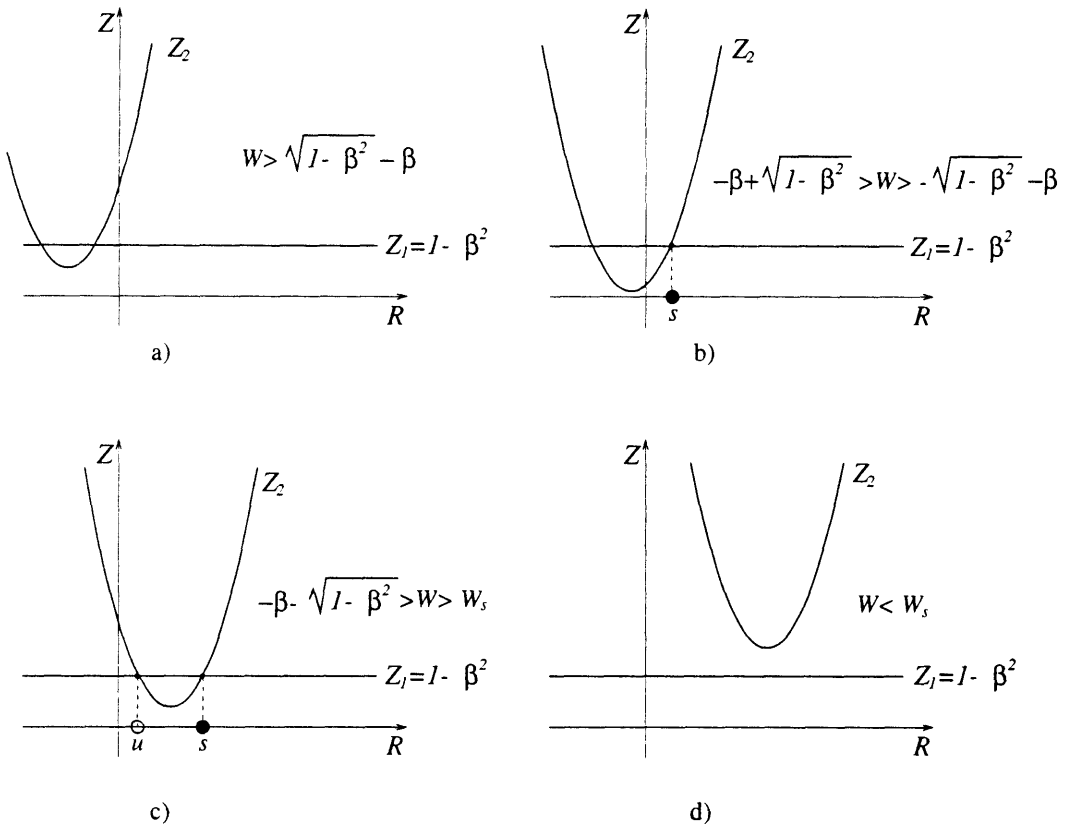

Figure 4-5: Graphical determination of the nontrivial fixed points and their stability in the case of linear viscous damping. a) no intersections; b) one intersection, s is stable; c) two intersections, s is stable, and u is unstable; d) no intersections.

dynamical system of the form

$$\begin{cases} X_T = (1 - W - \beta)\, Y - \beta X - (Y + \alpha X)\,(X^2 + Y^2)\,, \\ \\ Y_T = (1 + W + \beta)\, X - \beta Y + (X - \alpha Y)\,(X^2 + Y^2)\,. \end{cases} \tag{4.2.32}$$

The real part X and imaginary part Y are related to the action-angle variables by

$$X = -\sqrt{R}\sin\psi, \qquad Y = \sqrt{R}\cos\psi. \tag{4.2.33}$$

The system (4.2.32) is symmetric about the origin, as can be checked by substituting $X = -X$ and $Y = -Y$. This symmetry condition corresponds to the periodicity condition in ψ of (4.2.2). For each of the nontrivial fixed points s and u there exist two nontrivial fixed points, $s_{1,2}$ and $u_{1,2}$ whose coordinates are given by

$$X_{0\ 1,2}^{+} = \mp\sqrt{R_0^+}\sin\psi_0^+, \qquad Y_{0\ 1,2}^{+} = \pm\sqrt{R_0^+}\cos\psi_0^+, \tag{4.2.34}$$

for $s_{1,2}$, and

$$X_{0\ 1,2}^{-} = \mp\sqrt{R_0^-}\sin\psi_0^-, \qquad Y_{0\ 1,2}^{-} = \pm\sqrt{R_0^-}\cos\psi_0^-, \tag{4.2.35}$$

for $u_{1,2}$.

The stability properties of $s_{1,2}$ and $u_{1,2}$ and their regions of existence in the parameter space are identical to the ones of respectively s and u.

In figure 4-6 four sample phase plane XY are drawn for the same representative values of W and α, β of figure 4-1. Figure 4-6a is for $W > \sqrt{1-\beta^2} - \beta$ where the only fixed point is the origin. The origin is stable and trajectories spiral into it. For $W = -\beta$, the stable symmetrical fixed points $s_{1,2}$ corresponding to s are shown in figure 4-6b. For the region $W \in \left[W_s, -\sqrt{1-\beta^2} - \beta\right]$ figure 4-6c shows also the symmetrical unstable fixed points $u_{1,2}$. For $W < W_s$ the origin attracts all trajectories as can be seen in figure 4-6d.

4.3 Linear and quadratic viscous damping

When both β and γ are different from zero, equation (4.1.8) gives a dynamical system

$$\begin{cases} R_T = -2R\left(\alpha R + \sin 2\psi + \beta + \gamma\sqrt{R}\right) \equiv -H_\psi - G_R \\ \\ \psi_T = W + R + \beta - \cos 2\psi \equiv H_R - G_\psi. \end{cases} \tag{4.3.1}$$

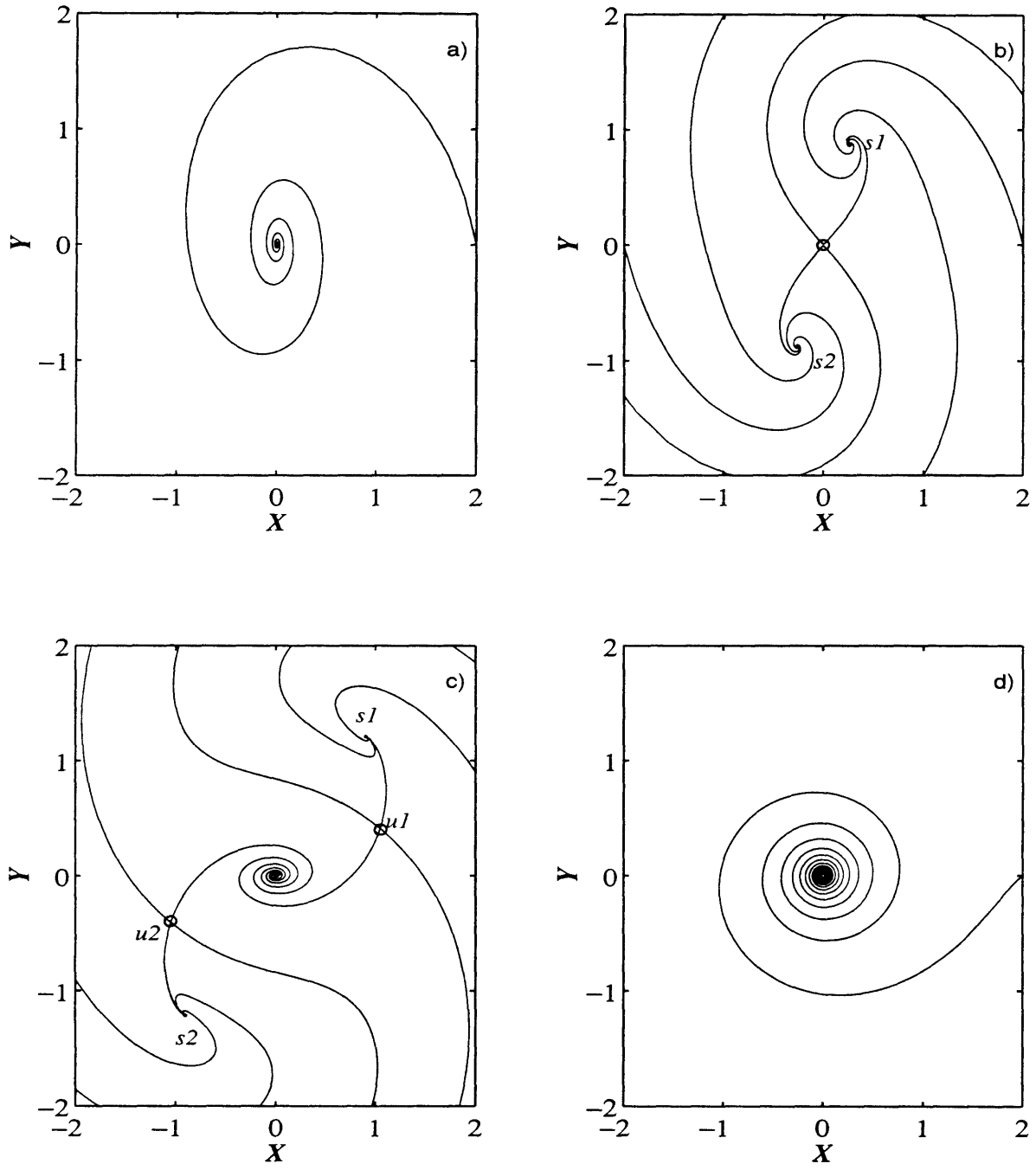

Figure 4-6: XY phase plane samples. a) $W = 2.00$, the origin is linearly stable. b) $W = 0.00$, origin unstable, there are two stable fixed points, $s_{1,2}$. c) $W = -2.05$ origin stable, two stable $s_{1,2}$ and two unstable $u_{1,2}$ nontrivial fixed points. d) $W = -6.00$, the origin is linearly stable.

The Hamiltonian defined in (4.2.3) remains unchanged while G includes also γ

$$G(R,\psi) = \frac{2}{3}\alpha R^3 + 2\beta R^2 + \frac{4}{5}\gamma R^{5/2}. \tag{4.3.2}$$

Compared to the preceding case, the overall features do not change significantly, but the equilibrium resonated amplitude must be somewhat smaller. Indeed we show that the region of instability is changed only by the linear term β and that the effect of quadratic damping is to decrease the resonated amplitude and the region of hysteresis.

The linear stability analysis of the trivial solution $R = 0$ is unchanged from subsection 4.2.1: the trivial solution is unstable for $|W+\beta| < \sqrt{1-\beta^2}$, stable otherwise. The condition for existence of instability interval, $\beta < 1$, again translates into (4.2.7). Therefore quadratic damping γ does not change the threshold for instability.

In action–angle coordinates, the algebraic equation in R whose roots R_0 are the nontrivial fixed points (analogous to (4.2.8)), is now

$$\left(1+\alpha^2\right)R^2 + 2\alpha\gamma R^{3/2} + \left(2W + 2\beta + 2\alpha\beta + \gamma^2\right)R + 2\beta\gamma R^{1/2} + (W+\beta)^2 = 1-\beta^2. \tag{4.3.3}$$

The above (4.3.3) does not have an explicit solution; the roots are found numerically. However, we can employ the graphical approach of the previous subsection to qualitatively analyze the nontrivial roots and discuss their stability.

Define of the two curves $Z_1 = 1-\beta^2$ and

$$Z_2 = \left(1+\alpha^2\right)R^2 + 2\alpha\gamma R^{3/2} + \left(2W + 2\beta + 2\alpha\beta + \gamma^2\right)R + 2\beta\gamma R^{1/2} + (W+\beta)^2 \tag{4.3.4}$$

in the auxiliary ZR plane as in figure 4-7. The expression Z_2 now contains a square root and therefore its graphic is defined only for $R > 0$; this is not a limitation since only $R > 0$ is physically meaningful. Indeed Z_2 intersects the Z axis at $Z = (W+\beta)^2$. Therefore, for $W > \sqrt{1-\beta^2} - \beta$, Z_2 has no intersections with Z_1, as can be seen in figure 4-7a. In the interval $|W+\beta| < \sqrt{1-\beta^2}$ there is one intersection and s is the corresponding fixed point, as shown in figure 4-7b. The fixed point u, which exist in the interval $W \in \left[W_s, -\sqrt{1-\beta^2} - \beta\right]$, is shown together with in s figure 4-7c. The two intersections collide when $W = W_s$, i.e. when Z_2 is tangent to Z_1 and finally for $W < W_s$ no intersections are possible since Z_2 lies above Z_1 (see figure 4-7d). At $W = W_s$, s and u undergo a saddle-node bifurcation.

The value W_s can be found by solving for R and W the condition for a tangent intersection

$$Z_2 = Z_1 \qquad \frac{\mathrm{d}Z_2}{\mathrm{d}R} = 0. \tag{4.3.5}$$

System (4.3.5) can be only be solved numerically. For each set of values of α, β, γ it gives $W_s = W_s(\alpha,\beta,\gamma)$; the case of linear viscous damping seen before is just a

particular case of (4.3.5) for which an explicit solution exists:

$$W_s(\alpha, \beta, 0) = \beta/\alpha - \sqrt{1 + 1/\alpha^2} - \beta \tag{4.3.6}$$

The existence of the fixed point u is dependent on whether $W_s < \sqrt{1-\beta^2} - \beta$, a condition that is verified numerically.

Using the graphical approach we can deduce the fixed points and their stability without solving explicitly (4.3.3). The Jacobian at R_0, ψ_0 has extra terms on the diagonal as compared to (4.2.28)

$$J(R_0, \psi_0) = \begin{bmatrix} -2\alpha R_0 - \gamma R_0^{1/2} & -4R_0\left(W + \beta + R_0\right) \\ 1 & -2\alpha R_0 - 2\gamma R_0^{1/2} - 2\beta \end{bmatrix}, \tag{4.3.7}$$

and the eigenvalues are given by

$$\lambda_{1,2} = -2\alpha R_0 - \beta - \frac{3}{2}\gamma R_0^{1/2} \pm \sqrt{-4R_0\left(W + \beta + R_0\right) + \beta^2 + \beta\gamma R_0^{1/2} + \frac{\gamma^2 R_0}{4}}. \tag{4.3.8}$$

The fixed point is unstable if and only if $\lambda_1 > 0$, i.e.

$$\begin{aligned} &-2R_0\left\{2\left(1+\alpha^2\right)R_0 + 3\alpha\gamma R_0^{1/2} + \beta\gamma R_0^{-1/2} + 2W + 2\beta + 2\alpha\beta + \gamma^2\right\} \equiv \\ &-2R_0\left\{\left.\frac{\mathrm{d}Z_2}{\mathrm{d}R}\right|_{R=R_0}\right\} > 0. \end{aligned} \tag{4.3.9}$$

Since $R_0 > 0$ by definition, the only possibility for a fixed point to be unstable is

$$\left.\frac{\mathrm{d}Z_2}{\mathrm{d}R}\right|_{R=R_0} < 0. \tag{4.3.10}$$

From the slope of Z_2 in the ZR plane at the intersection points of figure 4-7b and c, we deduce that, in their respective region of existence, s is always stable while u is always unstable.

The phase planes in action–angle and cartesian coordinates for the different cases are similar in all their features to the ones for linear damping only (c.f figure 4-1 and 4-2) and are therefore omitted.

Bifurcation diagram

The effect of quadratic damping is on the amplitude of the resonated wave. In figure 4-8 we show the bifurcation diagram (plot of $R_0\left(W; \alpha, \beta, \gamma\right)$ versus W) for fixed $\alpha = \beta = 0.4$ and different values of γ, 0.0, 0.4 and 0.8. For $\gamma = 0.0$, the diagram is the same as of figure 4-2a. For $\gamma = 0.4$ and $\gamma = 0.8$, the solid line representing R_0^+ is always below the corresponding one for $\gamma = 0$.

The topology of the fixed points is unaltered, that is $R = 0$, $W = \pm\sqrt{1-\beta^2} - \beta$

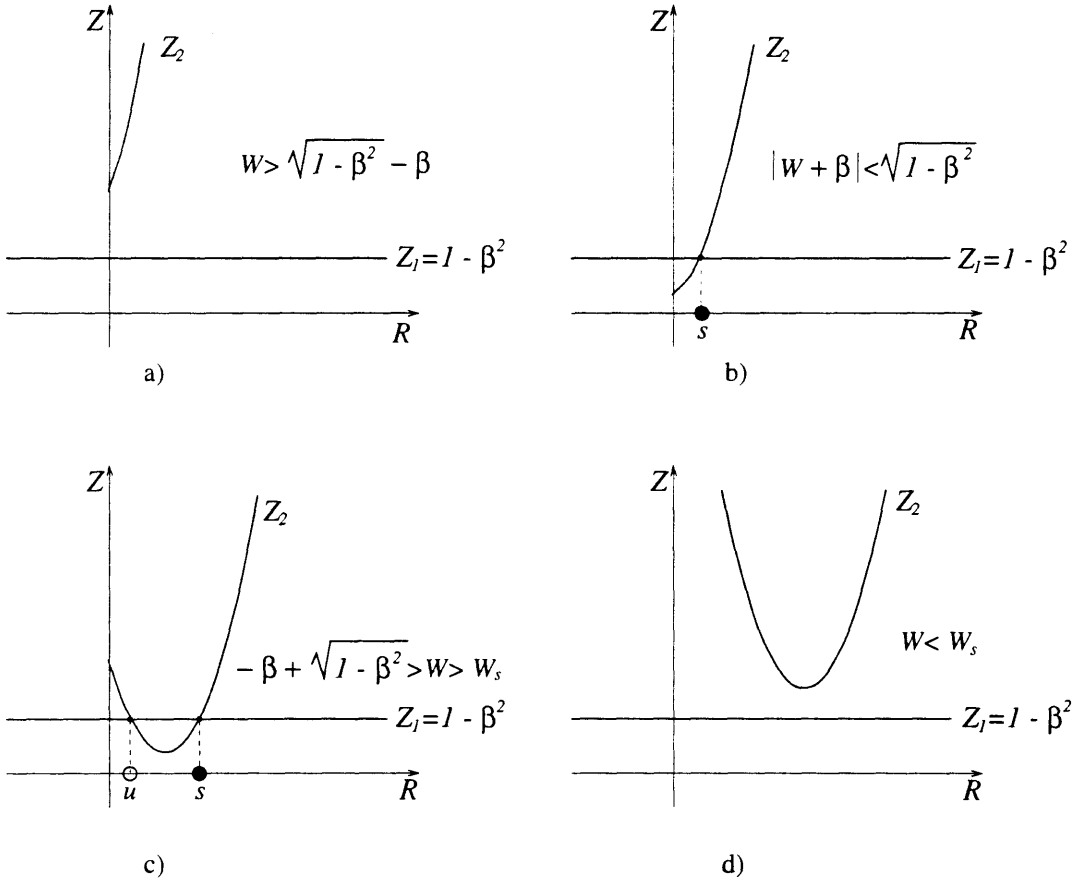

Figure 4-7: Graphical determination of the nontrivial fixed points and their stability in the case of viscous linear and quadratic damping.

are still respectively trans and sub critical pitchfork bifurcations and $W = W_s$ is still a saddle node. Figure 4-8 show that as γ increases, eventually u does not exist anymore and the saddle node bifurcation does not occur. In this case s is born in a transcritical bifurcation at both $W = \pm\sqrt{1-\beta^2} - \beta$ (see curve for $\gamma = 0.8$).

Figure 4-8 confirms that γ does not alter the region of instability. However, an increase in γ moves the saddle node SN toward $W = 0$ therefore reducing the interval of hysteresis.

To quantify the decrease in the response, we look at the maximum value of the nontrivial root s, $R_{0\,max}^{+}(\alpha, \beta, \gamma)$. It is obtained for a detuning W such that

$$\frac{\mathrm{d}}{\mathrm{d}W}(4.3.3) = 0, \tag{4.3.11}$$

and it occurs still at $W = -R_{0_{max}} - \beta$, but now with a value given by

$$R_{0_{max}} = \frac{1-\beta}{\alpha} - \frac{\gamma^2}{2\alpha^2}\left[\sqrt{1 + \frac{4\alpha}{\gamma^2}(1-\beta)} - 1\right], \tag{4.3.12}$$

which is smaller than the corresponding for linear viscous dissipation by the second term in γ (compare with (4.2.18)).

Region of instability in the $\Delta\omega/\omega_0\delta - \overline{A}'/b'\delta$ plane

As seen before, the addition of quadratic damping does not affect the size of the region of instability, which we recall is the interval $|W + \beta| < \sqrt{1-\beta^2}$ mapped onto a region of the $\Delta\omega/\omega_0\delta - \overline{A}'/b'\delta$ plane bounded by equation (4.2.20). The hyperbola is shown again in figure 4-9 for the same values of the coefficients of figure 4-4.

As can be seen in figure 4-8, with quadratic damping the value W_s of the saddle node bifurcation SN is closer to the value SP of the supercritical pitchfork bifurcation. Consequently in the $\Delta\omega/\omega_0\delta - \overline{A}'/b'\delta$ plane the curve SN is closer to the - branch SP of the hyperbola then in the case of linear damping only. To display this change, figure 4-9 shows SN for linear viscous damping only (as it is in figure 4-4) with a dashed line. The resulting region of hysteresis is therefore smaller than in the case $\gamma = 0$.

Recall that the curve SN can only be obtained numerically by solving (4.3.5) in terms of the variables $\Delta\omega/\omega_0\delta$ and $\overline{A}'/b'\delta$. Note that SN is no longer a straight line, but has a slight concavity towards the $\Delta\omega/\omega_0\delta$ axis. The region I, II, III, IV have the same meaning that in figure 4-2. Because the point of tangency of SN to SP is higher, region II is larger at the expenses of region III. As explained before region IV is instead smaller.

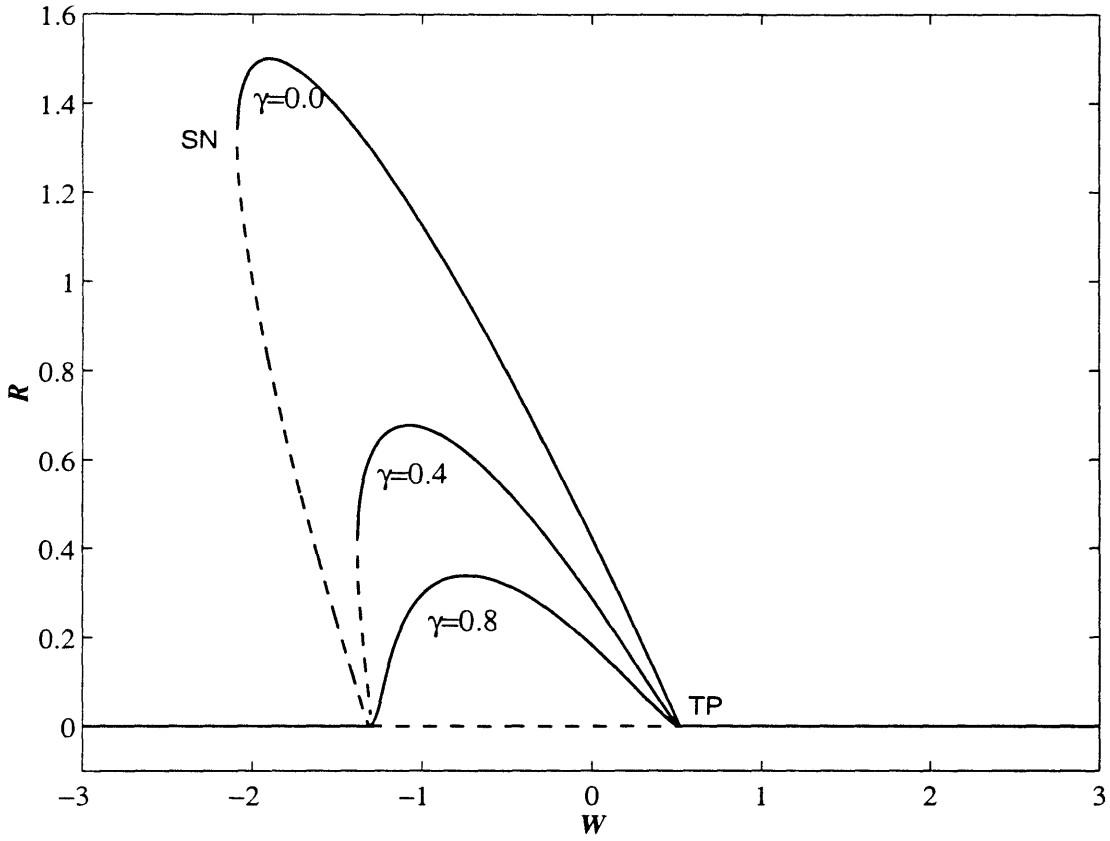

Figure 4-8: Bifurcation diagram for different values of quadratic viscous damping γ. The larger γ the smaller the stable fixed point action; the bandwidth of instability is not affected by γ.

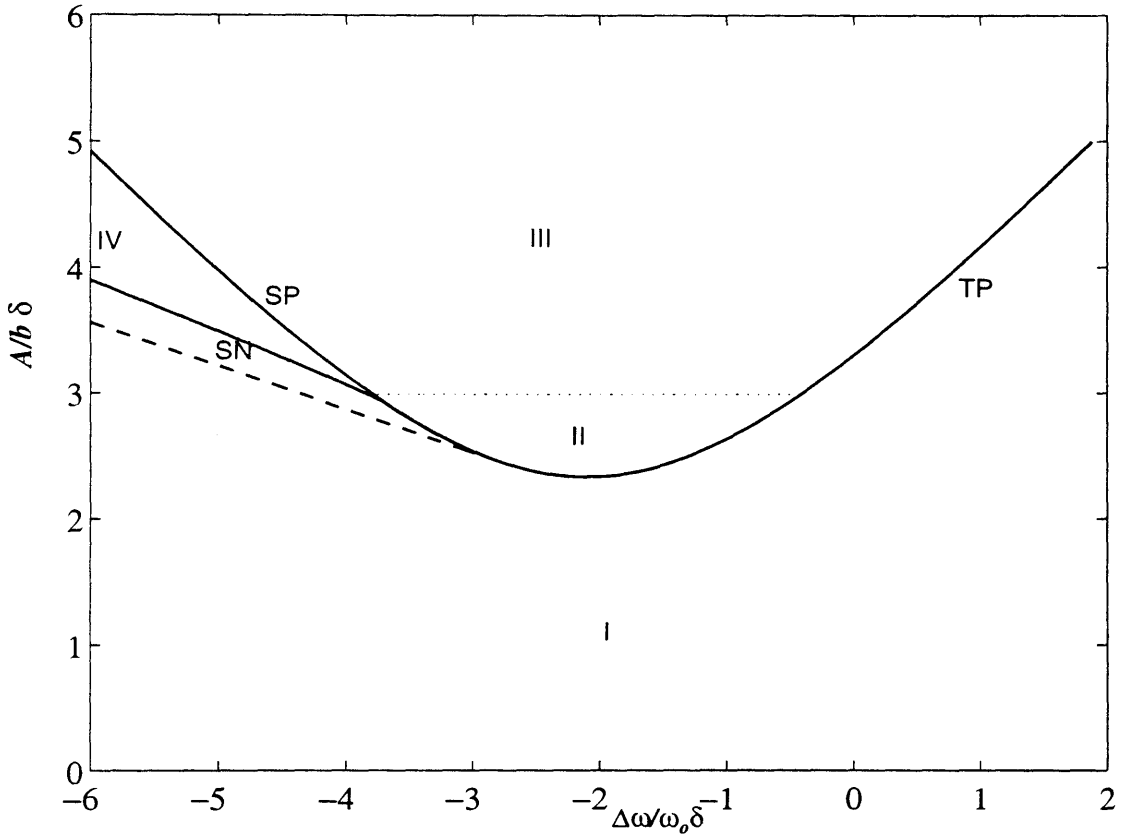

Figure 4-9: The regions of instability and hysteresis in the $\Delta\omega/\omega_0\delta - \overline{A}'/b'\delta$ plane for linear and quadratic viscous damping. The dashed line is SN for linear viscous damping. Region I: stable trivial fixed point. Region II and III: unstable trivial fixed point coexisting with s (region of instability). Region IV: stable trivial fixed fixed point coexisting with s and u (region of hysteresis)

4.4 Comparison with experiments in the wave channel

We now consider the forced oscillations experiments, in which a wave of frequency $2(\omega_0 + \Delta\omega)$ is generated by a piston wave maker at one end of the channel and the angular responses (including synchronous and subharmonic) of the gates are recorded together with the amplitude of the incident, reflected and transmitted waves. Here we report on the forced oscillation experiments.

To verify the features of the resonance diagram predicted in the previous section, Tran(1996) performed extensive experiments scanning the $\Delta\omega/\omega_0 - \overline{A}'/b'$ plane of figure 4-9.

The experiments were performed as follows. Once the natural frequency of oscillation is known from the free oscillation experiments, a series of scans in amplitude and frequency are made. During each scan wave frequency and amplitude are varied in a quasi static manner, i.e. by changing after every 150 seconds the amplitude or the frequency of the minimum step compatible with the instrumentation resolution (0.001 m and 0.0025 Hz approximately) without stopping the experiments.

Frequency scans. For fixed amplitude of the incident wave $\overline{A}'$, the frequency is varied from a positively detuned value outside the instability region, through the instability region, the hysteresis region down to a negatively detuned frequency minimum (reverse scan). The same range is followed backwards from negative to positive detuning (forward scan). In this way, by recording the angular response, the form of the bifurcation diagram is obtained and the possibility of hysteresis checked. The same is repeated for several distinct values of the incident wave ranging from 0.009 m to 0.025 m.

Amplitude scans. For fixed incident wave frequency, the amplitude is increased from a minimum to a maximum (forward scan) and then back (reverse scan). The same is repeated for several frequency both positively and negatively detuned.

Thus the entire plane $\Delta\omega/\omega_0 - \overline{A}'/b'$ is covered with sections parallel to the coordinate axis. In particular the lines SP of figure 4-9 is revealed by the forward scans, while the lines SN by the backward scans. Both backward and forward scans should reveal the TP + branch.

Frequency scans were made experimentally for Faraday waves by Hendersen and Miles(1991), who measured the hysteretic lines in the frequency-amplitude plane of the Faraday waves resonance.

4.4.1 Theoretical viscous dissipation coefficients

The theoretical values of the coefficients of the evolution equation c's, δ and f have been found in section 3.4.1, expression (3.4.5) and (3.4.6).

We first compare the region of instability and the hysteretic threshold curves in

the plane $\Delta\omega/\omega_0 - \overline{A}'/b'$ of figure 4-10.

The experimental points denoted by a empty circles are the lowest threshold subharmonic response ($\theta'_e > 0.1$ deg) obtained by increasing the amplitude for fixed frequency or increasing the frequency for fixed amplitude, that is by the forward frequency and amplitude scans. On the other hand, the stars denote the threshold subharmonic response ($\theta'_e < 0.1$ deg) obtained when, starting from a large resonated response, the wave amplitude is decreased to zero or, for a given amplitude, the frequency is decreased from a maximum, i.e. they are obtained from the reverse frequency and amplitude scans.

While the nonhysteretic + branch is confirmed quantitatively, the disagreement is significant in the low threshold amplitude and the region of hysteresis. This could be due to the following reasons.

On the theoretical side, c_L does not contain all possible linear damping effect, such as the meniscous effect, the effects of the friction of the hinges, of the measurement devise (potentiometer) and the hydraulic communication at the hinges and along the wall–gaps between the $\Omega^{\pm}$ fluid domains. In other words the predicted c_L is not large enough.

On the experimental side, low amplitude waves are difficult to generate and measure. But most of all, while around the threshold of the instability region the growth time tends to infinity, the amplitudes and the frequency were recorder over too short a time (150 secs) to reach steady state. Therefore, below a certain wave amplitude, growing or decaying transients, rather than several steady state have been recorded.

We have grouped together in the eight plots of figures 4-11 and 4-12 the frequency and amplitude scans. The massive data have been grouped and divided into two categories: backward (asterisks) and forward (empty circles) scans. Regardless of their belonging to a frequency or an amplitude scan, they are presented in the figures as frequency scans. Going from the first to the last, the amplitude of the incident wave is increasing. For example consider the first plot of figure 4-11 for $A' = 0.027b' = 0.010$ m. Any data point whose amplitude is 0.010 ± 0.0005 is plotted in correspondence of its forcing frequency, with an asterisk if it is reverse or a circle if it is forward.

The experimental width of the region of hysteresis is given by the length spanned by empty circles alone on the $\theta = 0$ line. From the same plot, we have a confirmation of the fact that for low incident wave amplitudes the region of hysteresis is hard to define. Indeed, in figure 4-11 for $\overline{A'}/b' = 0.027$, there are no nontrivial responses denoted by empty circles. This means that, in the region of instability, while nontrivial responses were found in the reverse scans, they were not observed in the forward ones, which strongly suggests that transients rather than steady states were measured.

In figure 4-12, for larger values of $\overline{A'}/b'$, the experimental region of hysteresis is smaller than in 4-11 and closer to the size predicted by the theory. Overall, it is remarkable that, regardless of the exact size, the predicted hysteresis and jumps phenomena are confirmed by the experimental observations.

Another feature of the comparisons of figures 4-11 and 4-12 is that the theoretical predicted nontrivial response is always larger than the experimental. This is due to the fact that, as pointed out also in section 3.4.1, not all the sources of dissipation are accounted for in the damping coefficients formulation.

In the next section we use the fitted values of the δc_L and $f c_Q$ found in section 3.4.1, expression (3.4.8).

4.4.2 Fitted viscous dissipation coefficients

Overall, the comparison with forced oscillation when δc_L and $f c_R$ are fitted to the free oscillation experimental data is more satisfactory (for the numerical values of the coefficients see section 3.4.1).

The comparison of the different regions in the $\Delta\omega/\omega_0 - \overline{A'}/b'$ plane is not dramatically improved, as can be seen in figure 4-13. In particular, the agreement is poor in the region of low $\overline{A'}/b'$, suggesting difficulties in running experiments at low amplitudes, as is explained in the previous subsection.

The comparison of the nontrivial steady states is instead more successful, as figures 4-14 and 4-15 show. The predicted steady state reproduce the experimental measurements for the wide range of incident wave amplitudes $\overline{A'}$. As a consequence of the increase of δc_L and $f c_Q$, both the theoretical region of instability and hysteresis are slightly smaller.

In summary, it can be said that the inherent features of the Stuart-Landau equation are confirmed by the experiments and that, upon proper tuning of the linear and quadratic damping coefficients, satisfactory quantitative agreement is achieved.

4.4.3 On the magnitude of α, β, γ

Using the fitted values of δc_L and $f c_R$ in (4.1.5), gives for the coefficients α, β, γ

$$\alpha = \frac{c_R}{c_N} = 0.590, \qquad \beta = \frac{\delta c_L}{c_F \overline{A'}/b'} = \frac{0.0099}{\overline{A'}/b'}, \qquad \gamma = \frac{f c_Q}{\sqrt{c_N c_F \overline{A'}/b'}} = \frac{0.1944}{\sqrt{\overline{A'}/b'}}. \tag{4.4.1}$$

In the present forced oscillation experiments, the ratio $\overline{A'}/b'$ ranges from 0.022 to 0.065, so that β ranges from 0.450 to 0.177, while γ ranges from 1.31 to 0.760.

Similarly, for the wave basin experiments, using expressions (3.4.9) and (3.4.11)

$$\alpha = 0.0831, \qquad \beta = \frac{0.0061}{\overline{A'}/b'}, \qquad \gamma = \frac{0.0719}{\sqrt{\overline{A'}/b'}}. \tag{4.4.2}$$

For an incident wave amplitude $\overline{A'} = 0.020$ m, (4.4.2) gives $\beta = 0.077$, $\gamma = 0.254$.

Hence, in the wave channel experiments $\{\alpha, \beta, \gamma\} \leq O(1)$, while in the basin

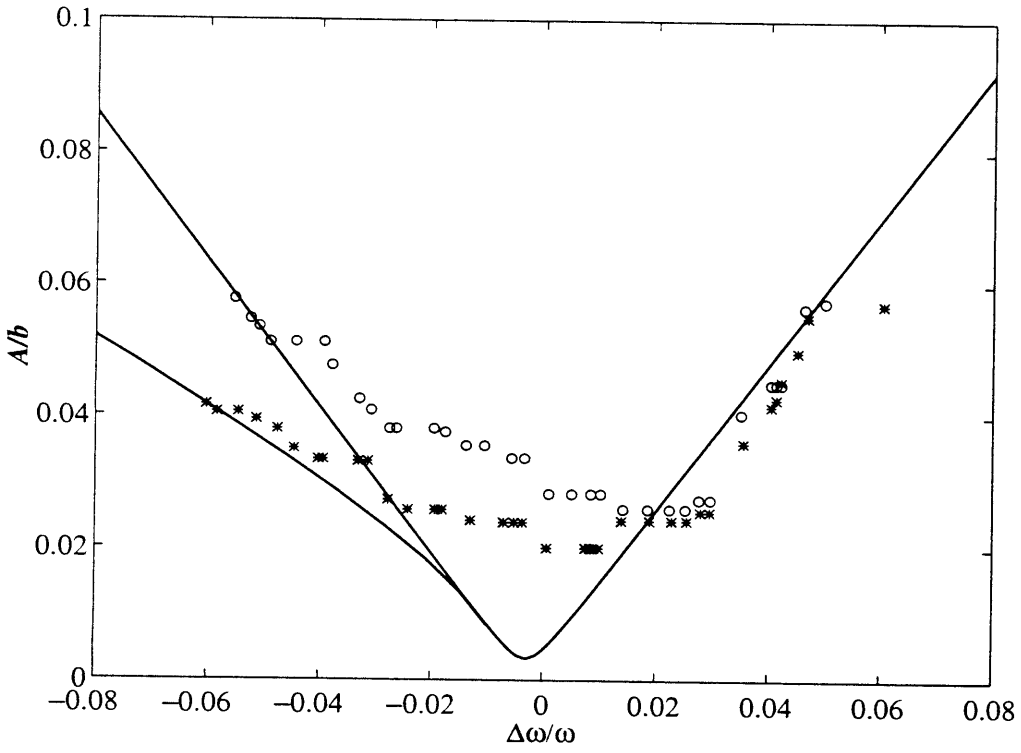

Figure 4-10: Experimental regions of instability and hysteresis compared with theory.

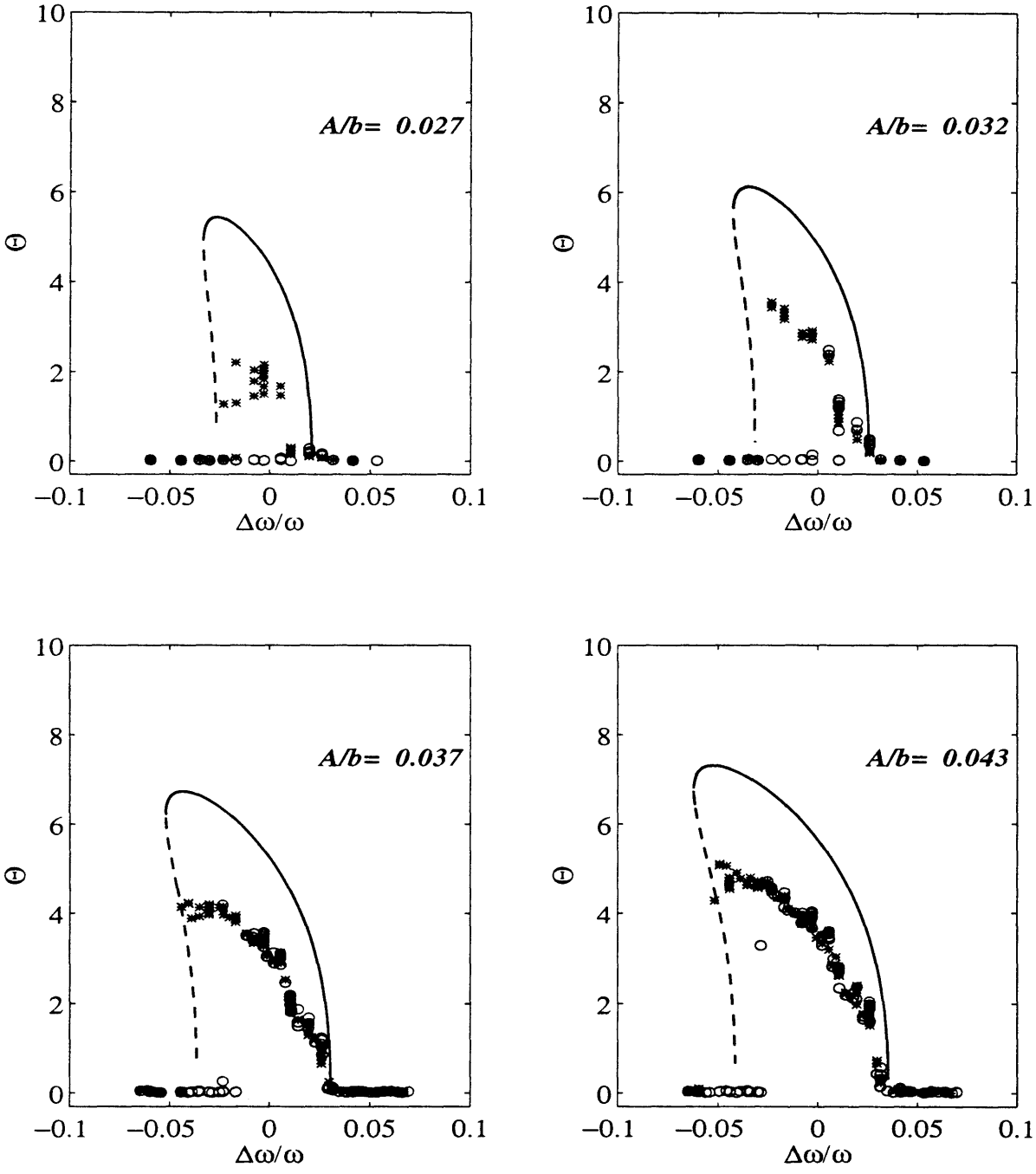

Figure 4-11: Frequency scans vs theory. θ is in degrees.

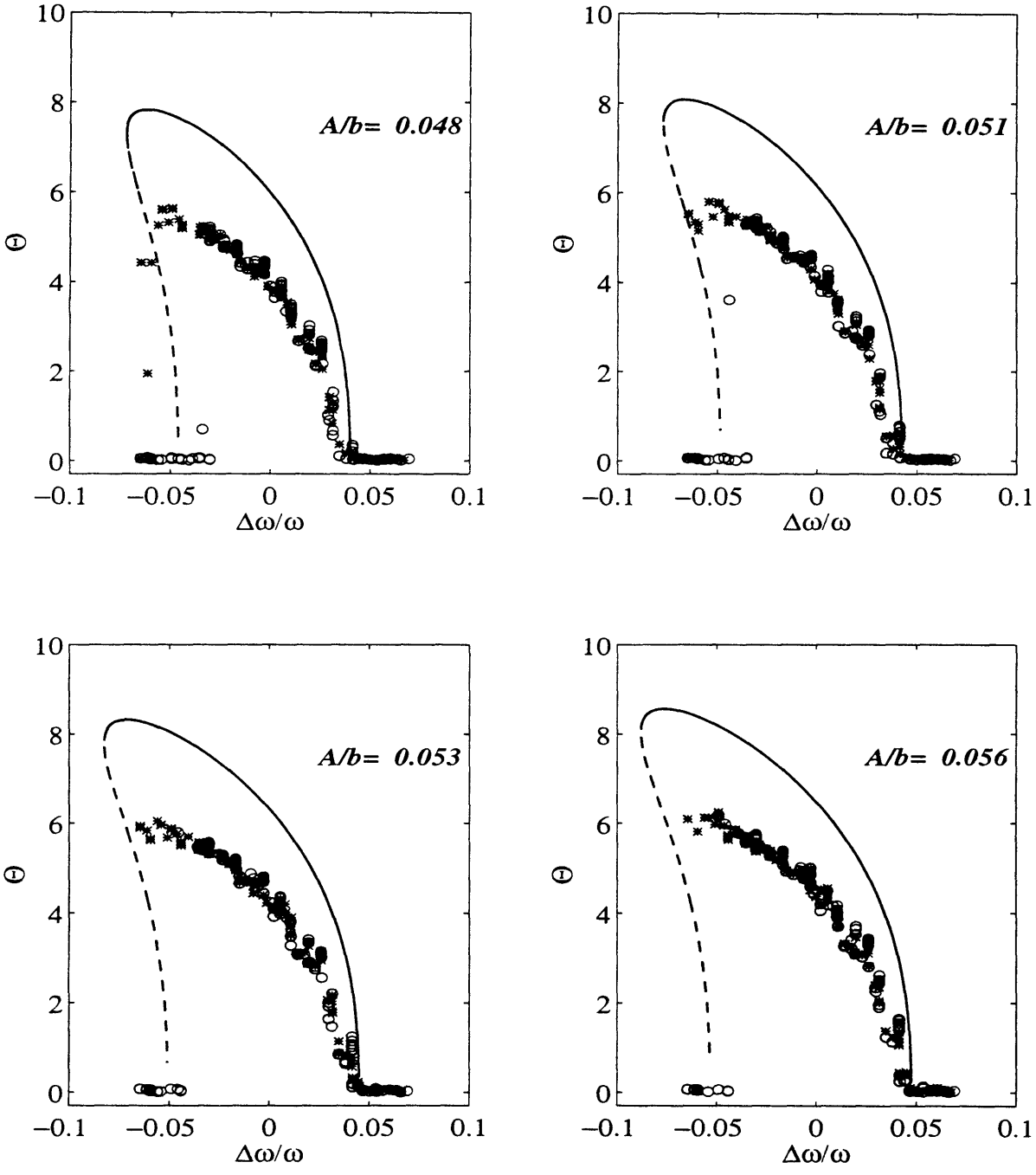

Figure 4-12: Frequency scans vs theory. θ is in degrees.

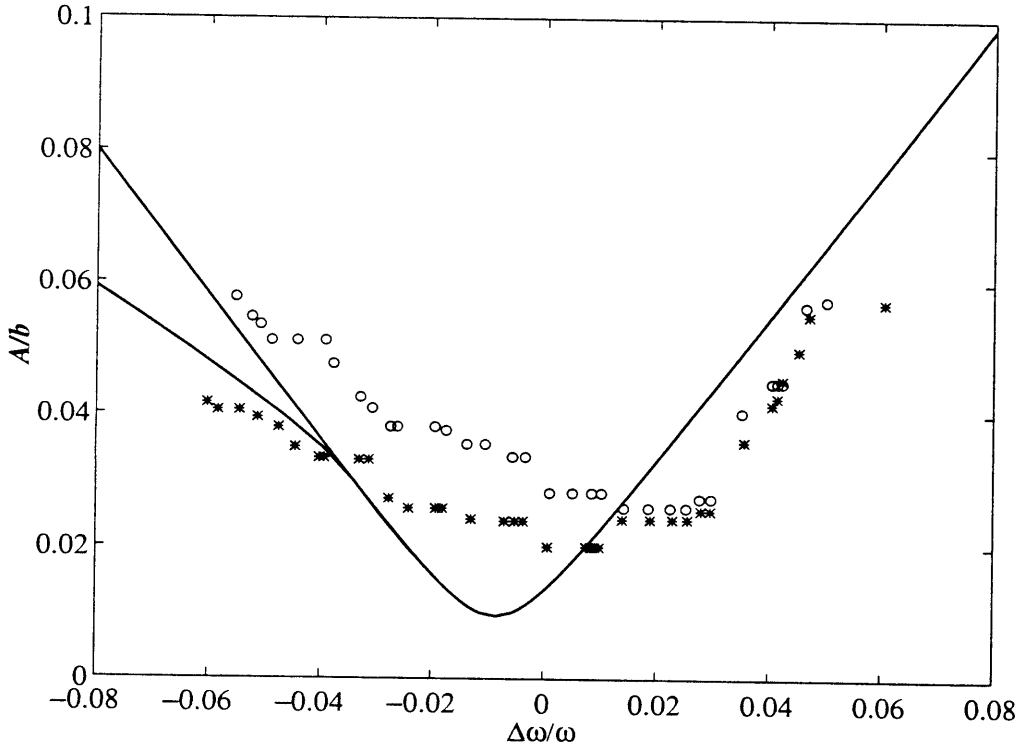

Figure 4-13: Experimental regions of instability and hysteresis compared with fitted theory.

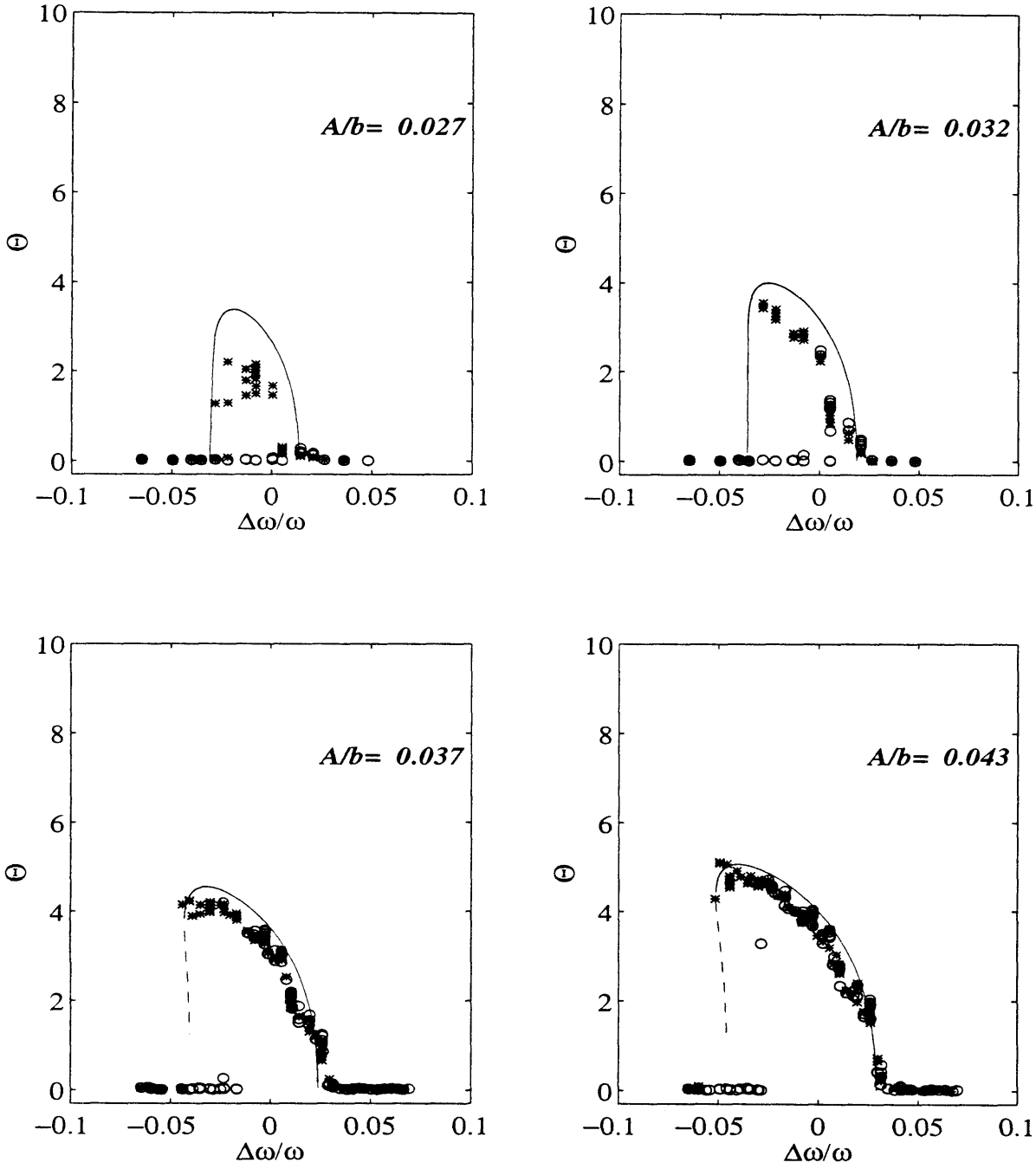

Figure 4-14: Frequency scans vs fitted theory. θ is in degrees.

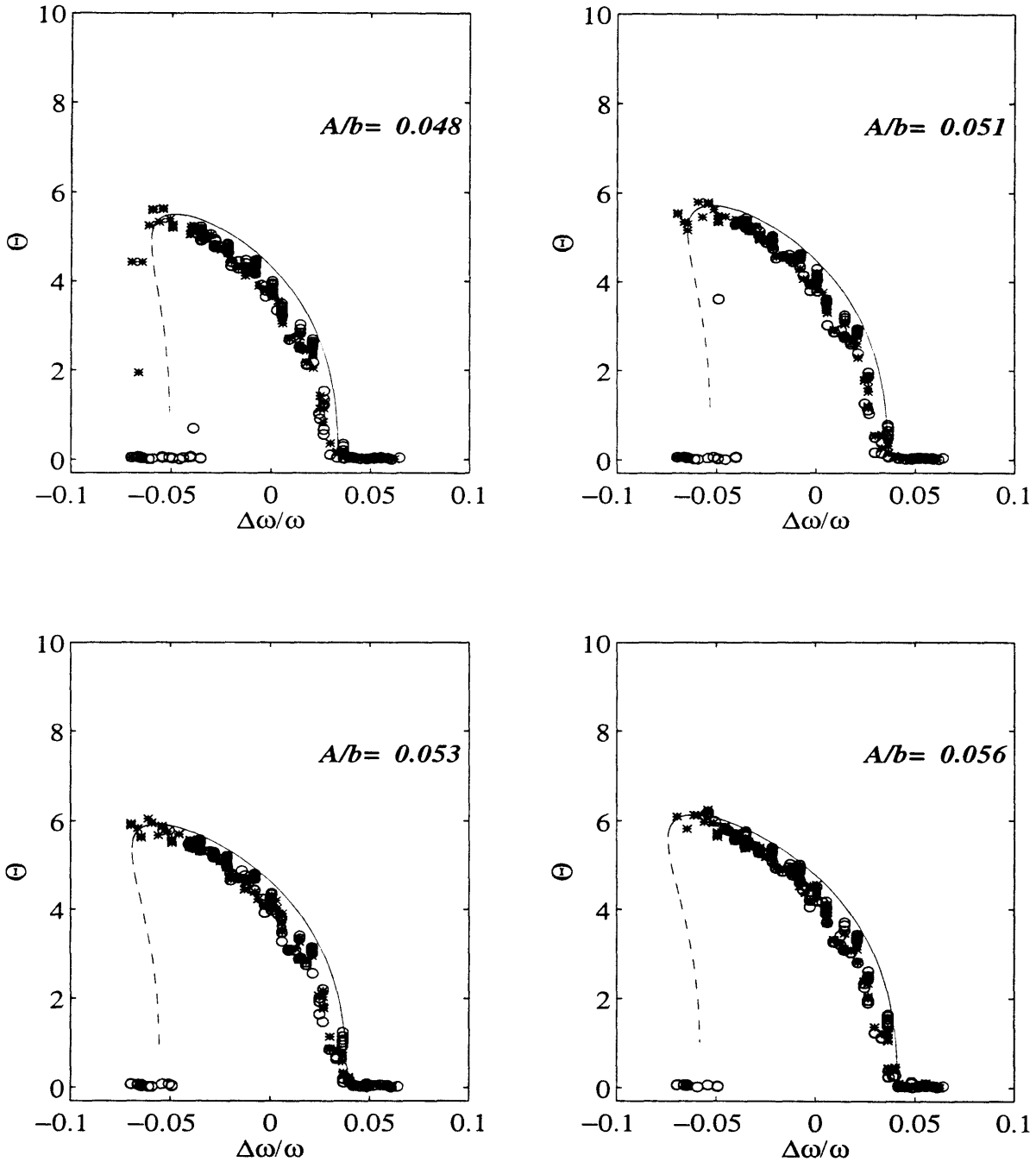

Figure 4-15: Frequency scans vs fitted theory. θ is in degrees.

$\{\alpha, \beta, \gamma\} = O(0.1)$. These last numerical values give support to the hypothesis

$$\{\alpha, \beta, \gamma\} \ll 1, \tag{4.4.3}$$

that is made in the next chapter, where local and global perturbation analysis is used to study equation (4.1.6) for $a \ll 1$.

Chapter 5

Modulated incident wave

5.1 Introduction

For a modulated incident wave, the evolution equation is given by expression (4.1.6)

$$-\mathrm{i}\vartheta_T = W\,\vartheta + (1+\mathrm{i}\,\alpha)\,\vartheta^2\vartheta^* + (1+a\cos\sigma T)\,\vartheta^* + (1+\mathrm{i})\,\beta\,\vartheta + \mathrm{i}\,\gamma|\vartheta|\,\vartheta, \qquad (5.1.1)$$

where a and σ are normalized amplitude and frequency of the modulation and are given by (4.1.7).

In action–angle coordinates, $\vartheta = \mathrm{i}\sqrt{R}\mathrm{e}^{\mathrm{i}\psi}$, the system reads

$$\begin{cases} R_T = -2R\left[\alpha R + (1+a\cos\sigma T)\sin 2\psi + \beta + \gamma\sqrt{R}\right] = -H_\psi - G_R, \\ \\ \psi_T = W + \beta + R - (1+a\cos\sigma T)\cos 2\psi = H_R - G_\psi, \end{cases} \qquad (5.1.2)$$

where the gradient function $G(R,\psi)$ is given by expression (4.3.2) and the hamiltonian function H is now time dependent

$$H(R,\psi,T) = \frac{1}{2}R^2 + R\,(W+\beta) - R\,(1+a\cos\sigma T)\cos 2\psi, \qquad (5.1.3)$$

Such a Hamiltonian system has solutions with stocastic behaviour, which appears as stochastic layers in a Poincaré map (see for example Liechtenberg and Lieberman(1991)). Because of dissipation, the eventual stocasticity should settle instead to a lower dimensional strange attractor.

Separating the real and immaginary part of (5.1.1) according to $\vartheta = X + \mathrm{i}Y$ yields

a nonautonomous dynamical system in cartesian coordinates

$$\begin{cases} X_T = (1 + a\cos\sigma T - W - \beta)\, Y - \beta X - (Y + \alpha X)\,(X^2 + Y^2) - \\ \qquad \gamma X\sqrt{X^2 + Y^2} = -H_Y - G_X, \\ Y_T = (1 + a\cos\sigma T + W + \beta)\, X - \beta Y + (X - \alpha Y)\,(X^2 + Y^2) - \\ \qquad \gamma Y\sqrt{X^2 + Y^2} = H_X - G_Y. \end{cases} \tag{5.1.4}$$

The gradient function $G(X, Y)$ is given by expression

$$G(X,Y) = \frac{\alpha}{2}\left(X^2 + Y^2\right)^2 + \frac{\beta}{2}\left(X^2 + Y^2\right) + \frac{\gamma}{2}\left(X^2 + Y^2\right)^{3/2}, \tag{5.1.5}$$

while the hamiltonian function H is now time dependent

$$H(X,Y,T) = \frac{1}{2}\left(X^2 - Y^2\right)(1 + a\cos\sigma T) + \frac{1}{2}(W + \beta)\left(X^2 + Y^2\right) + \frac{1}{4}\left(X^2 + Y^2\right)^2. \tag{5.1.6}$$

In the present chapter we wish to determine if modulation can cause further temporal resonances on the time scale of the modulation. Besides, the possibility of nonperiodic solutions and chaotic motion will be assessed.

To gain analytical insight on the complex dynamical behaviour of the above systems (5.1.2) or (5.1.4) both local and global analyses are pursued analytically. Such approximate analyses are based on the assumption that damping coefficients, α, β, γ, and forcing amplitude, a, are small. Indeed, in section 4.4.3 we saw that for the wave basin experiments not only $\alpha \ll 1$ but also that $\overline{A'}$ can be made large enough to meet the conditions $\beta \ll 1$, $\gamma \ll 1$.

Afterwards the features predicted by the perturbation theories will be compared with the experiments by direct numerical integration of (5.1.2) or (5.1.4).

In a paper on edge waves, similar questions have been studied by Gottlieb & Mei(1996) using the averaging techniques. Here we demonstrate the use of a powerful alternative, the multiple scales method. This method has been used by others in wave problem, e.g. Trulsen & Mei(1994).

5.2 Modulational resonances of the trapped wave

We begin by regarding the systems (5.1.2) and (5.1.4) as being exact. Let $\mu \ll 1$ be an ordering parameter and assume that damping coefficients and incident amplitude

have the following order of magnitude

$$\alpha = \mu^2 \alpha_2, \quad \beta = \mu^2 \beta_2, \quad \gamma = \mu^2 \gamma_2, \qquad a = \mu a_1. \tag{5.2.1}$$

Setting $\mu = 0$, system (5.1.2) gives the $O(\mu^0)$ limit in action-angle coordinates

$$\begin{cases} R_T = -2R \sin 2\psi \\ \\ \psi_T = W + R - \cos 2\psi. \end{cases} \tag{5.2.2}$$

Equivalently system (5.1.4) reduces in the same limit to

$$\begin{cases} X_T = (1 - W) Y - Y \left(X^2 + Y^2\right) \\ \\ Y_T = (1 + W) X + X \left(X^2 + Y^2\right), \end{cases} \tag{5.2.3}$$

5.2.1 The Hamiltonian limit

Both systems (5.2.2) and (5.2.3) are hamiltonian, with the hamiltonian functions given respectively by (5.1.3) and (5.1.6) with $a = 0$. Their results are of course a special case of the previous. From the definition of hamiltonian, the change in time of the hamiltonian calculated along a phase plane trajectory is given by

$$\frac{\mathrm{d}}{\mathrm{d}T} H\left(R(T), \psi(T)\right) = H_R R_T + H_\psi \psi_T = H_R \left(-H_\psi\right) + H_\psi H_R \equiv 0; \tag{5.2.4}$$

therefore the level curves of the hamiltonians are the trajectories in the phase plane. The fixed points can be described in simple form both in action-angle $\{R, \psi\}$

$$O = \{0, \psi_0\}, \qquad s = \{1 - W, 0\}, \qquad u = \left\{-1 - W, \frac{\pi}{2}\right\}, \tag{5.2.5}$$

and cartesian $\{X, Y\}$ coordinates

$$O = \{0, 0\}, \qquad s_{1,2} = \left\{0, \pm\sqrt{1 - W}\right\}, \qquad u_{1,2} = \left\{\pm\sqrt{-1 - W}, 0\right\}. \tag{5.2.6}$$

In (5.2.5), ψ_0 is given by $\cos 2\psi_0 = W$. Clearly, $s_{1,2}$ and s, $u_{1,2}$ and u are related by (4.2.34) and (4.2.35). $s_{1,2}$ exist for $W < 1$, while $u_{1,2}$ for $W < -1$. The stability can be inferred from the eigenvalues λ of the Jacobian $J(X, Y)$

$$J(X, Y) = \begin{bmatrix} -2XY & 1 - W - X^2 - 3Y^2 \\ \\ 1 + W + 3X^2 + Y^2 & -2XY \end{bmatrix} \tag{5.2.7}$$

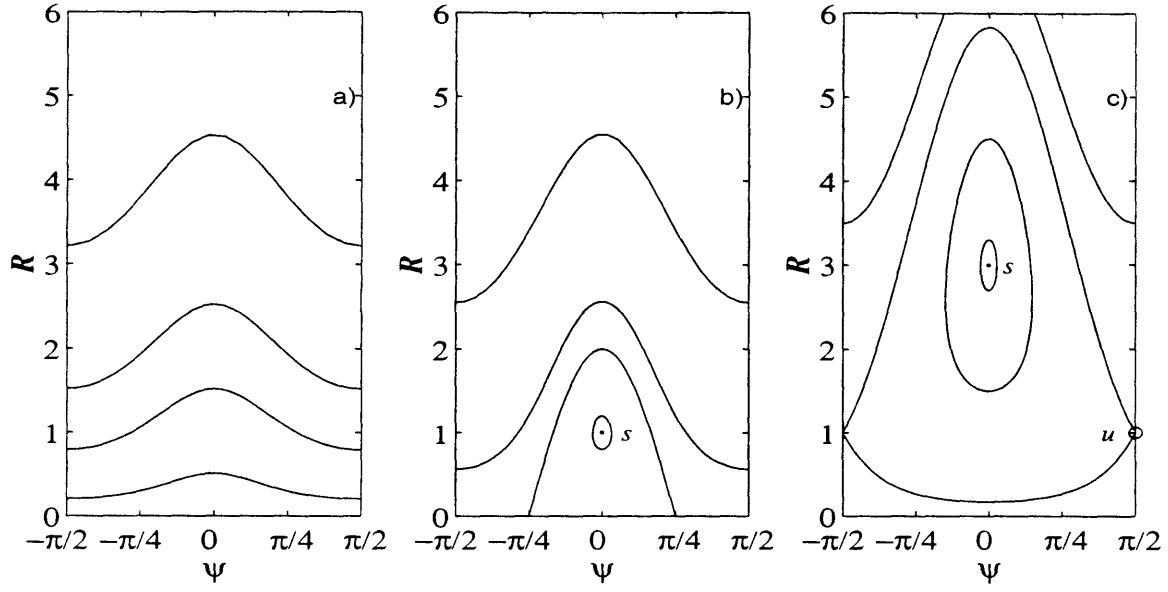

Figure 5-1: Phase plane samples in polar coordinates. a) $W = 2$ trajectories flow from left to right b) $W = 0$ there is one center, s c) $W = -2$ the saddle u is also present. Compare with figure 4-1 a) b) and c) with dissipation

evaluated at the fixed points. At the origin $\lambda = \pm\sqrt{1 - W^2}$, therefore the origin is a saddle for $|W| < 1$, a center for $|W| < 1$. For $s_{1,2}$ the eigenvalues are $\lambda = \pm 2\sqrt{W - 1}$ and since they exist only for $W < 1$, they are always centers. Conversely, the eigenvalues for $u_{1,2}$ are $\lambda = \pm 2\sqrt{-1 - W}$, and because they exist for $W < -1$, they are always saddles(unstable). Three phase plane samples representative of the possible scenarios, are shown both in polar, figure 5-1, and cartesian coordinates, figure 5-2 for respectively $W = 2$, $W = 0$ and $W = -2$.

The bifurcation diagram, i.e. the plot of the fixed points R_0 versus W is shown in figure 5-3. The inclined solid line originating at $W = 1, R = 0$ is the center s, for which $R_0^+ = 1 - W$, while the inclined dashed line originating at $W = -1, R = 0$ is the saddle u, for which $R_0^- = -1 - W$. To see the effect of dissipation, compare with the bifurcation diagrams of figures 4-2 or 4-8. The present hamiltonian case is the limit $\alpha, \beta, \gamma \to 0$, in which the saddle node SN goes to infinity. Indeed, as $\alpha, \beta \to 0$, expression (4.2.12) gives $W_s \to \infty$, expression (4.2.18) gives $R_{0\,max}^+ \to \infty$ and expression (4.2.8) becomes

$$(R + W)^2 = 1, \tag{5.2.8}$$

which has the roots u and s of (5.2.5). The same applies if quadratic damping γ is also included. Hence, at the leading order, the fixed point s is a center. Trajectories around

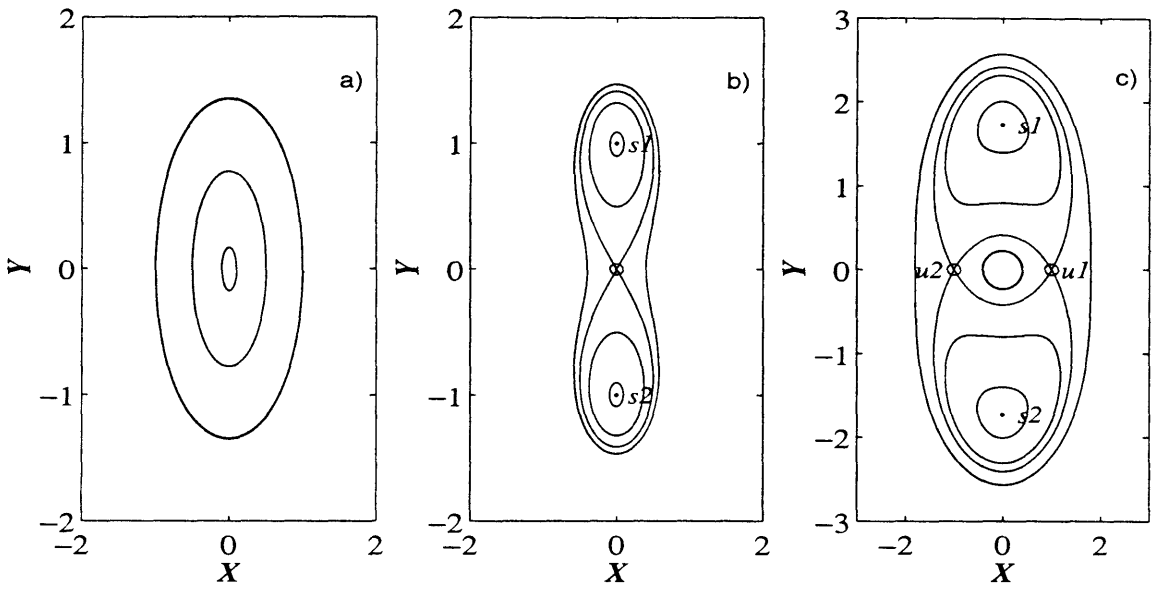

Figure 5-2: Phase plane samples in cartesian coordinates. a) $W = 2$ the origin is a center. b) $W = 0$ the origin is unstable and there are two centers $s_{1,2}$ encircled by two homoclinic orbits. c) $W = -2$ two saddles are also present, $u_{1,2}$; the heteroclinic connections separate the three domains of the centers. Compare with figure 4-6 a) b) and c) with dissipation

it oscillate harmonically with frequency equal to the eigenvalue $\lambda = 2\sqrt{1-W} \equiv 2\sqrt{R_0}$ (see figures 5-1bc and 5-2bc).

5.2.2 Effect of weak damping and wave forcing-no resonance

To see the effect of dissipation and forcing, we Taylor-expand system (5.1.2) about $R_0^+ = 1 - W$, $\psi_0^+ = 0$ in R and ψ up to third order and then substitute the following perturbation expansion

$$R = \sum_{p=0}^{3} \mu^p R_p + O(\mu^4), \qquad \psi = \sum_{p=0}^{3} \mu^p \psi_p + O(\mu^4). \tag{5.2.9}$$

At $O(\mu)$ sytem (5.1.4) gives

$$\begin{cases} R_{1_T} + \lambda^2 \psi_1 = 0 \\ \\ \psi_{1_T} - R_1 = -a_1 \cos \sigma T; \end{cases} \tag{5.2.10}$$

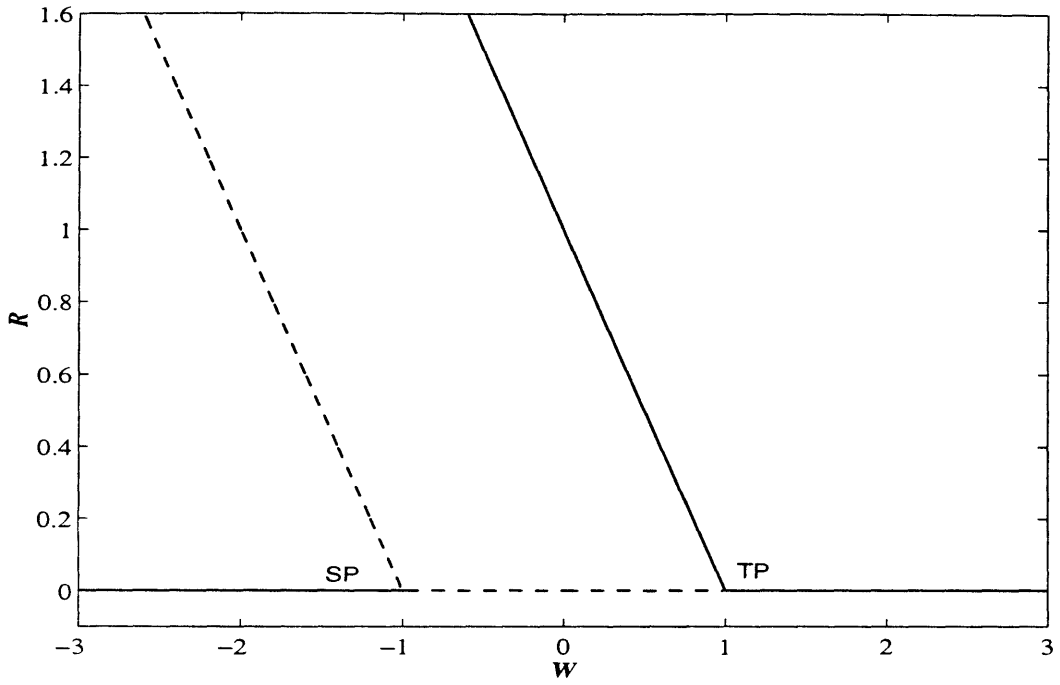

Figure 5-3: Bifurcation diagram for the Hamiltonian case; TP and SP are pitchfork bifurcation respectively transcritical and supercritical. Compared with 4-2 for viscous dissipation, the saddle node bifurcation point SN is at infinity

which is indeed the system governing an harmonic oscillator of natural frequency $\lambda \equiv 2\sqrt{R_0}$, forced at the frequency σ. The response is of the form

$$R_1 = R_{11}^{(n)}\, \mathrm{e}^{-\mathrm{i}\lambda T} + R_{11}^{(f)}\, \mathrm{e}^{-\mathrm{i}\sigma T} + *, \qquad \psi_1 = \psi_{11}^{(n)}\, \mathrm{e}^{-\mathrm{i}\lambda T} + \psi_{11}^{(f)}\, \mathrm{e}^{-\mathrm{i}\sigma T} + *. \tag{5.2.11}$$

Hence, at $O(\mu)$, both natural and forced frequencies are present. Through quadratic and cubic nonlinearities higher harmonics will be forced at higher orders, which in turn will cause resonance of the natural frequency. To describe the resulting slow time evolution, we let R_1 and ψ_1 be functions of $T_2 = \mu^2 T$.

At $O(\mu^2)$, the system governing R_2, ψ_2 is

$$\begin{cases} R_{2_T} + \lambda^2 \psi_2 = -\lambda^2 \psi_1 a_1 \cos\sigma T - 4R_1\psi_1 - \lambda^2\left(\lambda^2\alpha_2 + 4\beta_2 + 2\lambda\gamma_2\right)/8 \\ \\ \psi_{2_T} - R_2 = 2\psi_1^2 + \beta_2; \end{cases} \tag{5.2.12}$$

The quadratic terms above force the harmonics 2λ, 2σ, $\lambda \pm \sigma$ but not the natural frequency λ, unless the forcing frequency σ is near the values $\lambda/2$ or 2λ. In such cases the natural frequency is resonated respectively superharmonically or subharmonically; these possibilities are explored in the next sections. Away from these resonant values,

the response has the form

$$R_2 = R_{20} + R_{22}^{(n)}\,\mathrm{e}^{-\mathrm{i}2\lambda T} + R_{22}^{(f)}\,\mathrm{e}^{-\mathrm{i}2\sigma T} + R_{211}\,\mathrm{e}^{-\mathrm{i}(\lambda+\sigma)T} + R_{21,-1}\,\mathrm{e}^{-\mathrm{i}(\lambda-\sigma)T} + *, \quad (5.2.13)$$

$$\psi_2 = \psi_{20} + \psi_{22}^{(n)}\,\mathrm{e}^{-\mathrm{i}2\lambda T} + \psi_{22}^{(f)}\,\mathrm{e}^{-\mathrm{i}2\sigma T} + \psi_{211}\,\mathrm{e}^{-\mathrm{i}(\lambda+\sigma)T} + \psi_{21,-1}\,\mathrm{e}^{-\mathrm{i}(\lambda-\sigma)T} + *, \quad (5.2.14)$$

where each harmonic has an amplitude determined by solving system (5.2.12). For brevity their expressions are not reported.

Finally, at $O(\mu^3)$

$$\begin{cases} R_{3_T} + \lambda^2\,\psi_3 = -R_{1_{T_2}} - \lambda^2\psi_2 a_1\cos\sigma T - 4R_1\psi_1 a_1\cos\sigma T - 4R_2\psi_1 - 4R_1\psi_2 - \\ \qquad\qquad R_1\left(\lambda^2\,\alpha_2 + 2\beta_2 + \tfrac{3}{2}\lambda\,\gamma_2\right) \\ \psi_{3_T} - R_3 = -\psi_{1_{T_2}} + 4\psi_1\psi_2 + 2a_1\psi_1^2\cos\sigma T; \end{cases} \quad (5.2.15)$$

At this order the forced harmonics are λ, 3λ, σ, 3σ, $\lambda \pm 2\sigma$, $2\lambda \pm \sigma$ and include the natural frequency. Further resonances can occur if the forcing frequency σ is close to one of the following multiples of the natural: λ, 3λ, $\lambda/3$ which are respectively synchronous, subharmonic 1/3 and superharmonic 3 resonances. Away from the above values, removal of the secular terms proportional to $\exp\{-\mathrm{i}\lambda T)$ yields the evolution equation that describes the long term behaviour of $\left(R_{11}^{(n)},\ \psi_{11}^{(n)}\right)\exp\{-\mathrm{i}\lambda T)$

$$-\mathrm{i}R_{11_{T_2}}^{(n)} = \frac{\lambda^3\left[4\lambda^2 - \lambda^4 - 32 - 2\left(4 - \lambda^2 + 24\lambda^{-2}\right)\sigma^2 - \left(1 + 2\lambda^{-2} - 8\lambda^{-4}\right)\sigma^4\right]}{3\left(\sigma^2 - 4\lambda^2\right)\left(\sigma^2 - \lambda^2\right)^2}\,a_1^2 R_{11}^{(n)} - \frac{4}{\lambda}\left(\frac{1}{3} + \frac{4}{\lambda^2}\right)R_{11}^{(n)\,2}R_{11}^{(n)\,*} + \mathrm{i}\left(\frac{\lambda^2}{2}\alpha_2 + \frac{2}{3}\beta_2 + \frac{2}{3}\lambda\gamma_2\right)R_{11}^{(n)} - \frac{8\beta_2}{3\lambda}\,R_{11}^{(n)} \quad (5.2.16)$$

$$\psi_{11}^{(n)} = \frac{\mathrm{i}}{\lambda}R_{11}^{(n)}. \quad (5.2.17)$$

The first harmonic $R_{11}^{(n)}$ is modulated by the interaction with the forcing amplitude (term in $a_1^2 R_{11}^{(n)}$), by cubic interaction with itself (term in $R_{11}^{(n)\,2}R_{11}^{(n)\,*}$) and is dissipated by radiation damping (α_2) and viscosity (β_2, γ_2). Equation (5.2.17) is obtained from the second of (5.2.10).

From (5.2.16), the amplitude of $R_{11}^{(n)}$ is governed by

$$\left|R_{11}^{(n)}\right|_{T_2} = -\left(\frac{\lambda^2}{2}\alpha_2 + \frac{2}{3}\beta_2 + \frac{2}{3}\lambda\gamma_2\right)\left|R_{11}^{(n)}\right|. \quad (5.2.18)$$

As $T_2 \to \infty$, $\left|R_{11}^{(n)}\right| \to 0$. Hence, for σ away from λ, $\lambda/2$, $2\lambda, \ldots$ the natural mode is damped and the only response is the forced oscillation in phase with the modulation,

whose amplitude and phase are found from (5.2.10)

$$R_{11}^{(f)} = -\frac{a_1\lambda^2}{2\left(\sigma^2-\lambda^2\right)}, \qquad \psi_{11}^{(f)} = \mathrm{i}\frac{a_1\sigma}{2\left(\sigma^2-\lambda^2\right)}, \tag{5.2.19}$$

so that

$$R = R_0 - \frac{\mu a_1\lambda^2}{\sigma^2-\lambda^2}\cos\sigma T + O(\mu^2), \qquad \psi = \frac{\mu a_1\sigma}{\sigma^2-\lambda^2}\sin\sigma T + O(\mu^2). \tag{5.2.20}$$

The envelope of the trapped wave has an oscillating component of the same period as, and the same order of magnitude of, the modulation of the incident wave. Expression (5.2.20) of course becomes singular as $\sigma \to \lambda$, i.e. when synchronous resonance occurs.

5.2.3 Synchronous resonance with damping

Let the modulation amplitude be $O(\mu^3)$, $a = \mu^3 a_3$, and the frequency of the incident wave be slightly detuned from the natural, $\sigma = \lambda + \mu^2 d_2$. Damping terms are assumed to be $O(\mu^2)$

$$\alpha = \mu^2\alpha_2, \quad \beta = \mu^2\beta_2, \quad \gamma = \mu^2\gamma_2. \tag{5.2.21}$$

Following the same procedure outlined in the previous section, the $O(\mu)$ system is homogeneous

$$\begin{cases} R_{1_T} + \lambda^2\psi_1 = 0 \\ \\ \psi_{1_T} - R_1 = 0, \end{cases} \tag{5.2.22}$$

which corresponds to the undamped oscillator of (5.2.10) without forcing. The response has the form

$$R_1 = R_{11}\,\mathrm{e}^{-\mathrm{i}\left(\lambda+\mu^2 d_2\right)T} + *, \qquad \psi_1 = \psi_{11}\,\mathrm{e}^{-\mathrm{i}\left(\lambda+\mu^2 d_2\right)T} + *, \tag{5.2.23}$$

where $R_{11} = R_{11}(T_2)$, $\psi_{11} = \psi_{11}(T_2)$ are undetermined at this order.

At $O(\mu^2)$

$$\begin{cases} R_{2_T} + \lambda^2\psi_2 = -4R_1\psi_1 - \lambda^2\left(\lambda^2\alpha_2 + 4\beta_2 + 2\lambda\gamma_2\right)/8 \\ \\ \psi_{2_T} - R_2 = 2\psi_1^2 + \beta_2. \end{cases} \tag{5.2.24}$$

Thus only the zeroth and second harmonics are forced through quadratic terms. The solution is compactly written as

$$R_2 = R_{20} + R_{22}\,\mathrm{e}^{-\mathrm{i}2\left(\lambda+\mu^2 d_2\right)T} + *, \quad \psi_2 = \psi_{20} + \psi_{22}\,\mathrm{e}^{-\mathrm{i}2\left(\lambda+\mu^2 d_2\right)T} + *. \tag{5.2.25}$$

The amplitudes of the forced harmonics 0 and 2λ are easily found from (5.2.24).

At $O(\mu^3)$, the system governing the first harmonic λ is inhomogenoeous

$$\begin{cases} R_{3_T} + \lambda^2 \psi_3 = -R_{1_{T_2}} - 4R_2\psi_1 - 4R_1\psi_2 - R_1\left(\lambda^2\alpha_2 + 2\beta_2 + \frac{3}{2}\lambda\gamma_2\right) \\ \cdot \\ \psi_{3_T} - R_3 = -\psi_{1_{T_2}} + 4\psi_1\psi_2 - a_3\cos\left[(\lambda + \mu^2 d_2)\,T\right]; \end{cases} \tag{5.2.26}$$

since (5.2.22) is homogeneous, removing the secularity yields an evolution equation for R_{11}

$$-\mathrm{i}R_{11_{T_2}} = \left(\frac{1}{\lambda} + \frac{12}{\lambda^3}\right) R_{11}^2 R_{11}^* + \mathrm{i}\left(\frac{\lambda^2}{2}\alpha_2 + \beta_2 + \frac{3}{4}\lambda\gamma_2\right) R_{11} + \left(d_2 + \frac{2\beta_2}{\lambda}\right) R_{11} + \frac{\lambda}{4}\,a_3, \tag{5.2.27}$$

$$\psi_{11} = \frac{\mathrm{i}}{\lambda} R_{11}. \tag{5.2.28}$$

Equation (5.2.28) is again of Stuart-Landau form. The discussion of the fixed points is simplified by introducing the normalized damping coefficient

$$B = \left(\frac{\lambda^2}{2}\alpha_2 + \beta_2 + \frac{3}{4}\lambda\gamma_2\right)\left[\frac{a_3^2}{4}\left(\lambda + \frac{12}{\lambda}\right)\right]^{-\frac{1}{3}}, \tag{5.2.29}$$

the normalized detuning with a shift due to damping

$$D = \left(d_2 + \frac{2\beta_2}{\lambda}\right)\left[\frac{a_3^2}{16}\left(\lambda + \frac{12}{\lambda}\right)\right]^{-\frac{1}{3}}, \tag{5.2.30}$$

the normalized slow time

$$\tau = T_2\left[\frac{a_3^2}{16}\left(\lambda + \frac{12}{\lambda}\right)\right]^{\frac{1}{3}}, \tag{5.2.31}$$

and the normalized first harmonic response

$$r_{11} = R_{11}\left[\frac{4}{a_3}\left(\frac{1}{\lambda^2} + \frac{12}{\lambda^4}\right)\right]^{\frac{1}{3}}. \tag{5.2.32}$$

In terms of these variables, equation (5.2.28) becomes

$$-\mathrm{i}r_{11_\tau} = r_{11}^2 r_{11}^* + \mathrm{i}Br_{11} + Dr_{11} + 1. \tag{5.2.33}$$

Using action–angle variables, $r_{11} = \sqrt{\rho}\,\mathrm{e}^{\mathrm{i}\phi}$, and separating real and imaginary part of

(5.2.33), we obtain a dynamical system

$$\begin{cases} \rho_\tau = -2B\rho + 2\rho^{1/2}\sin\phi, \\ \\ \phi_\tau = \rho + D + \rho^{-1/2}\cos\phi, \end{cases} \tag{5.2.34}$$

whose fixed points can be found from the cubic equation

$$\rho^3 + 2D\rho^2 + \left(B^2 + D^2\right)\rho = 1. \tag{5.2.35}$$

The fixed points ρ_0, ϕ_0 of the above equation can be discussed graphically, in a similar manner as in the previous chapter. In the auxillary plane $\rho \sim Z$ of figure 5-4, consider the intersections of the curves $Z_1 = 1$ and $Z_2 = \rho^3 + 2D\rho^2 + (B^2 + D^2)\,\rho$, whose abscissas ρ_0 are the roots of (5.2.35). It is immediate to verify that there is one real and positive root for ρ if $D \notin [D'', D']$ and there are three real positive roots if $D \in [D'', D']$, where $D'' < D' < 0$ and D', D'' are the two roots of the tangency condition

$$Z_2 = Z_1, \qquad \frac{\mathrm{d}Z_2}{\mathrm{d}\rho} = 3\rho^2 + 4D\rho + B^2 + D^2 = 0. \tag{5.2.36}$$

Figure 5-4a,b and c depicts the three possible scenarios. Stability can be inferred from the same graph as follows. The eigenvalues of the jacobian evaluated at the fixed points

$$J(\rho_0, \phi_0) = \begin{bmatrix} -B & -2\rho_0\left(\rho_0 + D\right) \\ \\ \left(3 + D/\rho_0\right)/2 & -B \end{bmatrix}, \tag{5.2.37}$$

are given by

$$\lambda_{1,2} = -B \pm \sqrt{-3\rho^2 - 4D\rho - D^2}, \tag{5.2.38}$$

so that the fixed point is unstable whenever $\lambda_1 > 0$, i.e. when

$$-3\rho^2 - 4D\rho - D^2 - B^2 \equiv -\frac{\mathrm{d}Z_2}{\mathrm{d}\rho} > 0 \quad \Rightarrow \quad \frac{\mathrm{d}Z_2}{\mathrm{d}\rho} < 0. \tag{5.2.39}$$

Hence, the slope of Z_2 at the intesections with Z_1 gives the stability of the corresponding fixed points. For s_1 and s_2 the slope is positive and the fixed points are stable. On the other hand, u is unstable because the slope is negative. The two bifurcations that occur at D' and D'' are both of the saddle node type. To see this, let us decrease the value of D from positive values: when $D = D'$, s_2 and u are born and they drift apart as D continues to decrease. When $D = D'' < D'$, u and s_1 coalesce and disappear. These features can be seen in the bifurcation (or resonance) diagram of figure 5-5, where s_1, s_2 are respectively the upper/lower solid lines, while u is represented by a dashed line. The diagram for different values of damping B are represented. Note that for large enough damping B, the triple valued region is

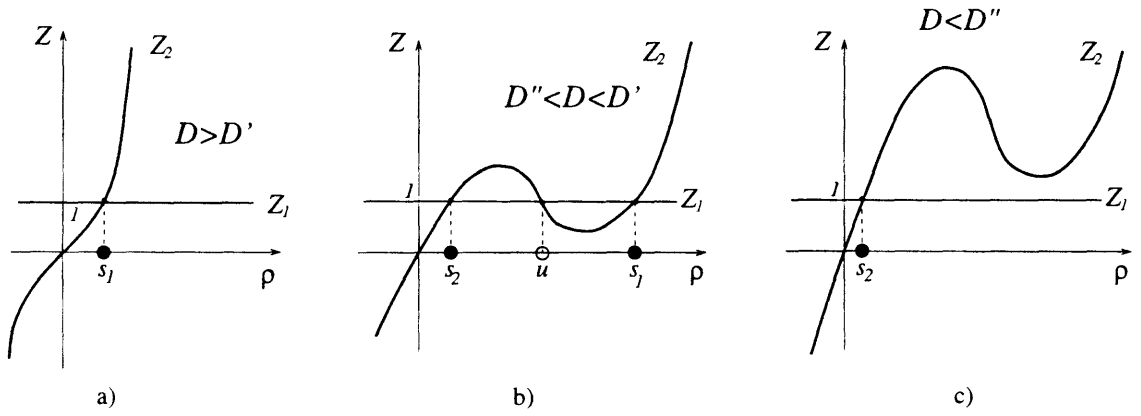

Figure 5-4: Graphical determination of the fixed points of system 5.2.34

absent. The threshold value for the disappearence of the triple valued region does not have a simple algebraic expression, but be found by the numerical solution of (5.2.35). Whenever the triple valued region exist, hysterisis and jump phenomena might occur.

The maximum value of the action, $\rho_{0_{max}}$ is achieved when

$$\frac{\mathrm{d}}{\mathrm{d}D}(5.2.35) = 0, \quad \text{i.e. at} \quad D = -\rho_{0_{max}} \tag{5.2.40}$$

at which

$$\rho_{0_{max}} = \frac{1}{B^2}. \tag{5.2.41}$$

Making use of (5.2.29), (5.2.30) and (5.2.32), we obtain a condition in terms of d_2, R_{11}, a_3 and the damping terms α_2, β_2, γ_2

$$d_2 = -|R_{11}|^2_{0_{max}} \frac{\lambda^2+12}{\lambda^{10/3}} - \frac{2\beta_2}{\lambda}, \qquad |R_{11}|_{0_{max}} = \frac{a_3}{2\lambda\alpha_2 + \frac{4}{\lambda}\beta_2 + 3\gamma_2}; \tag{5.2.42}$$

the amplitude of the response, $|R_{11}|_{0_{max}}$, grows with the amplitude of modulation and is limited by damping. Expression (5.2.42) depends also on the natural frequency $\lambda = 2\sqrt{1-W}$, where W is the detuning of the carrier wave defined by (4.1.5). The response for given a_3 and damping α_2, β_2, γ_2 varies with λ; the largest occurs when λ is such that

$$\frac{\mathrm{d}}{\mathrm{d}\lambda}|R_{11}|_{0_{max}} = 0, \tag{5.2.43}$$

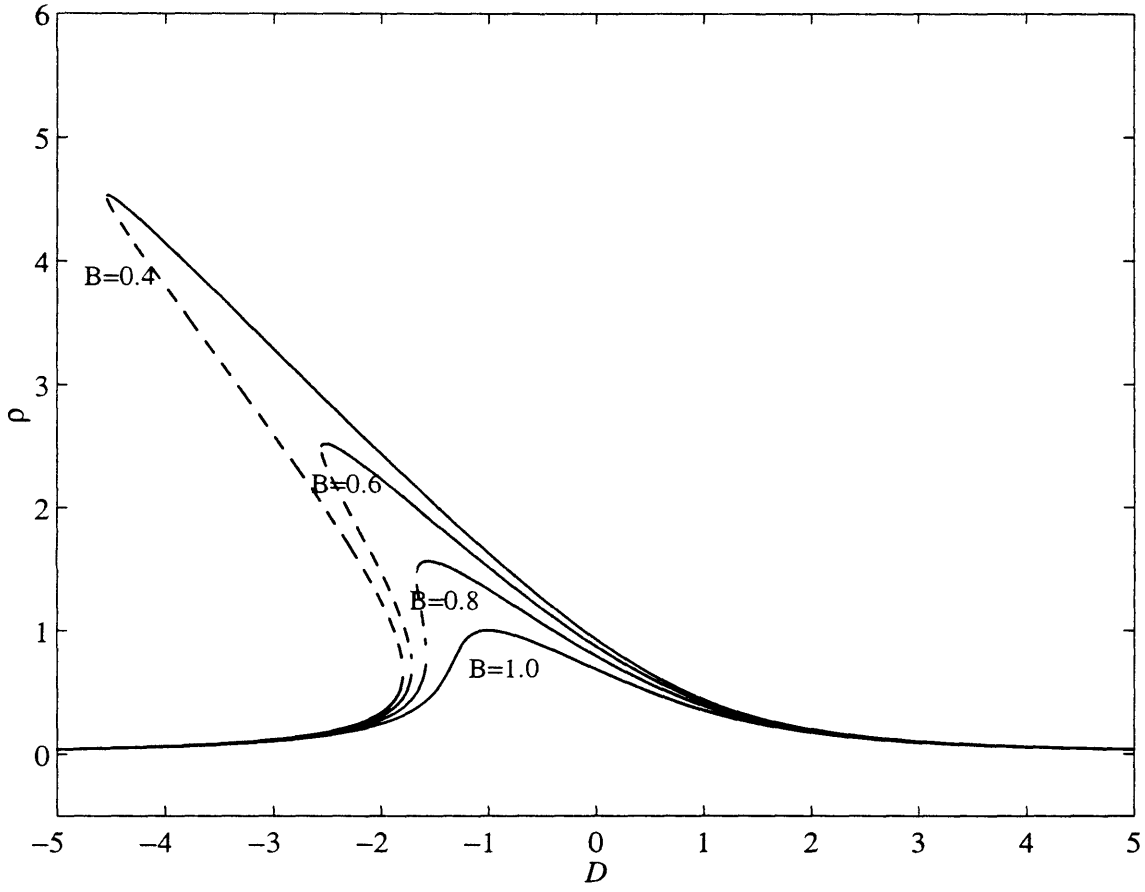

Figure 5-5: Bifurcation diagram for synchronous modulational resonance for different values of normalized damping. D includes a shift due to linear damping β_2.

which gives

$$\lambda = \sqrt{\frac{2\beta_2}{\alpha_2}} \quad \Rightarrow \quad W = 1 - \frac{\beta_2}{\alpha_2}, \tag{5.2.44}$$

and

$$|R_{11}|_{0_{max}} = \frac{a_3}{4\sqrt{2\alpha_2\beta_2} + 3\gamma_2}. \tag{5.2.45}$$

In order to verify the approximation of the present weakly nonlinear theory, we perform numerical integration of system (5.1.4) in the neighborhood of the synchronous resonance. All the numerical integrations in this and the following sections are carried out using a fourth order Runge–Kutta scheme with adaptive stepsize. The code driver makes use of the Numerical Recipes library and uses a numerical tolerance equal to 1.e-10. Subsequent spectra are generated using an FFT with 1024 data points and 15 sample points per period of the forcing $2\pi/\sigma$. The code driver makes use of the Matlab library for computing and plotting.

The detuning of the carrier wave is chosen to be zero, $W = 0$. Consequently the natural angular frequency of oscillation around the center is $\lambda = 2$. Synchronous resonance occurs when $\sigma = 2 + \mu^2 d_2$. In figure 5-6 two frequency spectra for $\alpha = \beta = \gamma = 0.01$ are shown. The first is for $a = 0.005$, representative of values of $\mu = O(a^{1/3}) = 0.15$, while the second is for $a = 0.015$, for which $\mu = O(a^{1/3}) = 0.25$. The power density spectrum of $R(T)$ obtained from numerical integration of (5.1.4) is shown with a solid line, while the harmonics calculated by the perturbation theory are denoted by empty circles. Because system (5.1.4) is nondimensional, the frequency horizontal axis and the power density vertical axis are both dimensionless. As predicted by the theory, only the forcing frequency σ and its higher harmonics are present. Clearly for values of $\mu < 0.15$ the differences are hardly appreciable.

As the frequency σ is varied around $\lambda = 2$, the amplitude of the first harmonic calculated from (5.2.35) (the circle in figure 5-6) is compared with the amplitude deduced from the spectrum of the numerical time series. The results are shown in the bifurcation diagram of figure 5-7. The plot is obtained by first solving in normalized coordinate ρ, D, equation (5.2.35) and then using expressions (5.2.30) and (5.2.32) to plot in the $\sigma - 2\mu|R_{11}|$ bifurcation plane:

$$2\mu|R_{11}| = \left[2\left(\frac{1}{\lambda^2} + \frac{12}{\lambda^4}\right)\right]^{-\frac{1}{3}} a^{-\frac{1}{3}}\rho^{\frac{1}{2}}, \quad \sigma = \lambda + \mu^2 d_2 = \lambda + \left[\frac{1}{16}\left(\lambda + \frac{12}{\lambda}\right)\right]^{\frac{1}{3}} a^{\frac{2}{3}} D - \frac{2\beta}{\lambda}. \tag{5.2.46}$$

Figure 5-7 is for $\alpha = \beta = \gamma = 0.01$, $a = 0.005$ and $a = 0.015$, i.e. the same values of figure 5-6. Thus only when σ is near λ, i.e. when the incident wave spectrum is narrow-banded, is the amplitude R_{11} significant. To check the accuracy of the theory for even larger values of μ, we also present a comparison for $a = 0.025$, i.e. $\mu = O(a^{1/3}) = 0.30$. For $a = 0.005$ the agreement is very good: numerical integration, represented by the empty circles, confirms the hump in the resonance diagram predicted by the theory

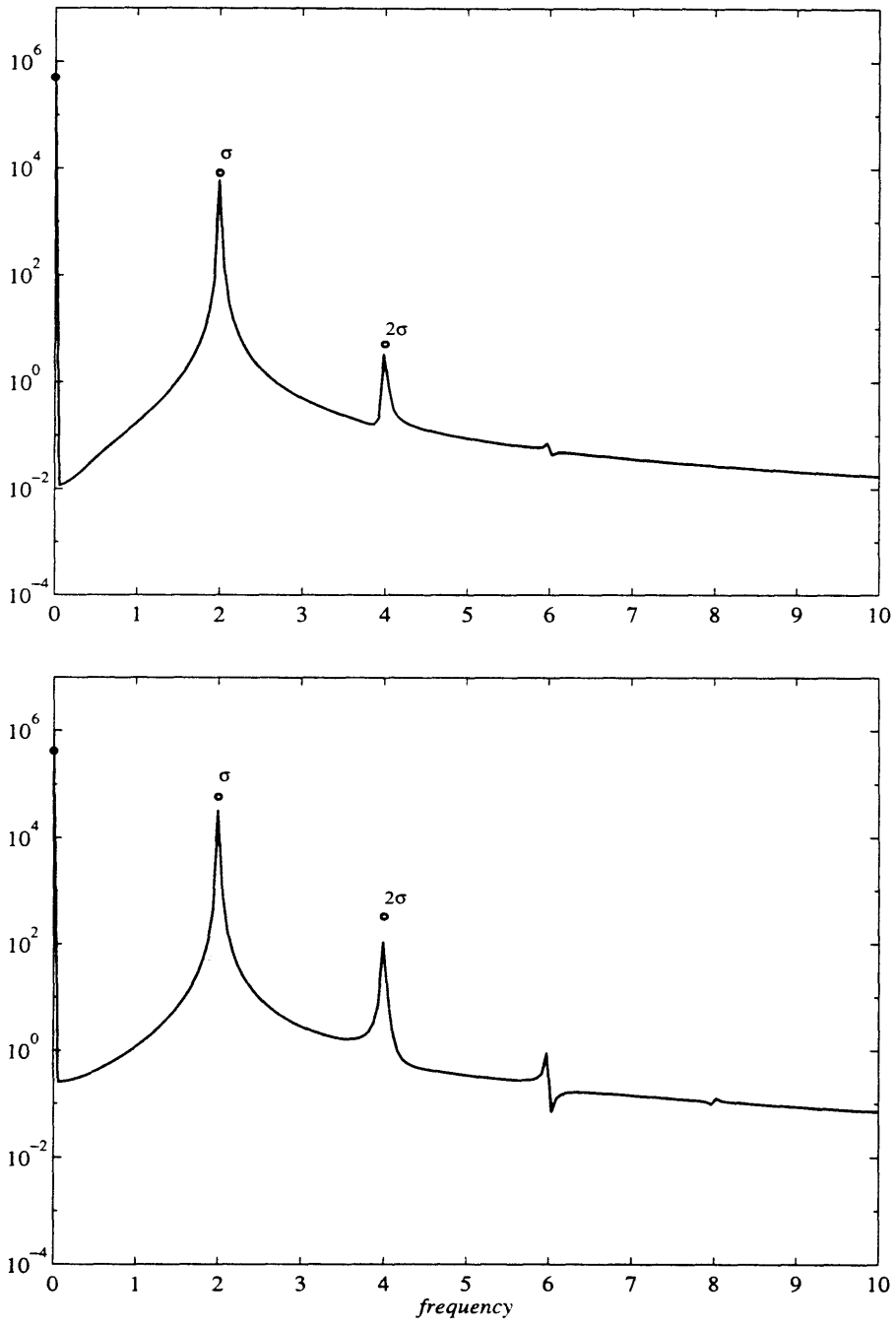

Figure 5-6: Spectra for $a = 0.005$, $a = 0.015$ and $\sigma = \lambda = 2$. Axis are dimensionless.

(represented with a solid line) with a maximum error smaller than 0.5%. For the larger value $a = 0.015$ the triple valued region is confirmed, but the upper theoretical branch is slightly greater than the numerical computed amplitudes. The same can be observed for $a = 0.025$. The relative difference between perturbation theory and numerics has been calculated to be within 0.5% for $\mu < 0.18$ and increasingly higher for larger values of μ.

For each point of the branches of figure 5-7 there is a corresponding attracting limit cycle in the phase plane $\psi \sim R$. In figure 5-8, the limit cycle for $\sigma = \lambda = 2$, $\alpha = \beta = \gamma = 0.01$ and $a = 0.005$ as described by the perturbation expansion up to $O(\mu^2)$ (solid line) is compared with the numerical simulation (dotted line); all trajectories are attracted to the limit cycle of frequency σ. A Poincaré section obtained by sampling every forcing cycle $2\pi/\sigma$ would yield a single point. The two cycles overlap almost completely.

For the larger value of the forcing amplitude, as seen in figure 5-5 and confirmed in figure 5-7, a single-valued and a triple-valued regions are possible. Correspondingly, one and two coexisting limit cycles appear in the phase plane $\psi \sim R$. In figure 5-9, for $\sigma = \lambda = 2$ and $a = 0.015$ the limit cycle as obtained from the perturbation theory (solid line) is compared with the one resulting from numerical integration; the two limit cycle are slightly off (see the point at $\sigma = \lambda = 2$ of the curve $a = 0.015$ in figure 5-7) In the second picture for $\sigma \simeq 1.9$ the two coexisting limit cycle are revealed by the theory and confirmed by numerical experiments. From figure 5-7 for $a = 0.015$ we know that the upper branch lies above the numerical findings; correspondingly the solid line outer limit cycle lies outside the corresponding numerical one. Still in figure 5-7 the lower theoretical and numerical branches coincides at $\sigma = 1.9$; indeed in figure 5-9 the analytical and numerical inner limit cycles coincide.

5.2.4 Subharmonic 1/2 resonance with damping

To analyse this resonance, let the modulation amplitude be $O(\mu^2)$, $a = \mu^2 a_2$. We also assume that the forcing frequency is detuned from the natural by an $O(\mu^2)$ quantity, i.e. $\sigma = 2(\lambda + \mu^2 d_2)$, and all damping terms are still $O(\mu^2)$

$$\alpha = \mu^2 \alpha_2, \quad \beta = \mu^2 \beta_2, \quad \gamma = \mu^2 \gamma_2, \tag{5.2.47}$$

so that the $O(\mu)$ system is again the free oscillator

$$\begin{cases} R_{1_T} + \lambda^2 \psi_1 = 0, \\ \\ \psi_{1_T} - R_1 = 0. \end{cases} \tag{5.2.48}$$

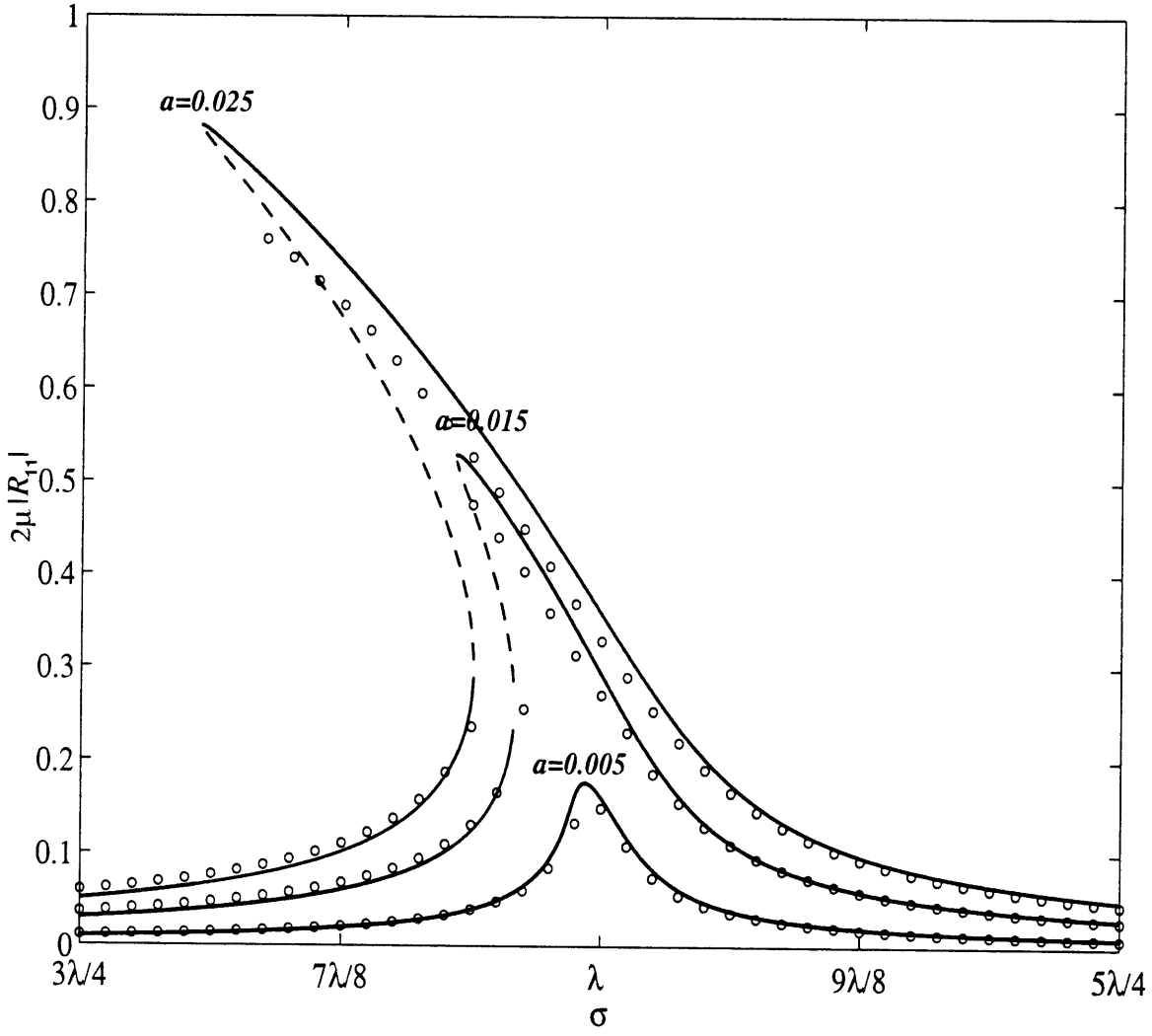

Figure 5-7: Bifurcation diagrams for $\alpha = \beta = \gamma = 0.01$. Solid and dashed lines denote the analytical solution, empty circles the numerical solution. Axis are dimensionless.

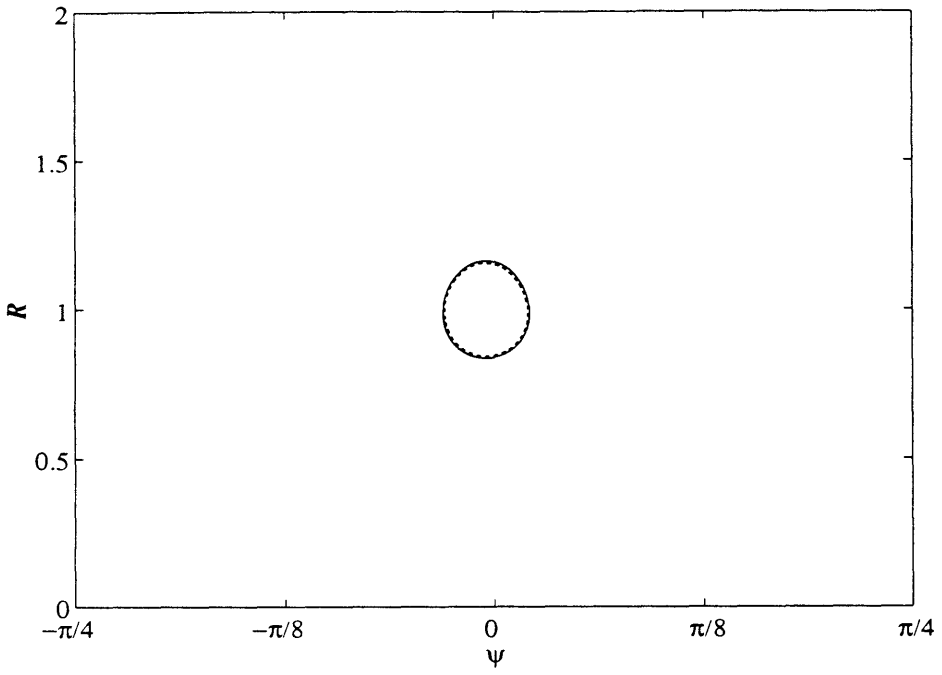

Figure 5-8: Limit cycle for $a = 0.05$ and $\alpha = \beta = \gamma = 0.05$ and $\sigma = \lambda = 2$

The response can be expanded in the form

$$R_1 = R_{11}\,\mathrm{e}^{-\mathrm{i}\left(\lambda+\mu^2 d_2\right)T} + *, \qquad \psi_1 = \psi_{11}\,\mathrm{e}^{-\mathrm{i}\left(\lambda+\mu^2 d_2\right)T} + *, \tag{5.2.49}$$

where $R_{11} = R_{11}(T_2)$, $\psi_{11} = \psi_{11}(T_2)$ are undetermined at this order.

At $O(\mu^2)$ the zeroth and second harmonics are forced through quadratic terms; the second harmonic is also forced by the modulation amplitude a_2

$$\begin{cases} R_{2_T} + \lambda^2\,\psi_2 = -4R_1\psi_1 - \lambda^2\left(\lambda^2\,\alpha_2 + 4\beta_2 + 2\lambda\,\gamma_2\right)/8 \\ \\ \psi_{2_T} - R_2 = 2\psi_1^2 + \beta_2 - a_2\cos\left[2\left(\lambda + \mu^2 d_2\right)T\right]. \end{cases} \tag{5.2.50}$$

The amplitudes of the forced harmonics 0 and 2λ are found from (5.2.24); the solution can be written as

$$R_2 = R_{20} + R_{22}\,\mathrm{e}^{-\mathrm{i}2\left(\lambda+\mu^2 d_2\right)T} + *, \quad \psi_2 = \psi_{20} + \psi_{22}\,\mathrm{e}^{-\mathrm{i}2\left(\lambda+\mu^2 d_2\right)T} + *. \tag{5.2.51}$$

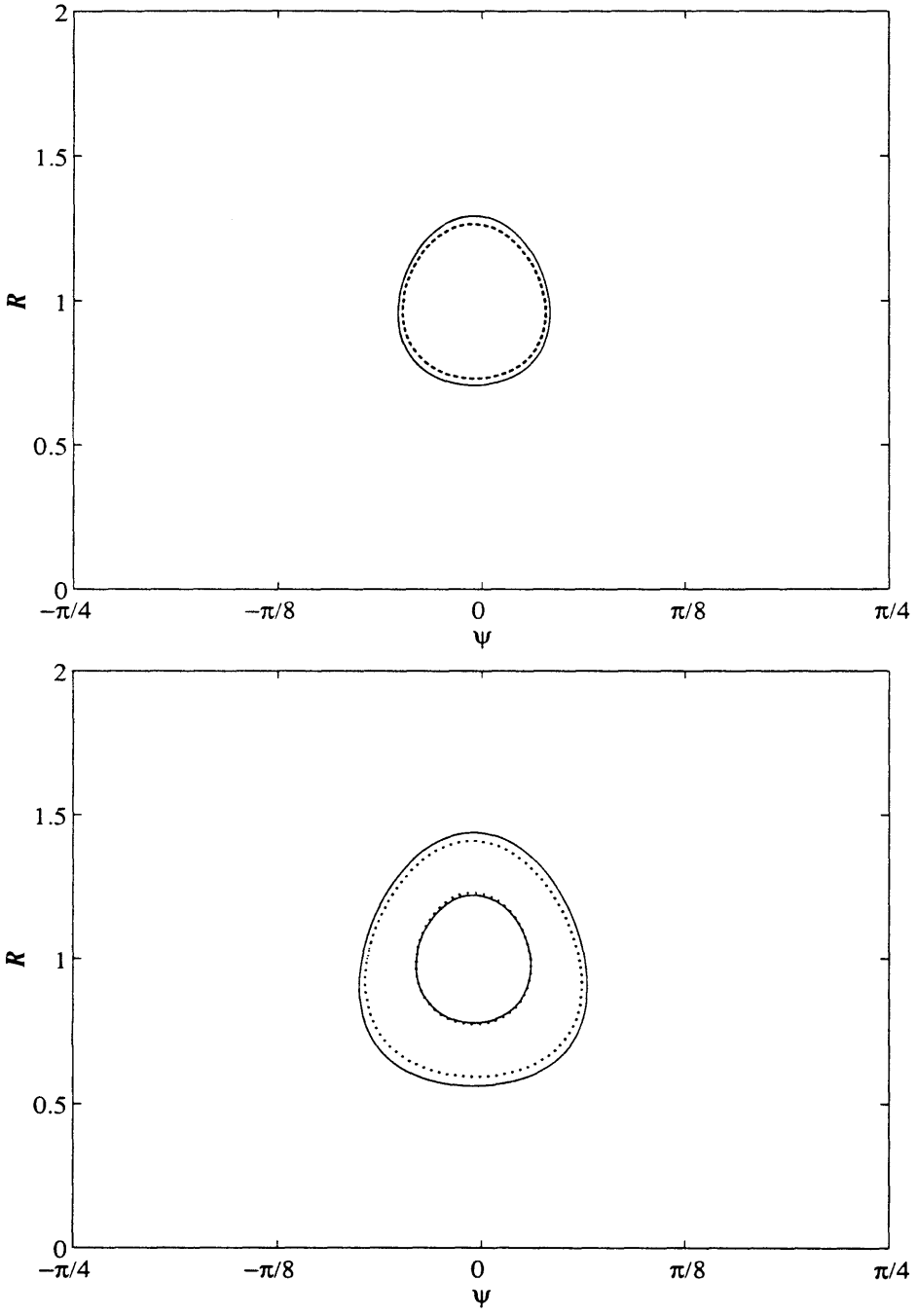

Figure 5-9: Limit cycles for $a = 0.25$ and $\alpha = \beta = \gamma = 0.05$ and $\sigma = \lambda$ in the single and triple valued region.

At $O(\mu^3)$, the system governing the first harmonic λ is inhomogenoeous

$$\begin{cases} R_{3_T} + \lambda^2 \psi_3 = -R_{1_{T_2}} - 4R_2\psi_1 - 4R_1\psi_2 - R_1\left(\lambda^2 \alpha_2 + 2\beta_2 + \frac{3}{2}\lambda\gamma_2\right) - \\ \qquad\qquad \lambda^2\psi_1 a_2 \cos\left[2\left(\lambda + \mu^2 d_2\right)T\right], \\ \psi_{3_T} - R_3 = -\psi_{1_{T_2}} + 4\psi_1\psi_2. \end{cases} \tag{5.2.52}$$

Since (5.2.48) is homogeneous, removal of the secularity yields an evolution equation for R_{11}

$$-\mathrm{i}R_{11_{T_2}} = \left(\frac{1}{\lambda} + \frac{12}{\lambda^3}\right) R_{11}^2 R_{11}^* + \mathrm{i}\left(\frac{\lambda^2}{2}\alpha_2 + \beta_2 + \frac{3}{4}\lambda\gamma_2\right) R_{11} + \left(d_2 + \frac{2\beta_2}{\lambda}\right) R_{11} + \left(\frac{\lambda}{4} + \frac{1}{\lambda}\right) a_2 R_{11}^*, \tag{5.2.53}$$

$$\psi_{11} = \frac{\mathrm{i}}{\lambda} R_{11}. \tag{5.2.54}$$

In comparison with the Stuart-Landau equation for synchronous resonance (5.2.28), only the forcing term is different.

Let us introduce the normalized damping coefficient (linear, effective)

$$B = \left(\frac{\lambda^2}{2}\alpha_2 + \beta_2 + \frac{3}{4}\lambda\gamma_2\right)\left[a_2\left(\frac{\lambda}{4} + \frac{1}{\lambda}\right)\right]^{-1}, \tag{5.2.55}$$

the normalized detuning with a shift due to linear damping

$$D = \frac{1}{a_2}\left(d_2 + \frac{2\beta_2}{\lambda}\right)\left(\frac{\lambda}{4} + \frac{1}{\lambda}\right)^{-1}, \tag{5.2.56}$$

the normalized slow time

$$\tau = T_2\, a_2\left(\frac{\lambda}{4} + \frac{1}{\lambda}\right), \tag{5.2.57}$$

and the normalized first harmonic response

$$r_{11} = \frac{R_{11}}{\sqrt{a_2}}\,\frac{2}{\lambda}\sqrt{\frac{\lambda^2 + 12}{\lambda^2 + 4}} \tag{5.2.58}$$

evolution equation (5.2.28) assumes the simplified form

$$-\mathrm{i}r_{11_\tau} = r_{11}^2 r_{11}^* + \mathrm{i}Br_{11} + Dr_{11} + r_{11}^*. \tag{5.2.59}$$

Using action–angle variables, $r_{11} = \sqrt{\rho}\,\mathrm{e}^{\mathrm{i}\phi}$, and sorting real and imaginary part of

(5.2.59) obtain a dynamical system

$$\begin{cases} \rho_\tau = -2\rho\,(B - \sin 2\phi)\,, \\ \\ \phi_\tau = \rho + D + \cos 2\phi, \end{cases} \tag{5.2.60}$$

whose fixed points are the equilibrium amplitude of the resonated natural frequency λ.

System (5.2.60) admits the trivial solution $\rho_0 = 0$, $\cos 2\psi_0 = -D$, which is unstable if a perturbation $\rho' \ll 1$ grows with time. Therefore let $\rho = 0 + \rho'$ and linearize the first of (5.2.60)

$$\rho'_\tau = -2B\rho' \mp \sqrt{1 - D^2}, \tag{5.2.61}$$

from which

$$\rho' \propto \mathrm{e}^{2\left(\mp\sqrt{1-D^2}-B\right)\tau}. \tag{5.2.62}$$

Hence the trivial fixed point is unstable for $|D| < \sqrt{1 - B^2}$, stable otherwise. Note that in order for the interval of instability to exist, the effective linear damping coefficient B must satisfy $B < 1$. Using definition (5.2.55) for B, it follows that for given damping coefficients $\alpha_2, \beta_2, \gamma_2$, instability of the trivial solution occurs only if the amplitude a_2 satisfies the inequality

$$a_2 > \left(\frac{\lambda^2}{2}\alpha_2 + \beta_2 + \frac{3}{4}\lambda\gamma_2\right)\left(\frac{\lambda}{4} + \frac{1}{\lambda}\right)^{-1}. \tag{5.2.63}$$

Since $\lambda = 2\sqrt{1 - W}$, as $W \to 1$ the threshold for a_2 decreases to zero. Using expression (4.1.5) for W, it follows that this temporal subharmonic resonance is more likely to occur when carrier wave amplitude $\overline{A'}$ and detuning $\Delta\omega$ fall near the right branch TP of the region of instability of figure 4-9.

The nontrivial fixed points are the roots ρ_0 of the equation

$$\rho^2 + 2D\rho + D^2 + B^2 = 1, \tag{5.2.64}$$

obtained by solving (5.2.60) for $\sin\psi$ and $\cos\psi$ and summing their squares. The roots are given by

$$\rho_0^{\pm} = -D \pm \sqrt{1 - B^2}, \tag{5.2.65}$$

which will be referred to respectively as s and u, $(s,\, u) = \left(\rho_0^+,\, \rho_0^-\right)$. Existence of the square roots in (5.2.65) requires $B > 1$; the condition $\rho > 0$ further requires that $D < \sqrt{1 - B^2}$ for s to exist, and that $D < -\sqrt{1 - B^2}$ for u to exist.

Stability can be inferred by considering the jacobian at the fixed points s and u

$$J(\rho_0^{\pm}, \phi_0^{\pm}) = \begin{bmatrix} 0 & -4\rho_0^{\pm}\left(\rho_0^{\pm} + D\right) \\ 1 & -2B \end{bmatrix}, \tag{5.2.66}$$

and then its eigenvalues

$$\lambda_{1,2}^{\pm} = -B \pm \sqrt{B^2 - 4\rho_0^{\pm}\left(D + \rho_0^{\pm}\right)}. \tag{5.2.67}$$

The fixed points are unstable when $\lambda_1^{\pm} > 0$, i.e. when

$$-4\rho_0^{\pm}\left(\rho_0^{\pm} + D\right) > 0. \tag{5.2.68}$$

Since $\rho_0^{\pm} > 0$, the last condition becomes

$$\rho_0^{\pm} > -D. \tag{5.2.69}$$

Comparing (5.2.69) with (5.2.65) it is immediate to see that s is always stable and u is always unstable.

We summarize the panorama of fixed points and their stability.

- $B > 1$. There is only the trivial solution, stable for any D.
- $B < 1$. For $D > \sqrt{1 - B^2}$, there is only the trivial solution, stable. For $|D| < \sqrt{1 - B^2}$ there is one stable nontrivial solution, s, and the trivial solution is unstable. Finally for $D < -\sqrt{1 - B^2}$, there are two nontrivial solution, one stable s and one unstable u, coexisting with the trivial solution, which is stable.

The bifurcation diagram is shown in figure 5-10. The solid lines represent stable roots, i.e. s and the origin for $|D| > \sqrt{1 - B^2}$; the dashed lines represent unstable roots, i.e. u and the origin for $|D| < \sqrt{1 - B^2}$ (interval of instability). The bifurcation at $D = \sqrt{1 - B^2}$ is a transcritical pitchfork (indicated by TP), while the one at $D = -\sqrt{1 - B^2}$ is supercritical (indicated by SP). Because the damping term in (5.2.59) is linear in r_{11} and does not contain quadratic or cubic terms, the nontrivial branches do not coalesce for $D < 0$ in a saddle node bifurcation, but are open and give unbounded response as $D \to -\infty$. As a consequence, the thoeoretical region of hysteresis is unbounded. Suppose we decrease the detuning D from some point 1, seen in figure 5-11. As the frequency is decreased down through 2, the null solution becomes unstable and the response increases along the branch 2-3, without going back to the null branch. Conversely, if we increase the frequency from negative detuning, say from point 4 in figure 5-11, the representative point hits the subcritical pitchfork at 5 and jumps on the stable branch (point 6); it remains there as we increase the frequency even further. Therefore, a jump phenomenon is still possible.

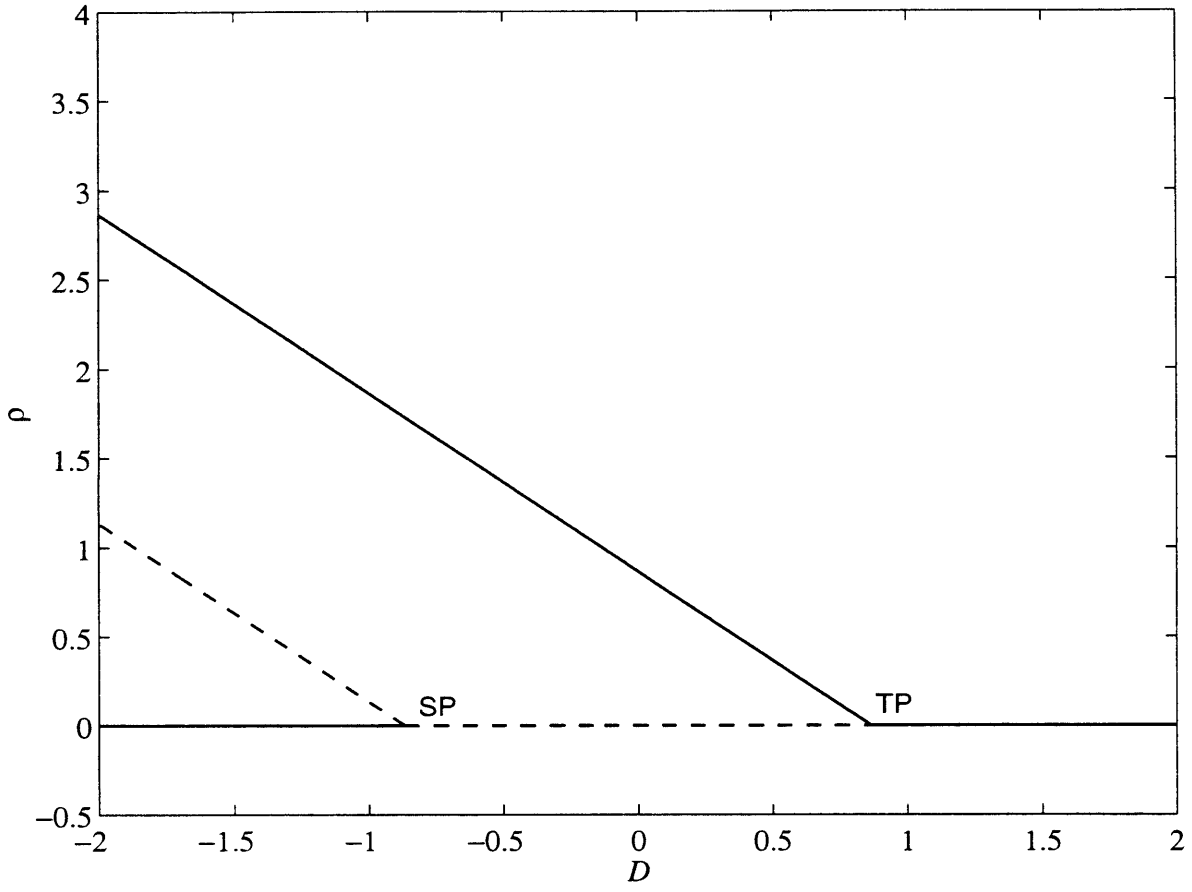

Figure 5-10: Bifurcation diagram for subharmonic modulational resonance for B=0.65

This is not a limitation since the theory is only local in a neighborhood of 2λ, where it will be shown to give reliable approximations for the response and the bandwidth of instability.

The band of instability is defined by $|D| < \sqrt{1-B^2}$; using expressions (5.2.55) and (5.2.56) the interval is mapped in a region of the $d_2 - a_2$ plane delimited by the hyperbola defined by $|D| = \sqrt{1-B^2}$

$$d_2 = \pm\sqrt{a_2^2\left(\frac{\lambda}{4}+\frac{1}{\lambda}\right)^2 - \left(\frac{\lambda^2}{2}\alpha_2 + \beta_2 + \frac{3}{4}\lambda\gamma_2\right)^2} - \frac{2\beta_2}{\lambda}, \tag{5.2.70}$$

which defines the region of instability in which subharmonic excitation is possible.

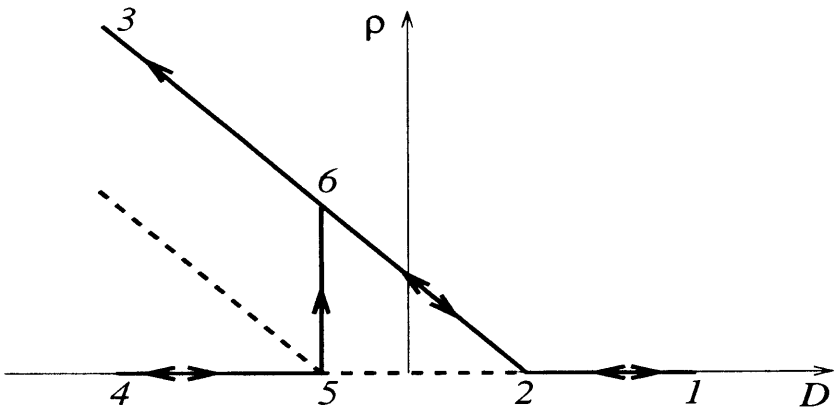

Figure 5-11: Jump phenomenon as D varies.

The vertex of the hyperbola lies at

$$d_2 = -\frac{2\beta_2}{\lambda}, \qquad a_2 = \left(\frac{\lambda^2}{2}\alpha_2 + \beta_2 + \frac{3}{4}\lambda\gamma_2\right)\left(\frac{\lambda}{4} + \frac{1}{\lambda}\right)^{-1} \tag{5.2.71}$$

The latter represents the marginal condition $D = 0$, $B = 1$ that marks the onset of instability and the existence of the nontrivial root s.

It is straightforward to see from (5.2.70) that as $\lambda \to 0$ (i.e. as $W \to 1$) the region of instability becomes the whole hals–plane $a_2 > 0$. At the same time the response decreases to zero, as can be deduced from (5.2.56) and the explicit expression of the nontrivial root $\rho = -D + \sqrt{1 - B^2}$. Recall form expression (4.1.5) for W, that the condition $W \to 1$ means that carrier wave amplitude $\overline{A'}$ and detuning $\Delta\omega$ fall near the right branch TP of the region of instability of figure 4-9. Therefore, for given carrier and modulated wave amplitudes, even if this temporal resonance is more likely to occur as the carrier wave detuning increases, the excited response becomes smaller in magnitude.

In figure (5-12) the region of instability is shown for $\alpha_2 = \beta_2 = \gamma_2 = 0.1$ and $\lambda = 2$ ($W = 0$). Along the + branch of (5.2.70), denoted by TP in figure 4-4, the origin loses stability in a transcritical pitchfork bifurcation; along the - branch, denoted instead by SP, the origin loses stability in a subcritical pitchfork bifurcation and the nontrivial response jumps to a finite value. Whenever the detuning d_2 and amplitude a_2 of the modulation fall inside the hyperbola (region II in figure 5-12), the finite amplitude subharmonic oscillation s will take place.

To the left of SP and above the vertex of the hyperbola (region III in figure 5-12) the stable nontrivial solution s coexists with the unstable u and the stable trivial fixed point.

In summary, the $d_2 - a_2$ plane is divided in the following regions.

- Region I. Only one stable trivial fixed point. Subharmonic resonance does not occur.
- Region II. The trivial fixed point is unstable and coexists with one stable nontrivial fixed point (s); subharmonic resonance always occur; jumps in the response are possible along SP for increasing d_2.
- Region III. One stable trivial fixed points coexisting with two nontrivial fixed point (s and u). Subharmonic resonance is conditional.

To complete the discussion of the fixed points, we show how the same results can be obtained with the graphical method. Define in the $\rho - Z$ plane of figure 5-13 the two curves $Z_1 = 1 - B^2$ and $Z_2 = \rho^2 + 2D\rho + D^2$, so that the nontrivial fixed point are the abscissas ρ_0 of their intersections in the region $\rho > 0$. Z_2 has its vertex on the $Z = 0$ axis at $\rho = -D$, so that there are respectively no, one (s) and two (s and u) intersections for $D > \sqrt{1 - B^2}$, $|D| < \sqrt{1 - B^2}$ and for $D < -\sqrt{1 - B^2}$. The three possible scenarios are depicted respectively in figure 5-13 a, b and c. Stability can be inferred graphically by considering the jacobian at the fixed points, expression (5.2.66), and then its eigenvalues (5.2.67). The fixed point is unstable when $\lambda_1 > 0$, i.e. when, at the points of intersection of Z_2 with Z_1, it holds

$$-4\rho(\rho + D) \equiv -2\rho\frac{\mathrm{d}Z_2}{\mathrm{d}\rho} > 0 \quad \Rightarrow \quad \frac{\mathrm{d}Z_2}{\mathrm{d}\rho} < 0. \tag{5.2.72}$$

Looking at the slope of Z_2 in figure 5-13b and c, it follows that s is always stable and u is always unstable. The interval $|D| < \sqrt{1 - B^2}$ (bandwidth of instability) is therefore the region in which subharmonic response takes place regardless of the initial condition.

Because the nontrivial fixed points are possible only in the quadrant $\rho > 0$, $Z > 0$ (see figure 5-13), the normalized damping must also satisfy the condition $Z_1 \equiv 1 - B^2 > 0$, which, using expression (5.2.55), gives the same condition (5.2.63) for a_2.

To verify the findings of the perturbation theory we compare them with the results of the numerical integration of the nondimensional system (5.1.2). We first fix the detuning of the carrier wave to $W = 0$, for which $\lambda = 2$ so that the subharmonic resonance is expected when $\sigma = 2\lambda = 4$. In figure 5-14 the wave spectra for $\sigma = 2.5\lambda = 5$ and $\sigma = 2\lambda = 4$ are shown. Solid line represent the power denstity spectrum from the numerical time series $R(T)$, while empty circle the harmonics calculated from the present perturbation theory. Indeed, in the first picture only the harmonic σ is present, while in the second a strong subharmonic $\sigma/2$ is resonated. The comparison is for $\alpha = \beta = \gamma = 0.01$. The harmonic calculated with the perturbation theory are denoted by an empty circle.

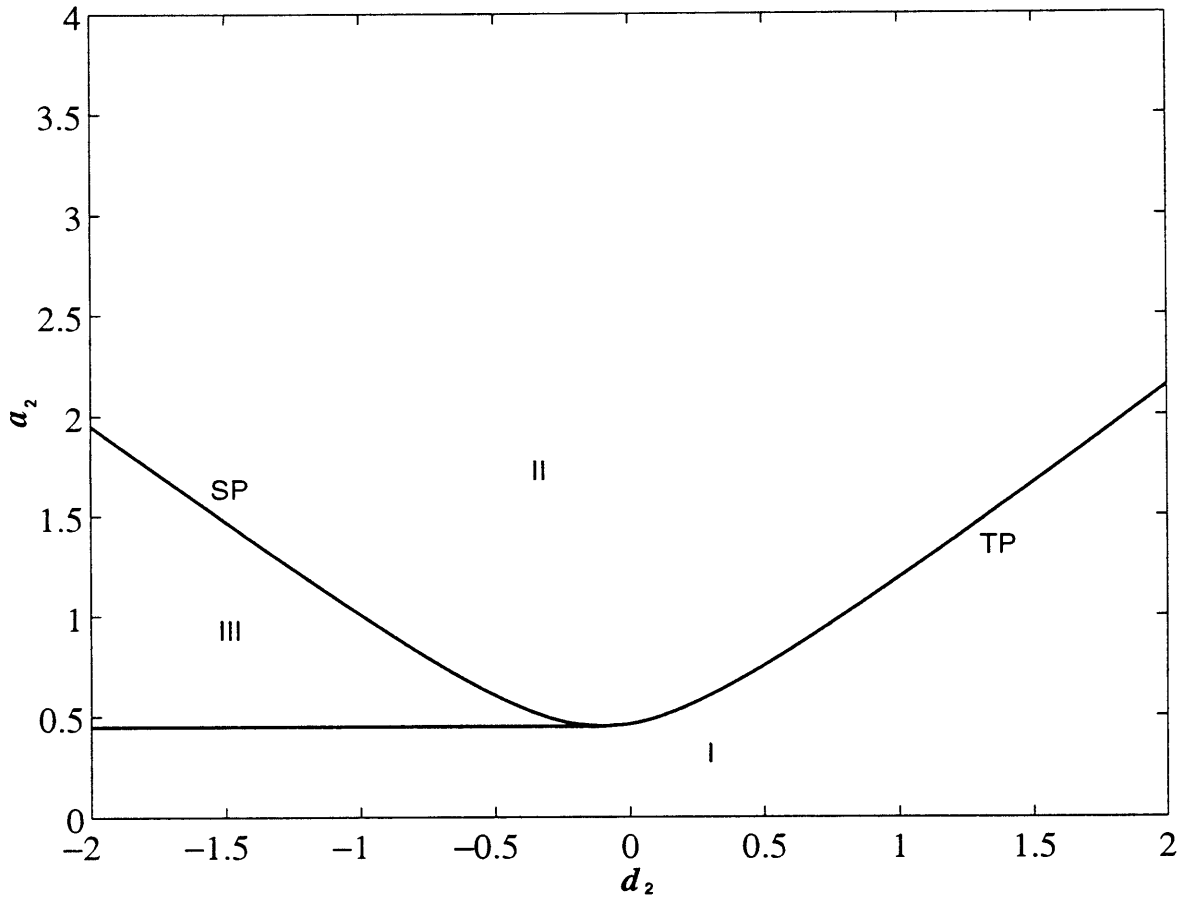

Figure 5-12: Region of instability for the subharmonic modulational resonance; $\alpha_2 = \beta_2 = \gamma_2 = 0.1$ $W = 0$ for which $B = 0.45$. Region I: stable trivial fixed point. Region II: unstable trivial fixed point coexisting with s (region of instability). Region III: stable trivial fixed fixed point coexisting with s and u

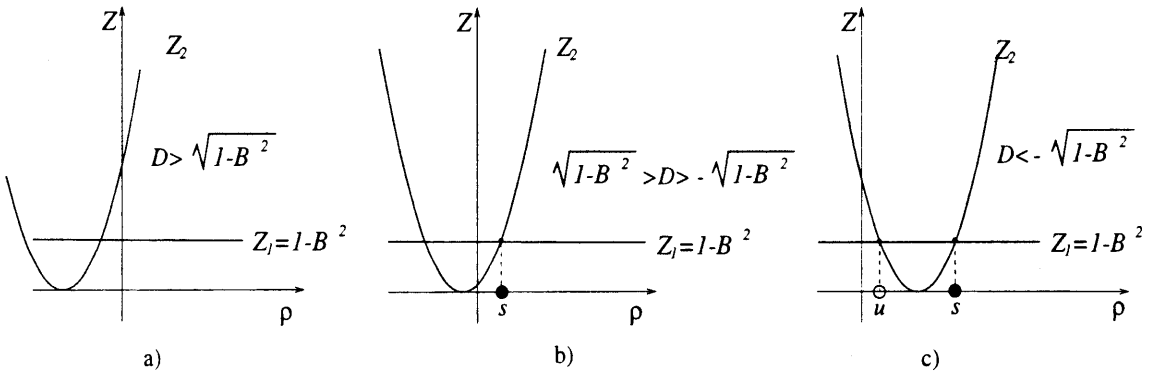

Figure 5-13: Graphical determination of the fixed points of system 5.2.60

For varying σ, the amplitude of the subharmonic $\sigma/2$ can be calculated from the spectrum and then compared with the prediction of the theory (the circle in figure 5-14). The result are the bifurcation diagrams of figure 5-15 and 5-16 in which the theoretical predictions of the amplitude of the first harmonic $2\mu|R_{11}|$ (solid lines) are compared with the result of the numerical integration (circles). The plots are obtained by first solving in normalized coordinate ρ, D, equation (5.2.65) and then using expressions (5.2.56) and (5.2.58) to plot in the $\sigma/2 - 2\mu|R_{11}|$ bifurcation plane:

$$\frac{\sigma}{2} = \lambda + \mu^2 d_2 = \lambda + \left(\frac{\lambda}{4} + \frac{1}{\lambda}\right) a\, D - \frac{2\beta}{\lambda}, \qquad 2\mu|R_{11}| = \frac{\lambda}{2}\sqrt{\frac{\lambda^2+4}{\lambda^2+12}}\,\sqrt{a\,\rho}. \quad (5.2.73)$$

The first two graphs in figure 5-15 are for $W = 0$ and $\alpha = \beta = \gamma = 0.01$, for which the threshold amplitude for resonance given by expression (5.2.63) is $a = 0.045$. Therefore we present the comparison for $a = 0.05$ and $a = 0.1$. In both cases the region of instability and the amplitude of the nontrivial roots are predicted by the theory with an error within 5%, which is satifactory for a comparison that occurs for values of $\mu = O(\sqrt{a}) \simeq 0.3$.

In figure 5-16 we fix $W = 0.6$ for which $\lambda = 1.26$; consequently, the threshold for resonance is lower $a = 0.025$ (recall that as $W \to 1$, $\lambda \to 0$, and the RHS of (5.2.63) tends to zero), and excitation of the response occurs for lower values of a. The first bifurcation diagram is for $a = 0.03$, $\mu = O(0.15)$, and shows agreement within 0.5% with the numerics. In the second diagram $a = 0.1$, $\mu = O(0.3)$. It is confirmed that for fixed a, going from $W = 0.0$ to $W = 0.6$ has increased the bandwidth of instability but decreased the response (compare with $a = 0.1$ in figure 5-15).

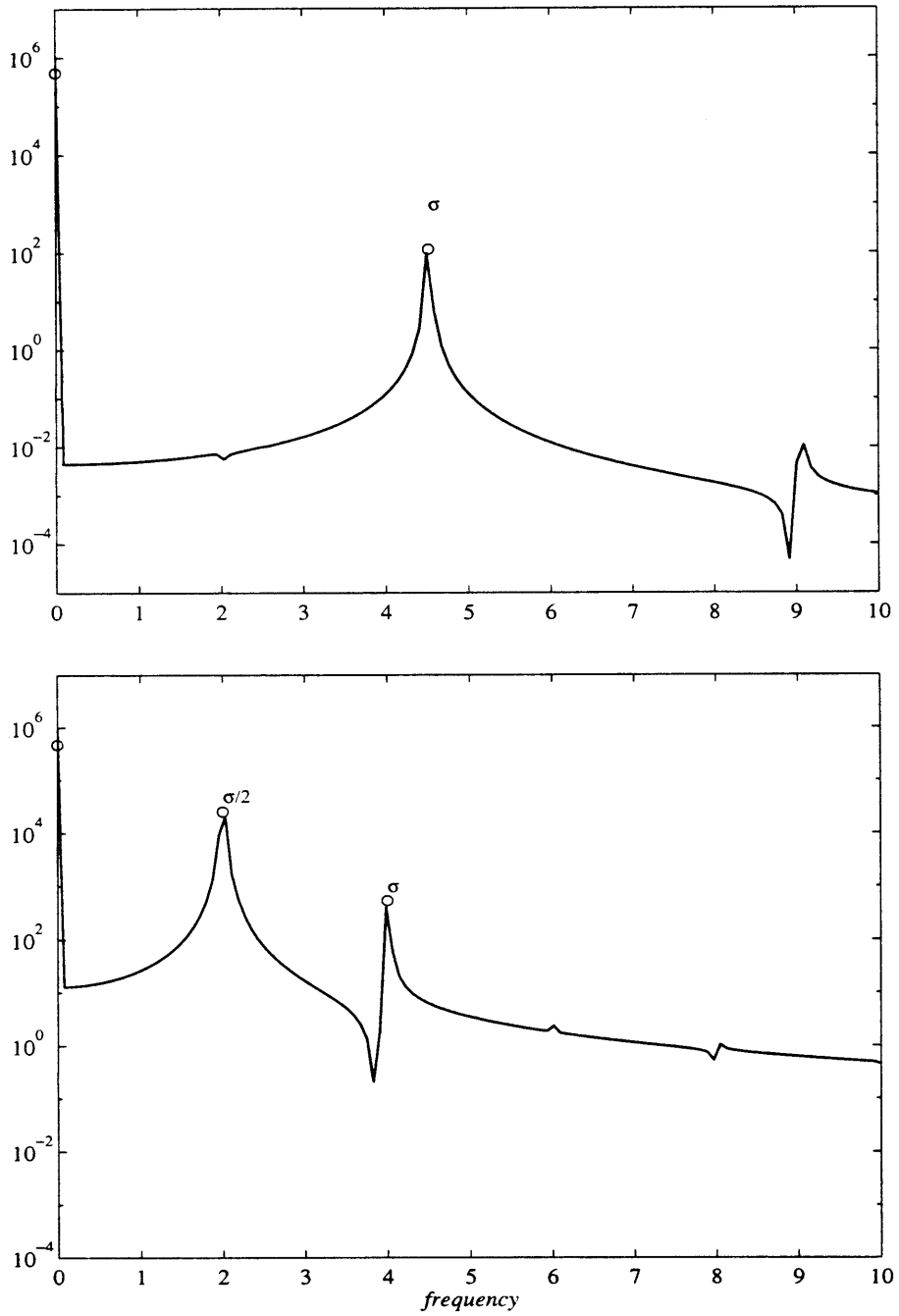

Figure 5-14: Spectra for $a = 0.05$ and respectively for $\sigma = 2.5\lambda$ showing no subharmonic resonance and for $\sigma = 2\lambda$ with pronounced subharmonic resonance. Axis are nondimensional.

The numerical simulation show also the real extension of the nontrivial stable branch in the negative detuning values. Indeed, from figures 5-15 and 5-16 it can be seen that as μ decreases the analytical solution is an increasingly better approximation. Because the stable nontrivial branch terminates for finite values of detuning, hysteretic cycles and jump phenomenon are possible also by modulational perturbation.

Finally a portrait of a limit cycle is shown in figure 5-17 for $\sigma = 2\lambda = 4$ (dotted line) and compared with the analytical solution approximate to $O(\mu^2)$ (solid line). The two asterisks in the Poincaré section (obtained by sampling the limit cycle every forcing cycle $2\pi/\sigma$) signify $4\pi/\sigma$ periodicity, i.e. a subharmonic component.

5.2.5 Superharmonic 2 resonance

For a modulational frequency $\sigma = (\lambda + \mu^2 d_2)/2$, we let the amplitude of the forcing be $O(\mu^{\frac{3}{2}})$

$$a = \mu^{\frac{3}{2}} a_{\frac{3}{2}}, \tag{5.2.74}$$

and the damping terms still $O(\mu^2)$

$$\alpha = \mu^2 \alpha_2, \quad \beta = \mu^2 \beta_2, \quad \gamma = \mu^2 \gamma_2. \tag{5.2.75}$$

The perturbation expansion is in powers of $\mu^{\frac{1}{2}}$

$$R = R_0 + \mu R_1 + \mu^{\frac{3}{2}} R_{\frac{3}{2}} + \mu^2 R_2 + \mu^{\frac{5}{2}} R_{\frac{5}{2}} + \ldots, \qquad \psi = 0 + \mu R_1 + \mu^{\frac{3}{2}} R_{\frac{3}{2}} + \mu^2 R_2 + \mu^{\frac{5}{2}} R_{\frac{5}{2}} \ldots \tag{5.2.76}$$

The $O(\mu)$ system is again the free oscillator of (5.2.10)

$$\begin{cases} R_{1_T} + \lambda^2 \psi_1 = 0, \\ \\ \psi_{1_T} - R_1 = 0. \end{cases} \tag{5.2.77}$$

At $O(\mu^{\frac{3}{2}})$, the harmonic $\lambda/2$ is forced

$$\begin{cases} R_{\frac{3}{2}_T} + \lambda^2 \psi_{\frac{3}{2}} = 0 \\ \\ \psi_{\frac{3}{2}_T} - R_{\frac{3}{2}} = -a_{\frac{3}{2}} \cos\left[(\lambda + \mu^2 d_2)\, T/2\right], \end{cases} \tag{5.2.78}$$

while at $O(\mu^2)$ the system is identical to (5.2.24)

$$\begin{cases} R_{2_T} + \lambda^2 \psi_2 = -4 R_1 \psi_1 - \lambda^2 \left(\lambda^2 \alpha_2 + 4\beta_2 + 2\lambda \gamma_2\right)/8 \\ \\ \psi_{2_T} - R_2 = 2\psi_1^2 + \beta_2. \end{cases} \tag{5.2.79}$$

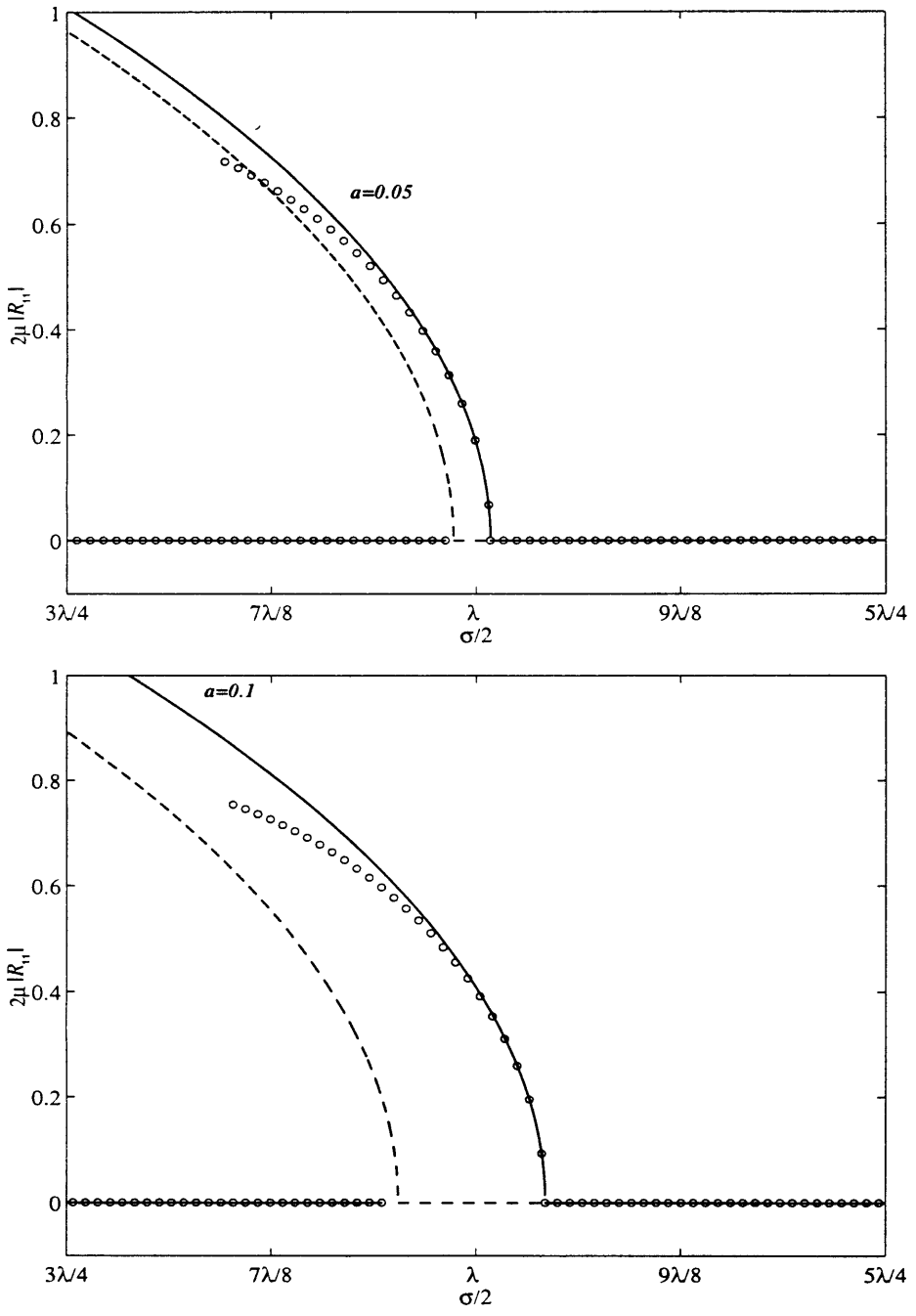

Figure 5-15: Bifurcation diagrams for $\alpha = \beta = \gamma = 0.01$ and $W = 0$. Solid and dashed lines denote the analytical solution (respectively stable and unstable); empty circles the numerical solution.

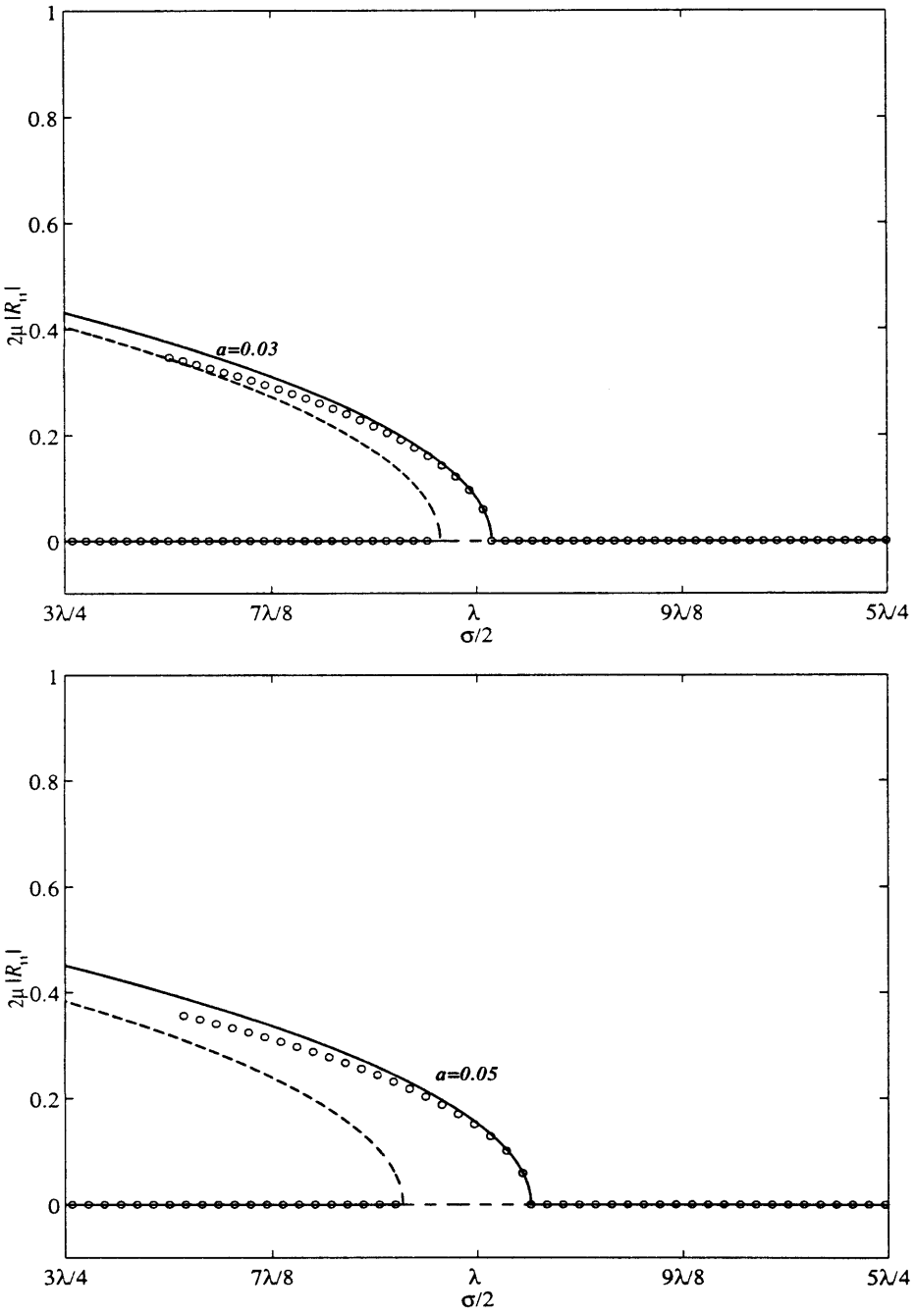

Figure 5-16: Bifurcation diagrams for $\alpha = \beta = \gamma = 0.01$ and $W = 0.6$. Solid and dashed lines denote the analytical solution (respectively stable and unstable); empty circles the numerical solution.

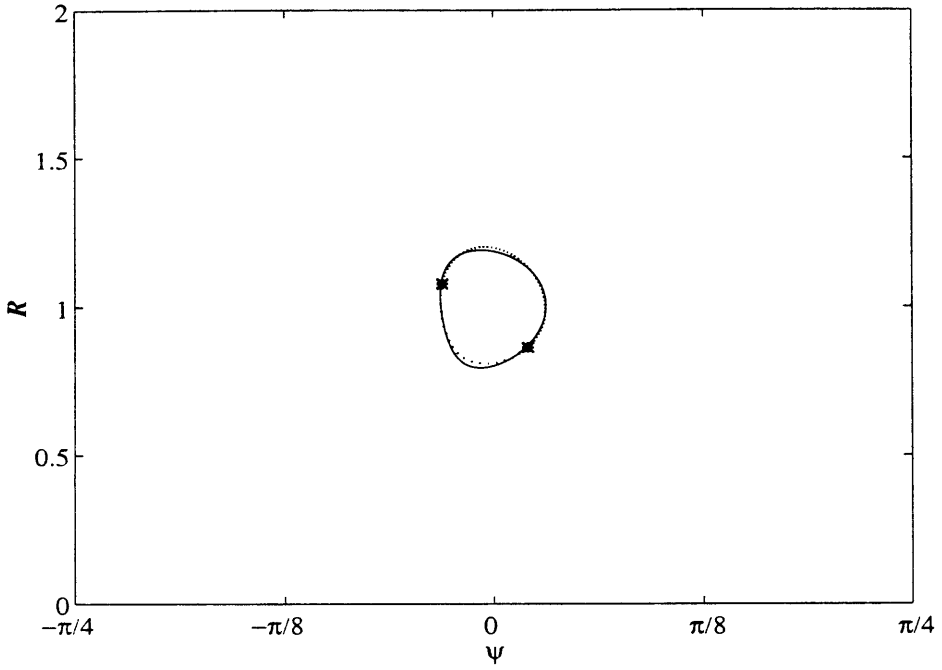

Figure 5-17: Limit cycle for $W = 0$, $a = 0.05$, $\alpha = \beta = \gamma = 0.01$ and $\sigma = 2\lambda = 4$

Through quadratic terms, $R_{\frac{3}{2}}$, $\psi_{\frac{3}{2}}$ force the natural frequency λ at $O(\mu^3)$:

$$\begin{cases} R_{3_T} + \lambda^2 \psi_3 = -R_{1_{T_2}} - 4R_2\psi_1 - 4R_1\psi_2 - R_1\left(\lambda^2\alpha_2 + 2\beta_2 + \frac{3}{2}\lambda\gamma_2\right) - \\ \qquad\qquad \lambda^2\psi_{\frac{3}{2}}\cos\left[(\lambda + \mu^2 d_2)\,T/2\right] - 4\psi_{\frac{3}{2}}\,R_{\frac{3}{2}} \\ \psi_{3_T} - R_3 = -\psi_{1_{T_2}} + 4\psi_1\psi_2 + 2{\psi_{\frac{3}{2}}}^2; \end{cases} \tag{5.2.80}$$

since (5.2.77) is homogeneous, removal of the secularity yields the desired evolution equation

$$-\mathrm{i}R_{11_{T_2}} = \left(\frac{1}{\lambda} + \frac{12}{\lambda^3}\right) R_{11}^2 R_{11}^* + \mathrm{i}\left(\frac{\lambda^2}{2}\alpha_2 + \beta_2 + \frac{3}{4}\lambda\gamma_2\right) R_{11} + \left(d_2 + \frac{2\beta_2}{\lambda}\right) R_{11} + \\ - \left(\frac{1}{3\lambda} + \frac{\lambda}{12}\right) {a_{\frac{3}{2}}}^2, \tag{5.2.81}$$

$$\psi_{11} = \frac{\mathrm{i}}{\lambda} R_{11}. \tag{5.2.82}$$

that describes how the natural frequency evolves under superharmonic forcing. The coefficient of the cubic, detuning and damping terms are the same as in the synchronous and subharmonic 1/2 forcing. The difference is the forcing term in $a_{\frac{3}{2}}$,

which has the same nature of the synchronus resonance case, i.e. appears alone. Let us introde the normalized damping coefficient

$$B = \left(\frac{\lambda^2}{2}\alpha_2 + \beta_2 + \frac{3}{4}\lambda\gamma_2\right)\left[\frac{4}{9}a_{\frac{3}{2}}^4\left(\lambda + \frac{12}{\lambda}\right)\left(1 + \frac{4}{\lambda^2}\right)^2\right]^{-\frac{1}{3}}, \tag{5.2.83}$$

the normalized detuning with shift due to damping

$$D = \left(d_2 + \frac{2\beta_2}{\lambda}\right)\left[\frac{a_{\frac{3}{2}}^4}{144}\left(\lambda + \frac{12}{\lambda}\right)\left(1 + \frac{4}{\lambda^2}\right)^2\right]^{-\frac{1}{3}}, \tag{5.2.84}$$

the normalized slow time

$$\tau = T_2\left[\frac{a_{\frac{3}{2}}^4}{144}\left(\lambda + \frac{12}{\lambda}\right)\left(1 + \frac{4}{\lambda^2}\right)^2\right]^{\frac{1}{3}}, \tag{5.2.85}$$

and the normalized first harmonic response

$$r_{11} = R_{11}\left[-\frac{12}{a_{\frac{3}{2}}^2}\frac{\lambda^2 + 12}{\lambda^2\left(\lambda^2 + 4\right)}\right]^{\frac{1}{3}}, \tag{5.2.86}$$

the evolution equation (5.2.81) assumes the simplified form

$$-\mathrm{i}r_{11_\tau} = r_{11}^2 r_{11}^* + \mathrm{i}Br_{11} + Dr_{11} + 1, \tag{5.2.87}$$

which is exactly the same as (5.2.33). Therefore, all the results found for the normalized forms of the synchronous resonance apply exactly for the present case, in particular for the fixed points and their stability and the bifurcation diagram.

5.3 Modulational resonance of the origin

For the hamiltonian system (5.2.3), the origin is a center for $|W| > 1$ and a saddle for $|W| < 1$ (see figure 5-2a, c). In the first case the frequency of oscillation around the center is $\lambda = \sqrt{W^2 - 1}$. If the linear viscous terms are small, say $\beta < O(\mu)$, at the leading order the origin remains an harmonic oscillator of natural frequency $\lambda = \sqrt{W^2 - 1}$, damped at higher order by α, β and γ. As seen in the previuos section 5.2, the modulational forcing $a\cos\sigma T$ can resonate such natural frequency λ synchronously, subharmonically or superharmonically whenever $\sigma = \lambda$, 2λ or $\lambda/2$. Because these further resonances add to a null state, they are less important compared to the previous case in which they add to an already developed nontrivial steady state. For completeness we nevertheless present the case of subharmonic resonance.

Let

$$\beta = \mu^2 \beta_2, \quad a = \mu^2 a_2. \tag{5.3.1}$$

We make no order of magnitude assumption for α and γ and consider a modulational frequency slightly detuned from twice the natural frequency, $\sigma = 2(\lambda + \mu^2 d_2)$. To study this resonance is mathematically more convenient to employ the representation in cartesian coordinates, $\theta = X = \mathrm{i}Y$. We Taylor-expand system (5.1.4) about the origin and use a perturbation expansion

$$X = \mu X_1 + \mu^2 X_2 + \mu^3 X_3 + \ldots, \qquad Y = \mu Y_1 + \mu^2 Y_2 + \mu^3 Y_3 + \ldots, \tag{5.3.2}$$

where $\mu \ll 1$ is an ordering parameter. Introducing the slow time variable $T_2 = \mu^2 T$, the time derivative becomes $\partial_T = \partial_T + \mu^2 \partial_{T_2}$.

The first order $O(\mu)$ describes a linear oscillator of natural frequency $\lambda = \sqrt{W^2 - 1}$

$$\begin{cases} X_{1_T} + (W-1) Y_1 = 0 \\ \\ Y_{1_T} - (W+1) X_1 = 0, \end{cases} \tag{5.3.3}$$

whose solution can be written as

$$X_1 = X_{11} \mathrm{e}^{-\mathrm{i}\lambda T} + *, \qquad Y_1 = Y_{11} \mathrm{e}^{-\mathrm{i}\lambda T} + *. \tag{5.3.4}$$

At $O(\mu^2)$ the zeroth and second harmonics are forced through quadratic terms

$$\begin{cases} X_{2_T} + (W-1) Y_2 = -\gamma \left(X_1^2 + Y_1^2/2 \right) \\ \\ Y_{2_T} - (W+1) X_2 = -\gamma \left(X_1^2/2 + Y_1^2 \right). \end{cases} \tag{5.3.5}$$

The solution can be written as

$$X_2 = X_{20} + X_{22} \, \mathrm{e}^{-\mathrm{i}2\left(\lambda + \mu^2 d_2\right) T} + *, \quad Y_2 = Y_{20} + Y_{22} \, \mathrm{e}^{-\mathrm{i}2\left(\lambda + \mu^2 d_2\right) T} + *. \tag{5.3.6}$$

At $O(\mu^3)$, the system governing the first harmonic λ is inhomogenoeous

$$\begin{cases} X_{3_T} + (W-1) Y_3 = -X_1^2 Y_1 - Y_1^3 + a_2 Y_1 \cos\left[2\left(\lambda + \mu^2 d_2\right) T\right] - \\ \\ \qquad\qquad \alpha \left(X_1 Y_1^2 + X_1^3 \right) - \beta_2 \left(X_1 + Y_1 \right) - \gamma \left(2 X_1 X_2 + Y_1 Y_2 \right) \\ \\ Y_{3_T} - (W+1) X_3 = X_1 Y_1^2 + X_1^3 + a_2 X_1 \cos\left[2\left(\lambda + \mu^2 d_2\right) T\right] - \\ \\ \qquad\qquad \alpha \left(X_1 Y_1^2 + X_1^3 \right) + \beta_2 \left(X_1 - Y_1 \right) - \gamma \left(X_1 X_2 + 2 Y_1 Y_2 \right). \end{cases} \tag{5.3.7}$$

Removal of the secularity yields an evolution equation of the form

$$-\mathrm{i}\,X_{11_{T_2}} = (b+\mathrm{i}c)\,|X_{11}|^2 X_{11} + \mathrm{i}\beta_2 X_{11} - \frac{W}{2\sqrt{W^2-1}}\,a_2 X_{11}^* + d_2 X_{11}. \tag{5.3.8}$$

where

$$b = \frac{12\left[W^2(1-2W^2)-1\right] + W(23W^2-3)\gamma^2}{6(W-1)(W^2-1)^{\frac{3}{2}}}, \quad c = \frac{2W\alpha}{W-1}\left[2\alpha + \frac{\gamma^2}{(W^2-1)}\right]. \tag{5.3.9}$$

Note that equation (5.3.8) was obtained without any restriction on the order of magnitude of α and γ.

The discussion of the fixed points of (5.3.8) is simplified by introducing the normalized cubic damping coefficient

$$B_c = \frac{c}{b} \equiv \frac{W\left[2\alpha + \gamma^2/(W^2-1)\right](W^2-1)^{\frac{3}{2}}}{\left[W^2(1-2W^2)-1\right] + W(23W^2-3)\gamma^2/12}, \tag{5.3.10}$$

the normalized linear damping coefficient

$$B_l = -\frac{\beta_2}{a_2}\,\frac{2\sqrt{W^2-1}}{W}, \tag{5.3.11}$$

the normalized detuning

$$D = -\frac{d_2}{a_2}\,\frac{2\sqrt{1-W^2}}{W}, \tag{5.3.12}$$

the normalized slow time

$$\tau = -a_2 T_2\,\frac{W}{2\sqrt{W^2-1}} \tag{5.3.13}$$

and the normalized first harmonic response

$$x_{11} = \frac{X_{11}}{\sqrt{a_2}}\left(\frac{2b\sqrt{W^2-1}}{|W|}\right)^{1/2} \tag{5.3.14}$$

In terms of these variables, evolution equation (5.3.8) becomes

$$-\mathrm{i}x_{11_\tau} = (1+\mathrm{i}B_c)x_{11}^2 x_{11}^* + \mathrm{i}B_l x_{11} + Dx_{11} + 1. \tag{5.3.15}$$

Equation (5.3.15) is formally identical to (4.1.8) of section 4.1 taken with $\gamma = 0$. Therefore all the discussion of the fixed points of that section applies here, when the coefficients α, β and W are substituted respectively by B_c, B_l and D.

In particular, there is a region of instability $|D| < \sqrt{1-B_l^2}$ in which subharmonic motion takes place, i.e. there is $O(\mu)$ oscillation of frequency $\sigma/2$. This is a long period oscillation of the trapped wave envelope, which take place only if $B_l > 1$, i.e.

if

$$a_2 > \beta_2 \frac{2\sqrt{W^2-1}}{W}. \tag{5.3.16}$$

As $|W| \to 1$ the right hand side of (5.3.16) tends to zero, rendering the resonance possible for any nonzero modulational amplitude.

5.4 Homoclinc tangle

In the previous section we have used local and weakly nonlinear analysis to determine the condition for subharmonic resonance around centers. For a modulational frequency σ nearly twice the natural frequency of the center, the envelope has been found to oscillate with frequency $\sigma/2$. This period-doubling phenomenon is the prerequisite of a period doubling cascade yielding chaotic solutions, and belongs to the category of local bifurcations.

For global bifurcations an analytical tool exists for predicting the onset of horseshoe tangle of a homoclinic orbit. This is the so called Melnikov method. The essence of the method is as follows.

Consider a nearly Hamiltonian system of the form

$$\begin{cases} R_T = f_1(R,\psi) + \mu\, g_1(R,\psi,T), \\ \\ \psi_T = f_2(R,\psi) + \mu\, g_2(R,\psi,T), \end{cases} \tag{5.4.1}$$

with $\mu \ll 1$ and g_1, g_2 periodic in T with period $2\pi/\sigma$, and whose unperturbed limit $\mu = 0$ is hamiltonian. Let the homoclinic orbit of the associated Poincaré map be denoted by $\left\{R^h(T),\, \psi^h(T)\right\}$. Then the zero of the Melnikov function

$$M = \int_{-\infty}^{\infty} \mathrm{d}T \;\left[f_1(R^h,\psi^h)g_2(R^h,\psi^h,T) - f_2(R^h,\psi^h)g_1(R^h,\psi^h,T)\right] \tag{5.4.2}$$

approximates the condition at which the stable and unstable manifolds of the perturbed Poincare' map intersect. Indeed, under the $O(\mu)$ perturbation, the degenerate structure of the homoclinic connection breaks and gives rise to two manifolds, one stable and one unstable, whose distance is proportional to M. The zero of M implies therefore a transverse intersection, which in turn implies horseshoe type of motion and is a prelude to global chaos. The Melnikov function, being calculated on the homoclinic orbit of the unperturbed system, is a function of the position in time $T_0 \in [0, 2\pi/\sigma]$ on which the first section is taken. For a thorough description of the method see Guckenheimer & Holmes(1984). In the context of the edge-wave Gottlieb & Mei(1995) have made extensive use of this method without and with linear damping. Here we extend their work to include both linear and quadratic damping.

For system (5.1.2) in the previous section we have analyzed the temporal resonances for damping α, β, γ and forcing a equal or smaller than $O(\mu)$. In the same spirit, let the damping coefficients and forcing be $O(\mu)$

$$\alpha = \mu\alpha_1, \quad \beta = \mu\beta_1, \quad \gamma = \mu\gamma_1, \qquad a = \mu a_1. \tag{5.4.3}$$

Then system (5.1.2) can be recast in the form

$$\begin{cases} R_T = -2R\sin 2\psi - \mu\, 2R\left(\alpha_1 R + \beta_1 + \gamma_1\sqrt{R} + a_1\cos\sigma T\sin 2\psi\right) = f_1 + \mu\, g_1, \\ \\ \psi_T = W + R - \cos 2\psi - \mu\left(\beta_1 + a_1\cos\sigma T\cos 2\psi\right) = f_2 + \mu\, g_2, \end{cases} \tag{5.4.4}$$

where the hamiltonian part f_1, f_2 has been described in figure 5-1. Note that orbits in the phase planes and in the Poincaré sections coincide when the orbits periods ratio to the the forcing period $2\pi/\sigma$ is an irrational number. If the ratio is a rational number m/n, then the Poincaré section is composed of m points visited n times every cycle.

First we analyze the homoclinic connection for $|W| < 1$, then the heteroclinic connections for $W < -1$.

5.4.1 Homoclinic orbit, $-1 < W < 1$

In figure 5-1b the orbits are plotted for $W = 0$. The homoclinic orbit is the hump that goes from $R = 0, \psi = -\pi/4$ to $R = 0, \psi = \pi/4$. Its expression R^h, ψ^h has been found by Gottlieb& Mei(1995); in terms of the present variables is

$$R^h(T - T_0;\, W) = \frac{2\left(1 - W^2\right)}{W + \cosh\left[2\sqrt{1 - W^2}\,(T - T_0)\right]}, \tag{5.4.5}$$

$$\psi^h(T - T_0;\, W) = \arctan\left\{\sqrt{\frac{1 - W}{1 + W}}\tanh\left[\sqrt{1 - W^2}\,(T - T_0)\right]\right\} \tag{5.4.6}$$

where $\left\{R^h(0;W), \psi^h(0;W)\right\} = \{2\,(1 - W)\,,\, 0\}$. Details of the derivation of these orbits and of the Melnikov function integrals are given in Appendix E; here we summarize the results.

The Melnikov function is given by

$$\begin{aligned} M(\sigma, T_0\,;\, W, \alpha_1, \beta_1, \gamma_1, a_1) = \int_{-\infty}^{\infty} \mathrm{d}T\ \left[f_1 g_2 - f_2 g_1\right]_{R=R^h,\,\psi=\psi^h} = \int_{-\infty}^{\infty} \mathrm{d}T\ 2R^h\ \times \\ \left[a_1\left(W + R^h\right)\sin 2\psi^h\cos\sigma T - \beta_1\sin 2\psi^h + \right. \\ \left.\left(W + R^h - \cos 2\psi^h\right)\left(\alpha_1 R^h + \beta_1 + \gamma_1\sqrt{R^h}\right)\right] \end{aligned} \tag{5.4.7}$$

Substituting expressions (5.4.5) and (5.4.6) into the integrands of (5.4.7), the Melnikov function (5.4.7) becomes

$$M(\sigma, T_0\,;\, W, \alpha_1, \beta_1, \gamma_1, a_1) = \Pi^{\alpha}(W)\alpha_1 + \Pi^{\beta}(W)\beta_1 + \Pi^{\gamma}(W)\gamma_1 - \Pi^{a}(\sigma, W)\, a_1\sin\sigma T_0 \tag{5.4.8}$$

where the functions Π have the expressions

$$\Pi^{\alpha}(W) = \int_{-\infty}^{\infty} \mathrm{d}T \; 2{R^h}^2 \left(W + R^h - \cos 2\psi^h\right) =$$
$$4\left[\left(1+2W^2\right)\left(\frac{\pi}{2} - \arctan\frac{W}{\sqrt{1-W^2}}\right) - 3W\sqrt{1-W^2}\right] \tag{5.4.9}$$

$$\Pi^{\beta}(W) = \int_{-\infty}^{\infty} \mathrm{d}T \; 2R^h \left(W + R^h - \cos 2\psi^h - \sin 2\psi^h\right) =$$
$$4\left[W\left(-\frac{\pi}{2} + \arctan\frac{W}{\sqrt{1-W^2}}\right) + \sqrt{1-W^2}\right] \tag{5.4.10}$$

$$\Pi^{\gamma}(W) = \int_{-\infty}^{\infty} \mathrm{d}T \; 2{R^h}^{3/2} \left(W + R^h - \cos 2\psi^h\right) =$$
$$4\sqrt{2}\left(1-W^2\right)^{5/2} \int_{-\infty}^{\infty} \mathrm{d}T \left\{W + \cosh\left[2\sqrt{1-W^2}\,(T-T_0)\right]\right\}^{-5/2} \tag{5.4.11}$$

$$-\Pi^{a}(\sigma, W) \sin\sigma T_0 = \int_{-\infty}^{\infty} \mathrm{d}T \; 2R^h \left(W + R^h\right) \sin 2\psi^h \cos\sigma T =$$
$$-\pi\sigma^2 \sin\sigma T_0 \cosh\left(\frac{\sigma \arccos W}{2\sqrt{1-W^2}}\right) \Big/ \sinh\left(\frac{\pi\sigma}{2\sqrt{1-W^2}}\right). \tag{5.4.12}$$

All but the third expression have been found by Gottlieb & Mei in Gottlieb & Mei(1995) an in an unpublished manuscript. The third integral Π^{γ}, can only be evaluated numerically due to its 5/2 power. Finally, the forcing term integral Π^{a} can be evaluated with the residue method. Details are given in Appendix E.

For fixed $\alpha_1, \beta_1, \gamma_1, W, \sigma$, equation (5.4.7), oscillates sinusoidally with T_0. Therefore the condition $M = 0$ is first met when

$$a_1 = \frac{\Pi^{\alpha}(W)\,\alpha_1 + \Pi^{\beta}(W)\,\beta_1 + \Pi^{\gamma}(W)\,\gamma_1,}{\Pi^{a}(\sigma, W)} \tag{5.4.13}$$

For fixed damping constants, homoclinic tangle occurs when the forcing amplitude a_1 is large enough. Compared with the edge-wave of Gottlieb & Mei(1995) for radiation damping only, the right hand side of (5.4.13) has two extra terms in β_1 and γ_1 which represent the contribution of respectively linear and quadratic viscous damping. Equation (5.4.13) is linear in $\alpha_1, \beta_1, \gamma_1$. Therefore, for fixed σ, W, the lower the values of the dissipation coefficients, the smaller the threshold.

On the other hand, for given values of the dissipation coefficients, expression (5.4.13) has a nonlinear dependence on both the detuning of the carrier wave W and on the frequency of modulation σ. To see this dependence we first vary the detuning W for constant σ and then vary σ for fixed W.

Figure 5-18a,b,c,d shows the dependence on W for $\sigma = 0.5, 2.0, 4.0$. First, in 5-18a,b,c, we show the coefficients of respectively α_1, β_1 and γ_1, that is the three

ratios

$$\frac{\Pi^{\alpha}(W)}{\Pi^{a}(\sigma,W)}, \qquad \frac{\Pi^{\beta}(W)}{\Pi^{a}(\sigma,W)}, \qquad \frac{\Pi^{\gamma}(W)}{\Pi^{a}(\sigma,W)}, \tag{5.4.14}$$

the first one being the ratio discussed by Gottlieb & Mei(1995). Then in 5-18d we plot the sum, equation (5.4.13), for $\alpha_1 = \beta_1 = \gamma_1 = 0.1$. For any given σ, the threshold goes to infinity as $W \to \pm 1$ and has a minimum which decreases in value and moves towards positive W as σ decreases. The latter is a common feature of all the three coefficients, which are shown to give similar contributions to the sum (5.4.13) for all the W away from $|W| = 1$.

Next, in figure 5-19a,b,c,d the dependence on σ for $W = -0.7, 0.0, 0.9$ is shown. Also in this case, W fixed and varying σ, the three ratios in (5.4.14) behave similarly. They all present a minimum that shift towards low frequency and decreases for increasing W. Hence positively detuned carrier waves with low frequency of modulation are more likely to yield homoclinic tangles.

The present findings are similar to the ones for the period doubling phenomenon. Also there, the threshold for the occurrence of resonance was lower as $W \to 1$, and of course lower for lower values of dissipation.

5.4.2 Heteroclinic orbits, $W < -1$

Heteroclinic orbits are curves that connect two saddles. For $W < -1$ there are two orbits that connect $\{R, \psi\} = \{-1 - W, -\pi/2\}$ to $\{-1 - W, \pi/2\}$ crossing the $\psi = 0$ axis above and below the center s. They are shown in figure 5-1c for $W = -2$ connecting the two saddles at $R = -(1 + W) = 1$, $\psi = \mp\pi/2$.

The parametric expressions of the orbits $R^{h\pm}$, $\psi^{h\pm}$ are

$$R^{h\pm}(T - T_0; W) = -(1 + W)\frac{\sqrt{-W}\cosh\left[2\sqrt{-1 - W}\,(T - T_0)\right] \pm 1}{\sqrt{-W}\cosh\left[2\sqrt{-1 - W}\,(T - T_0)\right] \mp 1}, \tag{5.4.15}$$

$$\psi^{h\pm}(T - T_0; W) = \arctan\left\{\sqrt{\frac{W}{1 + W}}\sinh\left[2\sqrt{-1 - W}\,(T - T_0)\right]\right\} \tag{5.4.16}$$

where the $\pm$ superscript refers respectively to the upper and lower orbits and for $T = T_0$, $\left\{R^{h\pm}(0; W), \psi^{h\pm}(0; W)\right\} = \left\{\left(\sqrt{-W} \pm 1\right)^2, 0\right\}$. For details see Appendix E.

Upon substitution of expressions (5.4.15) (5.4.16) into expression (5.4.7) obtain for each of the two orbits an expression which has the same form as (5.4.8) but with different values of the Π's

$$\Pi^{\alpha\pm}(W) = \mp 4W\left[(W - 2)\left(\arctan\sqrt{-1 - W} - \left\{\begin{array}{c}\pi\\0\end{array}\right\}\right) + 3\sqrt{-1 - W}\right], \tag{5.4.17}$$

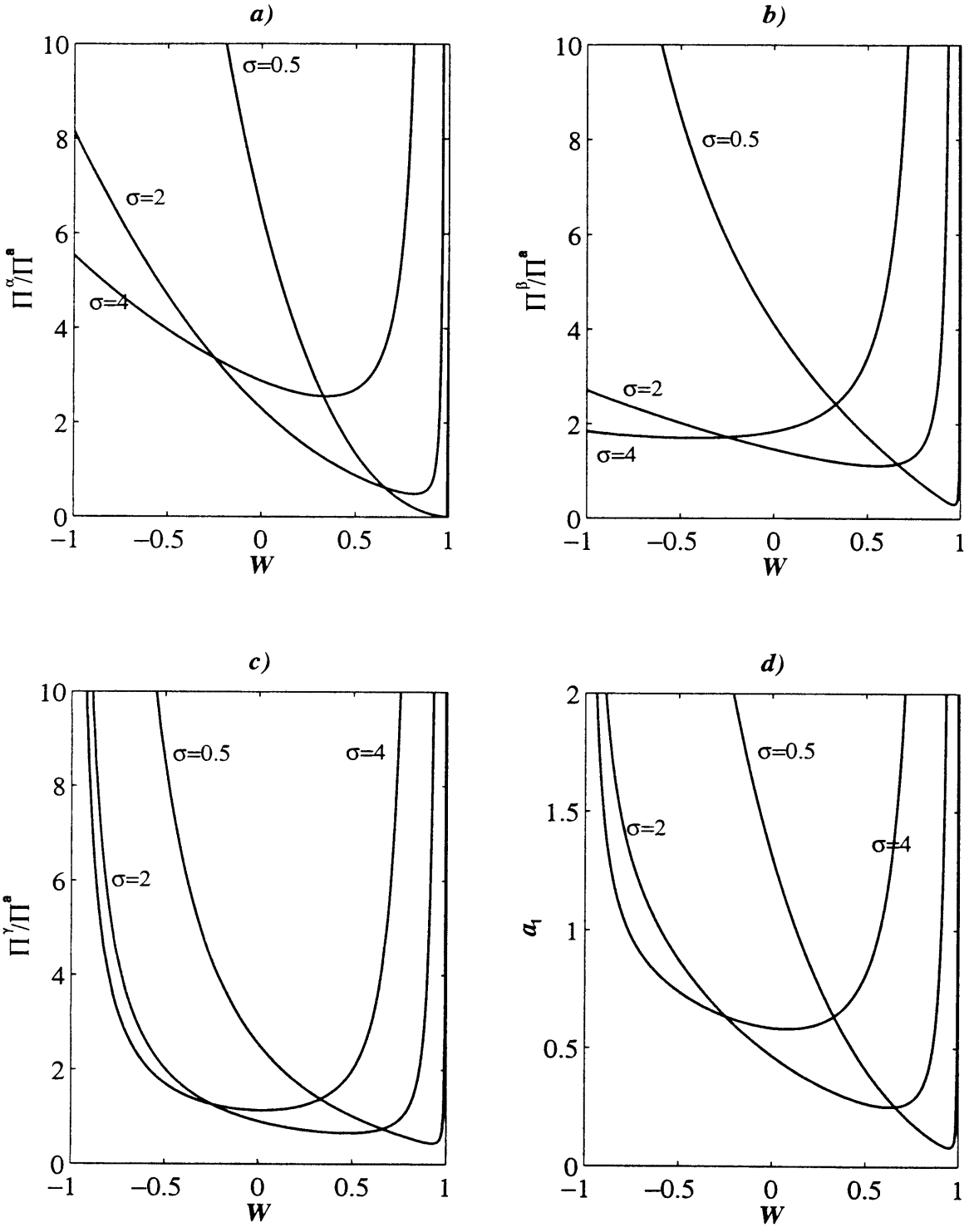

Figure 5-18: Melnikov's method for homoclinic tangle. a) factor for radiation damping α_1; b) factor for linear viscous damping β_1; c) factor for quadratic viscous damping γ_1; d) Thresholds for homoclinic tangle as a function of W for $\alpha_1 = \beta_1 = \gamma_1 = 0.1$

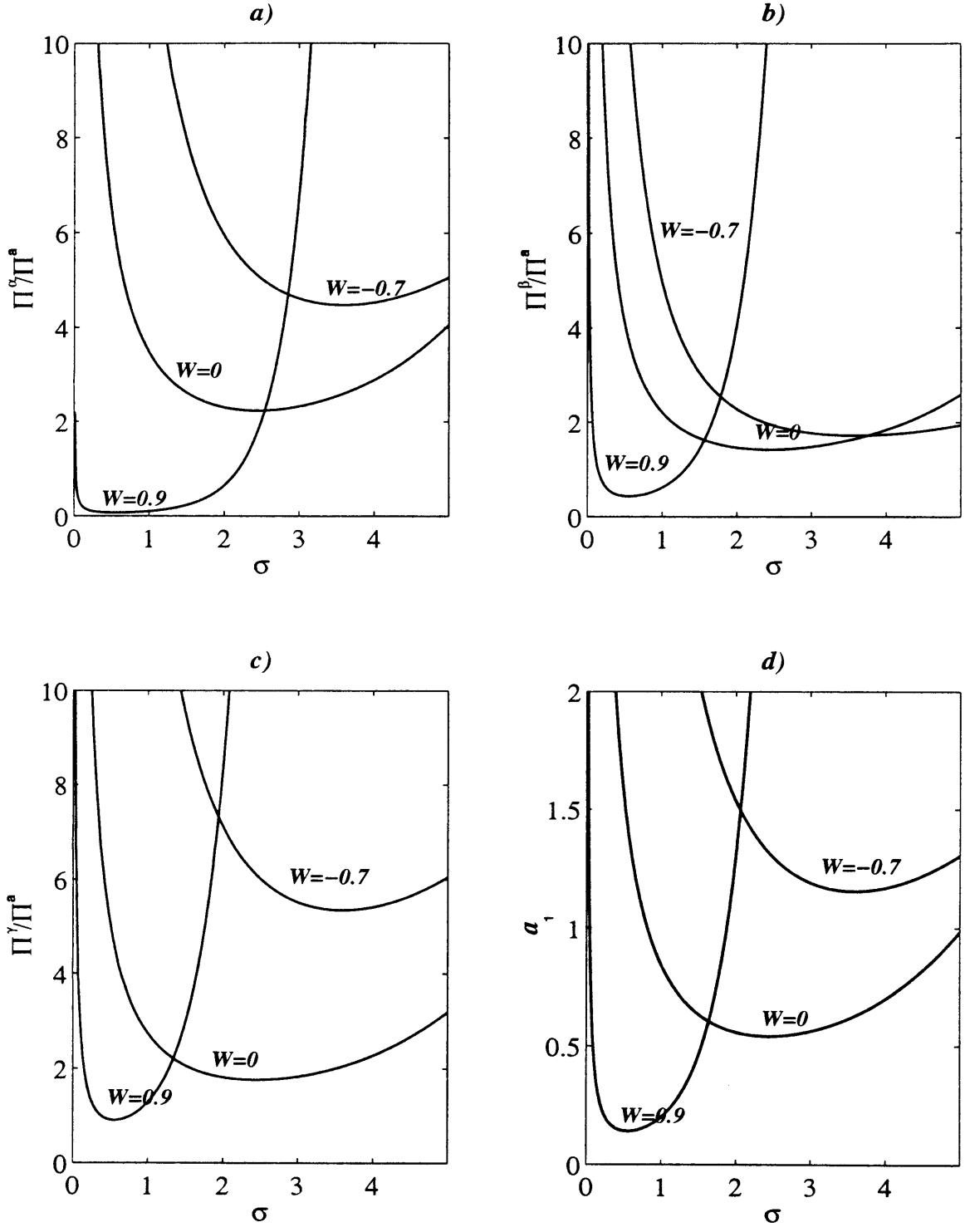

Figure 5-19: Melnikov's method for homoclinic tangle. a) factor for radiation damping α_1; b) factor for linear viscous damping β_1; c) factor for quadratic viscous damping γ_1; d) Thresholds for homoclinic tangle as a function of σ for $\alpha_1 = \beta_1 = \gamma_1 = 0.1$

$$\Pi^{\beta\pm}(W) = \pm 4\left[W\left(\arctan\sqrt{-1-W} - \left\{\begin{array}{c}\pi\\0\end{array}\right\}\right) + \sqrt{-1-W}\right], \tag{5.4.18}$$

$$\Pi^{\gamma\pm}(W) = \pm 4\,(1+W)^2\sqrt{W\,(1+W)}\int_{-\infty}^{\infty} dT \;\times$$
$$\cosh\left[2\sqrt{-1-W}\,(T-T_0)\right]\left\{\sqrt{-W}\cosh\left[2\sqrt{-1-W}\,(T-T_0)\right]\pm 1\right\}^{1/2}$$
$$\left\{\sqrt{-W}\cosh\left[2\sqrt{-1-W}\,(T-T_0)\right]\mp 1\right\}^{-5/2}, \tag{5.4.19}$$

$$\Pi^{a\pm}(\sigma, W) = \pi\sigma^2\frac{\cosh\left\{\sigma\left[\arccos\left(1/\sqrt{-W}\right) - \left\{\begin{array}{c}\pi\\0\end{array}\right\}\right]\Big/ 2\sqrt{-1-W}\right\}}{\sinh\left(\pi\sigma\,/2\sqrt{-1-W}\right)}. \tag{5.4.20}$$

The ratio $\Pi^{\alpha\pm}/\Pi^{a\pm}$ has been found in the case of edge waves by Gottlieb& Mei(1995).

Also in this case, $\Pi^{\alpha\pm}$ and $\Pi^{\beta\pm}$ can be evaluated directly, while $\Pi^{\gamma\pm}$ only numerically; the method of residues is used again to evaluate $\Pi^{a\pm}$. Details are given in Appendix E.

In figure 5-20a,b,c the three ratio of (5.4.14) are plotted for the lower and upper orbits respectively with solid and dashed lines. With the same linestyles, figure 5-20d shows the thresholds for $\alpha_1 = \beta_1 = \gamma_1$ of the two orbits.

For each orbit the contributions from the three dissipation sources (radiation, linear and quadratic viscous) behave similarly. For the lower orbit, increasing the value of σ decreases the contribution (see 5-20a,b,c) and their sum (see 5-20d). On the other hand, dashed lines show that for the upper orbit the effect of an increase in σ is to decrease the threshold.

The same conclusion can be drawn if we fix W and vary σ, as can be seen in figure 5-21a,b,c,d, where linestyles have the same meanings of figure 5-20. As the modulational frequency σ increases, for the upper orbits (dashed lines), the thresholds decrease, the opposite for the lower orbit (solid line).

Note that for detuning increasingly closer to -1, homoclinic tangle of the lower orbit occurs practically at $a_1 = 0$. On the other hand the threshold for the upper orbit is very high (> 1), so that large values of modulational amplitude a_1 are necessary for homoclinic tangle to occur.

It is of interest to compare the period-doubling threshold with the threshold for the homoclinic tangle, i.e. to compare expression (5.2.70) with (5.4.13).

Multiplication of expression (5.2.70) by μ^2 enables us to write the threshold condition for period doubling in terms of $\sigma = 2\,(\lambda + \mu^2 d_2)$ and a

$$\sigma = 2\left[\lambda \pm \sqrt{a^2\left(\frac{\lambda}{4}+\frac{1}{\lambda}\right)^2 - \left(\frac{\lambda^2}{2}\alpha + \beta + \frac{3}{4}\lambda\gamma\right)^2} - \frac{2\beta}{\lambda}\right], \tag{5.4.21}$$

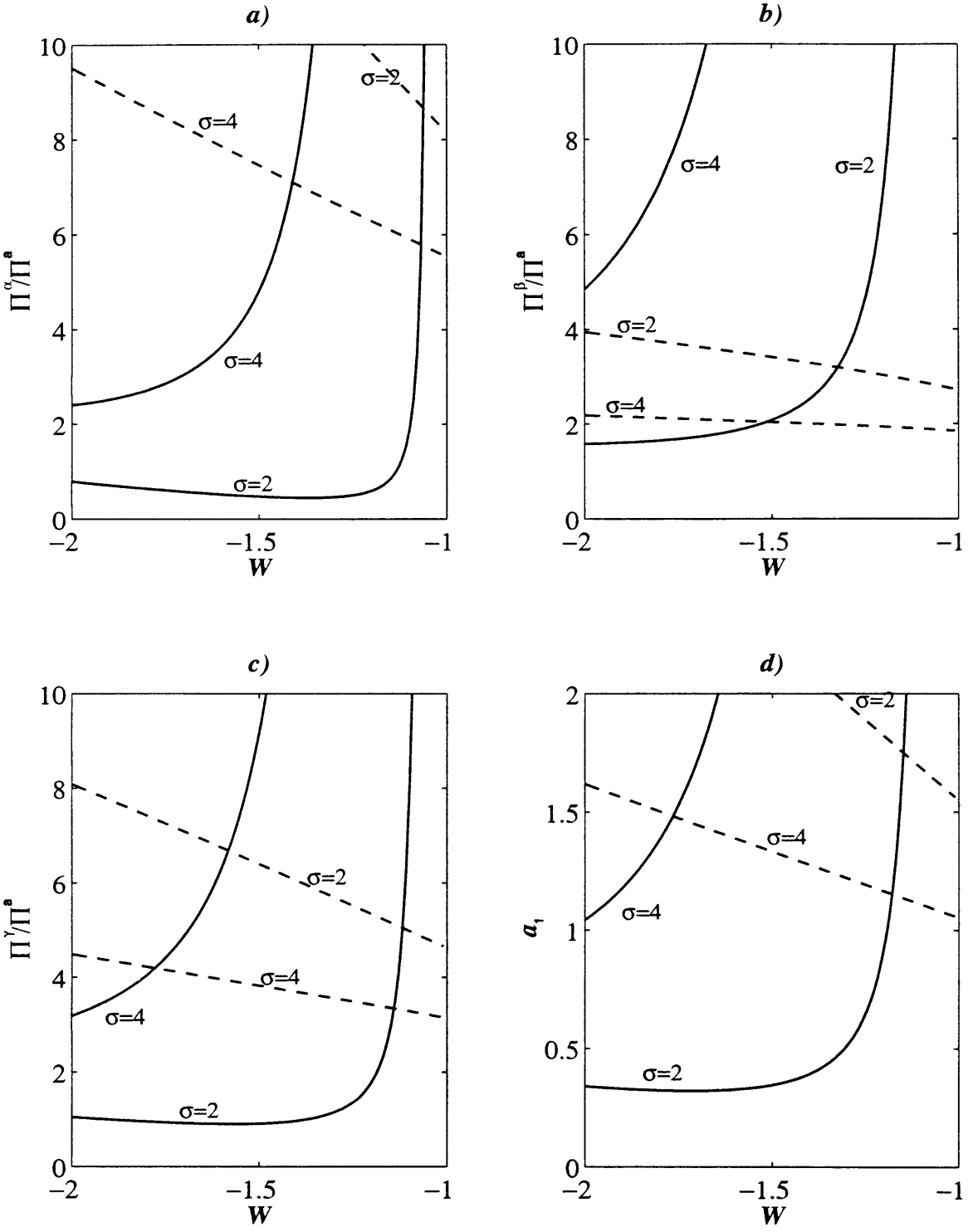

Figure 5-20: Melnikov's method for heteroclinic tangle; solid lines are for the lower connection, dashed lines are upper connection. a) factor for radiation damping α_1; b) factor for linear viscous damping β_1; c) factor for quadratic viscous damping γ_1; d) Thresholds for homoclinic tangle as a function of W for $\alpha_1 = \beta_1 = \gamma_1 = 0.1$

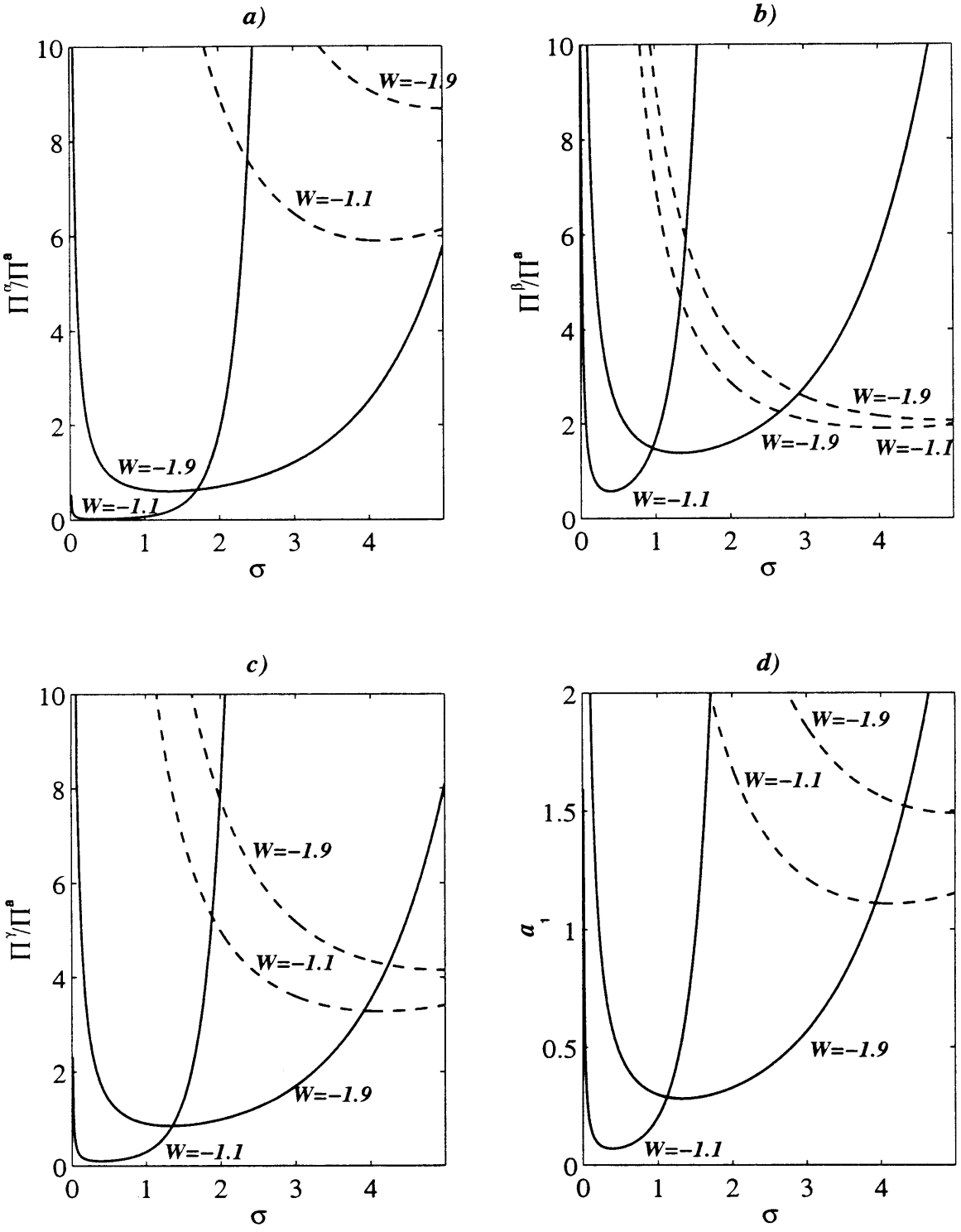

Figure 5-21: Melnikov's method for heteroclinic tangle; solid lines are for the lower connection, dashed lines are upper connection. a) factor for radiation damping α_1; b) factor for linear viscous damping β_1; c) factor for quadratic viscous damping γ_1; d) Thresholds for homoclinic tangle as a function of σ for $\alpha_1 = \beta_1 = \gamma_1 = 0.1$

where $\lambda = 2\sqrt{1-W}$. Similarly multiplication of (5.4.13) by μ yields

$$a = \frac{\Pi^{\alpha}(W)\,\alpha + \Pi^{\beta}(W)\,\beta + \Pi^{\gamma}(W)\,\gamma}{\Pi^{a}(\sigma, W)}. \tag{5.4.22}$$

The two thresholds (5.4.21) and (5.4.22) can now be plotted together in the $\sigma \sim a$ plane of figure 5-22, which is essentially a superposition of figure 5-12 and figure 5-18d for $\alpha = \beta = \gamma = 0.1$ and carrierrier wave detuning $W = 0$. The abscissa is labeled using the value of the natural frequency of the center, which in the present case is $\lambda = 2\sqrt{1-W} = 2$. Threshold (5.4.21) is plotted with a dashed line, together with the horizontal line that delimits region III (c.f. figures 5-12).

Above the threshold of Melnikov, homoclinic tangle is possible. In region II period doubling occurs, in region III synchronous and period doubled responses are both possible. Figure 5-22 shows that for a given modulational frequency σ, as the amplitude of the modulation a increases, period-doubling precedes homoclinic tangle. It can also be seen that natural frequency of the center λ and critical frequency for homoclinic tangle are of comparable magnitude.

Overall figure 5-22 shows the variety of dynamical response that can occur in the modulational parameter plane, ranging from horse-shoe motion above the Melnikov threshold to jump phenomenon with subharmonic motion when crossing the - branch SP from its left.

In the next section the response will be found numerically from the original Stuart-Landau equation and compared with the approximate results presented here.

5.5 Numerical experiments and chaotic oscillation

After having established bifurcation conditions respectively for period doubling, homoclinic and heteroclinic tangle, we turn to numerical experiments in order to find where synchronous, period doubled and chaotic motion actually occur. As $W \to 1$, the analysis of section 5.2.4 has shown that period doubled response is more likely to occur and the analysis of section 5.4 has shown that the threshold for homoclinc tangle tends to zero. Besides, our ultimate goal is to compare the theoretical results with the experiments in the wave basin, where for the carrier wave detuning W has been kept positive, $W \geq 0$. Therefore, we now focus on the interval of the carrier wave detuning $|W| \leq 1$, where only homoclinic tangle is possible.

We present numerical experiments, in which both the modulational frequency σ and the modulational amplitude a are varied over a fine grid in the $\sigma - a$ plane. In order to let the transients fade, for each value of σ and a the equations are integrated for two hundred cycles before being analyzed.

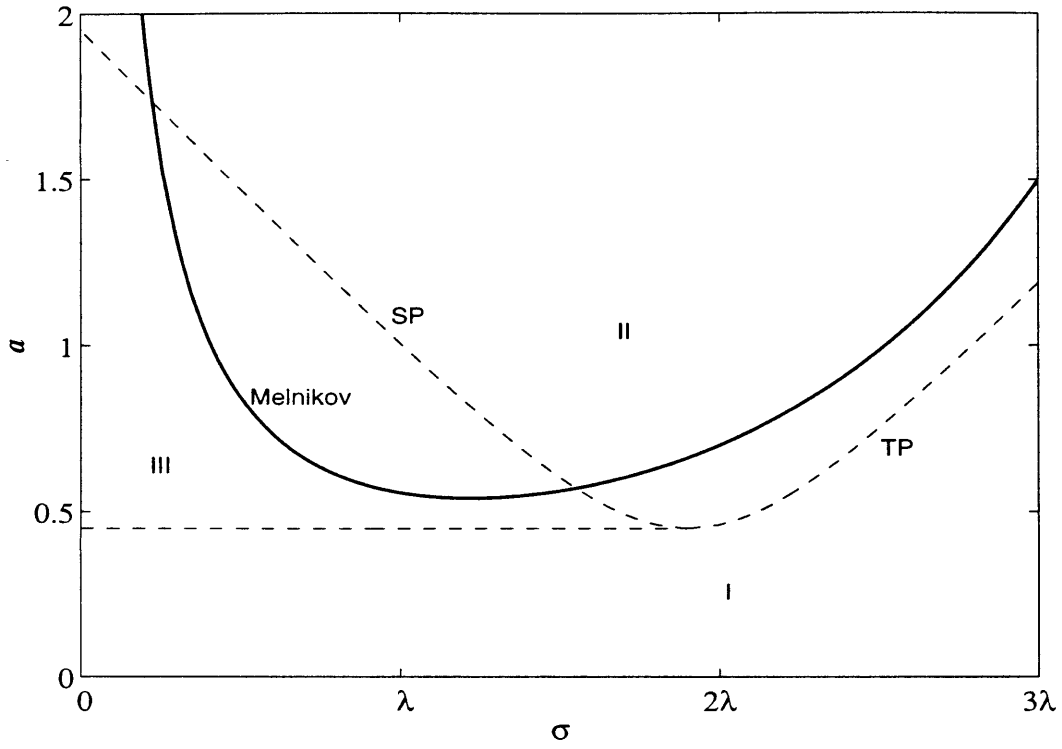

Figure 5-22: Threshold for heteroclinic tangles as a function of σ compared with the region of instability of the subharmonic resonance as in for $W = 0$ figure 5-12

If the response is synchronous with the forcing a white square tags the corresponding point in the $\sigma - a$ plane. Similarly, a light grey cell marks a period 2 response (subharmonic) and a black cell mark a non periodic response. In figure 5-23 we show the color correspondence with the possible orbits of the period doubling phenomenon.

Figure 5-24 shows the comprehensive result for $W = -\beta$. The parameter plane is explored by scanning the modulation frequency σ for increments of 0.035 and the modulation amplitude a of 0.015. For the widest range of the forcing parameters σ and a, the response is mostly synchronous (period 1), subharmonic (period 2) and chaotic; therefore in the parameter plane $\sigma\, a$, the predominant colors are white, light gray and black. Synchronous response (white) occurs for low values of a. As the amplitude is increased chaotic motion (black) or subharmonic response (light grey) prevail and finally for large amplitudes subharmonic response dominates.

To explain further figure 5-24, we take a slice at $\sigma = 2\lambda = 2\times 2\sqrt{1-W} = 2.09$, i.e. we increase the amplitude of modulation a for fixed frequency of modulation $\sigma = 2\lambda$. Details of the period doubling cascade to nonperiodic motion are shown in figures 5-25a–f, 5-26a–f, 5-27a–f, 5-28a–f and 5-29 5-30. For each type of response shown, the corresponding color can be found in the corresponding point of figure 5-24.

The time series of the real X and imaginary Y parts in figure 5-25a show that for $a = 0.380$ the response is synchronous with the forcing; the spectrum in figure

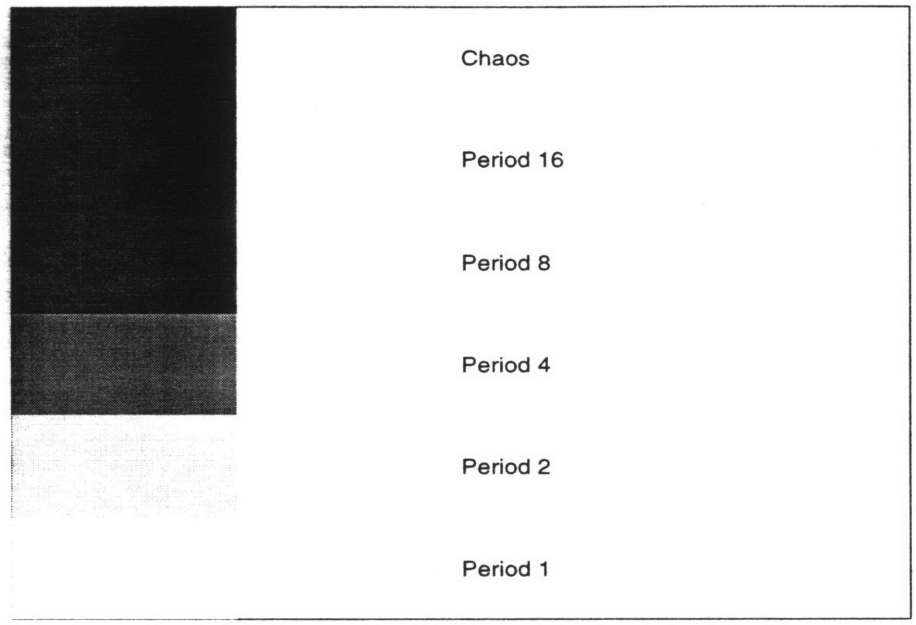

Figure 5-23: Colorbar of the response of the system

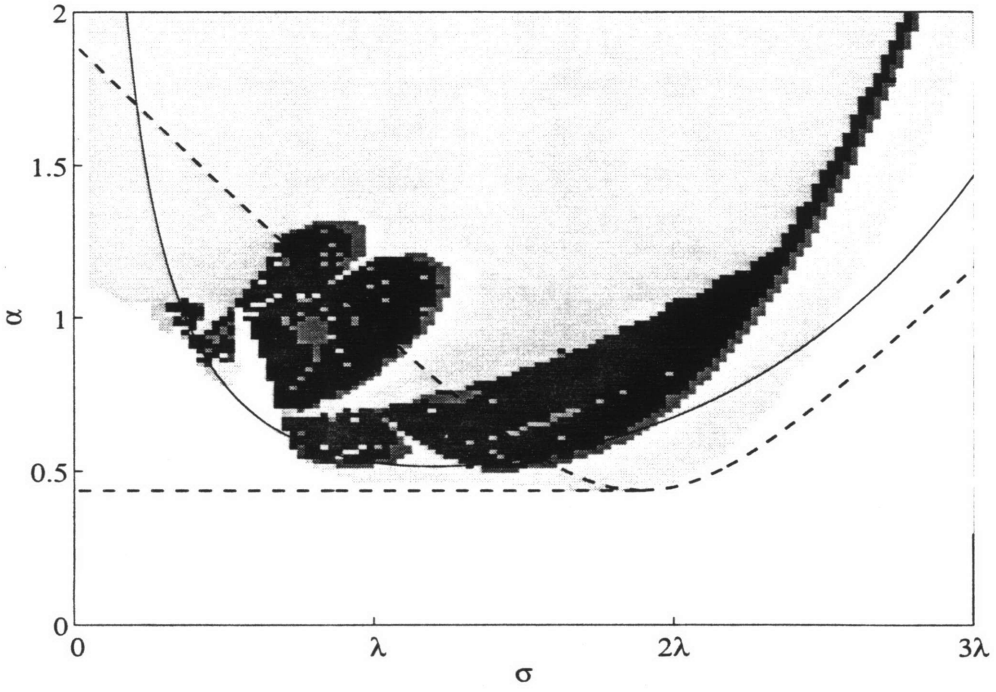

Figure 5-24: Chart of the response of the system for $\alpha = \beta = \gamma = 0.1$ and $W = -\beta$

5-25b has only one spike at σ. As the amplitude is increased above the threshold for subharmonic resonance, period doubling occurs and the response has frequency $\sigma/2 = \lambda = 2$ as the time series and the spectrum of respectively figure 5-25c and d show for $a = 0.680$. Such a behavior has been predicted by the nonlinear analysis of the previous section. We continue and find that around $a = 0.750$ a second bifurcation occurs which lead to period quadrupled oscillations. The time series of figure 5-25e and the spectrum of figure 5-25f are for $a = 0.780$. The time series shows a period 4 oscillation, confirmed by the spike at $\sigma/4$. Note that energy is present also at $3\sigma/4$. Further increase of a causes the response to double to period 8, 16 to infinity in a cascade that occurs in the narrow parameter range of $a = 0.793$ to $a = 0.799$. Period 8 motion is shown in figure 5-26a and b, for $a = 0.797$. In the latter a spike at $\sigma/8$ appears, accompanied by spikes at $\sigma = 3\lambda/8$ and $\sigma = 5\lambda/8$. Nonperiodic motion occurs for $a \in [0.780, 0.915]$. The time series of figure 5-26c for $a = 0.910$ show no periodicity and the spectrum of 5-26d shows that energy is distributed continuously over a wide frequency band, typical indicators of chaotic motion. Above $a = 0.915$ a strong subharmonic oscillation develops and persists for higher values of a. The orbit is symmetrical with respect to the origin (the mean of each of the two time series is zero) and does not have any energy at σ; all the energy is transferred to $\sigma/2$ and $3\sigma/4$. This can be seen in figure 5-25e and f, where $a = 1.080$. Now, the center of an orbit in the $X \sim Y$ plane is the amplitude of the response at $\omega = \omega_0 + \Delta\omega$. Therefore, in the case of these period doubled trajectories symmetric about the origin (and with zero mean) there is zero response at ω and all the energy is shifted at $\omega \pm \sigma/2$ and at $\omega \pm \sigma$. This frequency shift phenomenon is extensively analyzed in the next section.

The same bifurcation scenario can be highlighted via Poincaré sections of the trajectories in the X, Y, T or R, ψ, T spaces, with time of flight equal to $2\pi/\sigma$. The synchronous response for $a = 0.380$ is denoted by one point, as can be seen in 5-27a and b, respectively showing the XY plane and the $R\psi$ plane (see also 5-25a and b). The period doubled solution consists instead of two points visited alternatively as in figure 5-27c and d, where $a = 0.680$ (see also 5-27c and d). The period 4 oscillations found for $a = 0.780$, whose time series and spectrum are shown in figure 5-25e and f, appear as four points in the Poincaré sections of 5-27e and f. Each of the four points is visited every $4 \times 2\pi/\sigma$. Bifurcation to period 8 (as seen in figure 5-26a and b for $a = 0.797$) generates 8 points in the Poincaré maps, visited every $8 \times 2\pi/\sigma$. The corresponding sections are shown in figure 5-28a and b. Corresponding to the broad banded continuous spectrum of figure 5-26d, strange attractors, peculiar of chaotic motion, occur both in the XY and $R\psi$ planes of figure 5-28c and d. Finally the large amplitude subharmonic motion for $a > 0.915$ is represented by two points. In the XY plane the points are symmetrical about the origin; because the trajectory now encircle the origin, in the $R\psi$ plane, the ψ coordinate whirls around 2π every two period of the forcing and the Poicaré map has to be represented between $-\pi$ and π.

The response of the system along the slice cut at $\sigma = 2\lambda$, can be represented also

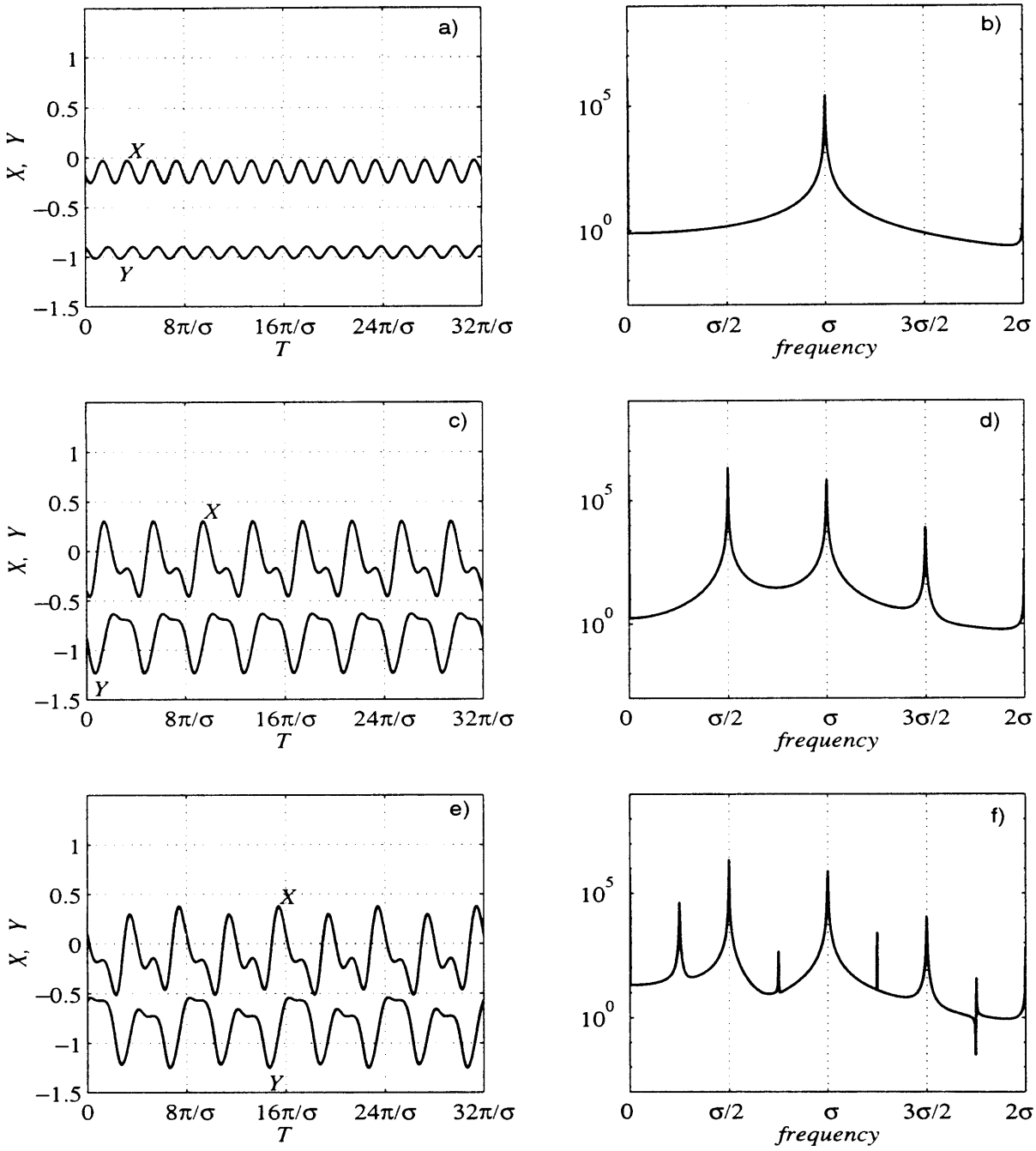

Figure 5-25: Time series and spectra for $W = -\beta$, $\sigma = 2\lambda = 4.18$ and $\alpha = \beta = \gamma = 0.1$. a), b) period 1 for $a = 0.380$; c), d) period 2 for $a = 0.680$; e), f) period 4 for $a = 0.780$.

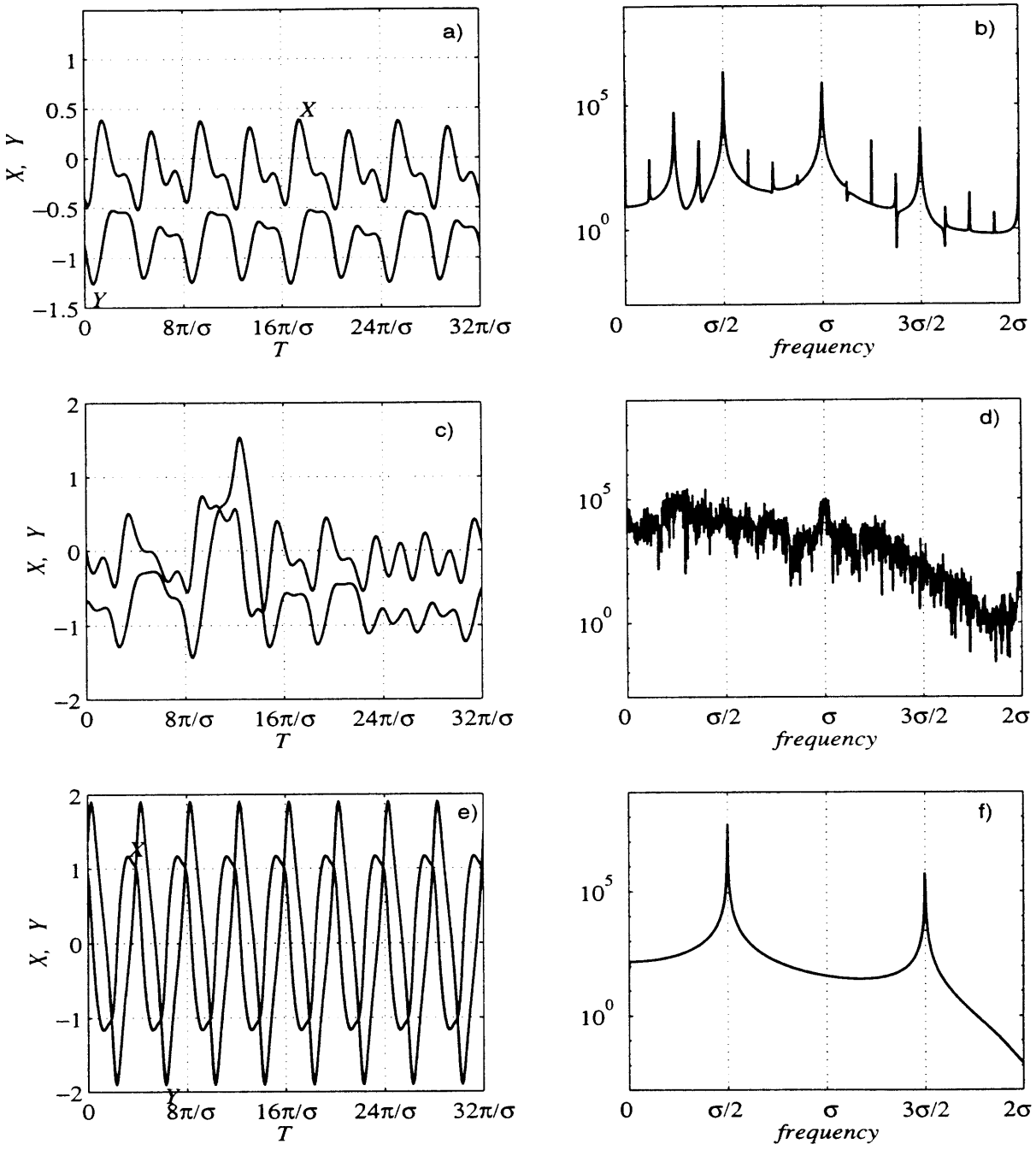

Figure 5-26: Time series and spectra for $W = -\beta$, $\sigma = 2\lambda = 4.18$ and $\alpha = \beta = \gamma = 0.1$. a), b) period 8 for $a = 0.797$; c), d) nonperiodic motion for $a = 0.910$; e), f) period 2 for $a = 1.080$.

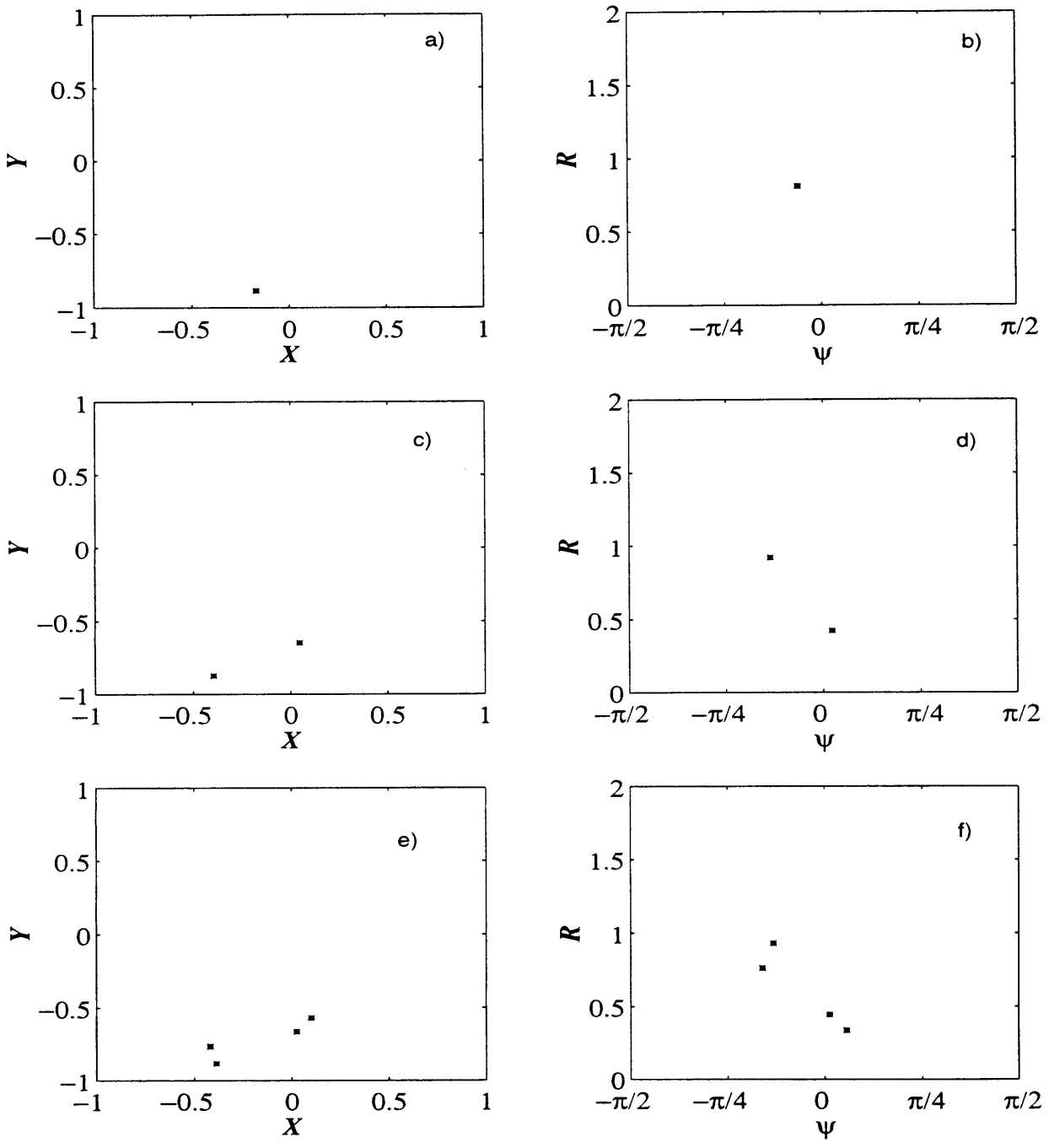

Figure 5-27: Poincaré sections for $W = -\beta$, $\sigma = 2\lambda = 4.18$ and $\alpha = \beta = \gamma = 0.1$. a), b) period 1 for $a = 0.380$; c), d) period 2 for $a = 0.680$; e), f) period 4 for $a = 0.780$. Compare with figure 5-25.

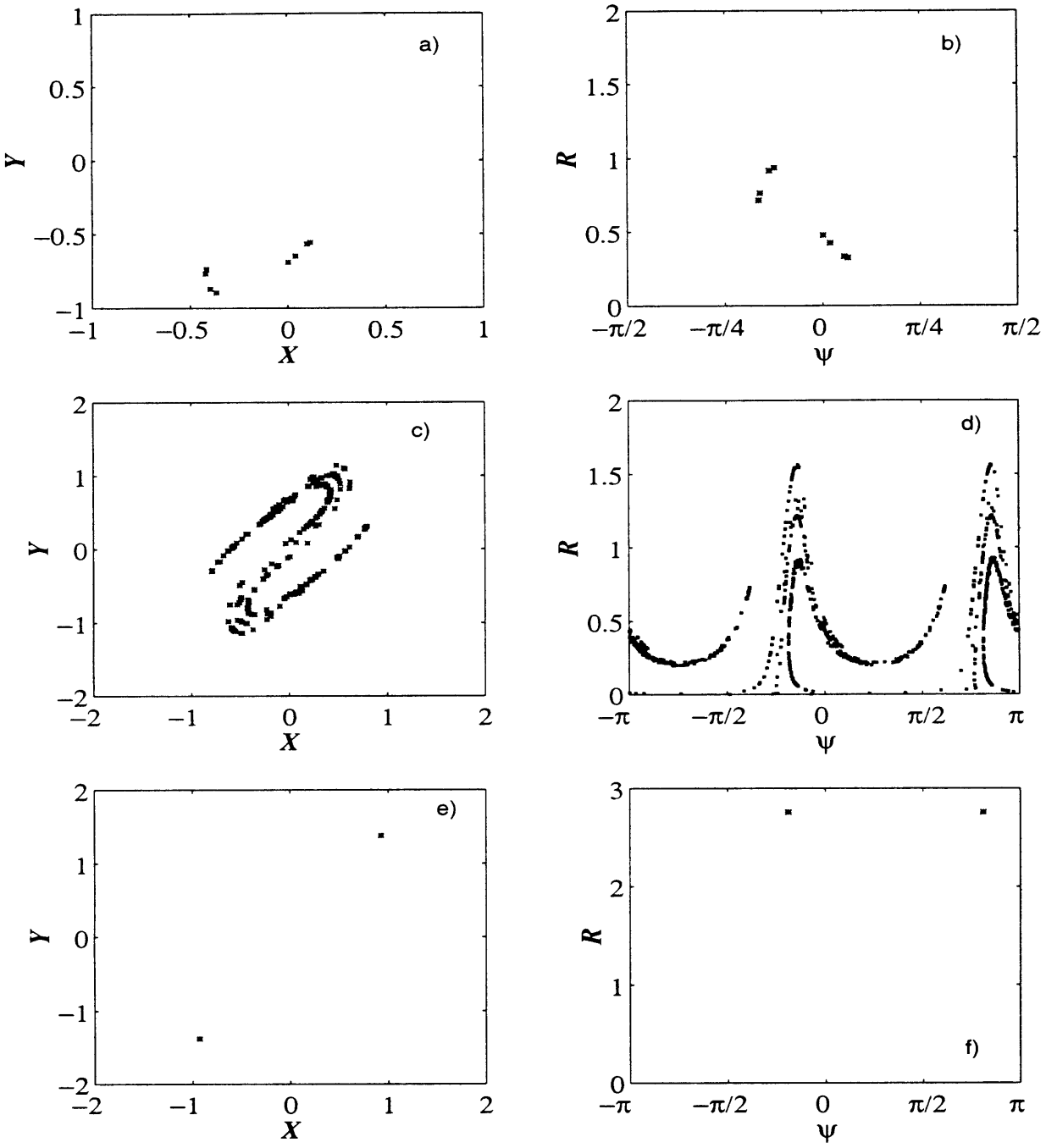

Figure 5-28: Poincaré sections for $W = -\beta$, $\sigma = 2\lambda = 4.18$ and $\alpha = \beta = \gamma = 0.1$. a), b) period 8 for $a = 0.797$; c), d) strange attractors for $a = 0.910$; e), f) period 2 for $a = 1.080$. Compare with figure 5-26.

with a bifurcation diagram. For each time series $X(T)$ or $Y(T)$, a local maximum is found. Then the time series is sampled every forcing period $2\pi/\sigma$, so to obtain the X or Y projection of the Poincaré section based on local maxima. The $1, 2, 4, 8, \ldots$ points of the section are then plotted versus the amplitude a so to obtain a bifurcation diagram of the Poincaré map of the motion. The result is plotted in figure 5-29, which contains a continuous description of the bifurcation phenomena occurring in the system for $\sigma = 2\lambda$. In such a figure, the response can be followed as a increases in its changes from synchronous to doubled, quadrupled, chaotic and finally subharmonic again.

The response is similar to many other bifurcation phenomena and period doubling cascade to chaos occurring in other branches of science and engineering. A collection of examples drawn from biology, physics and chemistry can be found in the introductory text of Strogatz(1995) or Drazin(1991). More detailed discussion can be found in the second edition of Liechtember and Liebermann(1994).

The analysis can be repeated for different values of σ, guided by the insight given by figure 5-24. In figure 5-30, we select $\sigma = \lambda$. Period doubling and chaos occur and even alternate as a is increased.

On the other hand for higher values of the modulational frequency no period doubling occurs. Instead the response remains synchronous for the values of a up to 2. This can be seen in figure 5-31, where an increase in a causes only an increase in the synchronous response.

We have considered also the effect of variations in W. Three of the charts so computed are shown respectively in figure 5-32, 5-33 and 5-34 respectively for $W = -0.5$, $W = -\beta$, $W = 0.4$ and $W = 0.8$. The analytical result is confirmed, that increasing W towards 1 lowers the threshold substantially. For $W = 0.9$ chaos and period doubling occur practically at $a = 0$. The theoretical thresholds for Melnikov and period doubling are also qualitatively confirmed.

This description gives an overview of the different responses over the parameter plane. Clearly, the description can be as detailed as desired, with the result that a period doubling cascade is reflected in a continuous shading of the plane.

5.6 Comparison with experiments in the wave basin

In the Gunther wave basin Tran(1996) has conducted a detailed experimental investigation of the possible modulational resonances of the envelope of the trapped wave. The experimental setup consists of an array of eleven full gates and two half gates places in a partition of the wave basin bounded by vertical walls. The two half gates are positioned by the vertical walls, so that modal periodicity is assured. Incident waves are generated at one end and absorbed by a beach at the other. For a detailed

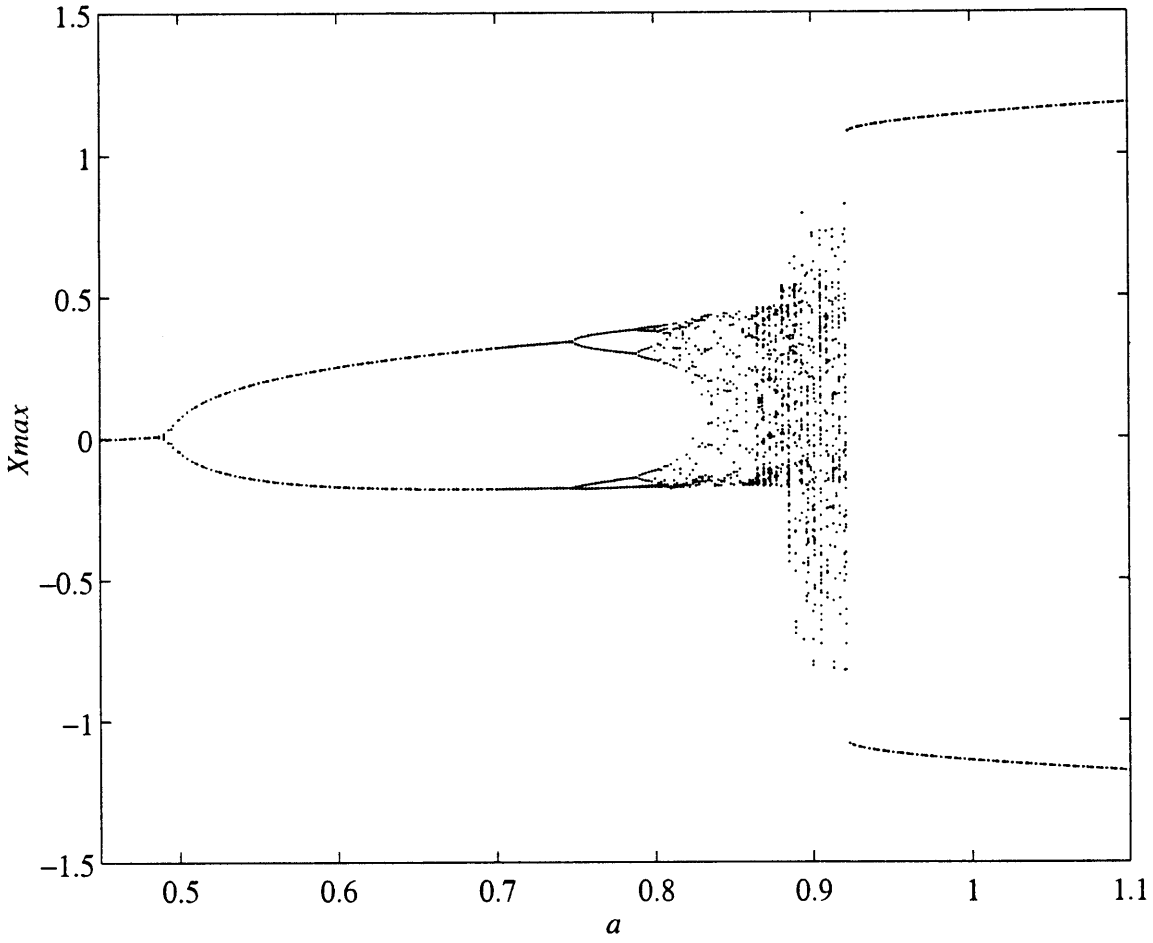

Figure 5-29: Period doubling cascade for $\sigma = 2\lambda$.

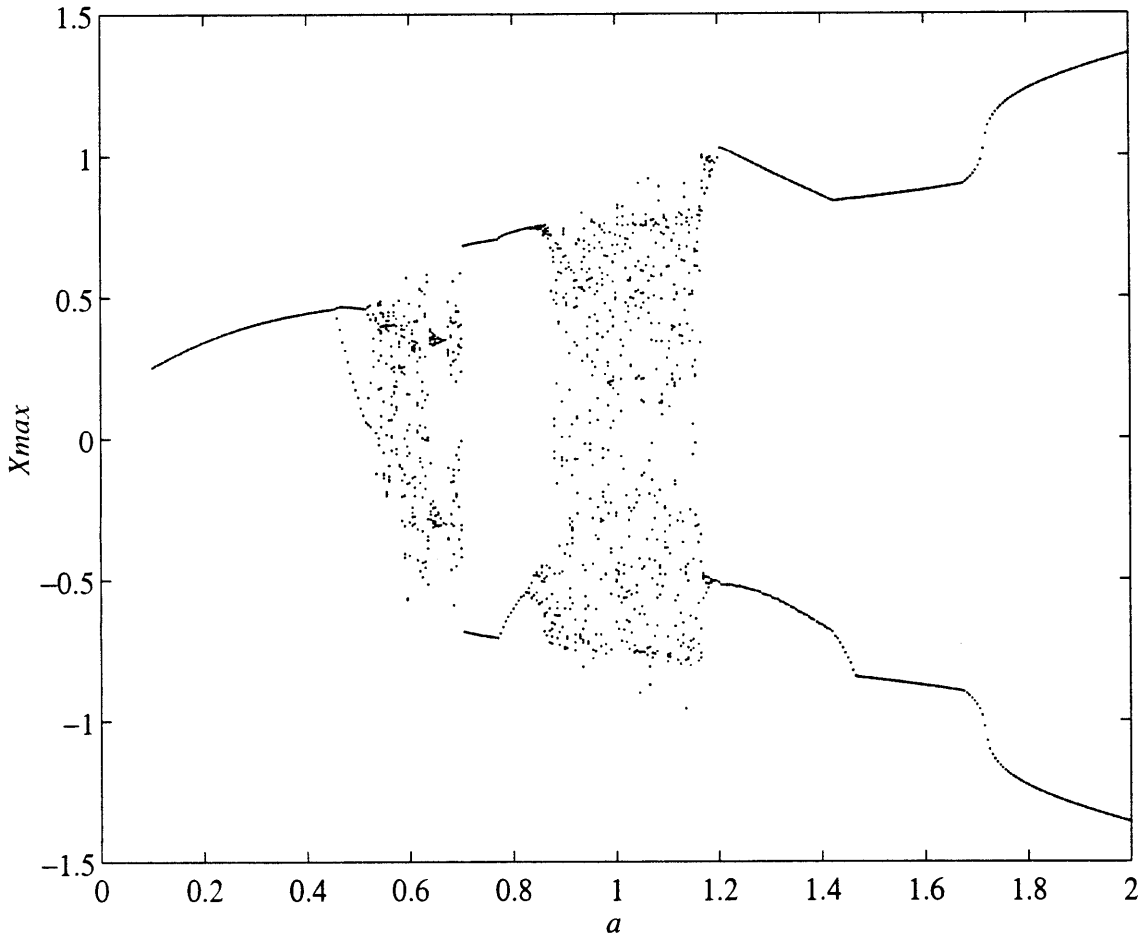

Figure 5-30: Period doubling cascade for $\sigma = \lambda$.

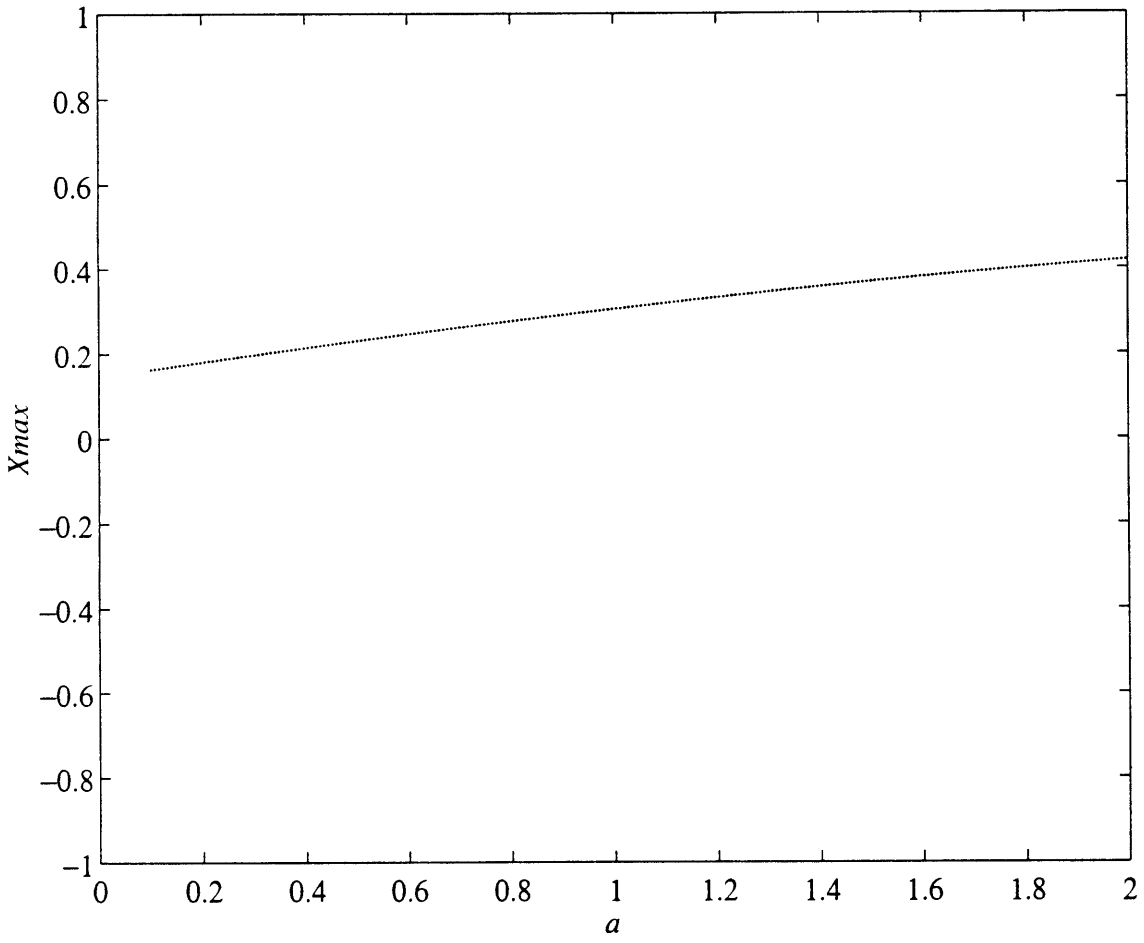

Figure 5-31: No bifurcation for high frequency of modulation; here $\sigma = 3\lambda$.

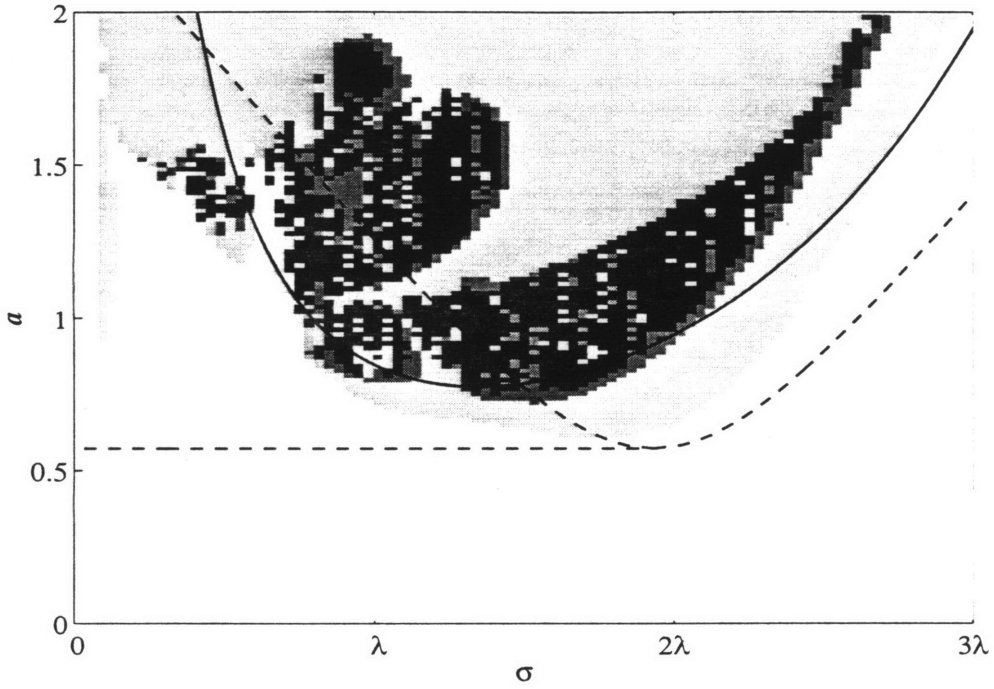

Figure 5-32: Chart of the response of the system for $\alpha = \beta = \gamma = 0.1$ and $W = -0.5$

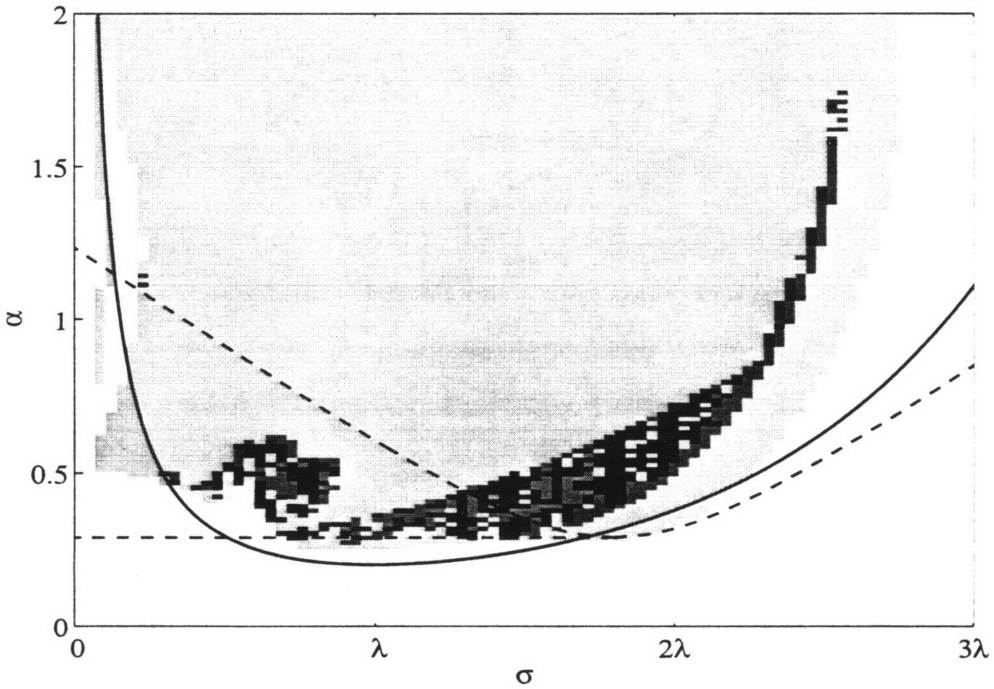

Figure 5-33: Chart of the response of the system for $\alpha = \beta = \gamma = 0.1$ and $W = 0.4$

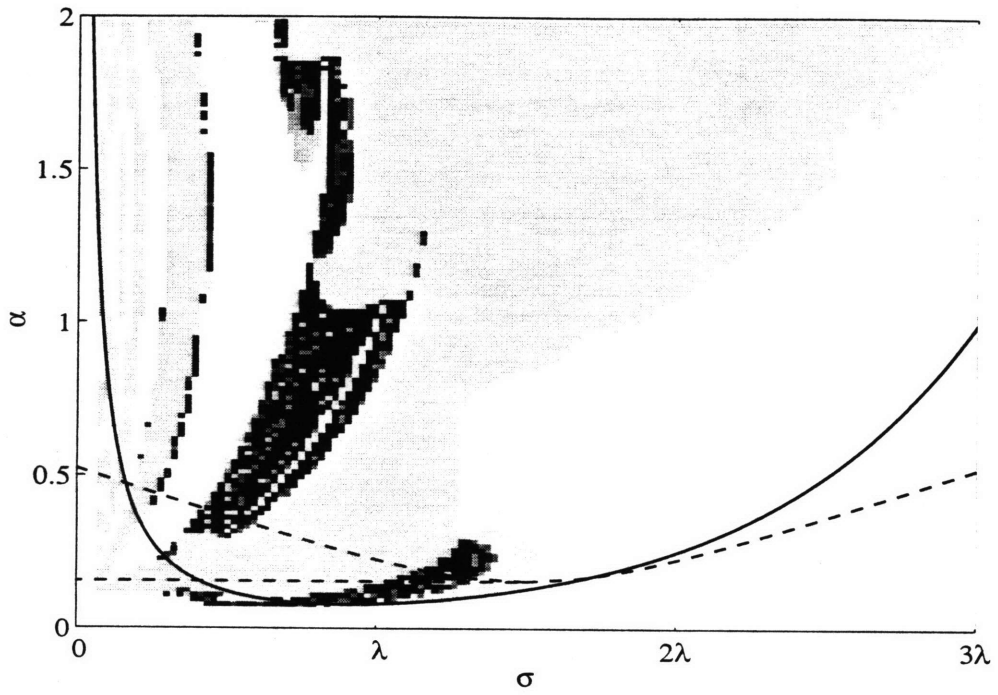

Figure 5-34: Chart of the response of the system for $\alpha = \beta = \gamma = 0.1$ and $W = 0.8$

description of the setup see Tran(1996).

5.6.1 Coefficients of the evolution equation

For the experiments in the wave basin, recall from section 3.4.2 that the theoretical coefficients of the evolution equations are

$$c_N = 27.330,\ c_R = 2.271,\ c_F = 1.630, \tag{5.6.1}$$

and the fitted values are

$$\delta c_L = 0.0031, \qquad f c_Q = 0.34. \tag{5.6.2}$$

Using the above values, in section 4.4.3 we found

$$\alpha = 0.0831, \qquad \beta = \frac{0.0061}{\overline{A'}/b'}, \qquad \gamma = \frac{0.0719}{\sqrt{\overline{A'}/b'}}. \tag{5.6.3}$$

5.6.2 The choice of the carrier wave amplitude and frequency.

Recall from 2.5.5 that the free surface elevation due to the incident wave reads, at a station $x = 0$

$$\left(\overline{A}_2 + \tilde{A}_2 \cos \Omega_2 t_2\right) \cos\left[2\left(1 + \epsilon^2 \omega_2\right) t\right] \tag{5.6.4}$$

In physical coordinates the above expression becomes

$$\left(\frac{\overline{A}'}{b'} + \frac{\tilde{A}'}{b'} \cos \Omega t'\right) \cos\left[2\left(1 + \frac{\Delta\omega}{\omega_0}\right) \omega_0 t'\right] \tag{5.6.5}$$

Hence, in the experiments, the incident modulated wave is defined by four physical parameters: the carrier wave amplitude $\overline{A}'$, the carrier wave detuning $\Delta\omega$, the modulation amplitude $\tilde{A}'$ and the modulational angular frequency Ω defined by

$$\Omega = \epsilon^2 \Omega_2 \, \omega_0 \tag{5.6.6}$$

For each choice of carrier wave amplitude $\overline{A'}$ and detuning $\Delta\omega/\omega_0$, we shall seek a region in the parameter plane $\Omega \sim \tilde{A}'$ for which the largest variety of modulational responses (synchronous, period doubled, chaotic) occurs within the physical constraint given by the experimental setup.

It has been shown in section 5.2.4 that the modulational frequencies with the lowest threshold for period doubling are around $\sigma = 2\lambda$, where $\lambda = 2\sqrt{1 - W}$ is the natural frequency of oscillation around the center of the hamiltonian limit of the dynamical system (5.1.2). We have also shown in figure 5-22, figures 5-32, 5-24, 5-33 and 5-34 that the natural frequency of the center λ and the critical frequencies for homoclinic tangle and chaotic oscillation are of the same magnitude. Therefore the four parameters of the incident modulated wave shall be chosen such that the condition for temporal subharmonic resonance is met. Then, around this condition, frequency Ω and amplitude $\tilde{A}'$ can be varied for the observation of bifurcations.

From section 5.2.4, the condition for subharmonic resonance

$$\sigma = 2\lambda = 4\sqrt{1 - W}, \tag{5.6.7}$$

can be recast in terms of the original variables using expressions (4.1.5) and (4.1.7)

$$\frac{\Omega/\omega_0}{c_F \overline{A}'/b'} = 4\sqrt{1 - \frac{\Delta\omega/\omega_0}{c_F \overline{A}'/b'}}. \tag{5.6.8}$$

Equation (5.6.8) gives the threshold modulational frequency Ω that causes modulational period doubling as a function of the amplitude $\overline{A}'$ and detuning $\Delta\omega$ of the

carrier wave. Equivalently we may solve (5.6.8) for $\Delta\omega$

$$\frac{\Delta\omega}{\omega_0} = c_F \frac{\overline{A'}}{b'} - \frac{\Omega^2}{16\omega_0^2} \frac{b'}{c_F \overline{A'}}, \tag{5.6.9}$$

which gives the threshold detuning of the carrier wave that causes period doubling of the gate envelope.

A second condition for subharmonic resonance of modulation is that the amplitude of modulation $a = \tilde{A}'/\overline{A'}$ be larger than the threshold given by the right hand side of (5.2.63). Upon multiplication by μ^2 and usage of (4.1.5), (5.2.63) can be rewritten in terms of the physical variables

$$\frac{\tilde{A}'}{\overline{A'}} > \left(\frac{\lambda^2}{2} \frac{c_R}{c_N} + \frac{\delta c_L}{c_F \overline{A'}/b'} + \frac{3}{4}\lambda \frac{f c_Q}{\sqrt{c_N c_F \overline{A'}/b}} \right) \left(\frac{\lambda}{4} + \frac{1}{\lambda} \right)^{-1}, \tag{5.6.10}$$

where $\lambda = 2\sqrt{1 - \Delta\omega b'/\omega_0 c_F \overline{A'}}$ is recalled.

Expressions (5.6.9), (5.6.10) can be used as follows. If two of the four parameters that define the incident wave, $\Delta\omega$, Ω, $\overline{A'}$, $\tilde{A}'$, are given, the remaining two can be chosen as to satisfy (5.6.9), (5.6.10). For example, let the frequency of modulation Ω be fixed. Then expression (5.6.9) gives $\Delta\omega$ for given $\overline{A'}$ and vice versa. Once $\Delta\omega$ and $\overline{A'}$ are chosen, (5.6.10) gives the minimum $a \equiv \overline{A'}/\tilde{A}'$ for subharmonic modulation to occur. These expressions have been used extensively to find the desirable condition for experiments, which, for a given modulational frequency Ω, consists of finding the carrier wave detuning that minimizes at the same time the carrier wave amplitude $\overline{A'}$ and the threshold for a.

As an example figure 5-35a represents condition (5.6.9) and figure 5-35b threshold (5.6.10) for $\Omega = 0.30$ rad/sec. It can be seen that for increasing detuning $\Delta\omega/\omega_0$ (ordinate of figure 5-35a) the resonance condition is met for increasing values of $\overline{A'}$ and, from figure 5-35b, for decreasing values of a. This corresponds in physical coordinates to the property that as $W \to 1$, the threshold for period doubling decreases (c.f. figures 5-22, 5-32, 5-24, 5-33 and 5-34).

In the wave basin, spurious undesired transverse waves are resonated for discrete values of $\Delta\omega/\omega_0$ both larger and smaller than zero. In the experiments we keep the sum $\overline{A'} + \tilde{A}'$ smaller than about 0.035 m, in order to prevent strong nonlinear effects in the incident waves and undesired higher reflections from the absorbing beach and the gates. Therefore even if larger values of $\overline{A'}$ have lower thresholds a, the optimal condition was finally chosen to be

$$\Delta\omega/\omega_0 = 0.00, \qquad \frac{\overline{A'}}{b'} = 0.0139/0.25 = 0.057, \tag{5.6.11}$$

for which, from (5.6.3)

$$\alpha = 0.083, \qquad \beta = 0.110, \qquad \gamma = 0.310. \tag{5.6.12}$$

5.6.3 Numerical integration.

With these coefficients we first carry out a detailed numerical investigation in the $\Omega \sim a$ plane in the same manner as in figures 5-32, 5-24, 5-33 and 5-34. The numerical integration is carried out first in nondimensional coordinates and then transformed in physical coordinates via

$$\frac{\overline{A'}}{\tilde{A'}} = a \equiv \frac{\overline{A}_2}{\tilde{A}_2}, \qquad \Omega = \sigma\omega_0 \, c_F \, \frac{\overline{A'}}{b'}. \tag{5.6.13}$$

The various scenarios are summarized in figure 5-36. The minimum threshold for subharmonic motion is predicted to be around $\Omega/2\pi = 0.045$ rad/sec. The region of chaotic motion appears in a band sandwiched by subharmonic response, the latter being the only response for large values of a. There is a large spot of period-four response, embedded in the chaotic band, for frequencies ranging approximately from 0.032 to 0.06. Also a thin period-four band separates the lower period-two region from the chaotic region. We will show that the period-two regions above and below the chaotic band differ in that the upper region is characterized by a marked downshift of the central peak by $\Omega/2$. Similar charts were obtained in section 5.5 for different values of α, β, γ, W and plotted in figures 5-32, 5-24, 5-33 and 5-34. In figure 5-36 also the bifurcation curves given by the Melnikov's theory and the multiple scales are plotted.

5.6.4 Comparisons

In corresponding experiments by Tran(1996), different frequencies of modulation were scanned, and for each of them increasing values of a were tested. The results are summarized in the chart of figure 5-37, which is plotted together with an enlargement of figure 5-36 to facilitate the recognition of the different areas. The most detailed records were taken for $\Omega/2\pi = 0.04$. Overall the various scenario predicted by the theoretical and numerical computations and confirmed by the experiments. First it can be seen that for any frequency, when the amplitude a is lower than ~ 0.6 the response remains synchronous. $\Omega = 0.04$, $a = 0.57$ is the lowest amplitude for which bifurcation to period doubling happens. There is a region of chaotic motion (denoted naturally by a (c) in figure 5-37) limited below and above by period-two motion; in the upper region, period-two is accompanied by the down-shift in the frequency of

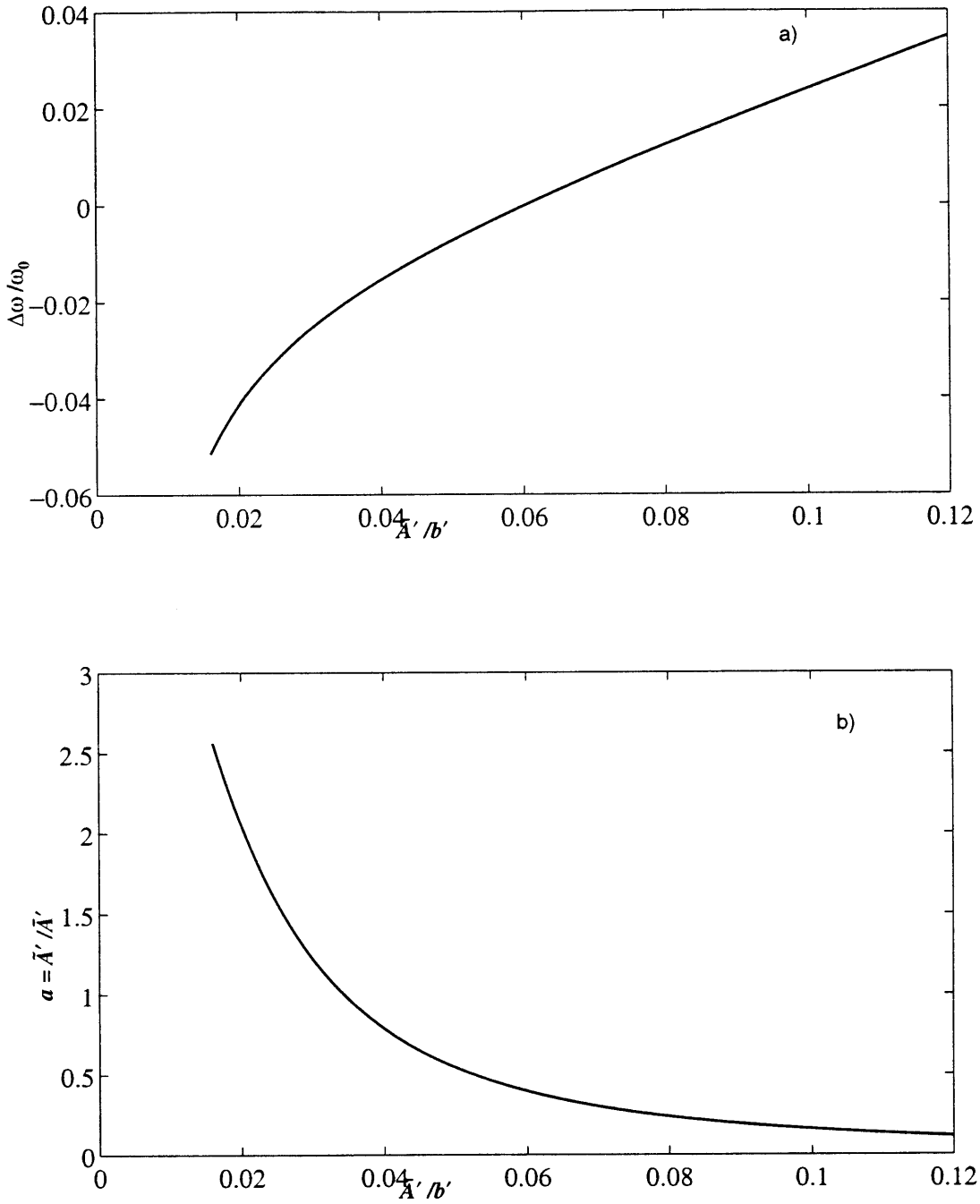

Figure 5-35: Experiments in the wave basin. For $\Omega = 0.05$ Hz, from plot a) $\overline{A}$ and $\Delta\omega$ are chosen. For the corresponding $\overline{A}$, above the curve in plot b) subharmonic resonance is expected.

response, as we are about to see.

A quantitative comparison with the experiments is further pursued as follows. Numerical integration of the dynamical system (5.1.4) is carried out in normalized variables for $\sigma = \Omega b'/\omega_0 c_F \overline{A}'$ and α, β, γ given in (5.6.3). The time series of the envelope $X(T), Y(T)$ is transformed in time series of the physical time $X(t'), Y(t')$ by using (4.1.5)

$$T = c_F \frac{\overline{A}'}{b'} \omega_0 t'. \tag{5.6.14}$$

Then the full time series in physical variables $\Theta'(t')$ is obtained by using the definition (4.1.5) of $\vartheta = X + \mathrm{i}Y$

$$\Theta'(t') = \sqrt{\frac{c_F \overline{A}'}{c_N b'}} \, (X + \mathrm{i}Y) \, \mathrm{e}^{-\mathrm{i}\omega_0 t'} + * = 2\sqrt{\frac{c_F \overline{A}'}{c_N b'}} \, [X(t') \cos \omega_0 t' + Y(t') \sin \omega_0 t'] \,, \tag{5.6.15}$$

The detuning of the carrier wave is chosen to be zero. Then the spectrum of the time series (5.6.15) is calculated. These theoretical results are compared with the experimental time series and the experimental spectra.

On the other hand, using the method based on the Hilbert transform devised by Melville(1983), the experimental envelope of the angular displacement can be extracted from the data, so as to obtain the experimental phase planes, Poincaré maps and spectra of the envelope, which can then be compared with the theoretical ones.

For the chosen sample frequency $\Omega/2\pi = 0.04$ Hz, each of the following figures contains four plots. In *a*) we show the theoretical time series (5.6.15) in rad versus sec. In *b*) we show the spectrum of (5.6.15). In *c*) we show with a continuous line the theoretical phase plane trajectories of the envelope X, Y calculated from (5.1.4) and transformed in radians. The asterisks represent the Poincarè map obtained by sampling every $2\pi/\sigma$ the nondimensional time series or, equivalently, sampling every $2\pi/\Omega$ the converted physical time series. Finally, in *d*) the spectrum of the envelope X is presented. In figures 5-40 to 5-53, the frequency of modulation $\Omega/2\pi$ is kept constant at 0.04 Hz, while the amplitude ratio a is increased to show the bifurcation sequence.

Theoretically, for small amplitude a, there are two coexisting limit cycle in the phase plane, which lie symmetricaly with respect to the origin. They represent oscillations of period $2\pi/\Omega$ around the fixed points for the steady amplitude case, i.e. around $s_{1,2}$ of figure 4-6b. A trajectory will tend to one or the other depending on the initial conditions. The corresponding two time series of the angular displacement are identical but for a phase shift equal to π. This can be clearly seen in figures 5-38 and 5-39. Figure 5-38c) shows lower limit cycle in the phase plane for $a = 0.20$, while 5-39c) shows the upper coexisting limit cycle for the same value of a. Comparison of

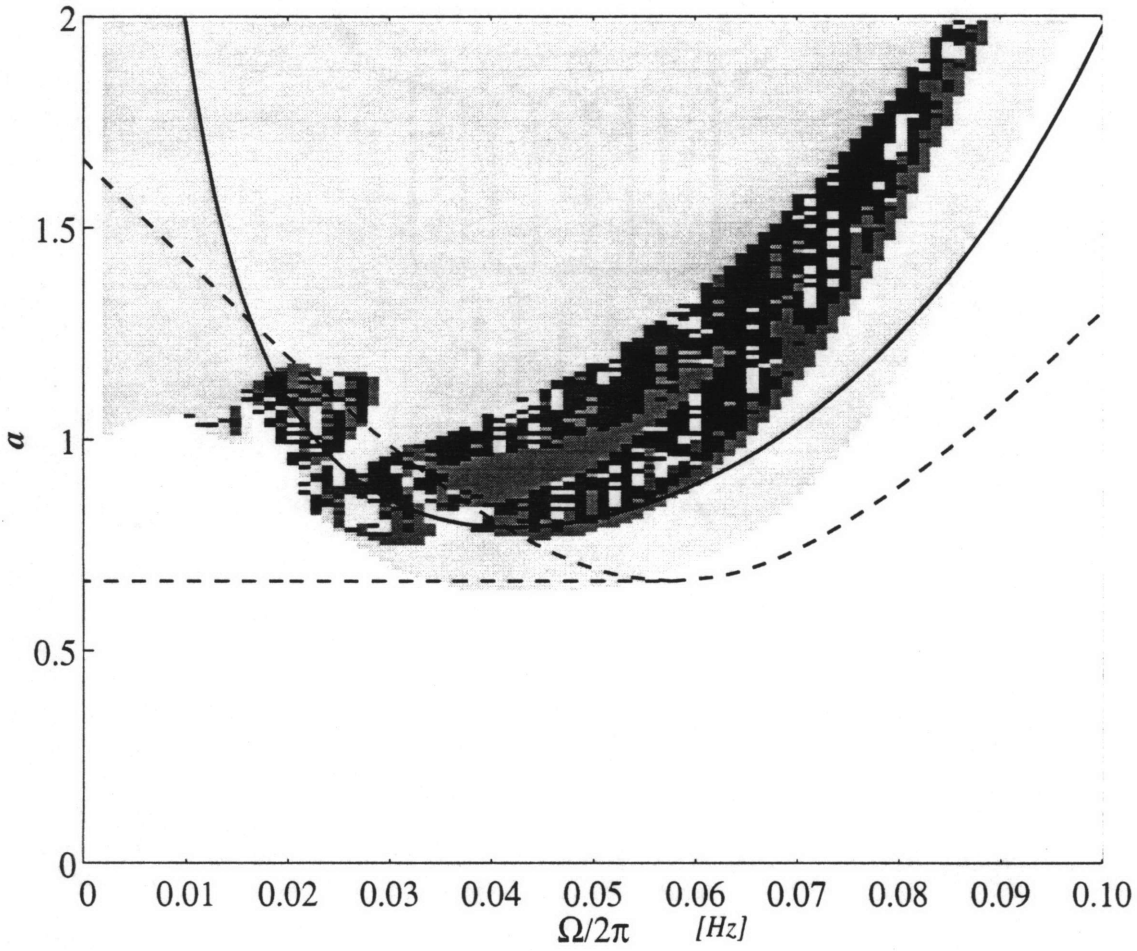

Figure 5-36: Experiments in the wave basin. Prediction by theory and numerics.

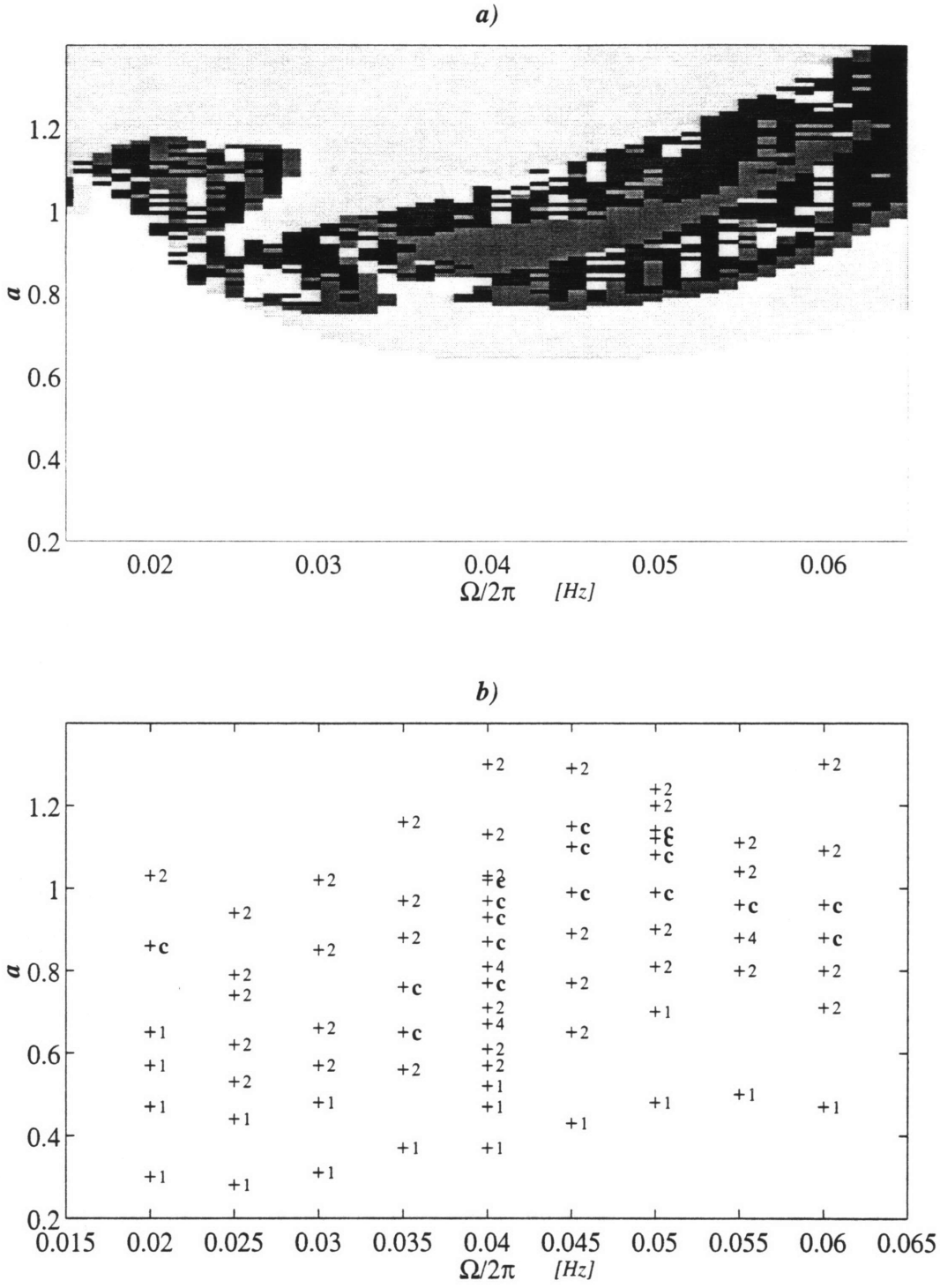

Figure 5-37: Experimental findings of Tran(1996) compared with the theory in the same parameter range (the axis of a) and b) are the same). The numbers 1,2, 4 stand for synchronous, period-two, period-four and c stands for chaos.

5-38a) with 5-39a) shows that indeed the two time series are identical but shifted by π. The spectra in b) and d) are indeed identical.

In the following we focus on the bifurcation route to chaos for the lower orbit. For large amplitude a the symmetry is lost and either chaotic motion occurs or a large period-four or period-two unique attractor exist in the phase plane.

For $a = 0.47$ below the threshold 0.57, the response is synchronous. In a) the envelope modulation has the same period of incident wave modulation; in b) the spectrum shows side bands at $(\omega_0 \pm \Omega)/2\pi = 0.7 \pm 0.04$ Hz, while in c) the Poincaré map has one fixed point; d) spectrum of the envelope shows the offset of the orbit in c) and a peak at $\Omega/2\pi$. The offset of the phase plane trajectory is the mean oscillation of the time series and measures the energy peak at half the carrier wave frequency, i.e. at $\omega_0/2\pi = 0.7$ Hz in b). The size of the limit cycle provides a measure of the amount of modulation in the gate rotation time series.

We point out a common property of all the spectra shown in b), that is, the left sidebands are consistently larger than the right sidebands. This appear to be an intrinsic characteristics of the nonlinearity of the Stuart-Landau equation.

We increase the value to $a = 0.63$ where bifurcation occurs. In figure 5-41a) subharmonic modulation is imperceptible in the time series and in b) the spectrum shows almost no side bands at $(\omega_0 \pm \Omega/2)/2\pi = 0.7 \pm 0.02$ Hz. Besides, in c) the two fixed points of the Poincaré map overlap, so that it is only the spectrum of the envelope in d) that shows a small peak at $(\Omega/2)/2\pi = 0.02$ Hz.

When the amplitude is increased to $a = 0.64$, subharmonic response is already fully developed. In figure 5-42a) subharmonic modulation is visible in the time series and the spectrum in b) shows small side bands at $(\omega_0 \pm \Omega/2)/2\pi = 0.7 \pm 0.02$ Hz. The Poincaré map in c) has two fixed point and the trajectory has an inside loop that decreases in size as the amplitude increase. The spectrum of the envelope in d) shows a peak at $(\Omega/2)/2\pi = 0.02$ Hz.

An increase of the amplitude to $a = 0.67$ renders the amplitude of the subharmonic response larger. In figure 5-43b) the side bands at $(\omega_0 \pm \Omega/2)/2\pi = 0.70 \pm 0.02$ Hz are larger, and the same in d) at $(\Omega/2)/2\pi = 0.02$ Hz. The inside loop of the phase plane trajectory in c) is now smaller and, when $a = 0.72$, figure 5-44c) shows that the inside loop is gone. In figure 5-44b) the subharmonic side bands at $(\omega_0 \pm \Omega/2)/2\pi = 0.70 \pm 0.02$ Hz are larger than the synchronous at $(\omega_0 \pm \Omega)/2\pi = 0.70 \pm 0.04$ Hz and in d) we see that the response at $(\Omega/2)/2\pi = 0.02$ Hz is dominant.

The period doubled orbit, bifurcates to a period-four when $a = 0.77$. In figure 5-45b) a small peak is born at $(\omega_0 \pm \Omega/4)/2\pi = 0.70 \pm 0.01$ Hz and in c) four fixed points appear in the Poincaré map. In d), the subarmonic at $(\Omega/4)/2\pi = 0.01$ Hz is evident.

For $a = 0.78$, nonperiodic motion has started. In figure 5-46a) the time series does not repeat itself; in b) the noise under the side bands is appreciable; and in c) we see the strange attractor. The spectrum in d) is broad banded with dominant peaks at

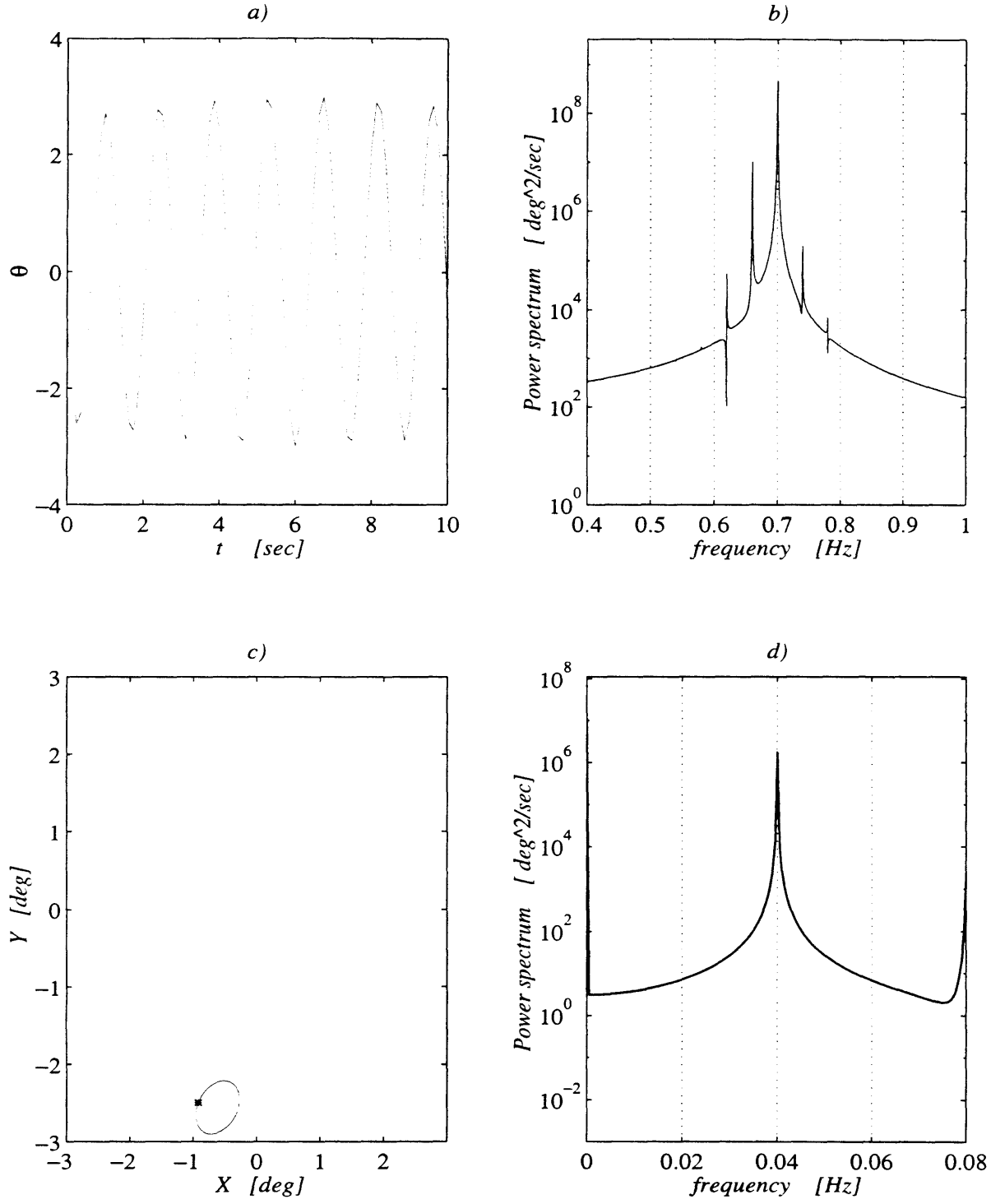

Figure 5-38: $\Omega/2\pi = 0.04$ Hz, $a = 0.20$, lower limit cycle. a) time series of angular displacement; b) spectrum shows small side bands at $(\omega_0 \pm \Omega)/2\pi = 0.7 \pm 0.04$ Hz; c) lower limit cycle; d) spectrum of the envelope shows the offset of the orbit in c) and a peak at $\Omega/2\pi$. Compare with 5-39.

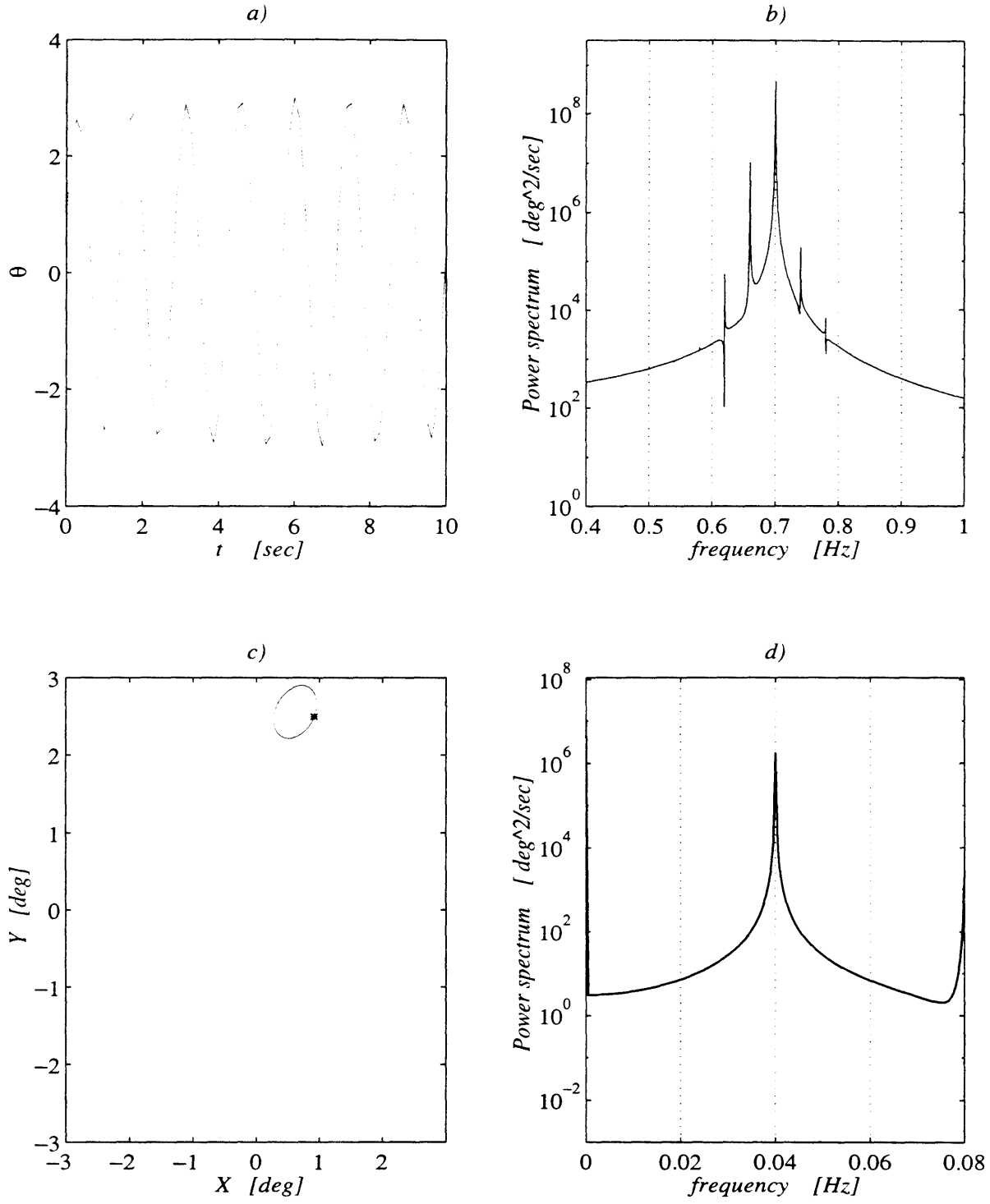

Figure 5-39: $\Omega/2\pi = 0.04$ Hz, $a = 0.20$, upper limit cycle. a) the time series of angular displacement is π out of phase with the time series of figure 5-38a); b) spectrum of the time series is identical to spectrum in figure 5-38b); c) upper limit cycle symmetrical to the cycle of 5-38b); d) spectrum of the envelope is identical to spectrum in figure 5-38b).

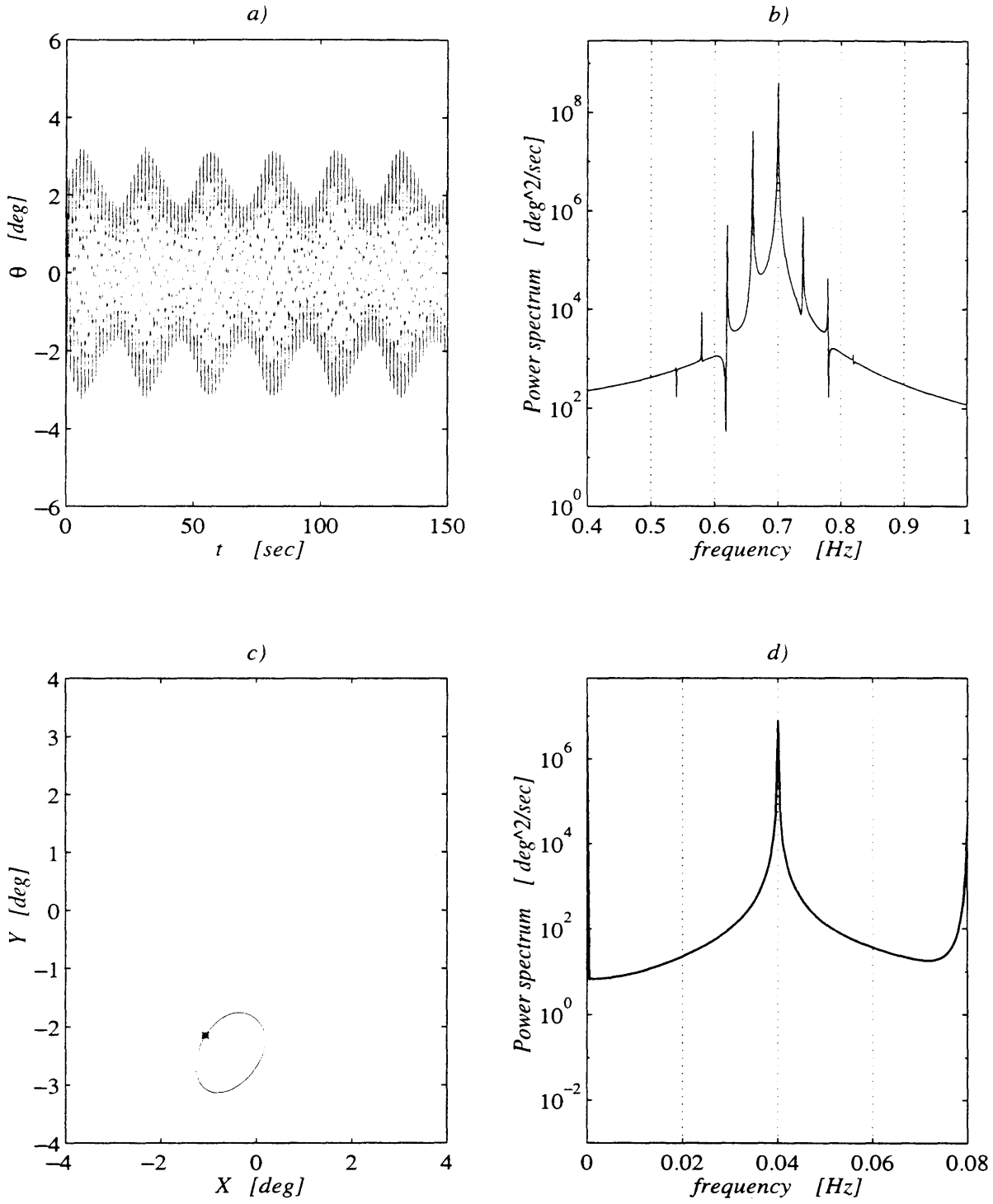

Figure 5-40: $\Omega/2\pi = 0.04$ Hz, $a = 0.47$, synchronous response. a) time series of angular displacement with modulation synchronous with incident wave; b) spectrum shows side bands at $(\omega_0 \pm \Omega)/2\pi = 0.7 \pm 0.04$ Hz; c) Poincaré map with one fixed point together with phase trajectory; d) spectrum of the envelope shows the offset of the orbit in c) and a peak at $\Omega/2\pi = 0.04$ Hz.

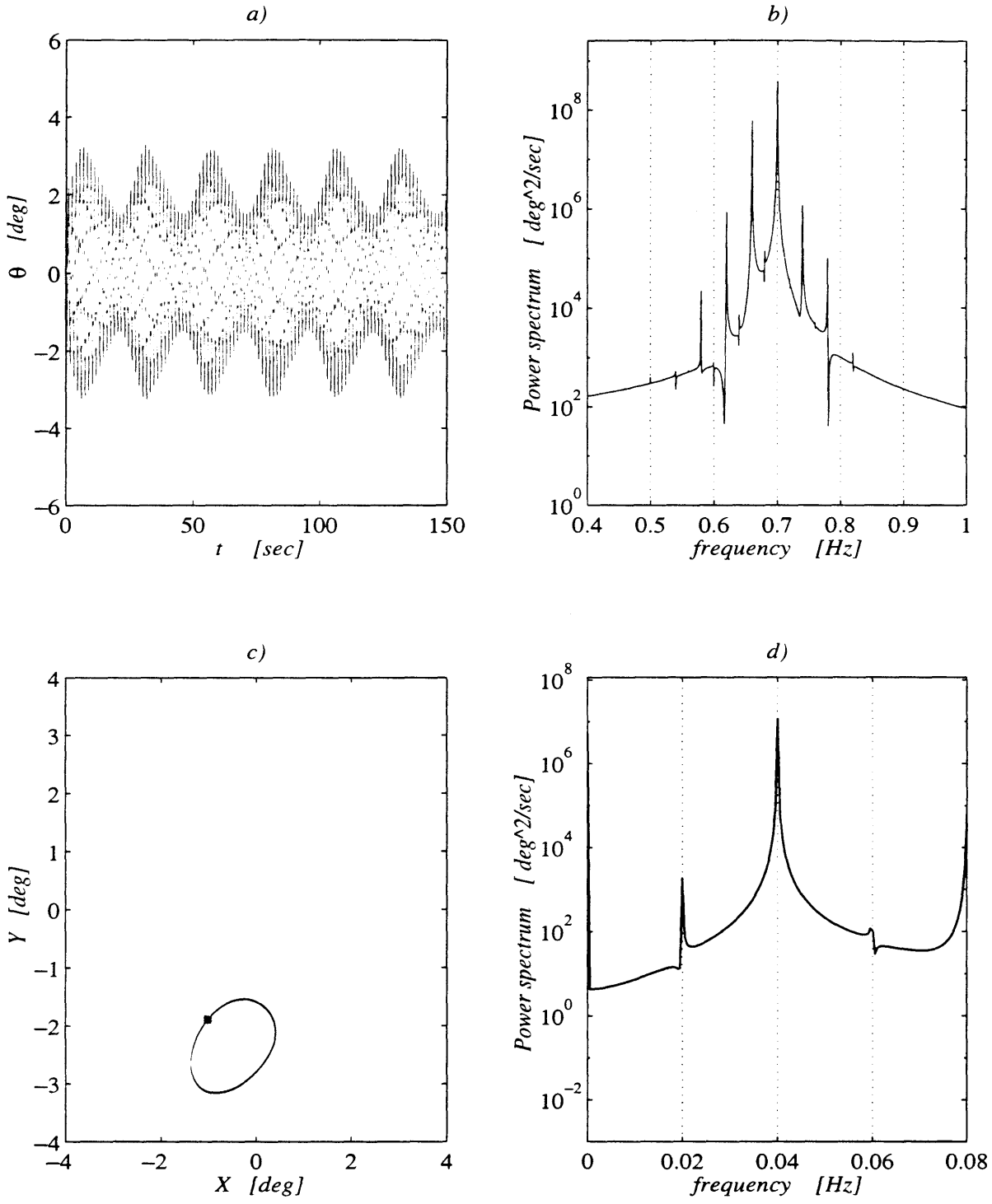

Figure 5-41: $\Omega/2\pi = 0.04$ Hz, $a = 0.63$, threshold for subharmonic response. a) subharmonic modulation is imperceptible in the time series; b) spectrum shows almost no side bands at $(\omega_0 \pm \Omega/2)/2\pi = 0.7 \pm 0.02$ Hz; c) The two fixed point of the Poincaré map overlap; d) spectrum of the envelope shows a small peak at $(\Omega/2)/2\pi = 0.02$ Hz.

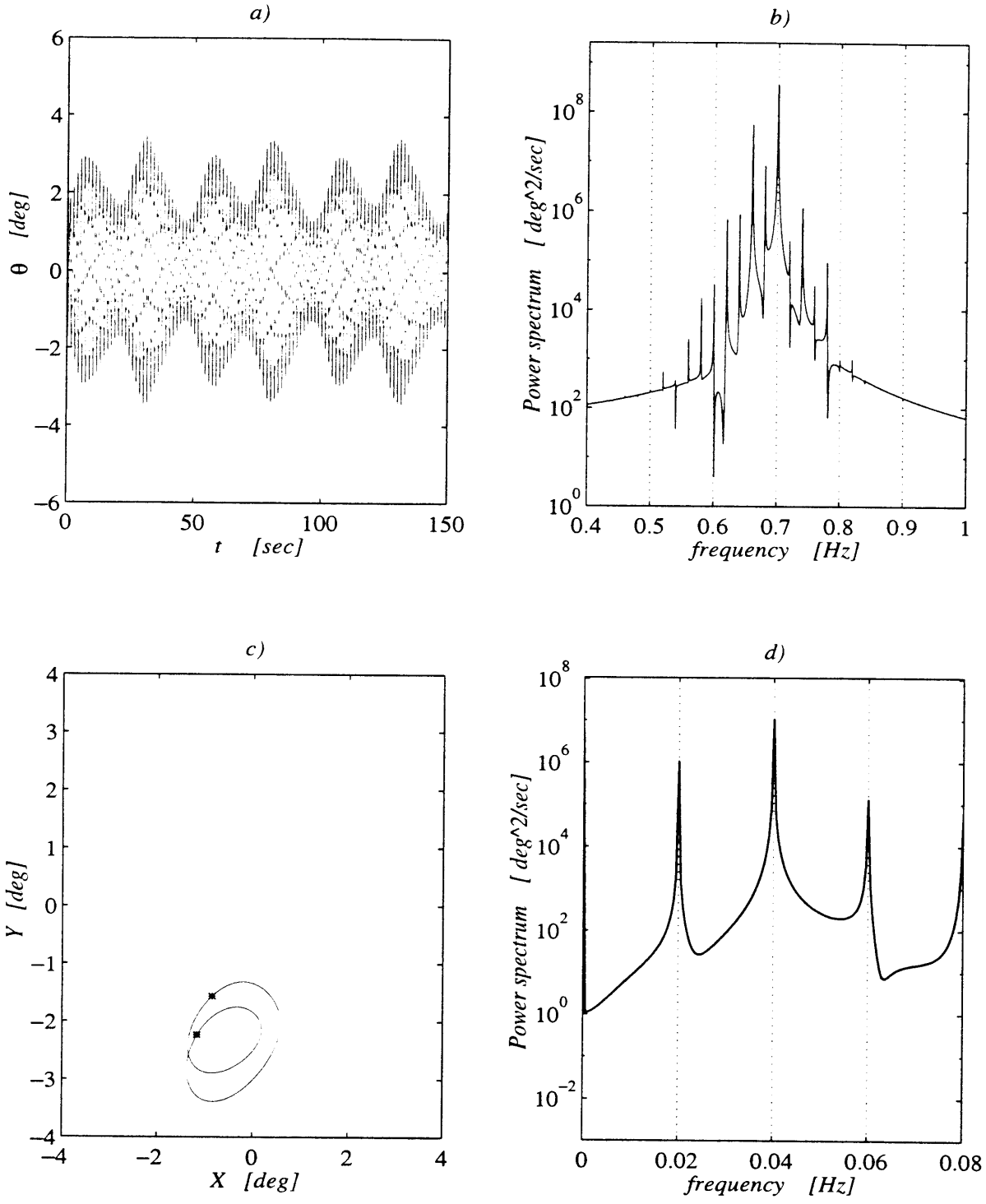

Figure 5-42: $\Omega/2\pi = 0.04$ Hz, $a = 0.64$, subharmonic response. a) subharmonic modulation is visible in the time series; b) spectrum shows small side bands at $(\omega_0 \pm \Omega/2)/2\pi = 0.70 \pm 0.02$ Hz; c) Poincaré map has two fixed point; d) spectrum of the envelope shows a peak at $(\Omega/2)/2\pi = 0.02$ Hz.

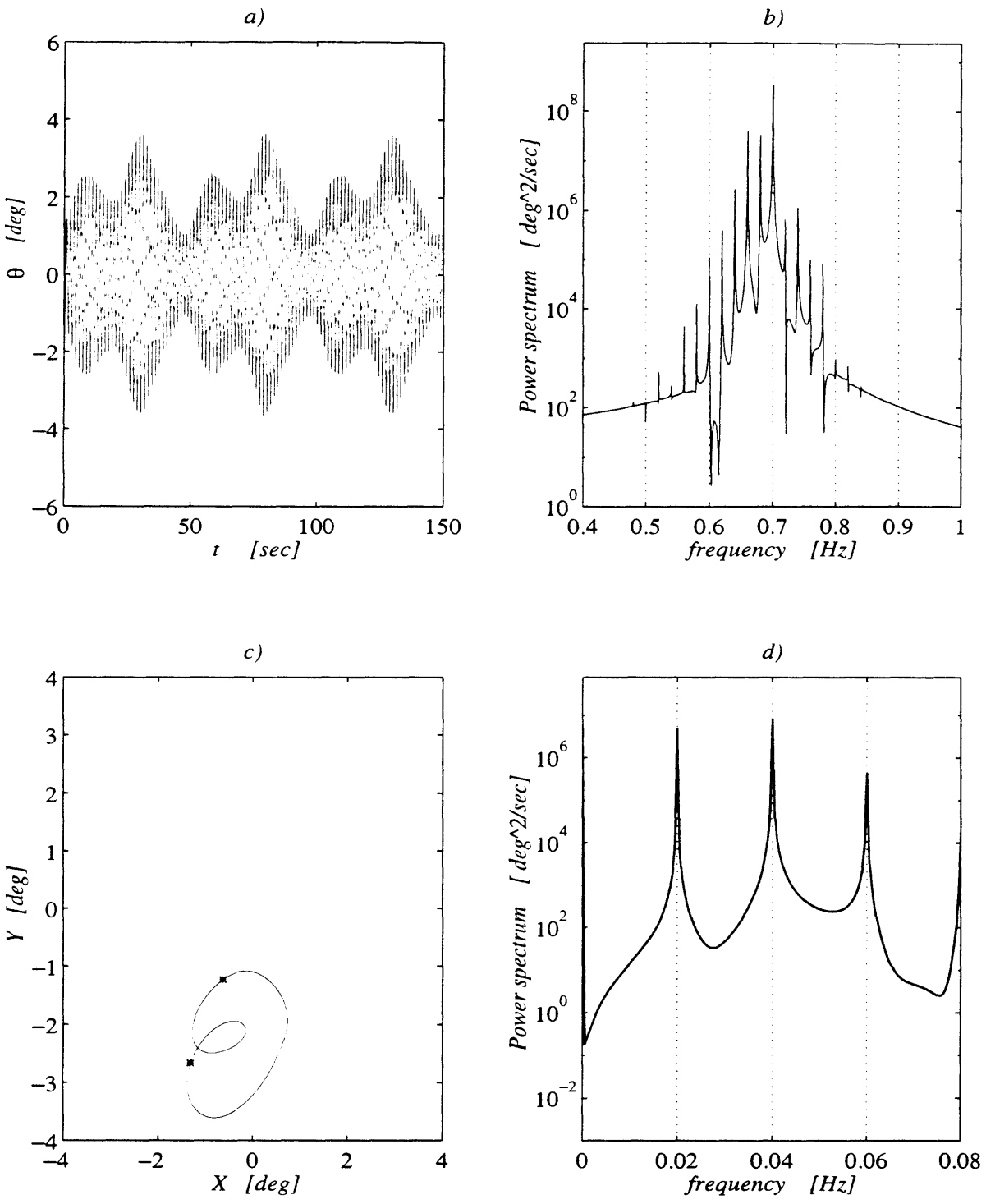

Figure 5-43: $\Omega/2\pi = 0.04$ Hz, $a = 0.67$, same as figure 5-42 but with larger side bands in b) at $(\omega_0 \pm \Omega/2)/2\pi = 0.70 \pm 0.02$ Hz and in d) at $(\Omega/2)/2\pi = 0.02$ Hz. Left sidebands in b) are consistently larger than the right ones.

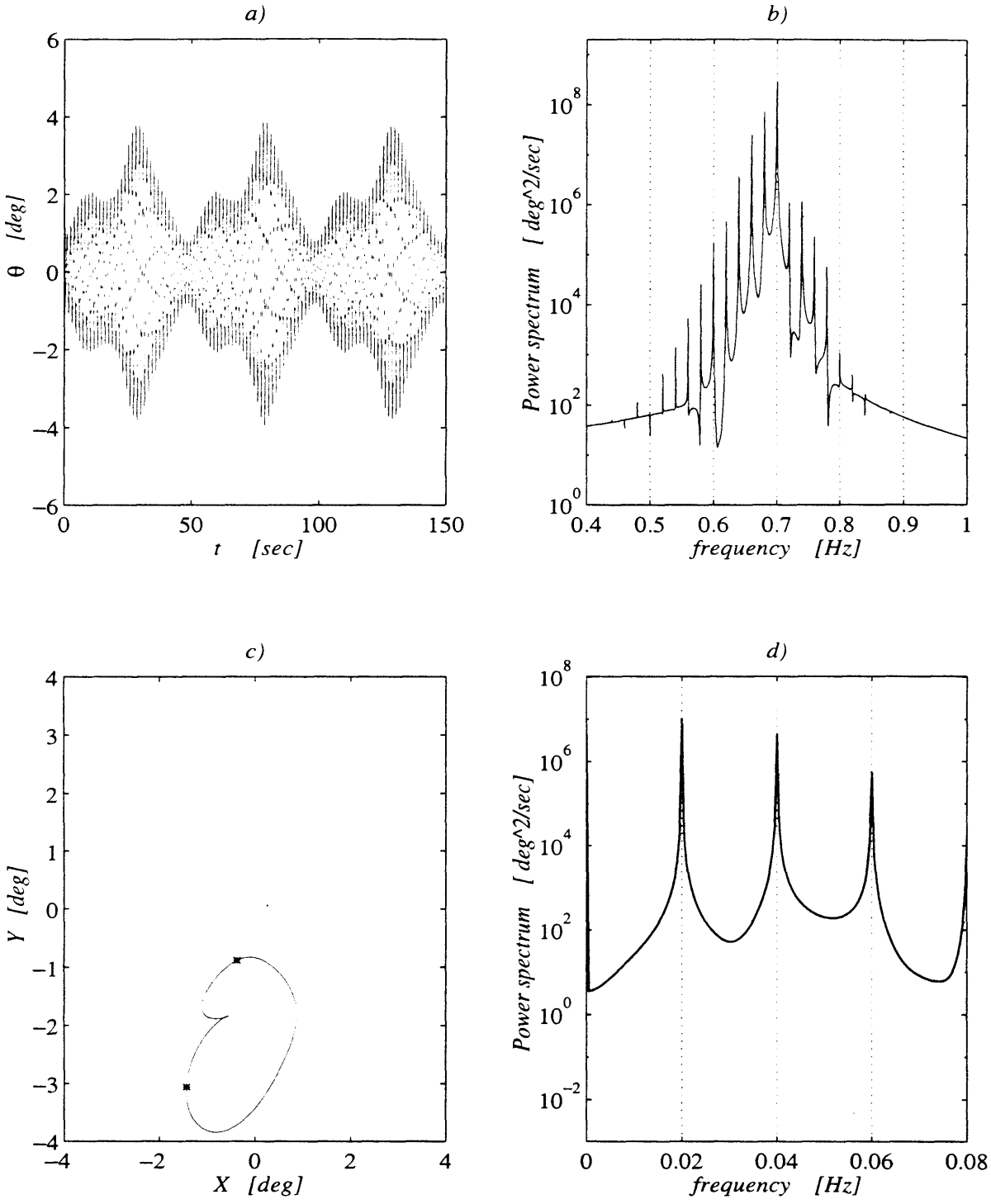

Figure 5-44: $\Omega/2\pi = 0.04$ Hz, $a = 0.72$, same as figure 5-42 but in b) the subharmonic side bands at $(\omega_0 \pm \Omega/2)/2\pi = 0.70 \pm 0.02$ Hz are larger than the synchronous at $(\omega_0 \pm \Omega)/2\pi = 0.70 \pm 0.04$ Hz; c) the trajectory does not loop twice anymore; d) the response at $(\Omega/2)/2\pi = 0.02$ Hz is dominant.

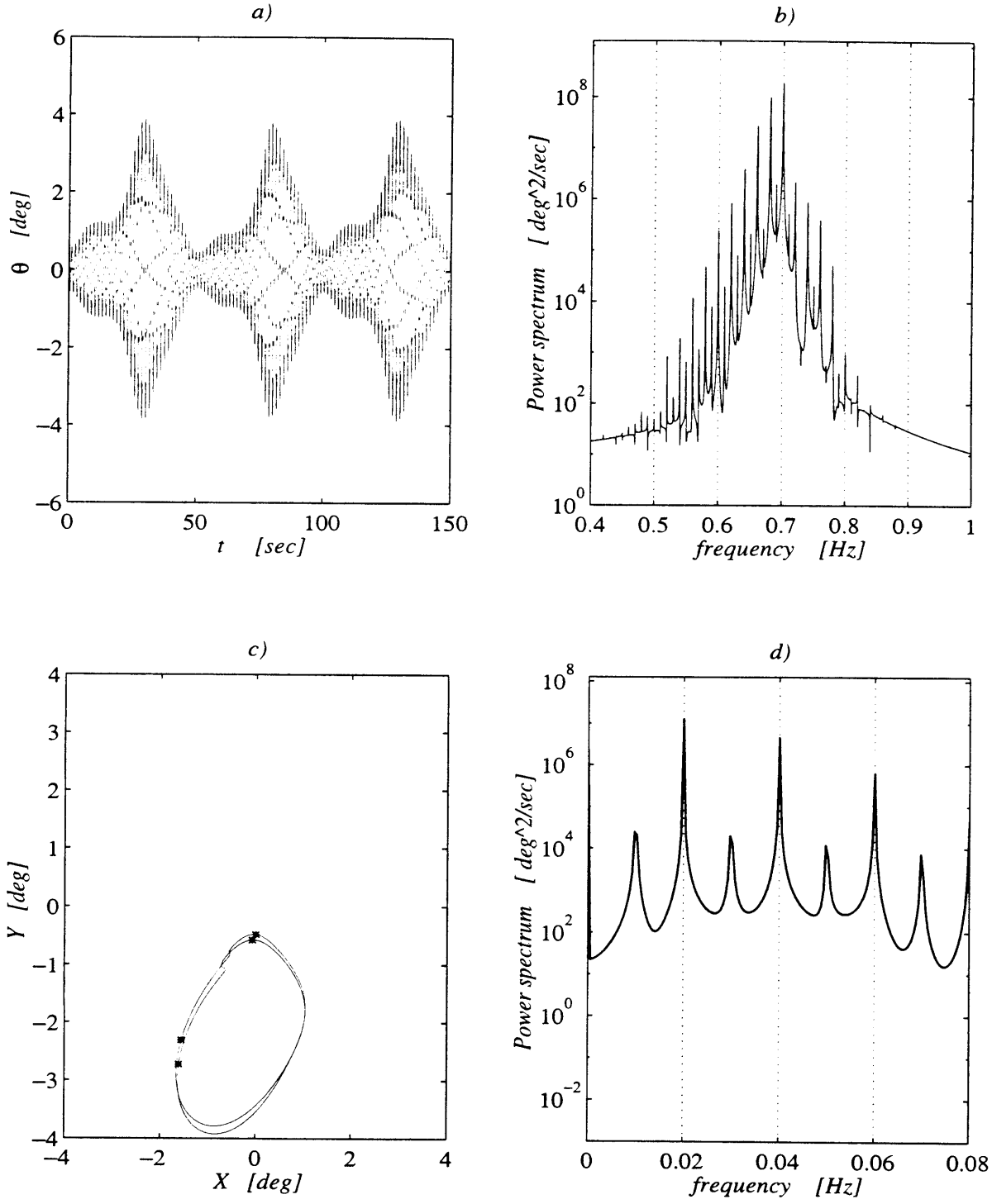

Figure 5-45: $\Omega/2\pi = 0.04$ Hz, $a = 0.77$, period four response. b) small band is born at $(\omega_0 \pm \Omega/4)/2\pi = 0.69$ Hz; c) four fixed points in the Poincaré map; d) subarmonic at $(\Omega/4)/2\pi = 0.01$ Hz is evident.

$(\Omega/2)/2\pi = 0.02$ Hz and at its higher harmonics.

Chaos is fully developed when $a = 0.81$, as can be seen in figure 5-47. The spectrum in b) maintains its peak at $\omega_0/2\pi = 0.70$ Hz but is broad banded. In c) the strange attractor occupies the four quadrants of the phase plane and in d) the noise level is almost uniform, but for a dominant peak at $\Omega/2\pi = 0.04$ Hz. Note how the strange attractor resembles the phase plane of figure 5-2b for the hamiltonian chaos. Indeed homoclinic tangle means infinite transverse intersections of the stable and unstable manifolds that are born when forcing breaks the homoclinic connection of figure 5-2b.

As was shown in the $\Omega \sim a$ plane of figure 5-37, there is an interval of a, in which period-four occurs. Figure 5-48, for $a = 0.87$, shows that this period-four occurs with a downshift by $(\Omega/4)/2\pi = 0.01$ Hz of the central peak response. This can be seen in b) where the peak of the spectrum is at $(\omega_0 - \Omega/4)/2\pi = 0.69$ Hz and there is no energy at $\omega_0/2\pi = 0.70$ Hz. Figure c) justifies this observation because the orbit is now symmetric with respect to the origin and has no offset anymore. Indeed in d) the dominant harmonic is at $(\Omega/4)/2\pi = 0.01$ Hz and there is no response at $\Omega/2\pi = 0.04$ Hz!

We increase a and chaotic motion occurs again. However, figure 5-49b) and d) show, for $a = 0.97$, that the maximum energy is still around $(\omega_0 - \Omega/4)/2\pi = 0.69$ Hz. Even further, when $a = 1.00$, the chaotic motion presented in figure 5-50 has the energy peak of the peak in b) shifting down to $(\omega_0 - \Omega/2)/2\pi = 0.68$ Hz; this shows in d) as a larger energy content at $(\Omega/2) = 0.02$ Hz. This shift, still in a broad-banded spectrum of a chaotic motion, is more pronounced in figure 5-51 for $a = 1.06$.

A slight increase of a by 0.01 completes the frequency downshift. At $a = 1.07$ figure 5-52a) shows that the time series modulation is again periodic and b) shows the frequency peak at $(\omega_0 - \Omega/2)/2\pi = 0.68$ Hz and the complete depletion of energy at $\omega_0/2\pi = 0.70$ Hz. Indeed, the trajectory in c) is symmetrical and has no offset and the envelope spectrum in d) shows no energy at $\Omega/2\pi = 0.04$ Hz! For larger modulational amplitudes a, the response stays subharmonic in the envelope and with the peak shifted by $(\Omega/2)/2\pi = 0.02$ Hz, as can be checked in figure 5-53 for $a = 1.20$. The time series is equivalent to a carrier signal at $\omega_0 - \Omega/2$ modulated at Ω, contrasting the fact that the forcing has carrier frequency $2\omega_0$ and is modulated at Ω.

The scenario depicted from picture 5-40 to 5-53 occurs also at other frequencies for different ranges of a, as is portraied in figures 5-36 and 5-37.

We now attempt a more quantitative comparison with the experiments. Are the theoretical and measured amplitudes of the limit cycles comparable in size? If a strange attractor exists now, does its shape and size compare and, finally, is the downshift phenomenon observed for large modulational amplitude actually taking place?

Consider figure 5-54 for the same parameters of figure 5-40, $\Omega = 0.04$ Hz and $a = 0.47$. The size and modulation of the theoretical time series, slightly overpredicts

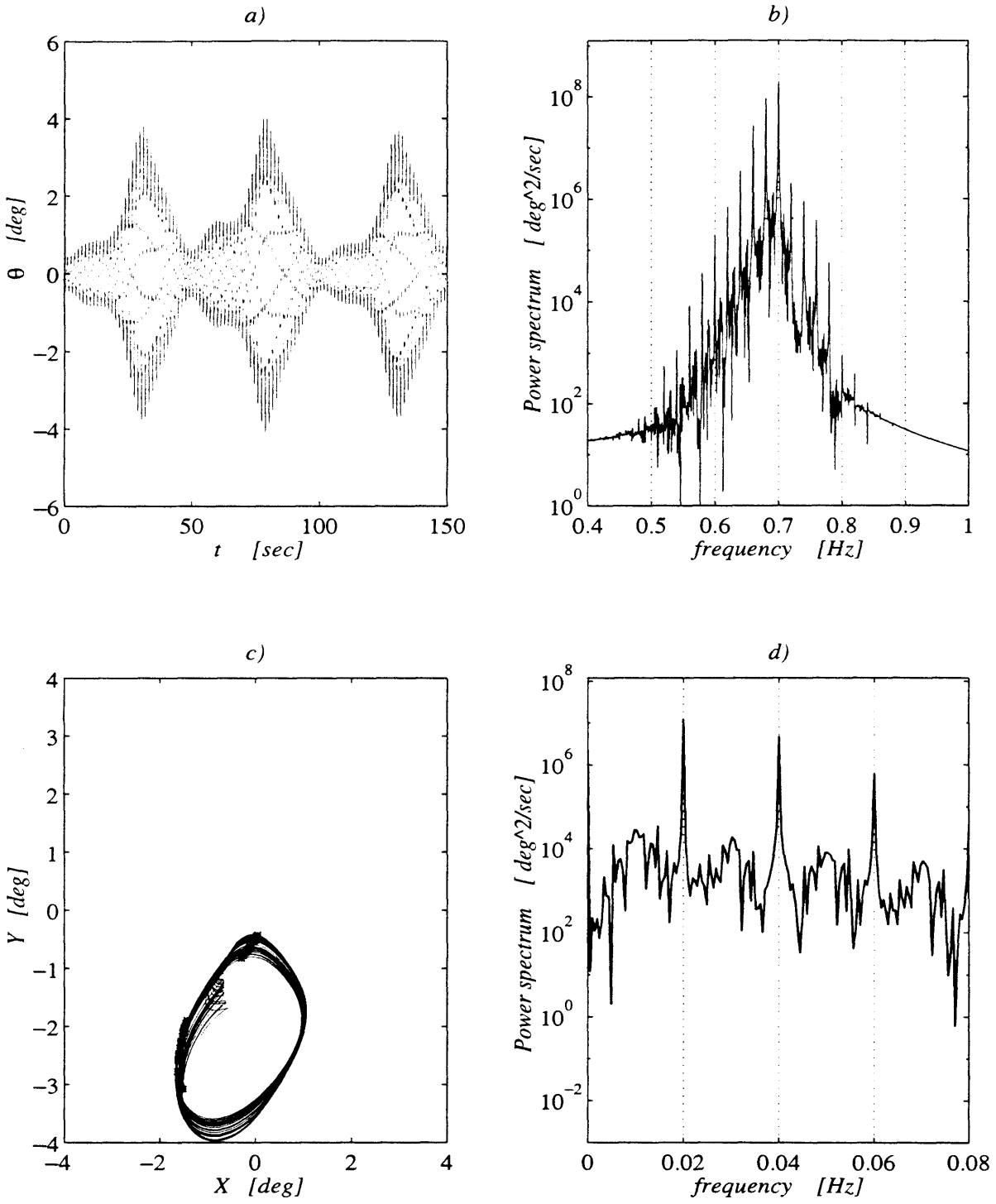

Figure 5-46: $\Omega/2\pi = 0.04$ Hz, $a = 0.78$, nonperiodic motion has started. a) time series does not repeat itself; b) the noise under the side bands is appreciable; c) the Poincaré map shows a strange attractor, the trajectory is still offset; d) the spectrum is broad banded with dominant peaks at $(\Omega/2)/2\pi = 0.02$ Hz and its higher harmonic.

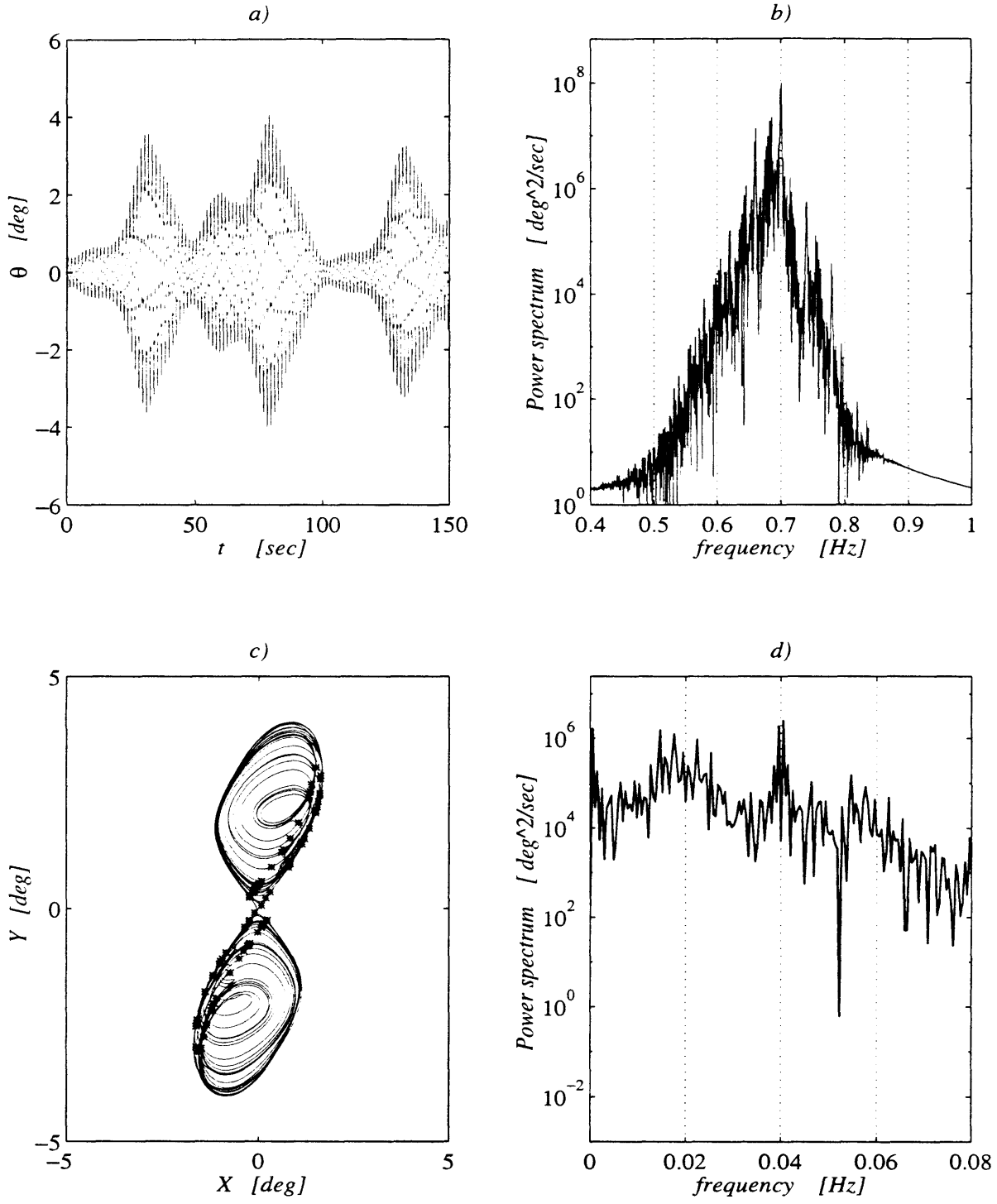

Figure 5-47: $\Omega/2\pi = 0.04$ Hz, $a = 0.81$, chaotic motion. b) the spectrum mantains its peak at $\omega_0/2\pi = 0.70$ Hz but is broad banded; c) strange attractor; d) the noise level is almost uniform, but for a dominant peak at $\Omega/2\pi = 0.04$ Hz.

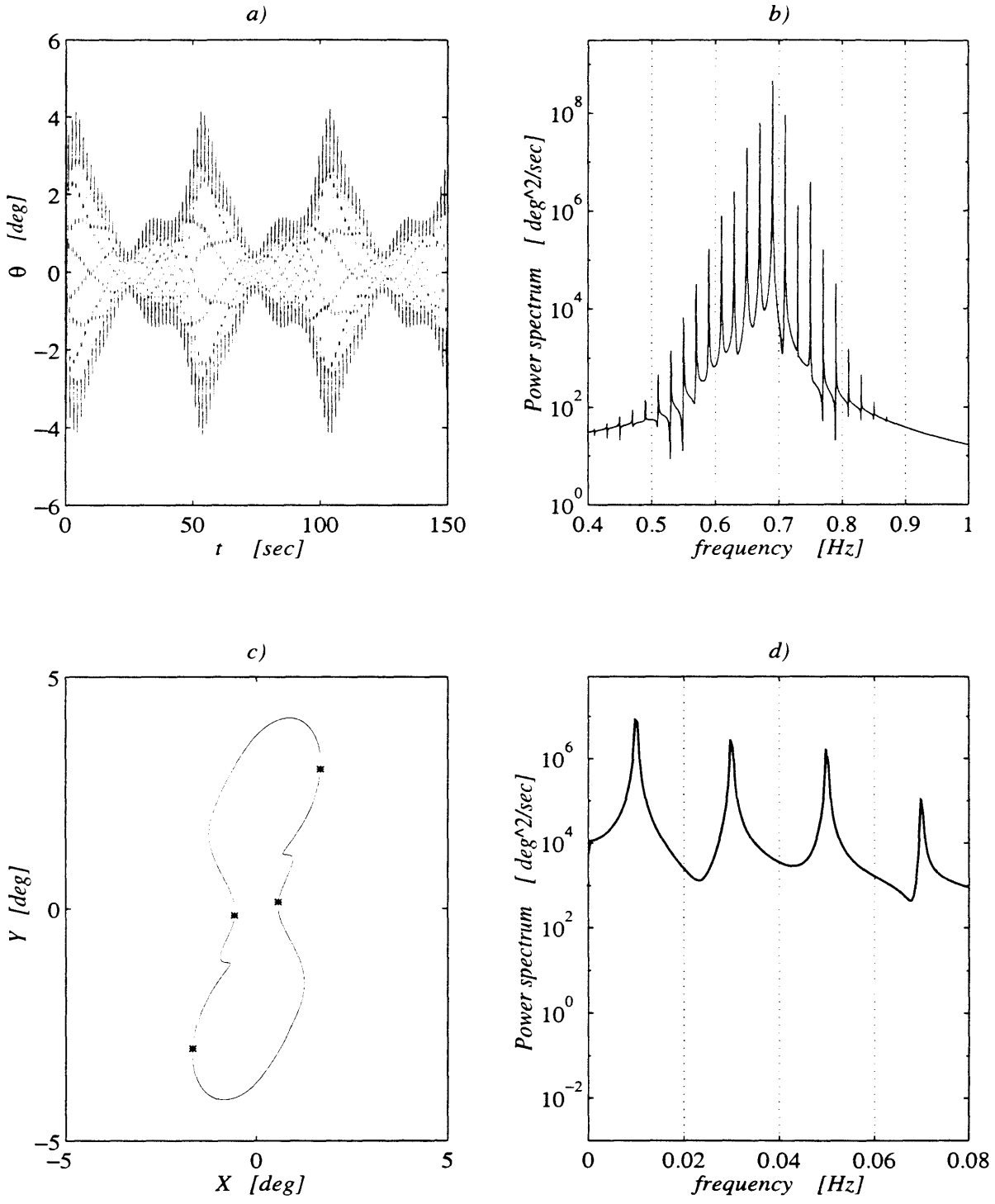

Figure 5-48: $\Omega/2\pi = 0.04$ Hz, $a = 0.87$, period four and downshift by $(\Omega/4)/2\pi = 0.01$ Hz. b) the peak of the spectrum is at $(\omega_0 - \Omega/4)/2\pi = 0.69$ Hz, there is no energy at $\omega_0/2\pi = 0.70$ Hz; c) the orbit is now symmetric with respect to the origin; d) the dominant harmonic is at $(\Omega/4)/2\pi = 0.01$ Hz, there is no response at $\Omega/2\pi = 0.04$ Hz!

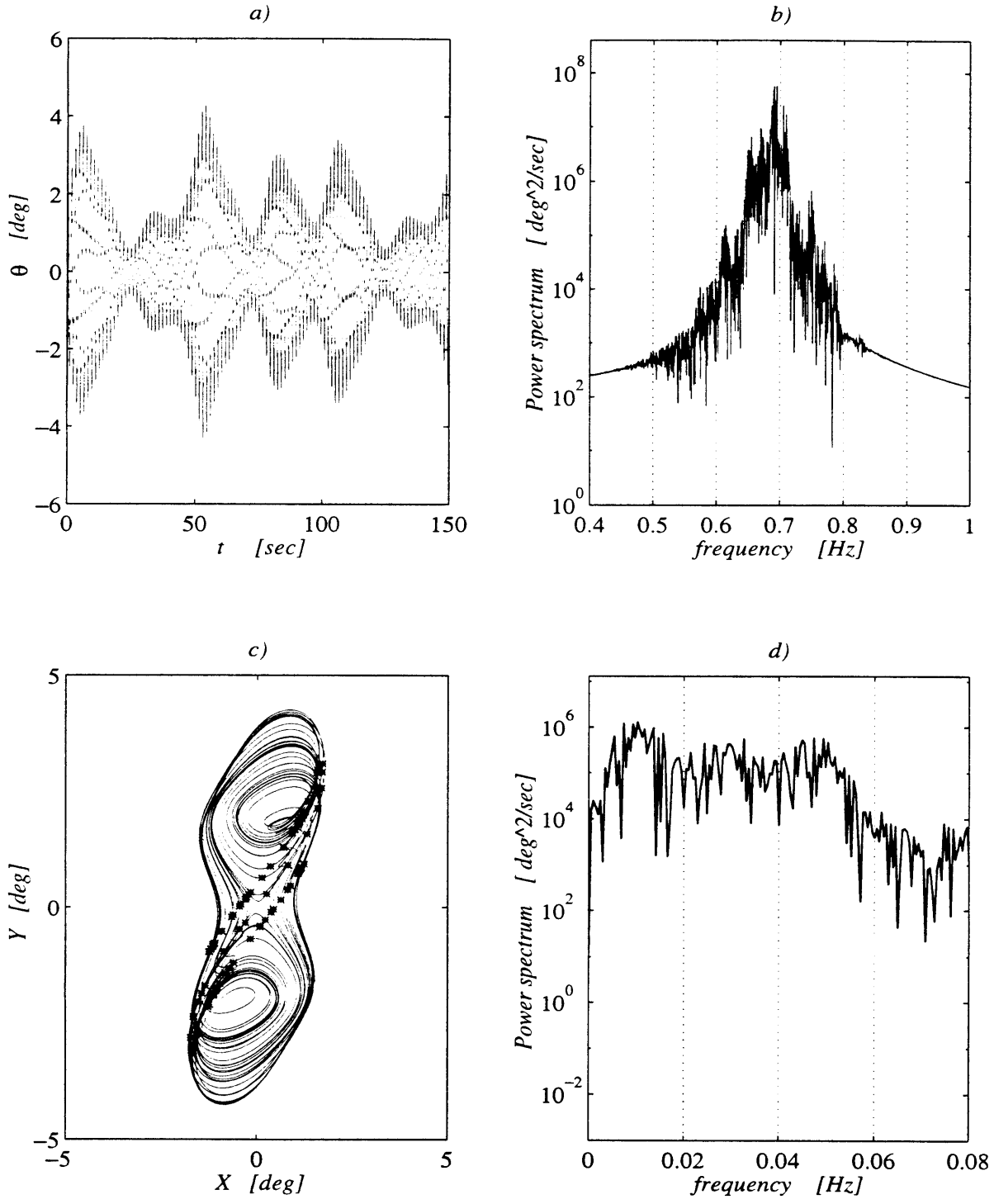

Figure 5-49: $\Omega/2\pi = 0.04$ Hz, $a = 0.97$, chaotic motion again; the maximum energy is still around $(\omega_0 - \Omega/4)/2\pi = 0.69$ Hz, as b) and d) show.

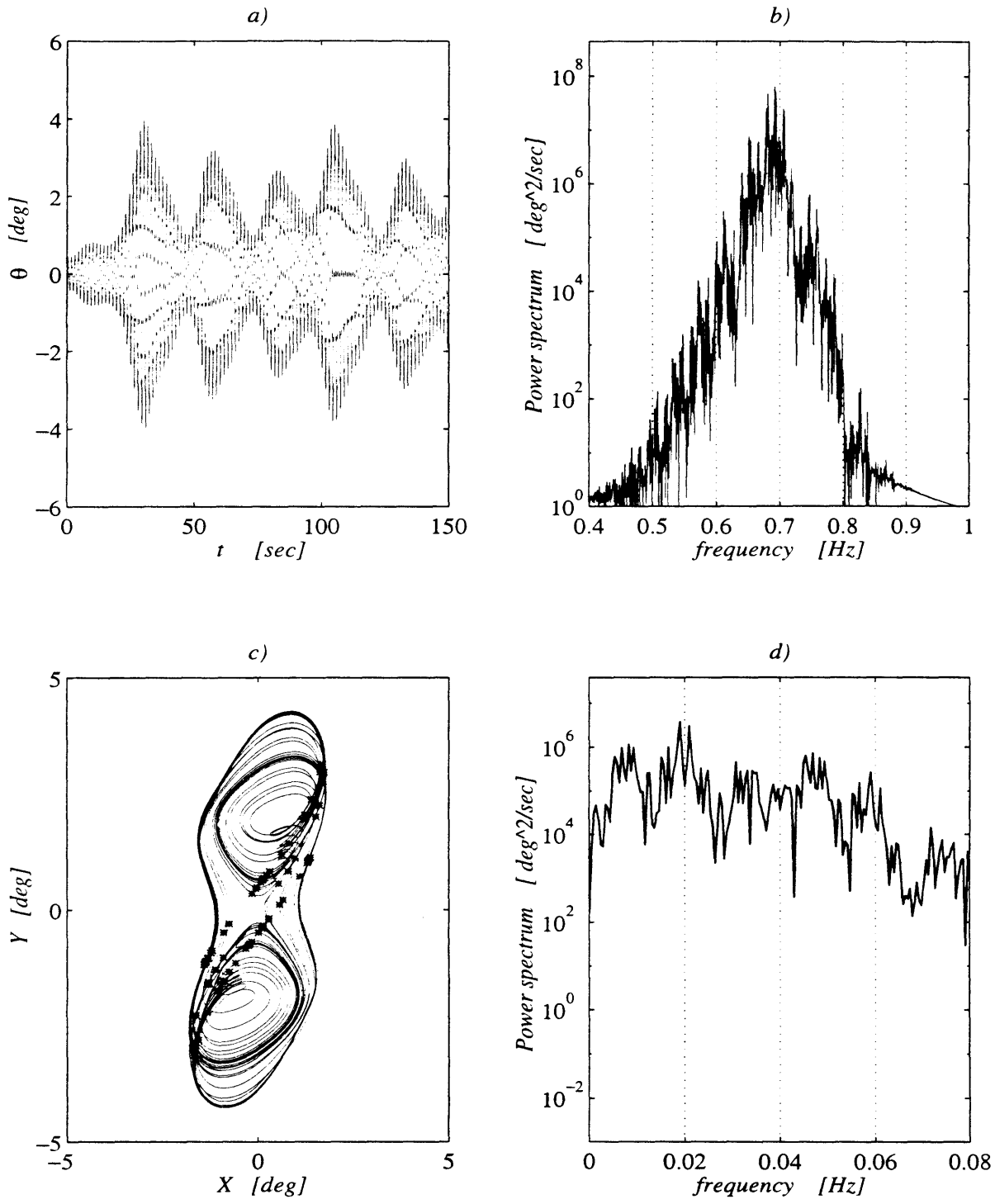

Figure 5-50: $\Omega/2\pi = 0.04$ Hz, $a = 1.00$, chaotic motion like in figure 5-49, but now in b) the energy peak is shifting down to $(\omega_0 - \Omega/2)/2\pi = 0.68$ Hz which shows in d) as a larger energy content at $(\Omega/2)/2\pi = 0.02$ Hz.

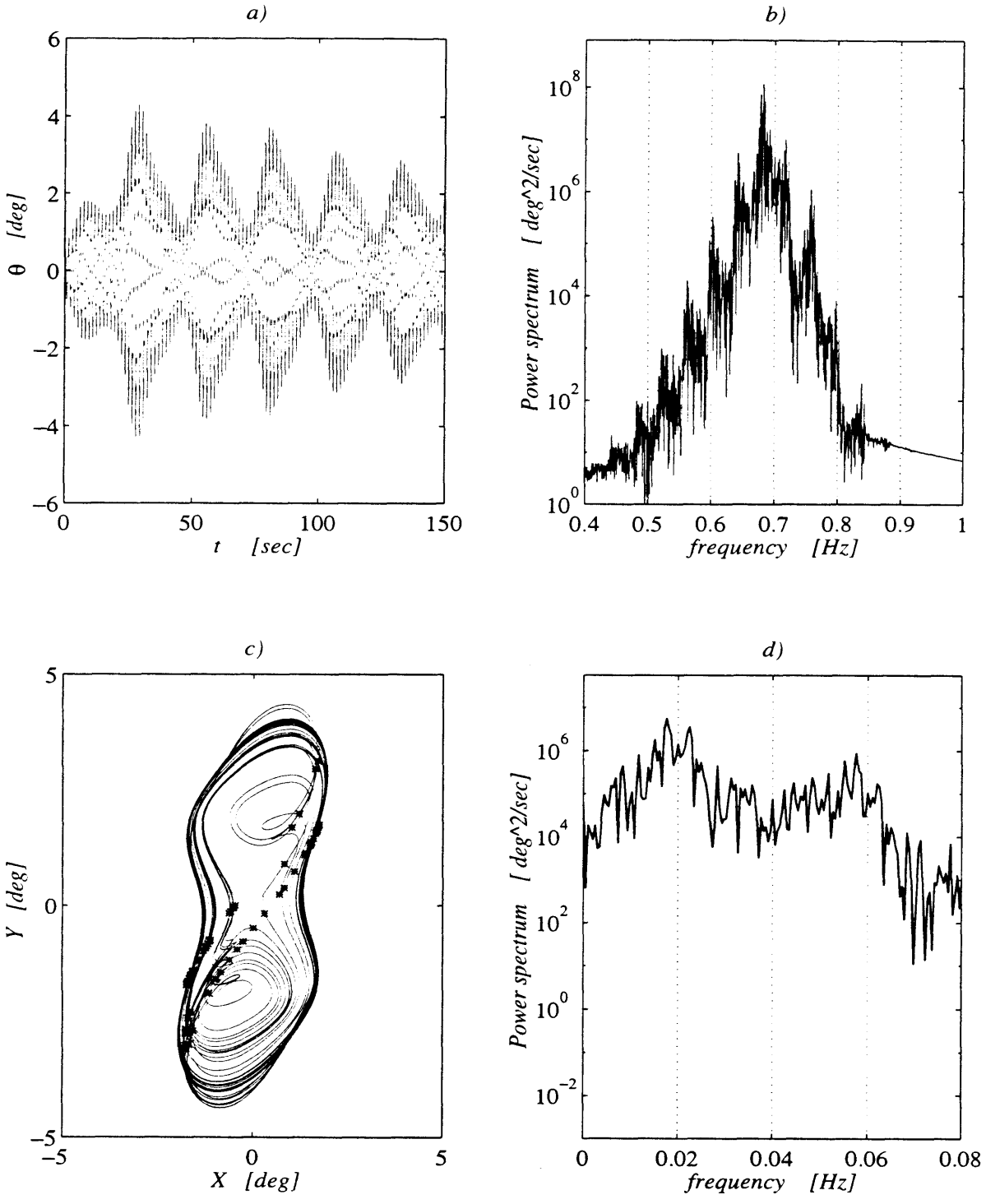

Figure 5-51: $\Omega/2\pi = 0.04$ Hz, $a = 1.06$, same as in figure 5-50, but now the shift is more pronounced.

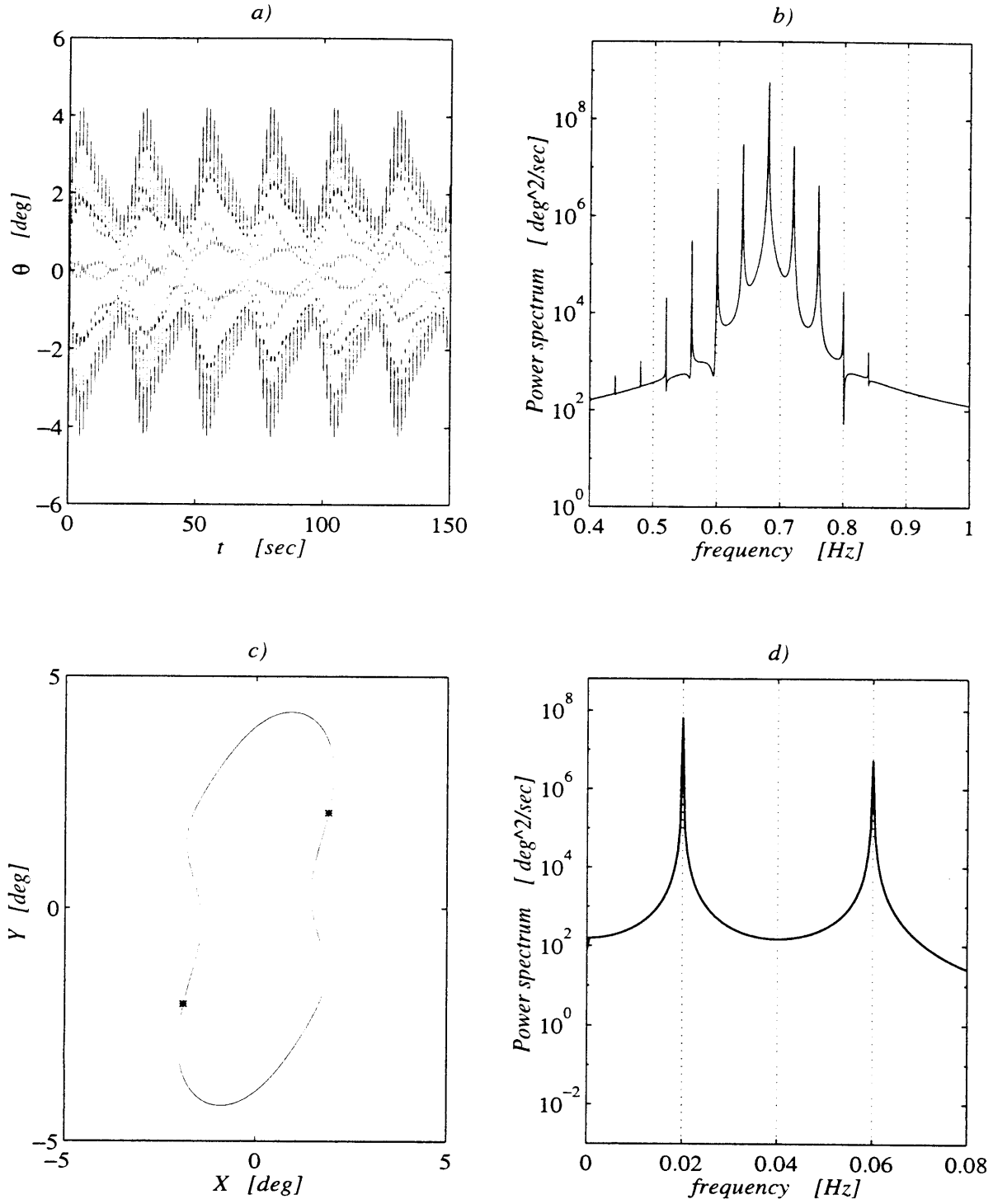

Figure 5-52: $\Omega/2\pi = 0.04$ Hz, $a = 1.07$, the downshift is completed. a) the time series modulation is periodic with period $2\pi/\Omega = 35.71\ldots$; b) the frequency peak is at $(\omega_0 - \Omega/2)/2\pi = 0.68$ Hz and there is no energy at ω_0; c) Poincaré map and trajectory are symmetric with respect to the origin, no offset; d) there is no energy at $\Omega/2\pi = 0.04$ Hz!

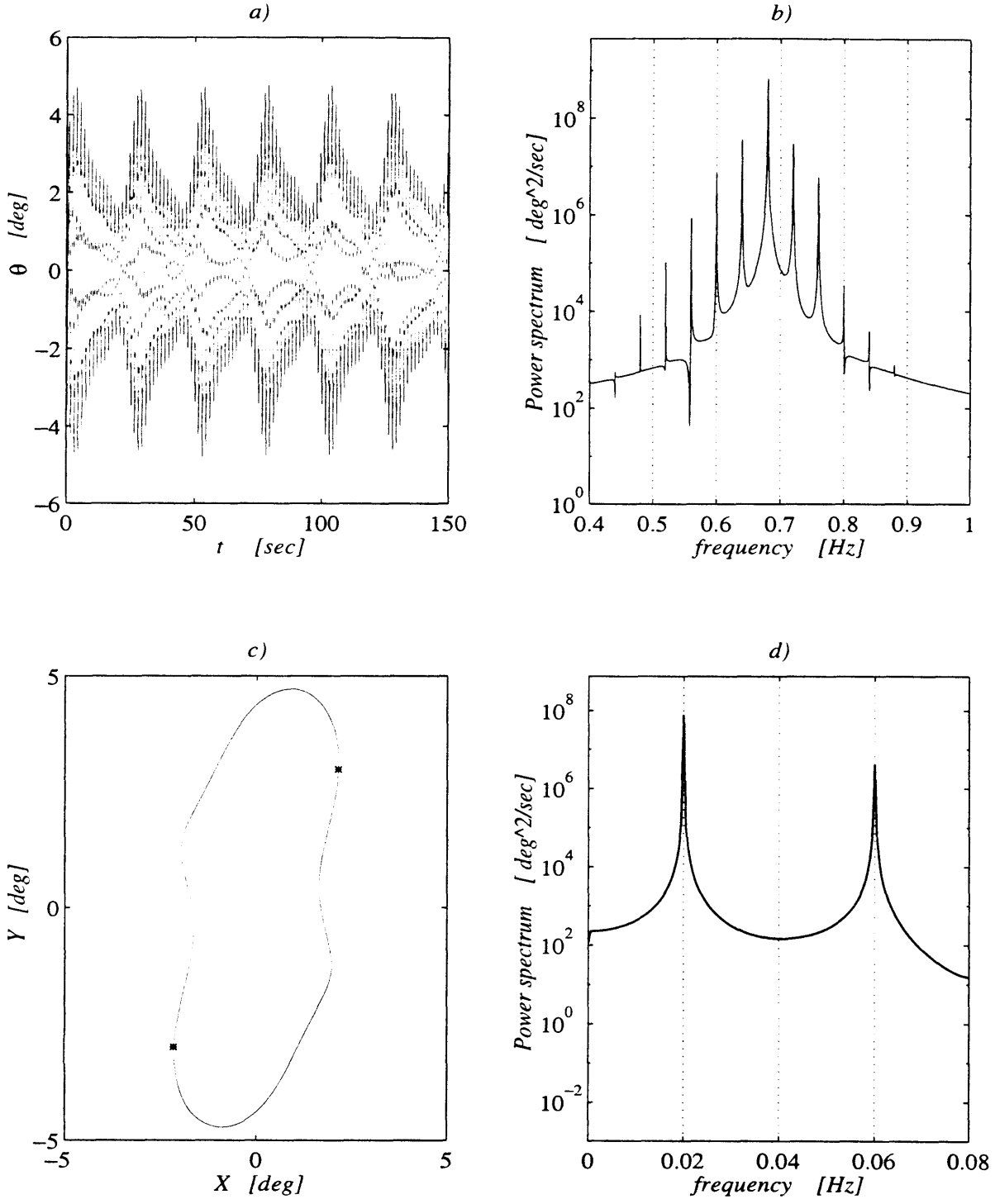

Figure 5-53: $\Omega/2\pi = 0.04$ Hz, $a = 1.20$; for larger modulational amplitudes a, the response stays subharmonic in the envelope and with the peak shifted by $(\Omega/2)/2\pi = 0.02$ Hz.

the experimental values. The offset from the origin of the theoretical limit cycle in figure 5-40c) is 2.45 deg and the average radius of the limit cycle is 1.00 deg, while in the experimental case the offset is 1.9 deg and the radius is 0.7 deg. The spectra in b) and d) are quite similar in showing the side bands at 0.70 ± 0.04 Hz. Note that in the experiments the left sideband is larger than the right sideband, confirming the theory.

The experimental limit cycle is rotated towards the negative X axis with respect to the theoretical one (c.f. figure 5-40). This is a consequence of the choice of the initial point in the experimental time series. Tran(1996) has shown that as the initial point is varied along the time series, the experimental limit cycle rotates around the origin, keeping the same distance from it. The choice of the initial point is arbitrary in the experiments, since it was not possible to keep track of the phase of the incident wave. On the other hand, in the theory the phase relation between the incident wave and the trapped wave is well defined by the form of the perturbation expansion. Therefore there is no ambiguity in the location of the two theoretical limit cycles. We stress that this indetermination has no effects on the spectra, the size of the attractors and their distance from the origin.

Next, for larger amplitude, $a = 0.57$, the experimental figure 5-55 show a period two modulational response. The spectrum in b) has two small side bands at $(\omega_0 \pm \Omega/2)/2\pi = 0.70 \pm 0.02$ Hz, smaller than the ones at $(\omega_0 \pm \Omega)/2\pi = 0.70 \pm 0.04$ Hz, but sufficient to generate the second loop in the phase trajectory of c). The asymmetry of the side bands is again confirmed. The Poincaré map has two points and the envelope spectrum in d) presents has a distinct peak at $(\Omega/2)/2\pi = 0.02$ Hz. The excursion of the time series, size of the spectra, Poincaré section and phase trajectory are comparable to 5-42, predicted for a slightly higher amplitude, $a = 0.64$.

In the theoretical computation we have seen that as the amplitude of the modulation increases to $a = 0.72$, the size of the subharmonic sidebands at $(\omega_0 \pm \Omega/2)$ in the time series spectrum grow, the smaller loop of the phase trajectory shrink and the frequency peak at $\Omega/2$ in the envelope spectrum becomes dominant. Indeed the experimental plots of figure 5-56 confirm all these when $a = 0.61$. The subharmonic modulational response at $\Omega/2$ is larger than the synchronous at Ω as both the spectra in b) and d) show. Again, the asymmetry of the side-bands is observed. The smaller loop of the phase plane trajectory is almost gone and the trajectory is heart-shaped. The Poincaré section still consists of two points.

Then, around $a = 0.77$ transition to chaotic oscillation occurs in the experiments. Figure 5-57a) shows the nonperiodic modulation of the time series, while b) its broad-banded spectrum, which still retains the dominant peaks at $\omega_0/2\pi = 0.70$ Hz and $(\omega_0 \pm \Omega)/2\pi = 0.70 \pm 0.02$ Hz. The phase trajectories in c) shapes as a strange attractor and the map has a fractal structure. Finally, the spectrum of the envelope has energy distributed continuosly at all the frequencies, but retains most of his energy around Ω, $\Omega/2$. This figure should be compared with figure 5-46 for $a = 0.78$.

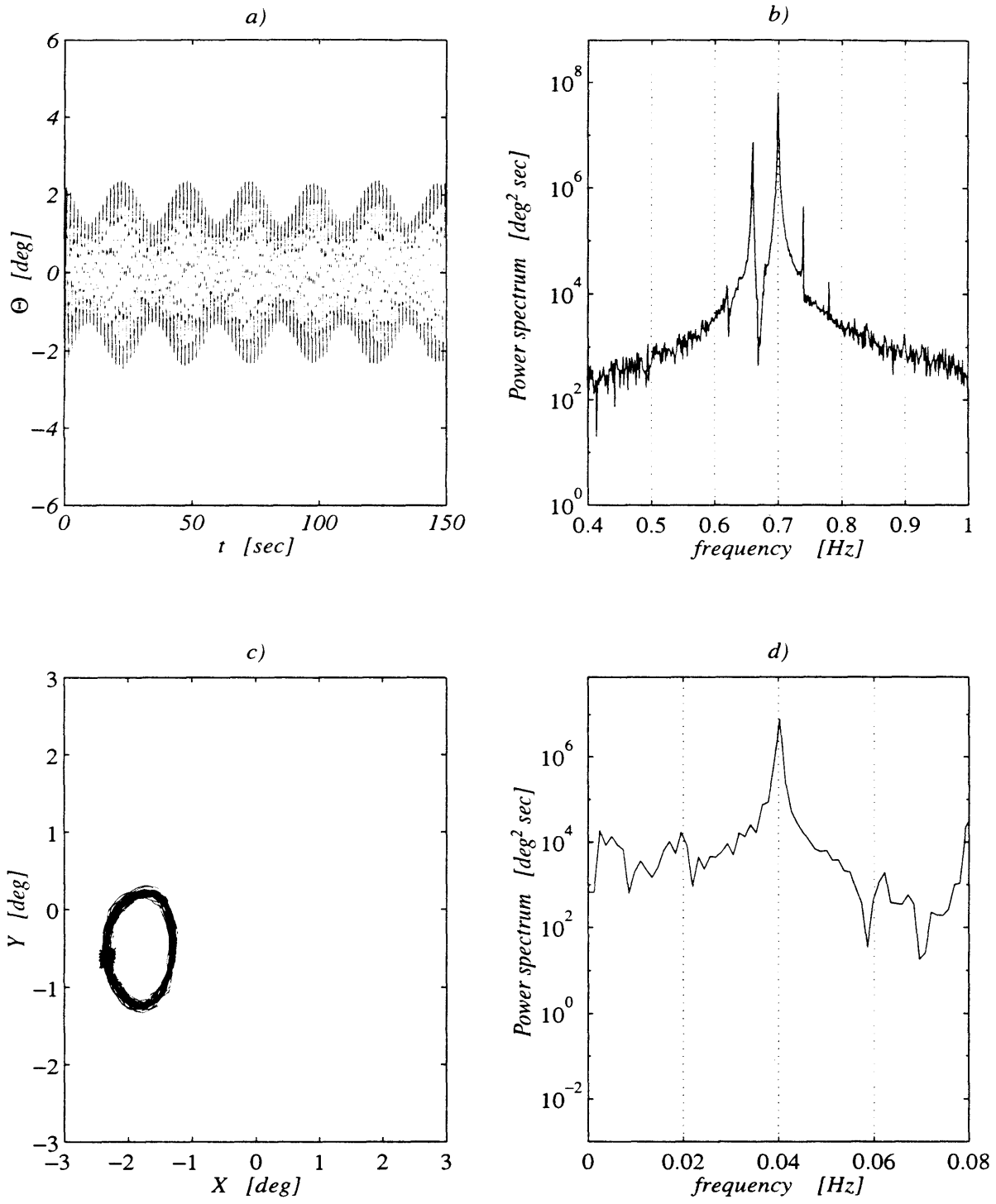

Figure 5-54: Experiments for $\Omega/2\pi = 0.04$ Hz, $a = 0.47$; a) experimental time series showing synchronous modulation; b) spectrum of the time series showing asymmetry in the side-bands c) Poincaré section has one point; d) spectrum of the envelope has one peak at $\Omega/2\pi = 0.04$ Hz.

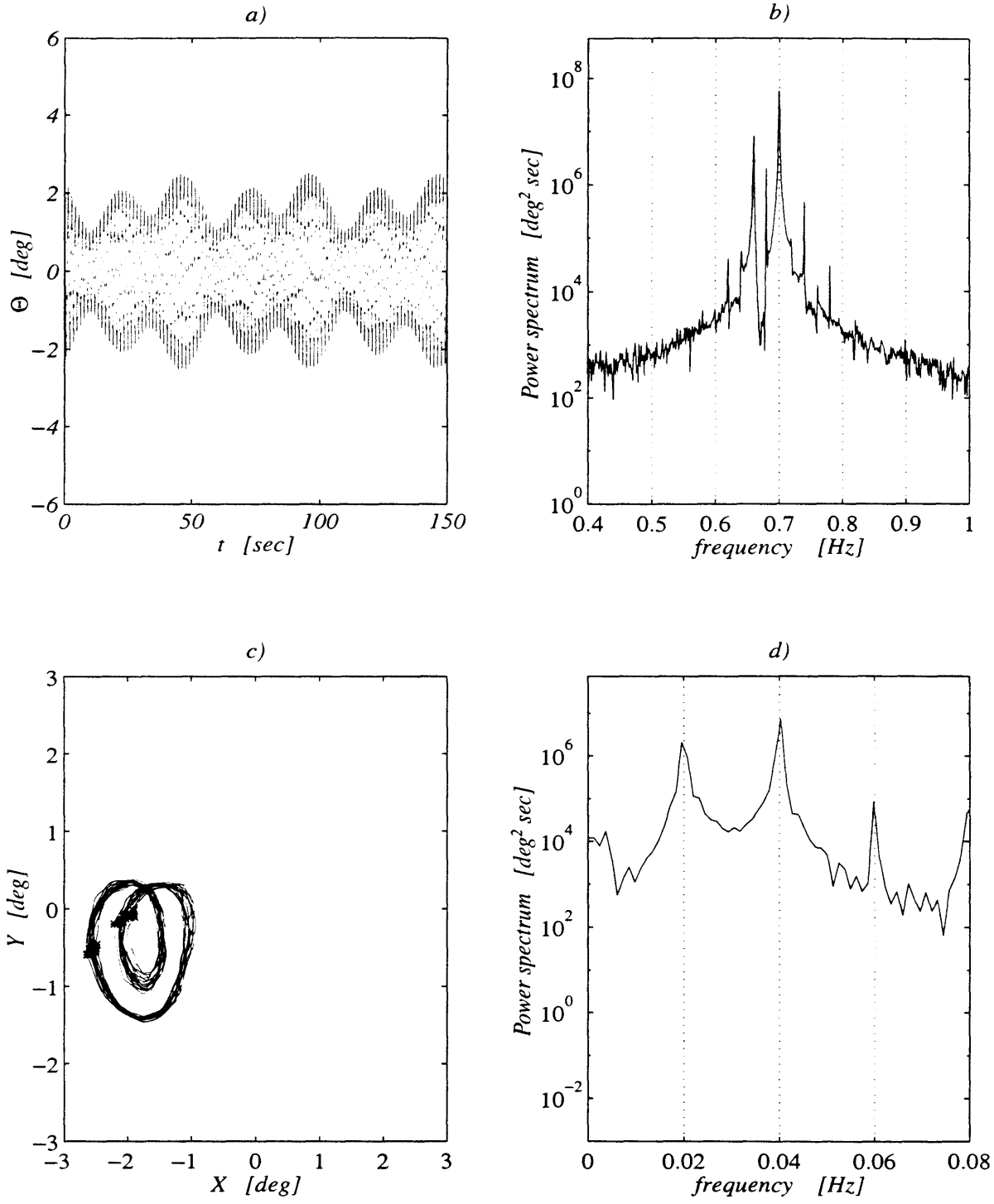

Figure 5-55: Experiments for $\Omega/2\pi = 0.04$ Hz, $a = 0.57$; period-two modulational response. a) the experimental time series shows period doubled envelope; b) the spectrum has two small side bands at $(\omega_0 \pm \Omega/2)/2\pi = 0.70 \pm 0.02$ Hz; c) the phase trajectory has a second loop and the Poincaré section is made of two points; d) spectrum of the envelope has a distinct peak at $(\Omega/2)/2\pi = 0.02$ Hz.

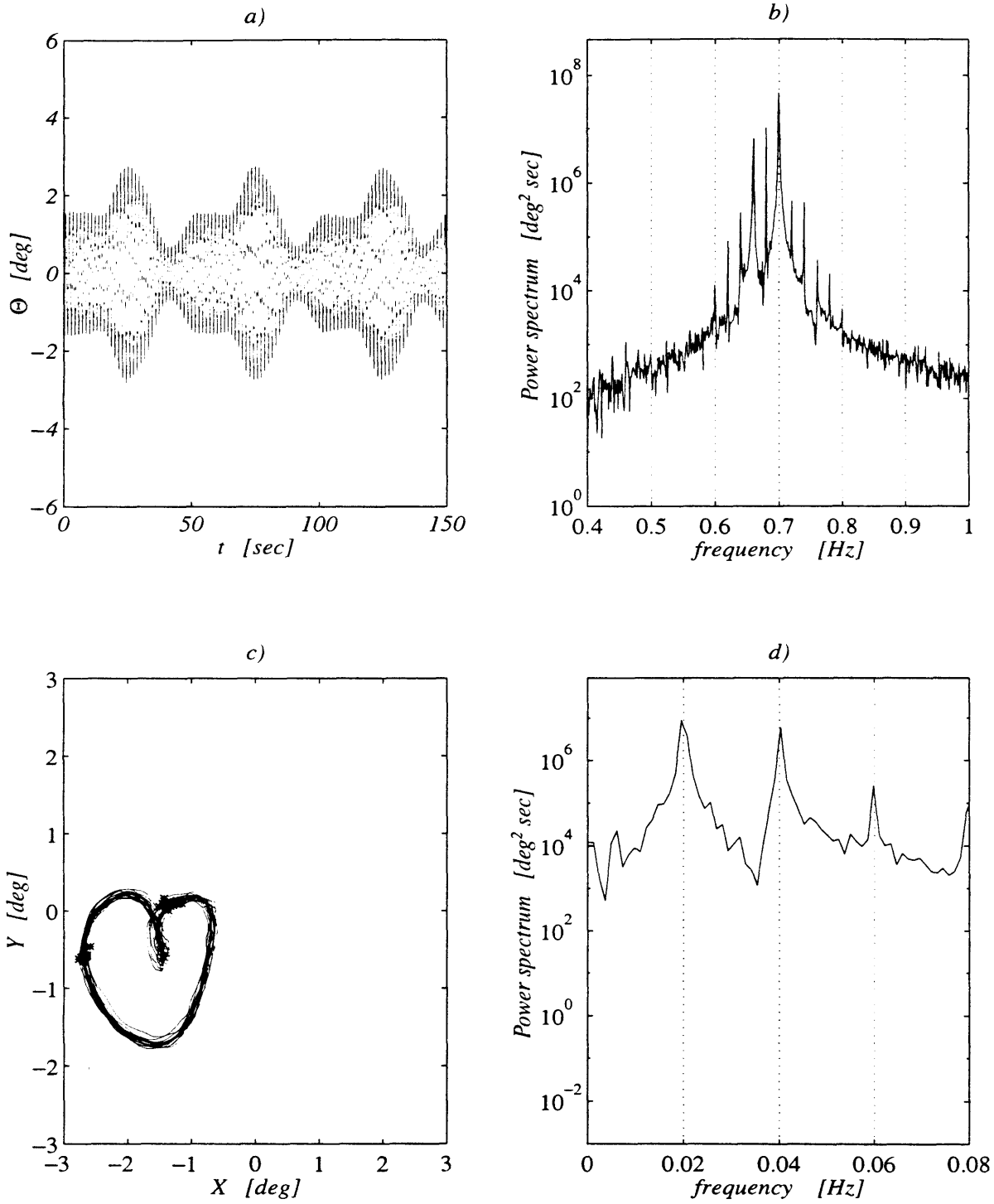

Figure 5-56: Experiments for $\Omega/2\pi = 0.04$ Hz, $a = 0.61$; period doubled response. b) spectrum of the time series has sidebands at $(\omega_0 \pm \Omega/2)/2\pi = 0.70 \pm 0.02$ Hz larger than those at $(\omega_0 \pm \Omega)/2\pi = 0.70 \pm 0.04$ Hz; c) the second loop of phase trajectory has shrunk; d) envelope spectrum shows large subharmonic peak at $(\Omega/2)/2\pi = 0.02$ Hz.

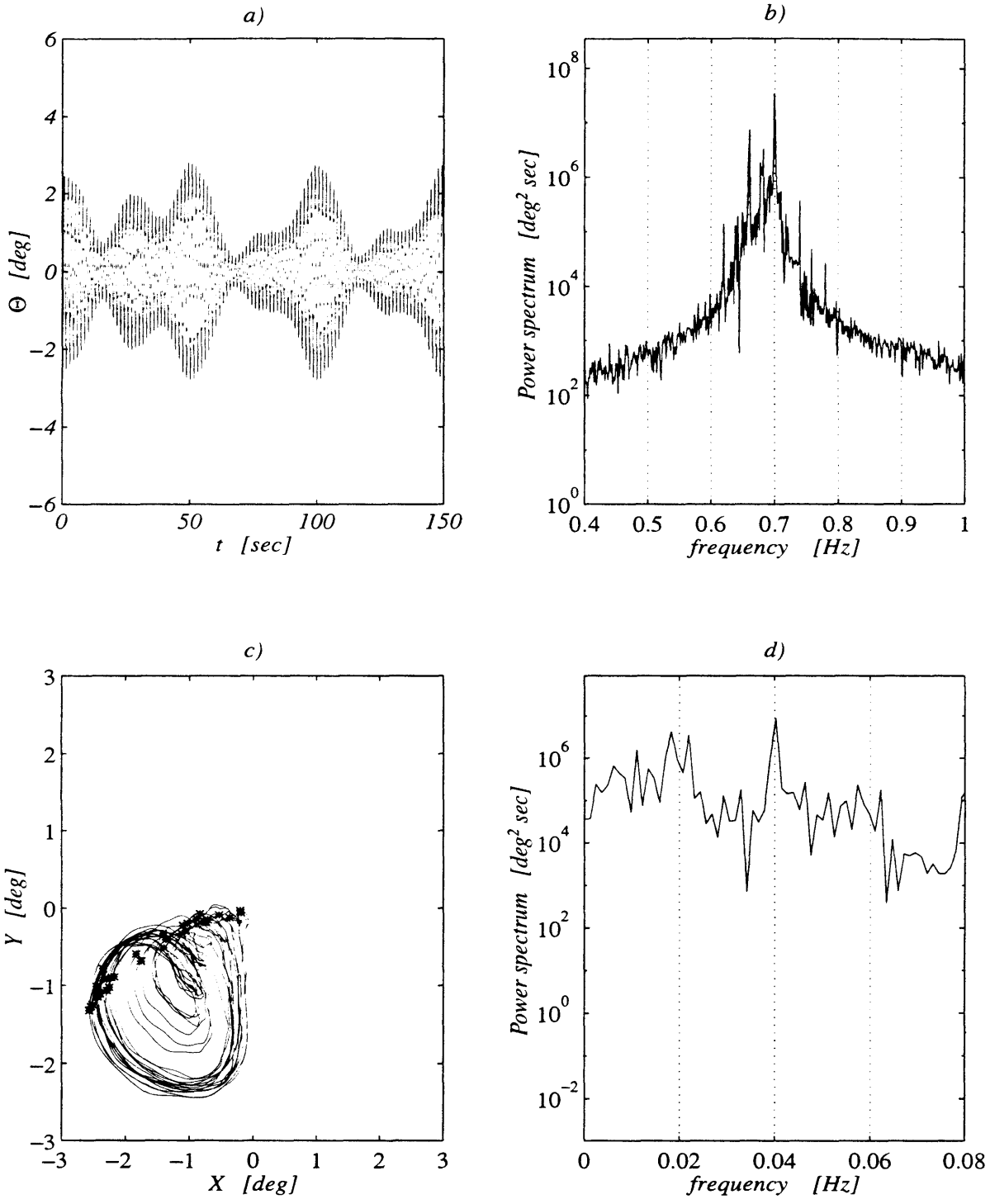

Figure 5-57: Experiments for $\Omega/2\pi = 0.04$ Hz, $a = 0.77$; transition to chaotic oscillations. a) time series envelope is non-periodic; b) energy spectrum has considerable energy away from carrier and modulational frequency; c) early stage of the strange attractor with fractal Poincaré section; d) broad-banded spectrum of the envelope.

Chaotic oscillations then maintain until $a = 1.02$. The next three figures, 5-58, 5-59 and 5-60 show the realization for respectively $a = 0.87$, 0.93 and 1.02 of the strange attractor. The three time series have all non-periodic modulation, their spectra are broad banded and the Poincaré maps have a fractal structure. Finally the spectra of the envelope are all broad-banded, with energy distributed over all the low-modulational frequency range. The time series a), their spectra b), the envelope spectra d) and most of all the shape and size of the strange attractor are in broad agreement with theoretical predictions, as shown by figures 5-47, 5-49, 5-50 and 5-51.

The period-four trajectory bifurcating from the period-doubled (denoted in figure 5-37 by a 4), has been observed in two cases only by a small peak at $(\Omega/4)/2\pi = 0.01$ Hz but with a Poincaré section not defined enough to see the four points. The symmetrical period-four phase trajectory corresponding to figure 5-48 was not observed.

Note that the frequency downshift for large amplitude of modulation is observed, as figure 5-61 and 5-62 show respectively for $a = 1.03$ and $a = 1.30$. The phase trajectories in 5-61c) and 5-62c) are symmetrical and have Poincaré sections with two points. The shape and size are close to the ones predicted theoretically (c.f. figures 5-52 and 5-53 for $a = 1.02$ and $a = 1.20$). Also, the spectrum of the envelope in 5-61d) and 5-62d) has a dominant peak at $(\Omega/2)/2\pi = 0.02$ Hz and no energy at $\Omega/2\pi = 0.02$ Hz. The spectra of the time series in 5-61b) and 5-62b) both have peaks at $(\omega_0 - \Omega/2)/2\pi = 0.68$ Hz with two side-bands shifted by $\pm\Omega/2\pi = \pm 0.04$ Hz. Again, like in the theory, the left side-band is larger then the right one.

Summing up, the experiments of Tran(1996) have essentially confirmed the theoretical findings. In particular the same sequence of bifurcations leading to nonperiodic motion have been found and the theoretical strange attractors and phase planes shapes have been reproduced. Besides, the downshift of the central peak of the response occurs in a manner perfectly similar to the theoretical predictions. In all the experimental spectrum the left side band is always larger than the right side band, confirming yet another aspect of the theoretical findings.

More comparisons of the theory and experiments are collected in Appendix F.

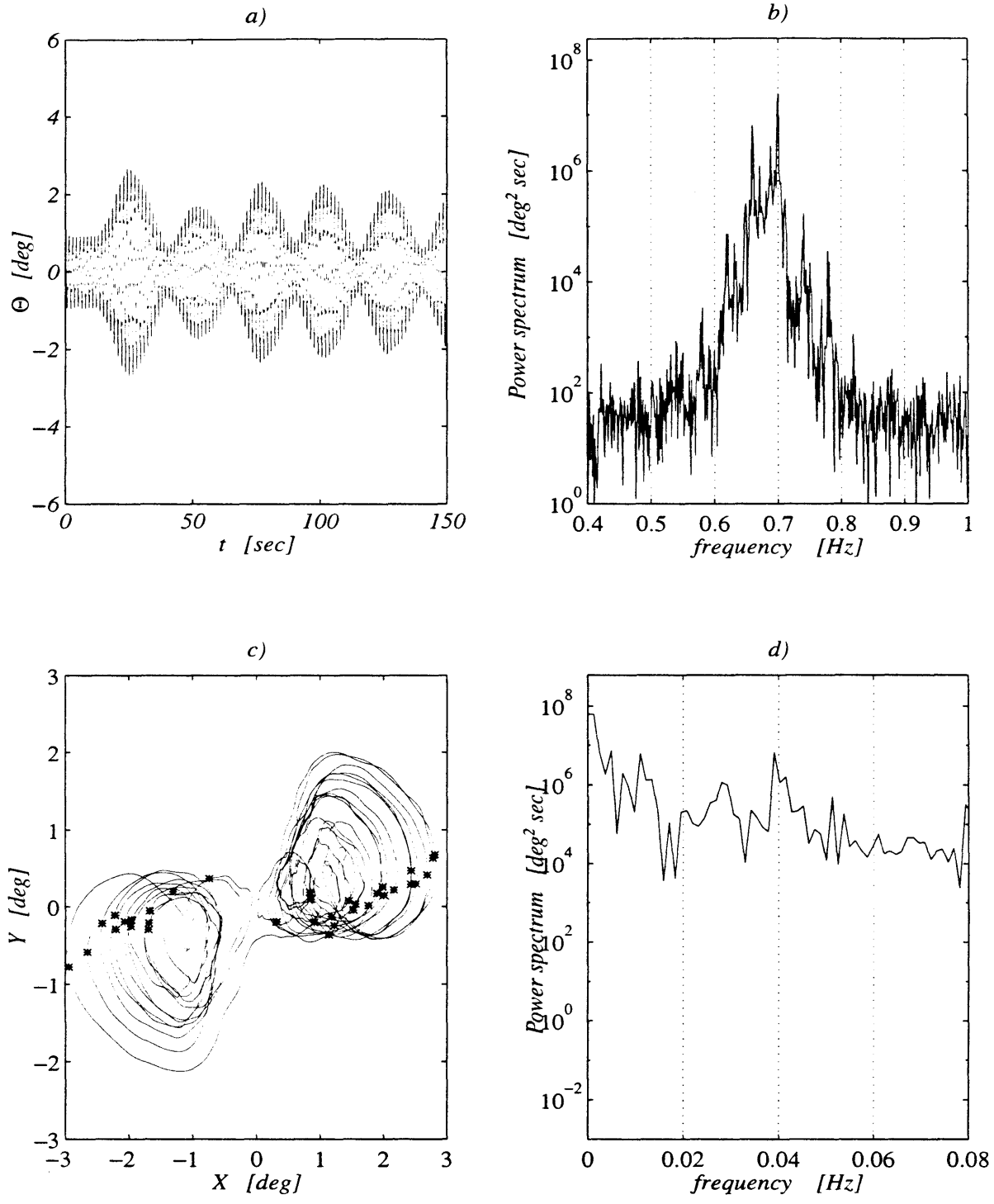

Figure 5-58: Experiments for $\Omega/2\pi = 0.04$ Hz, $a = 0.87$; chaotic oscillations. a) time series envelope is non-periodic; b) energy spectrum has considerable energy away from carrier and modulational frequency; c) experimental strange attractor with fractal Poincaré section; d) broad-banded spectrum of the envelope.

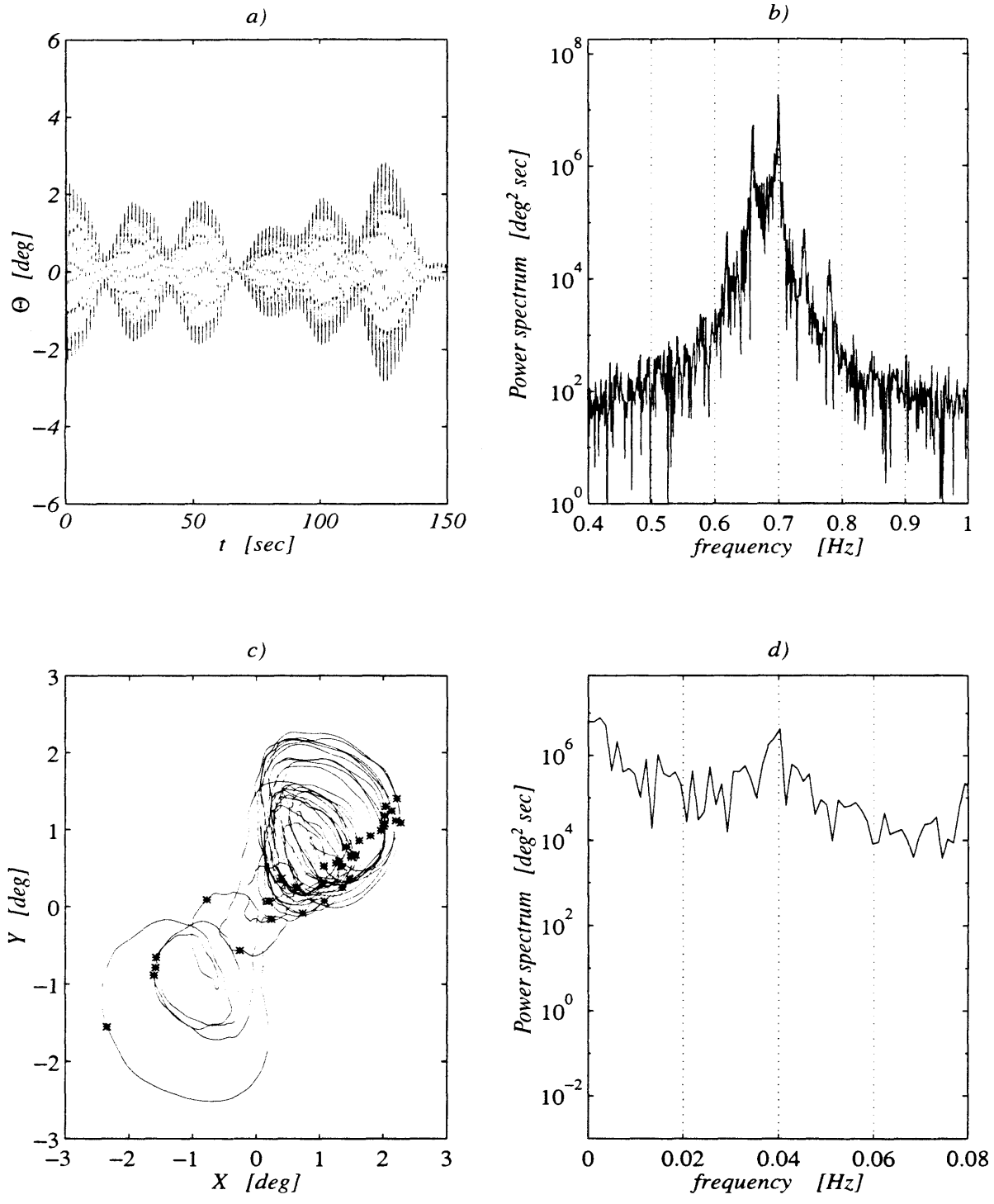

Figure 5-59: Experiments for $\Omega/2\pi = 0.04$ Hz, $a = 0.93$; same as figure 5-58. Energy is continuously spread across the frequencies both in b) and d).

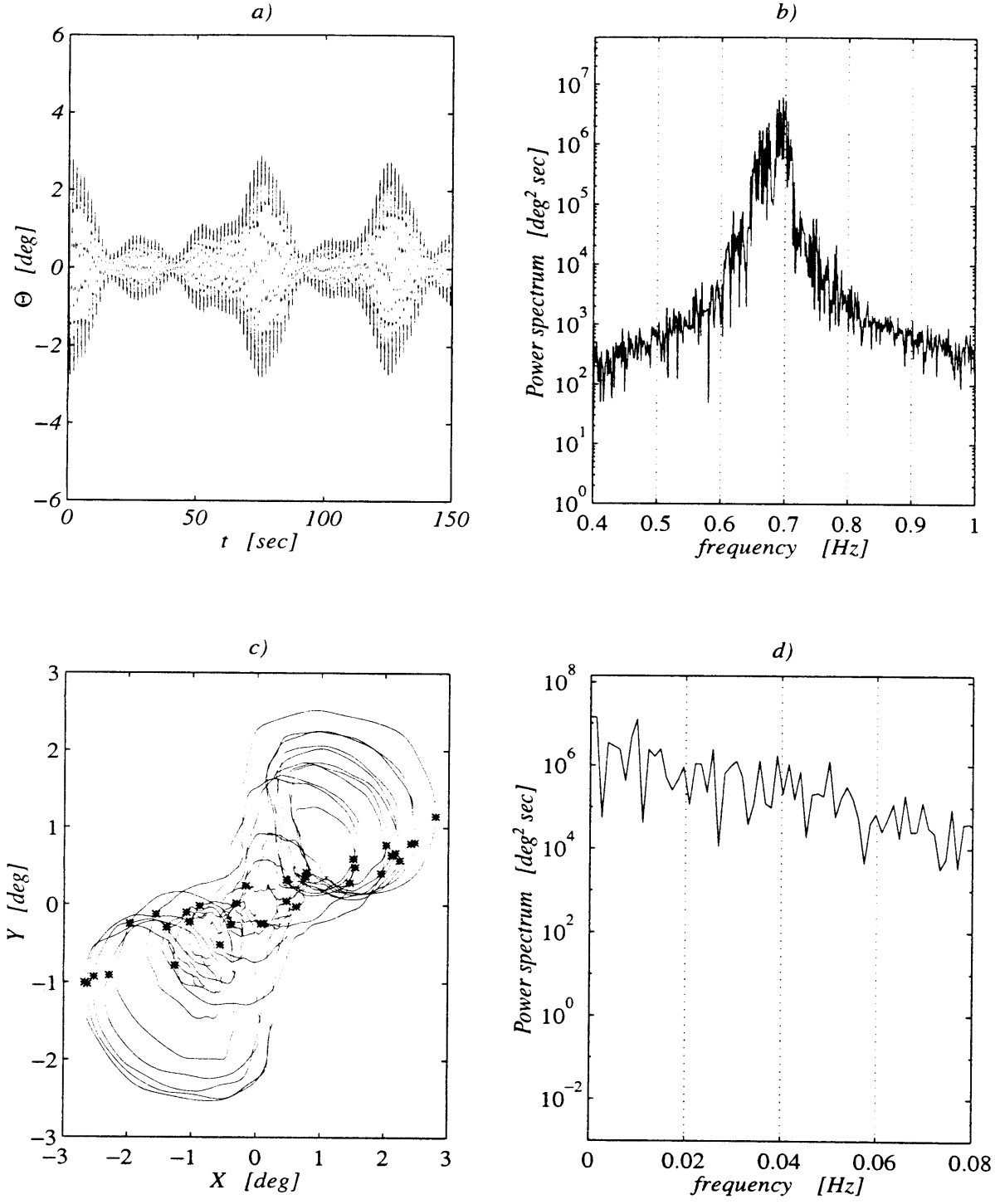

Figure 5-60: Experiments for $\Omega/2\pi = 0.04$ Hz, $a = 1.02$; same as figure 5-58. Energy is continuosly and homogeneously spread across the frequencies both in b) and d). The form of the strange attractor in c) is reaffirmed.

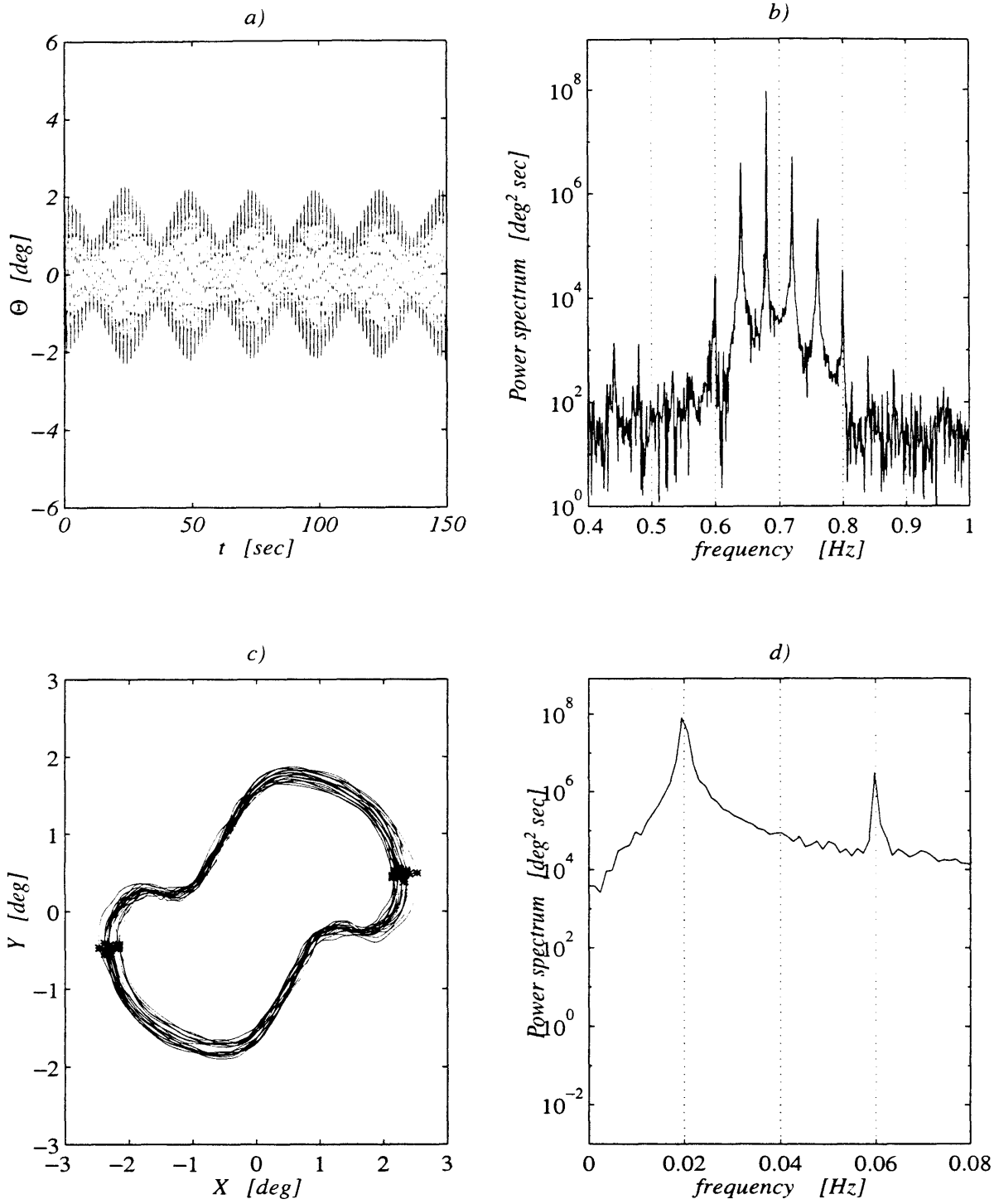

Figure 5-61: Experiments for $\Omega/2\pi = 0.04$ Hz, $a = 1.03$; frequency down-shift. a) time series show no apparent sign of period doubled envelope, but the fast oscillation is at $\omega_0 - \Omega/2$ rather than at ω_0; b) the central peak is at $(\omega_0 - \Omega/2)/2\pi = 0.68$ Hz and side bands are at $\pm\Omega/2\pi = \pm 0.04$ Hz from it; c) period-two Poincaré section with phase trajectory symmetric with respect to the origin; d) peak response is at $(\Omega/2)/2\pi = 0.02$ Hz and no energy response at $\Omega/2\pi = 0.04$ Hz

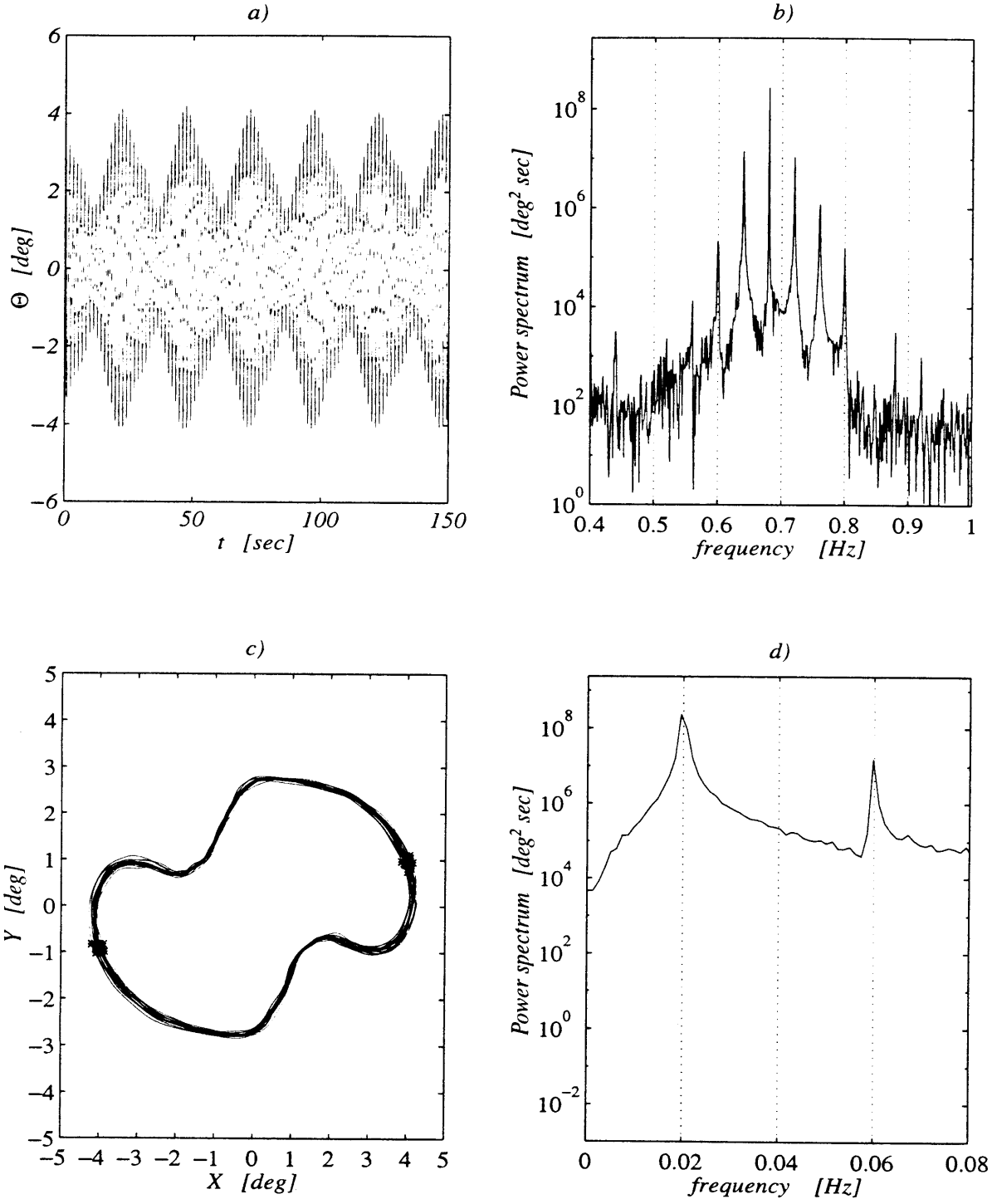

Figure 5-62: Experiments for $\Omega/2\pi = 0.04$ Hz, $a = 1.30$; same as figure 5-61. The time series, spectra, size of pahse trajectory are all larger for larger modulational amplitude.

Chapter 6

Conclusions

By choosing a realistic model of the Venice Gates, we have considered the out-of-phase subharmonic motion due to forcing by the incident waves.

We have shown that this phenomenon is due to a nonlinear mechanisms of resonance, and we have developed linear and nonlinear theories that describe and parametrically quantifies its dependence on the gates, the channel and the incident wave characteristics.

Any articulated array of gates possesses several eigen–modes of oscillation whose frequencies are determined by the linear eigen–value theory of Chapter 1 and section 2.5.2. These eigen–modes are characterized by trapped waves around the gates, so that energy does not leak away. We have shown that gate inclination is irrelevant and that even vertical gates, as long as they are articulated, can support natural modes of trapped waves. Laboratory evidence has then confirmed that subharmonic oscillation of vertical gates forced by normally incident waves is through the resonance of the trapped wave.

The linear theory has allowed a discussion of the parametric dependence of the eigen–frequency on the gate and channel characteristics. We have shown that gates with larger inertia have smaller eigen–frequency, i.e. heavier gates oscillate slower. For fixed inertia of the gate, an increase in the displaced volume induces an increase in the eigen–frequency. Indeed, in this case the restoring force increases and the gate takes a shorter time to move back towards the rest position. The effect of an increase of the gate width is to decrease the frequency. Finally, for fixed gate characteristics, deeper channel are accompanied by higher natural frequencies. This effect is more pronounced for heavier gates.

Based on the linear theory, we are able to suggest possible solution for the unwanted resonances. The first solution is to decrease the natural frequency below the range excitable by the local incident wave frequencies. This can be accomplished either by decreasing the displaced volume and/or the water depth or by increasing the gate inertia and/or gate width. The second solution is to render the gates so buoyant

that their natural frequency is above the cutoff frequency. For the inclined gates, where buoyancy and first moment of the gate are constrained to yield the design inclined equilibrium position, the theory needs to be modified.

We point out that the second solution would not solve completely the problem. In fact, an array of articulated gates has a large number of modes depending on the number of gates in the modal spatial period. The larger the number of gates in a spatial period, the lower the corresponding eigen–frequency. Therefore even if the first few modes could be pushed above the cutoff frequency, some lower frequency modes would then become excitable by the incident wave.

Therefore lowering the eigen–frequency of the first mode is the most viable solution; for inclined gates this can be accomplished by increasing the gate width.

In Chapter 2 we have deduced an evolution equation of the Stuart-Landau type governing the angular motion of the gate system. This evolution equation is common to several other wave phenomena, such as the subharmonic resonance of edge wave on a sloping beach or the Faraday wave in a small container. In the latter cubic radiation damping is absent and damping is given by viscosity only.

In the present context, it was necessary to carry the Taylor expansions of the boundary conditions and of the equation of motion of the gate up to third order. For the kinematic and dynamic conditions of the gate, these expansions were mathematically tractable because the gate has only one degree of freedom, that is roll about a fixed axis at the bottom hinges. The determination of the coefficients of the evolution equation has involved the solution of several diffraction and radiation problems. Because of the simplicity of the boundaries, we have used separation of variables and obtained a series representation of the wave potential. The integration of the wave potential on the fluid boundaries has been carried out numerically. We showed that, at the second order, the trapped wave radiates energy to infinity through its second harmonic and receives it from the incident wave, so that a finite amplitude equilibrium angular displacement is attained.

Knowledge of the evolution equation has allowed the prediction of important quantities such as the frequency band in which the phenomenon occurs and the equilibrium amplitude of the resonated modes and therefore the maximum opening between contiguous gates. It has been possible to discuss the parametric dependence of these quantities on the gate and channel characteristics for given incident wave amplitude.

We have shown that the heavier the gate (the smaller the natural frequency) the larger the angular response to a given incident wave amplitude. Heavier gates oscillates slower and with larger amplitude. We have also shown that, for any fixed value of the inertia, an increase in the displaced volume induces a decrease in the response, which comes with an increase of the natural frequency. Same effect can be achieved by an increase of the water depth.

We discussed the frequency band in which the trapped wave is unstable and showed that as the inertia increases (the response increases) it decreases and eventually be-

comes zero when the natural period and the angular response become infinite! Heavier gates have a larger response which is increasingly more difficult to excite.

Conversely, for any fixed value of the inertia, an increase of the displaced volume or of the water depth induces an increase in the bandwidth of instability.

This analysis allowed us to design the laboratory experiments that maximize the features of the phenomenon, yet keeping the values comparable with the prototype case. The gate were designed with small inertia and large buoyancy.

More delicate is the choice that minimize the phenomenon, since smaller response is associated with larger instability bandwidth and vice versa. Most of all, we have shown that increasing the gate width with the purpose of decreasing the natural frequency, might come with an undesired increase of the angular response.

In the inviscid theory of Chapter 2, radiation damping is the mechanism which limits the peak amplitude at resonance. Losses due to the viscosity of the fluid also limit the resonated amplitude. The gap between adjacent gates is designed to be thin (of the order of 10^{-1}m) and the corners sharp; localized losses and vortex shedding may become important for out-of-phase motion of large amplitude. In Chapter 3, we have introduced in a systematic way the frictional effects. In a formal perturbation expansion, the boundary layer correction appears in the forcing terms on the boundaries and in the equation of motion at the third order. The resulting evolution equation contains a linear term with real and imaginary parts, which have the effect of limiting the resonated amplitude and shifting the resonance diagram. We have shown that boundary layer effects are more important for low inertia and high buoyancy.

Using a simple model of an oscillating piston, we have included the effect of separation at the gate corners. Its torque acting on the gate generates a quadratic term in the final evolution equation, which limits even further the resonated amplitude.

In Chapter 4 we employed the dynamical system theory to study how different dissipation mechanisms affect the resonance peaks. Compared with the theory of Rockliff(1978) and Miles(1990), the linear dissipation term produces a shift in the resonance curves, reduces the interval in which the resonance occurs and reduces the equilibrium amplitudes. On the other hand the quadratic term only limits the equilibrium amplitude. The experiments of Tran(1996) have given evidence of the hysteresis phenomenon, intrinsic to the Stuart-Landau equation, and confirmed the shape, form and values of the theoretical resonance diagrams. The overall agreement with the experiments is satisfactory, even though the theory slightly overestimates the experimental values. This is due to having neglected other sources of damping such as radiation of higher order harmonics and friction in the hinges and measurement devices. Fitting of the linear and quadratic dissipation coefficients to the data, shows that linear, quadratic and cubic dissipation are sufficient to model the phenomenon.

Since the three inlets of the Venice Lagoon are not likely to be subjected to strictly monocromatic waves, we have considered the effects of an incident wave with slowly modulated amplitude, corresponding to a narrow-banded spectrum. With an ampli-

tude periodic in time, the evolution equation becomes a second order nonautonomous dynamical system. Local and global analysis have been used to investigate modulational resonances and transition to chaos.

In order to study modulational resonance, we have extended the multiple scales analysis employed by Trulsen & Mei(1995) to include dissipation. Transition to chaos has been predicted by the Melnikov method and by i.e. extending the work of Gottlieb & Mei(1995) to include linear and quadratic damping. Using the local and global bifurcation criteria, we have individuated region in the parameter plane of modulational frequency versus modulational amplitude in which period doubling cascade leads to chaos.

Extensive numerical investigation of the above parameter plane have confirmed qualitatively the analytical predictions, and delineated the various regions of existence of the different responses. For low modulational amplitude the modulational angular response of the subharmonic eigen–mode is synchronous with the forcing. Increase of the amplitude causes bifurcation (through the temporal resonance mechanisms revealed by the multiple scale analysis of the Stuart-Landau equation) to subharmonic motion and further period doubling until modulational chaos is attained. Above this region of chaos, for modulational amplitude of the same order as the carrier wave amplitude, period doubled response of the envelope is the only response. This last type of long term response is represented by an orbit in the phase plane of the envelope that is symmetric about the origin. We have shown that, in the spectrum of the gate rotation, this corresponds to a downshift of the central frequency from half the incident carrier wave of a quantity equal to half the modulational frequency. The response is in this case much larger than the non-shifted non-resonant response occurring for the same modulational amplitude but at larger modulational frequency.

Numerical findings have shown that for sufficiently high frequency of modulation, no temporal resonances of any kind is possible. This means that large side bands do not alter the resonance phenomenon induced by the carrier wave frequency.

We conclude that in a wide band spectrum with the central peak around twice the natural frequency of the mode, the side band frequencies can modify the ampolitude with qualitative change.

We have shown that in all the theoretically calculated spectra of the subharmonic angular response the left side band is always larger than right one. Such an asymmetry is therefore intrinsic to the nonlinearities of the Stuart–Landau equation.

We remark that period doubling cascade route to chaos, homoclinic tangle, chaotic oscillation and strong period two symmetrical orbits implying downshift have been shown to be all intrinsic features of the sinusoidally forced Stuart-Landau equation.

The experiments of Tran(1996) have successfully confirmed all of the above findings both qualitatively and quantitatively. In particular the same sequence of bifurcations leading to nonperiodic motion have been found and the theoretical strange attractors and phase planes shapes have been reproduced. Besides, the downshift of

the central peak of the response occurs in a manner similar to the theoretical predictions. In all the experimental spectrum the left side band is always larger than the right one, confirming yet another aspect of the theoretical findings.

We have proven that the validity of this weakly nonlinear analysis, and of the evolution equation that it yields, goes well beyond the order of magnitude limits in which it was derived, in that it captures phenomena that occur on a much larger temporal scale than the theoretical ones.

In the present theory we have not investigated mode-mode interaction, which is a second mechanism that can lead to chaotic oscillations. Indeed, the linear theory has shown that the eigenfrequencies of the modes can be close on the frequency axis and the nonlinear theory has shown that mode 1 and mode 2 region of resonance overlap. Chaotic motion can occur in the same manner as in the modal competition of the experiment of Ciliberto & Gollub(1984) for Faraday waves or in the theory of bubble resonance of Mei &Zhou (1992) by acoustic sounds. This is an aspect worth investigating both theoretically and experimentally.

The theory and experimental comparison presented here are for vertical gates. For practical design it is desirable to extend our theory to the cases of the inclined gates. It is expected thta all the qualitative findings regarding the resonance diagrams, hysteresis phenomena and the narrow banded wave spectra apply also to the trapped mode for inclined gates, since its evolution equation is of the same type but with different coefficients.

In the case of inclined gates, while the perturbation scheme will be identical in principle, the determination of the coefficients will be attainable only by a numerical approach. In particular, each of the radiation and diffraction problem that we have seen in Chapter 2 can be solved by either the hybrid element method or the boundary element method. However, the computational domain will still be periodic in the direction of the gate array and therefore Fourier expansion in the y coordinate along the gate array will be possible for each perturbation problem. This observation reduces the numerical computational domain from a three- to a two-dimensional one. Each potential, from the trapped wave to the second harmonic forced by nonlinearities, will be expressed by a Fourier series with unknown coefficients. Each of these coefficients will then be found by solving a two dimensional Helmholtz equation in the vertical plane either with the HEM or the BEM. The coefficients of the evolution equation will then be obtained by numerical integration on the boundaries. The inclusion of viscous dissipation will follow the same formal path and make use of the representation of the wave potential in the same manner seen in Chapter 3.

For the prototype inclined gate, it is likely that inertia effect will be more important than viscous effect, rendering the response of the array even closer to a inviscid model in which the only dissipation mechanism is radiation damping.

Another aspect that merits investigation is the determination of the nonlinear motion of and the drift force on the gate array in a plane incident wave field, away

from the eigen–frequencies of the trapped wave. This strictly two dimensional problem will be an extension of the drift and nonlinear forcing on the two dimensional block in beam seas of Agnon& Mei(1985).

Appendix A

Taylor expansion of equation of motion of the gate

A.1 Torque induced by the term Gz

We deduce the torque by Gz by first integrating in z from $-h$ to 0

$$\begin{aligned}\mathcal{T}_p^I = &\int_{y_1}^{y_2} \mathrm{d}y \left\{ - \int_{-h}^{0} \mathrm{d}z\, Gz \left[z + h - a\epsilon\Theta + (z+h)\epsilon^2\Theta^2 - \frac{5}{6}\epsilon^3\Theta^3 \right] + \right. \\ &\left. \int_{-h}^{0} \mathrm{d}z\, Gz \left[z + h + a\epsilon\Theta + (z+h)\epsilon^2\Theta^2 + \frac{5}{6}\epsilon^3\Theta^3 \right] \right\} = \\ &\int_{y_1}^{y_2} \mathrm{d}y \left\{ \int_{-h}^{0} \mathrm{d}z\, Gz \left(2a\epsilon\Theta + \frac{5}{3}\epsilon^3\Theta^3 \right) \right\} = \\ &- (y_2 - y_1) \left(\epsilon\, G\, a h^2 \Theta + \epsilon^3 G\, a h^2 \frac{5}{6} \Theta^3 \right), \end{aligned} \tag{A.1.1}$$

and then integrating from zero to the free surface $\epsilon\zeta'^{\pm}$

$$\begin{aligned}\mathcal{T}_p^{II} = &\int_{y_1}^{y_2} \mathrm{d}y \left\{ - \int_{0}^{\epsilon\zeta'^{+}} \mathrm{d}z\, Gz \left[z + h - a\epsilon\Theta + (z+h)\epsilon^2\Theta^2 - \frac{5}{6}\epsilon^3\Theta^3 \right] + \right. \\ &\left. \int_{0}^{\epsilon\zeta'^{-}} \mathrm{d}z\, Gz \left[z + h + a\epsilon\Theta + (z+h)\epsilon^2\Theta^2 + \frac{5}{6}\epsilon^3\Theta^3 \right] \right\} = G \int_{y_1}^{y_2} \mathrm{d}y\ \times \\ &\left\{ - \frac{1}{3}\epsilon^3 \left(\zeta^{+^3} - \zeta^{-^3} \right) - \frac{h}{2}\epsilon^2 \left(\zeta^{+^2} - \zeta^{-^2} \right) + \frac{a}{2}\epsilon^3\Theta \left(\zeta^{+^2} + \zeta^{-^2} \right) \right\}. \end{aligned} \tag{A.1.2}$$

As pointed out earlier, the free surface displacement $\zeta^{\pm}$ is evaluated according to (2.2.25), which can be expanded for small ϵ

$$\zeta^{\pm} = \zeta^{\pm}(\xi^{\pm}, y, t) = \zeta^{\pm} \left(\pm a - (\zeta^{\pm} + h)\,\epsilon\Theta \pm \frac{a}{2}\epsilon^2\Theta^2\ , y, t \right). \tag{A.1.3}$$

Equation (A.1.3) states that the free surface is evaluated at a point which is at an $O(\epsilon)$ distance from $\pm a$; therefore we can repeatedly Taylor expand in (A.1.3) as follows

$$\begin{aligned}\zeta^{\pm} = & \\ & \left[\zeta^{\pm}\right]_{x=\pm a} + \left(-(\zeta^{\pm}+h)\,\epsilon\Theta \pm \frac{a}{2}\epsilon^2\Theta^2\right)\left[\zeta_x^{\pm}\right]_{x=\pm a} + \frac{1}{2}\left(-(\zeta^{\pm}+h)\,\epsilon\Theta\right)^2\left[\zeta_{xx}^{\pm}\right]_{x=\pm a} = \\ & \left[\zeta^{\pm}\right]_{x=\pm a} - \epsilon\left\{h\Theta\left[\zeta_x^{\pm}\right]_{x=\pm a} + \Theta\left[\zeta^{\pm}\zeta_x^{\pm}\right]_{x=\pm a}\right\} + \epsilon^2\left\{\pm\frac{a}{2}\Theta^2\left[\zeta_x^{\pm}\right]_{x=\pm a} + \right. \\ & \frac{h^2}{2}\Theta^2\left[\zeta_{xx}^{\pm}\right]_{x=\pm a} + h\,\Theta^2\left[\zeta_x^{\pm^2}\right]_{x=\pm a} + \frac{1}{2}\Theta^2\left[\zeta^{\pm^2}\zeta_{xx}^{\pm}\right]_{x=\pm a} + \\ & \left. h\Theta^2\left[\zeta^{\pm}\zeta_{xx}^{\pm}\right]_{x=\pm a}\right\} + O(\epsilon^3) \end{aligned} \tag{A.1.4}$$

Substituting this last expression of $\zeta^{\pm}$ in (A.1.2) and retaining only the terms up to $O(\epsilon^3)$ we obtain

$$\mathcal{T}_p^{II} = \int_{y_1}^{y_2} dy \left\{-\epsilon^2 G\,\frac{h}{2}\,\Delta\zeta^2 - \epsilon^3 G\left(\frac{1}{3}\Delta\zeta^3 - a\Theta\,\overline{\zeta^2} - h^2\Theta\Delta\zeta\zeta_x\right)\right\}, \tag{A.1.5}$$

The following shorthand notations have been introduced

$$\Delta(\cdot) = \left[(\cdot)^+\right]_{x=a} - \left[(\cdot)^-\right]_{x=-a}, \qquad \overline{(\cdot)} = \frac{1}{2}\left\{\left[(\cdot)^+\right]_{x=a} + \left[(\cdot)^-\right]_{x=-a}\right\}, \tag{A.1.6}$$

which signifies respectively the jump and the average of the quantity $(\cdot)$ across the two sides of the gates.

A.2 Torque induced by the term $\epsilon\Phi_t$

We first integrate with respect to z from $-h$ to 0. Retaining only the part of the moment arm that contributes to $O(\epsilon^3)$, we have:

$$\begin{aligned}\mathcal{T}_p^{III} = \int_{y_1}^{y_2} dy \left\{-\int_{-h}^{0} dz\,\epsilon\Phi_t^+\left[z+h-a\epsilon\Theta+(z+h)\epsilon^2\Theta^2\right] + \right. \\ \left. \int_{-h}^{0} dz\,\epsilon\Phi_t^-\left[z+h+a\epsilon\Theta+(z+h)\epsilon^2\Theta^2\right]\right\}\end{aligned} \tag{A.2.1}$$

We Taylor-expand $\Phi_t^{\pm}$ about $x = \pm a$ in the same manner as in expression (2.4.5)

$$\begin{aligned}\epsilon\Phi_t^{\pm} = & \epsilon\left[\Phi_t^{\pm}\right]_{x=\pm a} - \epsilon^2(z+h)\,\Theta\left[\Phi_{tx}^{\pm}\right]_{x=\pm a} + \\ & \epsilon^3\left\{\pm\frac{a}{2}\Theta^2\left[\Phi_{tx}^{\pm}\right]_{x=\pm a} + \frac{1}{2}(z+h)^2\Theta^2\left[\Phi_{txx}^{\pm}\right]_{x=\pm a}\right\},\end{aligned} \tag{A.2.2}$$

and substitute back in (A.2.1). Retaining only the terms up to $O(\epsilon^3)$ we obtain

$$\mathcal{T}_p^{III} = \int_{y_1}^{y_2} \mathrm{d}y \int_{-h}^{0} \mathrm{d}z \, \left\{ -\epsilon \Delta\Phi_t(z+h) + \epsilon^2 \left[\Theta \Delta\Phi_{tx}(z+h)^2 + 2\,\Theta\, a\overline{\Phi_t} \right] - \right.$$
$$\left. \epsilon^3 \left[3\,\Theta^2\, a\overline{\Phi_{tx}}(z+h) + \Theta^2 \Delta\Phi_t(z+h) + \frac{1}{2}\,\Theta^2 \Delta\Phi_{txx}(z+h)^3 \right] \right\}, \qquad \text{(A.2.3)}$$

where use has been made of the shorthand notation (A.1.6).

We now integrate in z from 0 to $\zeta^{\pm}$:

$$\mathcal{T}_p^{IV} = \int_{y_1}^{y_2} \mathrm{d}y \left\{ -\int_0^{\epsilon\zeta^+} \mathrm{d}z\, \epsilon \Phi_t^+ \left[z + h - a\epsilon\Theta + (z+h)\epsilon^2\Theta^2 \right] + \right.$$
$$\left. \int_0^{\epsilon\zeta^-} \mathrm{d}z\, \epsilon \Phi_t^- \left[z + h + a\epsilon\Theta + (z+h)\epsilon^2\Theta^2 \right] \right\}. \qquad \text{(A.2.4)}$$

Observe that this integral in z is of the order $O(\epsilon)$ because of the limits of integration; thus it is sufficient to retain terms only up to $O(\epsilon^2)$ in the Taylor expansion of Φ_t (A.2.2) and in the integrand in (A.2.4). The latter therefore becomes

$$\mathcal{T}_p^{IV} = \int_{y_1}^{y_2} \mathrm{d}y \left\{ \int_0^{\epsilon\zeta^+} \mathrm{d}z \, \left[-\epsilon(z+h) \left[\Phi_t^+\right]_{x=a} + \epsilon^2\, \Theta\, (z+h)^2 \left[\Phi_{tx}^+\right]_{x=a} + \epsilon^2 \Theta \left[\Phi_t^+\right]_{x=a} \right] + \right.$$
$$\left. \int_0^{\epsilon\zeta^-} \mathrm{d}z \, \left[\epsilon(z+h) \left[\Phi_t^-\right]_{x=-a} - \epsilon^2\, \Theta\, (z+h)^2 \left[\Phi_{tx}^-\right]_{x=-a} + \epsilon^2 \Theta \left[\Phi_t^-\right]_{x=-a} \right] \right\}. \qquad \text{(A.2.5)}$$

This expression can be further simplified because of the $O(\epsilon)$ dimension of the interval of integration in z. Indeed, $\left[\Phi_t^{\pm}\right]_{x=\pm a}$ and $\left[\Phi_{tx}^{\pm}\right]_{x=\pm a}$ can in turn be Taylor expanded in powers of z about $z = 0$ and then integrated from 0 to $\epsilon\zeta^{\pm}$. Let f denote either $[\Phi_t]_{x=\pm a}$ or $[\Phi_{tx}]_{x=\pm a}$, then

$$f = [f]_{z=0} + z\,[f_z]_{z=0} + O(z^2) \qquad \text{(A.2.6)}$$

Upon substitution of the above Taylor expansions for the velocity potential and straightforward evaluation of the integral in z, expression (A.2.5) becomes

$$\mathcal{T}_p^{IV} = \int_{y_1}^{y_2} \mathrm{d}y \left\{ -\left[\Phi_t^+\right]_0 \left(\epsilon^3 \frac{1}{2} \zeta^{+^2} + \epsilon^2 h \zeta^+ \right) - \epsilon^3 \left[\Phi_{tz}^+\right]_0 \frac{h}{2} \zeta^{+^2} + \epsilon^3 \Theta \left[\Phi_{tx}^+\right]_0 h^2 \zeta^+ + \right.$$
$$\epsilon^3 \Theta a \left[\Phi_t^+\right]_0 \zeta^+ + \left[\Phi_t^-\right]_0 \left(\epsilon^3 \frac{1}{2} \zeta^{-^2} + \epsilon^2 h \zeta^- \right) + \epsilon^3 \left[\Phi_{tz}^-\right]_0 \frac{h}{2} \zeta^{-^2} -$$
$$\left. \epsilon^3 \Theta \left[\Phi_{tx}^-\right]_0 h^2 \zeta^- + \epsilon^3 \Theta a \left[\Phi_t^-\right]_0 \zeta^- \right\}. \qquad \text{(A.2.7)}$$

In order to avoid unwieldy notation, the symbol $[(\cdot)^{\pm}]_0$ means that the quantity between brackets is evaluated at $x = \pm a$ and $z = 0$. Finally, we substitute the free

surface expansion (A.1.4) in the above, disregard terms of $O(\epsilon^4)$, and obtain

$$\mathcal{T}_p^{IV} = \int_{y_1}^{y_2} dy \left\{ -\epsilon^2 h \Delta_0 \left(\Phi_t \zeta\right) + \right.$$
$$\left. \epsilon^3 \left[-\frac{1}{2} h \Delta_0 \left(\Phi_{tz} \zeta^2\right) - \frac{1}{2} \Delta_0 \left(\Phi_t \zeta^2\right) + \Theta h^2 \Delta_0 \left(\Phi_t \zeta\right)_x + 2\,\Theta\, a \overline{(\Phi_t \zeta)^0} \right] \right\} \quad \text{(A.2.8)}$$

where the operators $\Delta_0(\cdot)$ and $\overline{(\cdot)^0}$ have the same meaning as in (A.1.6) with the addition that quantities (read: Φ and all its derivatives) are evaluated at $z = 0$.

A.3 Torque induced by the term $\epsilon^2 \frac{1}{2} |\nabla\Phi|^2$

It is sufficient to replace $\epsilon\Phi_t$ by $\epsilon^2 \frac{1}{2} |\nabla\Phi|^2$ in the final expressions (A.2.3) and (A.2.8). Corresponding to equation (A.2.3) we get

$$\mathcal{T}_p^{V} = \int_{y_1}^{y_2} dy \int_{-h}^{0} dz \left\{ -\epsilon^2 \frac{1}{2} \Delta |\nabla\Phi|^2 (z+h) + \epsilon^3 \left[\frac{1}{2} \Theta \Delta |\nabla\Phi|_x^2 (z+h)^2 + a\,\Theta \overline{|\nabla\Phi|^2} \right] \right\}, \quad \text{(A.3.1)}$$

and to (A.2.8)

$$\mathcal{T}_p^{VI} = \int_{y_1}^{y_2} dy \left\{ -\epsilon^3 \frac{h}{2} \Delta_0 \left(|\nabla\Phi|^2 \zeta \right) \right\}. \quad \text{(A.3.2)}$$

The total pressure torque can be obtained by summing all the contributions. From the hydrostatic pressure Gz we sum expressions (A.1.1) for $\mathcal{T}_p^I$ and (A.1.5) for $\mathcal{T}_p^{II}$. From the linear and quadratic dynamic pressure $\epsilon\Phi_t + \frac{\epsilon^2}{2}|\nabla\Phi|^2$ we sum expressions (A.2.3),(A.2.8),(A.3.1) and (A.3.2) for $\mathcal{T}_p^{III}$ and $\mathcal{T}_p^{VI}$. Rearranging terms of same powers in ϵ and separating the terms that contain integrals in z from terms that are simply evaluate at $z = 0$, we obtain finally

$$\mathcal{T}_p =$$
$$\epsilon \int_{y_1}^{y_2} dy \int_{-h}^{0} dz \left\{ -\Delta\Phi_t (z+h) \right\} +$$
$$\epsilon^2 \int_{y_1}^{y_2} dy \int_{-h}^{0} dz \left\{ \Theta \Delta \Phi_{tx} (z+h)^2 + 2\,\Theta\, a \overline{\Phi_t} - \frac{1}{2} \Delta |\nabla\Phi|^2 (z+h) \right\} -$$
$$\epsilon^3 \int_{y_1}^{y_2} dy \int_{-h}^{0} dz \left\{ 3\,\Theta^2\, a \overline{\Phi_{tx}} (z+h) + \Theta^2 \Delta \Phi_t (z+h) + \frac{1}{2} \Theta^2 \Delta \Phi_{txx} (z+h)^3 - \right.$$
$$\left. \frac{1}{2} \Theta \Delta |\nabla\Phi|_x^2 (z+h)^2 - a\Theta \overline{|\nabla\Phi|^2} \right\} -$$
$$\epsilon^2 \int_{y_1}^{y_2} dy \left\{ G \frac{h}{2} \Delta\zeta^2 + h \Delta_0 \left(\Phi_t \zeta\right) \right\} -$$
$$\epsilon^3 \int_{y_1}^{y_2} dy \left\{ G \left(\frac{1}{3} \Delta\zeta^3 - a\Theta \overline{\zeta^2} - h^2 \Theta \Delta \zeta \zeta_x \right) + \frac{1}{2} h \Delta_0 \left(\Phi_{tz} \zeta^2\right) + \frac{1}{2} \Delta_0 \left(\Phi_t \zeta^2\right) - \right.$$

$$\Theta h^2 \Delta_0 \left(\Phi_t \zeta\right)_x - 2\,\Theta\, a\overline{(\Phi_t \zeta)^0} + \frac{h}{2}\,\Delta_0 \left(|\nabla \Phi|^2 \zeta\right)\Big\} -$$

$$\epsilon\, G\, a h^2 \left(y_2 - y_1\right) \Theta \; - G\, \frac{5}{6}\, a h^2 \left(y_2 - y_1\right)\, \Theta^3 + O(\epsilon^4). \tag{A.3.3}$$

Appendix B

Solution of the forced second harmonic by eigenfunction expansions

B.1 Waves generated by forcing at the free surface

In order to solve the following boundary value problem

$$F^{\pm\ S}_{p_{xx}} + F^{\pm\ S}_{p_{zz}} - p^2\pi^2 F^{\pm S}_p = 0 \qquad \text{in} \quad \Omega^{\pm}, \tag{B.1.1}$$

$$GF^{\pm S}_{p_z} - 4F^{\pm S}_p = \Gamma^{\pm}_p(x) \qquad z = 0, \tag{B.1.2}$$

$$F^{\pm S}_{p_z} = 0 \qquad z = -h, \tag{B.1.3}$$

$$F^{\pm S}_{p_x} = 0 \qquad x = 0, \tag{B.1.4}$$

In addition, propagating waves must be outgoing to $x \to \pm\infty$. We expand $F^{\pm S}_p$ in terms of the following eigenfunctions

$$F^{\pm S}_p = \sum_{l=0}^{\infty} \tilde{F}^{\pm S}_{pl}(x) \cosh K'_l(z+h), \tag{B.1.5}$$

where $\{Z'_l(z)\} \equiv \{\cosh K'_l(z+h)\}$ are the eigenfunctions of the following Sturm-Liouville problem in z

$$\frac{\mathrm{d}^2 Z'}{\mathrm{d}z^2} - K'^2 Z' = 0 \qquad z \in [-h, 0] \tag{B.1.6}$$

$$G\frac{\mathrm{d}Z'}{\mathrm{d}z} - 4Z' = 0 \qquad z = 0 \tag{B.1.7}$$

$$\frac{\mathrm{d}Z'}{\mathrm{d}z} = 0 \qquad z = -h \tag{B.1.8}$$

with K' assuming the discrete values

$$K'_l = \begin{cases} k' & \text{for } l = 0 \\ \mathrm{i}k'_l & \text{for } l = 1, 2, \ldots \end{cases} \tag{B.1.9}$$

where k' is the real root of

$$4 = Gk' \tanh k'h \tag{B.1.10}$$

and the k'_l are the real roots of

$$4 = -Gk'_l \tan k'_l h. \tag{B.1.11}$$

Recall from (2.5.54), (2.5.55) and (2.5.60) that G is the eigenfrequency of the trapped wave, so that $k' > k$ and $k'_l < k_l$. This fact implies the possibility of short-crested propagating wave in addition to long-crested propagating waves. The coefficients $\tilde{F}^{\pm S}_{pl}(x)$ of expansion (B.1.5) are found by orthogonality

$$\tilde{F}^{\pm S}_{pl}(x) = \frac{1}{C'_l} \int_{-h}^{0} \mathrm{d}z \, F^{\pm S}_p(x, z) \cosh K'_l(z + h) \tag{B.1.12}$$

where

$$C'_l = \int_{-h}^{0} \mathrm{d}z \, \cosh^2 K'_l(z + h) = h + \frac{G}{4} \sinh^2 K'_l h. \tag{B.1.13}$$

Now, the ordinary differential equation that governs each of the $\tilde{F}^{\pm S}_{pl}(x)$ can be simply obtained by multiplying the Helmholtz equation (B.1.1) by $Z'_l(z) = \cosh K'_l(z + h)$ and integrating in z from $-h$ to 0. The first term on the left hand sides gives:

$$\int_{-h}^{0} \mathrm{d}z F^{\pm\ S}_{p_{xx}} Z'_l = \frac{\mathrm{d}^2}{\mathrm{d}x^2} \int_{-h}^{0} \mathrm{d}z F^{\pm S}_p Z'_l = C'_l \tilde{F}^{\pm\ S}_{pl_{xx}}. \tag{B.1.14}$$

Integration by parts of the second term of (B.1.1) yields:

$$\int_{-h}^{0} \mathrm{d}z F^{\pm\ S}_{p_{zz}} Z'_l = \left[F^{\pm S}_{p_z} Z'_l\right]_{-h}^{0} - \left[F^{\pm S}_p Z_{l_z}\right]_{-h}^{0} + \int_{-h}^{0} \mathrm{d}z F^{\pm S}_p Z_{l_{zz}} = \frac{Z'_l(0)}{G} \Gamma^{\pm}_p + K'^2_l C'_l \tilde{F}^{\pm S}_{pl}, \tag{B.1.15}$$

where use has been made of (B.1.6), (B.1.7) and (B.1.8) for $Z'_l(z)$ and of (B.1.2), (B.1.3) for $\tilde{F}^{\pm S}_{pl}$. The desired equation for $\tilde{F}^{\pm S}_{pl}$ is therefore

$$\tilde{F}^{\pm\ S}_{pl_{xx}} + \left(K'^2_l - p^2\pi^2\right) \tilde{F}^{\pm S}_{pl} = -\frac{\cosh K'_l h}{G\, C'_l} \Gamma^{\pm}_p(x). \tag{B.1.16}$$

The boundary condition for the above ordinary differential equation (B.1.16) at the gate surface $x = 0$ can be obtained by multiplying (B.1.4) by $Z'_l(z) = \cosh K'_l(z + h)$

and integrating in z from $-h$ to 0:

$$\tilde{F}^{\pm\ S}_{pl_x} = 0, \tag{B.1.17}$$

As $x \to \pm\infty$, we require $\tilde{F}^{\pm S}_{pl}$ to remain bounded or to be an outgoing wave. The general solution is the sum of the homogeneous and the particular solution and can be found using the method of variation of parameters. Let $\alpha'^2_{pl} = K'^2_l - p^2\pi^2$. Note that α'_{pl} is real not only for $p = 0$ and $l = 0$ ($\alpha'_{00} = k'$) but also for $p = 1, 2, \ldots, P$ and $l = 0$, $\alpha'_{p0} = \sqrt{k'^2 - p^2\pi^2}$, where P is the largest integer for which $k' > P\pi$; these cases correspond to one long crested propagating wave, α'_{00}, and P short-crested propagating wave, α'_{p0}. In the remaining cases α'_{pl} is immaginary: $\alpha'_{p0} = \mathrm{i}\sqrt{-k'^2 + p^2\pi^2}$ for $l = 0$ and $p = P+1, P+2, \ldots$, which represent short crested evanescent waves, and $\alpha'_{pl} = \mathrm{i}\sqrt{k'^2_l + p^2\pi^2}$ for $l = 1, 2, \ldots$ and $p = 0, 1, 2, \ldots$ corresponding to both long ($p = 0$) and short ($p = 1, 2, \ldots$) crested evanescent waves. This definition of α'_{pl} allows us to write the homogeneous solution of (B.1.16) for any p, l as:

$$c_1^{\pm}\mathrm{e}^{\mathrm{i}\alpha'_{pl}x} + c_2^{\pm}\mathrm{e}^{-\mathrm{i}\alpha'_{pl}x}. \tag{B.1.18}$$

For real α'_{pl} the solution represents a travelling wave, for imaginary α'_{pl}, an evanescent or unbounded mode. With this understanding, we can write the general solution of (B.1.16) as:

$$\begin{aligned}\tilde{F}^{\pm S}_{pl} &= c_1^{\pm}\mathrm{e}^{\mathrm{i}\alpha'_{pl}x} + c_2^{\pm}\mathrm{e}^{-\mathrm{i}\alpha'_{pl}x} - \\ &\frac{\cosh K'_l h}{G\,C'_l}\left\{-\mathrm{e}^{\mathrm{i}\alpha'_{pl}x}\int^x \frac{\mathrm{e}^{-\mathrm{i}\alpha'_{pl}t}\Gamma_p^{\pm}(t)}{W(t)}\mathrm{d}t + \mathrm{e}^{-\mathrm{i}\alpha'_{pl}x}\int^x \frac{\mathrm{e}^{\mathrm{i}\alpha'_{pl}t}\Gamma_p^{\pm}(t)}{W(t)}\mathrm{d}t\right\}\end{aligned} \tag{B.1.19}$$

where the Wronskian $W(x)$ is given by:

$$W(x) = \begin{vmatrix} \mathrm{e}^{\mathrm{i}\alpha'_{pl}x} & \mathrm{i}\alpha'_{pl}\mathrm{e}^{\mathrm{i}\alpha'_{pl}x} \\ \mathrm{e}^{-\mathrm{i}\alpha'_{pl}x} & -\mathrm{i}\alpha'_{pl}\mathrm{e}^{-\mathrm{i}\alpha'_{pl}x} \end{vmatrix} = -2\mathrm{i}\alpha'_{pl}. \tag{B.1.20}$$

Upon substitution of the expression for $\Gamma_p^{\pm}$ (2.5.88) in (B.1.19), integration and application of the boundary conditions at $x = 0$ and $x = \pm\infty$, the solution is found to be:

$$\begin{aligned}\tilde{F}^{\pm S}_{pl} &= -\frac{\cosh K'_l h}{G\,C'_l}\sum_{q=-\infty,\neq 0}^{\infty}\sum_{m=0}^{\infty}\sum_{n=0}^{\infty}\times \\ &\frac{a_{pqmn}}{(\alpha_{qm}+\alpha_{p+q,n})^2 + \alpha'^2_{pl}}\left[\mathrm{e}^{\mp(\alpha_{qm}+\alpha_{p+q,n})x} - \frac{\mathrm{i}}{\alpha'_{pl}}(\alpha_{qm}+\alpha_{p+q,n})\,\mathrm{e}^{\pm\mathrm{i}\,\alpha'_{pl}x}\right].\end{aligned} \tag{B.1.21}$$

The first exponential fuction is always decaying as $x \to \pm\infty$ and consists of convolution products of the first order trapped wave with itself. This part of the solution is always real. The second exponential represents the waves associated with the roots of the second harmonic dispersion relation, K'_l: this second part of the solution is complex when α'_{pl} is real (propagating mode) and real when α'_{pl} is immaginary (evanescent mode). We remark that if G is sufficiently large (i.e. the dimensional eigenfrequency is sufficiently low), not only $k < \pi$ but also $k' < \pi$, which means $P = 0$, i.e. that there is only one propagating mode: the long crested $\alpha'_{00} \equiv K'_0 \equiv k'$.

B.2 Waves generated by forcing at the gate surface

The boundary value problem for $F^{\pm W}_{pl}$ is governed by

$$F^{\pm W}_{p_{xx}} + F^{\pm W}_{p_{zz}} - p^2\pi^2 F^{\pm W}_{p} = 0 \qquad \text{in} \quad \Omega^{\pm}, \tag{B.2.1}$$

$$GF^{\pm W}_{p_z} - 4F^{\pm W}_{p} = 0 \qquad z = 0, \tag{B.2.2}$$

$$F^{\pm W}_{p_z} = 0 \qquad z = -h, \tag{B.2.3}$$

$$F^{\pm W}_{p_x} = 2(z+h)c_p \pm \Lambda_p(z) \qquad x = 0. \tag{B.2.4}$$

and the radiation condition. We follow the same path as for $F^{\pm S}_{pl}$. First $F^{\pm W}_{pl}$ is expressed as an eigenfunction expansion in terms of the set $\{Z'_l(z)\}$

$$F^{\pm W}_{p} = \sum_{l=0}^{\infty} \tilde{F}^{\pm W}_{pl}(x) \cosh K'_l(z+h), \tag{B.2.5}$$

with the coefficients $\tilde{F}^{\pm W}_{pl}(x)$ defined as

$$\tilde{F}^{\pm W}_{pl}(x) = \frac{1}{C'_l} \int_{-h}^{0} \mathrm{d}z \, F^{\pm W}_{p}(x,z) \cosh K'_l(z+h). \tag{B.2.6}$$

A homogeneous ordinary differential equation governing $\tilde{F}^{\pm W}_{pl}(x)$ is found by multiplication of Helmoltz equation (B.2.1) by $Z'_l(z)$, integration in z from $-h$ to 0 and use of boundary conditions (B.2.2)(B.2.3) for $F^{\pm W}_{pl}$ and (B.1.7)(B.1.8) for $Z'_l(z)$:

$$\tilde{F}^{\pm W}_{pl_{xx}} + \left(K'^2_l - p^2\pi^2\right) \tilde{F}^{\pm W}_{pl} = 0. \tag{B.2.7}$$

By multiplication of boundary condition (B.2.4) by $Z'_l(z)$ and integration in z from $-h$ to 0, we get

$$\tilde{F}^{\pm W}_{pl_x} = \frac{2D'_l c_p}{C'_l} \pm \tilde{\Lambda}_{pl} \tag{B.2.8}$$

where

$$D'_l = \int_{-h}^{0} \mathrm{d}z\,(z+h)\cosh K'_l(z+h) = \frac{1}{K'^2_l}\left[\left(\frac{4h}{G}-1\right)\cosh K'_l h + 1\right], \tag{B.2.9}$$

and $\tilde{\Lambda}_{pl}$ is the expansion coefficient of the forcing function $\Lambda_p(z)$ in terms of the eigenfunctions $Z'_l(z)$

$$\tilde{\Lambda}_{pl} = \frac{1}{C'_l}\int_{-h}^{0} \mathrm{d}z\,\Lambda_p(z)\cosh K'_l(z+h). \tag{B.2.10}$$

To evaluate the above coefficient we use expression (2.5.90) for $\Lambda_p(z)$ to get:

$$\begin{aligned}\tilde{\Lambda}_{pl} = \frac{\epsilon_p}{4C'_l}\sum_{q=-\infty,\neq 0}^{\infty}\int_{-h}^{0}\mathrm{d}z\,\cosh K'_l(z+h)\left\{-\frac{a}{2}b_q + b_{p+q}\sum_{n=0}^{\infty}\beta_{qn}\times\right.\\ \left.\left[K_n\sinh K_n(z+h) - (z+h)\alpha_{qn}^2\cosh K_n(z+h)\right]\right\} =\\ \frac{\epsilon_p}{4C'_l}\sum_{q=-\infty,\neq 0}^{\infty}\left\{-\frac{a\,b_q}{2K'_l}\sinh K'_l h + b_{p+q}\sum_{n=0}^{\infty}\beta_{qn}\left[C'_{nl} - \alpha_{qn}^2 D'_{nl}\right]\right\},\end{aligned} \tag{B.2.11}$$

where

$$\begin{aligned}C'_{nl} = \int_{-h}^{0}\mathrm{d}z\,K_n\,\sinh K_n(z+h)\,\cosh K'_l(z+h) =\\ \frac{1}{\left(K'^2_l - K_n^2\right)}\left[K_n^2 + \left(\frac{4}{G^2} - K_n^2\right)\cosh K_n h\,\cosh K'_l h\right],\end{aligned} \tag{B.2.12}$$

$$\begin{aligned}D'_{nl} = \int_{-h}^{0}\mathrm{d}z\,(z+h)\,\cosh K_n(z+h)\,\cosh K'_l(z+h) = \frac{1}{\left(K'^2_l - K_n^2\right)^2}\\ \left\{K_n^2 + K'^2_l + \left[\frac{8}{G^2} - K_n^2 - K'^2_l + \frac{3h}{G}\left(K'^2_l - K_n^2\right)\right]\cosh K_n h\,\cosh K'_l h\right\}.\end{aligned} \tag{B.2.13}$$

Note that for any n, l, p, not only C'_{nl} and D'_{nl}, but also (B.2.11) for $\tilde{\Lambda}_{pl}$ are real. When computing C'_{nl} and D'_{nl} a numerical singularity arises for $n = l \to \infty$ in expressions (B.2.12) and (B.2.13). In fact, because of the nature of the dispersion relations (2.5.55) for k_n and (2.5.116) for k'_l, the roots $k'_l \to k_n \to n\pi$ and in both expressions (B.2.12) and (B.2.13) the denominator goes to zero. Such a singularity is only a result of the explicit integration in z for $K'_l \neq K_n$. Indeed if we let $K'_l = K_n$

and let $n \to \infty$, we have:

$$C'_{nn} = \int_{-h}^{0} \mathrm{d}z \, K_n \sinh K_n(z+h) \cosh K_n(z+h) = \frac{1}{2} \sinh^2 K_n h = -\frac{1}{2} \sin^2 k_n h \to 0 \tag{B.2.14}$$

$$D'_{nn} = \int_{-h}^{0} \mathrm{d}z \, (z+h) \cosh^2 K_n(z+h) = \frac{h^2}{4} + \frac{\cos^2 k_n h}{4G^2 k_n^4} \left(2Gk_n^2 h - 1\right) \to \frac{h^2}{4} \tag{B.2.15}$$

In the numerical evaluation of $\tilde{\Lambda}_{pl}$, we simply perform numerical integration for C'_{nl} and D'_{nl} so that such a singularity is completely by-passed. Once the coefficients $\tilde{\Lambda}_{pl}$ are calculated, application of the radiation condition at $x = \pm\infty$ allows us to determine $\tilde{F}^{\pm W}_{pl}$:

$$\tilde{F}^{\pm W}_{pl} = -\frac{\mathrm{i}}{\alpha'_{pl}} \left(\tilde{\Lambda}_{pl} \pm \frac{2D'_l c_p}{C'_l} \right) \mathrm{e}^{\pm \mathrm{i}\, \alpha'_{pl}\, x}. \tag{B.2.16}$$

Hence the expansion coefficients $F_p^{\pm}(x,z)$ have the solution

$$F_p^{\pm} = F_p^{\pm S} + F_p^{\pm W} = \sum_{l=0}^{\infty} \left[\tilde{F}^{\pm S}_{pl}(x) + \tilde{F}^{\pm W}_{pl}(x) \right] \cosh K'_l(z+h), \tag{B.2.17}$$

with expressions (B.1.21) for $\tilde{F}^{\pm S}_{pl}(x)$ and (B.2.16) for $\tilde{F}^{\pm W}_{pl}(x)$.

The above expression (B.2.16) contains the unknown Fourier expansion coefficients c_p of the angular motion. Such coefficients can now be determined by substituting in the gate motion equation (2.5.96) the expression for $F_p^{\pm}$. It is immediate to verify that:

$$\Delta F_p = -\mathrm{i} \sum_{l=0}^{\infty} \frac{4D'_l c_p}{\alpha'_{pl} C'_l} \cosh K'_l(z+h), \tag{B.2.18}$$

i.e. that the equation of motion of the gate is unforced. Indeed, from equation (2.5.96) obtain respectively for gate one and two

$$(-4\,I + G\,C)\, q^I = \sum_{p=0}^{\infty} \sum_{l=0}^{\infty} \frac{8D'^2_l \sin p\pi(1-r)}{p\pi \alpha'_{pl} C'_l} c_p, \tag{B.2.19}$$

$$\frac{r}{1-r} (-4\,I + G\,C)\, q^{II} = -\sum_{p=0}^{\infty} \sum_{l=0}^{\infty} \frac{8D'^2_l \sin p\pi(1-r)}{p\pi \alpha'_{pl} C'_l} c_p. \tag{B.2.20}$$

Recalling expression (2.5.99) of the expansion coefficients c_p, observe that equations (B.2.19) and (B.2.20) represent a linear homogeneous system in q^I and q^{II} with nonzero determinant of the coefficient matrix (G is the eigenvalue given by (2.5.62)). Therefore the only solution is the trivial $q^I = q^{II} = 0$, i.e. $c_p = 0, \quad p = 0, 1, 2 \ldots$ The angular motion is zero (with a nontrivial pressure and velocity fields and a radiated wave!).

The final form of $\tilde{F}^{\pm W}_{pl}$ is therefore

$$\tilde{F}^{\pm W}_{pl} = -\frac{\mathrm{i}}{\alpha'_{pl}}\tilde{\Lambda}_{pl}\mathrm{e}^{\pm \mathrm{i}\,\alpha'_{pl}\,x}. \tag{B.2.21}$$

Appendix C

Alternate solution of the forced second harmonic with a Green's function

C.1 Formalism of solution

The solution for the forced wave (2.5.91) can also be found with the aid of a Green's function rather than a direct eigenfunction expansion. Although the formalism is quite different, the Green's function is eventually expanded in terms of the same eigenfunctions as the previous solution. We outline the procedure for insight and for checking the results in Appendix B.

Consider the governing equations (2.5.100) to (2.5.103) for $F_p^{\pm}$ defined in the plane $\Omega^{\pm}$; for simplicity here we anticipate the result $c_p \equiv 0$. The associated problem defining the desired Green's function $\Psi_p^{\pm}$ is the one of an oscillating point source at x_0, z_0:

$$\Psi^{\pm}_{p_{xx}} + \Psi^{\pm}_{p_{zz}} - p^2\pi^2\Psi^{\pm}_p = \delta(x-x_0)\delta(z-z_0) \quad \text{in} \quad \Omega^{\pm}, \tag{C.1.1}$$

$$G\Psi^{\pm}_{p_z} - 4\Psi^{\pm}_p = 0 \qquad z = 0, \tag{C.1.2}$$

$$\Psi^{\pm}_{p_z} = 0 \qquad z = -h, \tag{C.1.3}$$

$$\Psi^{\pm}_{p_x} = 0 \qquad x = 0, \tag{C.1.4}$$

$$\Psi^{\pm}_p \quad \text{outgoing at} \quad \pm\infty. \tag{C.1.5}$$

Once $\Psi_p^{\pm}(x, z; x_0, z_0)$ is determined, application of Green's formula

$$\iint_{\Omega_p^{\pm}} F_p^{\pm}\left(\partial_{xx}+\partial_{zz}\right)\Psi_p^{\pm} - \Psi_p^{\pm}\left(\partial_{xx}+\partial_{zz}\right)F_p^{\pm} = \int_{\partial\Omega_p^{\pm}} F_p^{\pm}\frac{\partial\Psi_p^{\pm}}{\partial n} - \Psi_p^{\pm}\frac{\partial F_p^{\pm}}{\partial n}, \tag{C.1.6}$$

to $F_p^{\pm}(x, z)$ and $\Psi_p^{\pm}(x, z; x_0, z_0)$ with the help of their respective governing equations

(2.5.100) to (2.5.103) and (C.1.1) to (C.1.5), yields

$$F_p^{\pm}(x_0, z_0) = \int_{-h}^{0} \mathrm{d}z\, \Psi_p^{\pm}(0, z; x_0, z_0)\, \Lambda_p(z) \mp \frac{1}{G} \int_0^{\pm\infty} \mathrm{d}x\, \Psi_p^{\pm}(x, 0; x_0, z_0)\, \Gamma_p^{\pm}(x). \quad \text{(C.1.7)}$$

We anticipate that $\Psi_p^{\pm}$ is symmetric with respect of an exchange between x, z and x_0, z_0 so that the last expression can be rewritten as

$$F_p^{\pm}(x, z) = \int_{-h}^{0} \mathrm{d}z_0\, \Psi_p^{\pm}(0, z_0; x, z)\, \Lambda_p(z_0) \mp \frac{1}{G} \int_0^{\pm\infty} \mathrm{d}x_0\, \Psi_p^{\pm}(x_0, 0; x, z)\, \Gamma_p^{\pm}(x_0), \quad \text{(C.1.8)}$$

where the integration are carried in x_0 and z_0.

C.2 Determination of Green's function

We now turn to the determination of $\Psi_p^{\pm}$. Let ψ_p be the Green's function of the following simplified problem in the entire xz plane for a source at x_0, z_0:

$$\psi_{p_{xx}} + \psi_{p_{zz}} - p^2\pi^2\psi_p = \delta(x - x_0)\delta(z - z_0) \quad \text{(C.2.1)}$$

$$G\psi_{p_z} - 4\psi_p = 0 \qquad z = 0, \quad \text{(C.2.2)}$$

$$\psi_{p_z} = 0 \qquad z = -h, \quad \text{(C.2.3)}$$

$$\psi_p \quad \text{outgoing at} \quad \pm\infty. \quad \text{(C.2.4)}$$

By the method of images it is obvious that $\Psi_p^{\pm}$ is given by:

$$\Psi_p^{\pm} = \psi_p(x, z; x_0, z_0) + \psi_p(x, z; -x_0, z_0), \quad \text{(C.2.5)}$$

where $x_0 \gtrless 0$ for $\Psi_p^{\pm}$. Now, ψ_p can be calculated by solving for its fourier transform $\tilde{\psi}_p$, defined by

$$\tilde{\psi}_p(\alpha, z) = \int_{-\infty}^{\infty} \mathrm{d}x\, \mathrm{e}^{-\mathrm{i}\alpha x}\psi_p(x, z), \quad \text{(C.2.6)}$$

and then taking its inverse

$$\psi_p(x, z) = \frac{1}{2\pi} \int_{-\infty}^{\infty} \mathrm{d}\alpha\, \mathrm{e}^{\mathrm{i}\alpha x}\tilde{\psi}_p(\alpha, z). \quad \text{(C.2.7)}$$

The boundary value problem for $\tilde{\psi}$ is:

$$\tilde{\psi}_{p_{zz}} - \left(\alpha^2 + p^2\pi^2\right)\tilde{\psi}_p = \mathrm{e}^{-\mathrm{i}\alpha x_0}\delta(z - z_0) \quad \text{(C.2.8)}$$

$$G\tilde{\psi}_{p_z} - 4\tilde{\psi}_p = 0 \qquad z = 0, \quad \text{(C.2.9)}$$

$$\tilde{\psi}_{p_z} = 0 \qquad z = -h, \quad \text{(C.2.10)}$$

or its equivalent

$$\tilde{\psi}_{p_{zz}} - \left(\alpha^2 + p^2\pi^2\right)\tilde{\psi}_p = 0 \tag{C.2.11}$$

$$G\tilde{\psi}_{p_z} - 4\tilde{\psi}_p = 0 \qquad z = 0, \tag{C.2.12}$$

$$\tilde{\psi}_{p_z} = 0 \qquad z = -h, \tag{C.2.13}$$

$$\left[\tilde{\psi}_p\right]_{z_0^+} - \left[\tilde{\psi}_p\right]_{z_0^-} = 0, \tag{C.2.14}$$

$$\left[\tilde{\psi}_{p_z}\right]_{z_0^+} - \left[\tilde{\psi}_{p_z}\right]_{z_0^-} = \mathrm{e}^{-\mathrm{i}\alpha x_0}. \tag{C.2.15}$$

The second jump condition (C.2.15) can be derived by integrating (C.2.8) across z_0. In terms of

$$\kappa(\alpha) = \sqrt{\alpha^2 + p^2\pi^2}, \quad z_> = \max(z, z_0), \quad z_< = \min(z, z_0), \tag{C.2.16}$$

the solution for $\tilde{\psi}_p$ can be expressed in compact form as

$$\tilde{\psi}_p = \frac{\mathrm{e}^{-\mathrm{i}\alpha x_0}}{\kappa(\alpha)} \frac{4\sinh\kappa(\alpha)z_> + G\kappa(\alpha)\cosh\kappa(\alpha)z_>}{4\cosh\kappa(\alpha)h - G\kappa(\alpha)\sinh\kappa(\alpha)h} \cosh(z_< + h). \tag{C.2.17}$$

In order to obtain ψ_p we must then calculate the integral (C.2.7):

$$\psi_p(x,z) = \frac{1}{2\pi}\int_{-\infty}^{\infty} \mathrm{d}\alpha \frac{\mathrm{e}^{-\mathrm{i}\alpha(x-x_0)}}{\kappa(\alpha)_p} \frac{4\sinh\kappa(\alpha)z_> + G\kappa(\alpha)\cosh\kappa(\alpha)z_>}{4\cosh\kappa(\alpha)h - G\kappa(\alpha)\sinh\kappa(\alpha)h} \cosh(z_< + h). \tag{C.2.18}$$

On the real α axis there can be poles if α is a root of

$$4\cosh\kappa(\alpha)h - G\kappa(\alpha)\sinh\kappa(\alpha)h = 0. \tag{C.2.19}$$

Such roots are given by $\kappa(\alpha) = K_l'$, where K_l' are the familiar roots defined in (2.5.114). Solving $\sqrt{\alpha^2 + p^2\pi^2} = K_l'$ for α, we find that the poles of $\tilde{\psi}_p$ occur exactly at $\alpha = \pm\alpha_{pl}'$ defined before in (B.1.18): $\alpha_{pl}'^2 = K_l'^2 - p^2\pi^2$. Hence, if p is 0 or any of the first P integers, on the real axis Re α there are two poles, $\alpha = \pm\alpha_{p0}' \equiv \pm\sqrt{k'^2 - p^2\pi^2}$. All the remaining poles are on the immaginary axis, $\alpha = \pm\alpha_{pl}' \equiv \pm\mathrm{i}\sqrt{k_l'^2 + p^2\pi^2}$, $l = 1, 2, \ldots$. This case is indicated in figure C-1a. On the other hand, if p is one of the integers greater than P, then all the poles are on the immaginary axis: $\alpha = \pm\alpha_{p0}' \equiv \pm\mathrm{i}\sqrt{-k'^2 + p^2\pi^2}$ and $\alpha = \pm\alpha_{pl}' \equiv \pm\mathrm{i}\sqrt{k_l'^2 + p^2\pi^2}$, $l = 1, 2, \ldots$; this second case in indicated in figure C-1b. In the first case, the radiation condition must be invoked in order to define the improper integral; we choose a path of integration that is indented below α_{p0}' and above $-\alpha_{p0}'$. Then we apply the residue method: for $x > x_0$ we close the path of integration with a semicircle of infinitely large radius in the upper half plane so that its contribution is null as Im$\alpha \uparrow \infty$ (Jordan's lemma); such a path contains the real pole α_{p0}' and all the infinite number of immaginary

poles on $\mathrm{Im}\,\alpha > 0$ (see figure C-1a,b). For $x < x_0$ we close the path with a semicircle in the lower half plane so to include the real poles $-\alpha'_{p0}$ and all the infinite number of immaginary poles on $\mathrm{Im}\,\alpha < 0$. Evaluation of all the residues gives the desired integral as a series expansion. In the second case in which there are no real poles, no indentation on the real axis is necessary, though we still use the residue method to calculate the integral, with the same choice of circular paths. The calculation of the residues is straightforward and can be obtained by making repeated use of (C.2.19). We write hereafter the result in compact form valid for any p:

$$\psi_p(x,z;x_0,z_0) = -\mathrm{i}\sum_{l=0}^{\infty} \frac{\mathrm{e}^{\mathrm{i}\alpha'_{pl}|x-x_0|}}{2C'_l\alpha'_{pl}} \cosh K'_l(z+h)\cosh K'_l(z_0+h) \qquad \text{(C.2.20)}$$

In such a representation we have made extensive use of the complex representation for K'_l and α'_{pl}; we remark that for $p \le P$ only the first term of the series is complex (and corresponds to the propagating mode), while for $p > P$ all the terms in the series are real (and correspond to evanescent modes). For example, for $p < P$ the series (C.2.20) is equal to:

$$\begin{aligned}\psi_p(x,z;x_0,z_0) = -\mathrm{i}\,\frac{\mathrm{e}^{\mathrm{i}\sqrt{k'^2-p^2\pi^2}|x-x_0|}}{2C'_0\sqrt{k'^2-p^2\pi^2}} \cosh k'(z+h)\cosh k'(z_0+h) - \\ \sum_{l=1}^{\infty} \frac{\mathrm{e}^{-\sqrt{k'^2_l+p^2\pi^2}|x-x_0|}}{2C'_l\sqrt{k'^2_l+p^2\pi^2}} \cos k'_l(z+h)\cos k'_l(z_0+h) \qquad \text{(C.2.21)}\end{aligned}$$

The desired Green function is then simply obtained according to (C.2.5)

$$\Psi^{\pm}_p(x,z;x_0,z_0) = -\mathrm{i}\sum_{l=0}^{\infty} \frac{\mathrm{e}^{\mathrm{i}\alpha'_{pl}|x-x_0|} + \mathrm{e}^{\mathrm{i}\alpha'_{pl}|x+x_0|}}{2C'_l\alpha'_{pl}} \cosh K'_l(z+h)\cosh K'_l(z_0+h). \qquad \text{(C.2.22)}$$

C.3 Solution as a boundary integral

Finally, evaluation of the line integrals in expression (C.1.8) yelds $F^{\pm}_p$. The first integral on the gate surface is:

$$\begin{aligned}\int_{-h}^{0} \mathrm{d}z_0 \Psi^{\pm}_p(0,z_0;x,z)\,\Lambda_p(z_0) = \\ -\mathrm{i}\sum_{l=0}^{\infty}\int_{-h}^{0}\mathrm{d}z_0 \frac{\mathrm{e}^{\mathrm{i}\alpha'_{pl}|x|}}{C'_l\alpha'_{pl}} \cosh K'_l(z+h)\cosh K'_l(z_0+h)\,\Lambda_p(z_0) = \\ -\mathrm{i}\sum_{l=0}^{\infty}\frac{\tilde{\Lambda}_{pl}}{\alpha'_{pl}}\,\mathrm{e}^{\pm\mathrm{i}\alpha'_{pl}x}\cosh K'_l(z+h), \qquad \text{(C.3.1)}\end{aligned}$$

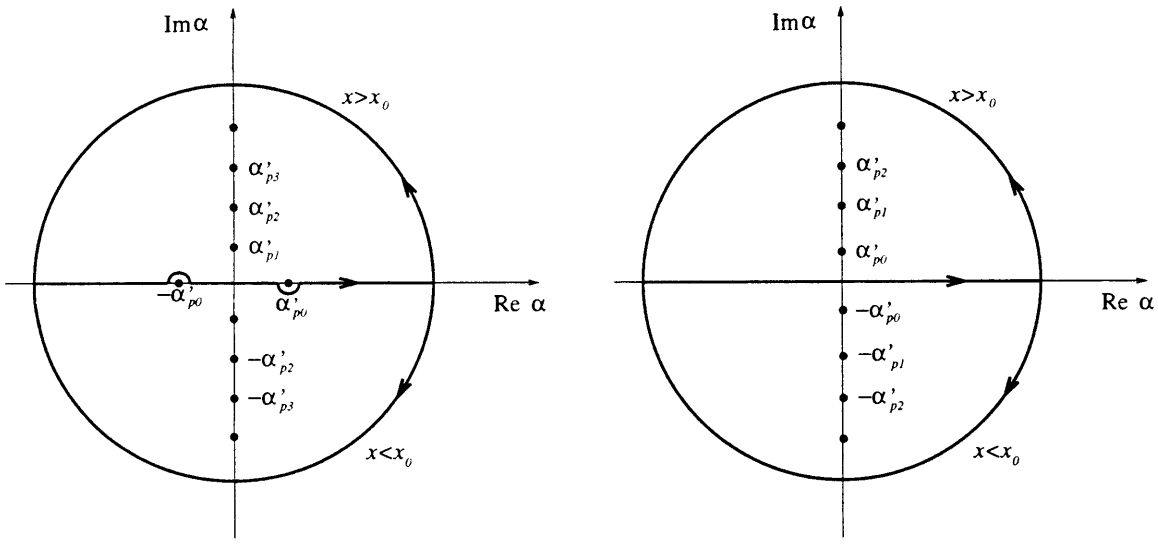

Figure C-1: The complex α plane. On the real axis are indicated the $P+1$ real poles, corresponding to propagating waves. The remaining poles on the immaginary axis correspond to evanescent modes. The upper(lower) contour is for $x > x_0 (x < x_0)$.

which is exactly the eigenfunction expansion of F_p^W! The second integral is also straightforward but lengthy; upon substitution of expressions (C.2.22) for $\Psi_p^{\pm}$ and (2.5.88) for $\Gamma_p^{\pm}(x_0)$ we find:

$$\mp\frac{1}{G}\int_0^{\pm\infty} \mathrm{d}x_0\, \Psi_p^{\pm}(x_0,0;x,z)\,\Gamma_p^{\pm}(x_0) = \pm\frac{\mathrm{i}}{G}\sum_{l=0}^{\infty}\frac{\cosh K_l' h}{2C_l'\alpha_{pl}'}\cosh K_l'(z+h)\,\times$$

$$\left[\int_0^x \mathrm{d}x_0\left(\mathrm{e}^{\mathrm{i}\alpha_{pl}'(x-x_0)}+\mathrm{e}^{\mathrm{i}\alpha_{pl}'(x+x_0)}\right)\Gamma_p^{\pm}+\int_x^{\infty}\mathrm{d}x_0\left(\mathrm{e}^{\mathrm{i}\alpha_{pl}'(-x+x_0)}+\mathrm{e}^{\mathrm{i}\alpha_{pl}'(x+x_0)}\right)\Gamma_p^{\pm}\right] =$$

$$-\frac{1}{G}\sum_{l=0}^{\infty}\frac{\cosh K_l' h}{C_l'}\cosh K_l'(z+h)\sum_{q=-\infty,\neq 0}\sum_{m=0}\sum_{n=0}\times$$

$$\frac{a_{pqmn}}{(\alpha_{qm}+\alpha_{p+q,n})^2+{\alpha_{pl}'}^2}\left[\mathrm{e}^{\mp(\alpha_{qm}+\alpha_{p+q,n})x}-\frac{\mathrm{i}}{\alpha_{pl}'}(\alpha_{qm}+\alpha_{p+q,n})\,\mathrm{e}^{\pm\mathrm{i}\,\alpha_{pl}'x}\right]. \quad \text{(C.3.2)}$$

which is instead the eigenfunction expansion of F_p^F! Hence the two method of solution yield the identical result.

Appendix D

The coefficients of the evolution equation

The coefficient c has the following expression

$$c = \frac{1}{G}\int_0^1 \mathrm{d}y \int_0^\infty \mathrm{d}x\, 4f_{11}^{+^2} + \int_0^1 \mathrm{d}y \int_{-h}^0 \mathrm{d}z\, 4(z+h)q_{11}f_{11}^{+} + 2Iq_{11}^2, \tag{D.1.1}$$

where the last term on the right hand side means

$$2Iq_{11}^2 = 2I + 2\frac{rI}{1-r}\,(1-1/r)^2 = 2I/r. \tag{D.1.2}$$

Carrying out the integrals, obtain

$$c = \frac{2}{G}\sum_{i=1}\sum_{j_1=0}\sum_{j_2=0}\frac{\beta_{ij_1}\beta_{ij_2}}{\alpha_{ij_1}+\alpha_{ij_2}}\cosh K_{j_1}h\cosh K_{j_2}h + \sum_{i=1}\sum_{j=0}\beta_{ij}b_iD_j + \frac{2I}{r} \tag{D.1.3}$$

The complex coefficient $c\,(c_N + \mathrm{i}\,c_R)$ is evaluated numerically but for the last terms arising from the nonlinear buoyancy:

$$\begin{aligned}
c\,(c_N + \mathrm{i}\,c_R) = {} & \frac{1}{G}\int_0^1 \mathrm{d}y \int_0^\infty \mathrm{d}x\, f_{11}^{+}\Big\{-2f_{11}^{+}\left(f_{22_{xx}}^{+} + f_{22_{yy}}^{+}\right) + 4\left(f_{11_x}^{+}f_{22_x}^{+} + f_{11_y}^{+}f_{22_y}^{+}\right) + \\
& 4f_{22}^{+}\left(f_{11_{xx}}^{+} + f_{11_{yy}}^{+}\right) - \frac{12}{G^2}f_{11}^{+}f_{22}^{+} - 3\left(f_{11_y}^{+^3}\right)_y - 3\left(f_{11_x}^{+^3}\right)_x + \frac{f_{11}^{+}}{G^2}\left(f_{11_x}^{+^2} + f_{11_y}^{+^2}\right) + \\
& \frac{f_{11}^{+^2}}{G^2}\left(f_{11_{xx}}^{+} + f_{11_{yy}}^{+}\right) - 3\left(f_{11_x}^{+^2}f_{11_{yy}}^{+} + f_{11_y}^{+^2}f_{11_{xx}}^{+}\right) + \frac{11}{G^4}f_{11}^{+^3} - f_{11_x}^{+}f_{11_y}^{+}f_{11_{xy}}^{+}\Big\} + \\
& \int_0^1 \mathrm{d}y \int_{-h}^0 \mathrm{d}z\, q_{11}\Big\{(z+h)\left(-2f_{11}^{+}f_{22_{zz}}^{+} + 2f_{11_z}^{+}f_{22_z}^{+} + 10q_{11}^2f_{11}^{+}\right) - 10\,a(z+h)^2q_{11}^3 + \\
& (z+h)^3q_{11}^2f_{11_{zz}}^{+} - 2f_{11}^{+}f_{22_z}^{+} + aq_{11}\left(4f_{22}^{+} - f_{11}^{+}f_{11_{zz}}^{+} + f_{11_z}^{+^2}\right)\Big\} +
\end{aligned}$$

$$\int_0^1 \mathrm{d}y\, q_{11}\, \frac{f_{11}^+}{G}\left[-4hf_{22}^+ + \frac{{f_{11}^+}^2}{G}\left(1+\frac{2h}{G}\right)5h^3 q_{11}^2 - 3aq_{11}f_{11}^+\right] +$$
$$\frac{G}{2}\left[ah^2(y_2-y_1)+S\right]\left[1+\left(\frac{1}{r}-1\right)^3\right] \qquad \text{(D.1.4)}$$

In the above expression the real part $c\,c_N$ is given by all the terms containing f_{11}^+ and q_{11} (recall that $f_{11}^\pm$ and q_{11} are real), and by the products of the real part of f_{22}^+ and f_{11}^+ and/or q_{11}, i.e. by the products of all the evanescent modes, and by the last nonlinear buoyancy term. The immaginary part $c\,c_F$ is instead given by the products of the immaginary part of f_{22}^+ and f_{11}^+ and/or q_{11}, i.e. by the products of the $P+1$ radiated modes of the outgoing second harmonic wave and the first order trapped wave.

The last coefficient $c\,c_F$ originates from the quadratic products of $g_{22}^\pm$ and $f_{11}^\pm$ and does not have the symmetry property of the other coefficients, since $g_{22}^+(x,z) \neq g_{22}^-(-x,z)$. Therefore the integrals have to be carried out on both boundaries $\partial\Omega_1^\pm$. The expression of $c\,c_F$ is

$$\begin{aligned}
&c\,c_F = \\
&\frac{1}{G}\int_0^1 \mathrm{d}y \left\{ \int_{-\infty}^0 \mathrm{d}x\, f_{11}^- \left[-f_{11}^- g_{22_{xx}}^- + 2f_{11_x}^- g_{22_x}^- + 2g_{22}^- \left(f_{11_{xx}}^- + f_{11_{yy}}^- \right) - \frac{6}{G^2} f_{11}^- g_{22}^- \right] + \right. \\
&\left. \int_0^\infty \mathrm{d}x\, f_{11}^+ \left[-f_{11}^+ g_{22_{xx}}^+ + 2f_{11_x}^+ g_{22_x}^+ + 2g_{22}^+ \left(f_{11_{xx}}^+ + f_{11_{yy}}^+ \right) - \frac{6}{G^2} f_{11}^+ g_{22}^+ \right] \right\} + \\
&\int_0^1 \mathrm{d}y \int_{-h}^0 \mathrm{d}z\, q_{11} \left\{ (z+h)\left(-\overline{f_{11} f_{22_{zz}}} + \overline{f_{11_z} f_{22_z}} \right) - \overline{f_{11} f_{22_z}} + 2a\overline{g_{22}} \right\} - \\
&-\frac{2h}{G}\int_0^1 \mathrm{d}y\, q_{11}\overline{f_{11} g_{22}}.
\end{aligned} \qquad \text{(D.1.5)}$$

Integration can be carried out explicitly to give

$$\begin{aligned}
c\,c_F = &\frac{1}{2}\sum_{m=1}\sum_{n=0}\sum_{n'=0} \beta_{mn}\beta_{mn'} \cosh K_n h \cosh K_{n'} h \times \\
&\left[\frac{(\alpha_{mn}+\alpha_{mn'})\left(\frac{3}{G^2}+K_{n'}^2\right) - 2{K_0'}^2 \alpha_{mn'}}{(\alpha_{mn}+\alpha_{mn'})^2 + {K_0'}^2} \right] - \frac{2a}{{K_0'}^2}\sum_{m=1} b_m^2 - \\
&\frac{GK_0'}{2\cosh {K_0'}^2 h}\sum_{m=1}\sum_{n=0} b_m \beta_{mn} F_{n0}' + \frac{3h}{2}\sum_{m=1}\sum_{n=0} b_m \beta_{mn} \cosh K_n h,
\end{aligned} \qquad \text{(D.1.6)}$$

where

$$\begin{aligned}
F_{n0}' = &\int_{-h}^0 \mathrm{d}z\, (z+h) K_n \sinh K_n(z+h) \sinh K_0'(z+h) = \\
&K_0'\left(\frac{C_{n0}'}{K_n^2} - D_{n0}' \right) + \left(h - \frac{1}{GK_n^2} \right) \cosh K_n h \sinh K_0' h.
\end{aligned} \qquad \text{(D.1.7)}$$

The first triple summation in (D.1.6) is the contribution of the free surface integrals, while the remaning summations are the contribution of the gate surface integrals.

Appendix E

Details for Melnikov's method

E.1 Homoclinic orbit, $-1 < W < 1$

System (5.4.4)

$$\begin{cases} R_T = -2R\sin 2\psi - \mu\, 2R\left(\alpha_1 R + \beta_1 + \gamma_1\sqrt{R} + a_1\cos\sigma T\sin 2\psi\right) = f_1 + \mu\, g_1, \\ \\ \psi_T = W + R - \cos 2\psi - \mu\left(\beta_1 + a_1\cos\sigma T\cos 2\psi\right) = f_2 + \mu\, g_2, \end{cases} \tag{E.1.1}$$

for $\mu = 0$ has an homoclinic connection when $|W| < 1$. Its parametric expression can be found using the constant value of the Hamiltonian on the orbit itself

$$H(R,\psi) = H(0,\psi_0) = 0. \tag{E.1.2}$$

Using expression (5.1.3) for the Hamiltonian with $a = 0$ gives

$$R\left(\frac{R}{2} + W - \cos 2\psi\right) = 0, \qquad \Longrightarrow \qquad R = 2\cos 2\psi - 2W. \tag{E.1.3}$$

Substitution in the second of (E.1.1) with $\mu = 0$ (i.e. in f_2) gives a first order equation in ψ only

$$\psi_T = \cos 2\psi - W, \tag{E.1.4}$$

whose solution ψ^h with the initial conditions $\psi^h = 0$ for $T = T_0$ is

$$\tan\left[\psi^h(T - T_0;\, W)\right] = \sqrt{\frac{1-W}{1+W}}\tanh\left[\sqrt{1-W^2}\,(T - T_0)\right] \tag{E.1.5}$$

Substitution of (E.1.5) back into (E.1.3) yields

$$R^h(T - T_0;\, W) = \frac{2\,(1-W^2)}{W + \cosh\left[2\sqrt{1-W^2}\,(T - T_0)\right]}. \tag{E.1.6}$$

where $R = 2(1 - W)$ for $T = T_0$.

The Melnikov function is given by

$$M(\sigma, T_0\,;\, W, \alpha_1, \beta_1, \gamma_1, a_1) = \int_{-\infty}^{\infty} \mathrm{d}T\ \left[f_1 g_2 - f_2 g_1\right]_{R=R^h,\psi=\psi^h} = \int_{-\infty}^{\infty} \mathrm{d}T\ 2R^h \times \left[a_1\left(W + R^h\right)\sin 2\psi^h \cos\sigma T - \beta_1 \sin 2\psi^h + \left(W + R^h - \cos 2\psi^h\right)\left(\alpha_1 R^h + \beta_1 + \gamma_1\sqrt{R^h}\right)\right] \quad \text{(E.1.7)}$$

Substituting expressions (E.1.6) and (E.1.5) into the integrands of (E.1.7), the Melnikov function becomes

$$M(\sigma, T_0\,;\, W, \alpha_1, \beta_1, \gamma_1, a_1) = \Pi^{\alpha}(W)\alpha_1 + \Pi^{\beta}(W)\beta_1 + \Pi^{\gamma}(W)\gamma_1 - \Pi^{a}(\sigma, W)\, a_1 \sin\sigma T_0. \quad \text{(E.1.8)}$$

We discuss each partial Π of (E.1.8).

Radiation damping, α_1.

$$\Pi^{\alpha}(W) = \int_{-\infty}^{\infty} \mathrm{d}T\ 2{R^h}^2\left(W + R^h - \cos 2\psi^h\right) = 8\left(1 - W^2\right)^3 \int_{-\infty}^{\infty} \frac{\mathrm{d}T}{\left\{W + \cosh\left[2\sqrt{1 - W^2}\,(T - T_0)\right]\right\}^3}. \quad \text{(E.1.9)}$$

The above integral has a closed form solution which can be found on Gradshteyn & Ryzhik(1979) or by direct integration using MACSYMA

$$\Pi^{\alpha}(W) = 4\left[\left(1 + 2W^2\right)\left(\frac{\pi}{2} - \arctan\frac{W}{\sqrt{1 - W^2}}\right) - 3W\sqrt{1 - W^2}\right] \quad \text{(E.1.10)}$$

Linear viscous damping, β_1.

$$\Pi^{\beta}(W) = \int_{-\infty}^{\infty} \mathrm{d}T\ 2R^h\left(W + R^h - \cos 2\psi^h - \sin 2\psi^h\right) = 4\left(W^2 - 1\right)\int_{-\infty}^{\infty} \mathrm{d}T\, \frac{W^2 - 1 + \sqrt{1 - W^2}\sinh\left[2\sqrt{1 - W^2}\,(T - T_0)\right]}{\left\{W + \cosh\left[2\sqrt{1 - W^2}\,(T - T_0)\right]\right\}^2} \quad \text{(E.1.11)}$$

The part of the integral above in sinh gives zero contribution because sinh is odd in T and the denominator is an even function of T. Therefore

$$\Pi^{\beta}(W) = 4\left(1 - W^2\right)^2 \int_{-\infty}^{\infty} \frac{\mathrm{d}T}{\left\{W + \cosh\left[2\sqrt{1 - W^2}\,(T - T_0)\right]\right\}^2}. \quad \text{(E.1.12)}$$

Also this last integral has a closed form solution which is

$$\Pi^{\beta}(W) = 4\left[W\left(-\frac{\pi}{2} + \arctan\frac{W}{\sqrt{1-W^2}}\right) + \sqrt{1-W^2}\right]. \tag{E.1.13}$$

Quadratic viscous damping, γ_1.

$$\Pi^{\gamma}(W) = \int_{-\infty}^{\infty} \mathrm{d}T 2{R^h}^{3/2}\left(W + R^h - \cos 2\psi^h\right) = 4\sqrt{2}\left(1-W^2\right)^{5/2}\int_{-\infty}^{\infty}\frac{\mathrm{d}T}{\left\{W + \cosh\left[2\sqrt{1-W^2}\,(T-T_0)\right]\right\}^{5/2}}. \tag{E.1.14}$$

The above integral (E.1.14) can only be evaluated numerically. By letting

$$2\sqrt{1-W^2}\,(T-T_0) = \log\frac{1}{x}, \tag{E.1.15}$$

we get

$$\Pi^{\gamma}(W) = 16\sqrt{2}\left(1-W^2\right)^3\int_0^1\frac{\mathrm{d}x}{x\left[W + \cosh\left(\log(x)\right)\right]^{5/2}}. \tag{E.1.16}$$

Forcing term, a_1

$$-\Pi^{a}(\sigma, W)\,\sin\sigma T_0 = \int_{-\infty}^{\infty}\mathrm{d}T\; 2R^h\left(W + R^h\right)\sin 2\psi^h\,\cos\sigma T = 2\left(1-W^2\right)\times \int_{-\infty}^{\infty}\mathrm{d}\tau\,\frac{(W^2 - 2 - W\cosh\tau)\,\sinh\tau\,\cos\left[\sigma\left(\frac{\tau}{2\sqrt{1-W^2}} + T_0\right)\right]}{(W+\cosh\tau)^3}, \tag{E.1.17}$$

where the following change of variable has been made

$$2\sqrt{1-W^2}\,(T-T_0) = \tau. \tag{E.1.18}$$

If we rewrite the cosine function as

$$\cos\left[\sigma\left(\frac{\tau}{2\sqrt{1-W^2}} + T_0\right)\right] = \cos\frac{\sigma\tau}{2\sqrt{1-W^2}}\,\cos\sigma T_0 - \sin\frac{\sigma\tau}{2\sqrt{1-W^2}}\,\sin\sigma T_0 \tag{E.1.19}$$

and recall that the integral from $-\infty$ to ∞ of odd functions is zero, we reduce integral (E.1.17) to

$$-\Pi^{a}(\sigma, W)\sin\sigma T_0 = -2\left(1-W^2\right)\times \sin\sigma T_0\int_{-\infty}^{\infty}\mathrm{d}\tau\,\frac{(W^2 - 2 - W\cosh\tau)\,\sinh\tau\,\sin\frac{\sigma\tau}{2\sqrt{1-W^2}}}{(W+\cosh\tau)^3}, \tag{E.1.20}$$

The last integral can be evaluated with the residue method. Consider the path 1234 in the complex plane $\mathrm{Re}\tau \sim \mathrm{Im}\tau$ of figure E-1. From the residue theorem, the integral on the complex path 1234 of the integrand of (E.1.20) is

$$\int_{1234} \mathrm{d}\tau \, \frac{(W^2 - 2 - W\cosh\tau)\,\sinh\tau\,\sin\frac{\sigma\tau}{2\sqrt{1-W^2}}}{(W+\cosh\tau)^3} = 2\pi\mathrm{i}\sum_{j=1}^{2}\mathrm{Res}_j \tag{E.1.21}$$

where Res_j are the residues of the integrand calculated at the two poles

$$\tau = \mathrm{i}\,\arccos W, \quad \text{and} \quad \tau = \mathrm{i}\,(2\pi - \arccos W)\,. \tag{E.1.22}$$

Integral (E.1.20) is the limit for $R \to \infty$ of the 1-2 part of the integral in (E.1.21). It is straightforward to find that, as the abscissa $\pm R$ of the two parts 2-3 and 4-1 of the path goes to infinity, their contributions go to zero (c.f. (E.1.21) for $\tau = \pm R + \mathrm{i}\mathrm{Im}\tau$ and figure E-1). Therefore the only contributions to (E.1.21) come from the parts 1-2 and 4-1.

Since

$$\int_{34} = -\cosh\frac{2\pi\sigma}{2\sqrt{1-W^2}}\int_{12} \tag{E.1.23}$$

The desired integral (E.1.20) is given by

$$\int_{\infty}^{\infty} \mathrm{d}\tau \, \frac{(W^2 - 2 - W\cosh\tau)\,\sinh\tau\,\sin\frac{\sigma\tau}{2\sqrt{1-W^2}}}{(W+\cosh\tau)^3} = \frac{2\pi\mathrm{i}\sum_{j=1}^{2}\mathrm{Res}_j}{1-\cosh\frac{2\pi\sigma}{2\sqrt{1-W^2}}}. \tag{E.1.24}$$

Evaluation of the residues with the aid of MACSYMA gives

$$\int_{\infty}^{\infty} \mathrm{d}\tau \, \frac{(W^2 - 2 - W\cosh\tau)\,\sinh\tau\,\sin\frac{\sigma\tau}{2\sqrt{1-W^2}}}{(W+\cosh\tau)^3} = -\frac{\pi\sigma^2\cosh\left(\frac{\sigma\arccos W}{2\sqrt{1-W^2}}\right)}{2\,(1-W^2)\sinh\frac{\pi\sigma}{2\sqrt{1-W^2}}}. \tag{E.1.25}$$

Finally, substitution of the above (E.1.25) in (E.1.20) yields

$$-\,\Pi^a(\sigma,W)\sin\sigma T_0 \;= -\sin\sigma T_0\;\pi\sigma^2\cosh\left(\frac{\sigma\arccos W}{2\sqrt{1-W^2}}\right)\Big/\sinh\left(\frac{\pi\sigma}{2\sqrt{1-W^2}}\right), \tag{E.1.26}$$

that is

$$\Pi^a(\sigma,W) = \pi\sigma^2\cosh\left(\frac{\sigma\arccos W}{2\sqrt{1-W^2}}\right)\Big/\sinh\left(\frac{\pi\sigma}{2\sqrt{1-W^2}}\right). \tag{E.1.27}$$

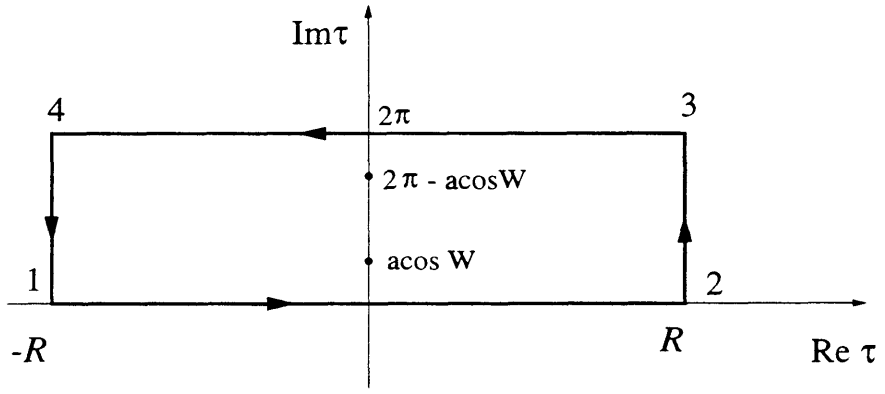

Figure E-1: Path in the complex plane for the residue method; homoclinic orbit

E.2 Heteroclinic orbits, $W < -1$

System (E.1.1) with $\mu = 0$ has two heteroclinic connection for $W < -1$. Their parametric expressions can be found using the costant value of the Hamiltonian on the orbits themselves

$$H(R, \psi) = H(-1 - W, \mp\pi/2) = -\frac{1}{2}(1 + W)^2. \tag{E.2.1}$$

Using expression (5.1.3) for the Hamiltonian with $a = 0$ gives

$$R\left(\frac{R}{2} + W - \cos 2\psi\right) = -\frac{1}{2}(1 + W)^2, \tag{E.2.2}$$

from which

$$R = -W + \cos 2\psi \pm \sqrt{(1 + \cos 2\psi)(-1 - 2W + \cos 2\psi)}. \tag{E.2.3}$$

Substitution in the second of (E.1.1) with $\mu = 0$ (i.e. in f_2) gives a first order equation in ψ only

$$\psi_T = \pm \frac{1}{2\cos\psi\sqrt{-W - 1 + \cos^2\psi}}, \tag{E.2.4}$$

whose solutions $\psi^{h\pm}$ with the initial conditions $\psi^h = 0$ for $T = T_0$ is

$$\tan\left[\psi^{h\pm}(T - T_0;\, W)\right] = \pm\sqrt{\frac{W}{1 + W}}\sinh\left[2\sqrt{-1 - W}\,(T - T_0)\right] \tag{E.2.5}$$

Substitution of (E.2.5) back into (E.2.3) yields

$$R^{h\pm}(T-T_0;\,W) = -(1+W)\frac{\sqrt{-W}\cosh\left[2\sqrt{-1-W}\,(T-T_0)\right]\pm 1}{\sqrt{-W}\cosh\left[2\sqrt{-1-W}\,(T-T_0)\right]\mp 1}, \qquad \text{(E.2.6)}$$

where the $\pm$ superscript refers respectively to the upper and lower orbits and for $T = T_0$, $R^{h\pm} = \left(\sqrt{-W}\pm 1\right)^2$.

The Melnikov function is given by

$$M(\sigma, T_0\,;\, W, \alpha_1, \beta_1, \gamma_1, a_1) = \int_{-\infty}^{\infty} dT\ [f_1 g_2 - f_2 g_1]_{R=R^{h\pm},\,\psi=\psi^{h\pm}} = \int_{-\infty}^{\infty} dT\ 2R^{h\pm}\ \times$$
$$\left[a_1\left(W + R^{h\pm}\right)\sin 2\psi^{h\pm}\cos\sigma T - \beta_1 \sin 2\psi^{h\pm} + \right.$$
$$\left.\left(W + R^{h\pm} - \cos 2\psi^{h\pm}\right)\left(\alpha_1 R^{h\pm} + \beta_1 + \gamma_1\sqrt{R^{h\pm}}\right)\right] \qquad \text{(E.2.7)}$$

Substituting expressions (E.2.6) and (E.2.5) into the integrands of (E.2.7), the Melnikov function becomes

$$M(\sigma, T_0\,;\, W, \alpha_1, \beta_1, \gamma_1, a_1) = \Pi^{\alpha^\pm}(W)\alpha_1 + \Pi^{\beta^\pm}(W)\beta_1 + \Pi^{\gamma^\pm}(W)\gamma_1 -$$
$$\Pi^{a}(\sigma, W)\, a_1 \sin\sigma T_0. \qquad \text{(E.2.8)}$$

We discuss each partial Π of (E.2.8).

Radiation damping, α_1.

$$\Pi^{\alpha^\pm}(W) = \int_{-\infty}^{\infty} dT\ 2{R^{h\pm}}^2\left(W + R^{h\pm} - \cos 2\psi^{h\pm}\right) = 4\,(-1-W)^3\sqrt{-W}\times$$
$$\int_{-\infty}^{\infty} dT \frac{\sqrt{-W}\cosh\left[2\sqrt{-1-W}\,(T-T_0)\right]\pm 1}{\left\{\sqrt{-W}\cosh\left[2\sqrt{-1-W}\,(T-T_0)\right]\mp 1\right\}^3}\cosh\left[2\sqrt{-1-W}\,(T-T_0)\right]. \qquad \text{(E.2.9)}$$

The above integral has a closed form solution which can be found on Gradshteyn & Ryzhik(1979) or by direct integration using MACSYMA

$$\Pi^{\alpha^\pm}(W) = \mp 4W\left[(W-2)\left(\arctan\sqrt{-1-W} - \left\{\begin{array}{c}\pi\\0\end{array}\right\}\right) + 3\sqrt{-1-W}\right]. \qquad \text{(E.2.10)}$$

Linear viscous damping, β_1.

$$\Pi^{\beta^\pm}(W) = \int_{-\infty}^{\infty} dT\ 2R^{h\pm}\left(W + R^{h\pm} - \cos 2\psi^{h\pm} - \sin 2\psi^{h\pm}\right) =$$
$$4\sqrt{-W}\,(1+W)^2\int_{-\infty}^{\infty} dT\ \times$$
$$\frac{\cosh\left[2\sqrt{-1-W}\,(T-T_0)\right] + (-1-W)^{-\frac{1}{2}}\sinh\left[2\sqrt{-1-W}\,(T-T_0)\right]}{\left\{\sqrt{-W}\cosh\left[2\sqrt{-1-W}\,(T-T_0)\right]\mp 1\right\}^2} \qquad \text{(E.2.11)}$$

The part of the integral above in sinh gives zero contribution because sinh is odd in T and the denominator is an even function of T. Therefore

$$\Pi^{\beta^{\pm}}(W) = 4\sqrt{-W}\,(1+W)^2 \int_{-\infty}^{\infty} \mathrm{d}T \, \frac{\cosh\left[2\sqrt{-1-W}\,(T-T_0)\right]}{\left\{\sqrt{-W}\cosh\left[2\sqrt{-1-W}\,(T-T_0)\right] \mp 1\right\}^2}. \tag{E.2.12}$$

Also this integral has a closed form solution which is

$$\Pi^{\beta^{\pm}}(W) = \pm 4\left[W\left(\arctan\sqrt{-1-W} - \left\{\begin{array}{c}\pi\\0\end{array}\right\}\right) + \sqrt{-1-W}\right]. \tag{E.2.13}$$

Quadratic viscous damping, γ_1.

$$\Pi^{\gamma^{\pm}}(W) = \int_{-\infty}^{\infty} \mathrm{d}T 2R^{h\pm\,3/2}\left(W + R^{h\pm} - \cos 2\psi^{h\pm}\right) =$$

$$4\sqrt{W\,(1+W)}\left(1+W^2\right)^2 \int_{-\infty}^{\infty} \mathrm{d}T \frac{\left\{\cosh\left[2\sqrt{-1-W}\,(T-T_0)\right] \pm 1\right\}^{\frac{1}{2}}}{\left\{\cosh\left[2\sqrt{-1-W}\,(T-T_0)\right] \mp 1\right\}^{\frac{5}{2}}}. \tag{E.2.14}$$

The above integral (E.2.14) can only be evaluated numerically. By letting

$$2\sqrt{-1-W}\,(T-T_0) = \log\frac{1}{x}, \tag{E.2.15}$$

we get

$$\Pi^{\gamma^{\pm}}(W) = 4\sqrt{-W}\left(1+W^2\right)^2 \int_0^1 \mathrm{d}x \, \frac{\left[\cosh\left(\log(x)\right) \pm 1\right]^{\frac{1}{2}}}{x\left[\cosh\left(\log(x)\right) \mp 1\right]^{\frac{5}{2}}}. \tag{E.2.16}$$

Forcing term, a_1

$$-\Pi^{a}(\sigma, W)\,\sin\sigma T_0 = \int_{-\infty}^{\infty} \mathrm{d}T\; 2R^{h\pm}\left(W + R^{h\pm}\right)\sin 2\psi^{h\pm}\,\cos\sigma T =$$

$$2\,(1+W)\sqrt{-W}\int_{-\infty}^{\infty} \mathrm{d}\tau \;\times$$

$$\frac{\left(2W - \sqrt{-W}\cosh\tau \mp 1\right)\sinh\tau\,\cos\left[\sigma\left(\frac{\tau}{2\sqrt{-1-W}} + T_0\right)\right]}{\left(\sqrt{-W}\cosh\tau \pm 1\right)^3}, \tag{E.2.17}$$

where the following change of variable has been made

$$2\sqrt{-1-W}\,(T-T_0) = \tau. \tag{E.2.18}$$

If we rewrite the cosine function as

$$\cos\left[\sigma\left(\frac{\tau}{2\sqrt{-1-W}}+T_0\right)\right]=\cos\frac{\sigma\tau}{2\sqrt{-1-W}}\cos\sigma T_0-\sin\frac{\sigma\tau}{2\sqrt{-1-W}}\sin\sigma T_0 \tag{E.2.19}$$

and recall that the integral from $-\infty$ to ∞ of odd functions is zero, we reduce integral (E.2.17) to

$$-\Pi^a(\sigma,W)\sin\sigma T_0=-2\,(1+W)\sqrt{-W}\times$$
$$\sin\sigma T_0\int_{-\infty}^{\infty}\mathrm{d}\tau\,\frac{\left(2W-\sqrt{-W}\cosh\tau\mp 1\right)\sinh\tau\,\sin\left(\frac{\sigma\tau}{2\sqrt{-1-W}}\right)}{\left(\sqrt{-W}\cosh\tau\pm 1\right)^3}, \tag{E.2.20}$$

The last integral can be evaluated with the residue method. Consider the path 1234 in the complex plane $\mathrm{Re}\tau\sim\mathrm{Im}\tau$ of figure E-2 which is identical to the one of figure E-1, but for the fact that now it encircles the poles of the upper/lower orbits, respectively at

$$\tau=\mathrm{i}\arccos\left(\mp\frac{1}{\sqrt{-W}}\right),\quad\text{and}\quad\tau=\mathrm{i}\left[2\pi-\arccos\left(\mp\frac{1}{\sqrt{-W}}\right)\right]. \tag{E.2.21}$$

Using the residue theorem, the integral on the complex path 1234 of the integrand of (E.2.20) is

$$\int_{1234}\mathrm{d}\tau\,\frac{\left(2W-\sqrt{-W}\cosh\tau\mp 1\right)\sinh\tau\,\sin\left(\frac{\sigma\tau}{2\sqrt{-1-W}}\right)}{\left(\sqrt{-W}\cosh\tau\pm 1\right)^3}=2\pi\mathrm{i}\sum_{j=1}^{2}\mathrm{Res}_j \tag{E.2.22}$$

where Res_j are the residues of the integrand calculated at the two poles in $\mathrm{Im}\tau\in[0,2\pi]$. Using the same argument of the previous section, we deduce that the only contributions to (E.2.22) come from the parts 1-2 and 4-1.

Since

$$\int_{34}=-\cosh\frac{2\pi\sigma}{2\sqrt{-1-W}}\int_{12} \tag{E.2.23}$$

The desired integral (E.2.20) is given by

$$\int_{\infty}^{\infty}\mathrm{d}\tau\,\frac{(W^2-2-W\cosh\tau)\sinh\tau\,\sin\frac{\sigma\tau}{2\sqrt{1-W^2}}}{(W+\cosh\tau)^3}=\frac{2\pi\mathrm{i}\sum_{j=1}^{2}\mathrm{Res}_j}{1-\cosh\frac{2\pi\sigma}{2\sqrt{1-W^2}}}. \tag{E.2.24}$$

Evaluation of the residues with the aid of MACSYMA gives

$$\int_{\infty}^{\infty}\mathrm{d}\tau\,\frac{\left(2W-\sqrt{-W}\cosh\tau\mp 1\right)\sinh\tau\,\sin\left(\frac{\sigma\tau}{2\sqrt{-1-W}}\right)}{\left(\sqrt{-W}\cosh\tau\pm 1\right)^3}=$$

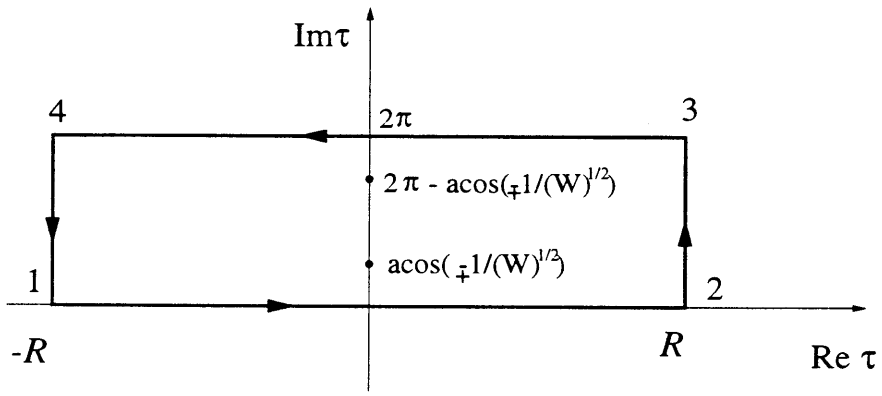

Figure E-2: Path in the complex plane for the residue method; heteroclinic upper and lower orbits

$$\pi\sigma^2 \frac{\cosh\left\{\sigma\left[\arccos\left(1/\sqrt{-W}\right)-\left\{\begin{array}{c}\pi\\0\end{array}\right\}\right]\Big/2\sqrt{-1-W}\right\}}{2\sqrt{-W}\,(1+W)\sinh\left(\pi\sigma\,/2\sqrt{-1-W}\right)}. \qquad \text{(E.2.25)}$$

Finally, substitution of the above (E.2.25) in (E.2.20) yields

$$\Pi^a(\sigma,W)=\pi\sigma^2 \frac{\cosh\left\{\sigma\left[\arccos\left(1/\sqrt{-W}\right)-\left\{\begin{array}{c}\pi\\0\end{array}\right\}\right]\Big/2\sqrt{-1-W}\right\}}{\sinh\left(\pi\sigma\,/2\sqrt{-1-W}\right)}. \qquad \text{(E.2.26)}$$

Appendix F

Further comparisons with experiments for modulated waves

Here we present further comparisons of the theoretical prediction with the experimental findings. The frequency of modulation is fixed at $\Omega/2\pi = 0.045$ Hz and increasing values of a are considered. The scenario is similar to the one described for $\Omega/2\pi = 0.040$ Hz in Chapter 5.6.4.

First, in figure F-1 we show the synchronous response for $a = 0.430$. Then, figure F-2 shows a period doubled response for $a = 0.640$. Chaotic motion is reported in the three figures F-3, F-4 and F-5, for $a = 0.810$, 0.827 and $a = 0.990$ respectively. Finally one sample case of the period-two response involving frequency downshift is shown in figure F-6.

The experiments are reported in figure F-7 to F-12. Figure F-7 shows the synchronous response for $a = 0.43$ and must be compared with figure F-1. Figure F-8 shows the subharmonic response for $a = 0.65$ and must be compared with figure F-2 for $a = 0.64$.

Besides the similarity of the syncronous and subharmonic responses, figures F-9, F-10 and F-11, for $a = 0.89$, 0.99 and 1.10 respectively, show how similar is the shape and size of the experimental strange attractor with the theoretical one (compare with figures F-3, F-4 and F-5).

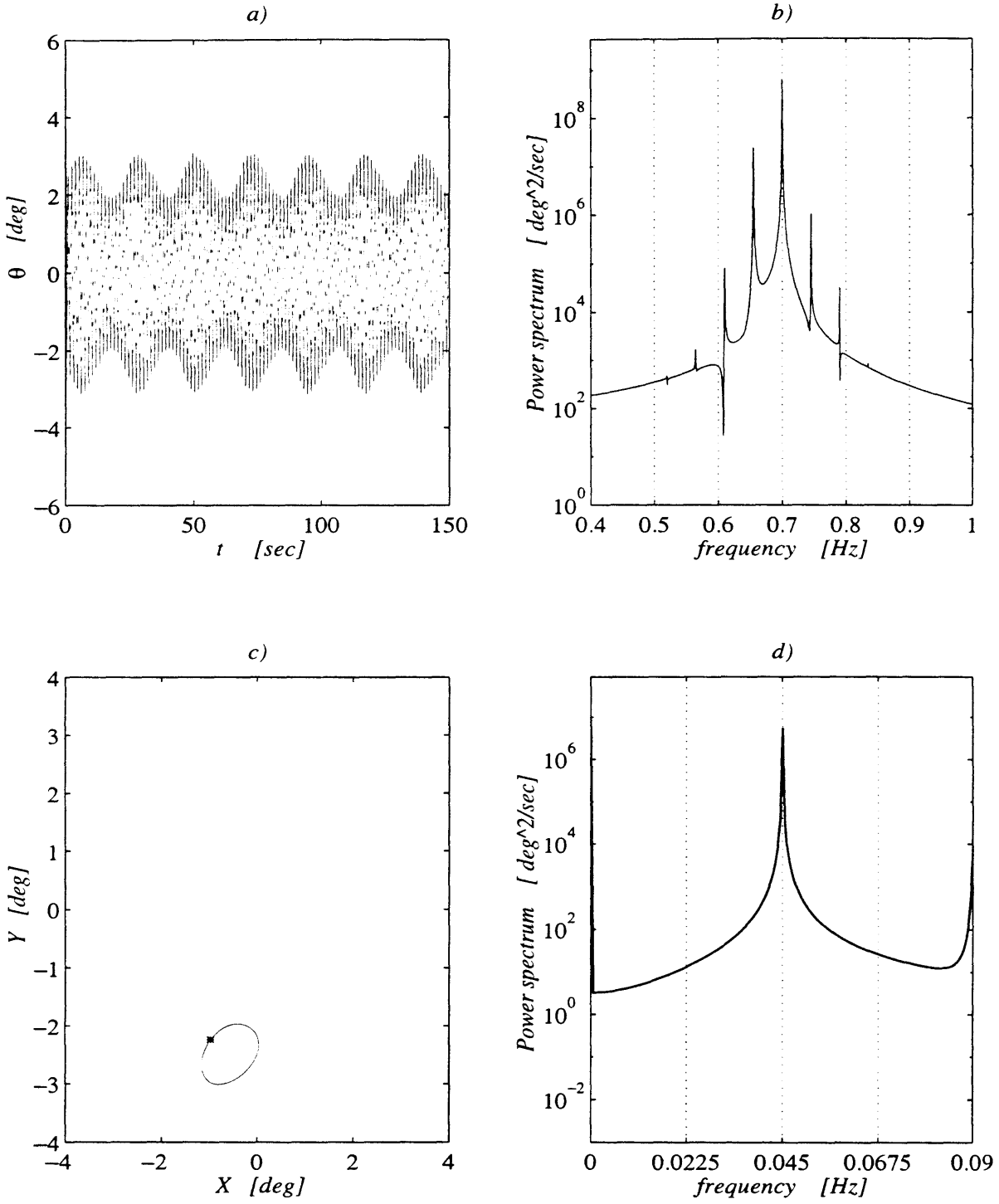

Figure F-1: $\Omega/2\pi = 0.045$ Hz, $a = 0.43$, synchronous response. a) time series of angular displacement with modulation synchronous with incident wave; b) spectrum shows side bands at $(\omega_0 \pm \Omega)/2\pi = 0.7 \pm 0.045$; c) Poincaré map with one fixed point together with phase trajectory; d) spectrum of the envelope shows the offset of the orbit in c) and a peak at $\Omega/2\pi$.

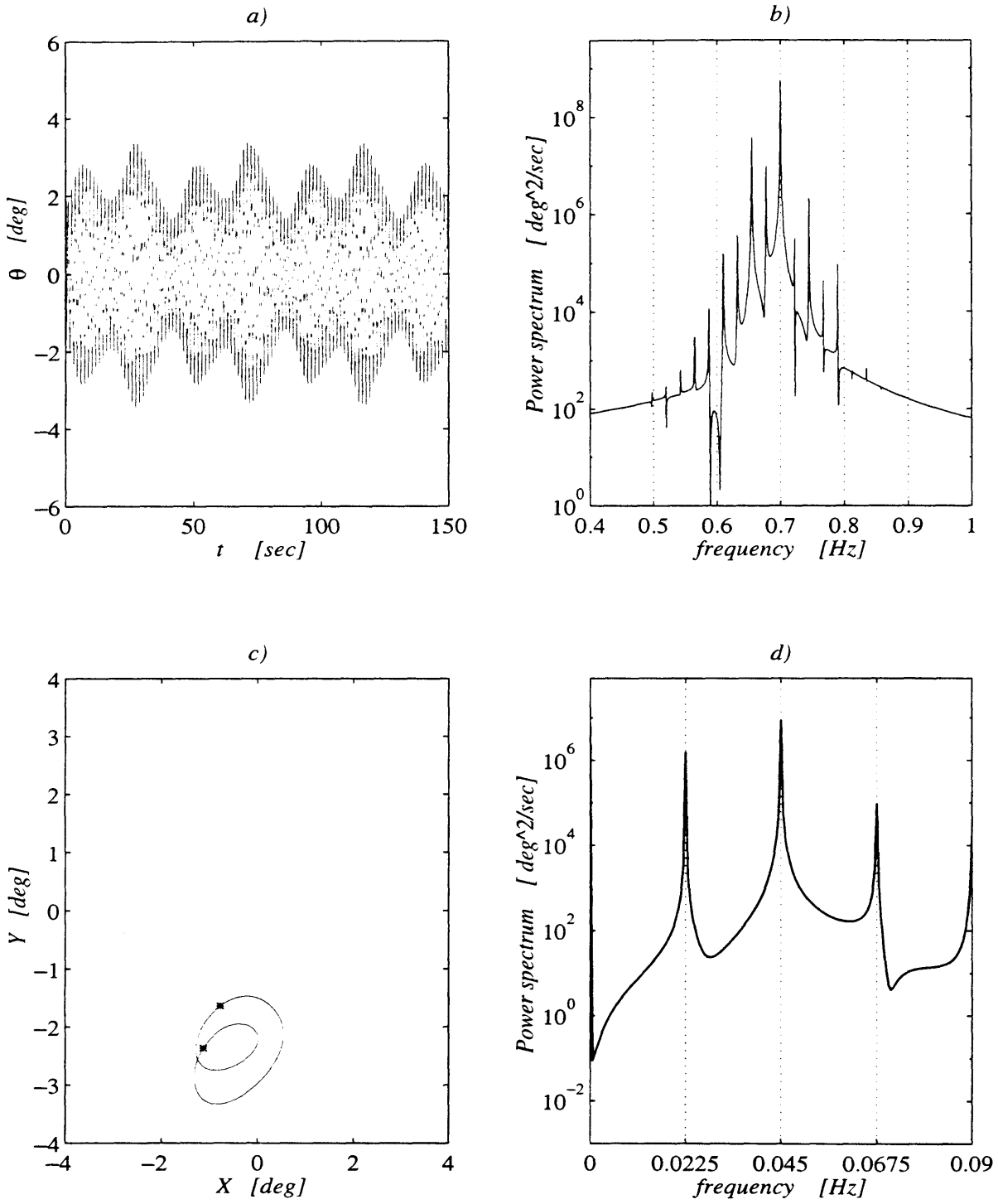

Figure F-2: $\Omega/2\pi = 0.045$ Hz, $a = 0.64$, subharmonic response. a) subharmonic modulation is visible in the time series; b) spectrum shows small side bands at $(\omega_0 \pm \Omega/2)/2\pi = 0.7 \pm 0.0225$ Hz; c) Poincaré map has two fixed point; d) spectrum of the envelope shows a peak at $(\Omega/2)/2\pi = 0.0225$ Hz.

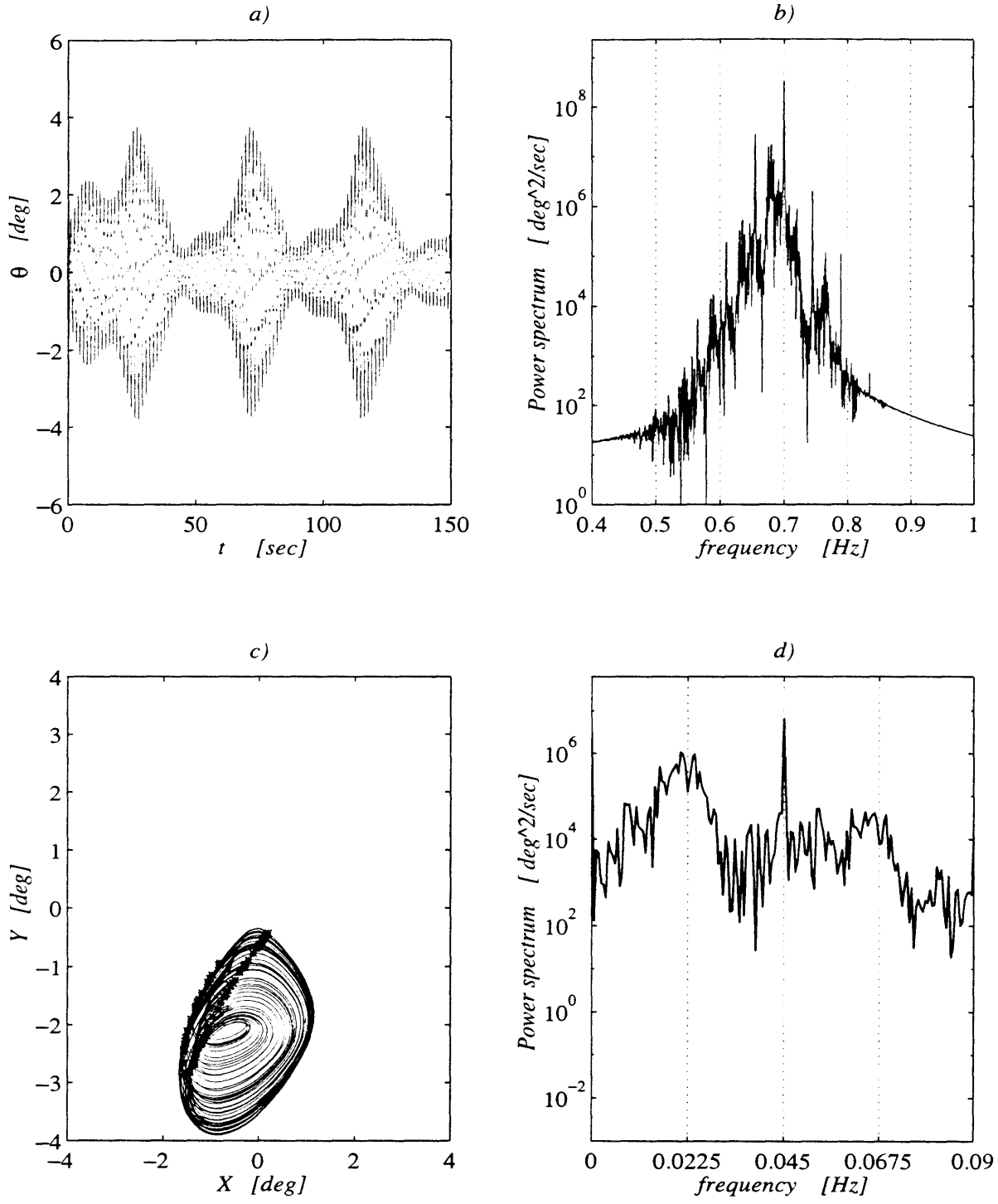

Figure F-3: $\Omega/2\pi = 0.045$ Hz, $a = 0.81$, nonperiodic motion has started. a) time series does not repeat itself; b) the noise under the side bands is appreciable; c) the Poincaré map shows a strange attractor, the trajectory is still offset; d) the spectrum is broad banded with dominant peaks at $\Omega/2$ and its higher harmonic.

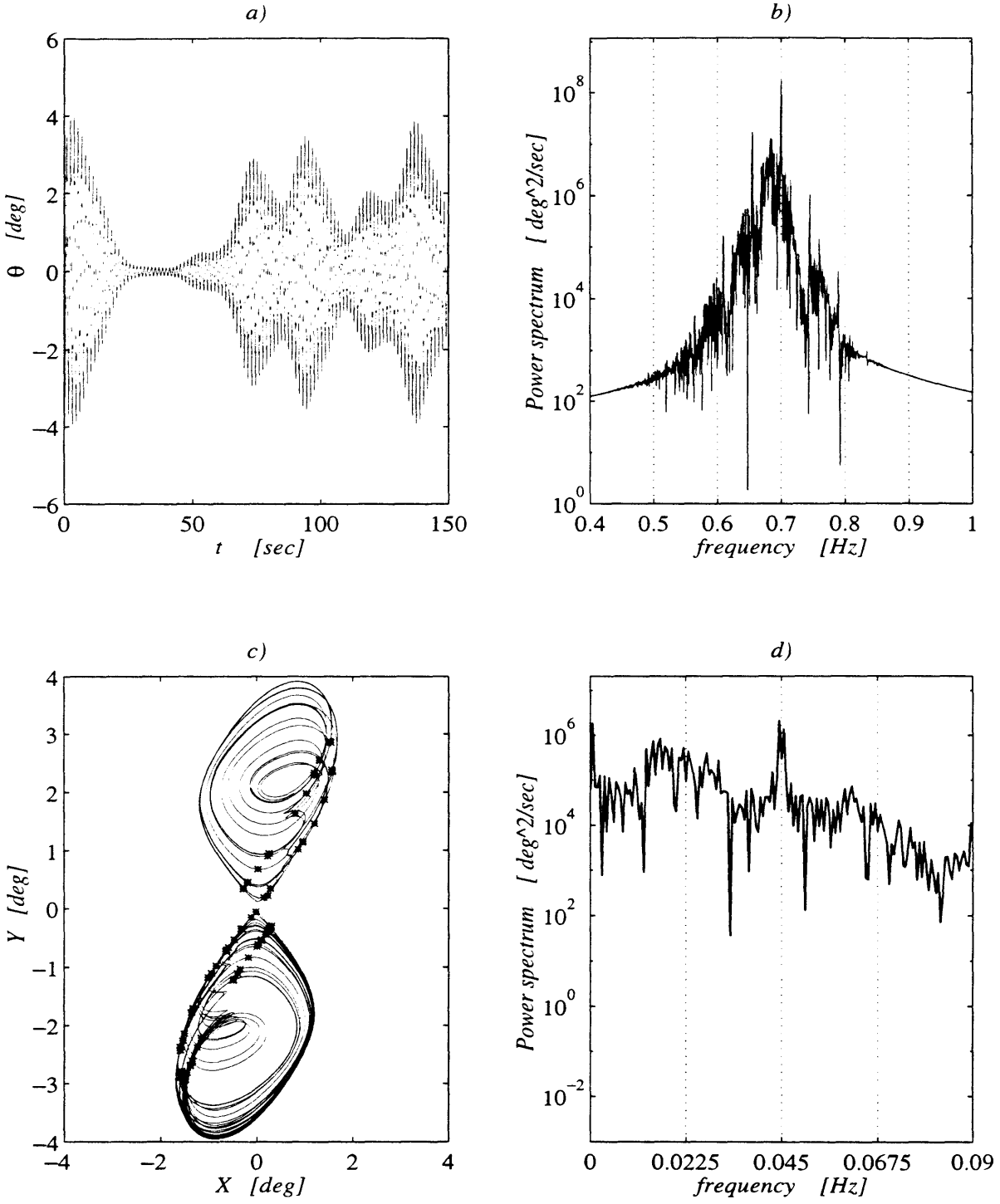

Figure F-4: $\Omega/2\pi = 0.045$ Hz, $a = 0.827$, chaotic motion. b) the spectrum mantains its peak at ω_0 but is broad banded; c) strange attractor; d) the noise level is almost uniform, but for a dominant peak at Ω

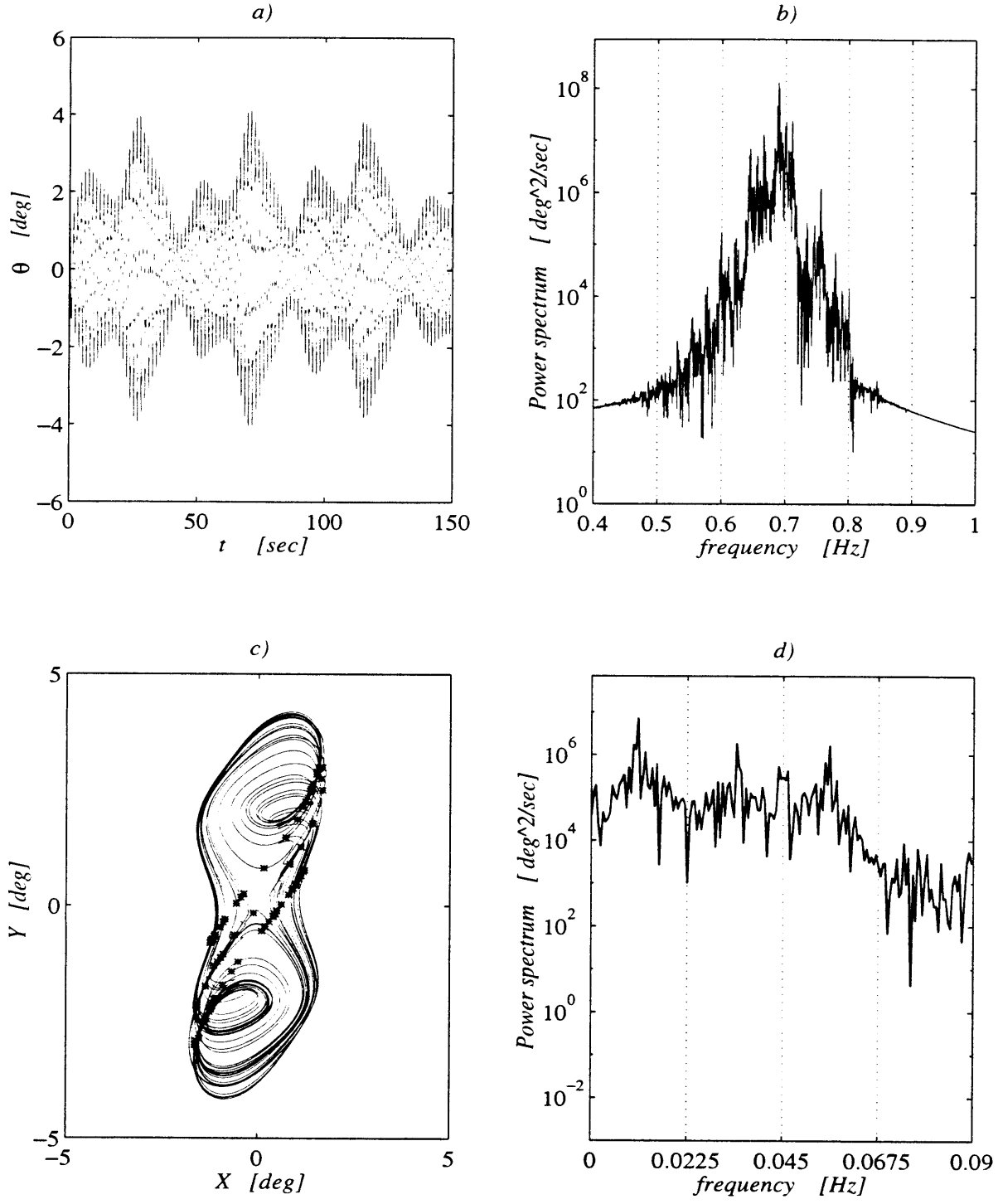

Figure F-5: $\Omega/2\pi = 0.045$ Hz, $a = 0.99$, chaotic motion.

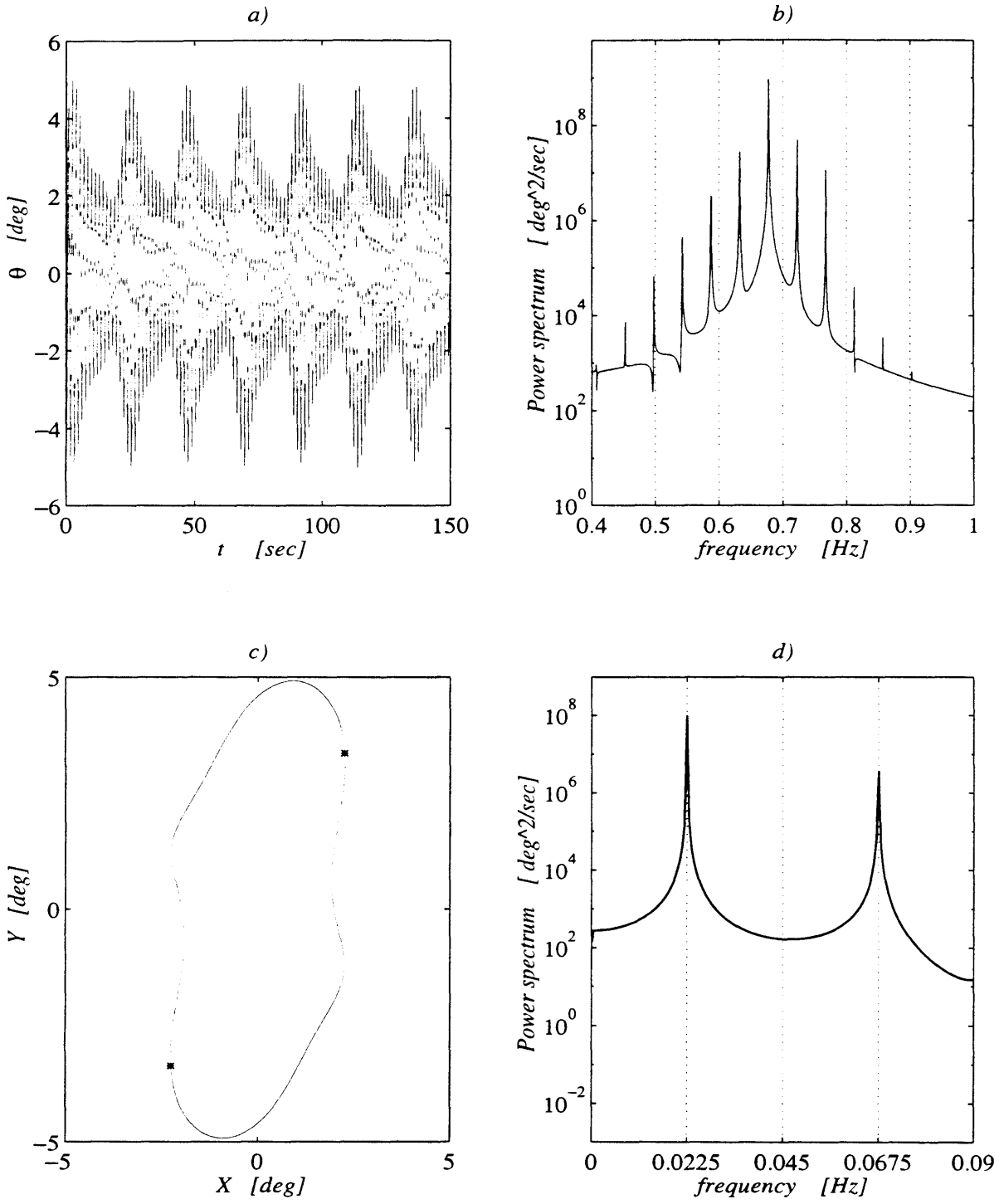

Figure F-6: $\Omega/2\pi = 0.045$ Hz, $a = 1.29$, frequency downshift. a) the time series modulation is periodic with period $2\pi/\Omega = 35.71\ldots$; b) the frequency peak is at $(\omega_0 - \Omega/2)/2\pi = 0.6775$ Hz and there is no energy at $\omega_0/2\pi = 0.700$ Hz; c) Poincaré map and trajectory are symmetric with respect to the origin, no offset; d) there is no energy at Ω!

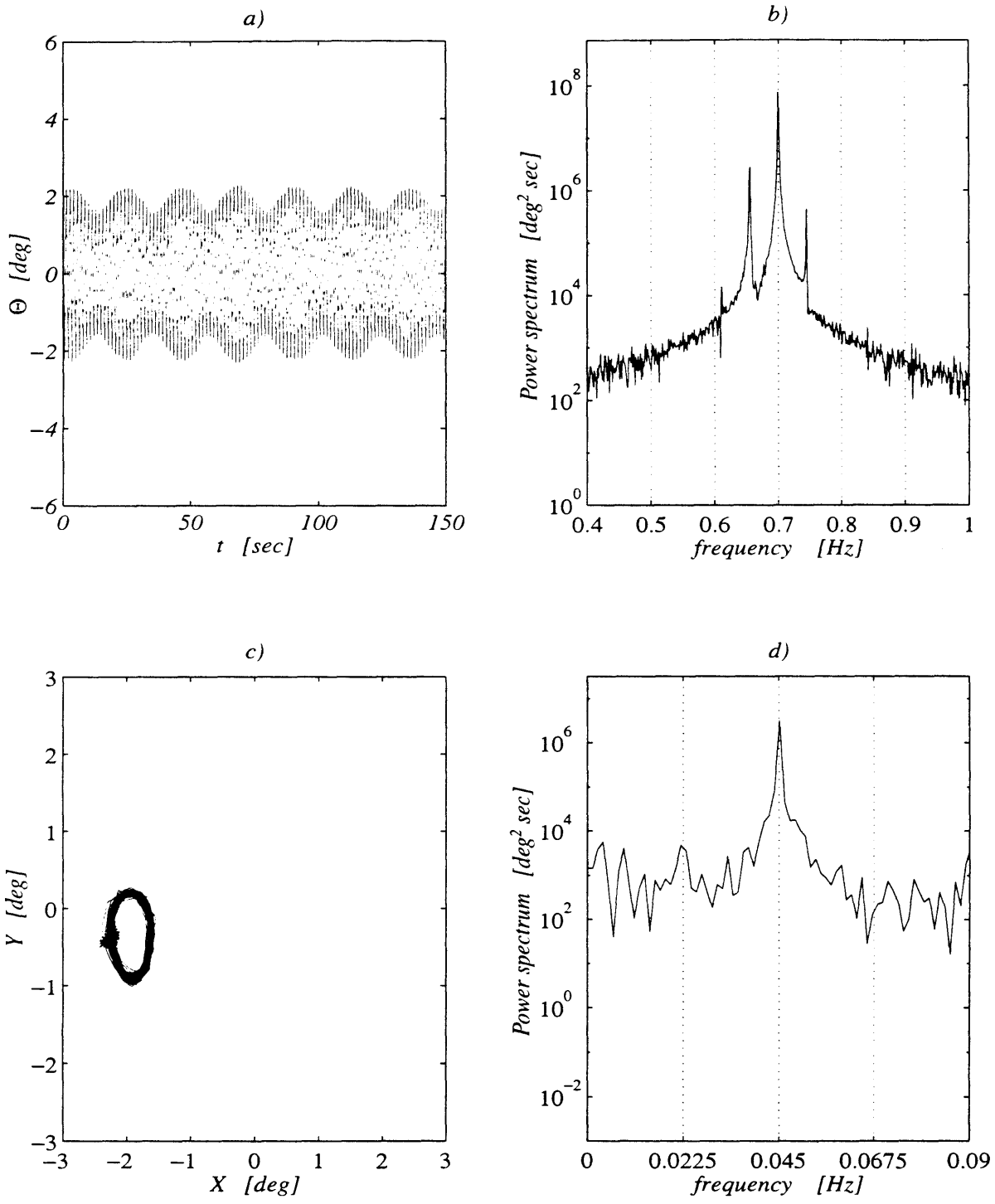

Figure F-7: Experiments for $\Omega/2\pi = 0.045$ Hz, $a = 0.43$; a) experimental time series showing synchronous modulation; b) spectrum of the time series showing asymmetry in the side-bands c) Poincaré section has one point; d) spectrum of the envelope has one peak at Ω.

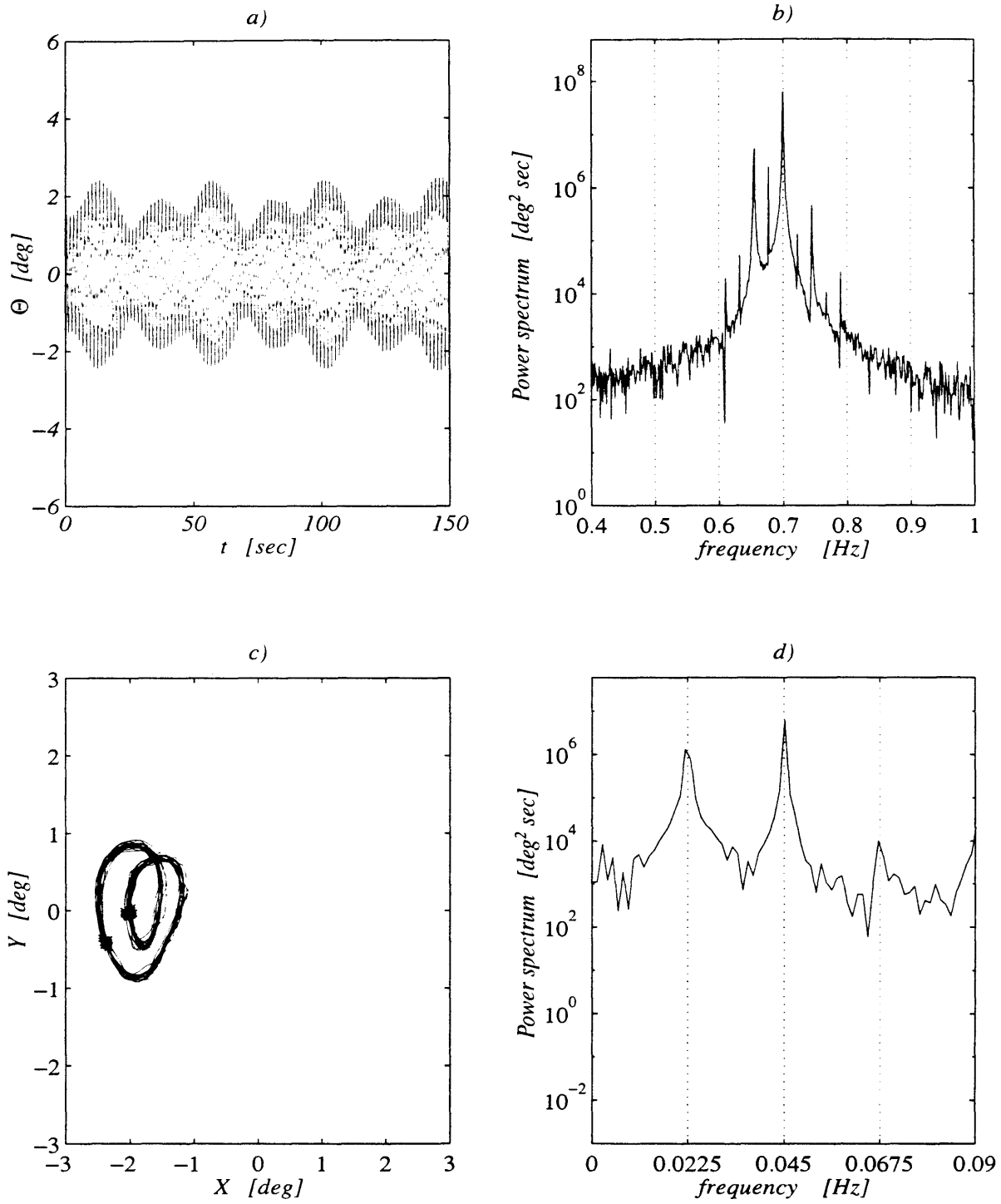

Figure F-8: Experiments for $\Omega/2\pi = 0.045$ Hz, $a = 0.65$; period-two modulational response. a) the experimental time series shows period doubled envelope; b) the spectrum has two distinct side bands at $(\omega_0 \pm \Omega/2)/2\pi = 0.70 \pm 0.0225$ Hz; c) the phase trajectory has a second loop and the Poincaré section is made of two points; d) spectrum of the envelope has a distinct peak at $(\Omega/2)/2\pi = 0.0225$ Hz.

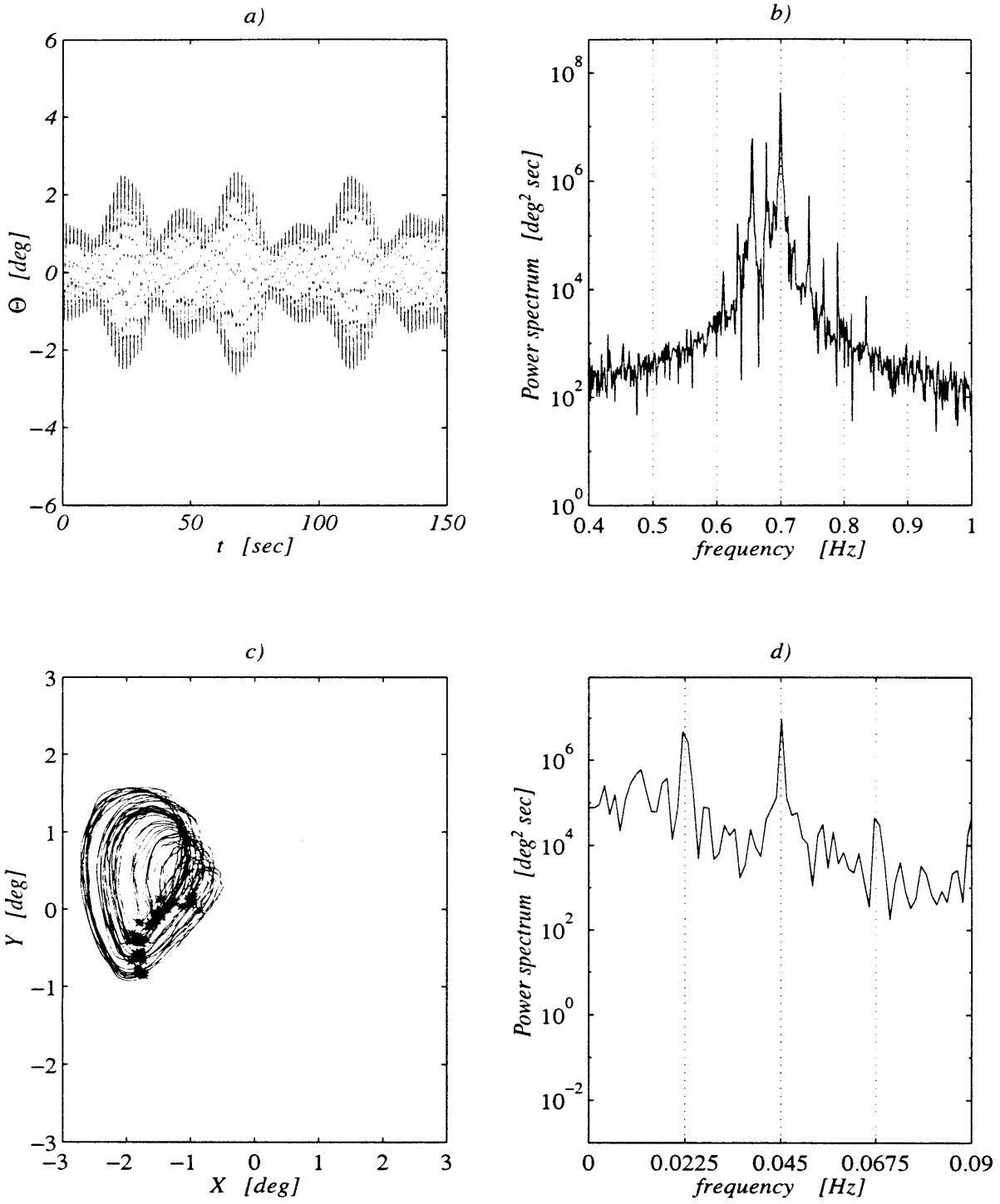

Figure F-9: Experiments for $\Omega/2\pi = 0.045$ Hz, $a = 0.89$; transition to chaotic oscillations. a) time series envelope is non-periodic; b) energy spectrum has considerable energy away from carrier and modulational frequency; c) early stage of the strange attractor with fractal Poincaré section; d) broad-banded spectrum of the envelope.

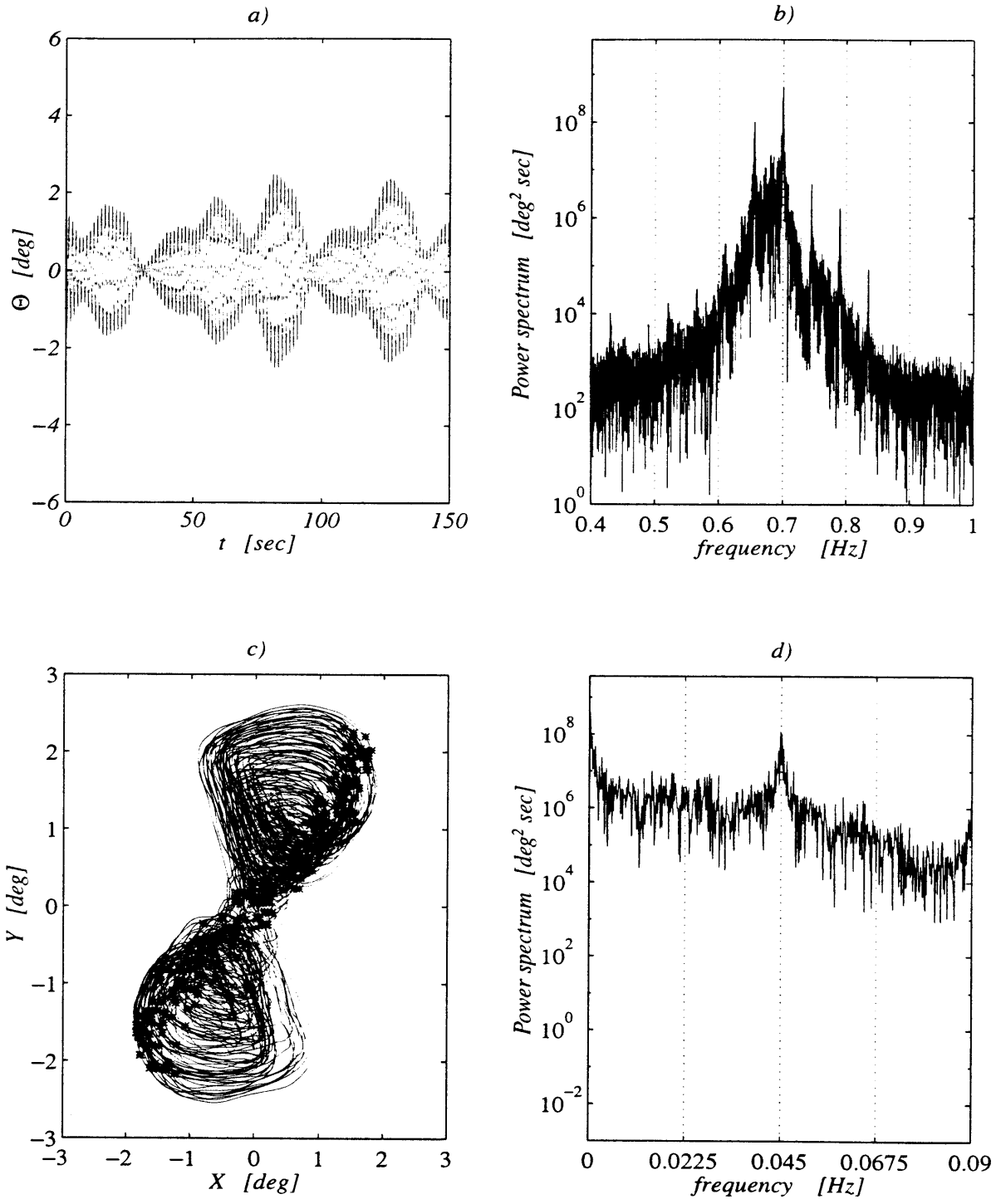

Figure F-10: Experiments for $\Omega/2\pi = 0.045$ Hz, $a = 0.99$; chaotic oscillations. a) time series envelope is non-periodic; b) energy spectrum has considerable energy away from carrier and modulational frequency; c) experimental strange attractor with fractal Poincaré section; d) broad-banded spectrum of the envelope.

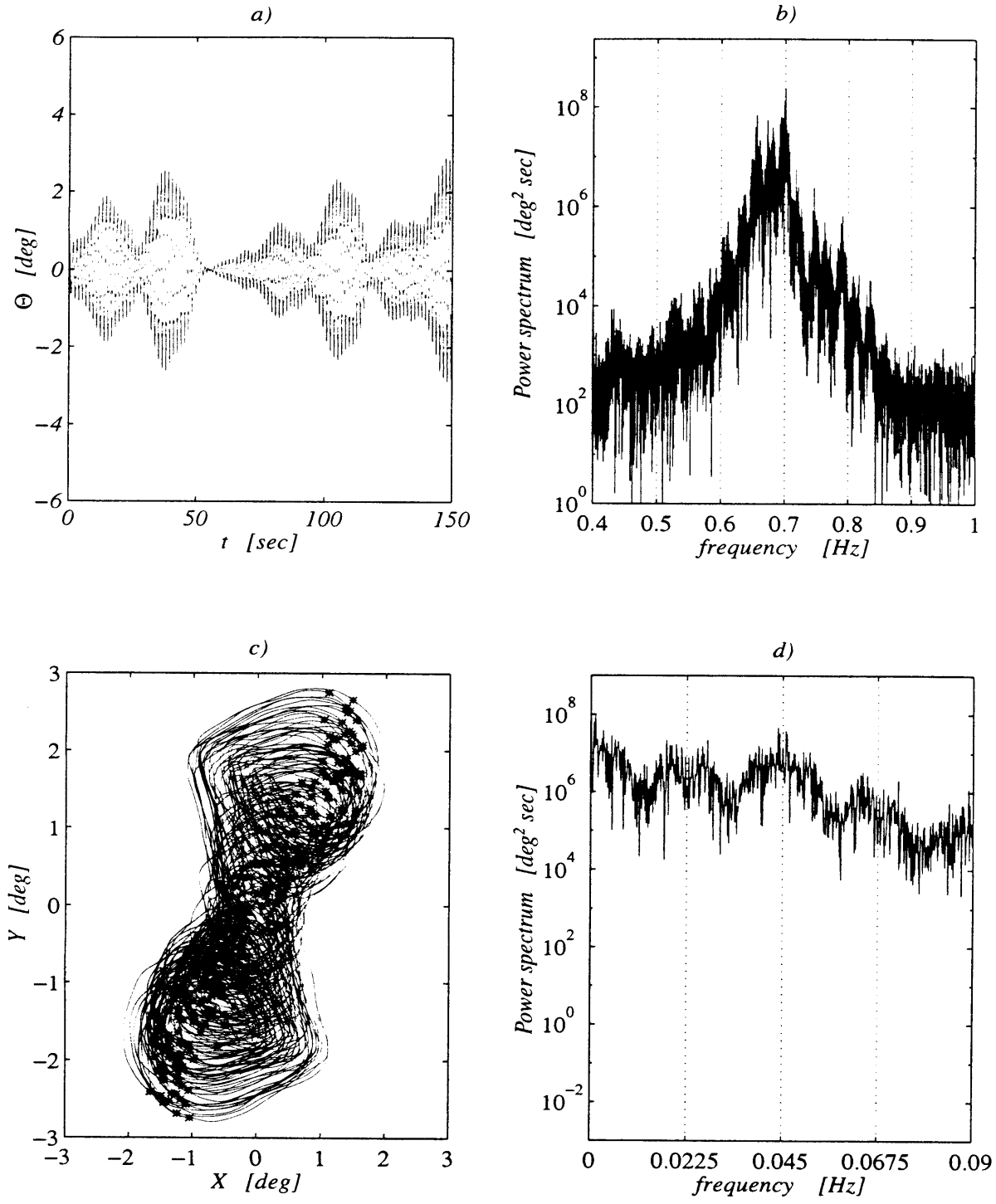

Figure F-11: Experiments for $\Omega/2\pi = 0.045$ Hz, $a = 1.10$; same as figure 5-58. Energy is continuously spread across the frequencies both in b) and d).

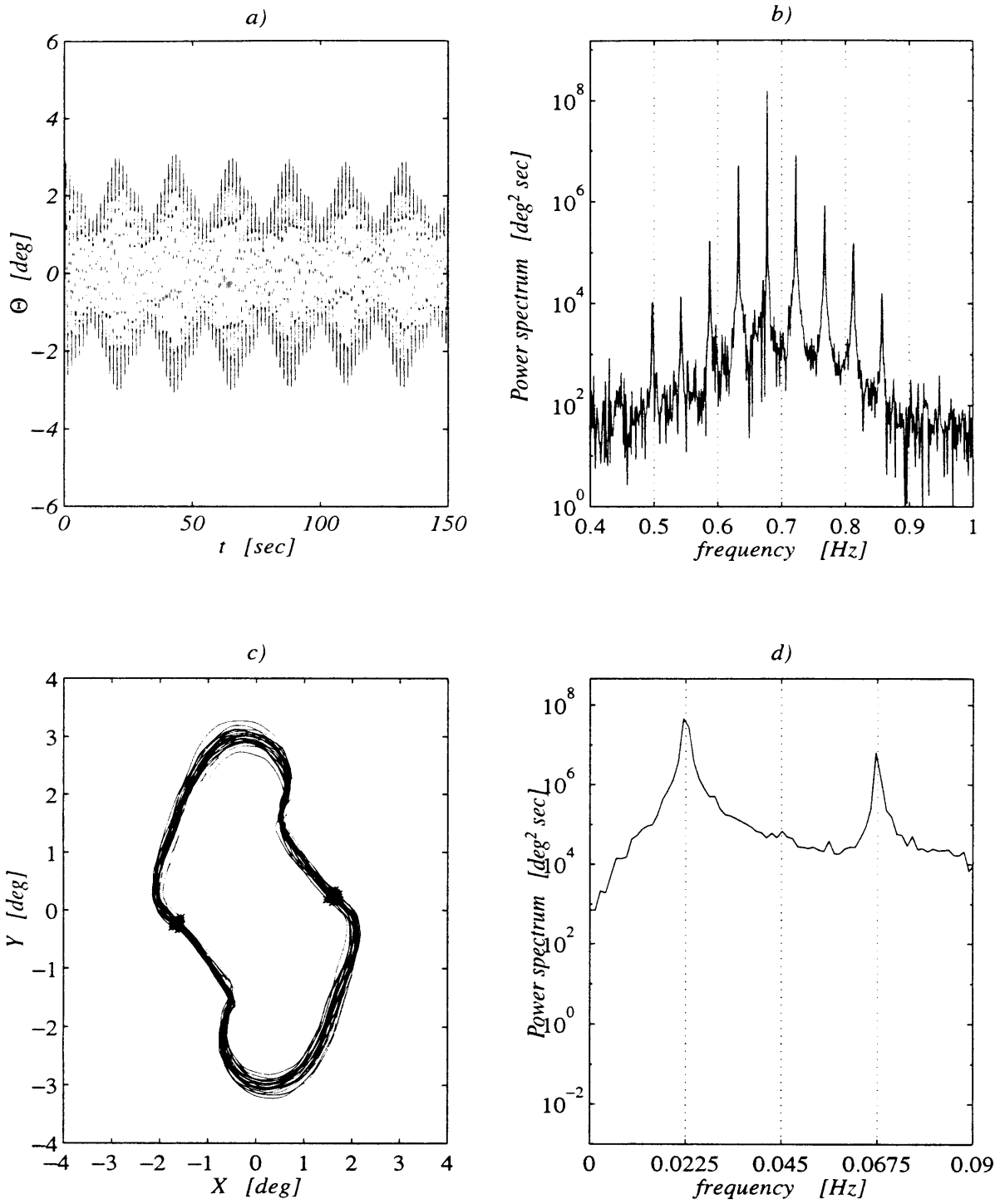

Figure F-12: Experiments for $\Omega/2\pi = 0.045$ Hz, $a = 1.29$; frequency down-shift. a) time series show no apparent sign of period doubled envelope, but the fast oscillation is at $\omega_0 - \Omega/2$ rather than at ω_0; b) the central peak is at $(\omega_0 - \Omega/2)/2\pi = 0.6775$ Hz and side bands are at $\pm\Omega/2\pi = 0.045$ Hz from it; c) period-two Poincaré section with phase trajectory symmetric with respect to the origin; d) peak response is at $(\Omega/2)/2\pi = 0.0225$ Hz and there is no energy response at $\Omega/2\pi = 0.045$ Hz.

Bibliography

AGNON, Y. & MEI, C. C. 1985 Slow-drift motion of a two-dimensional block in beam seas. *J. of Fluid Mech.* **151**, 279-294.

BLONDEAUX, P., SEMINARA G. & VITTORI, G. 1993*a* Linear response of the gate system for protection of the Venice Lagoon. Note I. Transverse free modes. *Rend. Mat. Acc. Lincei* A **59**, 291-298.

BLONDEAUX, P., SEMINARA G. & VITTORI, G. 1993*b* Linear response of the gate system for protection of the Venice Lagoon. Note II. Excitation of transverse subharmonic modes. *Rend. Mat. Acc. Lincei* A **59**, 299-305.

CILIBERTO, S. & GOLLUB, J. P. 1985 Chaotic mode competition in parametrically forced surface waves. *J. of Fluid Mech.* **158**, 381-398.

CONSORZIO "VENEZIA NUOVA" 1988*a*. Modelli fisici delle paratoie a spinta di galleggiamento (in Italian). Technical Report 291 by *Estramed SpA*.

CONSORZIO "VENEZIA NUOVA" 1988*b*. Study on the influence of the inclination angle and the gate shape on gate response. Studio 2.2.10. Technical Report by *Delft Hydraulics*

DAILY, J. W. & HARLEMAN, D. R. F. 1966 *Fluid Dynamics.* Addison-Wesley, Reading, MA.

DORE, B. D. 1969 The decay of oscillations of a non-homogeneous fluid within a container. *Proc. Cambridge Philos. Soc.* **65**, 301-307.

DRAZIN, P. G. 1992 *Nonlinear Systems.* Cambridge University Press, London.

JOHNS, B. 1968 A boundary layer method for the determination of the viscous damping of small amplitude gravity waves. *Q. J. Mech. Appl. Math.* **21**, 93-103.

FONTANET, P. 1961 Theory of the generation of a cylindrical wave by a straight-fronted wave generator. *La Houille Blanche* **1**, 3-31.

FONTANET, P. 1961 Theory of the generation of a cylindrical wave by a straight-fronted wave generator. *La Houille Blanche* **2**, 174-197.

GOTTLIEB, O. & MEI, C. C. Local and global bifurcation of edge waves. Submitted to *Journal of Bifurcation & Chaos.*

GRADSHTEYN, I. S. & RYZHIK, I. M. 1979 *Table of Integrals, Series and Products.* Academic Press, NY.

GREENSPAN, H. P. 1968 *The theory of rotating fluid.* Cambridge University Press, London.

GUZA, R. T. & BOWEN, A. J. 1976 Finite amplitude Stokes edge waves. *J. Marine Res.* **34**, 269-293.

HENDERSON, D. M. & MILES, J. W. 1991 Faraday waves in 2:1 internal resonance. *J. of Fluid Mech.* **222**, 449-470.

HENDERSON, D. M. & MILES, J. W. 1990 Parametrically forced surface waves. *Ann. Rev. Fluid Mech.* **22**, 143-165.

JOHNS, B. 1968 A boundary layer method for the determination of the viscous damping of small amplitude gravity waves. *Q. J. Mech. Appl. Math.* **21**, 93-103.

JORDAN, D. W. & SMITH, P. 1986 *Nonlinear Ordinary Differential Equations.* Clarendon Press, Oxford.

LICHTENBERG, A. J. & LIEBERMANN, M. A. 1992 *Regular and Chaotic Dynamics.* Springer-Verlag, Berlin.

LO, E. & MEI, C. C. 1985 A numerical study of water-wave modulation based on a higher-order nonlinear Schrödinger equation. *J. of Fluid Mech.* **150**, 395-416.

MADSEN, O. S. 1973 A three dimensional wave maker, its theory and application. *J. of Hydr. Res.* **12**, 205-222.

MADSEN, O. S. 1970 Wave generated by a piston-type wave maker. *Proc. Twelfth Conf. Coastal Engineering*, ASCE **1**, 589-609.

MEI, C. C. 1989 *The applied dynamics of ocean surface waves.* World Scientific, Teaneck, NJ.

MEI, C. C. & LIU, X. 1973 The damping of surface gravity waves in a bounded liquid. *J. of Fluid Mech.* **59**, 239-256.

MEI, C. C., SAMMARCO, P., CHAN E. S. & PROCACCINI, C. 1994 Subharmonic resonance of proposed storm gates for Venice Lagoon. *Proc. R. Soc. Lond.* A **444**, 463-479.

MEI, C. C. & ZHOU, X. 1991 Parametric resonance of a spherical bubble *J. of Fluid Mech.* **229**, 29-50.

MELVILLE, W. K. 1982 Wave modulation and breakdown. *J. of Fluid Mech.* **128**, 489-506.

MILES, J. W. 1990 Parametrically excited standing edge waves. *J. of Fluid Mech.* **214**, 43-57.

MILES, J. W. 1993 On Faraday waves. *J. of Fluid Mech.* **248**, 671-683.

MINZONI, A. A. & A. J. WHITHAM 1977 On the exitation of edge waves on beaches. *J. of Fluid Mech.* **79**, 273-287.

OGILVIE, T. F. 1984 Second-order hydrodynamic effects on ocean platforms. *Paper presented at Intl Workshop on Ship and Platform Motions, University of California at Berkeley*

ROCKLIFF, N. 1976 Finite amplitude effects in free and forced edge waves. *Math. Proc. Cambridge Philos. Soc.* **83**, 257-265.

SAMMARCO, P. & MEI, C. C. 1995 Weakly nonlinear theory of subharmonic resonance of Venice gates. *Proc. Twelfth Ital. Conf. Theor. Appl. Mech.,* AIMETA, 281-286.

STROGATZ, S. H. 1994 *Nonlinear Dynamics and Chaos* Addison-Wesley, Reading, MA.

TRAN, H. 1996 Experiments on subharmonic resonance of Venice Lagoon Storm Gates. *M.S. thesis, MIT, Dept. of Civil & Environmetal Engineering.*

TRULSEN, K. & MEI, C. C. 1995 Modulation of three resonanting gravity–capillary waves by a long gravity wave. *J. of Fluid Mech.* **290**, 345-376.

VARISCO, D. 1992 Interaction between flap gates and tidal current and waves. *Abstract 23rd Conf. Coastal Engineering*, ASCE.

VITTORI, G., BLONDEAUX, P. & SEMINARA G. 1996 Waves of finite amplitude trapped by oscillating gates *Proc. R. Soc. Lond.* A **452**, 791-811.

WEHAUSEN, J. V. & E. V. LAITONE 1960 *Handbuch der Physik*, edited by W. Flügge. Springer-Verlag, Berlin.